THE PHYSICAL REVIEW

VOLUME 93 Second Series NUMBER 3

FEBRUARY 1, 1954

Published for the

AMERICAN PHYSICAL SOCIETY

by the

AMERICAN INSTITUTE OF PHYSICS

Incorporated

LANCASTER, PA., AND NEW YORK, N. Y.

A journal of experi

Published by the American Institute of Physics
for the

AMERICAN PHYSICAL SOCIETY

Officers

President

ENRICO FERMI
Institute for Nuclear Studies
University of Chicago
Chicago 37, Illinois

Vice-President

H. A. BETHE
Cornell University
Ithaca, New York

Secretary

K. K. DARROW
Bell Telephone Laboratories
Office:
Columbia University
New York 27, New York

Treasurer

G. B. PEGRAM
Columbia University
New York 27, New York

Local Secretary
for the Pacific Coast

J. B. KAPLAN
University of California at Los Angeles
Los Angeles, California

Managing Editor

S. A. GOUDSMIT
Brookhaven National Laboratory
Upton, Long Island
New York

The Physical Review is pu

Entered as second class matter March

Assignment for mailing at special rate of post

Founded by E. L. Nichols in 1893

BOARD OF EDITORS

Associate Editors

W. A. Fowler
Kenneth Greisen
Charles Kittel
R. E. Marshak
W. K. H. Panofsky
V. F. Weisskopf

Assistant Editors

P. Morrison
G. Placzek

submitted to S. A. Goudsmit,
Upton, Long Island, New York. The
charge of $
reprints. Instructions

accepted papers in the process of pub
Business Manager, American Institute of
York 21, New York.

Subscription Price

Foreign Postage

Single Numbers

The following issues are available:

July, 1929;
December, 1941;
January, 1943-December, 1946;

Back numbers should be addressed to
55 Street, New York 22, New York.

of members of the American Physical
in the case of other subscribers.

Cornell University, Ithaca, New York.

Lancaster, Pennsylvania.
under the Act of March 3, 1879.
P. L. & R. of 1938, authorized January 29, 1941.

THE
PHYSICAL REVIEW

A journal of experimental and theoretical physics established by E. L. Nichols in 1893

SECOND SERIES, VOL. 93, NO. 3 FEBRUARY 1, 1954

Spectroscopy of the Solid State: Some of the Transition Elements*†

E. M. GYORGY AND G. G. HARVEY
Research Laboratory of Electronics and Department of Physics, Massachusetts Institute of Technology, Cambridge, Massachusetts

(Received August 3, 1953)

The $3P_{\frac{1}{2},\frac{3}{2}}$ emission curves of nickel, manganese, and iron have been obtained by using a vacuum recording spectrograph. A plausible interpretation of a number of features of the experimental bands is discussed.

EXPERIMENTAL DATA

WE have obtained the $3P_{\frac{1}{2},\frac{3}{2}}$ (valence to $M_{2,3}$) emission curves of nickel, manganese, and iron, using the spectrograph previously described.[1-3] A representative nickel emission band is shown in Fig. 1. It was recorded at a bombarding potential of 500 volts and a target current of 4 ma. The range shown is from 50 counts to 200 counts per second. Unfortunately, the long wavelength side of the emission band is near a region of anomalous background. This irregularity (Fig. 2) is the second order of irregularities in the background extending from approximately 100A to 120A that was observed by Skinner.[4] Skinner has shown the source of these anomalies to be connected with the absorption and dispersion of the $2p$ electrons of silicon in SiO_2, the main constituent of the glass of the grating. A comparison of the nickel emission band and the continuous spectrum makes it clear that the anomaly in the background is only appreciable at wavelengths larger than 209A. As a result, we may assume the background radiation is at the level indicated on the experimental curve. Figure 3 illustrates the manner in which satellite intensity increases as the bombarding potential is increased. To obtain these curves the target current was carefully adjusted to make the background emission of the three curves equal. The curves were observed, using the 200 counts-per-second scale of the counting-rate meter and a bombarding potential of 500, 600, and 700 volts. The respective target currents used were 4 ma, 3 ma, and 2.5 ma. The absolute intensity of the emission bands cannot be related to the target current and bombarding voltage, since the position of the focus of the electron beam on the target is not exactly reproducible. The kinks in the $3P_{\frac{1}{2},\frac{3}{2}}$ edges are due to the response time of the counting-rate meter and are not real.[1] The manganese emission band shown in Fig. 4 was recorded at a bombarding potential of 600 volts and a target current of 6 ma. The low intensity made it necessary to use the 100 counts-per-second scale of the counting-rate meter, the larger response time corresponding to the 100 counts-per-

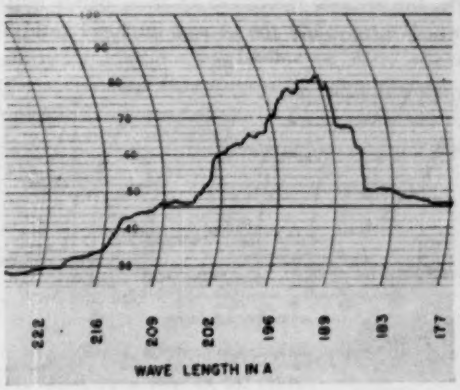

FIG. 1. Band emission curve of nickel. $E_b = 500$ volts, $I_b = 4$ ma.

* This work was supported in part by the Signal Corps, the Air Materiel Command, and the U. S. Office of Naval Research.

† The work reported here is based in part on a thesis submitted by E. M. Gyorgy to the Department of Physics, Massachusetts Institute of Technology, June, 1953, in partial fulfillment of the requirements for the degree of Doctor of Philosophy.

[1] E. M. Gyorgy and G. G. Harvey, Phys. Rev. **87**, 861 (1952).
[2] Piore, Harvey, Gyorgy, and Kingston, Rev. Sci. Instr. **23**, 8 (1952).
[3] R. H. Kingston, Phys. Rev. **84**, 944 (1951).
[4] H. W. B. Skinner, Trans. Roy. Soc. (London) **A239**, 95 (1940).

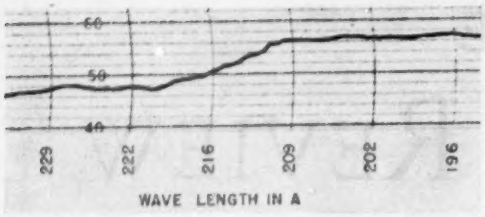

FIG. 2. Background radiation.

second scale, and the more rapid contamination of the sample made it impossible to obtain curves that were reproducible with the accuracy obtained for copper, nickel, and chromium.[1]

It was impossible to obtain a satisfactory iron emission band. The intensity and the ratio of intensity to background are low. The very rapid contamination of the sample made it imperative to record the curves rapidly. However, since the observed curves show more structure than previously obtained, it is probably worthwhile to consider them. The curve shown in Fig. 5 was recorded, using the 100 counts-per-second scale and 6-ma target current at 700 volts bombarding potential.

The experimental curves are modified to represent the distribution of the *s*-type and *d*-type electrons by the method given by Skinner.[4] The background of the experimental curves is eliminated. Then, to minimize the effect of fluctuations, we average the observed intensities. The average intensity with the ordinate divided by a factor proportional to the fourth power of the absolute energy is plotted as a function of energy. This curve is the superposition of the modified $3P_{\frac{1}{2}}$ and $3P_{\frac{3}{2}}$ emission bands. The structure introduced by the response time of the counting-rate meter is, of course, neglected. The distribution curve obtained for nickel is shown in Fig. 6. The modified experimental curve (dotted) shown in Fig. 1 has been added for comparison. In order to disentangle the $3P_{\frac{1}{2}}$ and $3P_{\frac{3}{2}}$ bands, the relative intensities of these bands must be known. We may find the correct intensity ratio if we

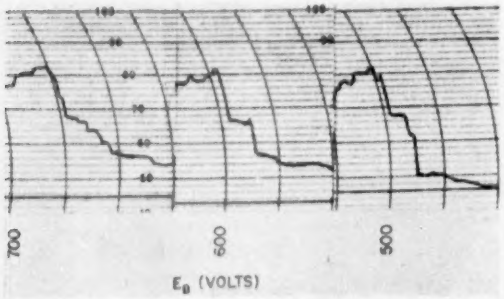

FIG. 3. Emission edges of nickel. (The background level is indicated for each curve.)

note that the shape of the experimental curve on the long wavelength side of the $3P_{\frac{1}{2}}$ emission edge is not altered as the satellite intensity is increased. In fact, the majority of the experimental curves used to obtain the average intensity, from which the modified distribution curve given in Fig. 6 is derived, was taken at 600 volts bombarding voltage. These curves showed the expected larger relative satellite intensity (Fig. 3).

On the basis of these observations we may then assume that the shape of the emission curve would be unchanged if the satellite intensity could be reduced to zero. In other words, to find the correct ratio of the

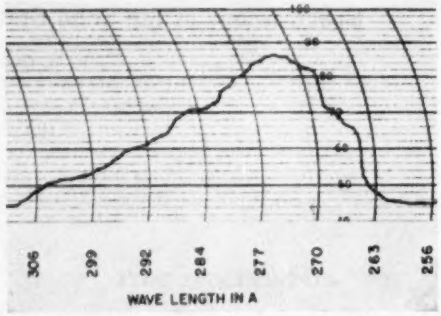

FIG. 4. Band emission curve of manganese. $E_b = 600$ volts, $I_b = 6$ ma.

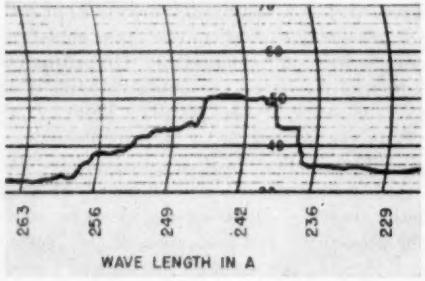

FIG. 5. Band emission curve of iron. $E_b = 700$ volts, $I_b = 6$ ma.

$3P_{\frac{1}{2}}$ to the $3P_{\frac{3}{2}}$ intensity, the $3P_{\frac{1}{2}}$ emission edge must be measured from the level of the background. The two bands can then be separated as indicated. The doubtful low-energy parts of the curves are dotted. The experimental observations concerning the shape of the other emission bands that were studied, and the intensity of the satellite emission, were the same as those of nickel. Consequently, we may separate the iron, and the manganese curves, as shown in Fig. 7 and Fig. 8. The modified experimental curves (dotted) have been added. Considering the low accuracy of the experimental iron emission bands, we would not expect the details of the distribution curve to be meaningful. In fact, below 50 volts the method of separation caused the separated curves to be somewhat oscillatory. For

the sake of clarity we have drawn a smooth curve, but in no case was the ordinate changed by more than 10 percent.

The experimental results are summarized in Table I. It should be emphasized that the deviations given are a reasonable limit on the error and are not the probable error. The reasonable limit is determined by considering possible inaccuracies in the calibration of the spectrograph and the inherent low accuracy of the long wavelength side of the experimental curves.

DISCUSSION

The density of states having d-like symmetry around the individual atoms of the lattice is presumably higher than the density of states having s-like symmetry. Also, at least for hydrogen-like wave functions, the $3d$, $3p$ transition has a greater probability than the $4s$, $3p$ transition. Hence, we might expect that the observed emission band represents only the five d bands. However, the experimental emission edges of copper,[1] which has a completely occupied d band, are as sharp as those

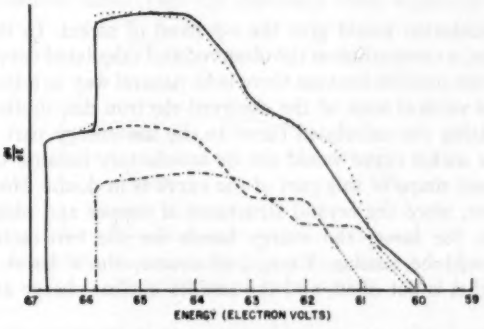

FIG. 6. Electron distribution in nickel.

observed for nickel, which has a partly filled d band. If the experimental emission curves represent only the d band, we would not expect the characteristic sharp edge at the high-energy side of the copper band. This is one of the observations that suggest that s-like states contribute an appreciable part to the experimental bands. In fact, if we assume that transitions from the s-p band to the $3P_{1,1}$ level have a greater probability than transitions from the five d bands, we are able to give a self-consistent interpretation of a number of features of the experimental bands. The copper d and s-p bands would then be roughly represented as shown in Fig. 9. (Part of the s-p band is indicated by the dashed line.) We may note that this curve portrays, except for the relative height of the s-p and d bands, the general features predicted for the energy bands of copper; that is, a narrow, filled d band protruding in the middle of a wider valence band. It should be stressed that the only reason for postulating that the transition probabilities are such as to make the integrated intensity of the d band less than that of the

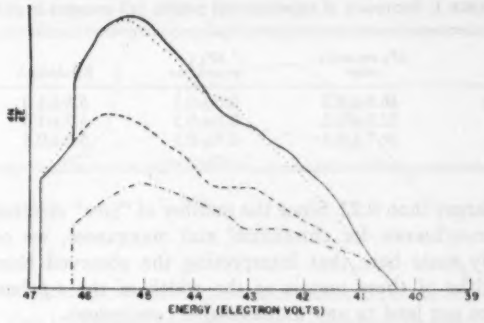

FIG. 7. Electron distribution in manganese.

s-p band is that this postulate leads to the most plausible conclusions to put forward at the present time.

The width of the conduction bands of the metals of the first two periods of the periodic table are given quite accurately by the Sommerfeld free-electron approximation.[4] On the basis of the calculations of the copper s-p band by Slater[5] and Krutter,[6] we may expect the same to be true for the transition elements because according to these calculations the electrons in the s-p band behave approximately as free electrons, except in the immediate neighborhood of the nuclei of the ions. In Table II we compare the width of the observed emission bands with the width of the s-p band calculated for free electrons. With the assumption that the half of the d band associated with positive electron spin is filled, the number of electrons per atom in the s-p band of nickel, iron, and copper may be obtained from magnetic measurements. The agreement for copper and nickel is good and helps to substantiate the representation of the s-p band shown in Fig. 9. The agreement for iron is not as satisfactory, but the discrepancy could be explained by assuming that the free-electron approximation is not applicable without modification to electrons in the s-p band of iron or that the number of conduction electrons obtained from the magnetic measurements is incorrect. In fact, Seitz,[7] to account for the cohesive energy of iron, suggests that half the d band of iron is not filled, and that consequently the number of conduction, or "free," electrons

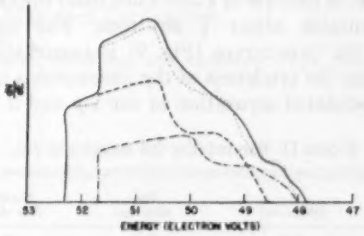

FIG. 8. Electron distribution in iron.

[5] J. C. Slater, Phys. Rev. **49**, 537 (1936).
[6] H. M. Krutter, Phys. Rev. **48**, 664 (1935).
[7] F. Seitz, *Modern Theory of Solids* (McGraw-Hill Book Company, Inc., New York, 1940), p. 430.

TABLE I. Summary of experimental results (all energies in ev).

	$3P_{\frac{1}{2}}$ emission edge	$3P_{\frac{1}{2},\frac{3}{2}}$ separation	Bandwidth
Mn	46.8±0.2	0.6±0.1	5.8±1.0
Fe	52.3±0.2	0.6±0.1	3.7±1.0
Ni	66.7±0.2	0.9±0.1	5.8±0.5

is larger than 0.22. Since the number of "free" electrons is not known for chromium[1] and manganese, we can only state here that interpreting the observed bandwidths of these metals as the width of the *s-p* band does not lead to any unreasonable conclusions.

Now, in the light of the preceding discussion we might expect the analysis given by Jones, Mott, and Skinner[8] to be applicable to the *s-p* band of copper. Following their procedure we expand ψ_k, the wave function of the electron in the *s-p* band, in the neighborhood of the nuclei in the form

$$\psi_k = a_s(k)\psi_{4s} + a_p(k)\psi_{4p},$$

where ψ_{4s} and ψ_{4p} are the free-atomic wave functions and k is the wave vector. In the case of an energy band derived from an atomic *s*-state and an atomic *p*-state of slightly higher energy they find that

$$a_p(k)^2 = (k/K_1)^2,$$

where $k = K_1$ at the edge of the first Brillouin zone. If we denote the number of electrons per unit energy range by dN/dE, we may regard

$$a_s(k)^2 dN/dE \text{ and } a_p(k)^2 dN/dE$$

as the numbers of *s* and *p* type electrons, respectively, corresponding to k in the *s-p* band. Then we have

$$(dN/dE)_s = a_s(k)^2 dN/dE = [1-(k/K_1)^2]dN/dE.$$

The approximate value of K_1 is given by $\Omega_K = 4/3\pi K_1^3$, where Ω_K is the volume of the zone. We replace k^2 and dN/dE by the corresponding expressions given by the free-electron approximation to obtain $(dN/dE)_s$ as a function of energy. To compare this calculated curve with the observed *s-p* emission band, we must normalize the latter to represent the same number of electrons per atom as the calculated curve. A simple calculation shows that in the case of a half-filled band the calculated curve contains about $\frac{5}{8}$ electrons. The agreement between the two curves (Fig. 9) is remarkably good, considering the crudeness of the assumptions involved. If the postulated separation of the *s-p* and *d* bands is correct, the width of the copper *d* band is approximately 3 volts. It must be remembered, however, that although the analysis described here helps to give qualitatively the general features of the conduction band, it is definitely incorrect in many details. For example, the electronic specific heat of copper predicted by the free-electron distribution is $0.6\times10^{-4}RT$ compared to the experimental value of $0.89\times10^{-4}RT$,[9] where R is the gas constant.

TABLE II. Bandwidths (all energies in ev).

	Observed	Free electron	Number of free electrons
Fe	3.7	2.6	0.22
Ni	5.8	5.3	0.6
Cu	7.1	7.1	1.0

[8] Jones, Mott, and Skinner, Phys. Rev. **45**, 379 (1934).

Since the *s-p* band calculated for copper fits the experimental data, we would expect that a similar

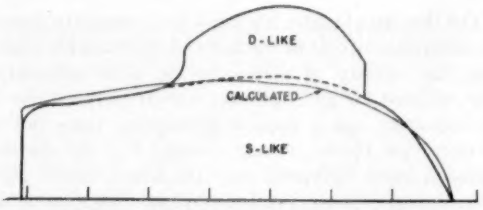

FIG. 9. The electron distribution of copper, showing the postulated *s-p* and *d* bands.

calculation would give the *s-p* band of nickel. In this case, a comparison of the observed and calculated curves is not possible because there is no natural way to adjust the vertical scale of the observed electron distribution. Fitting the calculated curve to the low-energy part of the nickel curve would not be satisfactory because the exact shape of this part of the curve is in doubt. However, since the crystal structures of copper and nickel are the same, the energy bands for the two metals should be similar. Except, of course, the *d* band of nickel is not filled, and the smaller nuclear charge and

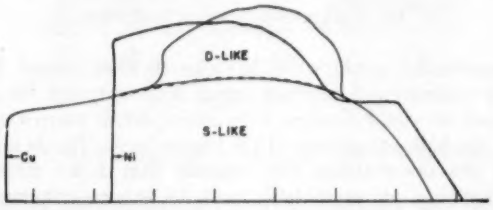

FIG. 10. The electron distribution of copper and nickel, showing the postulated *s-p* and *d* bands.

smaller lattice spacing might be expected to broaden the bands. We can attempt to separate the nickel *d* and *s-p* bands by analogy to copper, as shown in Fig. 10. This procedure would give an experimental width of the *d* band of approximately 3.6 ev. If we normalize the postulated nickel *d* band to represent 9.4 electrons, we can obtain a numerical value for the density of electrons at the Fermi edge. We then obtain 8.5 $\times10^{-4}RT$ for the electronic specific heat, which is in good agreement with the measured value 8.72×10^{-4}

[9] J. A. Kok and W. H. Keesom, Physica **3**, 1035 (1936).

RT.[10] The contribution of the s-p band to the density of electrons at the Fermi edge has been neglected, since it is an order of magnitude smaller than the contribution of the d band. These results are, of course, only qualitative, since we have also neglected any possible admixture of p-type electrons in the d band and any variation of the transition probability; but they show that the shape of the postulated d band is consistent with the observed electronic specific heat.

The s-p bands of iron, chromium, and manganese might also be expected to be similar to the one calculated for copper, even though the crystal structure of these metals is different. As in the case of nickel, there is no unique way to adjust the vertical scale of the observed curves. Furthermore, a comparison with the copper emission curve can no longer be expected to be valid. Therefore, we arbitrarily adjust the observed manganese curve to fit the calculated s-p band at 2.5 ev (Fig. 11). This procedure results in fair agreement of the low-energy parts of the observed and calculated curves. With less justification, the parabolic rise of the calculated curve is fitted to the bottom of the observed chromium band (Fig. 12). Although these separations

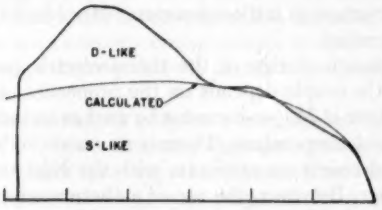

FIG. 11. The electron distribution of manganese, showing the postulated s-p and d bands.

of the observed electron distributions into the d and s-p bands are somewhat arbitrary, they form a basis for a discussion of the energy bands. The manganese curve has the expected behavior: a narrow unfilled d band and a wider conduction band. The d band is about 3.0 ev wide. The unfilled d band of manganese would indicate a large electronic specific heat, but certainly not as large as the observed value of $21\times10^{-4}RT$,[11] which is 2.5 times larger than that of nickel. The calculated s-p band of chromium obviously is not correct, since it

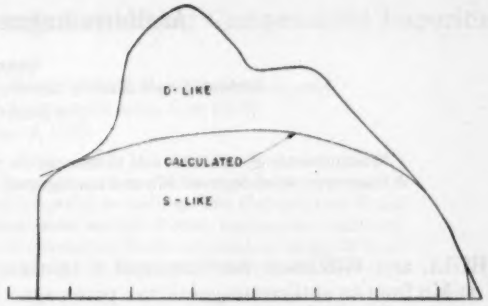

FIG. 12. The electron distribution of chromium, showing the postulated s-p and d bands.

requires that the d band be filled. However, the low-electronic specific heat of chromium indicates that the general features of the separation of the s-p and d bands may be correct. The measured value of the electronic specific heat of chromium is $1.9\times10^{-4}RT$,[12] only about two times larger than that expected from the s-p band alone. The postulated d band, which appears to drop to a low intensity at the emission edge, is consistent with the expected low density of states at the Fermi edge. The low-energy limit of the chromium band is not clearly marked, except perhaps by the inflection in the band, 3.4 ev below the emission edge. The latter interpretation does not fit the calculated s-p band shown, but since the separation of the d and s-p bands of chromium has less justification than the postulated separations discussed for the other metals, we shall not pursue this topic further. We shall not attempt to separate the iron s-p and d bands, since the accuracy of the experimental curves is too low to give us much confidence in the results. However, a comparison of the iron curve and the nickel curve shows that we might say that the d band of iron is about 2.2 ev wide.

ACKNOWLEDGMENT

We are indebted to Dr. R. H. Parmenter of the Solid-State and Molecular Theory Group at M.I.T. for many helpful discussions. One of us (E. M. Gyorgy) also wishes to express his appreciation for receiving a fellowship grant made possible by the International Business Machines Corporation.

[10] W. H. Keesom and C. W. Clark, Physica **2**, 513 (1935).
[11] Elson, Grayson-Smith, and Wilhelm, Can. J. Research **18**, 82 (1940).
[12] Estermann, Friedberg, and Goldman, Phys. Rev. **87**, 582 (1952).

Antiferromagnetism of Manganese

LYLE PATRICK*
Institute for the Study of Metals, University of Chicago, Chicago, Illinois
(Received October 22, 1953)

Measurements of resistance and thermoelectric power of Mn show anomalies near the Néel temperature. A thermocouple of degassed Mn and nondegassed Mn gives evidence of a Mn transition at 100°K.

SHULL and Wilkinson[1] have reported a transition in Mn from an antiferromagnetic to a paramagnetic state at 100°K. This temperature is known as the Néel temperature. One would expect changes in the electrical properties in the neighborhood of this transition, but no measurements of resistance or thermoelectric power have been reported for this temperature range. Because α-Mn is brittle, it cannot be obtained in wire form, and precise electrical measurements are difficult, but it is possible to soft-solder Cu wires to electrolytic chips, and this permits rough measurements to be made. Chemical analysis of the electrolytic chips showed a purity of over 99.9 percent, and the samples were degassed by heating for 3 hours at 450°C in a vacuum.

The measurements showed a broad resistance minimum at about 90°K, and at liquid nitrogen temperature (77°K) the temperature coefficient of resistance was still negative. The thermoelectric power of Mn against Cu changed sign at about 93°K. When a Mn specimen was used which had not been degassed, this change of sign occurred at about 85°K. The progressive increase of this temperature was also observed on a single specimen as the specimen was subjected to successively higher degassing temperatures between 100° and 300°C. The lower reversal of sign of the thermoelectric power of the nondegassed specimen suggests that it may have a lower Néel temperature. Potter and Huber[2] made measurements of the Mn lattice parameter as a function of H_2 content, and found that the parameter increased as much as 0.2 percent on absorption of H_2. With the increased lattice parameter one would expect a lower Néel temperature, since there is evidence that with a large enough increase in lattice parameter Mn would become ferromagnetic.[3]

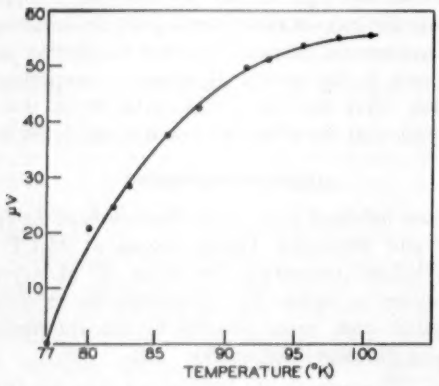

FIG. 1. Emf plotted against hot junction temperature for a thermocouple of degassed Mn *vs* nondegassed Mn with cold junction held at 77°K.

The change of sign of the thermoelectric power in the Mn-Cu couple depends on the properties of Cu as well as those of Mn, so it cannot be used as an indication of the Néel temperature. There is no reason to identify the broad resistance minimum with the Néel temperature either. However, the use of a thermocouple made of degassed Mn and nondegassed Mn seems much more promising. The assumption is made that there is a thermoelectric power at liquid nitrogen temperature because the degassed Mn is in a more highly ordered state, being farther from its transition temperature. Then with the cold junction held in liquid nitrogen one would expect the emf measured on warming the other junction to become constant after reaching the higher Néel temperature (that of the degassed specimen). Above this temperature the *effective* hot junction must move along the specimen so that it remains at the transition temperature. This behavior is found experimentally, as can be seen in Fig. 1, which shows that the emf levels off at about 55 microvolts near 100°K. This temperature is in good agreement with that of Shull and Wilkinson, which was also obtained with a degassed sample.

* Now at Westinghouse Research Laboratories, East Pittsburgh, Pennsylvania.

[1] C. G. Shull and M. K. Wilkinson, Revs. Modern Phys. **25**, 100 (1953).

[2] E. Vernon Potter and Ralph W. Huber, Phys. Rev. **68**, 24 (1945).

[3] R. M. Bozorth, *Ferromagnetism* (D. Van Nostrand Company, Inc., New York, 1951), p. 341.

Some Electrical Properties of Germanium Crystals Containing Compensated Impurities*

VERNON OZAROW
Department of Chemistry, Pennsylvania State University, State College, Pennsylvania, and Electronics Laboratory, General Electric Company, Syracuse, New York†

(Received September 3, 1953)

Compensated *n*-type germanium crystals containing both radioindium and radioantimony were prepared. The indium and antimony content was determined by radiochemical procedures. The Hall constant R and resistivity ρ of three compensated samples and one uncompensated sample of room temperature resistivity comparable to that of one of the compensated samples were measured in the temperature range 78°K to 393°K. The Hall mobility μ was calculated as R/ρ and compared with theoretically calculated values of μ.

MANY of the extrinsic electrical properties of germanium are interpreted in terms of the concentration of impurities as determined by measurements such as resistivity or Hall constant. It is generally recognized, however, that these measurements actually reflect the excess concentration of one type of impurity (donor or acceptor) over that of another (acceptor or donor). It is the purpose of this communication to give some preliminary results of measurements over the temperature range 78°K to 393°K of Hall constant, resistivity and Hall mobility obtained from samples of known total impurity concentration. Included for comparison is an uncompensated sample of about the same room temperature resistivity as one of the compensated samples.

The compensated samples were prepared by doping a melt (S-7) of 40-ohm-cm *n*-type germanium with Sb^{124} and In^{114} and growing the crystal from this melt. Another crystal (S-8) was prepared from the same purity material but doped with Sb alone. The concentration of each of the doping constituents in the resultant *n*-type crystal was determined by radiochemical analysis which gave results with an estimated precision of 7 percent. The Hall constant R and resistivity ρ were measured over the indicated temperature range using the techniques described by Dunlap.[1] The mobility μ was calculated as R/ρ. The data obtained are shown in the accompanying figures.

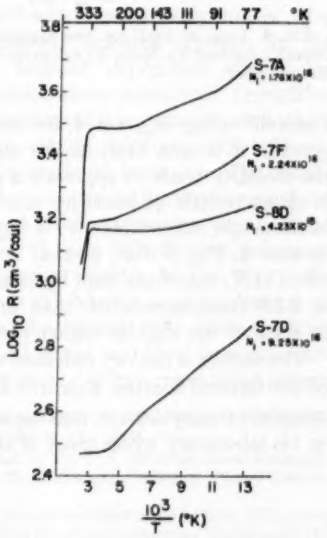

FIG. 1. Log$R$ *vs* $10^3/T$ as a function of total impurity content N_I.

Table I is a summary of the values of resistivity ρ, in concentration N_A, Sb concentration N_D, excess Sb concentration $(N_D-N_A)_A$ (as determined by radiochemical analysis), excess Sb concentration $(N_D-N_A)_H$ (as determined from the lowest value of the Hall constant[2] in the extrinsic range), and the total impurity concentration $N_I=N_D+N_A$.

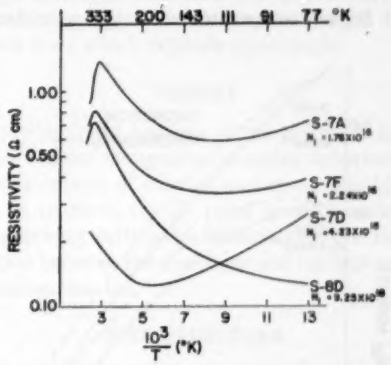

FIG. 2. ρ *vs* $10^3/T$ as a function of total impurity content N_I. Note: N_I values for S-7*D* and S-8*D* should be interchanged.

In Fig. 1, the values of Hall constant *vs* temperature are shown. It is seen that in the low-temperature range there is an increase in slope of these curves with increasing values of N_I. This indicates an apparent decrease in the number of carriers, which is not con-

* This work has been supported by the USAF Air Research and Development Command, USAF Air Materiel Command, Army Signal Corps, and Navy Bureau of Ships.

† Present address.

[1] W. C. Dunlap, Phys. Rev. **79**, 286 (1950).

[2] The factor r in the expression for the Hall constant $R=r/ne$ [where n is the concentration of carriers assumed equal to $(N_D-N_A)_H$, and e is their electric charge] was not taken into account here. This factor varies from 1.18 to 1.93 depending upon the relative amount of lattice and impurity scattering. This factor was also neglected in calculating the Hall mobility R/ρ. See, for instance, V. A. Johnson and K. Lark-Horowitz, Phys. Rev. **82**, 977 (1951) and H. Jones, Phys. Rev. **81**, 149 (1951).

TABLE I. Impurity content of the samples.

Sample	ρ(Ω cm)	N_D (atoms/cm³)	N_A (atoms/cm³)	$(N_D-N_A)_A$ atoms/cm³	$(N_D-N_A)_B$ atoms/cm³	$(N_I=N_D+N_A)$ atoms/cm³
S-7*A*	1.01	9.74×10^{15}	7.90×10^{15}	1.84×10^{15}	2.05×10^{15}	1.76×10^{16}
S-7*F*	0.58	1.36×10^{16}	0.88×10^{16}	4.82×10^{15}	3.96×10^{15}	2.24×10^{16}
S-7*D*	0.16	5.56×10^{16}	3.69×10^{16}	1.87×10^{16}	2.09×10^{15}	9.25×10^{16}
S-8*D*	0.45	...	...	...	4.23×10^{15}	4.23×10^{15}

sistent with an impurity activation energy of 0.01 ev.[8] With such a value of the activation energy, it is expected that essentially no electrons would drop from the conduction band into the donor level. The effect is particularly striking when comparing S-7*F* and S-8*D*, the samples having comparable room temperature resistivities. It is probable that this apparent decrease in carrier concentration can be explained in terms of r^2. In general, r has higher values where the ratio of impurity to lattice scattering is greater. The higher values of r correspond to large N_I and/or lower temperatures. Preliminary calculations indicate that by using the correct values of r the slopes of the curves are brought toward a horizontal position.

In Fig. 2, the values of logρ *vs* $1/T$ are plotted. The effect of N_I is illustrated in the low-temperature range by the tendency of the curves to approach a positive slope at higher temperatures for the specimens with higher N_I. Again the difference in behavior between S-7*F* and S-8*D* at these lower temperatures is quite striking.

In Figs. 3 and 4, logμ is plotted against log$T$. The theoretical values of μ were calculated according to

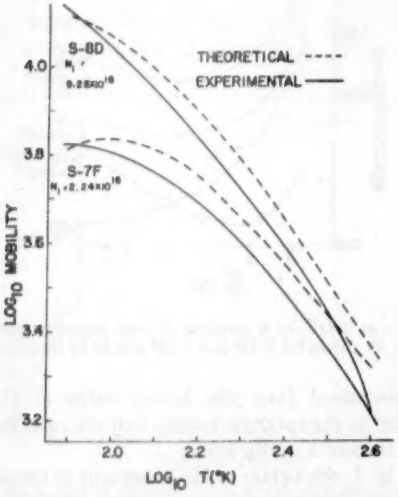

FIG. 3. Logμ *vs* log$T$ for two specimens having comparable room temperature resistivities but different total impurity contents. Note: N_I values for S-7*D* and S-8*D* should be interchanged.

[8] E. M. Conwell, Proc. Inst. Radio Engrs. **40**, 1327 (1952).

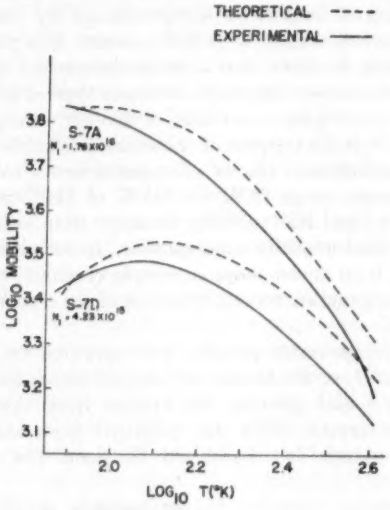

FIG. 4. Logμ *vs* log$T$ for two samples having different total impurity content N_I. Note: N_I values for S-7*D* and S-8*D* should be interchanged.

Conwell[3] using $m_{eff}=m/4$ for the electron mass. In general, it is seen that, as the temperature decreases, the mobility tends to approach a positive slope (which is characteristic of impurity scattering) most rapidly in those specimens where N_I is highest. It is interesting to note in Fig. 3 that, even at room temperature, the effect of N_I manifests itself by causing a higher mobility in S-8*D* (uncompensated) than in S-7*F* (compensated) in spite of the slightly higher resistivity of the latter.

The author is heavily indebted to Dr. W. C. Dunlap, of the General Electric Research Laboratory, who gave complete cooperation in making available the facilities in his laboratory where most of this work was done.

Paramagnetic Resonance Absorption of Mn^{++} in Single Crystals of $CaCO_3$*†

F. KENNETH HURD,‡ MENDEL SACHS, AND W. D. HERSHBERGER
University of California, Los Angeles, California

(Received August 17, 1953)

Paramagnetic resonance absorption of Mn^{++} at 9300 Mc/sec has been studied using single crystals of $CaCO_3$ containing 0.06 wt. percent Mn^{++} ions. The Mn^{++} spectrum consists of 30 well-resolved lines approximately 3.5 gauss wide and extending over a range of 1100 gauss with a large dependence upon angular orientation between crystal axes and external magnetic field. The theory pertaining to the Mn^{++} resonance absorption in the $CaCO_3$ crystal is developed and presented. The interpretation of the observed spectra is based upon crystalline field effects plus nuclear hyperfine interaction. The spectroscopic g factor is found to be essentially isotropic. The hyperfine structure factors A' and B' are found to be nearly equal. The fine structure constants D' and d' are determined. The values assigned are:

$$g_{\parallel}=2.0022, \quad g_{\perp}=2.0014, \quad A'=8.782\times10^{-3}\ \text{cm}^{-1},$$
$$D'=3.75\times10^{-3}\ \text{cm}^{-1}, \quad d'=4.00\times10^{-4}\ \text{cm}^{-1}, \quad B'=8.774\times10^{-3}\ \text{cm}^{-1}.$$

Small discrepancies between theory and experiment are found, as well as unexpected and unexplained line-splittings at certain angular orientations.

INTRODUCTION

INVESTIGATION of the effects of crystalline fields on paramagnetic resonance absorption spectra contributes to our knowledge of the solid state by revealing certain properties of the crystal and of the paramagnetic ion. They theory describing paramagnetic resonance in crystals is necessarily based upon a single crystal model. Several investigators[1] have observed and interpreted spectra in single crystals of alums, Tutton salts, and similar materials in which the crystalline field is that of the surrounding waters of hydration. Single crystals of non-hydrated inorganic compounds with suitable substitutional concentration of the paramagnetic ions have been unobtainable, and hence studies of these materials have previously been limited to powdered samples[2,3] which presumably consist of a large number of randomly oriented crystals. In the resulting spectrum, angular dependent effects are average; thus information about anisotropic crystalline fields is obscured. The present investigation used single $CaCO_3$ crystals of the calcite structure with 0.06 wt. percent Mn as a substitutional impurity. The calcite structure has trigonal symmetry in the nearest neighbors (the CO_3^{--} ions) and cubic symmetry in the next nearest neighbors (Ca^{++}). The 9300-Mc/sec paramagnetic resonance absorption spectra of the Mn^{++} observed in these crystals exhibited a large anisotropy as was to be expected for the trigonal field. Since the lines have a width of only 3.5 gauss, and their positions were determined with an accuracy of one gauss using proton resonance and since the effect of angular orientation on line position is large, the present work with calcite permits a precise comparison between the predictions of theory and experimental observations themselves. On the whole, the agreement between theoretical predictions and the results of experiment is good; however, small deviations greater than the experimental error are found, as well as a heretofore unobserved splitting of certain lines which depends upon angle.

THEORY

The predominant features of the magnetic behavior of doubly ionized manganese occurring substitutionally in a single crystal of calcium carbonate should be explained in terms of the D_3 point group symmetry[4] of the neighboring carbonate radicals and the magnetic interaction between the electronic and nuclear moments of the manganese ion.

FINE STRUCTURE

The fine structure splitting is caused by the crystalline field which leaves the magnetic levels doubly degenerate and the external magnetic field which lifts this degeneracy. The ground state of Mn^{++} is a ${}^6S_{\frac{5}{2}}$ state, and the nuclear spin is $I=5/2$. The total number of energy levels is $(2S+1)(2I+1)=36$. The selection rules for paramagnetic resonance absorption are $\Delta M=+1$, $\Delta m=0$ (where M and m are the electronic and nuclear magnetic quantum numbers respectively); hence the total number of transitions is 30.

The most general expression for the crystalline potential at the site of the Manganese nucleus is given by

$$V=\sum_{l=0}^{\infty}\sum_{m=-l}^{+l}\Lambda_l{}^m r^l Y_{lm}(\theta,\varphi), \tag{1}$$

where $\Lambda_l{}^m$ is the crystal field coefficient, r is the radius

* A preliminary account of this work was given by M. Sachs, Bull. Am. Phys. Soc. **28**, No. 6, 15 (1953).

† Work supported in part by the U. S. Office of Naval Research.

‡ Present address: Visiting Fulbright Professor, Fouad University, Cairo, Egypt.

[1] See W. Gordy *et al.*, *Microwave Spectroscopy* (John Wiley and Sons, Inc., New York, 1953) for a comprehensive bibliography to July, 1952.

[2] E. E. Schneider and T. S. England, Physica **17**, 221 (1951).

[3] W. D. Hershberger and H. N. Leifer, Phys. Rev. **88**, 714 (1952).

[4] Eyring, Walter and Kimball, *Quantum Chemistry* (John Wiley and Sons, Inc., New York, 1947).

of the magnetic ion, and $Y_{lm}(\theta,\varphi)$ is a spherical harmonic $P_l^m(\cos\theta)e^{im\varphi}$.

The calculation of the expectation value of the crystalline potential requires integration between d wave functions. The product $\psi_{3d}^*\psi_{3d}$ transforms under rotation like the base vector of the direct product $D_2\times D_2$ of the representations of the rotation group. Since the direct product

$$D_2\times D_2=\sum_{L=0}^{4} D_L,$$

the components of the potential V with $l>4$ will have vanishing diagonal matrix elements. The odd l components of the potential V are off diagonal in the orbital quantum number l. Since the excited orbitals are very far from the ground state, these components of V can be neglected.

Assuming the crystalline potential to be axial, the fine structure Hamiltonian $3\mathcal{C}_{fs}$ is

$$\begin{aligned}3\mathcal{C}_{fs}&=\boldsymbol{\mu}\cdot\mathbf{H}+V\\&=H(\mu_{x'}\sin\theta'\cos\varphi'+\mu_{y'}\sin\theta'\sin\varphi'+\mu_{z'}\cos\theta')\\&\quad+\Lambda_2^0 r^2P_2(\cos\theta')+\Lambda_4^0 r^4P_4(\cos\theta'),\end{aligned}\tag{2}$$

where (x', y', z') refer to the crystalline coordinate system and P_l is the Legendre polynomial.

In the case under study, the magnetic energy is much larger than the crystalline energy; hence the Hamiltonian (2) must be quantized with respect to the direction of magnetization in the crystal (z axis).

In order to rotate the Hamiltonian (2) from the primed to the unprimed frame of reference, use is made of the spherical harmonic addition theorem.

$$P_l(\cos\theta')=\frac{4\pi}{2l+1}\sum_{m=-l}^{+l}\bar{P}_l^m(\cos\tilde{\theta})\bar{P}_l^m(\cos\theta'')e^{im(\tilde{\varphi}-\varphi'')},\tag{3}$$

where $\bar{P}_l^m$ is the normalized associated Legendre polynomial, $\tilde{\theta}$ is the angle between the radial vector and the direction of magnetization, and θ'' is the angle between the direction of magnetization and the crystalline field axis.

The rotated Hamiltonian (2) is

$$\begin{aligned}3\mathcal{C}_{fs}&=\mu_z H_z+(4\pi/5)\Lambda_2^0 r^2\sum_{m=-2}^{+2}\bar{P}_2^m(\cos\tilde{\theta})\\&\quad\times\bar{P}_2^m(\cos\theta'')e^{im(\tilde{\varphi}-\varphi'')}+(4\pi/9)\Lambda_4^0 r^4\\&\quad\times\sum_{m=-4}^{+4}\bar{P}_4^m(\cos\tilde{\theta})\bar{P}_4^m(\cos\theta'')e^{im(\tilde{\varphi}-\varphi'')}.\end{aligned}\tag{4}$$

The eigenvalues of the Hamiltonian (4) will be calculated by first and second order perturbation theory. The matrix elements of the crystalline terms are diagonal when $m=0$, the matrix elements of the remaining terms in the summation are off diagonal, and their eigenvalues must be calculated by second-order perturbation theory. The second-order terms for the third factor in Eq. (4) will be neglected because of the small order of magnitude of Λ_4^0. The matrix elements of $P_l^m(\cos\tilde{\theta})$ are evaluated by noting that since they transform under rotation like the base vector of the D_l representation of the rotation group, their matrix elements have the same dependence on the magnetic quantum number M as the Wigner coefficients $S_{JMM_L}^{(LS)}$.[5] Hence, the matrix element of the associated Legendre polynomial is the product of the Wigner coefficient and a factor which depends upon the total angular quantum numbers of the ion but which is independent of M. Since the amount of orbital momentum produced by the crystalline-field distortion of the S state is unknown, these constants cannot be evaluated but will be left as empirical constants γ and δ. In the cases where the total quantum numbers are known (i.e., paramagnetic salts of the rare earth ions), these constants can be evaluated by the method described by Stevens.[6]

The matrix elements of the Legendre polynomials are

$$\begin{aligned}(M|P_2^0|M)&=\gamma[3M^2-S(S+1)],\\(M|P_2^1|M\pm1)&=\gamma\{(1\pm2M)[(3/2)(S\pm M+1)\\&\qquad\times(S\mp M)]^{\frac{1}{2}}\},\\(M|P_2^2|M\pm2)&=\gamma[(3/2)(S\pm M+2)(S\pm M+1)\\&\qquad\times(S\mp M)(S\mp M-1)]^{\frac{1}{2}},\\(M|P_4^0|M)&=\delta[35M^4-30S(S+1)M^2+25M^2\\&\qquad-6S(S+1)+3S^2(S+1)^2].\end{aligned}\tag{5}$$

Making use of Eq. (5), the eigenvalues of the Hamiltonian (4) become

$$\begin{aligned}E_M^{fs}&=g\beta HM+D'[(M^2-(1/3)S(S+1)]\\&\quad\times[(3g_{11}^2/g^2)\cos^2\theta-1]\\&\quad-\frac{2D'^2}{g\beta H_0}[M(4S(S+1)-1)-8M^3]\\&\quad\times\frac{g_{11}^2g_\perp^2}{g^4}\sin^2\theta\cos^2\theta\\&\quad+\frac{D'^2}{2g\beta H_0}[M(2S(S+1)-1)+2M^3]\\&\quad\times(g_\perp^4/g^4)\sin^4\theta+d'[35M^4-30S(S+1)M^2\\&\quad+25M^2-6S(S+1)+3S^2(S+1)^2]\\&\qquad\cdot\left(35\frac{g_{11}^4}{g^4}\cos^4\theta-30\frac{g_{11}^2}{g^2}\cos^2\theta+3\right),\end{aligned}\tag{6}$$

where

$$D'=(3/2)\gamma\Lambda_2^0\langle r_{3d}^2\rangle_{Av},\quad d'=(1/8)\delta\Lambda_4^0\langle r_{3d}^4\rangle_{Av},$$

$$g=[g_{11}^2\cos^2\theta+g_\perp^2\sin^2\theta]^{\frac{1}{2}},\quad\cos\theta''=(g_{11}/g)\cos\theta$$

[5] E. Wigner, *Gruppentheorie* (Edwards Brothers, Inc., Ann Arbor, 1931).

[6] K. W. H. Stevens, Proc. Phys. Soc. (London) **A65**, 209 (1952).

and where θ is the angle between the magnetic field H and the crystalline field axis, and $g_{\parallel}$ and $g_{\perp}$ are the components of the spectroscopic splitting factor parallel and perpendicular to the crystalline-field axis, respectively. The d' term neglected by Bleaney[7] is of sufficient magnitude to be required in the interpretation of spectra exhibiting large axial crystalline-field effects.

HYPERFINE STRUCTURE

The hyperfine splitting is the result of a coupling between nuclear and electronic magnetic moments. The hyperfine structure Hamiltonian ($\mathcal{H}_{hfs}$) is

$$\mathcal{H}_{hfs}=AS_zI_z+\tfrac{1}{2}B(S_+I_-+S_-I_+), \tag{7}$$

where $S_{\pm}=S_x\pm iS_y$ and $I_{\pm}=I_x\pm iI_y$. S is the effective electronic spin, and I is the nuclear spin.

The eigenvalues of $\mathcal{H}_{hfs}$ are angularly dependent if A is not equal to B.[7] In the case under study, A is approximately equal to B; consequently the angular dependence of higher-order perturbation terms will be neglected. The eigenvalues of (7) calculated by first-, second-, and fourth-order perturbation theory are

$$\begin{aligned}E_{Mm}{}^{hfs}=K'Mm&+\frac{A'^2}{2g\beta H_0}\{M[I(I+1)-m^2]\\&-m[(S(S+1)-M^2]\}\\&+\frac{A'^4}{(2g\beta H_0)^3}[m^3\sigma(S)-M^3\sigma(I)+M^2m^3\tau(S)\\&-M^3m^2\tau(I)+M^4m\xi(I)-Mm^4\xi(S)\\&+m\eta_S(I)-M\eta_I(S)+Mm^2\zeta_S(I)\\&-M^2m\zeta_I(S)+M^3m^4-M^4m^3],\end{aligned} \tag{8}$$

where

$$\begin{aligned}&\sigma(x)=x(x+1)[4-3x(x+1)],\\&\tau(x)=[6x(x+1)-9],\quad \xi(x)=[3x(x+1)-1],\\&\eta_x(y)=[3x^2(x+1)^2y(y+1)-x^2(x+1)^2\\&\qquad-4x(x+1)y(y+1)+2x(x+1)],\\&\zeta_x(y)=[6x(x+1)y(y+1)-11x(x+1)-2y(y+1)+5],\\&K'=(1/g)[A'^2g_{\parallel}{}^2\cos^2\theta+B'^2g_{\perp}{}^2\sin^2\theta]^{\frac{1}{2}}.\end{aligned}$$

Combining Eqs. (6) and (8), we obtain the total energy eigenvalue:

$$E_{Mm}=E_M{}^{fs}+E_{Mm}{}^{hfs}, \tag{9a}$$

and the transition energy:

$$h\nu_0=E_{Mm}-E_{M-1,m}. \tag{9b}$$

Since in paramagnetic resonance absorption experiments the radiation frequency is kept constant and the magnetic field is varied, Eq. 9(b) is solved for H and the line position becomes (in units of gauss):

$$\begin{aligned}H=H_0&-D(2M-1)\left(3\frac{g_{\parallel}{}^2}{g^2}\cos^2\theta-1\right)\\&+\frac{2D^2}{H_0}[4S(S+1)-24M(M-1)-9]\\&\times\frac{g_{\parallel}{}^2g_{\perp}{}^2}{g^4}\sin^2\theta\cos^2\theta\\&-\frac{D^2}{2H_0}[2S(S+1)-6M(M-1)-3]\frac{g_{\perp}{}^2}{g^4}\sin^4\theta\\&-d\{140M^3-210M^2+[190-60S(S+1)]M\\&+30S(S+1)-60\}(35(g_{\parallel}{}^4/g^4)\cos^4\theta\\&-30(g_{\parallel}{}^2/g^2)\cos^2\theta+3)-Km\\&-\frac{A^2}{2H_0}[I(I+1)-m^2+m(2M-1)]\\&-\frac{A^4}{8H_0{}^3}\{(4M^3-6M^2+4M-1)[m\xi(I)-m^3]\\&+(3M^2-3M+1)[m^4-m^2\tau(I)-\sigma(I)]\\&+(2M-1)[m^3\tau(S)-m\zeta_I(S)]\\&+m^2\zeta_S(I)-m^4\xi(S)-\eta_I(S)\},\end{aligned} \tag{10}$$

where $D=D'/g\beta$, $d=d'/g\beta$, $H_0=h\nu_0/g\beta$, $A=A'/g\beta$, and $B=B'/g\beta$.

INTENSITIES

The observed transitions may be identified with electronic quantum numbers by means of their intensities. The intensity of magnetic dipole radiation is proportional to $(J+M)(J-M+1)$. Hence the intensities of transitions between the Zeeman levels of Mn^{++} occur in the ratios (the subscript denotes the upper of the two magnetic levels):

$$I_{\frac{5}{2}}:I_{\frac{3}{2}}:I_{\frac{1}{2}}:I_{-\frac{1}{2}}:I_{-\frac{3}{2}}=5:8:9:8:5. \tag{11}$$

EXPERIMENTAL METHOD

The crystals were prepared by cleaving them along the natural rhomdehedral cleavage planes of calcite to a size approximately 4 mm on a side and mounted at the desired orientation with wax onto a $\frac{1}{4}$-in. quartz rod. The orientation of the crystal with respect to the quartz rod was checked by means of optical gainiometer measurements and held to a precision of 20 min of arc.

Two mountings were used, one such that the c-crystallographic axis (which incidentally is the optic axis) was parallel to the axis of the quartz rod and a second with the c axis perpendicular to the axis of the quartz rod. Inasmuch as the crystalline electric field in calcite is

[7] B. Bleaney, Phil. Mag. 42, 441 (1951).

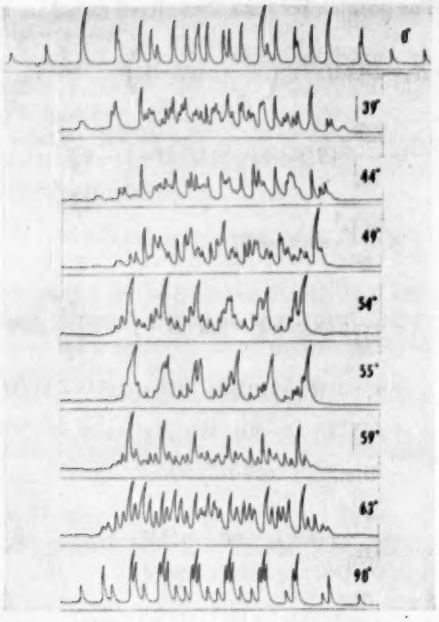

FIG. 1. Direct 9300-Mc/sec absorption curves of Mn^{++} 0.06 wt. percent in a single crystal of $CaCO_3$. The angle specified is that between the c-crystallographic axis and the external magnetic field. The 0° curve extends from 2732 gauss to 3872 gauss. The individual lines are symmetrical. The apparent asymmetry is due to the curvilinear coordinate of the Brush recorder.

predominately axial and lies along the c axis, most of the data were obtained with the latter crystal.

The experimental method was the same as that used by Hershberger and Leifer[3] in their investigation of powdered phosphors except for the method of mounting the sample and the method of measurement of the magnetic field. The crystals used in this investigation were natural calcite crystals which by chemical analysis were found to contain 6.02×10^{-3} wt. percent of Mn. The crystals cleaved along natural cleavage planes were mounted on a quartz rod which in turn was mounted in a holder which formed the end wall of a cylindrical resonant cavity operated in the circular electric or TE_{011} mode. The holder placed the quartz rod along the axis of the cavity and the sample at the center of the cavity. The holder was rotatable and graduated so that the crystal could be rotated through known angles. The resonant cavity placed in the magnetic field with its axis perpendicular to the externally applied magnetic field satisfied the condition for resonance, that is, rf magnetic field perpendicular to external magnetic field.

The general features of the detection systems have been previously described[3] and will be reviewed briefly to point out some modification with regard to field measurement.

The magnetic field is swept over the 1200-gauss range in approximately 10 min and is simultaneously swept 1 or 2 gauss at a 35-cps rate. The low-speed wide-range sweep is accomplished by varying the set point on an electronic regulator supply furnishing power for the main magnet coils while separate low inductance coils are employed to inject the 35 cps sweep. The band width of the detection system is approximately 3 cps. Changes in power transmitted through the cavity containing the sample are amplified by a narrow band 35-cps amplifier and are then detected and recorded using a square law detector and a phase detector followed by a two-channel brush recorder. This method of detection yields the derivative of the absorption curve but with a loss of its sign for the square law detector. Signals-to-noise ratios in excess of 1000 were obtained for samples of approximately $\frac{1}{4}$ gram and 6×10^{-2} wt. percent Mn, indicating that less than 10^{15} Mn^{++} ions may be detected.

The large signal-to-noise ratio permitted dc amplification of the transmitted power changes, yielding the absorption curves directly. Some such curves are shown in Fig. 1.

Magnetic field strength is measured by means of proton resonance. The proton resonance signal is detected and used as the information signal of a servo system which adjusts the proton resonance oscillator, keeping it centered on the proper frequency for the magnetic field. Hence, as the magnetic field is driven slowly through the desired range, the proton resonance oscillator follows automatically. The oscillator is hetrodyned with the harmonics of a General Radio Type 1100-A Secondary frequency standard, which are spaced at 100-kc/sec intervals. The hetrodyne signal is detected and amplified by a narrow-band low-frequency amplifier, such that zero beat gives an impulse to the marker pen on the brush recorder. These markers appear every 100 kc/sec which corresponds to approximately 23.5 gauss. The markers can be seen in Fig. 2. Actual data were taken from records for which the paper speed was greater than that shown in the figure in order to reduce the interpolation error. Linear interpolation is used between markers. The stability of the magnetic field and the tracking of the servo system are such that the maximum uncertainty of a field determination is approximately 1 gauss.

EXPERIMENTAL RESULTS

It was anticipated that the axial component of the crystalline electric field would be parallel the c axis of the crystal. To test the correctness of this assumption, one crystal was mounted with the c axis parallel ($c\parallel$) to the quartz rod, and data were taken every 10° for a total rotation of the crystal of 180°. Thus the c axis was kept perpendicular to the external magnetic field for all angular orientations. No angular change in the line position was noted; hence it was concluded that the (large) axial crystalline-electric field had no component perpendicular to the c axis and in fact coincided with the c axis.

A second crystal was mounted with the c axis per-

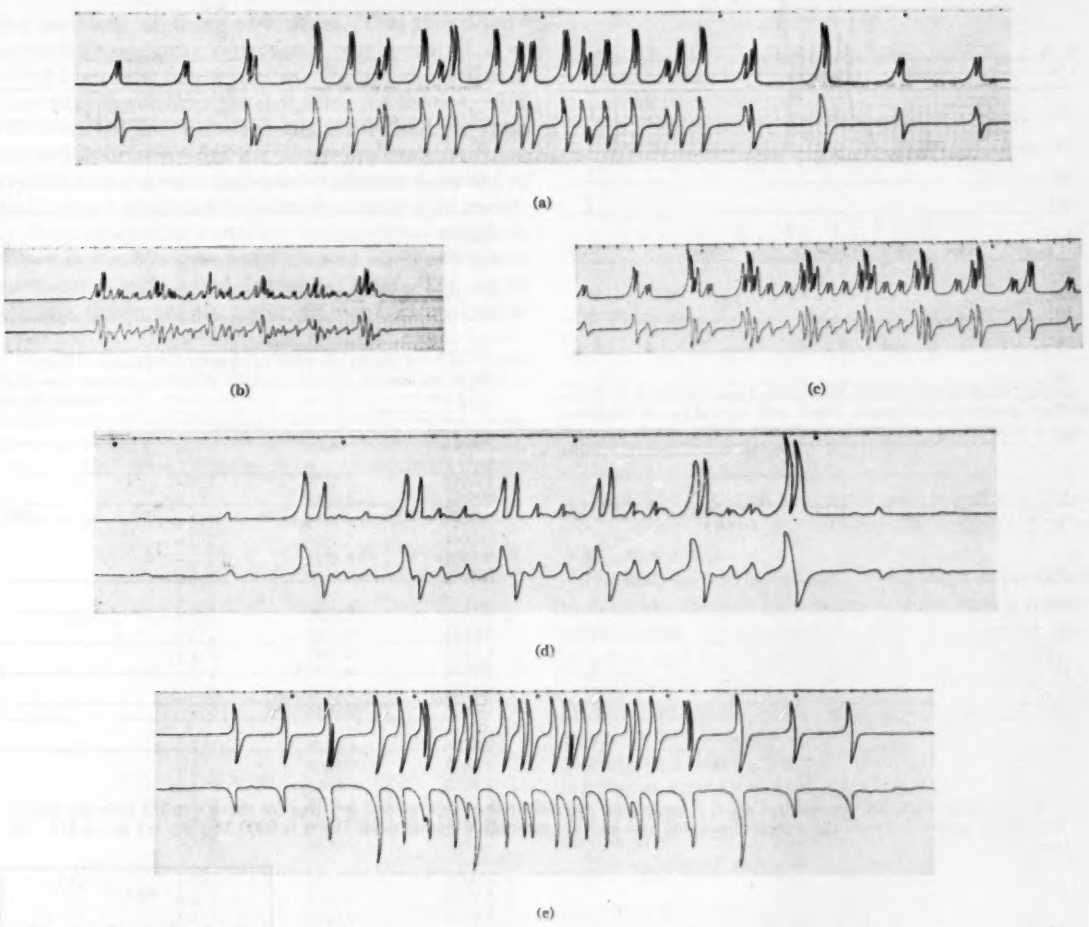

FIG. 2. Experimental records for $CaCO_3$:Mn 0.06 wt. percent. (a) $\theta=0°$; (b) $\theta=57°$; (c) $\theta=90°$; (d) powdered; (e) $\theta=0°$. Rf=9300 Mc/sec. The slope of the absorption curve is recorded except in the lower $\theta=0°$ case where the relationship between the slope and direct absorption is shown. The magnetic field markers appear at the top of the records.

pendicular ($c\perp$) to the quartz rod. Rotation for this crystal permitted orientation of the axial crystalline field with respect to the external magnetic field to any desired angle between 0° and 360°. Inasmuch as the mount did not allow absolute correlation between the c axis and the angular scale, the correlation was obtained experimentally at 90° by comparison between the $c\parallel$ and $c\perp$ data. A precision of 1° in the angular determination was obtained.

The angular dependence of the line positions is shown in Fig. 1 which record absorption directly. Figure 3 plots the $m=+5/2$ and $m=-5/2$ lines for the angles at which they may be determined with precision. It will be noted from Fig. 1 that many of the lines can be neither clearly resolved nor positively identified for angles between 0° and 90°. Note both in Figs. 1 and 3 the splitting of the $M=+5/2$, $+3/2$, $-1/2$, and $-3/2$ lines at intermediate orientations between 0°, 90°, and 180°. Figure 4 shows the angular dependence of the central ($M=+1/2$) lines to an enlarged scale where deviations from the line position at 90° are plotted for each of the six central ($M=+1/2$) lines. It is noted that the magnitude of the angular dependence is a function of the nuclear magnetic quantum number m increasing monotonically from $m=+5/2$ to $m=-5/2$, although the increase does not seem to be linear. The evidence of nonlinearity is not conclusive since overlapping of the lines reduces the precision at the angles where the shift is the greatest.

Figure 2 shows the appearance of the spectrum at 0°, 57°, 90°, and for a sample of the calcite which was powdered by grinding to give random crystal orientation. At 0° and at 90°, most of the 30 lines are seen to be well resolved. For this reason and for the reason that the theoretical expression for the line positions have maxima or minima in the angular dependent terms at these angles, they were chosen for precision measurements, and the interpretation is based principally upon

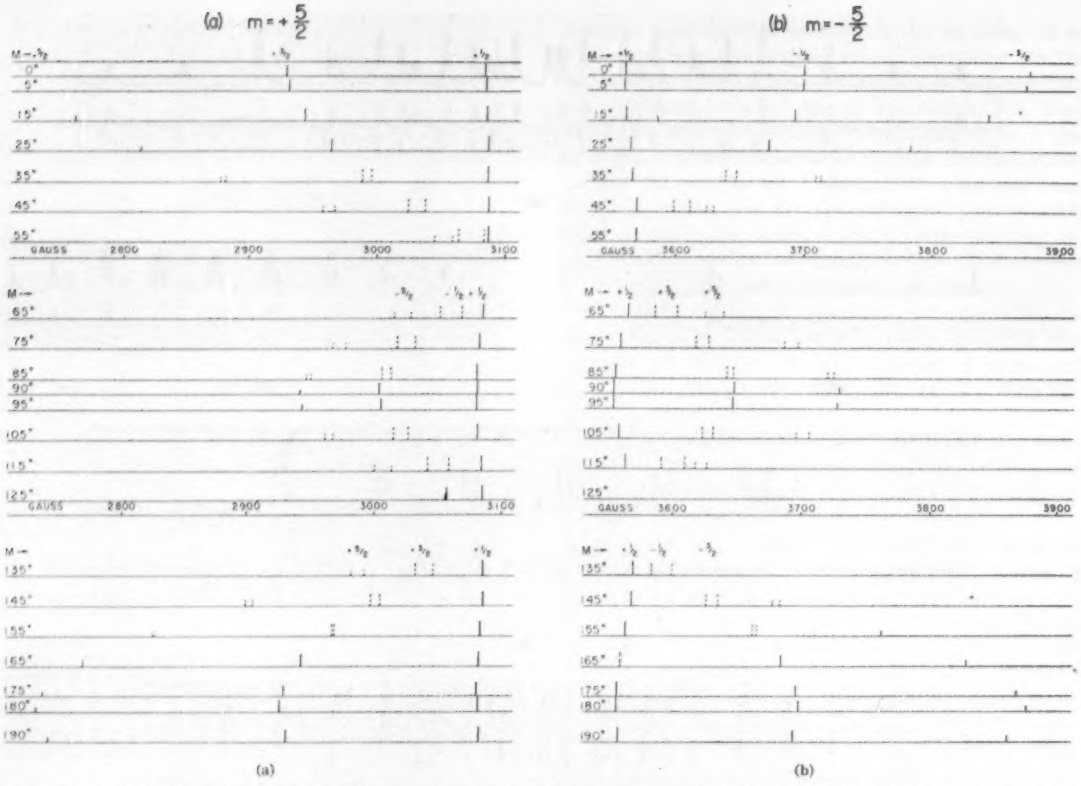

FIG. 3. Mn^{++} 0.06 wt. percent in $CaCO_3$. The angular dependent line position and splitting for the $m=\pm 5/2$ lines are shown for certain angles between the c-crystallographic axis and the external magnetic field. The rf is 9300 Mc/sec. (a) $m=+5/2$; (b) $m=-5/2$.

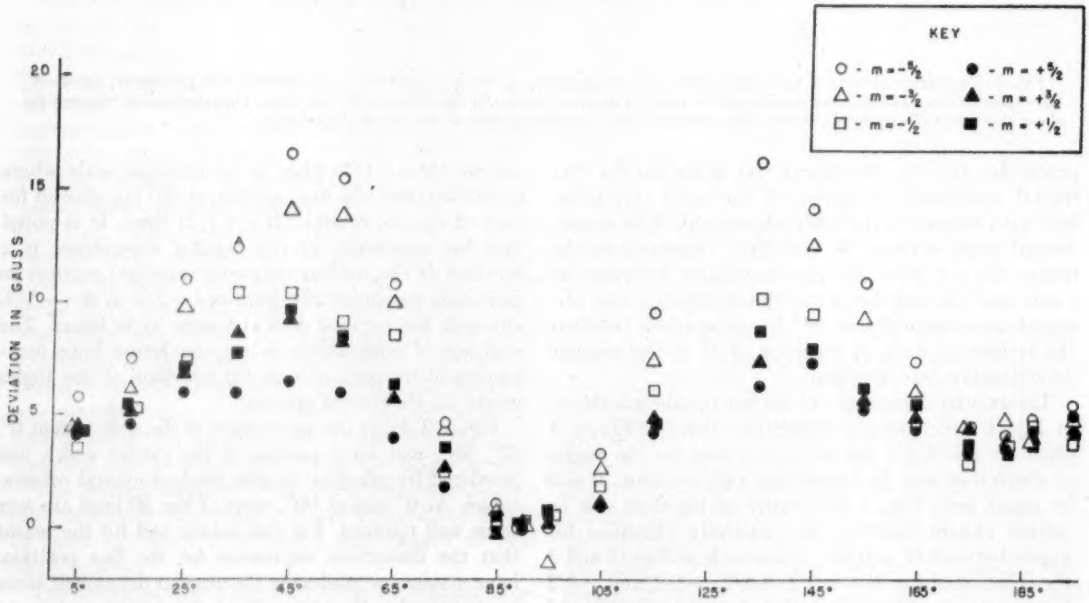

FIG. 4. Mn^{++} 0.06 wt. percent in $CaCO_3$; rf = 9300 Mc/sec. The angular dependence of the $M=+1/2$ lines is shown in terms of deviation from their position at $\theta=90°$. The angle θ is the angle between the c-crystallographic axis and the external magnetic field.

line positions at these two angles. The "powdered" curve shows angular dependence of the central $M=+1/2$ lines as a function of m. The $m=+5/2$ line is the strong line on the right (low field) and the $m=-5/2$ line is on the left. Increased angular dependence from $m=+5/2$ to $m=-5/2$ for these randomly oriented crystals shows up as a decreased maximum slope and as an increased separation between maximum slope points. A direct absorption curve for the powdered sample is shown in Fig. 5. Figure 5 also shows a direct absorption curve to a compressed horizontal scale. The major features shown are six major ($M=+1/2$) peaks plus

TABLE I. Resonance absorption lines (in gauss) for $CaCO_3$:Mn 0.06 wt. percent, rf=9300 Mc/sec. Line positions are known to ±1.0 gauss.

M	m	$\theta=0°$	$\theta=90°$
5/2	+5/2	2732.6	3226.2
	+3/2	2826.8	3319.9
	+1/2	2924.2	3415.8
	−1/2	3022.7	3515.0
	−3/2	3125.4	3617.9
	−5/2	3232.0*	3725.0
3/2	+5/2	2924.2	3157.9
	+3/2	3015.9	3248.8
	+1/2	3109.8	3342.1
	−1/2	3206.9	3439.1
	−3/2	3306.1	3538.6
	−5/2	3410.0*	3640.9
1/2	+5/2	3080.5	3077.4
	+3/2	3169.9	3166.5
	+1/2	3260.9	3258.1
	−1/2	3354.8	3352.2
	−3/2	3451.3	3447.9
	−5/2	3550.6	3546.7
−1/2	+5/2	3236.1	3000.4
	+3/2	3322.3	3087.7
	+1/2	3410.0*	3176.8
	−1/2	3503.0	3268.8
	−3/2	3596.9	3362.1
	−5/2	3693.3	3457.9
−3/2	+5/2	3428.1	2938.2
	+3/2	3510.9	3023.7
	+1/2	3596.9	3111.9
	−1/2	3687.1	3201.1
	−3/2	3778.4	3292.2
	−5/2	3872.4	3385.0

* Because of superpositions of lines, the accuracy here is ±2.5 gauss.

secondary peaks superposed upon a broad absorption curve. The powdered crystal curves also show the futility of an attempt to interpret data regarding crystalline fields when obtained from powdered samples.

The line position for each of the 30 lines at 0° and at 90° is tabulated in Table I. Figure 6 shows a plot of the line positions at 0° and 90° with the quantum number assignments indicated.

INTERPRETATION

In accordance with the customary practice, the lines are designated by the quantum numbers of the upper energy level involved in the transition corresponding to

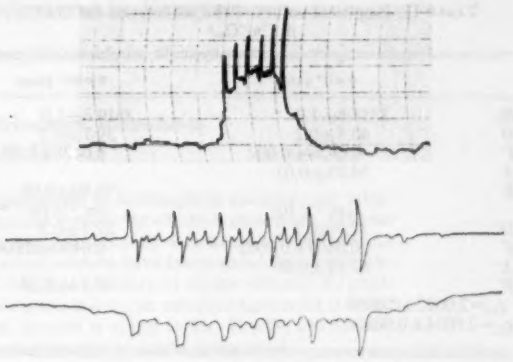

FIG. 5. Spectrum for a sample of $CaCO_3$:Mn 0.06 wt. percent, powdered by grinding. The direct absorption spectrum and its slope are shown below. The direct absorption spectrum to a compressed scale is shown above.

the line. Thus the line associated with the $M=+3/2\rightarrow+5/2$, $m=+3/2\rightarrow+3/2$ transition is designated $M=+5/2$, $m=+3/2$.

The lines intensities fall into three groups as predicted by Eq. (11). Further identification of the lines is readily accomplished by comparison with the leading fine structure and hyperfine structure terms of Eq. (10).

Empirical determination of the parameters of Eq. (10) for $\theta=0°$ yields the values $H_0=3318.6$ gauss, $D=40.5$ gauss, $d=0.0428$ gauss, $A=93.95$ gauss, and $g_\parallel=2.0022$ as given in Table II. Use of these values for the parameters gives agreement between observed and calculated line position within the estimated maximum experimental error of ±1.0 gauss.

The values of the parameters which give the best

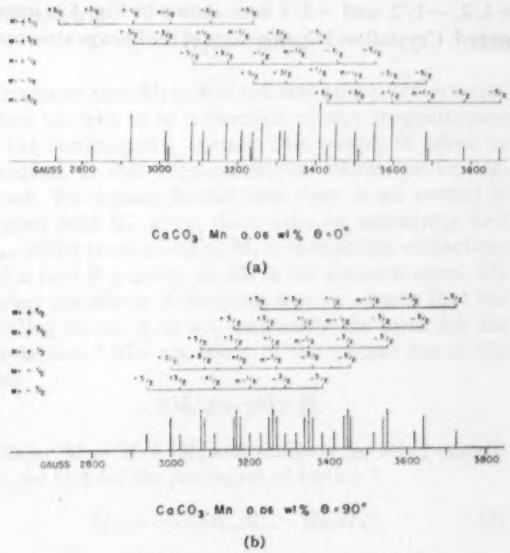

FIG. 6. Line positions and quantum number assignments. θ is the angle between the c-crystallographic axis and the external magnetic field. Rf=9300 Mc/sec.

TABLE II. Empirical values of the parameters for Mn^{++} in $CaCO_3$.[a]

	$\theta=0°$ gauss	$\theta=90°$ gauss
H_0	3318.6±1.0	3319.8±1.0
D	40.5±0.2	39.7±0.2
d	0.0428±0.002	0.0428±0.002
A	93.95±0.05	
B		93.90±0.05
	$cm^{-1}\times10^4$	$cm^{-1}\times10^4$
D'	37.9±0.2	37.1±0.2
d'	0.0400±0.0002	0.0400±0.0002
A'	87.82±0.08	
B'		87.74±0.08
$g_{\parallel}=2.0022\pm0.0006$		
$g_{\perp}=2.0014\pm0.0006$		

[a] A discrepancy in the two values of the constant D is noted. The value $D'=(37.5\pm0.4)\times10^{-4}$ cm^{-1} would give agreement between calculated and experimental line positions.

agreement between experimental and calculated values of line positions at 90° are $H_0=3319.8$ gauss, $D=39.7$ gauss, $d=0.0428$ gauss, $B=93.90$ gauss, $g_{\perp}=2.0014$. At this angle some difficulty is experienced in assigning best values to the parameters. The values assigned yield agreement between experimental and calculated line positions to within the maximum experimental error for all lines except the $M=+5/2$, $m=+5/2$ and the $M=-5/2$, $m=-5/2$ lines where the discrepancy is about four times the experimental error.

In an attempt to account for discrepancies, the effect of higher order terms of a trigonal symmetry, use of a small cubic symmetry contribution, and nuclear quadrupole effects have been examined and are found to be inadequate. The discrepancies, though small, are considered to be significant.

The angular dependent splitting of the $M=+5/2$, $+3/2$, $-1/2$, and $-3/2$ lines shown in Fig. 3 is unexpected. Crystalline imperfections of the lineage structure type would produce discrete angular dislocations of the crystal planes and might occur frequently enough throughout the crystal to yield two slightly different orientations of the crystal effectively, thereby giving rise to two equally intense lines of the angular dependent spacing observed. The hypothesis, although attractive, must be discarded inasmuch as it would demand the splittings for the $M=+5/2$ and $-3/2$ lines to be twice that for the $M=+3/2$ and $-1/2$ lines whereas the observation is that the $M=+5/2$, $-3/2$ lines are split less than the $M=+3/2$, $-1/2$ lines.

The significance of the crystalline-field-splitting terms D' and d' of Table II is shown in Eq. (6), where they are expressed as the products of three factors:

$$D'=(3/2)\gamma\Lambda_2{}^0\langle r_{3d}{}^2\rangle_{Av} \quad \text{and} \quad d'=(1/8)\delta\Lambda_4{}^0\langle r_{3d}{}^4\rangle_{Av}.$$

The coefficients $\Lambda_2{}^0$ and $\Lambda_4{}^0$ are the derivatives $(1/2!)(\partial^2V/\partial z^2)_0$ and $(1/4!)(\partial^4V/\partial z^4)_0$. The terms $\langle r_{3d}{}^2\rangle_{Av}$ and $\langle r_{3d}{}^4\rangle_{Av}$ are the mean square and mean fourth radii of the $3d$ shell of Mn^{++}. The terms γ and δ are numerical factors dependent upon the total angular quantum number of Mn^{++} in the crystal.

The mean square and mean forth radii can be calculated and will probably be known to a fair degree of accuracy. Experiments designed to determine the coefficients $\Lambda_2{}^0$ and $\Lambda_4{}^0$ will allow a determination of γ and δ and will therefore enable one to determine the quantity of orbital momentum introduced by means of the crystalline field distortion of the S state of Mn^{++}.

The assistance of J. S. Fuller, from whom the crystals were obtained, and of Professor R. J. Finkelstein is gratefully acknowledged. Special credit is due R. C. Mackey who was responsible for the electronic instrumentation. A detailed presentation of the instrumentation aspects of the work is in the process of preparation by Mr. Mackey and will be published in the future.

Magnetic Resonance Phenomena in Ferrites

FIELDING BROWN, *Sprague Electric Company, North Adams, Massachusetts*

AND

DAVID PARK, *Williams College, Williamstown, Massachusetts*

(Received August 13, 1953)

The resonant frequencies of the rotations of domain magnetization in ferrimagnetic materials are calculated by the use of the molecular field approximation, taking into account the effects of anisotropy, external field, and differences in magnetization and g values between the two sublattices. Resonance is found to occur in two frequency bands: one in a microwave band, which various workers have investigated experimentally, and one in the infrared, predicted earlier by Kaplan and Kittel. It is necessary to discuss critically the physical nature of the anisotropy field entering the equations; when this is done, an excellent agreement is found with the measurements of Yager *et al.* and Healy on single crystals of nickel ferrite. Finally, the relation between the theory presented here and experiments on sintered samples of ferrite is discussed.

INTRODUCTION

IN recent years several experiments have been performed on ferrites to find resonance phenomena analogous to those known to occur in ferromagnetic substances.[1-7] Two bands of resonance frequencies have been identified: a radio frequency band, probably corresponding to oscillations of the Bloch walls of the sample,[4] and a microwave band, probably due to domain rotations.[4] In addition, the theory of exchange resonance predicts a third frequency band in the infrared,[8] but this has not yet been verified experimentally.

The theory of the Bloch wall resonance is beyond the scope of these remarks, but the microwave and the predicted infrared resonance should both be due to the collective interactions of spins within each domain, and should, therefore, both be explainable by the same physical considerations. Most of the experiments on the microwave resonance, however, were done before the theory of ferrimagnetic resonance was worked out in detail,[9-12] and so the theoretical interpretation of these phenomena was given at the time and has since been discussed in terms borrowed from the theory of ferromagnetic resonance.[13] Essentially, it has been argued that the resonance is due to the motion of the net magnetization of the domain precessing in an aligning field consisting of an equivalent magnetocrystalline anisotropy field, taken to be the same as the anisotropy field determined from torque measurements on a saturated crystal, plus any externally applied magnetic field. The object of this paper is to derive an expression for the resonant frequencies to be expected in ferrimagnetic materials, to discuss the role played by the equivalent anisotropy field, and to compare this theory with experiment.

THEORY

To derive the equations of motion, we suppose that the ferrite possesses two oppositely directed magnetic sublattices, of magnetization $\mathbf{M}_1$ and $\mathbf{M}_2$. In the molecular field approximation, each lattice can be regarded as subjecting the other to an effective exchange field H_E proportional to its own magnetization: that acting on lattice 1 is

$$\mathbf{H}_{E1}=-\lambda\mathbf{M}_2, \tag{1a}$$

and similarly

$$\mathbf{H}_{E2}=-\lambda\mathbf{M}_1. \tag{1b}$$

We assume that $\mathbf{M}_1$ is directed along the positive z axis, which we take to be a direction of easy magnetization of the ferrimagnetic crystal. The sample is taken as spherical, so that demagnetization effects can be neglected. We assume further that there is an externally applied field H_0, along the z axis, an anisotropy field H_{A1}, which tends to orient $\mathbf{M}_1$ in the positive z direction, and a field H_{A2} acting on $\mathbf{M}_2$ in the opposite sense. We neglect the effects of damping, but we assume that the splitting factor, g, is not necessarily the same for the two lattices.[8] The equations of the motion are of the form

$$\partial\mathbf{M}/\partial t=\gamma\mathbf{M}\times\mathbf{H}.$$

Defining $M_+=M_x+iM_y$ and similarly for other quantities, we find for the precession of lattice 1,

$$\dot{M}_{1+}=-i\gamma_1(H_{1z}M_{1+}-H_{1+}M_{1z}). \tag{2}$$

In this situation, H_+ acting on each lattice is due entirely to the exchange field H_E of the other lattice;

[1] J. L. Snoek, Philips Tech. Rev. **8**, 353 (1948); Nature **160**, 90 (1947); Physica **14**, 207 (1948); H. G. Beljers and J. L. Snoek, Philips Tech. Rev. **11**, 313 (1949).
[2] Yager, Galt, Merritt, and Wood, Phys. Rev. **80**, 744 (1950).
[3] C. Kittel, J. phys. radium **12**, 292 (1951).
[4] G. T. Rado, Revs. Modern Phys. **25**, 81 (1953).
[5] Wijn, Gevers, and van der Burgt, Revs. Modern Phys. **25**, 91 (1953).
[6] D. W. Healy, Jr., Phys. Rev. **86**, 1009 (1952).
[7] Okamura, Torizuka, and Kojima, Phys. Rev. **88**, 1425 (1952).
[8] J. Kaplan and C. Kittel, J. Chem. Phys. **21**, 760 (1953).
[9] F. Keffer and C. Kittel, Phys. Rev. **85**, 329 (1952).
[10] R. K. Wangsness, Phys. Rev. **86**, 146 (1952).
[11] C. Kittel, Phys. Rev. **82**, 565 (1951); T. Nagamiya, Progr. Theoret. Phys. (Japan) **6**, 342 (1951).
[12] We follow Néel in using the term *ferrimagnetic* to describe phenomena characteristic of the magnetic structure of ferrites. Ferromagnetism and antiferromagnetism can both be regarded as special cases of ferrimagnetism.
[13] C. Kittel, Phys. Rev. **73**, 155 (1948).

in fact, from (1),

$$H_{1+}M_{1z}=H_{E2z}M_{2+},\quad H_{2+}M_{2z}=H_{E1z}M_{1+}.$$

In the limit of small oscillations, $H_{E1z}=H_{E1}$ and $H_{E2z}=-H_{E2}$, so we shall drop the subscript z and write (2) as

$$\dot{M}_{1+}=-i\alpha_1\gamma[(H_0+H_{A1}+H_{E1})M_{1+}+H_{E2}M_{2+}].$$

Similarly,

$$\dot{M}_{2+}=-i\alpha_2\gamma[(H_0-H_{A2}-H_{E2})M_{2+}-H_{E1}M_{1+}], \quad (3)$$

where

$$\alpha_1=\tfrac{1}{2}g_1,\quad \alpha_2=\tfrac{1}{2}g_2,\quad \text{and}\quad \gamma=e/mc.$$

The frequency at which such a system will resonate if driven is the frequency of free oscillation ω_0. Setting M_{1+} and M_{2+} each proportional to $e^{i\omega_0 t}$ and solving the resulting secular equation gives

$$\begin{aligned}-2\omega_0/\gamma=&(\alpha_1+\alpha_2)H_0+\alpha_1H_{A1}-\alpha_2H_{A2}+\alpha_1H_{E1}\\&-\alpha_2H_{E2}\pm\{[(\alpha_1-\alpha_2)H_0+\alpha_1H_{A1}\\&+\alpha_2H_{A2}+\alpha_1H_{E1}+\alpha_2H_{E2}]^2\\&-4\alpha_1\alpha_2H_{E1}H_{E2}\}^{\frac{1}{2}}. \quad (4)\end{aligned}$$

In the special case of antiferromagnetism we have $\alpha_1=\alpha_2\sim 1$, $H_{A1}=H_{A2}=H_A$, and $H_{E1}=H_{E2}=H_E$. Equation (4) then reduces to $\omega_0/\gamma=H_0\pm[H_A(H_A+2H_E)]^{\frac{1}{2}}$, as given earlier.[11] In the ferromagnetic case, $\alpha_2=H_{E1}=0$ and the above resonance condition gives $\omega_0/\gamma=\alpha_1\times(H_0+H_A)$ in agreement with the theory of ferromagnetic resonance.[13]

In most of the applications in which one is interested, the square root in (4) can be expanded. Corresponding to the upper sign we get

$$-\omega_0/\gamma=\alpha_1H_{E1}-\alpha_2H_{E2}+\frac{(\alpha_1^2H_{E1}-\alpha_2^2H_{E2})H_0+(\alpha_1^2H_{E1}H_{A1}+\alpha_2^2H_{E2}H_{A2})}{\alpha_1H_{E1}-\alpha_2H_{E2}}, \quad (5)$$

and to the lower,

$$\frac{\omega_0}{\gamma}=\frac{\alpha_1\alpha_2}{\alpha_2H_{E2}-\alpha_1H_{E1}}[(H_{E2}-H_{E1})H_0+H_{A1}H_{E2}+H_{A2}H_{E1}], \quad (6)$$

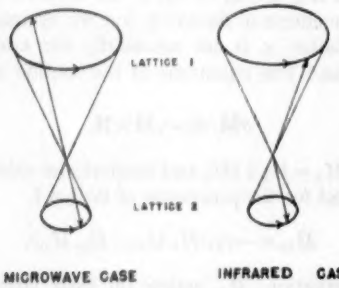

FIG. 1. Precessional motion of magnetic lattices in a ferrite for the two resonance cases treated. H_0 is parallel to axis of cones.

where in evaluating the root we have assumed that $\alpha_1H_{E1}<\alpha_2H_{E2}$ and that even the difference between these quantities is large compared to H_0, H_{A1}, and H_{A2}.

Equation (5) is, except for the corrections due to anisotropy and external field, the same as the formula of Kaplan and Kittel[8] for the infrared resonance. The resonant frequency (6), on the other hand, is of a different order of magnitude, falling in the range of microwave phenomena which we discussed earlier, for ω_0 is of the order of γH_0 or γH_A.

Let us now see what sort of lattice motions take place in these two ranges of frequencies. If we substitute (5) and (6) back into (3), we find that

$$M_{2+}\sim(\alpha_2/\alpha_1)M_{1+}\ \text{(infrared)},$$

and

$$M_{2+}\sim-(H_{E1}/H_{E2})M_{1+}\ \text{(microwave)}.$$

These motions are respectively in phase and in opposition to each other and are illustrated in Fig. 1. Clearly, the microwave motion flexes the bond coupling the two lattices very little, in contrast to the infrared motion which flexes it to the greatest possible degree. This accounts for the large difference between the two frequency ranges and shows why the frequency of the microwave oscillation is roughly independent of the quantities H_{E1} which describe the bond.

DISCUSSION

We can compare the predictions of Eq. (6) with available experimental data. Before doing this, however, we must examine the relation of H_{A1} and H_{A2}, as they appear in the resonance expression, to the so-called equivalent anisotropy field, designated as H_{AO}, which has been measured for nickel ferrite from the hysteresis loops of single crystals[14] and from the variation with crystal orientation of the external field necessary for ferrimagnetic resonance.[2,6]

Ordinarily, H_{AO} is defined in terms of the torque required to cause a small angular deviation of the magnetization of a specimen away from a direction of easy magnetization. The torque is proportional to the anisotropy constant and to the angular deviation θ and is written as $H_{AO}M_s\theta$, where M_s, the saturation magnetization, is M_1-M_2. But we can express it also in terms of H_{A1} and H_{A2}, each of which is assumed to act on the magnetization of the corresponding lattice so as to tend to align it with the axis of easy magnetization (that is, to orient M_1 in the positive z direction and M_2 in the negative one). In these terms, the torque is equal to $(M_1H_{A1}+M_2H_{A2})\theta$. Thus, we have

$$M_1H_{A1}+M_2H_{A2}=H_{AO}(M_1-M_2). \quad (7)$$

The use of (1) then allows us to write (6) as

$$\omega_0=\gamma\alpha_1\alpha_2\frac{M_2-M_1}{\alpha_2M_1-\alpha_1M_2}(H_{AO}+H_0). \quad (8)$$

[14] Galt, Matthias, and Remeika, Phys. Rev. 79, 391 (1949).

We can now compare the predictions of (8) with that of resonance experiments on single crystals of nickel ferrite. To do this we shall take M_1 equal to 865 and M_2 to 600 cgs so that $M_s=265$. Further $g(Ni^{2+})=2.20$ and $g(Fe^{3+})=2.00$, corresponding to a pure inverse spinel structure, which gives[8] $\alpha_2=1.00$ and $\alpha_1=1.03$. We may evaluate H_{AO} from the expression for the crystal anisotropy energy density, for small angular deviations,

$$f=pk_1\theta^2, \tag{9}$$

where k_1 is the first-order anisotropy constant of the crystal. Equation (9) follows from a standard expression for the anisotropy energy if $p=1$ for positive k_1 and $p=-\frac{3}{5}$ for negative k_1 as in the present case of ferrites in which the (111) direction is an easy direction of magnetization. The torque as given by (9) is

$$T=\partial f/\partial\theta=(4/3)k_1\theta.$$

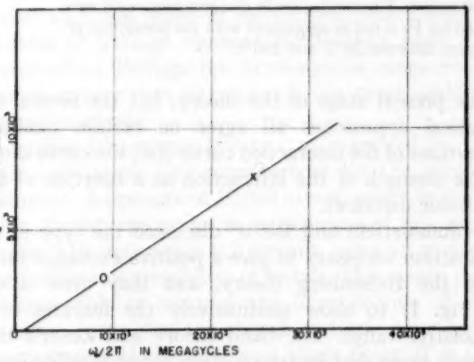

FIG. 2. Ferrimagnetic resonance conditions in single crystals of nickel ferrite. X—experimental data of Yager *et al.* (see reference 2); O—data of Healy; solid line is plot of present theory.

The anisotropy field H_{AO} is then equal to

$$H_{AO}=(4/3)(k_1/M_s). \tag{10}$$

If we insert the previously measured value[2] of $k_1=-6.27\times10^4$ ergs/cm^3, Eq. (10) gives $H_{AO}=315$ oersteds. A plot of (8) is given in Fig. 2, together with the available experimental data. The agreement is excellent, considering the probable accuracy of the constants used and the apparent variability[6] of the effective anisotropy constant from one crystal specimen to another. Further, the slope of the theoretical line in Fig. 2 represents a calculated g-value of 2.21, as compared with 2.25 and 2.19 as measured by Healy and Yager, respectively.

In addition to the data cited above for resonance in single crystals, we may compare the present results with the measurements of Okamura *et al.*[7] on spheres cut from sintered nickel ferrite and manganese ferrite. Figure 3 shows this comparison, where H_{AO} in each case has been taken to give the best fit with the experimental points. In the case of sintered nickel ferrite, a value of $\alpha_2=1.00$ has been used,[15] corresponding to our choice of $g(Fe^{3+})=2.00$, and α_1 has been adjusted to give the correct experimental slope. With M_1 and M_2 assumed the same as for the single crystals, the data yield a g factor for nickel in sintered nickel ferrite of 2.07.

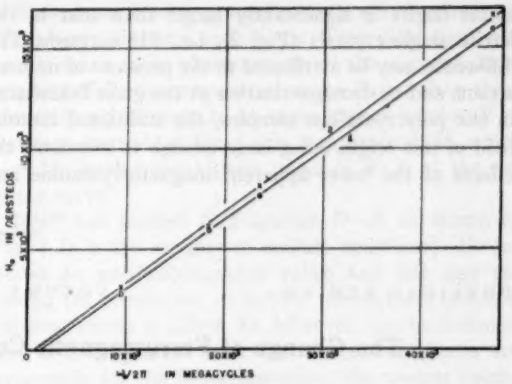

FIG. 3. Ferrimagnetic resonance conditions in sintered ferrites. X—experimental data of Okamura *et al.*[7] in nickel ferrite; O—data in manganese ferrite (same author); present theoretical prediction in each case is represented by solid curve.

A similar comparison is possible for the data[7] in sintered manganese ferrite. Again the experimental points are shown along with the theoretical curve computed for $H_{AO}=278$ oersteds, as given by Okamura, under the assumption that $\alpha_1=\alpha_2=1.00$, corresponding to observation,[15] and that $g(Fe^{3+})=g(Mn^{2+})=2.00$. (In this case the values of M_1 and M_2 do not enter the resonance condition.) The agreement is again satisfactory.

CONCLUSIONS

In view of the agreement with experiment of these ideas on the nature of the equivalent anisotropy field as applied to resonance in ferrites, it is of interest to speculate on the expected resonance frequencies in the closely related antiferromagnetic materials. From Eq. (7) it is found that H_{A1} and H_{A2} are appreciably smaller than H_{AO}. In fact, if we take $H_{A1}=H_{A2}$, it is found that $H_{A1}=90$ for sintered nickel ferrite. If we assume that the anisotropy fields in antiferromagnetic materials are of this same order of magnitude, the resonance frequencies to be expected may be somewhat lower than those predicted using a value of $H_{AO}\sim500$,[11] thus offering the possibility of observing antiferromagnetic resonance under less extreme experimental conditions than usually anticipated.

It may further be noticed that the internal field observed by Okamura[7] of 507 oersteds for sintered

[15] F. W. Lancaster and W. Gordy, J. Chem. Phys. **19**, 1181 (1951); L. R. Maxwell and T. R. McGuire, Revs. Modern Phys. **25**, 279 (1953).

nickel ferrite is significantly larger than that in the ferrite single crystals (Fig. 2), i.e., 315 oersteds. The difference may be attributed to the presence of internal strains and to demagnetization at the grain boundaries in the polycrystalline samples, the additional internal field of this origin being large enough to overcome the effects of the lower apparent magnetocrystalline anisotropy fields which must result from the random orientation of crystallites away from directions of easy magnetization.[16]

[16] After this work was completed an article by R. Wangsness [Phys. Rev. 91, 1085 (1953)] appeared in which is given a formula equivalent to (6) except that it does not contain the distinction between the phenomenological anisotropy field and that which enters the resonance expression.

PHYSICAL REVIEW VOLUME 93, NUMBER 3 FEBRUARY 1, 1954

The Change of Ferromagnetic Curie Points with Hydrostatic Pressure*

LYLE PATRICK†
Department of Physics, University of Chicago, Chicago, Illinois
(Received October 19, 1953)

The effect of pressure on the Curie temperature has been measured for 13 ferromagnetic materials, comprising 4 elements (Fe, Co, Ni, Gd), 7 metallic alloys, a ferrite, and a perovskite. Curie points ranged from 16°C (Gd) to 1120°C (Co), and pressures up to 9000 atmos. The results are in disagreement with two common forms of the interaction curve. The result obtained for Fe is not in agreement with the prediction of Kornetzki, based on volume magnetostriction measurements between 20°C and 100°C.

I. INTRODUCTION

Importance of Interatomic Distance

THE effect of pressure is considered to be that resulting from the change produced in interatomic distance, which is known to be an important parameter in the strength of magnetic interaction. Slater[1] first pointed out that ferromagnetism occurs only in those elements in which there is a large ratio of interatomic distance, D, to diameter of unfilled inner shell, d (usually a d shell, but in Gd it is the $4f$ shell). An accurate calculation of the magnetic interaction is still impossible at the present stage of the theory, but the several theoretical approaches all agree on certain qualitative features of the interaction curve (i.e., the curve showing the strength of the interaction as a function of interatomic distance).

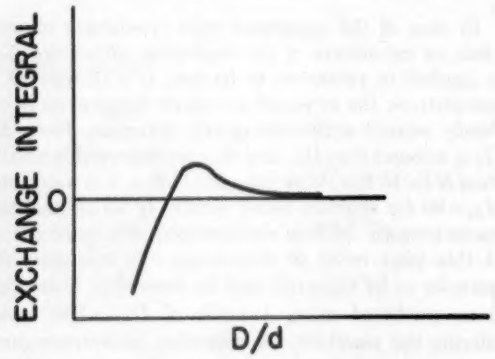

FIG. 1. Bethe interaction curve.

Sommerfeld and Bethe[2] discussed the type of wave function necessary to give a positive exchange integral in the Heisenberg theory, and they drew a curve (Fig. 1) to show qualitatively the features of this positive range. The band theory and Zener's theory both agree that ferromagnetism is not possible for very small or very large values of D, but the width of the ferromagnetic range is still an unsettled question. The salts of ferromagnetic elements, in which D is large, are paramagnetic rather than weakly ferromagnetic. On the other hand, Zener[3] has pointed out the importance of conduction electrons in coupling the d-shell spins. The salts may be paramagnetic because of the absence of conduction electrons.

The Forrer Correlation

Forrer[4] has made a correlation of magnetic interaction with interatomic distance, D, for Mn, Cr, Fe, Co, Ni and their compounds in which these elements retain their characteristic moments and in which coupling does not occur through intermediate atoms by the superexchange mechanism. He finds that as D increases the interaction changes, for each element, from antiferromagnetic to ferromagnetic and then to paramagnetic. The ferromagnetic range is roughly 10 percent

* Submitted in partial fulfillment of the requirements for the degree of Ph.D. at the University of Chicago. The work was done at the laboratory of the Institute for the Study of Metals, Chicago, Illinois.

† Now at Westinghouse Research Laboratories, East Pittsburgh, Pennsylvania.

[1] J. C. Slater, Phys. Rev. 36, 57 (1930).

[2] A. Sommerfeld and H. A. Bethe, *Handbuch der Physik* (J. Springer, Berlin, 1933), second edition, Vol. 24, No. 2, p. 596.

[3] C. Zener, Phys. Rev. 81, 440 (1951).

[4] R. Forrer, Ann. Physik 7, 605 (1952).

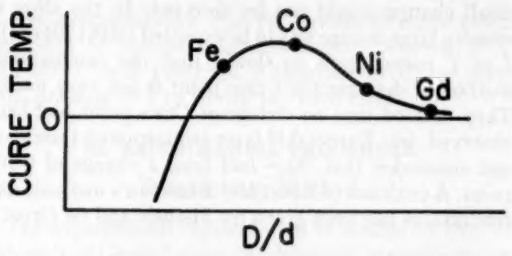

FIG. 2. Bozorth interaction curve.

of D—perhaps as little as 5 percent in Co. However, one must consider Zener's remarks about conduction electrons. The Forrer correlation overlooks the fact that the range of D in metals is rather limited. Dilution of ferromagnetic elements to increase the average distance does not work in metallic alloys because the conduction electrons of the added metal apparently fill the d band of the ferromagnetic element. The reduction of Curie point in such cases results from a reduction of average moment rather than from any distance effect. Perhaps the ferromagnetic range would be much greater than 10 percent if this range could be obtained in metals.

A narrow ferromagnetic range, as suggested by the Forrer correlation, has consequences for the present experiment. A pressure of 10 000 atmos, which is available in the laboratory for an experiment of this type, changes D by only about 0.2 percent, using an average value for the compressibility of metals. This means that it is impossible to measure any large portion of the interaction curve, but the change of Curie point with pressure does give the slope at a single point. If in Co the Curie temperature rises to 1400°K and falls to zero again within a range of 5 percent of D, the average rate of rise or fall must be over 10° per 1000 atmos. For Fe this figure is about 4°. This means that changes of this order of magnitude should be expected if the ferromagnetic range is as limited as Forrer suggests.

Interaction Curves

The Forrer correlation is an attempt to define the ferromagnetic range for single elements. The suggestion of Slater that D/d is the significant parameter for ferromagnetic interaction has led to attempts to draw a generalized interaction curve to include all ferromagnetic elements. The assumption is that D and d are the only important parameters in the strength of magnetic interaction; therefore a correlation is attempted, using a function of D and d as a "reduced" distance. Such attempts must prove futile if other important parameters exist (e.g., conductivity).

Figure 2 shows one such curve, drawn by Bozorth.[5] In this, Curie temperatures are plotted against D/d. However, the Curie temperature, on the assumption of a Weiss inner field, is proportional to $\mu^2 N$, in which μ is the atomic moment and N the Weiss field constant; and μ seems to be characteristic of the element, independent of D (the examples given by Forrer show this). Hence it would seem to be more logical to plot N as ordinate instead of the Curie temperature, in which case Ni, having the highest value of N, is at the top of the curve.

Néel[6] has plotted N/z against $D-d$, as shown in Fig. 3 (z is the number of nearest neighbors). He includes an antiferromagnetic range and has also extended the correlation to include interactions between different atoms in alloys. Fe, however, can be included only if it is assumed that next nearest neighbors are responsible for the ferromagnetism, the nearest neighbors being near the point where the curve crosses the axis, and therefore ineffective. He has found further evidence to support this curve; and has predicted an increase of Curie point with pressure in Fe of 0.79° per 1000 atmos and decreases in Co and Ni of 4.6° and 0.13°, respectively.

Reciprocal Effects

If a change of volume alters the magnetic interaction, there should be a reciprocal effect in which the change of intrinsic magnetization by a high field changes the volume of a ferromagnet. This effect has been measured as the volume magnetostriction, and more will be said of it later. Also, the loss of magnetization as the temperature is raised has an effect on the volume which shows up as an abnormal thermal expansion. This may be large enough, as in Invar, to compensate the normal thermal expansion over a certain temperature range. Both effects have been used to estimate the volume dependence of the interaction.

II. PREVIOUS RESULTS

There have been several unsuccessful or partly successful attempts to measure the change of Curie point with pressure. A short description of each of these will

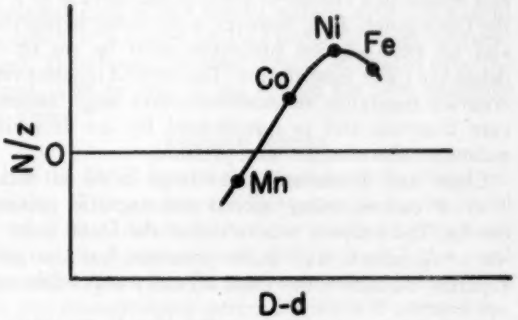

FIG. 3. Néel interaction curve.

[5] R. M. Bozorth, Bell System Tech. J. 19, 1 (1940).

[6] L. Néel, *Le Magnétisme* (University of Strasbourg, Strasbourg, 1939), Vol. 2, p. 65.

be given. Following this, a summary will be given of estimates of the change to be expected, based on the indications obtained from volume magnetostriction data and from estimates of the anomalous thermal expansion.

Measurements Using High Pressure

In 1931, Adams and Green[7] used the method which has been adopted for the present experiment; they used the sample as the core of a transformer and, with a constant small alternating current supplied to the primary, they measured the output of the secondary as a function of temperature. The drop in output at the Curie temperature is very sharp, and although it does not define the Curie point in the conventional way, the method is very satisfactory for finding a *change* in Curie point. Unfortunately Adams and Green could not obtain a stable temperature in their pressure apparatus. CO_2 was used as a pressure fluid, and there were strong convection currents set up in it by the internal furnace. Their results indicate an uncertainty in temperature of about 5°, and this masked all changes.

Steinberger[8] did not attempt to measure the change of Curie temperature but observed a change from ferro-

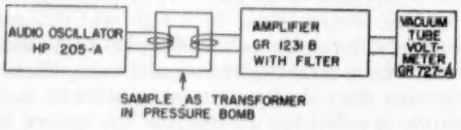

FIG. 4. Schematic diagram of experimental setup.

magnetic to paramagnetic for a 30Ni 70Fe alloy (weight percent) under pressure applied at room temperature. The great change was undoubtedly due to a change of Curie point, but Steinberger described it in terms of a change in permeability.

Michels *et al.*[9] have made measurements on two Monel alloys, using the change of slope of the resistance *vs* T curve as an indication of the Curie point. The ferromagnetic ordering lowers the resistance of a metal and results in a change of slope of the curve R *vs* T at the Curie point. This, however, is not sharp in practise, and an extrapolation procedure must be set up to define the Curie temperature. The method requires very accurate resistance measurements over large temperature intervals and is complicated by the fact that resistance also changes with pressure.

Ebert and Kussman[10] used large fields to obtain I *vs* T curves, using special nonmagnetic pressure bombs. The purpose was to define the Curie point in the conventional way under pressure; but the great experimental difficulties made accuracy impossible, and small changes could not be detected. In the alloy in which a large change was to be expected (30Ni 70Fe) the I *vs* T curve drops so slowly that the conventional method of defining the Curie point is not very useful. They decided that no change of Curie point had been observed, but Kornetzki[11] later reinterpreted their data and concluded that there had been a change of Curie point. A criticism of Ebert and Kussman's methods and conclusions has been given by Michels and de Groot.[12]

Predictions Based on the Reciprocal Effects

The predicted changes of Curie point with pressure are based on measurements of the thermal expansion anomaly or on measurements of volume magnetostriction. The latter cannot be carried out at high temperatures; thus they actually indicate the volume dependence of the magnetic interaction at the temperature at which they are carried out. This will be discussed under the results on Fe and Fe-Si alloys.

Slater[13] has used the Clapeyron equation as if the transformation from magnetic to nonmagnetic state were first order. The equation may be written $d\theta/dp = \Delta V/\Delta S$, in which θ is the Curie temperature. The volume change is estimated from the thermal-expansion anomaly, and the disordering entropy may be calculated, assuming dipoles with two orientations. Only order of magnitude is hoped for. For Ni, Slater has estimated an increase of Curie point with pressure of 0.05° per 1000 atmos.

If the transition is treated as second order, the corresponding Ehrenfest relation is $d\theta/dp = 3TV\Delta\alpha/\Delta C_p$ in which α is the linear coefficient of expansion and C_p the specific heat. These quantities do not show sharp discontinuities at the Curie point but an extrapolation method must be used. For Ni, Michels and de Groot[12] used average values of several determinations of $\Delta\alpha$ and ΔC_p and estimated the increase of Curie point with pressure to be 0.35° per 1000 atmos, which is in agreement with the result obtained in the present experiment. Ni was the only element for which sufficiently accurate experimental data were available.

In order to relate volume magnetostriction and change of Curie point with pressure, Kornetzki[14] has used the thermodynamic relation $(dV/dH)_p = -(dM/dp)_H$, where M is the total moment, and the assumption that the magnetization per gram, σ, is given by a relation of the form $\sigma = f(T/\theta)$. The relation derived from these is

$$\frac{1}{\theta}\frac{\partial\theta}{\partial p} = \frac{1}{T}\frac{\partial\omega}{\partial H} \Big/ \left(\rho\frac{\partial\sigma}{\partial T} - \frac{3\alpha}{K}\frac{\partial\omega}{\partial H}\right),$$

in which ω is the fractional change of volume, ρ the density, α the linear thermal expansion coefficient, and

[7] L. H. Adams and J. W. Green, Phil. Mag. **12**, 361 (1931).
[8] R. L. Steinberger, Physics **4**, 153 (1933).
[9] A. Michels *et al.*, Physica **4**, 1007 (1937); A. Michels and J. Strijland, Physica **8**, 53 (1941).
[10] F. Ebert and A. Kussman, Physik. Z. **39**, 598 (1938).
[11] M. Kornetzki, Physik. Z. **44**, 296 (1943).
[12] A. Michels and S. R. de Groot, Physica **16**, 249 (1950).
[13] J. C. Slater, Phys. Rev. **58**, 54 (1940).
[14] M. Kornetzki, Z. Physik **98**, 289 (1935).

K the compressibility. For Fe, Kornetzki made measurements of volume magnetostriction between 20°C and 100°C and predicted a decrease of Curie point with pressure of 5 to 10 deg per 1000 atmos.

III. EXPERIMENTAL PROCEDURE

Transformer Method

The experimental method used is similar to that of Adams and Green,[7] using the magnetic material as the core of a transformer, as demonstrated in Fig. 4, which shows the necessary equipment except for the pressure and furnace systems. The primary and secondary coils are wound on opposite arms of the picture frame sample so as to have very little direct coupling. The linkage is essentially through the sample only, and this fails at the Curie temperature.

A constant 1000-cy current is supplied to the primary, and the signal from the secondary is amplified, then measured as a function of temperature. The primary current was of the order of 0.1 amp, giving a magnetizing field of the order of 1 oersted; and the secondary voltage was amplified to about 10 v, then read on the vacuum-tube voltmeter.

The character of the output curve varies greatly from sample to sample but usually has the general features of Fig. 5. There is an inflection point between A and B and a very nearly linear portion in most cases from 90 percent of maximum output to 10 percent. If the maximum output remains the same under pressure, curves taken at different pressures are simply translated along the temperature axis by the amount of the change of Curie point, and this change is well defined even though the initial permeability curves are not used to define the Curie point itself. If the maximum output should change, a scale adjustment would have to be made before comparing the curves, and the interpretation would not be so simple. Fortunately no change over 10 percent in the maximum output under pressure ever occurred except in the two cases where it was difficult to get the sample in the usual form and Fe was used to complete the magnetic circuit. The initial permeability of Fe at room temperature is depressed by pressure, as was shown by Steinberger;[8] but near the Curie point the initial permeability seems to be unaffected by pressure.

The temperature range over which the drop from 90 percent of maximum output to 10 percent occurs is small in the elements (1.5° for Ni, as can be seen in Fig. 11); it is small in alloys if the Curie point does not depend much on the composition (as in 68 Permalloy); and it is small if the alloy is very homogeneous (as in Alumel, a fully annealed thermocouple wire). On the other hand Compensator alloy (70Fe 30Ni) is an example of a sample in which the drop occurs over a wide temperature range; nevertheless, the change under pressure is a simple translation along the temperature axis.

Measurements were made with different primary currents to verify that changes found were independent of the field. To detect irreversible effects, measurements were made with falling and with rising temperatures and after increases and decreases of pressure. No irreversible changes were found. Measurements were made at several pressures; within experimental error any changes were linear with pressure.

Pressure Equipment

In the application of pressure two separate sets of pressure equipment were used. One is designed to use a liquid as the pressure fluid, and the other is designed to use a gas; these will be referred to as the liquid system and the gas system.

A liquid system has been described by Bridgman.[15] It is used for temperatures up to 400°C, and the fact that an external furnace is used to heat the entire pressure bomb means that there is good temperature stability and a large gradient-free experimental region.

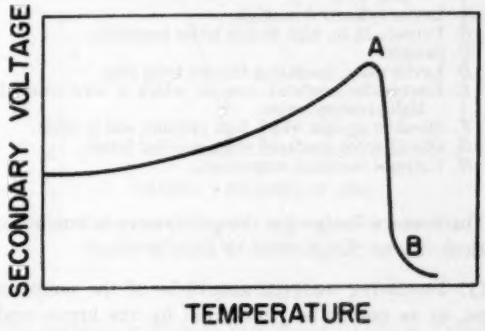

FIG. 5. General form of temperature dependence of voltage in secondary winding.

The gas system is used for higher temperatures (up to 1120°C). No liquid is known which will not decompose or react with other parts of the system at high temperatures; therefore an inert gas must be used, and argon has been found to be satisfactory. Also the hardened steel of the bombs softens with consequent rupture if it is heated for long periods at high temperatures. Therefore an internal furnace, insulated from the bomb, must be used. A gas system has been described by Yoder.[16]

Furnace Design

For the liquid system the whole bomb is heated externally. With an internal thermocouple it was found to be quite satisfactory to make measurements while allowing the temperature to drift at a rate of several degrees per hour. For Gd the bomb was cooled with dry ice, and measurements were made while it warmed up; this process took several hours.

[15] P. W. Bridgman, *The Physics of High Pressure* (G. Bel and Sons, London, 1949).
[16] H. Yoder, Trans. Am. Geophys. Union 31, 827 (1950).

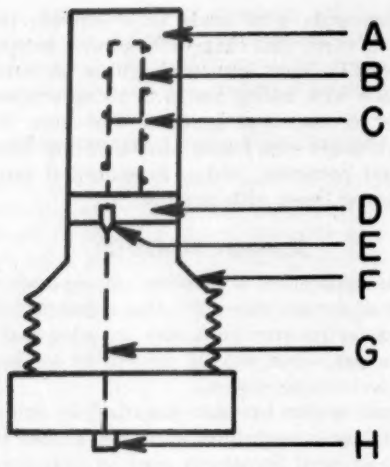

FIG. 6. Plug with furnace and insulation for gas system.

A. Lavite cylinder 3 in. high.
B. Furnace 2½ in. high within lavite insulation.
C. Sample.
D. Lavite plate, insulating furnace from plug.
E. Electrically insulated cone at which a wire enters the high-pressure region.
F. Shoulder against which high pressure seal is made.
G. One of seven insulated wires entering bomb.
H. External electrical connection.

The furnace design for the gas system is much more critical. Three things must be kept in mind:

(1) Insulating material should be of the nonporous type, so as not to be penetrated by the argon under pressure. Lavite was found to be very good. The heat loss is more than doubled if ordinary firebrick is used.

(2) Convection currents in the argon must be cut down to avoid high heat loss and to achieve stable temperatures. For this purpose, Yoder[16] used a horizontal bomb. With a vertical bomb, the closed top furnace shown in Fig. 6 was found to use only half the power of one which ran the whole length of the lavite cylinder *A*; and the temperature stability was greatly increased.

(3) All space should be filled. This makes it easier to reach high pressures and also cuts down the convection currents. Lavite was used not only between furnace and bomb (*A* and *D* in Fig. 6) but also within the fused quartz cylinder (*B* and *D* in Fig. 7) to fill space on both sides of the sample.

The heat capacity of the furnace is small and the heat loss is high under pressure so that it is difficult to hold the temperature constant. Two variacs were used to control the input voltage; the second, in conjunction with a step-down transformer, permitted fine adjustment (7.5-v full scale) and the temperature could be controlled by voltage adjustment so that the rate of drift was about 1° in 3 min; this was good enough to permit fairly accurate readings of temperature and secondary output.

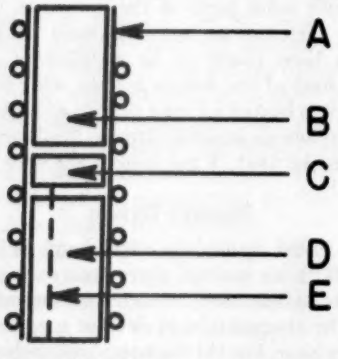

FIG. 7. Furnace with inner parts.

A. Fused quartz tube wound with 0.015 in. Pt wire.
B. Lavite cylinder above sample.
C. Ni ring surrounding sample.
D. Lavite cylinder below sample.
E. Electrically insulated wire from sample to cone.

Sample Design

In the liquid system the size of sample is limited only by the internal dimensions of the bomb itself as this region is a uniform temperature. In the gas system, however, the bomb is cool (about 100°C) so that only a small region at the center of the furnace is gradient-free, and the sample must be quite small. It consisted of two rings of the shape shown in Fig. 8, maximum diameter about ½ inch, held together by screws, and with the thermocouple wires between them. Total thickness is about 1/20 in. Mica rings of the same shape above and below provided insulation for the two windings, which were about 5 turns each of Chromel wire. This wire holds its shape well after being bent, and no cement was used. A nickel ring ¼ in. high (*C* of Fig. 7) which just fit into the quartz tube was used to surround the sample in order to smooth out the temperature gradients. This was separated from the sample by mica. When this assembly was placed at the hot spot of the furnace (*C* of Fig. 6), the sample was free of gradient, as could be verified by the sharp drop of secondary output at the Curie point. When the double-ring sample was placed in a temperature gradient, the drop occurred in two sections with a plateau at the halfway point. With no gradient in the sample, the temperature reading could be considered to be that of the sample, as the thermocouple wires then came out from

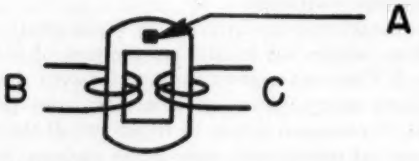

FIG. 8. Sample with windings.

A. Thermocouple junction between two rings.
B and *C*. Primary and secondary windings.

between the rings for about $\frac{1}{4}$ in. in a gradient-free region.

Temperature Measurement

For the liquid system it is convenient to have a thermocouple within the bomb, so that accurate measurements may be made while the temperature is drifting slowly. For the gas system an internal thermocouple is essential because of the large temperature gradients.

Birch[17] has investigated the effect of pressure on thermal emf, and the Chromel-Alumel couple was found to be independent of pressure within 10 microvolts as far as the calibration was carried (580°C and 4000 atmos). The entire path, including wire in the plug and the insulated cone (G and E in Fig. 6), must be of thermocouple wire. This is especially important in the gas system, as strong temperature gradients exist in just these places. It was found possible to obtain heavy Chromel and Alumel wire stock from which the cones were machined. However, there is still the problem that the complete circuit is made up of three different wires (the internal thermocouple, the cone, and the wire in the plug) and a perfect match of thermoelectric powers of these wires is impossible, so that a redistribution of gradients may look like a change of temperature. Such a redistribution does not occur in the liquid system when pressure is applied, but in the gas system the furnace power requirement doubles under pressure, and a redistribution of gradients is certainly to be expected. It was found that nearly all of the change in power requirement occurred between 1 and 400 atmos, and corresponding to this was an apparent Curie-point change of 2 or 3 deg. Hence measurements below 1000 atmos were not used. Measurements on Ni were made in both systems, and the results checked completely if data above 1000 atmos were used.

It should be emphasized that the precautionary measures are all for the purpose of measuring temperature *changes* under pressure. The Curie temperature itself does not enter into the experimental results and need not be known very accurately.

It will be noticed that measurements have been made using the thermocouple beyond its calibrated range; both temperature and pressure exceed the limits of Birch's calibration. The assumption is made that the thermoelectric power continues to be independent of pressure, but it would be desirable to have an extension of the calibration.

Pressure Measurements

Pressure measurements are made by finding the change in resistance of a Manganin wire gauge; this is the standard method and has been well calibrated.[18] The uncertainty (of about 0.1 percent) is insignificant in this experiment.

[17] F. Birch, Rev. Sci. Instr. **10**, 137 (1939).
[18] David Lazarus, Phys. Rev. **76**, 545 (1949).

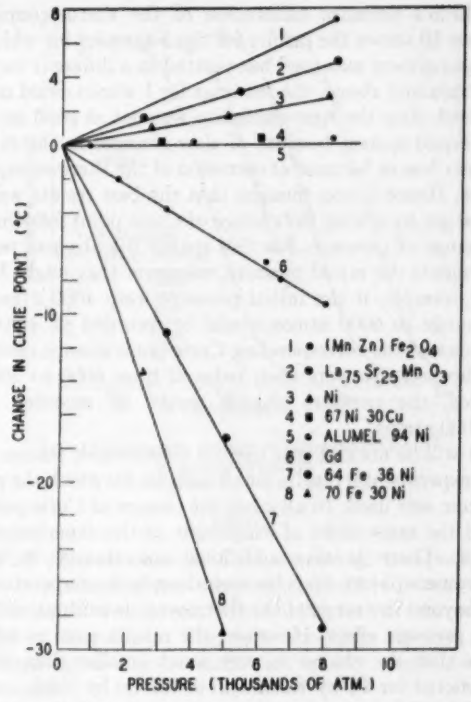
CHANGE IN CURIE POINT (°C)
PRESSURE (THOUSANDS OF ATM.)
1 • (Mn Zn) Fe2 O4
2 • La.75 Sr.25 Mn O3
3 ▲ Ni
4 ■ 67 Ni 30 Cu
5 • ALUMEL 94 Ni
6 • Gd
7 • 64 Fe 36 Ni
8 ▲ 70 Fe 30 Ni

FIG. 9. Change of Curie point *vs* pressure for 8 samples measured in the liquid system.

IV. RESULTS

The results are given in Figs. 9 and 10 and in Table I. Figure 9 shows the change in Curie point *vs* pressure for the 8 samples for which the liquid system was used. Consistent results are obtained in each case although the change is so small for Monel and Alumel that it is about the same order of magnitude as the uncertainty

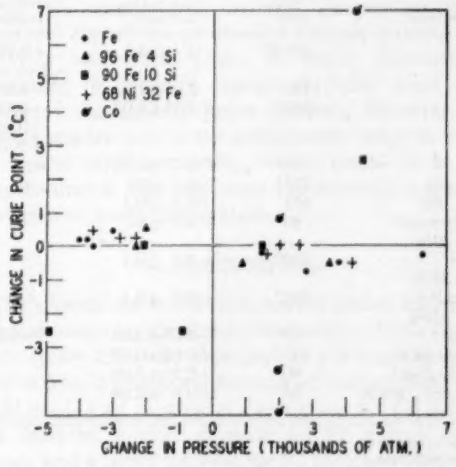

FIG. 10. Change of Curie point *vs* change of pressure for 5 samples measured in the gas system.

in Birch's pressure calibration of the thermocouple. Figure 10 shows the results for the 5 samples for which the gas system was used but plotted in a different way. As explained above, the readings for 1 atmos could not be used. Also the reproducibility was not as good as in the liquid system because of slow changes in the rate of heat loss or because of corrosion of the thermocouple wires. Hence it was thought that the best results were those got by noting the change of Curie point following a change of pressure. For this reason the abscissa zero represents the initial pressure, whatever that might be. For example, if the initial pressure were 4000 atmos, a change to 6000 atmos would be recorded as +2000 atmos and the corresponding Curie-point change noted. If the pressure were then reduced from 6000 to 2000 atmos, the pressure change would be recorded as −4000 atmos.

It will be noticed that there is considerable scatter of the experimental results for all samples for which the gas system was used. In all cases the change of Curie point is of the same order of magnitude as the experimental error. There is also additional uncertainty in the thermocouple readings because these high temperatures go beyond the range of the thermocouple calibration for the pressure effect. However, the results seem to indicate that the change is very much smaller than that predicted for Fe by Kornetzki or for Co by Néel.

Table I lists the change per 1000 atmos of all samples with an estimate of the experimental error based on the scatter in Figs. 9 and 10. This assumes a linear change of Curie point with pressure and does not include any error resulting from the effect of pressure on the thermocouple. More detailed information on the probable error can be obtained from the curves of output *vs* temperature for each sample at different pressures, but these are not reproduced here because of space limitations.

TABLE I. Change of Curie point with pressure.

Sample	Approx Curie temp	Deg change per 1000 atmos (+ indicates increase)	Predicted change
Fe	770°C	0 ±0.1	+0.79[a] −5 to −10[b]
Co	1120°	0 ±1	−4.6[a]
Ni	360°	+0.35±0.02	−0.13[a] +0.05[c] +0.35[d]
Gd	16°	−1.2 ±0.05	
96Fe 4Si	733°	−0.1 ±0.1	
90Fe 10Si	615°	+0.2 ±0.2	
Compensator	80°	−5.8 ±0.2	−5[b]
70Fe 30Ni Invar	210°	−3.6 ±0.1	
64Fe 36Ni Permalloy	606°	−0.1 ±0.1	
68Ni 32Fe Monel	50°	+0.07±0.03	+0.06[e]
Alumel 94Ni	143°	+0.04±0.02	
$Mn_1Zn_1Fe_2O_4$	90°	+0.9 ±0.04	
$La_{0.75}Sr_{0.25}MnO_3$	80°	+0.6 ±0.04	

[a] See reference 6.
[b] See reference 11.
[c] See reference 13.
[d] See reference 12.
[e] See reference 9.

Chemical Analysis of Samples

The Fe and Co were high purity samples obtained from the Institute's metallurgy section, and the Ni was a high purity sample (>99.9 percent) obtained from the Bell Telephone Laboratories. The Gd was prepared by A. Moskowitz under the direction of Dr. N. H. Nachtrieb, and the largest impurity shown by spectroscopic analysis was 0.1 percent Fe.

No chemical analysis was obtained for the commercial alloys Monel, Alumel, Invar, and Permalloy. The percentages shown in Table I are the usual percentages for these alloys.

The FeSi alloys reported as 96Fe 4Si and 90Fe 10Si were found to have 3.5 percent and 10.5 percent, respectively of Si. The ferrite was found to be represented approximately by the formula $Mn_1Zn_1Fe_2O_4$ (the Mn was 3 percent short, and the Zn was 5 percent short). The Compensator alloy contained 29.7 percent Ni. The formula $La_{0.75}Sr_{0.25}MnO_3$ represents the proportions which went into the preparation of this sample—no analysis was made subsequently.

Discussion of Results

Fe and Fe-Si Alloys

Fe is of special interest because of the decrease of Curie point with pressure of 5 to 10 deg per 1000 atmos predicted by Kornetzki, using volume magnetostriction measurements made between 20°C and 100°C. Smoluchowski[19] has also treated this problem, and he calculated the volume dependence of the Weiss constant from the same data. His calculations are $N^{-1}dN/d\omega = 44.1$ at 20°C and $N^{-1}dN/d\omega = 32.2$ at 100°C, a marked decrease with rising temperature. If one takes the point of view that interatomic distance D is the important factor and that the decrease of volume dependence with temperature is due to thermal expansion, then the conclusion is that the interaction curve rises sharply at the room temperature value of D in Fe but has reached the top of the curve at 770°C, for which D is about 1 percent greater—hence no change of Curie point with pressure in the present experiment. If this is so, a large decrease of Curie temperature could be obtained with a pressure of 50 000 atmos, which would reduce the lattice constant to its room temperature value.

Because 50 000 atmos is not available, the experiment was carried out on two Fe-Si alloys. Si reduces the lattice parameter of Fe and magnetically appears to act as a diluent, leaving the magnetic moment of the Fe atom unchanged up to about 5-percent Si by weight. The Curie point is lowered, and the combination of reduced D and lower Curie point results in a value of D

[19] R. Smoluchowski, Phys. Rev. **59**, 309 (1941); R. Smoluchowski, Phys. Rev. **60**, 249 (1941).

at the Curie point of the 10-percent Si alloy which is very nearly that of pure Fe at 20°C. If interatomic distance is the important parameter in magnetic interaction, a large decrease of Curie point with pressure should have been observed in the 10-percent Si alloy, in view of the volume dependence shown by the magnetostriction data.

Cobalt

The result for Co (no change with pressure) is in contradiction to the prediction of Néel (a decrease of 4.6° per 1000 atmos). However, the temperature of 1120°C is far beyond the 580°C to which the pressure calibration of the thermocouple was carried; therefore, the result cannot be regarded with the same certainty as those for the other samples.

Nickel

Although here again the result differs from Néel's prediction, there is rough agreement with predictions based on the volume magnetostriction and on the thermal expansion anomaly. Ni satisfies all the requirements for good experimental accuracy. The Curie temperature is low enough so that the liquid system may be used, the drop in output occurs within 2°, and there is no significant change in permeability under pressure. Figure 11 shows the output curves for several pressures.

Gadolinium

For this element the generalized interaction curves must predict an increase with pressure rather than the observed decrease. The inner incomplete shell is in this case the $4f$ shell with 7 electrons (a half-filled shell), and its small size results in a greater ratio of D/d and a greater value of $D-d$ than for any of the transition metals Fe, Co, or Ni.

Compensator Alloy

This is similar to the alloy which Steinberger reported as becoming paramagnetic under pressure (at room temperature). Kornetzki also predicted a decrease of about 5° per 1000 atmos from volume magnetostriction measurements, which agrees with the results found here.

Some doubts about the effect of phase change in this system had been expressed.[20] However the changes with pressure were found to be instantaneous and reversible and proportional to the applied pressure; hence, a phase change cannot be responsible. X-ray powder pictures showed that the sample was in the 2-phase region; the amount of body-centered (α) phase was estimated to be about 5 or 10 percent.

[20] R. M. Bozorth, *Ferromagnetism* (D. Van Nostrand Company, Inc., New York, 1951), p. 726.

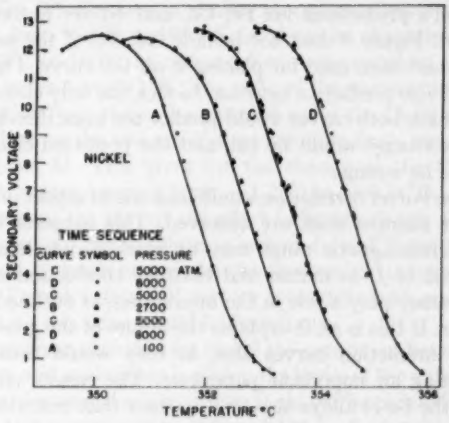

FIG. 11. Secondary voltage *vs* temperature for Ni at several pressures.

Invar

This alloy is close to Compensator in composition but is a single phase alloy (f.c.c.). The decrease of Curie point with pressure is smaller but of the same order of magnitude. The very abnormal thermal expansion gives a good indication of the result to be expected.

Permalloy

This is another Fe-Ni alloy, but one of the composition having scarcely any thermal expansion anomaly. Hence the negligible change of Curie point with pressure was to be expected.

Monel

The change here is in agreement with that found by Michels *et al.*

$La_{0.75}Sr_{0.25}MnO_3$

For this ceramic-type material (perovskite crystal structure) Zener[21] has proposed a formula relating conductivity and Curie point. It would therefore be interesting to compare change of Curie point with change of conductivity under pressure. However, the formula applies only in the temperature range in which the conductivity is metallic, which would be at low temperatures in this case since the material is a semiconductor at room temperature.

V. CONCLUSIONS

The generalized interaction curves shown in Figs. 2 and 3 are not consistent with the results of this experiment. Apart from the objection to plotting the Curie point in Fig. 2 which was mentioned earlier, this curve would predict an increase of Curie point for Gd instead of a decrease, a large decrease for Fe instead of no change, and a larger increase for Ni than was observed.

[21] C. Zener, Phys. Rev. 82, 403 (1951).

Néel's predictions for Fe, Co, and Ni are not confirmed. Figure 3 does not include Gd, but if the same rules had been used for placing it on the curve, Fig. 3 would also predict an increase. In fact, the only element for which both curves would predict the same direction of the change would be Gd, and the predicted change would be wrong.

The Forrer correlation would lead one to expect much larger changes than are observed. This suggests that the ferromagnetic range may be much wider than 10 percent of D in metals and that the conduction electrons may play a role in the interaction, as outlined by Zener. If this is so, it explains the failure of the generalized interaction curves also, as they would then be omitting an important parameter. The results on Fe and the Fe-Si alloys also tend to show that interatomic distance is not an all-important parameter.

One may still suppose that the interaction curve for a single element takes the form of Fig. 1. The fact that some large decreases of Curie point with pressure have been found but no large increases suggests that there may be a steep rise of the interaction curve as it crosses over from the antiferromagnetic region but only a gradual fall at large D. This is supported by the fact that there are no large values of negative volume magnetostriction reported nor large positive thermal expansion anomalies.

VI. ACKNOWLEDGMENTS

The writer wishes to thank his sponsor, Dr. A. W. Lawson, for advice and discussions of the problem.

Thanks are due various people for samples and assistance in the preparation of samples. Dr. R. M. Bozorth of the Bell Telephone Laboratories supplied three of the samples. Dr. N. H. Nachtrieb and Mr. A. Moskowitz prepared the Gd and perovskite samples. Mr. K. K. Ikeuye and Mr. E. Selmanoff prepared the FeSi alloy and gave assistance with other samples. Mr. N. D. Nachtrieb and Mr. K. Lindholm assisted in preparing a number of samples.

This research was supported in part by the U. S. Office of Naval Research.

PHYSICAL REVIEW VOLUME 93, NUMBER 3 FEBRUARY 1, 1954

The Influence of Pressure on the Curie Temperature of Iron and Nickel*

R. SMOLUCHOWSKI
Carnegie Institute of Technology, Pittsburgh, Pennsylvania
(Received October 26, 1953)

A comparison is made between Patrick's measurements of the change of Curie temperature under pressure and theory based on a Brillouin function. The agreement is fair.

THE usual assumption in the molecular-field theory of magnetism is that the saturation magnetization at absolute zero is independent of volume. An alternate procedure[1,2] based on the Brillouin function and on experimental volume magnetostriction data gives explicit values for N, the volume dependent field constant, and for I_0, the volume dependent saturation magnetization at absolute zero. The agreement with experimental data such as specific heat and with some magnetocaloric effects is satisfactory for coupled pairs of spins ($j=1$). Up until now there were no data available for comparing the predicted influence of pressure on the Curie temperature with experiments. The recent very interesting results obtained by Patrick[3] make such a comparison between experiment and theory possible.

This comparison can be made in several ways depending upon which of the necessary extrapolations seems to be most reliable. One of them is to use the formula

$$\frac{1}{\theta}\frac{\partial\theta}{\partial\omega}=\frac{1}{N}\frac{\partial N}{\partial\omega}+\frac{1}{I_0}\frac{\partial I_0}{\partial\omega}, \tag{1}$$

in which $\partial\omega$ is the relative change of volume dV/V. Using, in the right side of (1), the values (for $j=1$) given in reference 2, one obtains -1.7 at room temperature for nickel and $+21.2$ at 100°C for iron. These are the highest temperatures for which volume magnetostriction data are available. Since compressibility at the Curie points is not known, one has to use room temperature values which give for the relative decrease of volume at 1000-atmos pressure 0.55×10^{-3} and 0.6×10^{-3} for nickel and iron, respectively. One obtains thus for the change of the Curie temperature of nickel the value $+0.57$ deg and the value -13.3 deg for iron as compared with the observed $+0.35\pm0.03$ and 0 ± 0.2, respectively. The comparison for nickel, in view of the many assumptions and extrapolations, is fair whereas for iron it appears to be off by two orders of magnitude. It should be observed, however, that the above calcu-

* This work was supported by a U. S. Atomic Energy Commission contract.
[1] R. Smoluchowski, Phys. Rev. 59, 309 (1941).
[2] R. Smoluchowski, Phys. Rev. 60, 249 (1941).
[3] L. Patrick, this issue [Phys. Rev. 93, 384 (1954)].

lation actually gives the pressure effect for a density corresponding to about room temperature and not for the density at the Curie temperature. For nickel the variation of N with temperature and with volume is very small, and thus an extrapolation to the rather low Curie temperature is good. For iron, N changes with temperature and with volume one to two order of magnitude faster than for nickel, and the extrapolation to the rather high Curie temperature is naturally quite poor. This can also be seen from the rapid decrease of $N^{-1}\partial N/\partial\omega$ with increasing temperature which indicates a pressure effect which decreases rapidly with decreasing density in spite of a certain parallel increase of compressibility. Actually the absence of a measurable effect for iron is in agreement with a reasonable extrapolation of the low temperature values as obtained by means of formula (1).

Another way to compare the theory with experiment is to calculate explicitly the Curie temperatures using the formula

$$\theta=\frac{j+1}{3j}\frac{I_0N}{k}(jg\mu_B), \tag{2}$$

and substituting the values for I_0 and N from Tables I and II in reference 2. This procedure has the advantage that it avoids to a certain extent the difficulties of the previous calculation, but, on the other hand, it has the obvious drawback that the uncertainty of the absolute values of I_0 and N is much greater than the rather small uncertainty of their volume dependence used in Eq. (1). For nickel one obtains the values (at constant volume) $\theta_v=668.6$ and 667.6°K for the 0°C and 20°C densities as compared with the constant pressure value $\theta_p=631$°K. The total thermal expansion of nickel from 0 or 20°C up to the Curie temperature is about 28 times larger than the change of volume under 1000 atmos, and thus one gets an increase of the Curie temperature by 1.3°C which is reasonably close to that predicted by Eq. (1). For iron, a similar procedure gives a range of θ_v from 980°K to 1060°K for densities characteristic of 20°C to 100°C as compared with the constant pressure value $\theta_p=1047$°K. The ratio of the volume change resulting from thermal expansion up to the Curie temperature to the volume change resulting from pressure is about 55. This gives for the change of the Curie point values ranging from −1.2°C to +0.24°C. The reversal of the sign of the effect indicates clearly that, as expected, the absolute values of I_0 and N for iron are not accurate enough for the purpose of comparison with Patrick's data and that an agreement with experiment on this basis would be fortuitous.

It appears thus that for nickel the agreement between theory and experiment is within the limits of the validity of the theoretical assumptions. It should be pointed out that this agreement is obtained for $j=1$ whereas the alternative assumption $j=\frac{1}{2}$ would lead to a wrong sign and an effect fifteen times too big. As is well known, this model of coupled spins applies well to saturation magnetization of nickel near room temperature and to the paramagnetic region.[4] For iron a quantitative comparison encounters serious difficulties although, qualitatively, the theory is in accord with the smallness of the observed effect. In this case there is only a slight preference for the assumption $j=1$. Although this very simple model of isolated elementary magnets applies so surprisingly well to pure metals, its validity for alloys is questionable. These would require a more advanced theory based either on the Slater approach[5] or on other treatments in which a more detailed picture of the electronic configurations and interactions is used. New data on the volume magnetostriction, admittedly difficult to measure, at various temperatures would be of great value for the theory.

[4] R. Becker and W. Döring, *Ferromagnetismus* (J. Springer, Berlin, 1939).

[5] J. C. Slater, Phys. Rev. **36**, 57 (1930); **49**, 537 (1936); **58**, 54 (1940).

Paramagnetic Resonance Absorption of Carbazyl and Hydrazyl*

C. KIKUCHI,† *Brookhaven National Laboratory, Upton, New York and Michigan State College, East Lansing, Michigan*

AND

V. W. COHEN, *Brookhaven National Laboratory, Upton, New York*

(Received October 9, 1953)

The paramagnetic resonance spectra of single crystals of carbazyl and hydrazyl show distinct anisotropies, which appear to be associated with the microscopic magnetic susceptibility within the molecule in the vicinity of the unpaired electron. This leads to an asymmetry in the absorption line of a polycrystalline specimen. The hyperfine structures of the two radicals in a benzene solution show that in carbazyl the two N atoms are nonequivalent in that the odd electron spends approximately twice as long in the vicinity of one, compared to the other.

SINCE the discovery of the phenomena of paramagnetic absorption of free radicals in 1949,[1] these compounds have attracted considerable interest for two principal reasons. In the first place, they offer a means of making precision magnetic field measurements in regions in which nuclear resonance methods cannot be used conveniently; in the second place, they offer a means of exploring certain aspects of electromagnetic interactions in atoms, ions, and molecules, that cannot be determined adequately by other methods. In the present report we shall be concerned only with the latter aspect. A preliminary report of our investigations on the absorption properties of two closely related free radicals, α,α-diphenyl-β-picryl hydrazyl and picryl-*n*-amino carbazyl was given earlier.[2] In the present paper, a more detailed report of our results will be presented in order to see in what ways molecular structure affects the absorption properties of free radicals.

I. THEORY

The reason for the absorption of microwaves by free radicals arises from the fact that these compounds possess unpaired electrons. These electrons are essentially microscopic magnetic probes, with which the magnetic field inside of molecules can be explored. When a molecule of a free radical is placed in a steady magnetic field, its unpaired electron may assume either parallel or antiparallel orientations with respect to the applied magnetic field. If, for the moment, the internal magnetic field is neglected, the energies associated with the parallel and antiparallel orientations are $+\frac{1}{2}g\beta H$ and $-\frac{1}{2}g\beta H$, respectively, where β is the Bohr magneton and H the applied magnetic field. If now an oscillating magnetic field is applied at right angles to the steady field, a large number of electrons will undergo spin reorientation. The condition for this is given by

$$h\nu=\Delta E=E_+-E_-, \tag{1}$$

where $E_\pm$ are the eigenvalues of the operator

$$\mathcal{H}=g\beta\mathbf{S}\cdot\mathbf{H}, \tag{1'}$$

ν the frequency of the oscillating field, and ΔE the separation of the two magnetic states. The spectroscopic splitting factor, or the g factor, is then defined by

$$g\equiv h\nu/\beta H. \tag{2}$$

For free electrons, this value is known to be 2.0023. For electrons in molecules, however, there may be a small but measurable deviation from the free electron g value.

In molecules, however, the internal magnetic field is not necessarily zero. It is customary, however, to define the g value as given by Eq. (2). Since the deviation of the g value from that of the free electron may be ascribed to internal magnetic fields, the deviation may be taken as a measure of the internal magnetic field, i.e.,

$$g=g_e+\Delta g, \tag{3}$$

where g_e is the free electron g value. The quantity Δg may depend upon a number of different factors, such as the nuclear and molecular magnetic fields, the crystal orientation, and even the applied magnetic field. To take these various possibilities into account we shall rewrite the resonance condition, given by Eq. (1'), in the form

$$\mathcal{H}'=\beta\mathbf{S}\cdot\mathbf{g}\cdot\mathbf{H}, \tag{4}$$

where $\mathbf{S}$ and $\mathbf{H}$ are the electron spin operator and the applied magnetic field respectively, and $\mathbf{g}$ the so-called g tensor of rank two. This tensor may be related to the microscopic susceptibility χ by the relation

$$\mathcal{H}'=g_e\beta\mathbf{S}\cdot(\mathbf{I}+4\pi\chi)\cdot\mathbf{H}. \tag{4'}$$

II. EXPERIMENTAL PROCEDURE

The free radical specimen to be investigated is placed in a cylindrical transmission cavity as shown in Fig. 1. This is 17 mm in length and in diameter, operating in the TE_{011} mode. In this mode, the electric and the

* Work performed at Brookhaven National Laboratory under the auspices of the U. S. Atomic Energy Commission.

† Present address—Naval Research Laboratory, Washington, D. C.

[1] Holden, Kittel, Merritt, and Yager, Phys. Rev. **77**, 147 (1949). C. H. Townes and J. Turkevich, Phys. Rev. **77**, 148 (1949).

[2] Cohen, Kikuchi, and Turkevich, Phys. Rev. **85**, 379 (1952).

transverse magnetic fields vanish along the axis, while the longitudinal magnetic field, which causes the electron to flip over, is a maximum at the center and falls off sinusoidally toward the top and bottom of the cavity. The sample under study is mounted upon a quartz rod which extends axially into the center of the cavity. According to this arrangement, it is possible to rotate the sample about an axis along the cylinder axis. The cavity is placed between the poles of the magnet, in such a way that the oscillating magnetic field vector is at right angles to the steady field. With this arrangement, the steady field produces a splitting of the electron energy levels and the oscillating field causes the electron to make transitions from one magnetic substate to another. These transitions will occur, if the resonance condition is satisfied. Such transitions are accompanied by an absorption of energy of $h\nu$ by the electron, which in turn results in the attenuation of the transmitted microwave power.

A block diagram of the experimental arrangement is shown in Fig. 2. Microwave power is furnished by 2K33A klystron. The detector crystal A is used with a wave meter to measure frequency. The cavity is coupled to the wave guide at each side with iris holes. The output crystal signal is fed either directly to an oscilloscope or through an intermediate vacuum tube voltmeter used as an audio-amplifier. The "Q" of the cavity is about 10 000.

The magnet is powered by dc using a constant voltage transformer, a "Variac," a full-wave selenium rectifier, an L-C filter, and a variable rheostat. For occasional use, where high stability is required, a high-capacity 130-volt storage battery is floated across the filtered dc.

The klystron frequency of approximately 23 050 Mc/sec was kept as constant as possible with manual stabilization. The magnetic field was modulated with 60-cps ac adjustable up to 80 gauss. The oscilloscope sweep was synchronized to the same 60-cps line. The oscilloscope then displayed the microwave absorption as a function of field over the range of the field modulation.

It should be pointed out that despite the simplicity of the electronic system and absence of a specially designed low-noise amplifier, a good signal was displayed from a sample of approximately 10^{-8} mole of carbazyl.

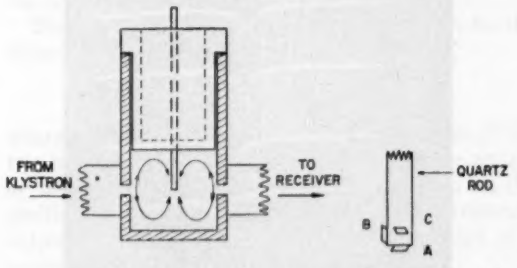

FIG. 1. Cavity and crystal orientations. The specimen being investigated is placed at the center of the cavity. To rotate the crystal about the three mutually perpendicular axes, A, B, and C, the crystal was mounted on the quartz rod as shown in the inset.

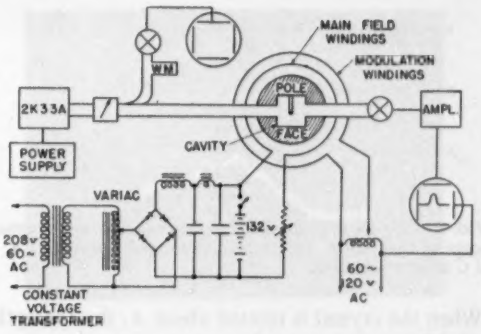

FIG. 2. Schematic arrangement of the apparatus.

III. CRYSTALLINE ANISOTROPY OF PICRYL-*N*-AMINO CARBAZYL[3]

The absorption of a polycrystalline sample of this free radical is a line about 7 gauss broad showing marked structure, in which the components shift rapidly as the sample is rotated. The absorption spectrum of a single crystal, however, is a single narrow line whose width is about half a gauss but whose position depends upon the crystal orientation. When a polycrystalline sample of hydrazyl is simultaneously mounted on the quartz rod, the carbazyl pip is observed to move from one edge of the hydrazyl line to the other as the quartz rod is rotated. Furthermore, for a certain orientation, the absorption pip of carbazyl is stationary. For this orientation, the carbazyl pip coincided with the center of the polycrystalline hydrazyl pip. Consequently, for our investigations, the stationary carbazyl g value was taken as 2.0036. All measurements were made relative to this value.

When examined under the microscope, the carbazyl crystal is seen to be triclinic, with a broad face and a long edge. A typical specimen had the dimensions 0.2 mm×0.2 mm×0.1 mm.[3] An axis normal to the broad face was designated as the A axis, the one parallel to the long edge, the B axis, and the one perpendicular to both A and B, the C axis. To rotate the crystal about these mutually perpendicular axes, the crystal was mounted on the quartz rod with a spot of stopcock grease as shown in Fig. 1. For example, to rotate about the A axis, the broad face of the crystal was placed against the end of the rod. Furthermore, in order to facilitate relative measurements, a second crystal was mounted on the quartz rod. This was oriented so that its pip did not move as the quartz rod rotated. All operations involving the selecting, mounting, and orienting of the crystals were carried out under a binocular stereomicroscope.

[3] Synthesized by J. Turkevich, Department of Chemistry, Princeton University, Princeton, New Jersey.

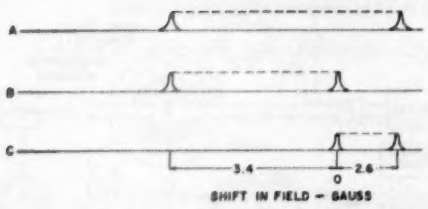

FIG. 3. The pips indicate the extreme positions of the carbazyl absorption line when the crystal is rotated about the A, B, and C axes, respectively.

When the crystal is rotated about A, the absorption pip is observed to move from one side to the other of the stationary pip, the extreme positions corresponding to -4.2 and 1.8 gauss, respectively. For orientation B, on the other hand, the absorption pip remains on one side, and for orientation C, on the other side of the stationary pip. These results are given schematically in Fig. 3. The behavior of the absorption pip with respect to the stationary one is illustrated by the oscilloscope traces given in Fig. 4. In Fig. 5, the dependence of the resonance pip upon the angle of orientation is given. It is observed that the resonance pip follows the $\cos^2$ law, as is to be expected for a tensor of rank 2.

IV. CRYSTALLINE ANISOTROPY IN α, α DIPHENYL-β-PICRYL HYDRAZYL[4]

The crystalline effects observed in carbazyl prompted us to look for similar effects in hydrazyl. An examination

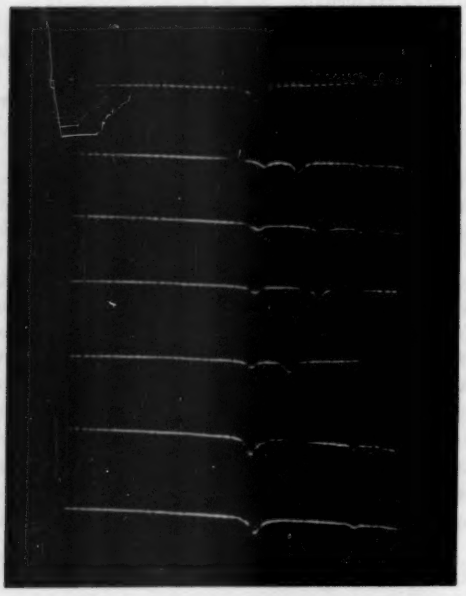

FIG. 4. Paramagnetic resonance absorption of carbazyl and hydrazyl.

[4] Presented to us by S. Liebson and M. Garstens, Naval Research Laboratory, Washington, D. C.

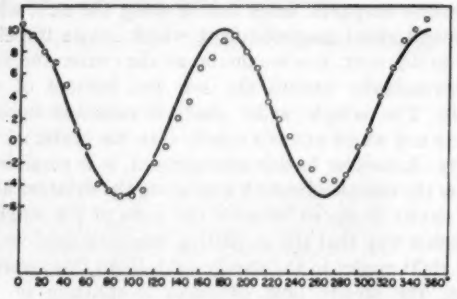

FIG. 5. Angular dependence of absorption pip when a carbazyl crystal is rotated about the A axis. The solid line is the plot of $5\ (3\cos^2\theta-1)$.

of the line shape of hydrazyl revealed that it is asymmetric, as is the case for polycrystalline carbazyl. Subsequently, our efforts were directed towards growing crystals of hydrazyl of the appropriate size. This was achieved by dissolving hydrazyl in carbon disulfide or carbon tetrachloride and permitting the solvent to evaporate slowly. It was possible in this manner to grow crystals a few millimeters in length and a few tenths of a millimeter in width. Microscopic examination of these crystals revealed that the external crystal symmetry is similar to that of carbazyl.

The investigation of the crystalline effect was carried out in a manner discussed above. However, because of the greater line width, amounting to about 1.5 gauss, it was necessary to use a somewhat larger crystalline sample. Typical behavior of the absorption pip as the crystal is rotated is shown in Fig. 6. Figure 7 shows the angular dependence of the g value for the hydrazyl. The total angular variation of the g value is smaller

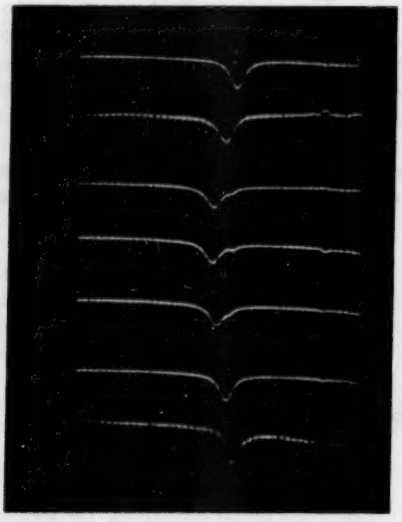

FIG. 6. The oscilloscope traces, taken at 30° intervals show the effect of rotating a hydrazyl crystal about the B axis.

than for carbazyl, amounting to 3.6 gauss for orientation A, as compared with the value 6 gauss for carbazyl.

V. HYPERFINE STRUCTURES OF CARBAZYL[5] AND HYDRAZYL

The hyperfine structure absorption spectra for both hydrazyl and carbazyl, dissolved in benzene, are presented in Fig. 8. In order to obtain these results, the signal from the rectifying crystal was amplified by a Ballantine ac voltmeter and then fed into the oscilloscope. For hydrazyl, a 1/320 molar solution was prepared by dissolving a known weight of hydrazyl into a known volume of benzene. This solution was placed in a small quartz tube and inserted axially into the cavity. The volume of the solution was about 0.050 cc and the total amount of hydrazyl was estimated at 10^{-7} mole. When the hydrazyl concentration was further reduced by dilution, the intensities of the hyperfine components were reduced but there was no observable change in the structure. Similar investigations were carried out for carbazyl. However, because of the limited supply of this compound, its concentration was estimated visually by comparison with known hydrazyl solutions.

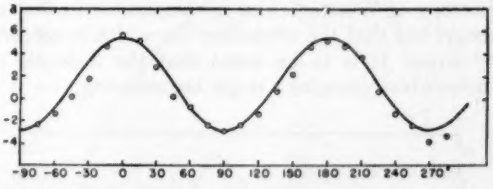

FIG. 7. Angular dependence of hydrazyl absorption pip when a crystal is rotated about the A axis. The solid line is the plot of $2.8\ (3\cos^2\theta-1)$.

The striking difference in the structures of the two spectra can be readily accounted for in terms of the times that the electron spends on the two nitrogens. As has been pointed out by Hutchison *et al.*,[6] the structure for the hydrazyl spectrum is explained by assuming that the unpaired electron spends nearly equal times at the two nitrogens. In carbazyl, on the other hand, the electron appears to spend about twice as much time on one nitrogen as compared to the other. In both cases the $\mathbf{I}_1\cdot\mathbf{I}_2$ interaction is negligible.

The magnetic interaction term giving rise to the hyperfine structure is of the form

$$\mathcal{H}=g\beta\mathbf{S}\cdot\mathbf{H}+a_1\mathbf{I}_1\cdot\mathbf{S}+a_2\mathbf{I}_2\cdot\mathbf{S},$$

where $\mathbf{I}_1$ and $\mathbf{I}_2$ are the nuclear spin operators of the two nitrogens, and a_1 and a_2 depend upon the square of the s-state wave function of the electron at the position of the two nuclei. In general, for arbitrary values of a_1 and a_2, the spectrum should consist of 9

[5] H. S. Jarrett has also investigated the hfs of carbazyl. See J. Chem. Phys. **21**, 761 (1953).

[6] Hutchison, Pastor, and Kowalsky, J. Chem. Phys. **20**, 534 (1952).

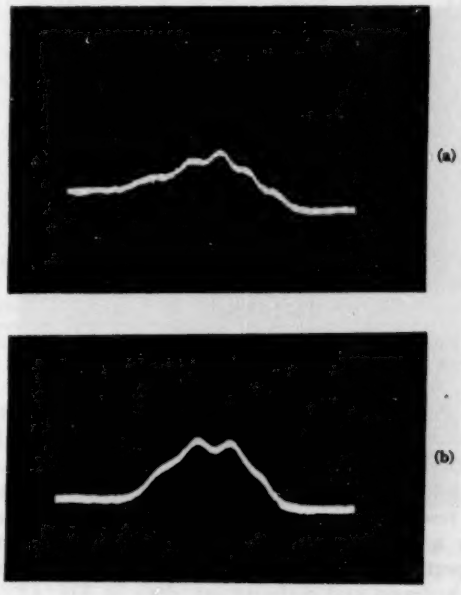

FIG. 8. The hyperfine structure absorption spectra of (a) hydrazyl and (b) carbazyl. The separation of the two main peaks in carbazyl is about 5/4 of the component separation in hydrazyl.

components. This can be seen readily by taking a vertical section of the plot given in Fig. 9. The abscissa a_2/a_1 is a measure of the nonequivalence of the two nitrogens. However, for the particular value of $a_2/a_1=1$ some of the components will coalesce, giving a spectrum of 5 lines with relative intensities, 1:2:3:2:1. Also, for $a_2/a_1=2$, the spectrum should consist of 7 components with the relative intensities 1:1:2:1:2:1:1. The calculated spectral contours for the cases $a_2/a_1=1$ and $a_1/a_2=2$ are given in Figs. 10 and 11, respectively. For the case of hydrazyl the ratio of the line half-width to the component separation was adjusted to give a plot as nearly resembling the experimental spectrum as possible. From a comparison of the two spectra, the peak-to-peak separation of hydrazyl to that of carbazyl

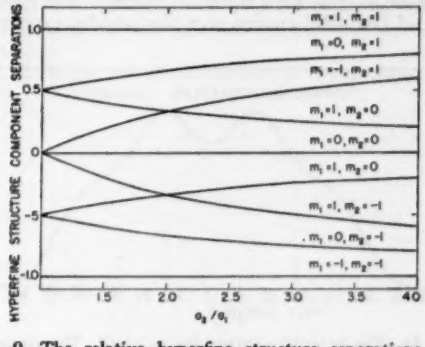

FIG. 9. The relative hyperfine structure separations to be expected for various degrees of nonequivalence of the two nitrogens.

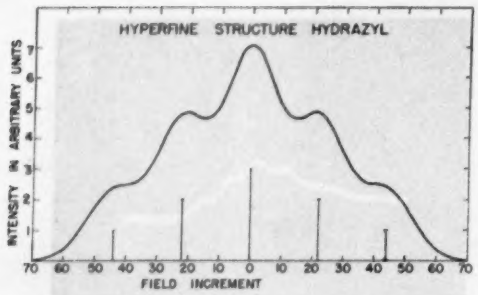

FIG. 10. The line shape expected for $a_2/a_1=1$. The vertical lines indicate the position of the hyperfine structure components. The line width and spacing scale factor were adjusted to give a contour resembling the hydrazyl spectrum.

was found to be 4:5. From these results, and further assuming that $a_2/a_1=2$, the plot given in Fig. 11 is obtained.

As will become clearer in the discussion to follow, the resonant structures of the free radicals appear to play a prominent role in determining the absorption properties of these compounds. The structural formulas for hydrazyl and carbazyl are given in Fig. 12. The main difference between these two is the additional bond connecting the phenyl groups in the case of carbazyl. This has the effect of increasing the number of resonance structures. Thus, it is reasonable to suppose that the unpaired electron spends more time on the nitrogen adjacent to the amino group. A way to test this would be to synthesize carbazyl with another isotope of nitrogen, N^{15}, in a known position.

VI. DISCUSSION

As we have indicated earlier, a conspicuous feature of the absorption lines is its asymmetry. This asymmetry can be readily accounted for by the crystalline anisotropy as discussed previously. If one assumes that the absorption line observed is a statistical summation of many lines because of randomly oriented crystallites, one obtains curves shown in Figs. 13 and 14 for hydrazyl and carbazyl, respectively. The dotted curves give the profiles to be expected if the crystallite line width is zero, and the solid curves give the profiles expected if the line widths are assumed to be 1.5 and 0.5 gauss for hydrazyl and carbazyl, respectively. It is difficult to compare these results with experimental curves because the specimens that were used were not large enough to average statistically over all crystallites. In the specimens that were investigated, the absorption lines showed irregularities, which changed when the sample was rotated. Figure 15 shows the profile of Wurster's blue. It is seen that this spectrum is also slightly asymmetric. The small pip appearing on the shoulder and in the wing is caused by a small crystal of carbazyl. From the motion of the carbazyl pip, we infer that the anisotropy of Wurster's blue is comparable to that of carbazyl but that the crystallite line width is appreciably larger. It is to be noted that the molecule of Wurster's blue contains a single benzene ring.

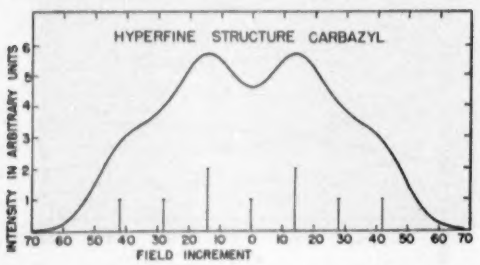

FIG. 11. The spectral contour for $a_2/a_1=2$. The component separation is taken to be $\frac{1}{2}$ that of hydrazyl. The component line widths are the same.

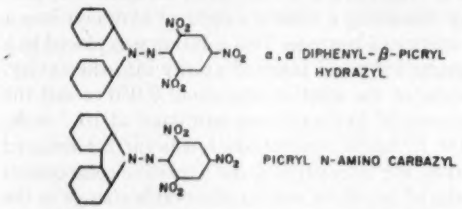

FIG. 12. Structural formulas of (a) α, α-diphenyl-β-picryl hydrazyl and (b) picryl-n-amino carbazyl.

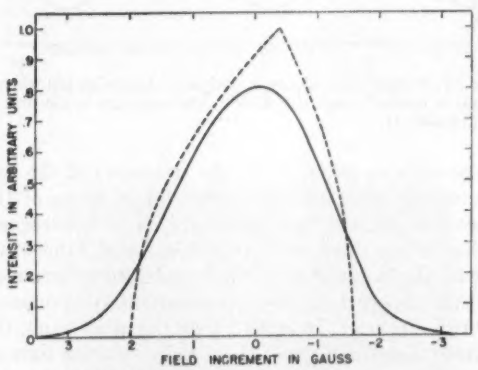

FIG. 13. Calculated line shape for polycrystalline hydrazyl. The dotted curve gives the expected line shape, if the crystallite line width were zero. The solid curve is obtained by assuming Gaussian shaped crystallite line of 1.5-gauss half-width.

These results lead one to suspect that perhaps the crystalline anisotropy is somehow attributable to the benzene ring. It seems reasonable, then, to suppose that the crystalline anisotropy is the result of the anisotropic microscopic susceptibility of the benzene ring. It was, therefore, anticipated that the anisotropies would be field-dependent. Measurements[7] carried out at a fre-

[7] These measurements were carried out in cooperation with G. Fraenkel and J. M. Hirshon of the Department of Chemistry, Columbia University, New York, New York.

quency of 9400 Mc/sec, showed the maximum anisotropy of carbazyl to be 2.4 gauss. The computed value, assuming a strict proportionality of the anisotropies to the applied magnetic field, is 9.4/23=2.45 gauss. A similar result has been observed for hydrazyl giving a maximum anisotropy in the X band of about 1 gauss.

It has been noted that the difference in the number of resonance structures of hydrazyl and carbazyl may have a profound effect upon their hyperfine structure. It is also possible that resonance structures affect the absorption line widths. The line width of carbazyl is considerably narrower than that of hydrazyl. According to Pauling, the stability of the free radicals is attributed to the large number of possible sites within the molecule for the unpaired electron. Thus, it is possible to think of the electron as 'hopping' at random from one molecular site to another. This would give rise to a motional narrowing of the line width, analogous to the

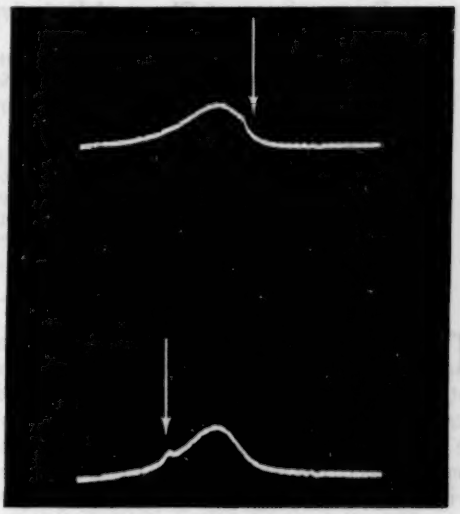

FIG. 15. The absorption spectrum of polycrystalline Wurster's blue shows a slight asymmetry. The sharp pips appearing on the shoulder and in the wing are due to carbazyl.

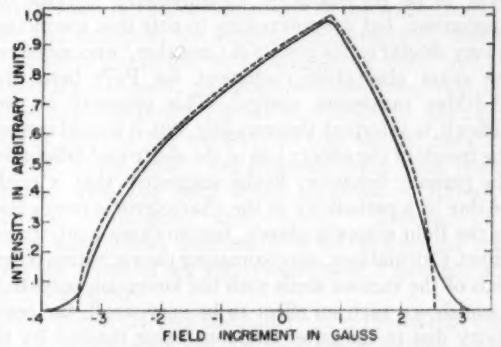

FIG. 14. The line shape of polycrystalline carbazyl. The half-width of the crystallite line is taken as 0.5 gauss.

narrowing of the proton resonance lines in liquids. Adapting the theory by Bloembergen, Pound, and Purcell,[8] there results for the order of magnitude of the line width[9]

$$H_{\frac{1}{2}}=\sim\frac{\beta(\Delta H)_{\mathrm{dip}}^{2}}{h}\tau_{ex},$$

where the quantity $(\Delta H)_{\mathrm{dip}}$ is the dipolar line width in the absence of any exchange effects and τ_{ex} the time associated with exchange effects. A reasonable value for $(\Delta H)_{\mathrm{dip}}$ is about 1000 gauss. Since the $2p$ electron orbitals are involved in the resonance exchange effects, a reasonable value for τ_{ex} is 10^{-14} sec. These values give a line width of the order of 0.1 gauss. The increase in the line width near liquid helium temperatures seems to support this exchange-motional narrowing hypothesis.[10]

It is a pleasure to acknowledge many interesting and stimulating discussions with Dr. M. Wolfsberg of Brookhaven National Laboratory, Professor J. Turkevich of Princeton University, Professor P. Weiss of Rutgers University, and Professor C. A. Hutchison of the University of Chicago during the progress of this investigation. Also we wish to thank Dr. S. Liebson and Dr. M. Garstens of Naval Research Laboratory for gift of hydrazyl, and also Professor G. Fraenkel and Mr. J. M. Hirshon of Columbia University for carrying out for us the measurements in the 9000-Mc/sec region.

[8] Bloembergen, Purcell, and Pound, Phys. Rev. 73, 679 (1948).
[9] P. W. Anderson and P. R. Weiss, Revs. Modern Phys. 25, 269 (1953).
[10] L. S. Singer and E. G. Spencer, J. Chem. Phys. 21, 939 (1953).

Energy Loss of Charged Relativistic Particles and the Element Periods*

TORBJÖRN WESTERMARK
Division of Physical Chemistry, Royal Institute of Technology, Stockholm, Sweden
(Received August 31, 1953)

The stopping power per electron for charged relativistic particles is known to be a function of the electron density of the matter traversed. As the latter is a periodic property of the elements, the stopping power should also be periodic. A calculation shows the energy loss to have maxima at the alkali metals and minima between them. It is suggested that this effect partly caused the periodicity found long ago by Crowther in in the absorption of Pa^{234} beta rays. Differences in stopping power for chemical isomers and element modifications are also discussed.

THE energy loss due to ionization and excitation during the passage of charged particles through matter is subject to a reduction at relativistic velocities because of the importance of distant encounters and the polarization of the intervening material. When this "density effect" has reached its full efficiency, the mean excitation potential in the Bethe-Bloch formula disappears. Then the energy loss formula takes the following form,[1]

$$-\frac{1}{n}\frac{dE}{dx}=\frac{2\pi e^4Z^2}{mc^2}\left\{\log\left[\frac{mc^2}{e^2}\left(\frac{mc}{\hbar}\right)^2\frac{1}{\pi n(1-\beta^2)}\right]-1\right\}, \quad (1)$$

after rearrangement to give the energy loss per electron/cm². The formula applies to "heavy" particles, e.g., protons and mesons, and should be somewhat modified for electrons.

As the electronic density n in (1) is a *periodic* function of the atomic number of the elements, the energy loss should also show periodicity at fixed velocity if (1) holds, (although this periodicity would be less pronounced than the atomic volume, for instance). Figure 1 shows the result of a calculation for the case of $(1-\beta^2)^{-\frac{1}{2}}=196.5$, which corresponds to 184 Gev for protons,[2] 29 Gev for π mesons, 21 Gev for μ mesons, and 100 Mev for electrons. The densities have been taken for ordinary temperature except for those elements existing as gases at this temperature, where the liquid density was taken.

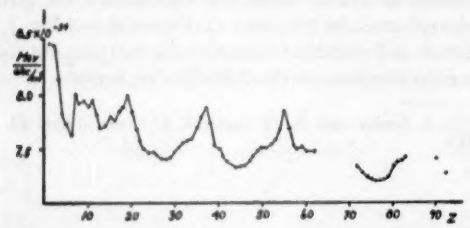

FIG. 1. Energy loss according to formula (1) as a function of atomic number. Note the peaks at $_{19}$K, $_{37}$Rb, and $_{55}$Cs and the intervening minima.

It is seen that the elements form a series of concave sections, each section containing one period and the maximum points corresponding to the alkali metals. The two first periods are less pronounced than the fourth and fifth because of individual deviations. There seem to be no published measurements suitable for comparison, but it is interesting to note that the picture is very similar to the results of Crowther,[3] who measured the mass absorption coefficient for Pa^{234} beta rays (2.3-Mev maximum energy). This property is very difficult to interpret theoretically, but it should contain the trends of the energy loss of the electrons.[4] Discussing the periodic behavior, Bothe suggested[4] that it might be due to a periodicity in the characteristic frequencies in the Bohr stopping theory, but no closer analysis was given. Calculations, approximating the excitation potentials of the various shells with the ionization potentials, have shown such an effect to be very small, the periodicity due to the outer electrons being masked by the inner ones. Even if the approximation used is somewhat in error, the density effect seems to be much larger even in this low-energy region. The observed deviations from a simple function of Z is, however, three or more times larger than the theoretical; therefore, it cannot yet be concluded that the periodic behavior observed by Crowther is due to the density effect only (despite the similarity in shape). The best procedure would be to measure the energy loss directly. Such studies are in progress here using 5-Mev electrons, where the energy loss due to radiation is not too large.

In addition to carbon, studied by Paul and Reich,[5] other element modifications should afford good opportunities of studying the density effect, e.g., arsenic whose yellow modification is expected to be 4 percent more effective in stopping than the gray one. Chemical isomers, e.g., organic compounds like diethylether and buthanol, should also differ. Melting processes should also be studied.

* Read before the Thirteenth International Congress of Pure and Applied Chemistry, Stockholm, August 1, 1953.

[1] H. Bethe and J. Ashkin, in *Experimental Nuclear Physics* edited by E. Segrè (John Wiley and Sons, Inc., New York, 1953), Vol. I, p. 225.

[2] 1 Gev (giga electron volt) = 10^9 ev.

[3] J. A. Crowther, Phil. Mag. 12, 379 (1906).

[4] W. Bothe, *Handbuch der Physik* (Springer Verlag, Berlin, 1933), Vol. 22, Part 2.

[5] W. Paul and H. Reich, Z. Physik 127, 429 (1950).

A New Method for Measuring Auger Transitions*

CHARLES E. ROOS
The Johns Hopkins University, Baltimore, Maryland
(Received July 14, 1953; revised manuscript received September 28, 1953)

The K fluorescence yields (w_K) of eight elements: zirconium, niobium, molybdenum, rhodium, palladium, silver, cadmium, and tin were measured by a new x-ray method involving the use of a NaI—Tl scintillation counter. This counter made it possible to detect the fluorescent x-rays radiated over an effective solid angle of 2π steradians. The values of w_K are Zr—0.645; Nb—0.713; Mo—0.714; Rh—0.779; Pd—0.782; Ag—0.814; Cd—0.819, and Sn—0.840, all with an accuracy of ±3 percent. These results confirm the theoretical predictions of Wentzel that $w_K/(1-w_K)$ is a function of Z^4, and they are in close agreement with the theoretically predicted values of Burhop and Pincherle.

INTRODUCTION

A KNOWLEDGE of the variation of the K fluorescence yield as a function of atomic number (Z) is of importance in studies of internal conversion of γ rays and of K capture.

Broyles, Thomas, and Haynes[1] have recently summarized most of the measurements of the Auger transitions and described the magnetic spectrograph, which they used to determine the K fluorescence yield (w_K) of Ba and Hg. Magnetic spectrographs have been used by several investigators[2–5] for the evaluation of the fluorescence yield of the elements of high atomic number ($Z>46$). These results are more accurate than those obtained with the older x-ray methods of Harms,[6] Compton,[7] Balderson,[8] and others.[9–14] Different observers have found differences of 25 percent in the measured values of w_K with elements of Z between 40 and 50 inclusive.

West, Meyerhof, and Hofstader[15] have shown that the NaI—Tl scintillation counter produces a voltage pulse proportional to the energy of the absorbed x-ray. The high density of the NaI crystal makes possible counters which are effectively 100 percent efficient for x-rays and sharply defines the effective region of the counter, thereby permitting accurate determination of the solid angle subtended by the counter. These features have made it possible to develop a method which has permitted more accurate measurement of the K fluorescence yields. The K fluorescence yields of eight of the elements with atomic numbers between 40 and 50 inclusive were determined by the use of the method described below.

EXPERIMENTAL PROCEDURE

Fluorescent radiation is emitted isotropically, and therefore the quantity of this radiation detected by a counter is strongly dependent upon the solid angle subtended by the counter. A counter was designed to detect this radiation over a solid angle of effectively 2π. If the primary radiation is well collimated, then by changing the solid angle subtended by the counter one can distinguish between the primary and fluorescent radiation. A diagram of the experimental equipment is shown in Fig. 1.

The power supply for the tungsten target x-ray tube both regulated the current and, using the Pepinsky[16] circuit for voltage regulation, stabilized the voltage to 1 part in 10 000. This supply has been briefly described by Swartz and Byerly.[17] Voltages of 35–40 kev and currents of 10 ma were used in this experiment.

The general radiation of the x-ray tube was passed through two sets of collimating slits and then diffracted by a calcite crystal. This monochromatic radiation was passed through the monitor slit which served to divide it, allowing part of the x-ray line to reach a Geiger-Müller counter (argon at 70 cm), used as a monitor, and the remaining part to reach the NaI—Tl scintillation counter.

A 3-mil foil of each of the elements investigated was placed in the path of the beam, almost in contact with

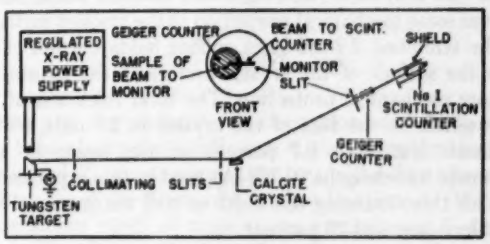

FIG. 1. Experimental arrangement.

* Taken from a thesis submitted in partial satisfaction of the requirements for the degree of Doctor of Philosophy at The Johns Hopkins University.

[1] Broyles, Thomas, and Haynes, Phys. Rev. 89, 715 (1953).
[2] O. Huber *et al.*, Helv. Phys. Acta 25, 3 (1952).
[3] E. Kondaiah, Phys. Rev. 83, 471 (1951).
[4] H. M. Neuman and I. Perlman, Phys. Rev. 81, 958 (1951).
[5] I. Bergstrom and S. Thubin, Phys. Rev. 79, 539 (1950).
[6] M. Harms, Ann. Physik 82, 87 (1920).
[7] A. H. Compton, Phil. Mag. 8, 961 (1929).
[8] M. Balderson, Phys. Rev. 27, 676 (1926).
[9] R. J. Stephenson, Phys. Rev. 51, 637 (1937).
[10] W. Bothe, Z. Physik 37, 547 (1926).
[11] I. Backhurst, Phil. Mag. 22, 737 (1936).
[12] E. Arends, Ann. Physik 22, 281 (1935).
[13] D. K. Berkey, Phys. Rev. 45, 437 (1934).
[14] H. Küstner and E. Arends, Ann. Physik 22, 443 (1935).
[15] West, Meyerhof, and Hofstader, Phys. Rev. 81, 141 (1951).
[16] R. Pepinsky and P. Jarmatz, Rev. Sci. Instr. 19, 247 (1948).
[17] G. Swartz and E. H. Byerly, Rev. Sci. Instr. 19, 273 (1948).

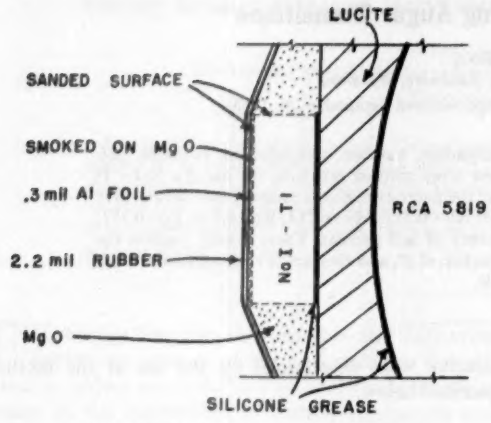

FIG. 2. Detail of NaI—Tl crystal mounting.

the surface of the NaI—Tl crystal, where it subtended a solid angle of effectively 2π steradians. In this position the counter detected both the fluorescent radiation and the portion of the original beam which was not absorbed in the foil. The same foil was then moved 35 cm away from the crystal and placed for convenience at the monitor slit. In this position the solid angle subtended by the counter was negligible. Since the fluorescent radiation is isotropic, less than 0.4 percent of it was detected, whereas the counter still detected the same quantity of the transmitted x-rays, except for the small effects of scattering. The difference between the readings obtained in the above two positions is therefore due to the fluorescent radiation. From the ratio of this fluorescent radiation to the intensity of the incident beam with no absorbers, the fluorescence yield can be obtained.

SCINTILLATION COUNTER MOUNTING

The mounting of the NaI—Tl crystal, which permits the foil to be placed closer than 4 mils to the crystal is shown in Fig. 2. The crystal was packed with MgO. In order to get a very thin layer (0.3 mil) on the front face of the crystal, the MgO was deposited there as smoke from burning Mg ribbon. This layer must be thin so that the x-rays are not appreciably absorbed. The Al foil (0.3 mil) serves as a light and moisture barrier and gives some mechanical protection to the smoked surface. The stretched 2.2-mil latex rubber holds the foil close to the surface of the crystal and gives the mounting more mechanical protection. The total thickness of all materials at the face of the crystal is 2.7 mils, which absorb less than 0.7 percent of the beam at the longest wavelengths (0.7284A) used in this experiment. With this mounting the width at half maximum of the 32-kev line was 28 percent.

RESULTS

A typical pulse-height spectrum obtained with the foil at the crystal is shown in Fig. 3. It is the sum of two basically Gaussian distributions—the spectra of the fluorescent and the transmitted incident radiation. The pulse-height distribution obtained with the foil 35 cm away from the crystal is the spectrum of the transmitted portion of the incident beam.

The two curves were subtracted graphically, and the broken line curve thus obtained represents the fluorescent radiation. This curve has its maximum at approximately the point where the K_α lines would be expected. The curve is not quite symmetrical, being broader on the high-energy side. This is to be expected since the contribution of the K_β line would tend to add more to the high-energy side.

One set of these curves was obtained for each of the eight elements investigated, although only the set for rhodium is shown here. The curves for zirconium and niobium showed almost complete separation of the peaks, while those for cadmium and tin showed relatively less separation. A pulse-height spectrum of the direct beam was also determined when the above curves were obtained.

In Fig. 3 it is seen that the points for higher pulse-height settings taken with the foil at the slit often lie slightly below the same points taken with the foil at the counter. This effect was observed on all of the eight sets of curves. Due to the Gaussian nature of these curves, the fluorescent radiation can be assumed to make no contribution at pulse heights of 36 to 46 volts. This difference can be attributed to scattering. The correction for this effect was made by drawing only one curve in the above region and then drawing the Gaussian curve for the transmitted radiation so that in the 17- to 27-volt region it is symmetric to the single curve drawn at 36 to 46 volts.

A planimeter was used to measure the difference between the curve for the transmitted x-rays drawn as mentioned above and the curve obtained for the combination of transmitted and fluorescent radiation (foil at crystal). The spectrum for the direct beam was plotted and measured and from the ratio of these two areas the ratio of fluorescent to incident radiation was determined. These ratios are given in the first line of Table I.

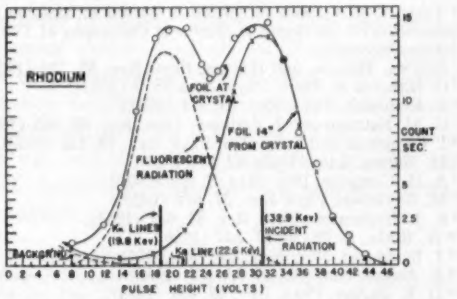
RHODIUM
FOIL AT CRYSTAL
FOIL 14" FROM CRYSTAL
FLUORESCENT RADIATION
(32.9 Kev) INCIDENT RADIATION
Kα LINES (19.8 Kev)
Kβ LINE (22.6 Kev)
BACKGROUND
COUNT/SEC.
0 2 4 6 8 10 12 14 16 18 20 22 24 26 28 30 32 34 36 38 40 42 44 46
PULSE HEIGHT (VOLTS)

FIG. 3. Pulse height spectra obtained with 3-mil rhodium foil in beam of 32.9-kev x-rays.

TABLE I. Ratio of fluorescent to incident radiation.

Element	Zr	Nb	Mo	Rh	Pd	Ag	Cd	Sn
Graphs	0.0574	0.0633	0.0601	0.0502	0.0732	0.0853	0.1116	0.1410
Integrated counts	0.0613	0.0653	0.0625	0.0531	0.0755	0.0877	0.1121	0.1431
Corrected integrated counts	0.0573	0.0625	0.0604	0.0497	0.0739	0.0858	0.1104	0.1395

The above integrations could also be obtained directly by setting the pulse-height analyzer so as to count all pulses above 8 volts. It is possible to obtain statistics of 1–2 percent by this means in a relatively short time. The ratios obtained are given in the second line of Table I.

It is seen that the ratios for these integrated counts are all approximately 5 percent higher than those obtained with a planimeter. This is to be expected, since with this procedure allowance must still be made for scattering.

At wavelengths longer than that of the K edge, x-rays do not eject K electrons, and consequently no K fluorescent radiation is produced. Using these lower energy x-rays, the difference in the measured transmission of the foil in the two positions (at crystal and 35 cm away) will be due to the scattered x-rays. The ratio of these two readings gives $N_{35}/N_{\text{crystal}}=\exp(-\mu_\gamma t)$, where μ_γ is an "effective scattering coefficient" and t the thickness of the foil. The work of Coade[18] indicates that over the wavelength region between the K edge of the elements investigated and the wavelength of the incident radiation, the scattering coefficient should roughly decrease by a factor of two for all eight elements. If the ratio of transmitted to incident radiations is N_t, then

$$N_t[\exp(\mu_\gamma t/2)-1]=S,$$

where S is the fraction of the incident beam lost by scattering. The value of S was determined for each element, and subtracted from the directly integrated ratios in Table I to give the corrected values shown in line 3.

Since the effect of scattering is of the order of 5 percent of the fluorescent radiation, errors of even 20 and 40 percent in the application of this correction would cause errors of only 1 to 2 percent in the value of the fluorescence yields. Since the corrected values obtained by the two independent methods agree to within an average of 1 percent, it seems reasonable to conclude that the total error due to the effects of scattering is less than 2 percent. Because of their better statistics, the integrated counts are considered more reliable than the data from the pulse-height spectra graphs.

There are, in addition to the above, other sources of error to be considered. As was mentioned earlier, when the foil is 35 cm from the crystal, 0.4 percent of the fluorescent radiation is still detected by the counter.

The rubber, Al foil, and MgO at the face of the NaI—Tl crystal will absorb more of the fluorescent than primary radiation. This is due to the longer wavelengths of the fluorescent radiation and also to the fact that it has a longer average path in the mounting materials. The primary radiation, unlike the fluorescent, is collimated and its path is therefore always perpendicular to the crystal surface. The effect of this greater absorption is also 0.4 to 0.3 percent, and the result of the above two effects is to reduce the experimental value of the measured fluorescence radiation 0.8 percent.

The background counting rate for pulse heights corresponding to photons of 3–12 kev is observed to depend upon the history of the NaI—Tl crystal. This effect was independently observed earlier at this university by Class.[19] Megill and Emigh[20] have also observed the long-term phosphorescence of the NaI—Tl crystal. Exposure to light can increase the background rate in the 6-kev region as much as 5 times, and in the 10-kev region 2 times. This increased rate decays with a half-life on the order of 10 minutes. The exposure of the crystal to an intense beam of 30-kev x-rays can also raise this background level 5–10 percent. This effect, which perhaps can be attributed to phosphorescence, varies very much with different crystals.

With the use of a crystal selected so that this phosphorescence was reduced, this effect still caused the measured fluorescence value to be approximately 0.6 percent too high. This error effectively cancels with the 0.8-percent error mentioned above.

The important sources of error in these experimental ratios are either statistical in origin or due to effects of scattering. These errors are each less than 2 percent.

RELATION OF EXPERIMENTAL RATIOS TO FLUORESCENT YIELD

It can be shown that the number of incident x-rays (dI_x) absorbed photoelectrically by the ejection of a K photoelectron from atoms in a layer dx of the foil is given by

$$dI_x=\tau\frac{(r-1)}{r}N_0e^{-\mu_1 x}dx, \qquad (1)$$

where τ is the photoelectric absorption coefficient; μ_1, the total absorption coefficient; r, the absorption jump ratio; and N_0, the number of photons in the direct beam.

Because of the Auger effect only a fraction w_K (the K fluorescence yield) of those atoms which lose a K electron will radiate a K x-ray. These fluorescent K x-rays must, however, pass through the rest of the foil before

[18] E. Coade, Phys. Rev. **36**, 1109 (1930).

[19] C. M. Class, J. Opt. Soc. Am. (to be published).

[20] L. R. Megill and C. R. Emigh, Phys. Rev. **92**, 1081(A) (1953).

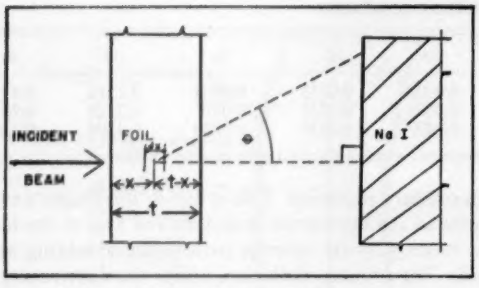

FIG. 4. Diagram showing relationship of t, θ, x, and dx to the foil and NaI—Tl crystal.

they are detected by the crystal and many are therefore reabsorbed. Furthermore, they are radiated isotropically, and the thickness of the foil through which they must pass depends upon the angle θ as seen in Fig. 4. Therefore, the number (dI_j) of K x-rays from the layer dx which are detected by the counter is given by

$$dI_j=\frac{dI_s w_K}{2}\int_0^{\pi/2} e^{-\mu_j(t-x)\sec\theta}\sin\theta d\theta dx, \qquad (2)$$

where t is the thickness of the foil. The difference in the integral between $\theta=90°$ and the actual experimental θ of 89° is less than 0.01 percent.

Allowing for the difference in absorption coefficients of the α_1, α_2, and β lines in the K series, and integrating expression (2) over all dx, the following expression is obtained:

$$I_T=\sum_j C_j\int_0^t dI_j dx=\tau\frac{w_K I_0(r-1)}{2r}\sum_j C_j\int_0^t e^{-\mu_1 x}$$

$$\times\int_0^{\pi/2} e^{-\mu_j(t-x)\sec\theta}\sin\theta d\theta dx=\frac{w_K I_0}{r}(r-1)\sum_j C_j\Gamma_j, \quad (3)$$

where C_j is the intensity of each line relative to the total intensity of the K series, and Γ_j is defined to be $\frac{1}{2}\tau$ times the double integral.

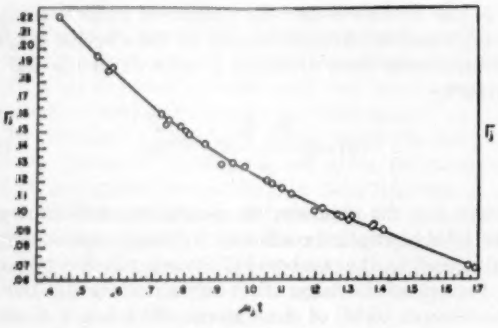

FIG. 5. Plot of

$$\frac{\tau}{2}\int_0^t e^{-\mu_1 x}\int_1^\infty\frac{e^{-\mu_j(t-x)v}}{v^2}dvdx$$

or Γ_j as a function of $\mu_j t$.

If $\sec\theta$ is set equal to v and substituted in the last integral in expression (3), one obtains

$$\int_0^{\pi/2} e^{-\mu_j(t-x)\sec\theta}\sin\theta d\theta=\int_1^\infty\frac{e^{-av}}{v^2}dv, \qquad (4)$$

where $a=\mu_j(t-x)$. This integral is recognized as the Gold[21] integral, which has been tabulated.

Using Gold's values for part of the integral, it was relatively simple to evaluate Γ_j using a small electronic computer (IBM-604). The values of Γ_j obtained are plotted against $\mu_j t$ in Fig. 5. The values of τ and $\mu_1 t$ may vary by more than 100 percent for neighboring points on the curve; yet the value of Γ_j is seen to be primarily a function of $\mu_j t$.

The foil thicknesses—3 mil—were chosen so that $\mu_j t$ was approximately equal to 1, the optimum value for accurate measurement. The same part of the same foil was used for both the fluorescent and absorption measurements eliminating errors due to variations in thickness of the foil and small impurities. Furthermore,

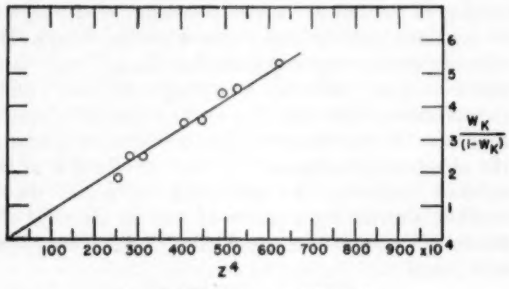

FIG. 6. Plot of Z^4 vs $w_k/(1-w_k)$.

it is not necessary to measure t with precision since the fluorescence yield depends upon $\mu_1 t$ and $\mu_j t$, which were obtained directly from the experimental measurements.

Wavelengths corresponding to those of the $K_{\alpha 1}$, $K_{\alpha 2}$, and K_β lines of the eight elements were isolated from the general radiation of tungsten by the 1.5-meter Bragg single crystal spectrometer. This spectrometer was calibrated and checked by use of the K absorption limits of tin, silver, cadmium, molybdenum, and zirconium.

Before evaluation of the K fluorescence yield it is also necessary to know the absorption jump ratio. The experimental values obtained by different investigators range from 6.7[22] to 7.8[23] in the case of silver. Despite this uncertainty in the value of r, the above values would cause only a 1.3-percent difference in the value of $(r-1)/r$. This difference is, however, of the same order of magnitude as the errors probably introduced by the scattering corrections.

[21] E. Gold, Proc. Roy. Soc. (London) **A82**, 62 (1908).
[22] L. H. Martin and K. C. Lang, Proc. Roy. Soc. (London) **A137**, 199 (1931).
[23] R. J. Spencer, Phys. Rev. **38**, 1932 (1931).

TABLE II. Values of K fluorescence yields.

Element	Zr	Nb	Mo	Rh	Pd	Ag	Cd	Sn
Present results	0.645	0.713	0.714	0.779	0.781	0.813	0.819	0.840
Theoretical[a]	0.67		0.71	0.75	0.78	0.79	0.81	0.83
Magnetic spectrograph[b]						0.83	0.83	
Stephanson[c]	0.69		0.735	0.77		0.81	0.79	0.81
Backhurst[d]			0.785	0.801	0.835	0.838	0.846	0.855
Arends[e]			0.724			0.795		0.825
Berkey[f]			0.79			0.72	0.70	0.66
Balderson[g]			0.97			0.88		
Compton[h]			0.68					

[a] See references 25 and 26. [b] See reference 2. [c] See reference 9. [d] See reference 11. [e] See reference 12. [f] See reference 13. [g] See reference 8. [h] See reference 7.

FINAL RESULTS

Using the relative intensity of the K lines, from Williams,[24] the weighted contribution of each integral was obtained and summed. With this value, the ratio of fluorescent to incident x-rays, and the value of $(r-1)/r$ which was chosen to be 0.860 for all elements, Eq. (3) was evaluated for w_k. The results are shown in Table II.[2,7-9,11-13,25,26]

The agreement between the scintillation counter results and the theoretical results of Burhop[25] and Pincherle[26] is excellent, in view of the approximations made in the theory. The values for silver and cadmium obtained with the magnetic spectrometer are little over one percent higher than the results from the scintillation counter method. Two samples of silver of different thicknesses were measured as a check on the consistency of the results. The value obtained for the K fluorescence yield of the first sample was 0.817 and that of the second was 0.810.

Wentzel[27] has predicted that $w_K/(1-w_K)$ should vary as the fourth power of Z. The scintillation counter values are seen to give a very close fit to this relationship for the elements studied, as seen in Fig. 6. For $Z>50$, it is quite possible that due to the effects of screening and relativity this relationship is no longer valid, as Broyles, Thomas, and Haynes[1] have mentioned.

With further improvement in scintillation counter techniques, it will be relatively simple to extend this method to the measurement of the L fluorescence yields of elements such as lead and tungsten and to measure the K fluorescence yields of elements such as iron and copper. By making the well-known correction for K escape of iodine,[17] this method also permits rapid and accurate measurement of the K fluorescence yields of elements of high atomic number. Improvement in resolution of the scintillation counter should make it possible to make more accurate corrections for scattering.

The author wishes to express his sincere appreciation to Professor J. A. Bearden for his constant encouragement and helpful counsel and to Professor L. Madansky for his suggestion of, and his interest in, this problem. Professor Rasetti, Professor Madansky, and Professor Hanna furnished the photomultiplier tube and the NaI—Tl crystals used in this work. Mr. W. Etchison, of the computation laboratory, assisted in the evaluation of the integrals needed in this work.

[24] E. J. Williams, Proc. Roy. Soc. (London) **A130**, 310 (1930).
[25] E. H. S. Burhop, Proc. Roy. (London) **A148**, 272 (1935).
[26] L. Pincherle, Nuovo cimento **12**, 81 (1935).
[27] G. Wentzel, Z. Physik **43**, 524 (1927).

Energy Loss and Straggling of Electrons*

CHARLES WARNER, III,† AND FRITZ ROHRLICH‡
Palmer Physical Laboratory, Princeton University, Princeton, New Jersey
(Received October 13, 1953)

The energy-straggling distribution and the most probable energy loss for 15.7-Mev electrons in Cu is calculated. Corrections for the resonance effect, bremsstrahlung, the polarization effect, and multiple scattering are included. The results are in very satisfactory agreement with recent experiments. The discrepancy in the most probable energy loss in Au is also discussed.

RECENTLY very accurate experiments on the energy loss and straggling of 15.7-Mev electrons were carried out.[1] They show good agreement with theory for Al and lighter elements, but they disagree with theoretical expectations for Au.[2] No comparison of the Cu data with theory could be made since calculations for this element were not available. In this note we want to report on such calculations.

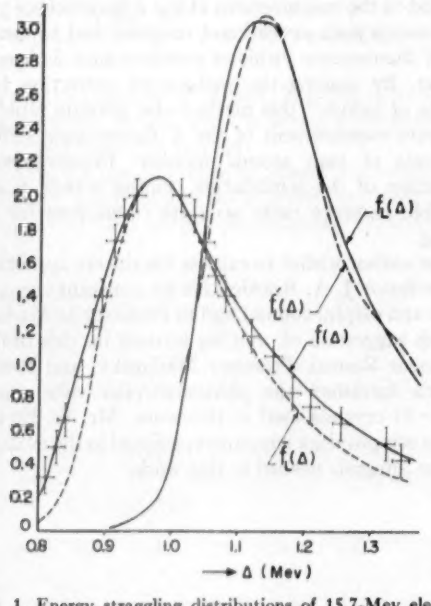

FIG. 1. Energy straggling distributions of 15.7-Mev electrons in Cu as a function of the energy loss Δ. Solid curves: Landau distribution $f_L(\Delta)$ and final theoretical distribution $f(\Delta)$, both normalized to unity. Dashed curves: Landau distribution $f_L(\Delta)$ with maximum coinciding with $f(\Delta)$ for the purpose of shape comparison and Blunck-Leisegang approximation $f_L'(\Delta)$ normalized to unity. (See reference 4.) The experimental results are from references 1 and 8.

The basic Landau distribution for energy straggling[3] was corrected for the following effects in this order:

(a) The resonance effect. The Williams-Landau theory does not take into account correctly those large but infrequent losses which result from ionization energies in the vicinity of S_0, the separation energy between soft and hard collisions.

(b) Bremsstrahlung. The Landau curve involves collision loss only.

(c) The polarization effect (density effect).

(d) Multiple scattering.

The first two effects will mainly broaden the distribution but will shift its maximum only slightly. The last two effects will only shift the whole distribution but not affect its shape.

For Cu the K-electron ionization energy $I_K < S_0 = 0.0589$ Mev. The Landau curve can be corrected, therefore, for the resonance effect by folding it into a gaussian distribution whose half-width is a certain average over the ionization energies of the atom.[4] The bremsstrahlung correction is then applied by folding the resultant distribution into the radiation loss distribution. The latter can easily be found to be of the form

$$f_B(\Delta)d\Delta = B\exp(-B\Delta)(B\Delta)^{xA-1}d\Delta/\Gamma(xA),$$

where Δ is the energy loss, x is the target thickness, and Γ is the gamma function. The constants A and B are found by approximating the cross section for bremsstrahlung $\sigma(\Delta)$ for small Δ,

$$\sigma(\Delta)d\Delta = A\exp(-B\Delta)d\Delta/\Delta.$$

This expression is a very good approximation in the Δ region of interest.[5]

The corrections (a) and (b) shift the maximum of the distribution from 1.130 Mev to 1.155 Mev. The polarization effect has recently been calculated very

* Part of this work is a summary of a thesis submitted by one of the authors (C.W.) to the Department of Physics, Princeton University, in partial fulfillment of the requirements for the degree of Bachelor of Arts.

† Now at the Department of Physics, Harvard University, Cambridge, Massachusetts.

‡ Now at the Department of Physics, State University of Iowa, Iowa City, Iowa.

[1] Goldwasser, Mills, and Hanson, Phys. Rev. **88**, 1137 (1952).

[2] C. N. Yang and J. M. Kennedy (unpublished numerical work for Au).

[3] E. J. Williams, Proc. Roy. Soc. (London) **A125**, 445 (1929); L. Landau, J. Phys. (U.S.S.R.) **8**, 201 (1944).

[4] O. Blunck and S. Leisegang, Z. Physik **128**, 500 (1950). It should be pointed out here that the approximation to the Landau curve in terms of four gaussians is not at all as accurate (less than 2 percent) as claimed by these authors. The approximate curve, $f_L'(\Delta)$ is shown for comparison in Fig. 1.

[5] This approximation was first applied to electron straggling by W. Schultz, Z. Physik **129**, 530 (1951). For further details of this and the other corrections and for numerical values the reader is referred to the B.A. thesis of one of us (C.W.) (unpublished).

accurately by Sternheimer.[6] From his paper one finds for our case −0.187 Mev for this correction, yielding 0.968 Mev for the most probable energy loss, Δ_p. Finally, a small correction for multiple scattering should be applied. This can be done by replacing the target thickness by an effective thickness[7] which in this case increases Δ_p by 0.9 percent or 0.009 Mev. Thus, the final theoretical value in Cu is

$$\Delta_p = 0.977 \text{ Mev}.$$

The theoretical straggling distribution, $f(\Delta)$, is shown in Fig. 1 together with the uncorrected Landau curve $f_L(\Delta)$ (both normalized to unity). For the purpose of comparing the shapes of these two distributions, $f_L(\Delta)$ is also plotted in a reduced vertical scale and a shifted energy scale so that its maximum coincides with the maximum of $f(\Delta)$. The experimental points with errors of ±0.015 Mev in energy and ±5 percent in counting rate are also shown.[8] Both the shape and the most probable energy loss are seen to be in very satisfactory agreement.

If we use for Au the polarization correction of Sternheimer[6] (−0.134 Mev) instead of the approximate Fermi value (−0.055 Mev), we find $\Delta_p = 0.966$ Mev compared with an experimental value of 0.902 Mev. The reduction of the discrepancy from 0.143 Mev to 0.064 Mev is appreciable but not sufficient. However, the good agreement for all the other elements including Cu suggests that further experiments and a careful check of the calculations will yield agreement also for Au.

We are grateful to Dr. Yang for letting us see the unpublished calculations on Au by him and Dr. Kennedy and for two profitable discussions.

[6] R. M. Sternheimer, Phys. Rev. **88**, 851 (1952), and **91**, 256 (1953).

[7] C. N. Yang, Phys. Rev. **84**, 599 (1951).

[8] We are grateful to Dr. Hanson for communicating these results to us.

PHYSICAL REVIEW VOLUME 93, NUMBER 3 FEBRUARY 1, 1954

One-to-Two Millimeter Wave Spectroscopy. IV. Experimental Methods and Results for OCS, CH_3F, and H_2O†

WILLIAM C. KING* AND WALTER GORDY
Department of Physics, Duke University, Durham, North Carolina

(Received September 17, 1953)

Design details are given of the harmonic generator and detector which made possible precision spectroscopy in the one-to-two mm wave region. The signal-to-noise ratio obtained on OCS rotational lines is 7 to 1 at 1.0-mm wavelength; 30 to 1 at 1.1 mm; and better than 100 to 1 at 1.4 mm and above. A useful tuning and measuring technique is made possible by the ability of the new system to detect several klystron harmonics at once and, hence, spectral lines in several different regions at the same time. The applications of the methods in the measurement of centrifugal distortion of molecules is illustrated with OCS, for which $D_J = 1.310 \pm 0.010$ kc/sec is obtained, and with CH_3F, for which $D_J = 57.8 \pm 1.0$ kc/sec and $D_{JK} = 445 \pm 4$ kc/sec are obtained. A new water-vapor line, the $2_{2,0} \rightarrow 3_{1,3}$ rotational line, has been measured at 183 311.30±0.30 Mc/sec.

INTRODUCTION

THE present paper is the fourth in a series reporting measurements of spectral lines in the one-to-two mm wave region. The experimental methods which made possible high-resolution spectroscopy in this essentially uncharted region of the electromagnetic spectrum will be described here in some detail. These methods were described earlier by one of us (W.G.) at the North Carolina Meeting of the American Physical Society (March, 1953) and briefly in the first paper of this series.[1]

† This research was supported by the United States Air Force under a contract monitored by the Office of Scientific Research, Air Research and Development Command. It is part of a thesis submitted by W. C. King in partial fulfillment of the requirements for the Ph.D. degree at Duke University.

* Present address: Radiation Laboratory, The Johns Hopkins University, Baltimore, Maryland.

[1] W. C. King and W. Gordy, Phys. Rev. **90**, 319 (1953).

EXPERIMENTAL METHODS

Harmonic Generator and Detector

The instrument and techniques developed earlier in this laboratory[2] extended high-resolution spectroscopy down to approximately 2 mm. Like the earlier methods, the present ones employ crystal harmonic generators driven by klystrons as the source of energy and crystal rectifiers for detection. The improvement in performance results principally from the changes in details of design of these components. The limit of applicability of the earlier harmonic generators and detectors which employed commercial, coaxially mounted crystals was found to be near 2-mm wavelength. Some improvement in the multiplier design

[2] Smith, Gordy, Simmons, and Smith, Phys. Rev. **75**, 260 (1949); Gilliam, Johnson, and Gordy, Phys. Rev. **78**, 140 (1950).

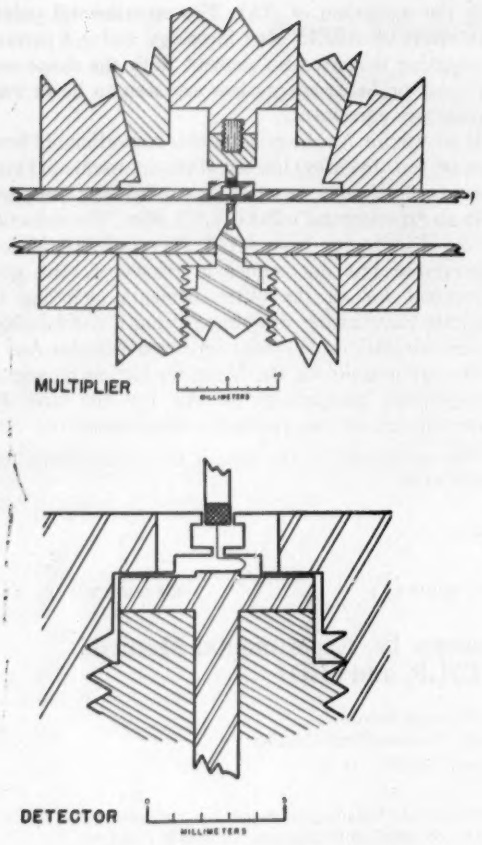

FIG. 1. Cross-section details of multiplier and detector (see also Fig. 2).

was made by Johnson,[3] who cut windows in the coaxial crystal cartridge of the harmonic generator so that the harmonic energy could be radiated directly down the mm waveguide. He also improved the mm wave detector by removing the crystal from its coaxial cartridge and mounting it in one face of the waveguide. With these improvements he was able to detect energy from klystron harmonics at wavelengths as short as 1.8 mm but measured no spectral lines below 2-mm wavelength. Simmons[4] reported making an improvement in the crystal multiplier by similarly mounting the crystal directly in the smaller waveguide. The Columbia group[5] were able by similar methods to measure spectral frequencies as high as 88 kMc/sec (3.4-mm wavelength).

[3] Johnson, Slager, and King, Rev. Sci. Instr. (to be published). Also given by C. M. Johnson at the third conference on Ultra-High Frequencies, held in Washington, D. C., February 1953 (unpublished).

[4] Reported orally by J. W. Simmons at the conference on Microwave Spectroscopy held by the New York Academy of Sciences (November 9–10, 1951).

[5] Nethercot, Klein, and Townes, Phys. Rev. 86, 798 (1952).

While some improvement in performance in the previously worked two-to-three mm region was apparently obtained by use of waveguide mounts of silicon crystals, efforts to extend their range to shorter wavelengths were unsuccessful. It occurred to us that one cause of this failure might be the large size of the crystal and pick-up probe which were being employed. Consequently, we removed a 1N26 silicon crystal from its mount, fractured it into a number of pieces, and selected and repolished a piece which was small as compared with the wavelength which we hoped to detect. We constructed a small pick-up probe by simply extending a 2-mil tungsten cat-whisker directly across the smaller guide. It was then possible to mount these small elements into the mm waveguide through holes which were small as compared with the size of the guide. Thus, no drastic cutting of the guide was necessary. With the first multiplier and detector units made in this way, spectral lines were immediately detected near one mm wavelength.

We now cut and shape the crystal chips with a small diamond wheel and if necessary polish the face of the chip to flatness with optical rouge. The back side of the silicon slab is sputtered or plated with nickel to make it easier to solder it to the conducting post.[6]

Cross-section details of the detector and multiplier are given in Figs. 1 and 2. Photographs of the components are shown in Fig. 3. The loop or bend necessary to give flexibility to the cat-whisker is placed just outside the smaller guide so that it also gives some choking action to decrease the loss of harmonic energy. However, in line with previous experience gained in this laboratory, we have avoided the use of ordinary chokes in order to make the system broad banded.

In both the multiplier and detector a differential screw mechanism is used so that a critical adjustment of the pressure of the whisker upon the face of the crystal can be made (see Figs. 1–3). The effective pitch of the differential screw is 364 turns per in. The cone into which the screw mechanism fits must be accurately machined and lapped so that the crystal will pass through the small hole without striking the wall of the guide. To avoid breaking the crystal, one will find it a good practice to adjust the screw so that the crystal will be outside the wall of the guide before he inserts the assembly into the cone. He then advances the crystal through the hole until it makes contact with the whisker. For the multiplier, the instant of contact can be judged by the sudden change in the output power of the klystron caused by the change in impedance resulting from the contact. Usually the first contact is the best, although an improvement can sometimes be made by a slight increase in the pressure or by a shift to a new spot on the crystal. In both the multiplier and detector, provision is made for rotation of the crystal mount so

[6] We are indebted to R. B. Belser, of the Georgia Institute of Technology, for suggesting this soldering aid.

that different points of contact can be made. Before the crystal is rotated, it should be screwed back so that it will not strike the whisker while the rotation is being made.

For the detector, one can usually judge when contact is made by the change in the noise output of the amplifier. However, evidence of detected energy is a much more reliable indication of contact. Hence it is desirable whenever possible to know that a detectable amount of harmonic energy is being generated by the multiplier. If the contact of the multiplier crystal is adjusted as directed, one can usually obtain detectable harmonic power with only a few trial settings of the waveguide tuning plungers. Nevertheless, it is good practice when one is making readjustments or changes in the detector to make sure that the harmonic generator is left in good adjustment. Likewise, it is advisable when one is readjusting the multiplier to leave the detector undisturbed.

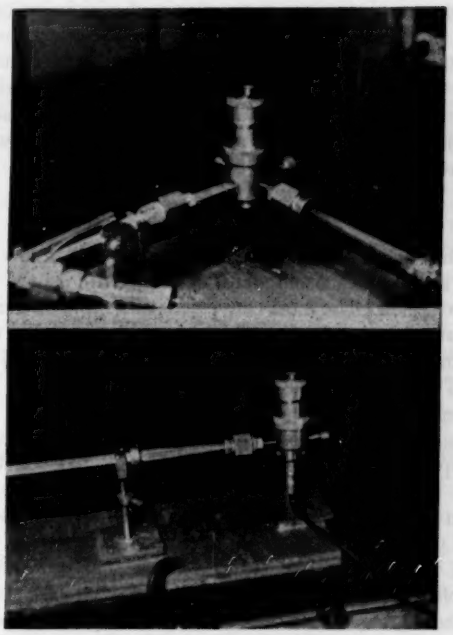

FIG. 3. Photograph of multiplier unit (upper figure) showing connector to klystron (left) and to absorption cell (right). Lower figure shows detector unit with electroformed transition section to K-band absorption cell.

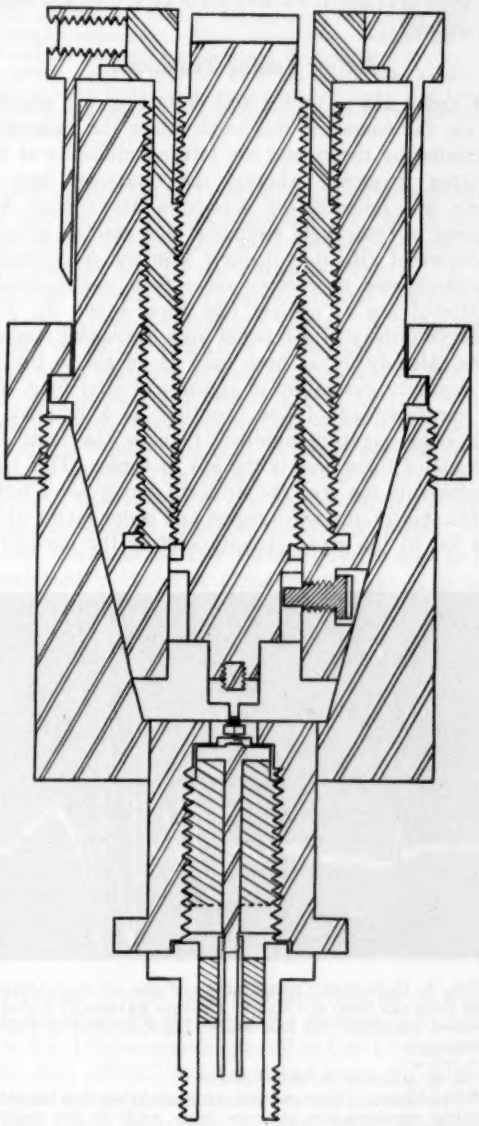

FIG. 2. Cross-section details of detector showing differential screw mechanism and the output connector. An identical differential screw arrangement is used for the multiplier unit.

The tungsten cat-whisker is pointed by electrolytic etching.[7] The end to be pointed is allowed barely to make contact with the surface film of a 10 normal solution of KOH. (The concentration is not critical, and other electrolytic agents can be used). An ac current is then passed through the whisker and solution until action at the end of the whisker ceases, usually in about one second. The amount of the current is not particularly critical. We use a 6-v 60-cy ac source. After the pointing, the solution is washed off, and the point is examined under a microscope. Often it is necessary to repeat the process in order to obtain a satisfactory point. A resharpening of the whisker is necessary after a few readjustments of the point of contact. Sometimes the point of the whisker is blunted by excess pressure, and sometimes it is burned off in the multiplier unit by excess power. If for unknown reasons the performance of the units drops, it is advisable for one to examine the whisker points under the microscope.

[7] R. Beringer, Phys. Rev. **70**, 53 (1946).

Some evidence has been obtained which indicates that high humidity adversely effects the operation of the multiplier and detector in the shorter mm range. This is believed to result from a water film which collects on the crystal surface. We consequently use a heating coil to keep the multiplier and detector units slightly warmer than the room temperature.

Electronic Components

The electronic amplifiers and display systems are the same as those used for the lower-frequency mm wave region.[8] The most convenient and rapid of these is the simple video system which employs a modified type *P* amplifier having a band width of about 6000 cps with a low frequency cutoff of about 100 cps. The sweep rate is adjusted so that the mode contour and broad signals from reflections are filtered, whereas the sharp absorption line signal is largely passed. With this broad-banded amplifier, and absorption line has been seen and measured on the cathode-ray oscilloscope at 1.03-mm wavelength.

A more sensitive system employs low-frequency repeller modulation[8] (of the order of 4000 cps) with a phase lock-in detector and a narrow-band amplifier and automatic recording of the line. The system used for the present work is essentially that given in a paper by Gilliam, Johnson, and Gordy[8] on techniques for the two-to-three mm region. We have found, however, that we obtain better discrimination against reflections by tuning the amplifier to twice the frequency of the repeller modulation (compare, for example, Figs. 6 and 7). To give this system best sensitivity, one must optimize the amplitude of repeller modulation for the line width expected (this is best accomplished by recording a known line), and one must, of course, make proper phase adjustment of the reference voltage which controls the lock-in detector. Another obvious but important adjustment is the tuning rate of the tube. The latter must be properly regulated for the time constants of the recorder and the bandwidth of the amplifier. For the optimum sensitivity and resolution, the klystron frequency must be stabilized by an external cavity.

Experience has shown that for the mm wave region, where harmonic generators of low power must be used as sources, better results are obtained with the repeller modulation at audio rather than at radio frequencies. Furthermore, at this time, repeller modulation is superior to Stark modulation because no Stark cells of sufficiently low loss for the shorter mm region have yet been developed. Parallel plate-type cells are under development.

A New Tuning Technique

A useful aid to tuning and measuring was evolved during the course of this work. Since the harmonics generated by the crystal are integral multiples of the klystron frequency whereas the rotational lines of linear or symmetric-top molecules are almost, but because of centrifugal stretching not exactly, integral multiples of $2B_0$, it is possible with the spectrometer described here to observe more than one molecular rotational line at a time (see Figs. 4 and 5). This multiple display of rotational lines has useful applications. Already it has been used as an aid to tuning, for accurate evaluation of centrifugal stretching, and for measurement of line breadths[9] as a function of rotational quantum number. Perhaps the most important of these uses is the aid to tuning. This trick circumvents the need for stringent waveguide filtering in the shorter mm wave region and is one factor which has led to the rapid exploitation[10] of the one-to-two

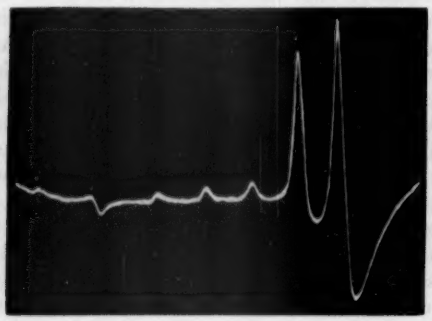

FIG. 4. The 8th, 10th, 12th, 14th, 16th, 18th, and 20th (from right to left) rotational lines of OCS obtained with the 4th to 10th klystron harmonic. Frequencies range from 97 kMc/sec to 243 kMc/sec (3.08 mm to 1.23 mm wavelength).

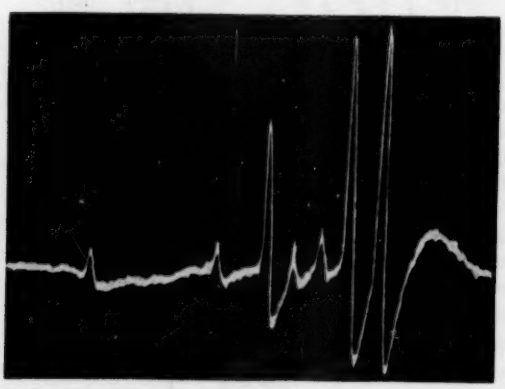

FIG. 5. Cathode-ray presentations of the $J=2\rightarrow3$ transition (the three tall lines) of CH_3F at 1.96-mm wavelength and of the $J=3\rightarrow4$ transition (the four weaker lines) of CH_3F at 1.47-mm wavelength.

[8] Gordy, Smith, and Trambarulo, *Microwave Spectroscopy* (John Wiley and Sons, Inc., New York, 1953), Chap. I.

[9] R. S. Anderson (to be published).

[10] In addition to the measurements made in our own laboratory, spectral measurements are now being made in the region at Columbia University [J. A. Klein and A. H. Nethercot, Phys. Rev. **91**, 1018 (1953)] and at John Hopkins University [Gallagher, Bedard, and Johnson (private communication)].

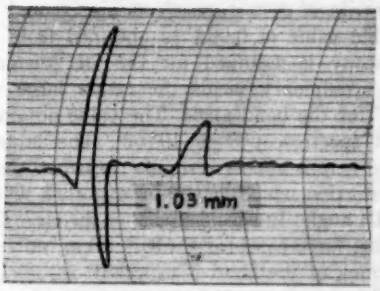

FIG. 6. Recorder tracing of the $J=21\rightarrow22$ (stronger) and $J=23\rightarrow24$ (weaker) lines of OCS occurring at 1.12 and 1.03-mm wavelength respectively. These results were obtained with the 11th and 12th harmonic energy from a K-band Raytheon klystron and with a small G-band cell of 20-cm length. The receiver is tuned to twice the klystron modulation frequency. The tracing represents approximately the second derivative of the absorption line contour.

mm region since the first description of our experiments. But the primary factors responsible for this development are the exceptionally broadbanded and effective multiplier and detector units described above.

To tune the microwave components with this method, one must choose a convenient "tuner" molecule such as OCS or OCSe, which has a rotational line in the region to be searched as well as a number of lines at lower frequencies. A klystron is then selected which gives harmonics coinciding with a group of rotational lines of the "tuner" molecule, including the one in the region of search. This allows a stepwise peaking of rotational lines of higher and higher frequency until the spectrometer is tuned in the desired region. The "tuner" molecules are then replaced by the ones to be investigated. A new line found in this way does not necessarily lie in the expected region but may correspond to an absorption of any harmonic passed by the waveguide filter. To verify the harmonic identification one can tune the klystron (or use a different one) so that the same line is observed by a different order of harmonic. This "crossfire" method was used in making certain the frequency of the H_2O line reported here. We found the line by first peaking the system on the sixteenth rotational line of OCS with the energy of the eighth harmonic of a K-band tube; we found the line again with a sixth harmonic from a J-band QK-291 klystron by first peaking the system on the tenth and fifteenth OCS lines.

Sensitivity

The signal-to-noise ratio obtained thus far on OCS rotational lines with the use of the recorder techniques is 7 to 1 at 1.0-mm wavelength, 30 to 1 at 1.1 mm, and better than 100 to 1 at 1.4 mm and above. In obtaining these signal-to-noise ratios we used a cell of 20-cm length and only $\frac{1}{4}$-cc volume. Most molecules absorb so strongly in this region that a longer cell is less effective. In the region of 2 mm and above, where it is now possible to obtain signal to noise ratios on power better than a thousand to one, a cell of K-band guide 6 m long has been used with excellent results on weak lines.

TABLE I. Observed transitions of $O^{16}C^{12}S^{32}$. $B_0=6081.494\pm0.10$ Mc/sec; $D_J=1.310\pm0.010$ kc/sec.

Oscillator harmonic	Transition	Frequency in Mc/sec Calculated	Frequency in Mc/sec Observed	Wavelength in mm
6	11→12	145 946.80	145 946.79±0.30	2.06
7	13→14	170 267.45	170 267.49±0.35	1.76
8	15→16	194 586.35	194 586.44±0.40	1.54
9	17→18	218 903.22	218 903.27±0.45	1.37
10	19→20	243 217.84	243 218.09±0.50	1.23
11	21→22	267 529.94	267 529.56±0.55	1.12
12'	23→24	291 839.27	291 839.22±0.60	1.03

MEASUREMENT OF CENTRIFUGAL STRETCHING IN MOLECULES

Rotational lines up to the $J=23\rightarrow24$ transition at 291.8 kMc/sec (1.027 mm) have been measured for $O^{16}C^{12}S^{32}$. The twenty-fourth line, which represents the highest spectral frequency measured to date with microwave spectroscopy, could barely be seen on the scope with the wide-band audio-amplifier but with a cell length of 20 cm gave a signal about 7 times the noise level on the recorder (see Fig. 6). The rotational lines were found to fit, within the limits of error, the theoretical formula

$$\nu=2B_0(J+1)-4D_J(J+1)^3,$$

with $B_0=6081.494\pm0.010$ mc/sec and $D_J=1.310\pm0.010$ kc/sec. Because of the cubic variation of the centrifugal stretching term, it is evident that D_J can now be measured much more accurately with microwave spectroscopy than it could when only the region above 2 mm could be reached. For the $J=7\rightarrow8$ transition at 3.09 mm, the centrifugal stretching term amounts to only 2.68 Mc/sec, whereas for the 23→24 transition at 1.03 mm it amounts to 72.44 Mc/sec. Furthermore, with the new technique of displaying several rotational lines, one can observe the stretching term directly by the separation of the lines on the scope or recorder without a measurement of the absolute frequencies or a knowledge of B_0. For this reason also, the centrifugal stretching constant D_J can now be more accurately obtained than was possible before. In Table I is a comparison of the measured frequencies of OCS with those calculated with the above formula.

In a symmetric-top molecule, there are two stretching constants, D_J and D_{JK}, which are observable from microwave measurements. These have already been measured at lower frequencies for the methyl halides but are being remeasured with the new techniques. This remeasurement has been completed for methyl fluoride. The results are given in Table II. The value of D_J, 57.8±1.0 kc/sec, agrees only roughly with the previous value, 32.5 kc/sec, obtained from the first

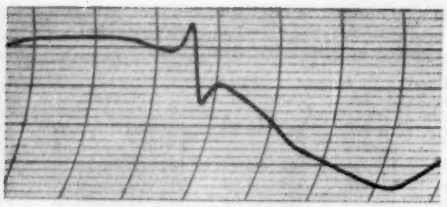

FIG. 7. Recorder tracing of the $2_{2,0} \rightarrow 3_{1,3}$ line of water vapor at 1.64-mm wavelength. The receiver is tuned to the fundamental frequency of the klystron modulation voltage (4 kc/sec). The tracing represents approximately the first derivative of the absorption line contour.

and second rotational lines only. Figure 5 is a photograph of the third and fourth transitions as displayed upon the scope.

WATER VAPOR LINE

A resonant absorption line has been found in water vapor at 183 311.30±0.30 Mc/sec. Its Stark effect has not yet been observed, but it can be identified with certainty from its position as the $2_{2,0} \rightarrow 3_{1,3}$ rotational line. Figure 7 shows a recorder tracing of the line.

Only two water vapor lines are expected[11] to fall in the entire microwave region between one mm and one m. A knowledge of the positions of these lines has practical significance for microwave propagation. Both have now been located experimentally. The $5_{2,3} \rightarrow 6_{1,6}$ transition occurring at 1.35 cm was first measured[12] during World War II after a radar band had unfortunately been developed in the same region.

The absorption coefficient and line-breadth parameter of the 1.62-mm line will be measured later in this laboratory. The observed frequency occurs only 1200 Mc/sec from that predicted by King, Hainer, and Cross.[11] Consequently, their predicted absorption coefficient of 6.838×10^{-3} cm^{-1} for the line should be approximately correct. Had the line occurred at a radically different frequency from that predicted, the predicted absorption coefficient, which varies rapidly with frequency, would also have been greatly in error.

[11] King, Hainer, and Cross, Phys. Rev. **71**, 433 (1947).
[12] G. E. Becker and S. H. Aulter, Phys. Rev. **70**, 300 (1946).

If centrifugal distortion effects are ignored and the reasonable value of 0.96A as obtained from infrared spectroscopy is assumed for the OH distance, the $2_{2,0} \rightarrow 3_{1,3}$ frequency yields the rather large value of 105° 56′ for the bond angle. The value obtained from infrared spectroscopy[13] is 105° 3′. The larger value obtained here is almost certainly caused by the centrifugal distortion which would be expected to open up the HOH angle. In consideration of the large OH bond stretching force constant 8×10^{-5} d/cm, no significant lengthening of the bond is expected. Insufficient data are obtainable from microwave spectroscopy on H_2O alone for evaluation of its centrifugal distortion constant. Progress is being made, however, in the evaluation[14] of these constants for D_2O and HDO, which have more abundant microwave spectra.

TABLE II. Observed transition of CH_3F. $B_0 = 25\,536.12 \pm 0.05$ Mc/sec; $D_J = 57.8 \pm 1.0$ kc/sec; $D_{JK} = 445 \pm 4$ kc/sec.

Oscillator harmonic	Transition J	K	Frequency in Mc/sec Calculated	Observed	Wavelength in mm
4	1→2	0	102 142.59	102 142.56±0.20	2.94
		1	102 140.81	102 140.86±0.20	
6	2→3	0	153 210.30	153 210.44±0.30	1.96
		1	153 207.63	153 207.65±0.30	
		2	153 199.62	153 199.58±0.30	
8	3→4	0	204 273.70	204 273.69±0.40	1.47
		1	204 270.14	204 270.09±0.40	
		2	204 259.46	204 259.48±0.40	
		3	204 241.66	204 241.71±0.40	

Mr. W. B. Francis, of the Duke University Instrument Shop, constructed the multiplier and detector, and it is a credit to his careful machine work that even the first models performed well. Mr. Frank Trippe, electronics technician, of the microwave laboratory, made all electronic components for the spectrometer. Mr. C. A. Burrus helped to obtain the experimental results.

[13] G. Herzberg, *Infrared and Raman Spectra* (D. Van. Nostrand Company, Inc., New York, 1945), p. 489.
[14] D. W. Posener and M. W. P. Strandberg, J. Chem. Phys. **21**, 1401 (1953).

The Stopping Powers of Various Elements for Protons of Energies from 400 to 1050 kev*

ARTHUR B. CHILTON,† JOHN N. COOPER, AND JAMES C. HARRIS
Ohio State University, Columbus, Ohio

(Received August 6, 1953)

The proton-stopping powers of the elements nitrogen, neon, argon, krypton, xenon, nickel, and copper are reported in the energy range from 400 kev to 1050 kev. Comparisons are made with results of other experimental work and with theory. The measured stopping powers show a dependence on particle velocity and on the atomic number of the stopping element in general conformity with the theory of N. Bohr. For proton energies below 700 kev, the ratio of atomic stopping power to $Z^{\frac{1}{2}}$ for nickel and copper is lower than the corresponding ratio for the gases. Energy loss straggling is reported for nickel and copper and is of the same order of magnitude as theory predicts.

I. INTRODUCTION

THE energy loss of particles as they traverse matter is a topic of great interest in modern physics. Bethe[1] and Bloch[2] have derived expressions for stopping power on the assumption that the particle velocity is much greater than the "velocities" of all electrons in the atoms of the stopping material. In order to extend the range of validity of these expressions to lower particle velocities, correction terms have been computed[3–5] to allow for the deficiency in stopping power of the K electrons. Protons of energies from 400 kev to 1050 kev, the region covered in this report, are so slow that formulas for the stopping power of the heavier elements for these particles require also corrections for deficiencies of electrons of the higher shells. For a few gaseous elements these corrections have been estimated and stopping power values for low-energy protons predicted,[6] but the approximations required to get numerical data make the accuracy of the results somewhat uncertain. Experimental data are thus needed to supplement theoretical calculations.

Bohr[7] has provided a formula applicable to moderately slow protons through heavy media. Although it is not expected to give absolutely accurate predictions, it has been shown to give approximately the correct dependence of stopping power upon proton velocity and atomic number of the medium traversed for protons of 350 to 550 kev passing through metallic foils.[8] The testing of these predictions in stopping power dependence at other energy ranges and through other types of media is desirable.

Another facet of the stopping-power problem which is of interest is the extent of difference to be expected at these low energies between values for media in the condensed state as compared with gaseous media. This aspect of the problem has been widely studied,[9] and is summarized in a review article by Taylor.[10] At high, though still nonrelativistic, particle velocities special stopping effects attributable to the condensed or conducting state of the stopping media are probably small, since the number of outer electrons seriously affected by the state of condensation is a small proportion of the total number of electrons in the atoms of the stopping medium. At low particle velocities the relative importance of the outer electrons to stopping power becomes greater, so that a difference in stopping power between gaseous and nongaseous elements, if it occurs, would be most likely to appear at the lower particle energies.

II. OUTLINE OF EXPERIMENTAL TECHNIQUE

The experiments were carried out by using protons accelerated by a Van de Graaff generator. The basic method was that utilized and described by Madsen and Venkateswarlu.[11] In this technique an energy spectrum for a certain proton reaction with some target material is obtained first without, and then with, a stopping medium inserted in the proton beam. The amount of material inserted is sufficient to slow, but not completely to stop, the protons of the beam. The energy loss suffered by the protons in the stopping material is indicated by the shift in the resonance peaks of the reaction spectrum, whereas the straggling in this energy loss is indicated by the increase in width of the peaks.[12]

* Supported in part by the U. S. Atomic Energy Commission through a contract with the Ohio State University Research Foundation.

† Commander, Civil Engineer Corps, U. S. Navy. Work performed under the sponsorship of the U. S. Office of Naval Research and the supervision of the U. S. Naval Postgraduate School. Present address: Bureau of Yards and Docks, Department of the Navy, Washington, D. C.

[1] H. A. Bethe, Ann. Physik **5**, 325 (1930).
[2] F. Bloch, Ann. Physik **16**, 285 (1933).
[3] M. S. Livingston and H. A. Bethe, Revs. Modern Phys. **9**, 245 (1937).
[4] L. M. Brown, Phys. Rev. **79**, 297 (1950).
[5] M. C. Walske, Phys. Rev. **88**, 1283 (1952).
[6] J. O. Hirschfelder and J. L. Magee, Phys. Rev. **73**, 207 (1948).
[7] N. Bohr, Kgl. Danske Videnskab. Selskab, Mat.-fys. Medd. **18**, No. 8 (1948).
[8] S. D. Warshaw, Phys. Rev. **76**, 1759 (1949).
[9] For example, see Ellis, Rossi, and Failla, Phys. Rev. **86**, 562 (1952), and references.
[10] A. E. Taylor, Repts. Progr. in Phys. **15**, 49 (1952).
[11] C. B. Madsen and P. Venkateswarlu, Phys. Rev. **74**, 648, 1782 (1948).
[12] No resonance peaks, shifted or unshifted, are shown herein since their shapes were quite usual. No significant asymmetry in the energy loss distribution was expected on a theoretical basis, nor was any observed.

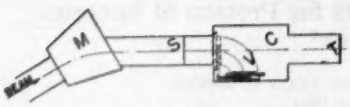

FIG. 1. Schematic diagram of the apparatus. Protons from the Van de Graaff generator are deflected to the slit S by the analyzing magnet M. The valve V has a slot covered by a thin foil of either copper or nickel. For calibration runs the valve V is lowered so the beam falls directly on the target T. The stopping power of the foil is obtained by raising V into the beam. For determining the stopping powers of gases, the chamber C is filled to a pressure of two to six mm of mercury.

The method as originally described was applied only to foils, but with minor modifications it is readily applicable to gases.

The apparatus utilized is shown schematically in Fig. 1. The proton beam, after passing through the analyzing magnetic field, proceeded through a defining slit into a box which performed the combined functions of gas chamber, target holder, and Faraday cage. This chamber had at the entrance a flap valve covered with a thin foil. This valve could be moved into or out of the beam by a shaft through a gas-tight seal. When the foil was in the beam, the valve was clamped against a gasketed valve seat. When the valve was in this position, the gas chamber would be left evacuated for experiments wherein the energy losses in the foil itself were measured. After the energy losses in the foil were known, appropriate gases could be introduced into the chamber, and energy losses in the gases could be determined. The foils used were either nickel or copper. The gases studied were nitrogen, neon, argon, krypton, and xenon.

The targets used for this work were either of lithium fluoride or of aluminum. The resonance energy levels for the (p,γ) reactions are accurately known for these target elements.[13,14] For study of the foils both types of target were used. Only the lithium fluoride targets were utilized for the study of the stopping powers of gases, because the yield from the shifted aluminum resonances was too low for satisfactory measurements. The targets used were a few kev thick in terms of the energy loss of the entering protons.

The voltage of the cap of the Van de Graaff generator was stabilized in standard manner by detecting any unbalance in proton current intercepted by the defining slits and automatically altering the corona drain to bring the beam back to a balanced position between the slits. The cap potential was determined from the current in the coils of the analyzing magnet, which was calibrated by use of precisely known (p,γ) resonances. The magnet current was provided by a motor-generator set and was regulated electronically. The variation in beam voltage due to magnet current fluctuations was less than 200 volts at one-Mev beam energy.

[13] F. Ajzenberg and T. Lauritsen, Revs. Modern Phys. **24**, 321 (1952).
[14] Bröström, Huus, and Tangen, Phys. Rev. **71**, 661 (1947).

The proton currents used were about 0.5 to 1.0 microampere. For such currents reaction yields were adequate to give statistically good points on the resonance curves but the currents were not so strong as to cause severe heating of the foils.

III. STOPPING MATERIALS

The copper and nickel foils varied from 0.03 to 0.1 mil in thickness (about 0.67 to 2 mg/cm^2). They were purchased from the Chromium Corporation of America, Waterbury, Connecticut, which had prepared them by a process of electrolytic deposition. These foils were a little thicker than are commonly used for such low-energy experiments, but a thicker foil has the advantages of minimizing the effect of errors in thickness estimation and of errors due to minute surface deposits of carbon or oxide. Ease in measurement and handling was also provided. The foils were trimmed to a rectangular shape, weighed in a microanalytical balance, and measured dimensionally under a low-powered microscope.

In order to insure thickness uniformity, a technique was developed which permitted the determination of statistical variations in foil thickness from spot to spot. Figure 2 shows the rather simple apparatus used for this determination. A thin source of polonium alpha particles was screened from a thin-window Geiger counter tube by a metal plate containing a small ($\frac{1}{32}$-in. diameter) hole of about the same size as the intense core of the proton beam from the accelerator. A platform containing the source was movable with reference to the Geiger tube. With the foil removed, data were first taken of counting rate as a function of height of the movable platform from the fixed surface. This gave a curve similar to curve (a) at the right side of Fig. 2. The steepness of the curve is determined by the range-straggling of the alpha particles. The experiment was repeated with a foil interposed over the hole. A curve (b) of similar shape, but displaced by amount A, the air equivalent of the foil for alpha particle stopping, was determined.

The apparatus was then set at height H, in order to

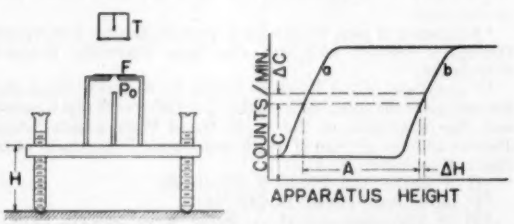

FIG. 2. Apparatus for measuring thickness variations in thin foils and typical curves obtained with the apparatus. Alpha particles from a thin polonium source (Po) pass through a small hole and are counted by the Geiger tube T. Curve (a) at the right is obtained by raising the source toward T. Then the thin foil F is placed over the hole and a curve (b) is obtained. The source is then set at height H and the counting rate determined with many different spots in the foil placed over the hole.

operate on a reasonably linear section of the steep part of the curve, and the counting rate was measured with various portions of the foil positioned over the hole. A change in counting rate Δc, when corrected for the natural statistical variations in source activity, indicated a change in air-equivalent of ΔH. The value of $\Delta H/A$ represented the fractional variation in thickness from the original spot to the new spot studied. The "counting statistics" provided a limit to the accuracy obtainable by this technique. For most of the foils used, a standard deviation of about 1.4 percent was obtained for the thickness variation, though the copper foils seemed on the average a little better than the nickel in this respect. This value was approximately equal to the standard deviation of the radiation counting process and, therefore, to the approximate limit of accuracy.

The chemical purities of the copper and nickel foils were determined by semiquantitative spectrographic analyses. The amounts of impurities were found to be very small, and no correction to the observed stopping powers was indicated. Four nickel foils and two copper foils were used in obtaining stopping power data. Each had a different thickness. Furthermore, each foil was cut into two pieces and in most cases each half was studied. One reason so many foil sections were used is that there was some difficulty with "carbonization" of the foils during bombardment. Foils were checked regularly, both visually and by repeated stopping power measurements, and they were discarded whenever the "carbon" layer became excessive.

The gases nitrogen and argon were purchased from the Linde Air Products Company in ordinary commercial pressurized cylinders with an expected purity of 99.6 percent or better. Because of the availability of these gases in large amounts at above atmospheric pressures, little opportunity for contamination by air leakage into the gas-chamber filling system was expected, and flushing and refilling was simple. Furthermore, the molecular stopping powers of the usual gases of the atmosphere are very close to those of nitrogen and argon, so that a small amount of contaminants would have little effect on stopping power results.

The gases neon, krypton, and xenon were purchased from the Linde Air Products Company and were supplied in glass flasks at approximately atmospheric pressure. After some gas had been used, the pressure was below atmospheric, and there was risk of air contamination during the gas-handling operations. Furthermore, the original purity guaranteed by the company permitted several percent contamination, mostly by other rare gases. For each of these three gases, therefore, a mass-spectrographic analysis was made on the residual gas in the flasks after the stopping power observations had been made. It was found that no appreciable contamination had been suffered by the krypton, enough by the neon to warrant a correction of about 7.5 percent in the final results, and a small amount by the xenon requiring correction of about 1.5 percent.

TABLE I. Summary of data on stopping power for protons.

(a) Nickel			(c) Nitrogen		
Proton energy (kev)	Stopping power [kev/(mg/cm²)]	Probable error (%)	Proton energy (kev)	Stopping power [kev/(mg/cm²)]	Probable error (%)
527	172	1.5	408	400	4.0
704	149	2.0	410	401	4.0
718	150	3.0	454	371	2.5
739	143	2.0	502	362	4.0
741	142	2.0	503	351	4.0
755	145	1.5	542	328	3.0
757	146	1.5	648	296	4.5
915	128	3.0	648	278	4.0
935	126	2.0	716	275	4.5
941	134	2.0	717	264	4.5
949	128	2.0	750	257	3.5
951	132	2.0	914	238	4.5
977	129	3.0	914	219	4.5
1000	127	2.0	942	217	3.5
1007	122	2.0	973	207	4.5
1046	120	2.5	974	228	4.5
1047	122	2.5	1001	209	4.0
1057	121	2.0			

(b) Copper			(d) Neon		
Proton energy (kev)	Stopping power [kev/(mg/cm²)]	Probable error (%)	Proton energy (kev)	Stopping power [kev/(mg/cm²)]	Probable error (%)
446	169	1.5	422	310	3.5
532	158	1.5	424	290	3.5
603	150	1.5	517	280	3.5
713	140	1.5	519	269	3.5
755	137	2.0	668	236	4.0
812	132	1.5	730	217	4.0
949	120	2.0	733	217	4.0
996	115	1.5	929	186	4.0
1006	112	2.0	930	191	4.0
1050	113	2.0	988	175	4.0
			992	188	4.0

(e) Argon			(g) Xenon		
Proton energy (kev)	Stopping power [kev/(mg/cm²)]	Probable error (%)	Proton energy (kev)	Stopping power [kev/(mg/cm²)]	Probable error (%)
421	225	3.5	437	121	3.5
476	224	2.0	441	121	3.0
519	215	3.5	536	111	3.5
567	207	2.5	538	115	3.5
662	176	4.0	679	91	3.5
713	187	2.5	679	95	3.5
778	176	2.5	748	87	3.5
929	154	4.0	750	93	3.5
932	155	4.0	943	78	4.0
971	154	3.0	969	77	3.5
989	149	4.0			

(f) Krypton		
Proton energy (kev)	Stopping power [kev/(mg/cm²)]	Probable error (%)
420	163	3.5
516	150	3.5
527	154	3.5
665	130	4.0
675	129	3.5
733	124	4.0
743	122	3.5
929	107	4.0
941	107	4.0
989	103	4.0

The scattering of particles in the stopping medium adds to the path length of the particle in the medium and would thus introduce a possible error, particularly in case of the gases, since the amount of material traversed (foil plus gas) was largest in these cases. However, the half-angle subtended by the target (with vertex at the window foil) was small (5.6°). Errors involved in ignoring the scattering factor were determined to be much smaller than the over-all experimental error.

IV. RESULTS

Table I lists for seven elements the measured values of the stopping power in kev/(mg/cm²) for several proton energies. The method by which the proton energy was assigned is described below.

When the average energy loss $\langle \Delta E \rangle_{Av}$ in the stopping medium is very small compared to the initial proton energy E_i, it is adequate to assign the observed $-\langle \Delta E \rangle_{Av}/\Delta x$ as $-dE/dx$ for the arithmetic mean of the initial and exit energies of the beam. However, when the energy loss is appreciable compared to E_i, the observed rate of energy loss should be assigned to some intermediate energy E_p other than the average. Warshaw[8] has commented on this matter and has proposed a correction based on the assumption that the stopping power is a linear function of proton energy over a small region.

In view of the great energy losses (~100 to 300 kev) in traversing our unusually large amounts of stopping material, it is important to consider the actual shape of the stopping power curve when determining E_p. In the energy region in question it is approximately true that

$$-dE/dx = kE^{-\gamma}, \tag{1}$$

where $\gamma = 0.5$ according to Eq. (3.5.7) of Bohr's[7] paper. The thickness of medium traversed Δx is given by

$$\Delta x = \int_{E_f}^{E_i} \frac{dE}{-(dE/dx)} = \frac{E_i^{\gamma+1} - E_f^{\gamma+1}}{k(\gamma+1)}, \tag{2}$$

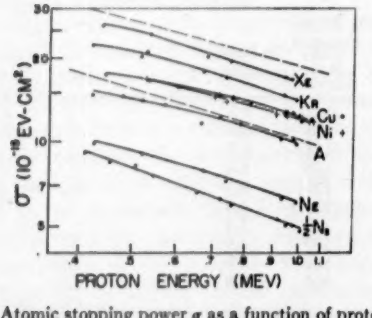

FIG. 3. Atomic stopping power σ as a function of proton energy for seven elements. Wherever two values from Table I were too close to plot separately, the plotted point represents an average value. The light, dashed lines are the predictions of Hirschfelder and Magee (see reference 6) for Xe and A.

where E_i and E_f are the initial and final proton energies, respectively.

If E_p is the energy of the protons for which $(E_i - E_f)/\Delta x$ is actually $-dE/dx$,

$$-\frac{dE}{dx}\Big]_{E_p} = \frac{E_i - E_f}{\Delta x} \tag{3}$$

and

$$\Delta x = (E_i - E_f)/kE_p^{-\gamma}. \tag{4}$$

If the expressions for Δx [Eqs. (2) and (4)] are equated and the resultant expression is solved for E_p, one obtains

$$E_p = \left[\frac{1}{\gamma+1} \cdot \frac{E_i^{\gamma+1} - E_f^{\gamma+1}}{E_i - E_f}\right]^{1/\gamma}. \tag{5}$$

If $(E_i + E_f)/2 = E_a$ and $E_i - E_f = \langle \Delta E \rangle_{Av}$, Eq. (5) may be expanded to give

$$E_p = E_a\left\{1 + \frac{(\gamma-1)}{24}\left(\frac{\langle \Delta E \rangle_{Av}}{E_a}\right)^2 + \text{other terms}\right\}. \tag{6}$$

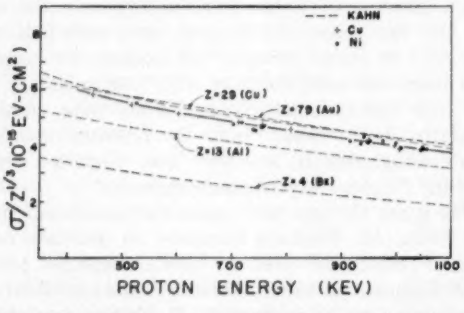

FIG. 4. The ratio of atomic stopping power σ to $Z^{\frac{1}{3}}$ as a function of proton energy for copper and nickel. For comparison, data derived from Kahn (see reference 15) are plotted for several metals to give the dashed curves.

The other terms involve higher powers of $\langle \Delta E \rangle_{Av}/E_a$ and may be neglected when $\langle \Delta E \rangle_{Av} < E_a$.

The probable error of each experimental stopping power value has been computed and appears in Table I. For the foils the probable error in $\langle \Delta E \rangle_{Av}$ was found to be about 2.2 kev and the error in foil thickness 1.1 percent. These values lead to total probable errors in the stopping power results of 1.5 to 3.0 percent. For the gases the error in $\langle \Delta E \rangle_{Av}$ was taken as 3.0 kev, the total error in equivalent gas thickness, including the effects of impurities, varied from 1.4 to 1.7 percent. The total probable error in the individual values of gas stopping power varied from 2.0 to 4.5 percent. These individual probable errors are only partially independent, since certain measurements were common to calculations of several individual values.

V. DISCUSSION OF RESULTS

In Fig. 3 the atomic stopping power in ev-cm² is plotted as a function of proton energy. Also shown are

the curves for xenon and argon predicted by Hirschfelder and Magee.[6] In both cases the experimental points lie below the theoretical curves by an amount somewhat greater than the computed probable error of the experimental points, the differences being of the order of 5 to 10 percent.

Bohr predicts [reference 7, Eq. (3.5.7)] that stopping power in this energy region is inversely proportional to particle velocity, so that a plot of stopping power *versus* proton energy should give a straight line on a logarithmic plot, with a slope of -0.5. From Fig. 3 it is clear that our data are in rough, though not precise, agreement with this prediction, as were previous data by Warshaw[8] in a lower energy range.

According to the same equation of Bohr referred to above, the atomic stopping power is proportional to the cube root of the atomic number for the heavier elements. If the values of atomic stopping power divided by $Z^{\frac{1}{3}}$ are plotted as a function of proton energy for each element, the plots should coincide to the extent that the theoretical prediction is correct. The comparison between the stopping power values for various

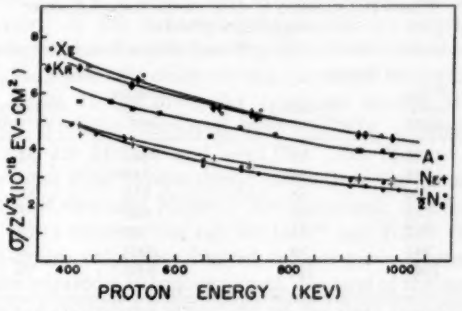

FIG. 5. The ratio of atomic stopping power σ to $Z^{\frac{1}{3}}$ as a function of proton energy for gases.

elements is made easier by such a plot. Figure 4 shows the data for the metals studied. Also included for the sake of comparison are curves for several metals derived from the results of Kahn.[15] It should be noted that our curves for nickel and copper are practically coincident. Kahn's curve for copper lies about 4 percent above ours. Madsen has also done some work on protons through copper,[16] but his curve lies in general about 13 percent below ours. The results on stopping power of metals provided by earlier workers[11,17] on beryllium and gold are not shown here, but are in substantial agreement with the work of Kahn.

In Fig. 5 the atomic stopping power σ divided by the cube root of the atomic number is shown as a function of proton energy for the gases studied. Weyl[18] has reported data for protons with energies up to 450 kev

[15] D. Kahn, Phys. Rev. **90**, 503 (1953).
[16] C. B. Madsen (private communication, 1953).
[17] T. Huus and C. B. Madsen, Phys. Rev. **76**, 323 (1949).
[18] P. K. Weyl, Phys. Rev. **91**, 289 (1953).

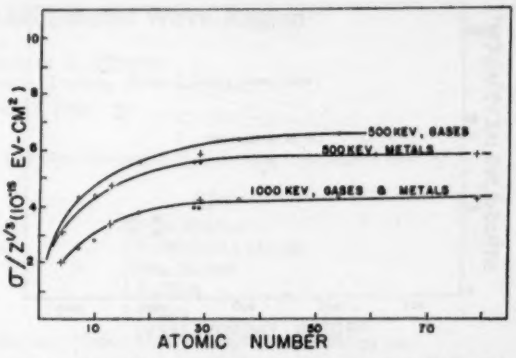

FIG. 6. The ratio of atomic stopping power σ to $Z^{\frac{1}{3}}$ as a function of atomic number Z at proton energies of 500 and 1000 kev. The open circles represent the results of this paper for gases and the closed circles for metals. The crosses represent the measurements of Kahn (see reference 15) for metals.

passing through argon. His results coincide essentially with ours where the regions of study overlap. Dunbar, Reynolds, Wenzel, and Whaling[19] have studied all the gases reported on herein for proton energies up to 600 kev. Within the region of overlap our data agree well with theirs for nitrogen, neon, and argon. For krypton their results are about 5 percent lower than ours, but for xenon they are about 15 percent higher.[20]

From the curves given in Figs. 4 and 5, data were obtained for Fig. 6 in which stopping power divided by cube root of atomic number is plotted as a function of atomic number. This is done for two values of proton energy: 500 kev and 1000 kev. If $\sigma/Z^{\frac{1}{3}}$ were constant, as Bohr's theory predicts for heavy elements, the curves would be horizontal lines. The curves fall off for low atomic numbers, but for $Z \gtrsim 25$ they show the expected horizontal character.

It is of particular interest to note the discrepancy between the results for the gases and the metals for the proton energy of 500 kev. Figure 3 indicates that this discrepancy begins to be apparent if the proton energy decreases to below about 700 kev. This confirms the conjecture that if differences exist between gaseous and condensed media, they should show up most strongly at low proton velocities, since the relative importance of the outer electrons becomes greater as the proton velocity decreases. Whether the deviation of the metals studied is due to their conduction properties or simply to their condensed state is not known. Future experimental work on nonconducting media in the condensed state would be desirable to answer this question.

[19] Dunbar, Reynolds, Wenzel, and Whaling, Phys. Rev. **91**, 496 (1953) and **92**, 742 (1953).
[20] This discrepancy for xenon was so far outside the probable error limit that a repetition of the measurements of energy loss in xenon and purity of the xenon sample was considered worthwhile. The two values of stopping power which were obtained were essentially in agreement with our earlier results.

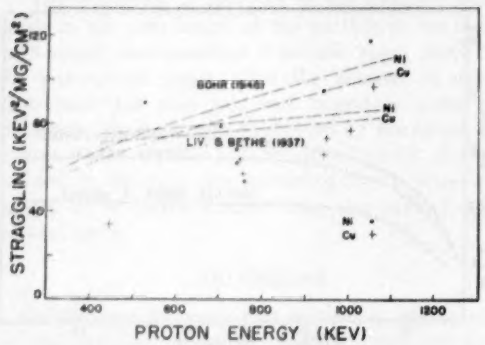

FIG. 7. Stopping power straggling (energy loss variance per unit thickness) as a function of proton energy. The dotted lines are calculated from theoretical expressions of Livingston and Bethe (see reference 3) and of Bohr (see reference 7).

VI. STOPPING POWER STRAGGLING

Associated with the idea of stopping power is the concept of "straggling" in energy loss of similar particles in traversing a given amount of stopping material. This effect is due to the statistical nature of the stopping process. This straggling has been treated theoretically for slow particles by Livingston and Bethe[3] and by Bohr.[7] Very little experimental work has been done for low-energy protons. Madsen and Venkateswarlu[11] have measured the straggling in beryllium foils for protons with energies between 400 and 1200 kev.

If ΔE is the energy loss of a particular particle in passing through a given layer of material and $\langle \Delta E \rangle_{Av}$ is the average value of the energy loss for a number of identical particles of the same incident energy, the mean square fluctuation is defined as

$$\Omega^2 = \langle (\Delta E - \langle \Delta E \rangle_{Av})^2 \rangle_{Av}, \qquad (7)$$

and the straggling in stopping power is given by $d(\Omega^2)/dx$. The straggling can be computed from the measured widths of the resonances in the shifted and unshifted yield curves (see reference 11).

The results on the straggling in energy loss of protons traversing the foils are shown in Table II. It was impossible to compute meaningful values of the straggling in gases from our experimental resonance curves. It is difficult to ascribe probable errors to the values tabulated for the straggling effect. The measurements are themselves of a statistical variable which is hardly greater than the errors themselves in energy losses. Furthermore, the errors are much more likely to be positive than negative, since any effects giving rise to variations in stopping power increase the computed value of straggling. The extent of the errors can be judged best by noting the spread in the individual points in the table.

In Fig. 7 the results are plotted along with calculations based on the theoretical expressions due to Bohr [reference 7, Eq. (3.5.8)] and to Livingston and Bethe [reference 3, Eq. (788)]. (The appropriate electron ionization energies were taken for I_n and 4/3 was used as the value for each κ_n.) The results are seen to be too erratic to do more than confirm the correctness in order of magnitude of both expressions. The formula of Bohr does seem to predict the general variation of the straggling with proton energy. The variations in foil thickness, even though small, may have a marked effect upon this straggling; such effect is obviously always to add to the observed straggling. This fact, coupled with the results of the thickness variation studies (outlined above) showing that the copper foils seem to be somewhat more uniform in thickness than the nickel foils, would seem to indicate strongly that the correct experimental curve for straggling is somewhat lower than the theoretical curves. The approximations made in developing the formula suggest that the predicted values might be too high for low proton energies.

TABLE II. Summary of data on the stopping power straggling of protons.

(a) Nickel		(b) Copper	
Proton energy (kev)	Straggling [kev²/(mg/cm²)]	Proton energy (kev)	Straggling [kev²/(mg/cm²)]
527	89	446	34
704	78	749	63
739	68	755	57
741	61	945	65
757	54	949	72
941	94	1004	76
1046	116	1006	96

VII. ACKNOWLEDGMENTS

The authors are indebted to the other members of the staff of the Van de Graaff generator program for their assistance on many aspects of the stopping power work. We wish to express our gratitude to the Ohio State University Development Fund and to the Graduate School for financial support and to Professors S. K. Allison of the University of Chicago and Ward Whaling of the California Institute of Technology for helpful discussions.

Note added in proof: The authors have recently received Dr. C. B. Madsen's summary [Kgl. Danske Vid. Sels. Math.-fys. Medd. **27**, 13 (1953)] of his stopping power results for Be, Cu, Ag, and Au. Aside from the previously noted discrepancy for Cu, the results fit well into the $\sigma/Z^{\frac{1}{2}}$ *vs* Z curves of Fig. 6. Furthermore, Madsen reports measurements for straggling in Cu which are consistent with those in Table II.

Spectrum of DBr in the One-Millimeter Wave Region*

WALTER GORDY AND CHARLES A. BURRUS†
Department of Physics, Duke University, Durham, North Carolina
(Received October 21, 1953)

From measurements on the 0→1 transition of DBr at 1.18-mm wavelength the following information has been obtained:

	DBr^{79}	DBr^{81}
eQq(Br)	533±3 Mc/sec	455±3 Mc/sec
B_0	127 358.2±0.3 Mc/sec	127 280.0±0.3 Mc/sec
B_e	1286_{18} Mc/sec	1285_{38} Mc/sec
r_0	1.42136_2A	1.42136_2A
r_e	1.414_{40}A	1.414_{39}A

Values of α obtained from infrared spectroscopy by Keller and Nielsen were employed in calculating the equilibrium values.

WITH the new mm-wave methods already described,[1] the $J=0\rightarrow1$ rotational transitions of DBr^{79} and DBr^{81} have been measured at 1.18-millimeter wavelength. Both Br^{79} and Br^{81} have a nuclear spin of $\frac{3}{2}$, and the Br nuclear quadrupole interactions split the transitions into triplet components having relative intensities of 1, 2, and 3. The lines were easily seen and measured on the cathode-ray scope with an amplifier of 6-kc/sec band width (see Fig. 1).

Table I gives the observed and calculated frequencies and Table II the molecular constants derived from them. We also employed the auxiliary constants, $D=2.8$, 2.8 Mc/sec and $\alpha=1257$, 1258 Mc/sec for DBr^{79} and DBr^{81}, respectively, taken from the infrared data of Keller and Nielsen.[2] No observable difference was found between the r_0's for DBr^{79} and DBr^{81}. The equilibrium values are limited to four-place accuracy by the infrared α values employed. Because of the small effects of centrifugal stretching on the 0→1 transition, the infrared D value does not limit the accuracy of B_0. The B values of Keller and Nielsen are in complete agreement with ours to the four significant figures which they quote.

The Br nuclear coupling, eQq, with the coupling per unbalanced p electron from atomic beam measurements,[3] yields the number of unbalanced p electrons of Br in DBr as

$$U_p=(eQq)_{\text{mol}}/2(eQq)_{\text{atom}}=0.69.$$

With hybridization and other small effects neglected, a bond ionic character of 31 percent is indicated. This U_p value is in good agreement with that of 0.65 predicted from the nuclear coupling-electronegativity relation,[4] $U_p=1-|x_A-x_B|/2$.

Deuterium bromide has the smallest moment of inertia of any molecule so far measured with microwave electronic methods. It should prove worthwhile for optical spectroscopists to measure the wavelength separation of its higher J transitions very precisely in order to obtain a check on the velocity of light. Rank,

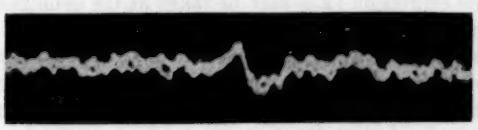

FIG. 1. Cathode-ray trace of the $F=\frac{3}{2}\rightarrow\frac{5}{2}$, $J=0\rightarrow1$, line of DBr^{81} at 1.18-mm wavelength.

TABLE I. $J=0\rightarrow1$ transitions of DBr^{79} and DBr^{81}.

$F\rightarrow F'$	Frequency in Mc/sec: Calculated[a]	Observed
	DBr^{79}	
$\frac{3}{2}\rightarrow\frac{1}{2}$	254 572.0	254 572.2±0.5
$\frac{3}{2}\rightarrow\frac{3}{2}$	254 678.5	254 678.6±0.5
$\frac{3}{2}\rightarrow\frac{5}{2}$	254 811.8	254 812.9±1.0
	DBr^{81}	
$\frac{3}{2}\rightarrow\frac{1}{2}$	254 437.7	254 439.4±1.5
$\frac{3}{2}\rightarrow\frac{3}{2}$	254 526.8	254 526.7±0.5
$\frac{3}{2}\rightarrow\frac{5}{2}$	254 637.9	254 638.0±0.5

[a] Calculated with ν_0's and eQq's given in Table II.

TABLE II. Characteristic constants of deuterium bromide.[a]

	DBr^{79}	DBr^{81}
eQq(Br)	533±3 Mc/sec	455±3 Mc/sec
$\nu_0(0\rightarrow1)$[b]	254 705.2±0.5 Mc/sec	254 548.9±0.5 Mc/sec
B_0	127 358.2±0.3 Mc/sec	127 280.0±0.3 Mc/sec
B_e	1286_{18} Mc/sec	1285_{38} Mc/sec
r_0	1.42136_2A	1.42136_2A
r_e	1.414_{40}A	1.414_{39}A

[a] Atomic masses employed are those tabulated in reference 4.
[b] Rotational frequency corrected for nuclear quadrupole splitting.

* This research was supported by the United States Air Force under a contract monitored by the Office of Scientific Research, Air Research and Development Command.
† Shell Company Fellow.
[1] W. C. King and W. Gordy, Phys. Rev. 90, 319 (1953). See also Part IV of same series. Phys Rev. (to be published).
[2] F. L. Keller and A. H. Nielsen, Phys. Rev. 91, 235 (1953).
[3] J. G. King and V. Jaccarino, Phys. Rev. 91, 209 (1953).
[4] Gordy, Smith, and Trambarulo, *Microwave Spectroscopy* (John Wiley and Sons, Inc., New York, 1953), p. 284.

Ruth, and Vander Sluis[5] have attempted to check the velocity of light by comparing microwave and optical constants of HCN; but the results do not agree well with the accurate, recent values[6] from other sources. Better results might be obtained with DBr. The separations of the rotational lines of DBr (in a sample with one Br isotope concentrated) are three times those of HCN. Effects of the nuclear hyperfine structure are easily calculable with the known coupling constants, and for relatively high J values they can be neglected entirely. There is hope that DCl (first rotational line near 0.9 mm) can be reached with the present mm-wave techniques. If so, it would provide a still more desirable link between optical and radiofrequency measurements.

We wish to thank Dr. Albert Jache for preparing the sample of DBr.

[5] Rank, Ruth, and Vander Sluis, Phys. Rev. 86, 799 (1952).
[6] J. W. M. DuMond and E. R. Cohen, Revs. Modern Phys. 25, 691 (1953).

PHYSICAL REVIEW VOLUME 93, NUMBER 3 FEBRUARY 1, 1954

Theory of Fine Structure Pressure Broadening of Spectral Lines*

MAKOTO TAKEO AND SHANG-YI CH'EN
Department of Physics, University of Oregon, Eugene, Oregon
(Received May 26, 1953)

The difference of pressure broadenings and shifts of the doublet components of the principal series lines of alkalis is treated in an approximate manner. Applying the perturbation method and the Franck-Condon principle to the Michels, deBoer, and Bijl model of compressed atoms in the doublet P states, it is shown that the doublet separation becomes smaller with increasing pressure at rather low pressure. Consequently, the shift of the $^2P_{\frac{1}{2}}$ must be smaller than that of the $^2P_{\frac{3}{2}}$ component of the principal series. The attractive forces are recalculated with the inclusion of the quadrupole moment for the $^2P_{\frac{1}{2}}$ state. This consideration requires the splitting of the state according to the magnetic quantum numbers so that the $^2P_{\frac{1}{2}}$ component will be 1.12 times larger in half-width than $^2P_{\frac{3}{2}}$ in the approximation of the collision theory. This result is in good agreement with experimental values.

I. INTRODUCTION

NONE of the theoretical work on the theory of the pressure broadening of spectral lines has served to explain the well-established experimental fact[1] that under the influence of a foreign gas at high pressure the shifts and half-widths of the different components of a multiplet are different, i.e., the so-called fine structure pressure effect, although in the case of self-broadening good theoretical work has been reported.[2] The reason may be to the lack of knowledge of the intermolecular forces, repulsive and attractive, including excited states.

In this article alkali atoms are treated as perturbed by rare gases in a rather approximate manner. Without the formation of chemical bonds in this case, rare gases serve to compress the electron clouds of radiating or absorbing atoms. The ambiguity of the separation of two molecules coming from the thermal motion of molecules will be disregarded so that the Hamiltonian concerned is a definite function of separation.

II. OVERLAP EFFECT

A. Perturbation Method Applied to a Compressed Atom

The Michels, deBoer, and Bijl model[3] of a compressed molecule may be used for the repulsive forces. The Franck-Condon principle is assumed in the absorption process starting from a spherically symmetric ground state. Thus the model is comparable to the replacement of the compressing molecules by a spherical infinite potential wall, such that

$$V(r)=0 \quad \text{for } 0\leq r<r_0,$$
$$=\infty \quad \text{for } r_0\leq r. \tag{2.1}$$

Assuming that the energy change of the atomic state is small in comparison with the energy level separations, the perturbation method is applied. Using the Dirac δ function,[4] the perturbation energy may be written as follows:

$$V(r)=\lim_{\Delta r\to 0}\sum_{k=0}^{\infty}\delta(r-(r_0+k\Delta r)). \tag{2.2}$$

The expression (2.2) may be taken as the definition of our potential wall if the discontinuity of (2.1) at the boundary is neglected. Denoting the wave function of the unperturbed state n of the absorbing atom without relativistic correction by ψ_n, the new energy and new normalized wave function are

$$W=W_n+(n|V|n)+\sum_j{}'\frac{(n|V|j)(j|V|n)}{W_n-W_j}, \tag{2.3}$$

$$\psi=\psi_n+\sum_j{}'\frac{(j|V|n)}{W_n-W_j}\psi_j. \tag{2.4}$$

The primed summation implies the exclusion of the

* This work was supported by a research grant from the National Science Foundation.
[1] S. Y. Ch'en, Phys. Rev. 58, 1051 (1940); E. D. Clayton and S. Y. Ch'en, Phys. Rev. 85, 68 (1952); S. Y. Ch'en and D. A. Kohler, Phys. Rev. 90, 1019 (1953).
[2] H. M. Foley, Phys. Rev. 69, 616 (1946).
[3] Michels, deBoer, and Bijl, Physica 4, 981 (1937).
[4] L. I. Schiff, *Quantum Mechanics* (McGraw-Hill Book Company, Inc., New York, 1951), p. 50.

state n from the sum. The matrix element can be easily evaluated:

$$(n'|V|n)=\int_{r_0}^{\infty} R_n^*(r)R_{n'}(r)r^2dr, \text{ when } l=l', \quad m_l=m_{l'},\ s=s', \quad (2.5)$$
$$=0, \text{ otherwise,}$$

where r_0 is the radius of the boundary surface of the infinite potential wall. $R_n(r)$ is the radial part of the wave function ψ_n. The selection rule (2.5) justifies the validity of (2.3) and (2.4) in the degenerate states.

In (2.3), if the denominator of the sum is replaced by the average value ΔW, the summation in the numerator can be carried out directly using the sum rule:

$$\sum_j{}'(n|V|j)(j|V|n)=(n|V^2|n)-(n|V|n)^2. \quad (2.6)$$

Owing to the special feature of the perturbation energy, $(n|V^2|n)$ is equal to $(n|V|n)$. Therefore, (2.3) leads to

$$W=W_n+\left(1+\frac{1}{\Delta W}\right)(n|V|n)-\frac{1}{\Delta W}(n|V|n)^2. \quad (2.7)$$

It often happens that the summation in (2.3) has a very poor convergence and requires many wave functions, and this is also true for the evaluation of the average value ΔW. However, (2.7) has an advantage over (2.3) in that ΔW is practically independent of r_0 over an appreciable range of r_0.

The difficulty of evaluation of ΔW may be lessened by using the variation method. This can give the maximum energy value using only the wave functions of the state concerned and lower-lying states.

B. Variation Method Applied to a Compressed Atom

The resonance lines will be more specifically considered. The trial function for the first excited state is written as

$$(1+AH')\psi_1-\int\psi_0^*\psi_1(1+AH')d\tau\psi_0,$$

which is orthogonal to the ground state wave function ψ_0. Here, A is the variation parameter and H' is the perturbation expressed by (2.2) interacting with the singly excited state ψ^1. The energy to be minimized is

$$W=\frac{\int[\psi_1^*(1+AH')^*-A\psi_0^*(1|H'|0)](H_0+H')\times[(1+AH')\psi_1-A(0|H'|1)\psi_0]d\tau}{\int|(1+AH')\psi_1-A(0|H'|1)\psi_0|^2d\tau} \quad (2.8)$$

where we have written

$$\int\psi_0^*\psi_1(1+AH')d\tau=A(1|H'|0).$$

By the selection rule (2.5), H' is not diagonal with respect to the principal quantum number, so that H_0 and H' do not commute with each other. However, the calculation is rather simple. After minimization, (2.8) leads to

$$W=\frac{[W_1+(1|V|1)+A\{2(1+W_1)(1|V|1)+\frac{1}{2}r_0^2[(R_1^2)']_{r=r_0}-2(0|V|1)^2\}+A^2\{(1+W_1)(1|V|1)+\frac{1}{2}r_0^2[(R_1^2)']_{r=r_0}-(1|V|0)^2[2+W_1-(0|V|0)]-\frac{1}{2}(1|V|0)r_0^3[(R_0R_1)']_{r=r_0}\}]}{1+2A(1|V|1)+A^2\{(1|V|1)-(0|V|1)^2\}} \quad (2.9)$$

with

$$A=-\frac{W_1(1|V|1)+\frac{1}{4}r_0^2[(R_1^2)']_{r=r_0}-(0|V|1)^2}{W_1(1|V|1)+\frac{1}{2}r_0^2[(R_1^2)']_{r=r_0}-(1|V|0)^2[1+W_1-(0|V|0)]-\frac{1}{2}(1|V|0)r_0^3[(R_0R_1)']_{r=r_0}} \quad (2.10)$$

and the matrix elements defined by (2.5). W_1 is the energy of the unperturbed first excited state and R_0 the radial wave function of the unperturbed ground state. The primed parentheses imply the derivative with respect to r.

The two methods give good results for hydrogen atoms in the states $1s$, $2s$, and $2p$, compared with calculations by ten Seldam and deGroot, for r_0 greater than 4 or 5A.[5]

C. Atomic Field under Compression

The atomic field in which the valence electron moves may change with pressure. If we assume the Thomas-Fermi-Dirac statistical model for the atomic core, the effective nuclear charge for the valence electron at r from the nucleus is expressed by

$$(Z-1)e\chi(r)+e, \quad (2.11)$$

where $\chi(r)$ is the solution of the Thomas-Fermi-Dirac equation with $r=bx$, b being equal to $0.886a_0/(Z-1)^{\frac{1}{3}}$ and Z being the atomic number of the absorbing atom. However, the boundary conditions must be such that

$$\chi(0)=1, \quad \left(\frac{d\chi(x)}{dx}\right)_{x=x_0}=\frac{\chi(x_0)}{x_0}. \quad (2.12)$$

Therefore, the pressure dependence of this quantity (4.1) can be deduced from that of $\chi(r)$. This treatment may be compared with the calculation of the polarizability of compressed argon by ten Seldam and deGroot.[6]

The solution of the Thomas-Fermi-Dirac equation for zero pressure will be denoted by $\chi_0(r)$, and a small quantity $\Delta\chi_p(r)$ will be added when compressed. Thus

[5] S. R. deGroot and C. A. ten Seldam, Physica **12**, 669 (1946).
[6] C. A. ten Seldam and S. R. deGroot, Physics **18**, 809 (1952).

we can write for the atomic field:

$$V_0(r)=-\frac{e^2}{r}\{(Z-1)\chi_0(r)+1\}-\frac{(Z-1)e^2\Delta\chi_p(r)}{r}, \quad (2.13)$$

with $\chi_p(r)=\chi_0(r)+\Delta\chi_p(r)$. The $\chi_0(r)$ vanishes at finite r, and $\Delta_p(r)$ is much larger than $\chi_0(r)$ for large r. The boundary condition (2.12) leads to

$$\left(\frac{d\Delta\chi_p(x)}{dx}\right)_{x=x_0}\sim\frac{\Delta\chi_p(x_0)}{x_0}\sim\frac{\chi_p(x_0)}{x_0}. \quad (2.14)$$

D. Doublet Separation

Now we are ready to write down the doublet separation. The spin-orbit energy of the nl state is given by

$$\tfrac{1}{2}l\zeta_{nl} \quad \text{if} \quad j=l+\tfrac{1}{2}, \quad (2.15)$$

$$\tfrac{1}{2}(l+1)\zeta_{nl} \quad \text{if} \quad j=l-\tfrac{1}{2}, \quad (2.16)$$

$$\zeta_{nl}=\frac{\hbar^2}{2m^2c^2}\int_0^\infty |R_{nl}(r)|^2\frac{dV_0}{dr}rdr, \quad (2.17)$$

where V_0 is the potential energy of the valence electron. Using the wave function (2.4) and the rule associated with (2.6), we arrive at the following expression for (2.17):

$$\zeta_{nl}=d_{nl,\,nl}+\frac{2}{\Delta W}\sum_{n'}{}'(nl|V|nl)d_{n'l,\,nl}+\frac{(Z-1)e^2\hbar^2}{2m^2c^2}\chi_p(r_0)(1-b)\langle 1/r^3\rangle_{nl}. \quad (2.18)$$

The symbols are

$$d_{n'l,\,nl}=\frac{\hbar^2}{2m^2c^2}\int_0^\infty R_{n'l}{}^*R_{nl}\frac{1}{r}\frac{d}{dr}\times\left(-\frac{e^2}{r}\{(Z-1)\chi_0(r)+1\}\right)r^2dr,$$

and

$$\langle 1/r^3\rangle_{nl}=\int_0^\infty |R_{nl}(r)|^2\frac{1}{r}dr.$$

If the pressure is so low that the point $r=r_0$ is well outside of the atomic core ($r_0>3$A for Rb), the third term in (2.18) vanishes. Since the ΔW is negative, one can conclude that for moderate pressure the doublet separation is smaller with increasing pressure. By the sum rule the second term of (2.18) may be rewritten as follows:

$$\sum_{n'}{}'(nl|V|n'l)d_{n'l,\,nl}=\frac{\hbar^2}{2m^2c^2}\int_{r_0}^\infty |R_{nl}(r)|^2\frac{1}{r}\frac{d}{dr}\times\left[-\frac{e^2}{r}\{(Z-1)\chi_0(r)+1\}\right]r^2dr. \quad (2.19)$$

Well outside the atomic core, the potential field is hydrogenic:

$$\sum_{n'}{}'(nl|V|n'l)d_{n'l,\,nl}=\frac{\hbar^2}{2m^2c^2}\int_{r_0}^\infty |R_{nl}(r)|^2\frac{e^2}{r}dr.$$

Thus, (2.18) leads to

$$\zeta_{nl}=d_{nl,\,nl}-\frac{\hbar^2}{|\Delta W|\,m^2c^2}\int_{r_0}^\infty |R_{nl}|^2\frac{e^2}{r}dr. \quad (2.20)$$

This may be valid up to pressures of several hundred atmospheres, where the radius r_0 of the infinite potential wall is of the order of magnitude 5A.

The formula (2.20) leads to the conclusion that the line shift of the $^2P_{\frac{1}{2}}$ component is smaller than that of the $^2P_{\frac{3}{2}}$ in the principal series, as is easily seen from Fig. 1. With notation designated in the figure, the shifts are

$$^2P_{\frac{1}{2}}: \quad b'+b-a-c, \quad (2.21)$$

$$^2P_{\frac{3}{2}}: \quad 2a+b-2b'-c. \quad (2.22)$$

This difference of shift is what is observed under perturbation due to helium. It may easily be seen, however, that if the third term of (2.18) becomes larger than the second term due to the change of the effective nuclear field by high pressure, the shift of the $^2P_{\frac{1}{2}}$ is greater than that of the $^2P_{\frac{3}{2}}$, as has been observed at very high pressures.[7]

To find the half-width in the presence of valence forces only, we have to take into consideration the fluctuation of r_0. According to kinetic theory, the probability of finding the atom with a volume between v

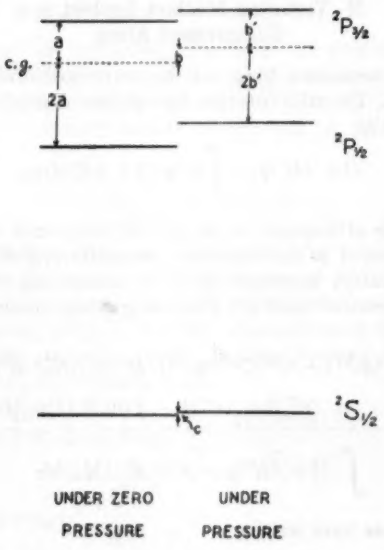

FIG. 1. Energy change of state under pressure.

[7] J. Robin and S. Robin, Compt. rend. 233 1019 (1951).

and $v+dv$ is given as

$$C\exp\left[\frac{(v-v_0)^2}{2kT}\left(\frac{\partial p_0}{\partial v_0}\right)_T\right]dv,$$

where C is a normalizing factor. v may be taken as the volume of the atom and v_0 and p_0 as the mean values of volume and pressure, respectively. This fluctuation gives the half-width of the hypothetical line of the center of gravity of the doublet concerned. Denoting radii r_0 of the spheres giving the half intensities of the maximum by $r_{\frac{1}{2}}$ and $r_{-\frac{1}{2}}$ ($r_{\frac{1}{2}}>r_{-\frac{1}{2}}$), the half-widths of the doublet components are

$$^2P_{\frac{1}{2}}:\quad d(r_{-\frac{1}{2}})-d(r_{\frac{1}{2}})-[b'(r_{\frac{1}{2}})-b'(r_{-\frac{1}{2}})],$$
$$^2P_{\frac{3}{2}}:\quad d(r_{-\frac{1}{2}})-d(r_{\frac{1}{2}})+2[b'(r_{\frac{1}{2}})-b'(r_{-\frac{1}{2}})],$$

where $d(r)=b(r)-c(r)$. Therefore, the half-width of the $^2P_{\frac{3}{2}}$ component is slightly smaller than that of the $^2P_{\frac{1}{2}}$ at moderate pressures. Since the distribution of r_0 is nearly symmetrical about its mean value, the steeper potential curve at smaller r_0 causes an asymmetrical intensity distribution $I(\nu)$ with a long tail toward the violet.

III. DENSITY EFFECT

The compressed atoms are polarizable. The polarizability depends largely on the charge distribution of an atom. From the above analysis, angular quantum numbers are good under compression. As the commutation relation shows, the charge distribution for $J=\frac{1}{2}$ is spherically symmetric whereas that for $J=\frac{3}{2}$ is not and provides an introduction of an electric quadrupole moment Q defined by

$$Q=Q_{zz}-Q_{xx}, \tag{3.1}$$

with

$$Q_{xx}=-e\int x^2|\psi_n|^2d\tau=Q_{yy},\quad Q_{zz}=-e\int z^2|\psi_n|^2d\tau,$$

where x, y, z are the rectangular coordinates with origin at the nucleus, $-e$ the electronic charge, and ψ_n the normalized wave function of a compressed atom originally in the state n.

It is not practicable to attempt to develop a perturbation theory for heavy atoms. Therefore, we will develop a simple calculation of the second order interation energy between two atoms in the 0 and 0′ states respectively. According to Buckingham's analysis,[8] the polarizability could be divided into groups due to each atomic shell. The perturbing molecule may be replaced by a one-electron system. Thus at a great separation, R, the energy reads

$$W=-\sum_{n,n'}{}'\frac{|(nn'|V|00')|^2}{W_n+W_{n'}-W_0-W_{0'}}, \tag{3.2}$$

with

$$V(R)\sim\frac{e^2}{R^3}(xx'+yy'-2zz'), \tag{3.3}$$

referring to the coordinate systems x, y, z and x', y', z', parallel to each other with z and z' in the direction of R and with the origins at the nuclei of each atom.

The summation in (3.2) may be understood to exclude the states degenerate to and including the 0 and 0′ states. Practically this restriction is unnecessary except for hydrogen atoms.

If the denominator of (3.2) can be replaced by an average with $\Delta W+\Delta W'$, we can use the sum rule

$$\sum_{n,n'}{}'|(nn'|V|00')|^2=(00'|V^2|00')-\sum{}''|(nn'|V|00')|^2.$$

$\sum''$ is summed up over all degenerate states to and including the 00′ states. Because of the odd parity of (3.3) the second term vanishes in this case. Furthermore, we will assume that the primed atom is spherically symmetric. Then with Q given by (3.1), we have

$$W=-\frac{e^4}{R^6}\frac{2}{\Delta W+\Delta W'}\left[-\frac{Q}{e}+(0|r^2|0)\right](0'|z'^2|0'). \tag{3.4}$$

The van der Waals energy for the initial state $^2S_{\frac{1}{2}}$, in the present case of absorption, is of the same magnitude regardless of the final states.

Introducing the ^2P wave functions for the J representation into (3.1), the quadrupole moments are

$$\begin{aligned}&Q=\tfrac{1}{5}e(0|r^2|0), &&\text{for } ^2P_{\frac{3}{2}},\ |m|=\tfrac{3}{2},\\ &Q=-\tfrac{1}{5}e(0|r^2|0), &&\text{for } ^2P_{\frac{3}{2}},\ |m|=\tfrac{1}{2},\\ &Q=0, &&\text{for } ^2P_{\frac{1}{2}},\ |m|=\tfrac{1}{2}.\end{aligned} \tag{3.5}$$

Therefore, from (3.4) the level $^2P_{\frac{3}{2}}$ splits into two subgroups according to their magnetic quantum numbers, m: assuming that $\Delta W+\Delta W'$ is approximately equal for all of the above-indicated states, the ratio of van der Waals energies is

$$(^2P_{\frac{3}{2}}^{\frac{3}{2}}):(^2P_{\frac{3}{2}}^{\frac{1}{2}}):(^2P_{\frac{1}{2}}^{\frac{1}{2}})=4:5:6. \tag{3.6}$$

The superscripts on the right indicate the values of $|m|$.

However, there may be some question about the additivity of the van der Waals forces under the multiple interactions, when the atom concerned is in the anisotropic $^2P_{\frac{3}{2}}$ state, since the direction of the z axis may be chosen by one colliding molecule. In this case, the interaction energy (3.3) will be transformed to

$$V(R)=\frac{e^2}{R^3}\left[\sum_{xx'}\{\cos(x,x')-3\cos(x,R)\cos(x',R)\}xx'\right],$$

where (x, R) denotes the angle between the x axis and the vector R joining the two molecules. The coordinates are parallel to each corresponding axis. Finally, the spherically symmetric property of the primed atom

[8] R. A. Buckingham, Proc. Roy. Soc. (London) **A160**, 113 (1937).

leads to

$$W=-\frac{e^4}{R^6}\frac{(0'|z'^2|0')}{\Delta W+\Delta W'}[\sum_s\{1+3\cos^2(x,R)\}(0|x^2|0)]. \tag{3.7}$$

Thus, if the perturbing atoms are distributed in a spherically symmetric manner around the radiating atom, the values of (3.7) are the same for different J's, neglecting the small difference in $\Delta W+\Delta W'$. This is simply because of no preference in the choice of z axis in space.

If binary encounters are assumed, the energy (3.4) can be used. This is the case corresponding to the wing at the longer wavelength side of a line intensity distribution. Similarly, this is the case for low pressure—probably lower than a few tens of atmospheres. Then the total line intensity distribution for the $^2S_{\frac{1}{2}}-{}^2P_{\frac{1}{2}}$, component must be the superposition of the two different distributions for $|m|=\frac{3}{2}$ and $\frac{1}{2}$. The statistical weight for $|m|=\frac{3}{2}$ and $|m|=\frac{1}{2}$ states in $^2P_{\frac{1}{2}}$ is the same, neglecting the very small effect of the Boltzmann factor. Therefore, the line intensities should be nearly equal.

According to the Fourier integral theory of pressure broadening, if the shifts or half-widths are denoted by Δ, the ratios are given by using the result (3.6).[9]

$$\Delta(^2P_{\frac{1}{2}}{}^I):\Delta(^2P_{\frac{1}{2}}{}^{II}):\Delta(^2P_{\frac{1}{2}}{}^{III})=1.74:1.90:2.05.$$

Since the ratio of shift to half-width of a spectral line is 0.727 for the $1/R^6$ force law from Foley's formula, the half-width of the $^2P_{\frac{1}{2}}$ line must be given roughly by $(1.90+0.727\times0.31)/1.90$ of the half-width of the $^2P_{\frac{1}{2}}$ component. Thus the ratio of the half-width of the $^2P_{\frac{1}{2}}$ component to that of $^2P_{\frac{1}{2}}$ is about 1.12, while the experimental value for the Rb resonance line perturbed by argon ranges between two limits 1.01 and 1.29 with a mean value of 1.12, up to 40 atmospheres.[1]

Furthermore, we should call attention to the fact that the half-width is smaller for the line $^2P_{\frac{1}{2}}{}^{II}$ than for $^2P_{\frac{1}{2}}{}^{I}$. Then, the maximum intensity of the line $^2P_{\frac{1}{2}}{}^{II}$ must be larger than that of the line $^2P_{\frac{1}{2}}{}^{III}$, roughly in the ratio of 2.05/1.74. Surely the maximum intensity of the total intensity distribution in the line $^2P_{\frac{1}{2}}$ should appear slightly closer to the $^2P_{\frac{1}{2}}{}^{II}$ component, and, thus, with slightly diminished shift.

If the pressure increases up to a point where the simultaneous perturbers are distributed spherically in a symmetrical manner around the radiating atom as they would be in crystals, the difference in shift and half-width of the doublet components disappears. However, our theory can be applied to the wing at the longer wavelength side of the intensity distribution. This region corresponds to the binary interaction. Therefore, because of the split of the $^2P_{\frac{1}{2}}$ states at the wing, the intensity curve must be broadened more than that of the $^2P_{\frac{1}{2}}$ in the corresponding region. This agrees with observations.

In the case of light perturbers (helium), the long-range attractive force is quite small. Therefore, the interaction with a radiating atom occurs only at such a small distance that the repulsive force is appreciable. Then the greater part of the broadening scheme may follow from the treatment of Chapter II.

IV. SUMMARY

It is unfortunate that the lack of exact wave functions for large r and heavy atoms has made it impossible for us to discuss our theory in a more quantitative way. However, the qualitative results of our analysis on the relative broadening of the doublets of the principal series perturbed by rare gas pressure may be summarized as follows:

(1) The attractive force has very little influence on the relative shifts of the $^2P_{\frac{1}{2}}$ and $^2P_{\frac{3}{2}}$ components for all members of the principal series.

(2) If the violet shift is negative and the red shift positive, the repulsive force will give a greater shift to the $^2P_{\frac{1}{2}}$ component than to the $^2P_{\frac{3}{2}}$ component at low pressures, regardless of the magnitude of the attractive force involved. The relative shift will be reversed in magnitude at high pressures.

(3) If only the attractive force is involved in the interaction, the half-width and asymmetry of the $^2P_{\frac{1}{2}}$ component will always be larger than those of the $^2P_{\frac{3}{2}}$ component.

(4) If only the repulsive force is involved, the half-width of the $^2P_{\frac{3}{2}}$ component will be slightly smaller than that of the $^2P_{\frac{1}{2}}$ component. The asymmetry toward the violet will be of the same magnitude for both.

[9] The small van der Waals force for the initial state is neglected.

Level Densities of Nuclei from the Inelastic Scattering of 18-Mev Protons*

P. C. GUGELOT
Palmer Physical Laboratory, Princeton University, Princeton, New Jersey
(Received October 16, 1953)

The spectra of protons inelastically scattered from Al, Fe, Ni, Cu, Ag, Sn, Pt, and Au have been measured. The energy distribution of the scattered protons is represented only approximately by a Maxwellian distribution. The relative level densities of the target nuclei have been calculated from the proton spectra. The scattering cross sections are compared with the predictions of the statistical model. The results indicate that the observed energy variation of the level densities may not depend on the excitation energy of the residual nucleus primarily, but, instead, there is some evidence that it is a function of the energy of the emitted particle.

I. INTRODUCTION

SINCE Weisskopf and Ewing[1] proposed the statistical model for nuclear reactions, several experiments have been performed to test this theory. Many of the more recent measurements support its predictions.[2–6] Paul and Clarke[7] carried out an extensive survey of (n,p), (n,α), and $(n,2n)$ reactions. They were able to show that the $(n,2n)$ reaction cross sections are approximately in agreement with theory. However, the (n,p) and (n,α) reaction cross sections for the heavy elements are orders of magnitude larger than expected. Similar observations were made in the study of (γ,p) reactions.[8] Most of these experiments consisted of the measurement of reaction cross sections which are not sensitive to the assumptions incorporated into the statistical model. Usually, it is not possible to determine which of these assumptions is responsible for any disagreement between experimental and theoretical results.

The basic assumption underlying the theory is the Bohr assumption, which states that in a nuclear reaction a compound nucleus is formed which decays in all energetically possible modes independent of its formation. This hypothesis makes it possible to separate the formation of the compound system and its decay. The decay is assumed to be a free competition between all the different possible processes of de-excitation. The reaction cross section σ_{ab} for a reaction $A(a,b)B$ can then be written

$$\sigma_{ab}=\sigma_a\Gamma_b/\textstyle\sum_i\Gamma_i. \tag{1}$$

Here σ_a is the cross section for the formation of a compound nucleus C by the bombardment of A with a; Γ_i is the width for the emission of a particle i. The sum is extended over all possible particles which may energetically be emitted. Weisskopf calculated the probability per unit time $\eta=\Gamma/\hbar$ for the emission of a particle by using the principle of microscopic reversibility:

$$\eta_b=\frac{M}{\pi^2\hbar^3\omega_C(E_0)}\int_{\epsilon=0}^{\epsilon_{\max}}S_b\omega_B(E)\epsilon d\epsilon. \tag{2}$$

M is the mass of particle b; ω_C is the level density of compound nucleus C at an excitation energy E_0; ϵ is the energy of particle b; S_b is the cross section for the formation of nucleus C with excitation energy E_0 by bombarding B, which is in a state with excitation energy E, by particle b, which has kinetic energy ϵ; E is the excitation energy of B after b has been emitted; $E=E_0-Q_b-\epsilon$, where Q_b is the binding energy of b; $\epsilon_{\max}=E_0-Q_b$ is the maximum kinetic energy b can obtain. The integrand

$$nd\epsilon=\text{const}S_b\omega_B(E)\epsilon d\epsilon \tag{3}$$

represents the energy distribution of emitted particles.

The principle of detailed balancing relates the cross section S_b with the density of states ω_B. Generally, the cross section for the formation of a particular nuclear state depends on the properties of that state. In this theory S_b is assumed to be a monotonic function of the kinetic energy of particle b

$$S_b=\sum_{l=0}^{\infty}(2l+1)\pi\lambda^2T_l(\epsilon),$$

in which T_l is a transmission coefficient. This applies only if the nuclear states are densely packed. Furthermore, this assumption does not take account of the width of a level. Hence, the transition to each final state becomes equally probable, e.g., an n-fold degenerate level will be counted n times. The density of states ω_B and the actually observed level density ρ_B should then be related by $\omega_B=f\rho_B$, where f has the meaning of an oscillator strength and contains the square of the matrix element for the particular transition.

The density of states at a residual excitation energy E of the nucleus B is assumed to be only a function of the excitation energy of a particular residual nucleus. The possibility that ω_B depends also on the kinetic energy of the bombarding particle should not be ex-

* This work was supported by the U. S. Atomic Energy Commission and the Higgins Scientific Trust Fund.
[1] V. F. Weisskopf and D. H. Ewing, Phys. Rev. **57**, 472 (1940).
[2] B. C. Diven and G. M. Almy, Phys. Rev. **80**, 407 (1950).
[3] P. R. Byerly and W. E. Stephens, Phys. Rev. **81**, 473 (1951).
[4] Nabholz, Stoll, and Wäffler, Phys. Rev. **86**, 1043 (1952).
[5] Brolley, Fowler, and Schlacks, Phys. Rev. **88**, 618 (1952).
[6] Bleuler, Stebbins, and Tendam, Phys. Rev. **90**, 460 (1953).
[7] E. B. Paul and R. L. Clarke, Can. J. Phys. **31**, 267 (1953).
[8] O. Hirzel and H. Wäffler, Helv. Phys. Acta **20**, 373 (1947).

cluded, since the maximum angular momentum of C depends on the energy of the bombarding particle. Therefore, higher angular momenta states in B may be excited with increasing E_0. ω is generally called "level density," although it may not represent the density of actual levels.

Little is known about ω. Weisskopf assumes $\omega = b\exp[(aE)^{\frac{1}{2}}]$ and calculates a and b from the known levels at low excitation energy and at the neutron dissociation energy. Formula 3 shows that it is possible to obtain the level density function experimentally from the energy distribution of the emitted particles.

The observation of the energy spectrum of emitted particles gives a direct measurement of the differential cross section $\partial^2\sigma/\partial\epsilon\partial\Omega$. Hauser and Feshbach[9] have shown that the cross section should not depend on the angle of observation in the energy region where the statistical theory applies. However, angular anisotropy for emitted particles has already been observed in γ-induced reactions.[8,10-12] Courant[13] predicted an anisotropic angular distribution on the basis of a direct dipole interaction between incident γ ray and the subsequently emitted nucleon.

The spectra of the products of heavy-particle-induced reactions in the intermediate energy range have been investigated for inelastic scattering of 14-Mev neutrons by Stelson and Goodman,[14] Whitmore and Dennis,[15] and Graves and Rosen.[16] (p,n) reactions were investigated by Gugelot.[17] Deuteron-induced reactions are not considered here, since the stripping process, which does not involve a compound nucleus, complicates the discussion. From the observed spectra, the energy variation of ω_B can be calculated. All the results obtained so far show that the spectra are approximately of the form $nd\epsilon = \text{const}\epsilon^{-\epsilon/T}\epsilon d\epsilon$. The parameter T varies little over the whole periodic system and is of the order of 1 Mev. As a result of the experimental difficulties in the detection of neutrons, the uncertainties of these results are large, and the investigated energy range is small. For this reason, an attempt has been made here to measure the spectra of inelastically scattered protons for which these experimental difficulties do not exist. The calculation of the relative level density from proton measurements requires only a knowledge of the barrier penetrability S_p in Eq. (3). For a nuclear radius of $1.5\times10^{-13}A^{\frac{1}{3}}$ cm, S_p is given by Blatt and Weisskopf[18] and more recently by Shapiro.[19]

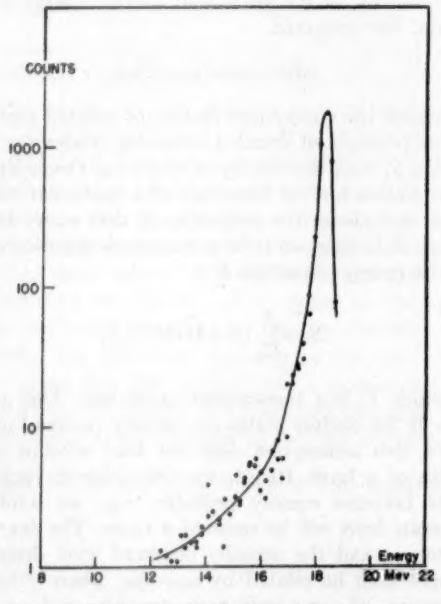

FIG. 1. The energy distribution of the protons in the incident beam.

II. EXPERIMENTAL SETUP

The focused and collimated 18.3-Mev proton beam of the cyclotron entered a 12-inch diameter scattering chamber with Al windows at 30, 60, 90, 120, and 150 degrees to the incident beam. The scattering chamber and NaI (Tl) scintillation detector are described by Likely and Franzen.[20] The beam was collected in a 5-inch long graphite Faraday cup. A 1-μf polystyrene precision condensor was connected between the cup and ground. The potential of the condensor could be measured by means of a quadrant electrometer, whose maximum deflection corresponded to about 1 volt. Calibration of the electrometer was carried out with a Rubicon potentiometer. The performance of the Faraday cup was checked by counting the number of scattered protons per unit charge collected as a function of the bias voltage on the cup. The counting rate stayed constant within 1 percent for a variation of the bias voltage between $+6$ and -6 volt.

The scattering foils used were 0.1- to 0.15-mil thick foils of Al, Fe, Ni, Cu, Ag, Sn, Pt, and Au. No correction for multiple scattering is necessary for this foil thickness. The foils were always mounted in such a way that their normal bisected the angle smaller than 90° between beam direction and detector.

The pulses from the RCA 5819 multiplier (in later experiments a Dumont K1186 was used) were amplified by a Los Alamos type 501 amplifier and displayed on

[9] W. Hauser and H. Feshbach, Phys. Rev. **87**, 366 (1952).
[10] Toms, Carroll, Rosenblum, and Stephens (to be published); M. E. Toms and W. E. Stephens, Phys. Rev. **88**, 160 (1952); Stephens, Toms, Carroll, and G. K. Rosenblum, Phys. Rev. **89**, 893 (1953).
[11] W. A. Butler and G. M. Almy, Phys. Rev. **89**, 893 (1953).
[12] Mann, Halpern, and Rothman, Phys. Rev. **87**, 146 (1952).
[13] E. D. Courant, Phys. Rev. **82**, 703 (1952).
[14] P. H. Stelson and C. Goodman, Phys. Rev. **82**, 69 (1951).
[15] B. G. Whitmore and G. E. Dennis, Phys. Rev. **84**, 296 (1951).
[16] E. R. Graves and L. Rosen, Phys. Rev. **89**, 343 (1953).
[17] P. C. Gugelot, Phys. Rev. **81**, 51 (1951).
[18] J. M. Blatt and V. F. Weisskopf, *Theoretical Nuclear Physics* (J. Wiley and Sons, Inc., New York, 1952), p. 352.
[19] M. M. Shapiro, Phys. Rev. **90**, 171 (1953).
[20] J. G. Likely and W. Franzen, Phys. Rev. **87**, 666 (1952).

a Tectronix 513D oscillograph which was fed through a line voltage regulator. The pulses were photographed on 35-mm film moving with a speed up to 5 cm/sec. The film was projected on a ground glass screen in front of which 65 regularly spaced microswitches were placed, each connected to a register.[21] The whole row of switches could be moved to follow the base line of the oscilloscope trace. The linearity of the complete system was checked by means of calibrated test pulses. It was not possible to obtain an energy resolution better than 3 percent (width at half-maximum of the elastic peak), whereas a multichannel discriminator showed that the actual resolution was 2 percent.

The pulse-height distributions were corrected for background, for the energy loss of the scattered protons in the Al windows, scattering foil and air path (total absorption about 25 mg/cm^2), and center-of-mass motion for the target elements up to Cu. Background runs were taken after each measurement. In general, three background runs were made: (1) with the scattering foil in place, but with an aluminum absorber of sufficient thickness to stop all protons between chamber window and detector, to detect the total γ-ray background; (2) with the same arrangement but without the scattering foil to detect the γ-ray background which originated in the collimators and collector cup; and (3) without scattering foil and without Al absorber to detect slit-scattered protons. There was no slit scattering observable in any run. At a pulse height corresponding to about 5 Mev, the γ-ray background increased very rapidly with decreasing pulse height, so that the proton spectra could not be taken below this energy.

To ascertain that no degraded protons reached the target, the energy distribution of the protons in the incident beam was measured by having the detector in place of the collector cup and operating the cyclotron at very low intensity. The results of this measurement are shown in Fig. 1. At 13 Mev the intensity is less than 0.1 percent of the main beam. The low-energy tail is probably produced by slit scattering. A gold collimator was used to define the beam. The actual measurements have been repeated at least twice for each element with slightly different collimator arrangements.

III. RESULTS

The results of the scattering experiments are presented as relative level-density functions. From Eq. (3) it is found that the quantity $n/\epsilon S_p$ is proportional to the level density of the residual nucleus. n is the experimentally observed number of protons per unit energy interval having kinetic energy ϵ; S_p is the cross section for the formation of a compound nucleus by protons as given by Weisskopf and Blatt.[18] The nuclear radius was assumed to be $1.5\times10^{-13}A^{\frac{1}{3}}$ cm.

[21] R. Britten, Phys. Rev. 88, 283 (1952).

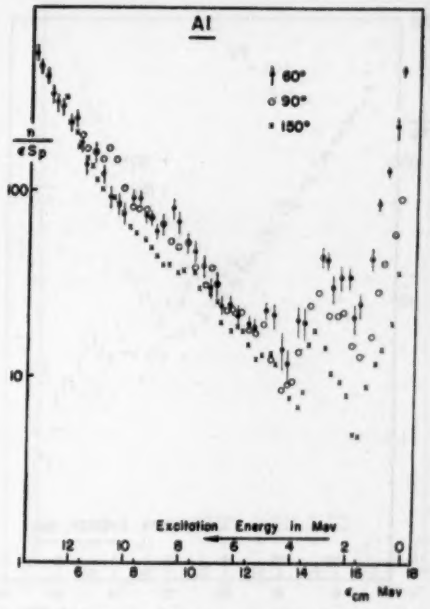

Fig. 2. The relative level density $\omega = n/\epsilon S_p$ of Al, obtained from the scattered proton energy distribution at 60°, 90°, and 150° to the incident beam.

A. Aluminum

Spectra were taken at 60°, 90°, and 150° to the incident beam. The results are shown in Fig. 2. The abscissa gives the energy in the center-of-mass system and the excitation energy of the residual nucleus. The ordinate is proportional to the level density in the residual nucleus for a region in which the compound nucleus theory holds. At zero excitation energy the elastic scattering is apparent. Up to 4-Mev excitation energy, the intensity fluctuates due to unresolved levels. Above 4 Mev the level structure is so dense that the spectrum becomes smooth, so that from here on the statistical model is applicable. The angular distribution of the scattered protons is seen to be isotropic, in agreement with the calculations by Hauser and Feshbach.[9] The spectrum is not purely Maxwellian. Defining nuclear temperature as $1/T = d\ln\omega/dE$, we find that T varies between 1.3 Mev and 2.7 Mev. Table I compares the values for T obtained from different experiments.

B. Iron, Nickel, and Copper

The results for these medium heavy elements are given in Figs. 3–5. The relative values for the level density are similar for the three elements considered. This is to be expected on the basis of the statistical model. However, in disagreement with this model is an anisotropic angular distribution of the emitted protons. More fast protons are emitted at 60° than at 150° to the incident beam, showing that a fraction of the re-

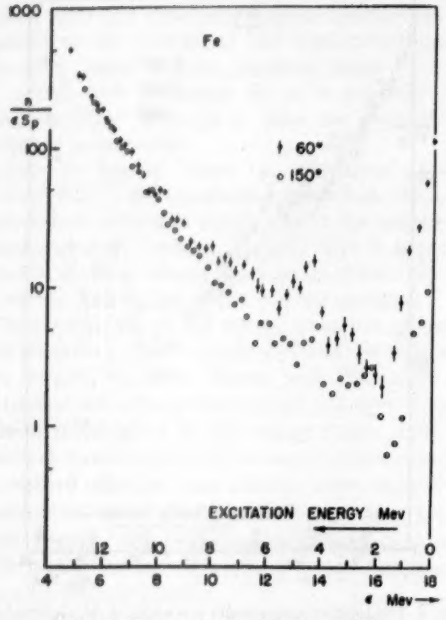

FIG. 3. The relative level density of Fe.

actions are due to interactions which cannot be described by the compound-nucleus theory.

Assuming that the backwards-scattered protons conform to the statistical description, we will confine the discussion in particular to the 150° data. This spectrum deviates again from a Maxwellian distribution: T increases with decreasing excitation energy. At $E=12$ Mev we find $T=1.3$ Mev. T increases to about 3 Mev at low excitation energies.

Table II compares data from different reactions.

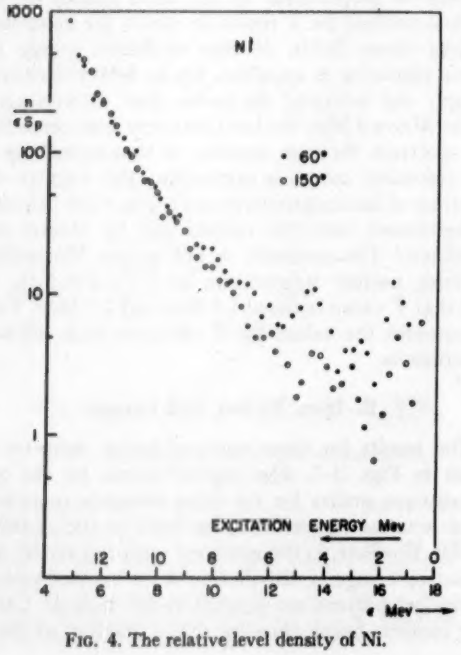

FIG. 4. The relative level density of Ni.

C. Silver and Tin

The relative level densities for silver and for tin are shown in Figs. 6 and 7. The protons having an energy larger than 8 Mev are emitted anisotropically. For these elements this effect is even more pronounced than for the medium heavy ones. Little difference is apparent between the results for Ag and those for Sn. The magic character of the proton number of Sn does not seem to have influence on the spectrum.

From the 150° data for Ag one finds that T changes from 0.8 Mev to about 3.5 Mev. The T values for Sn are approximately the same.

The measurement for Ag at 150° has been repeated for the normal incident proton energy of 18.3 Mev.

TABLE I. Values for $T=1/(d\log\omega/dE)$. ϵ_{max} is the maximum energy with which a particle can be emitted. $\Delta\epsilon$ is the energy interval of the emitted particle over which T is computed. ΔE is the interval of the residual excitation energy after emission of a particle with kinetic energy in the interval $\Delta\epsilon$.

Reaction	ϵ_{max}	$\Delta\epsilon$	ΔE	T	Ref.
Al(n,n)	13	1–2	12–9	1.0	a
Al(n,n)	14	1–4	13–10	1.1	b
Al(p,p)	28	10–25	18–3	3–6.5	c
Al(p,p)	17	5–7 8–12	12–10 9–5	1.3 2.7	d
Al(p,n)	11	2–5	9–6	1.3	e

[a] See reference 16.
[b] See reference 15.
[c] See reference 21.
[d] This paper.
[e] See reference 17.

Immediately afterwards the proton energy was reduced to 16.2 Mev and a run was made under the same conditions. These results are presented in Fig. 8. The ordinate of this plot is on an absolute scale, $\partial^2\sigma_{pp}/\partial\epsilon\partial\Omega$ being the cross section for inelastic scattering per Mev per steradian, ϵ the scattered proton energy, and S_p the formation cross section as defined by Blatt and Weisskopf. The slopes at equal excitation energy for both measurements do not agree: for $\epsilon_{max}=16$ Mev and $10<E<6$ Mev one finds $T=1.3$ Mev, whereas for $\epsilon_{max}=18$ Mev in the same excitation energy interval $T=1.8$ Mev. For the higher incident energy, $T=1.3$ Mev is obtained for $12<E<8$ Mev. Table III summarizes all available data.

D. Platinum and Gold

Figure 9 shows the results obtained from the inelastic scattering of protons from Pt. The relative level density of Au is very similar to that of Pt; it is therefore not reproduced. Several Pt runs have been carried out

with different beam and detector collimators. All results agreed with one another. The intensity of the scattered beam measured at 60° is almost uniformly three times as great as at 150°. A small admixture to the incident beam of a few percent of protons of degraded energy could have produced an apparent increase of the forward scattering, since the 60° elastic-scattering cross section is very much larger than that for 150° scattering. At 18 Mev measured values for the elastic-scattering cross section at 60° and 150° are 170 mb/sterad and 4 mb/sterad, respectively.[22] However, the energy distribution of the incident beam (Fig. 1) accounts for only 8 percent of the 60° scattered intensity at a proton energy of 12 Mev. Therefore, this amount of background cannot appreciably reduce the 60° intensity relative to the 150° intensity of scattered protons.

T varies between 0.7 Mev and about 2.8 Mev for the 150° data. The value for T at large excitation energy is just above the neutron binding energy. Table IV compares then the ratio of the level densities at the neutron binding energy and at 1-Mev excitation. In column 2 resolved levels are used, in column 3 the results of this experiment are used. For Al the agreement between the two ratios is fair, while for the other elements, the discrepancy amounts to at least a factor 100.

TABLE II. Values for T for Fe, Ni, and Cu. The symbols and references are the same as in Table I.

Reaction	ϵ_{max}	$\Delta\epsilon$	ΔE	T	Ref.
Fe(n,n)	14	1–4	13–10	0.76	a
Fe(n,n)	15	1–3	14–12	0.6	b
Fe(p,p)	18	5–8 10–16	13–10 8–2	1.36 2.6	d
Fe(p,n)	10	2–6	8–4	0.95	e
Ni(p,p)	18	5–8 10–16	13–10 8–2	1.2 2.6	d
Cu(n,n)	14	1–4	13–10	0.77	a
Cu(p,p)	18	5–8 10–16	13–10 8–2	1.2 2.6	d

in the residual nucleus cannot be very reliable, because the correction for the barrier penetration is large.

From the scattering of 14 Mev neutrons from Au, Graves and Rosen find $T=0.7$ Mev. From the Au(p,n)Hg reaction $T=0.8$ Mev was deduced.

IV. DISCUSSION

Several features of these results have to be discussed. The first and most general property of the deduced relative level density is that the density increases exponentially with excitation energy. Its variation with energy at high excitations is even more rapid than thermodynamical models predict. Secondly, the level densities of neighboring elements are very similar.

Since it is possible to obtain relative level densities only with these experiments, a normalization is necessary. A suitable excitation energy to fix the absolute value of ω is at about 1 Mev. At that excitation one knows that the level spacing is between 0.5 and 0.1 Mev. Another point where the level density is known

[22] P. C. Gugelot, Phys. Rev. 87, 525 (1952).

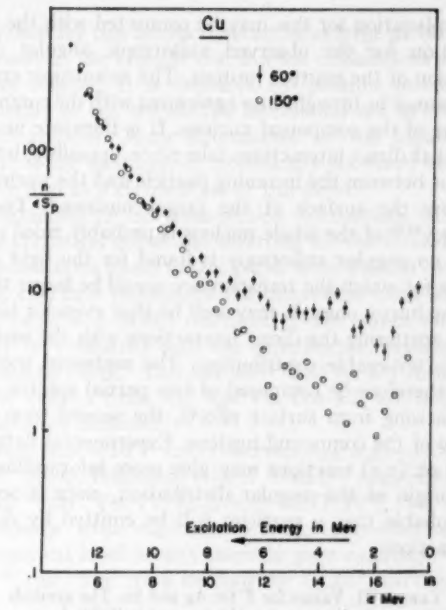

FIG. 5. The relative level density of Cu.

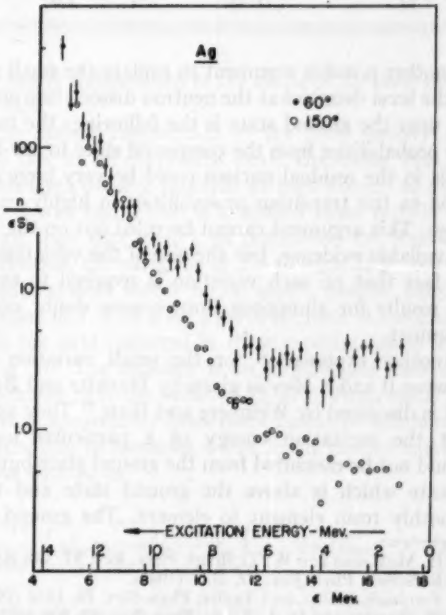

FIG. 6. The relative level density of Ag.

An explanation for this may be connected with the explanation for the observed anisotropic angular distribution of the emitted protons. The anisotropic emission cannot be brought into agreement with the common picture of the compound nucleus. It is therefore necessary that direct interactions take place—possibly, interactions between the incoming particle and the nucleons forming the surface of the target nucleus.[23] Transparency[24,25] of the whole nucleus is probably ruled out, since no angular anisotropy is found for the light elements for which the transparency would be larger than for the heavy ones. It may well be that even for backward scattering the direct interactions with the surface give a noticeable contribution. The measured spectra may therefore be composed of two partial spectra, the first arising from surface effects, the second from the decay of the compound nucleus. Experimental data on (p,α) or (n,α) reactions may give more information on the origin of the angular distribution, since it seems improbable that α particles will be emitted by direct interactions.

TABLE III. Values for T for Ag and Sn. The symbols and references are the same as in Table I.

Reaction	ϵ_{max}	$\Delta\epsilon$	ΔE	T	Ref.
Ag(n,n)	14	1–4	13–10	0.76	a
Ag(p,p)	18	5–8 11–15	13–10 7–3	1.0 3.5	d
Ag(p,p)	16	6–10	10–6	1.3	d
Rh(p,n)	14	2–6	12–8	0.85	e
Sn(n,n)	14	1–4	13–10	0.56	a
Sn(p,p)	18	5.5–8 11–14	12.5–10 7–4	0.9 2.8	d

Another possible argument to explain the small ratio for the level densities at the neutron dissociation energy and near the ground state is the following: the transition probabilities from the compound state to low-lying levels in the residual nucleus could be very large compared to the transition probabilities to highly excited states. This argument cannot be ruled out on the basis of available evidence, but the size of the variation and the fact that no such variation is required to explain our results for aluminum throws some doubt on this argument.

Another explanation for the small variation of ω between 0 and 8 Mev is given by Hurwitz and Bethe[26] and is discussed by Weinberg and Blatt.[27] They assume that the excitation energy of a particular nucleus should not be measured from the ground state but from a state which is above the ground state and varies smoothly from element to element. The ground state

[23] H. McManus and W. T. Sharp, Phys. Rev. **87**, 188 (1952).
[24] R. Serber, Phys. Rev. **72**, 1114 (1947).
[25] Fernbach, Serber, and Taylor, Phys. Rev. **75**, 1352 (1949).
[26] H. Hurwitz and H. A. Bethe, Phys. Rev. **81**, 898 (1951).
[27] I. G. Weinberg and J. M. Blatt, Am. J. Phys. **21**, 124 (1953).

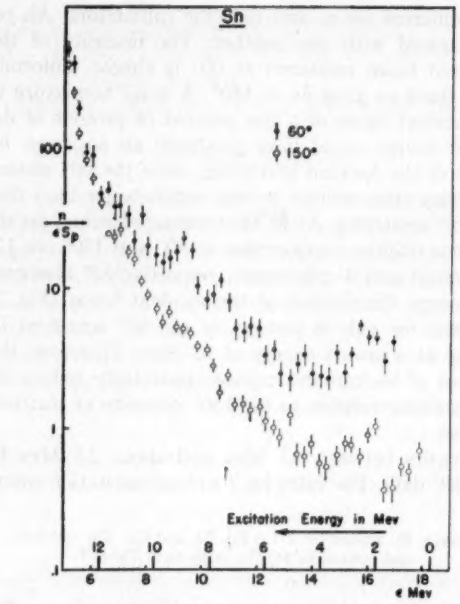

FIG. 7. The relative level density of Sn.

may be very much lower than this level for particularly stable nuclei. However, the similarity of the Ag and magic Sn spectra and of the Fe, Cu, and magic Ni spectra seems to refute this hypothesis.

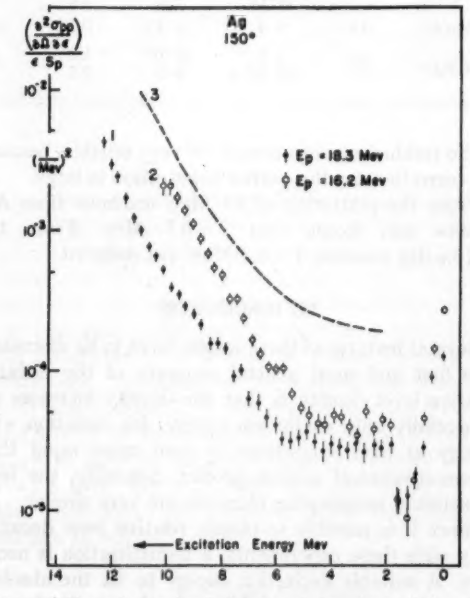

FIG. 8. The relative level density of Ag obtained from the scattering of 18.3-Mev and of 16.2-Mev protons. The values for $(1/\epsilon S_p)(\partial^2\sigma_{pp}/\partial\epsilon\partial\Omega)$ are absolute. Curve 3 presents the calculated value for $(1/\epsilon S_p)(\partial^2\sigma_{pp}/\partial\epsilon\partial\Omega)$ for 16.2-Mev incident protons. The level density used in the calculation is that obtained from the 18-Mev experiment.

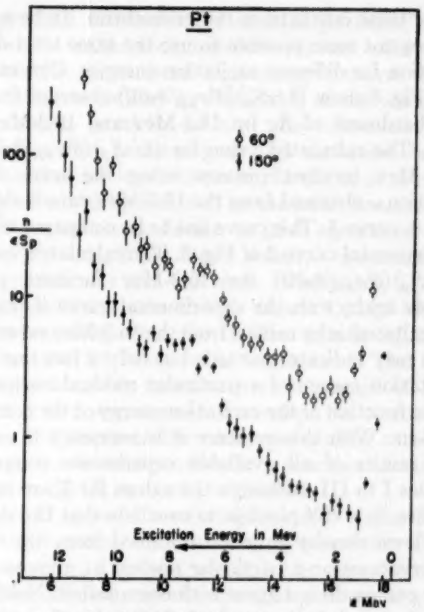

FIG. 9. The relative level density of Pt.

Another effect which may have to be considered to explain the observed angular anisotropy for the scattered protons is the electric excitation of nuclei by protons. This effect has been discussed by Weisskopf,[28] Mullin and Guth,[29] and Huby and Newns.[30] Total cross sections for this interaction can be as large as 10^{-28} cm². However, the angular distribution calculations are not very reliable. It is therefore not possible to conclude whether or not the electric interaction has to be taken into account. More information on the high-energy part of the spectrum of inelastically scattered neutrons may lead to a clarification of this point.

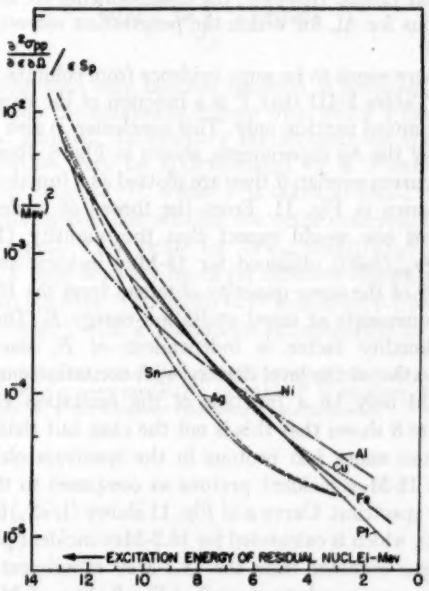

FIG. 10. A summary of the 150° experimental data.

[28] V. F. Weisskopf, Phys. Rev. **53**, 1018 (1938).
[29] C. J. Mullin and E. Guth, Phys. Rev. **82**, 141 (1951).
[30] R. Huby and H. C. Newns, Proc. Phys. Soc. (London) **A64**, 619 (1951).

Adhering to the cross-section calculations based on the statistical model but inserting for the level density the functions found in this paper from the 150° scattering, one may recalculate the theoretical cross sections for (n,p) and $(n,2n)$ reactions. These values for σ_{theor} may be compared with the experimental results from Paul and Clark.[7] This has been done for Rh (using the level density from Ag) and Pt. For Rh the following results are obtained:

$\sigma_{\text{theor}}(n,p)=10^{-26}$ cm², observed $\sigma_{\text{exp}}(n,p)=13\times10^{-26}$ cm². Using Weisskopf's level density: $\sigma_{\text{theor}}(n,p)=0.1\times10^{-26}$ cm². For Pt: $\sigma_{\text{theor}}(n,p)=3.7\times10^{-27}$ cm², which compares with $\sigma_{\text{exp}}(n,p)=3.10^{-27}$ cm², whereas the theoretical level density formula gave $\sigma_{\text{theor}}(n,p)=0.02$ 10^{-27} cm². The cross sections for $(n,2n)$ reactions are practically independent of the shape of the level density function.

TABLE IV. Ratio of level densities at the neutron binding energy and at 1-Mev excitation energy. Column 2, from neutron resonance experiments. Column 3, from the relative level densities in this paper.

Element	$\omega(O_n)/\omega(1)$	
Al	10	7
Fe	—	13
Ni	5.10^2	9
Cu	2.10^2	7
Ag	2.10^2	8
Sn	—	9
Pt	10^2	11

The energy dependence of the level density functions has to be considered next. Excluding that part of the level density function at high energy of excitation, it was found that ω increased more rapidly with energy than $\exp[(aE)^{\frac{1}{2}}]$, as postulated by Weisskopf. In addition, the variation of $T=(d\log\omega/dE)^{-1}$ over the periodic system seems to be small, smaller than the variation of T with E for a given element. A comparison of all the data collected in these experiments is shown in Fig. 10. The ordinate is on an absolute scale. It is remarkable that the value of $(1/\epsilon S_p)(\partial^2\sigma_{pp}/\partial\epsilon\partial\Omega)$ does not vary appreciably from one element to another.

According to formulas 1 and 2, the plotted quantity can be written as

$$\frac{\partial^2\sigma_{pp}}{\partial\epsilon\partial\Omega}\Big/\epsilon S_p=\frac{\sigma_p}{4\pi}\omega(E)\Big/\sum_i\int_0^{\epsilon_{\max^i}}S_i\omega(\epsilon_{\max^i}-\epsilon)\epsilon d\epsilon.$$

An isotropic angular distribution for the emitted protons is assumed. The sum has to be carried out over all

energetically possible reactions. By far the most probable reaction is, however, the (p,n) reaction; however, for Al the inelastic scattering of protons should also be considered. Setting $\omega(0)=1$ one may calculate

$$\frac{\sigma_p}{4\pi}\Big/\sum_i\int_0^{\epsilon_{\max}{}^i} S_i\omega(\epsilon_{\max}{}^i-\epsilon)\epsilon d\epsilon,$$

and this expression should then be equal to the ordinate of the measured curves at $E=0$. This has been carried out for those elements for which the threshold of the (p,n) reaction is known. The following results were obtained:

Al^{27}, 4.1×10^{-5} $(Mev)^{-2}$ calculated, and 1.6×10^{-5} $(Mev)^{-2}$ experimental;

Fe^{56}, 1.2×10^{-5} $(Mev)^{-2}$ calculated, and 10^{-5} $(Mev)^{-2}$ experimental;

Ag^{107}, 0.8×10^{-5} $(Mev)^{-2}$ calculated, and 1.5×10^{-5} $(Mev)^{-2}$ experimental.

The agreement is good, taking into account the rough assumptions. These results may show that cross section calculations on the basis of the statistical model give reliable results, provided the right level density functions are used. The results are very sensitive to ϵ_{max}; a variation of ϵ_{max} for Ag by 0.2 Mev gives a 26 percent variation in the computed values. However, the meaning of these estimates is rather doubtful. To be specific, it does not seem possible to use the same level density function for different excitation energies. Curves 1 and 2 of Fig. 8 show $(1/\epsilon S_p)(\partial^2\sigma_{pp}/\partial\epsilon\partial\Omega)$ observed from the bombardment of Ag by 18.3-Mev and 16.2-Mev protons. The calculated value for $(1/\epsilon S_p)(\partial^2\sigma_{pp}/\partial\epsilon\partial\Omega)$ for 16.2-Mev incident protons using the level density function ω obtained from the 18.3-Mev data is shown in Fig. 8, curve 3. This curve has to be compared with the experimental curve 2 of Fig. 8. The calculated value for $(1/\epsilon S_p)(\partial^2\sigma_{pp}/\partial\epsilon\partial\Omega)$ for 16.2-Mev incident protons agrees again with the experimental curve if one computes its value by using ω from the 16.2-Mev experiment. This may indicate that ω is not only a function of the excitation energy of a particular residual nucleus, but also a function of the excitation energy of the compound nucleus. With this evidence it is necessary to consider the results of all available experiments compiled in Tables I to III. Although the values for T are not very precise, it is still possible to conclude that the slopes of the level density function obtained from the various observations on a particular nucleus at a given excitation energy do not agree with one another. Neither can one find a definite trend of $T(E)$ with the excitation energy of the compound nucleus. The different values of T at high excitation energy obtained from (n,n) or from (p,p) scattering could be produced by a wrong Coulomb barrier penetration correction, due to either a depression of the barrier caused by surface vibration of an excited nucleus[31] or an incorrect estimate of the nuclear radius. However, the disagreements are already obvious for Al, for which the penetration correction is small.

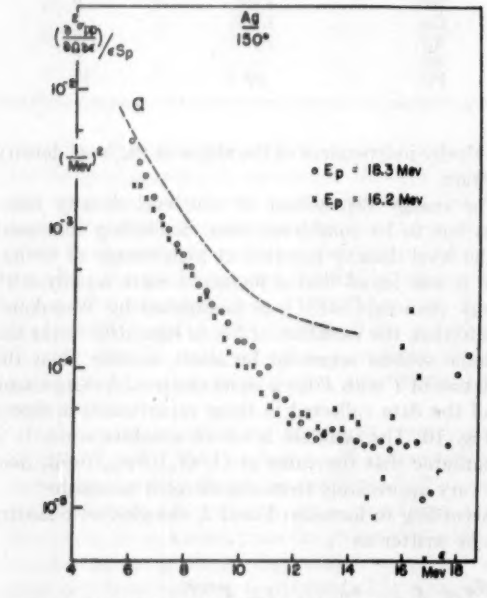

FIG. 11. $(1/\epsilon S_p)(\partial^2\sigma_{pp}/\partial\epsilon\partial\Omega)$ vs energy of the emitted protons obtained from the scattering of 18.3-Mev and 16.2-Mev protons by Ag. Curve a presents the calculated value of $(1/\epsilon S_p)(\partial^2\sigma_{pp}/\partial\epsilon\partial\Omega)$ for 16.2-Mev incident protons. The level density used in the calculation is that obtained from the 18-Mev experiment. Curve a is equivalent with curve 3 of Fig. 8.

There seems to be some evidence from columns 3 and 5 of Tables I–III that T is a function of the energy of the emitted particle only. This conclusion is also borne out by the Ag experiments, shown in Fig. 8. Here, the two curves overlap if they are plotted as a function of ϵ, as shown in Fig. 11. From the theory of nuclear reactions one would expect that the quantity $(1/\epsilon S_p)\times(\partial^2\sigma_{pp}/\partial\epsilon\partial\Omega)$ obtained for 18-Mev incident protons is 1/9 of the same quantity obtained from the 16-Mev measurements at equal excitation energy E. The proportionality factor is independent of E, since the derivative of the level density with excitation energy E should only be a function of the excitation energy. Figure 8 shows that this is not the case, but that there are too many fast protons in the spectrum obtained with 18-Mev incident protons as compared to the 16-Mev spectrum. Curve a of Fig. 11 shows $(1/\epsilon S_p)(\partial^2\sigma_{pp}/\partial\epsilon\partial\Omega)$, which is calculated for 16.2-Mev incident protons using ω obtained from the 18.3-Mev experiment. This curve corresponds to curve 3 of Fig. 8. At $\epsilon=5$ Mev the calculated curve a and the experimental curves approach each other, as one expects on the basis of the theory for

[31] E. Bagge, Ann. Phys. 33, 389 (1938).

a Maxwellian distribution of emitted particles.[22] It is possible to make noncompound nuclear effects responsible for the emitted high-energy protons. These direct interactions may be a function of the energy of the incoming particle, so that the observed level density has only a meaning at high excitation energy of the residual nucleus. However, the slopes of the level density obtained by Britten[21] by the inelastic scattering of 32-Mev protons by Al are in good agreement with our slopes for Al, if the "level density" is assumed to be a function of ϵ and not of E. In addition, $(1/\epsilon S_p) \times (\partial^2\sigma_{pp}/\partial\epsilon\partial\Omega)$ from the 32-Mev data is 7×10^{-5} Mev^{-2}, and that quantity from the 18-Mev data is 8.5×10^{-5} Mev^{-2} at $\epsilon=11.5$ Mev, in fair agreement. The error stays approximately constant over the range of ϵ for which the two measurements overlap. No correlation between the slopes of the two experimental curves is obtained, if ω is considered to be a function of the excitation energy E, as shown in Table I.

Figure 12 shows $T=-[d\log\omega(\epsilon)/d\epsilon]^{-1}$ taken from all available results on Al and Ag as a function of the particle energy. This plot shows better agreement between the different experiments than the values given for $T(E)$ in the tables. It should be kept in mind that the estimation of slopes from these spectra cannot be very precise.

It is now possible to understand the small variation of $(1/\epsilon S_p)(\partial^2\sigma_{pp}/\partial\epsilon\partial\Omega)$ for different elements as shown in Fig. 10. It is necessary to calculate

$$\omega(\epsilon)\Big/4\pi\int_0^{\epsilon_{\max}}\omega(\epsilon)\epsilon d\epsilon,$$

assuming that only neutron emission is probable; $\epsilon_{\max}$ represents the maximum energy with which a neutron can be emitted. To evaluate the integral the spectral distribution may be approximated by a Maxwellian distribution $\omega=\epsilon^{-\epsilon/T}$, where T is taken at small values of ϵ from which one obtains the main contribution to the integral. This yields for $(\partial^2\sigma_{pp}/\partial\epsilon\partial\Omega)/\epsilon S_p\sim\omega(\epsilon)/4\pi T^2$; T does not vary much for different elements and is about 0.8 Mev. Thus $\omega(0)/4\pi T^2$ is of order 0.1 Mev^{-2}, in agreement with a reasonable extrapolation to $\epsilon=0$

[22] The fact that $(1/\epsilon S_p)(\partial^2\sigma_{pp}/\partial\epsilon\partial\Omega)$ depends only on ϵ if the level density is $\omega=a\exp(E/T)$, in which T is constant, is also shown by K. J. Le Couteur (private communication).

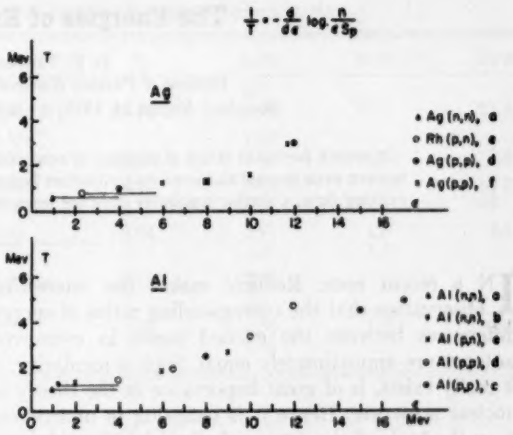

FIG. 12. $T=-[d\log\omega(\epsilon)/d\epsilon]^{-1}$ for Ag and Al vs energy of emitted protons. a: Graves and Rosen (see reference 16); b: Stelson and Goodman (see reference 15); c: Britten (see reference 21); d: this paper; 18.3-Mev incident protons; e: Gugelot (see reference 17); f: this paper; 16.2-Mev incident protons.

of the experimental plots. The ordinate is no longer a sensitive function of the threshold of the (p,n) reaction.

Using the hypothesis presented, one is able to recalculate the theoretical cross sections for (n,p) reactions which were measured by Paul and Clarke.[7] The cross section for $Ag(p,n)$ comes out to be about 10 mb with an uncertainty of a factor 2 resulting from the necessary extrapolation of the neutron spectrum to $\epsilon=0$. The measured cross section is 130 mb.

The evidence that ω is only a function of ϵ may have been caused by a misrepresentation of the form of the spectrum as given by Eq. (3), or by the fact that direct interactions are much more likely than had been expected. It cannot be concluded from the small amount of data available whether ω is a function of ϵ alone or a function of ϵ and the energy of the incoming particle. It will be necessary to obtain more experimental information from scattering and reaction experiments carried out in different energy ranges in order to check the evidence presented here and to be able to construct a model for the reaction mechanism.

The author would like to thank Mr. H. A. Lauter for his assistance and for reading most of the films, and he is especially grateful to Professor E. P. Wigner for many discussions about the statistical theory.

The Energies of Excited States of Nuclei

G. E. TAUBER† AND TA-YOU WU
Division of Physics, National Research Council, Ottawa, Canada
(Received August 24, 1953; revised manuscript received November 4, 1953)

A search for equal ratios of energies in even-even isotope nuclei observed by Redlich has been extended to even-even isotone and even-odd, odd-even isotope and isotone nuclei. It is found that on the basis of the existing data, a similar regularity does not seem to be present in these groups of nuclei.

IN a recent note, Redlich[1] makes the interesting observation that the corresponding ratios of energy differences between the excited states in even-even isotopes are approximately equal. Such a regularity, if it really exists, is of great importance in the theory of nuclear structure. Hence it is tempting to understand it on the basis of the current shell model. Consider two even-even isotope nuclei (Z,N), $(Z,N+2)$ and denote the energies of the excited states, measured from the ground state by E_1, E_2, E_3, etc. Redlich's observation that

$$E_2/E_1 \quad \text{or} \quad E_2/(E_2-E_1)$$

is approximately the same for the various even-even isotope nuclei can be taken to imply that the energy states, at least the lower ones showing this regularity, are mainly determined by the protons in the incomplete shell; for otherwise the addition of two more neutrons to the nucleus (Z,N) would have changed the configurations of the nucleus and hence the energy level pattern so that one would not expect the regularity observed by Redlich to be the rule. In fact, the regularity of Redlich can be readily understood if one assumes that in the even-even isotopic nuclei (Z,N), $(Z,N+2)$, $(Z,N+4)\cdots$, the energy levels are those determined by the proton configuration, the addition of successive pairs of neutrons bringing about a change in the "central field" part of the interaction and thereby changing the energy levels of the protons by a constant factor. For the heavier nuclei in which the "outer" protons and the "outer" neutrons are in very different shells, the interaction energy between a proton and a neutron in the incomplete shells is smaller than interaction energies between nucleons in the same shell. In this case the energies of the protons and of the neutrons may roughly be regarded as additive. If the spacings of levels of the proton configurations and of the neutron configurations taken separately are denoted by ΔE_N

TABLE I. Energy levels and ratios for even-Z, odd-N isotopes.[a] Energies are in Mev.

Z	Element	A	E_1	E_2	E_3	E_4	E_2/E_1	E_3/E_1	E_4/E_1
4	Be	7	0.429	4.6	6.56	7.16	10.7	15.3	16.7
							1.42*	1.55*	
		9	(1.5)	2.429	6.8	11.6	1.6	4.5	7.7
6	C	11	1.85	4.23	4.77	6.40	2.29	2.58	3.46
		13	0.7+	3.08+	3.69	3.89	4.4	5.3	5.6
8	O	15	5.29+	6.20−	6.84	7.61	1.29*	1.41	1.44
		17	0.875	3.07	3.86	4.56	1.25*	1.48*	1.70
10	Ne	21	0.35	1.73	2.84	3.73	4.9	8.1	10.7
		23	0.98	1.77	3.0		1.8	3.1	
12	Mg	25	0.58	0.98	1.58	1.98	1.7	2.7	3.4
		27	(0.99)	3.50			3.5		
14	Si	29	1.28	2.038	2.436	3.07	1.59	1.90	2.40
		31	0.73	1.23	1.48	1.73	1.7	2.0	2.4
18	A	37	1.49	2.56	3.50	4.40	1.72	2.35	2.95
		41	0.66	1.21	1.34	1.94	1.8	2.0	2.9
20	Ca	41	1.95	2.41	2.96	3.23	1.23	1.52	1.66
		43	0.56	1.0	1.65		1.8	2.9	
22	Ti	47	1.40	2.39	2.64	3.09	1.71	1.88	2.21
		49	1.35	1.70	2.41	3.11	1.26	1.78	2.30
82	Pb	207	0.55	0.87	1.60	2.05	1.6	2.9	3.7
		209	0.8	1.6	2.0	2.5	2.0	2.5	3.1
92	U	233*	0.0174	0.0757	0.1045	0.3765	4.35	6.00	21.64
		235	0.013	0.051			3.92		

[a] + and − denote parity; 0 ratios with corresponding parity; * lowest energy level omitted in finding the ratio; ( ) levels not found in β-decay schemes.

† National Research Laboratories Postdoctorate Fellow.
[1] M. G. Redlich, Proc. Natl. Acad. Sci. U. S. 30, 560 (1953).

TABLE II. Energy levels and ratios for odd-Z, even-N isotopes.[a] Energies are given in Mev.

Z	Element	A	E_1	E_2	E_3	E_4	E_2/E_1	E_3/E_1	E_4/E_1
3	Li	5	2.5	16.78			6.7		
		7	0.477	4.61	6.56	7.46	9.66	13.7	15.6
7	N	13	2.369^+	3.511^-	3.558^+		1.50[b]		
		15	5.28	5.31	6.33	7.16	1.00	1.20	1.36
9	F	17	0.536	3.10	3.86	4.35	5.78	7.20	8.11
		19	0.11	0.19	1.37	1.59	1.6	12	14
13	Al	25	0.45	0.95	1.81	1.94	2.1	4.0	4.3
		27	0.84	1.02	1.85		1.2	2.2	
17	Cl	33	0.76^+	1.89^+	2.84^-	4.22^-	2.50		
		35	0.6	1.5			2.5		
29	Cu	63	0.960	(1.44)	1.89	2.60	1.50	1.97	2.71
		65	1.12	1.49			1.33		

[a] See footnote a in Table I.

TABLE III. Energy levels and ratios in even-even isotones.[a] Energies are given in Mev.

Z	Element	A	N	E_1	E_2	E_3	E_2/E_1	E_3/E_1
4	Be	10	6	3.37	6.30	7.38	1.87	2.19
6	C	12	6	4.44	7.5	9.62	1.69	2.17
10	Ne	22	12	0.4	1.28	3.4	3.2	8.5
12	Mg	24	12	(1.38)	4.14	5.51	3.00	3.99
14	Si	28	14	1.80	4.47	4.91	2.48	2.73
12	Mg	26	14	1.84	2.85	4.00	1.55	2.17
				1.825	3.00	4.00	1.64	2.19
14	Si	30	16	2.3	3.6	4.9	1.6	1.8
16	S	32	16	2.25	4.34		1.93	
					3.81		1.69	
22	Ti	50	28	1.58	3.00	4.14	1.90	2.62
24	Cr	52	28	1.46	2.40	3.13	1.64	2.14
48	Cd	114	66	0.550	1.263	1.856	2.30	3.374
50	Sn	116	66	1.274	2.09	2.36	1.64	1.85
50	Sn	120	70	1.30	2.20		1.69	
52	Te	122	70	0.568	1.24		2.18	
56	Ba	138	82	1.44	2.42	2.88	1.68	2.00
58	Ce	140	82	1.60	2.09	2.42	1.31	1.51
76	Os	192	116	(0.283)	0.484	0.690	1.71	2.44
78	Pt	194	116	0.327	0.618	1.81	1.89	5.53
78	Pt	196	118	0.358	0.688		1.92	
80	Hg	198	118	0.411	1.087		2.64	

[a] See footnote a in Table I.

and ΔE_P, respectively, and if ΔE_P are smaller than ΔE_N by a factor 4 or 5, say, then the lower few levels of the nucleus will be essentially the levels of the proton configuration, and *vice versa*.

The above situation, however, does not obtain in general, especially in the case of the lighter nuclei in which the incomplete proton and neutron shells have the same quantum numbers. For such nuclei, it has been found necessary to consider all the protons and neutrons in the incomplete shells in order to account for the spin, magnetic moment, and energy levels of the nuclei.[2] In this case, it seems difficult to understand Redlich's regularity on the basis of the present shell model.

In view of these considerations, it is obviously of interest to extend the search of Redlich to see if similar regularities exist among (1) even-Z, odd-N isotopes, (2) odd-Z, even-N isotopes, (3) even-Z, even-N isotones, (4) even-Z, odd-N isotones, and (5) odd-Z, even-N isotones. From the recent compilations of nuclear energy levels,[3] we obtain the result given in the following tables.

From Table I for 11 groups of even-odd isotopes, it is seen that only in three cases, namely, O^{16}, O^{17}; Si^{29}, Si^{31}; A^{37}, A^{41} is there some approximate equality in the

[2] See, for example, D. R. Inglis, Phys. Rev. **87**, 915 (1952); Revs. Modern Phys. **25**, 390 (1953).

[3] G. Scharff-Goldhaber, Phys. Rev. **90**, 587 (1953); *Nuclear Data*, National Bureau of Standards Circular 499 (U. S. Government Printing Office, Washington, D. C., 1950); and Supplements; new nuclear data in Nuclear Science Abstracts, J. M. Hollander *et al.*, Revs. Modern Phys. **25**, 469 (1953).

TABLE IV. Energy levels and ratios in even-Z, odd-N isotones.[a] Energies are given in Mev.

Z	Element	A	N	E_1	E_2	E_3	E_4	E_2/E_1	E_3/E_1	E_4/E_1
2	He	5	3	1.76	2.6	16.64		1.5	9.45	
4	Be	7		0.430	4.6	6.4	7.16	10.0	15.0	16.7
								1.4[b]	1.6[b]	
4	Be	9	5	(1.5)	2.43	6.8	11.6	1.6	4.5	7.7
6	C	11		1.85	4.23	4.77	6.40	2.29	2.58	3.46
6	C	13	7	0.70$^+$	3.082$^+$	3.68	3.89	4.4	5.3	5.56
								1.20[b]	1.26[b]	
8	O	15		5.29$^+$	6.20$^-$	6.84	7.48	1.17	1.29[b]	1.41
10	Ne	23	13	0.98	1.77	3.0		1.8	3.1	
12	Mg	25		0.58	0.98	1.58	1.98	1.7	2.7	3.4
12	Mg	27	15	0.99	3.50			3.4		
14	Si	29		1.282	2.038	2.438	3.073	1.59	1.90	2.40
14	Si	31	17	0.73	1.23	1.48	1.73	1.7	2.0	2.4
16	S	33		0.85	1.90	2.17	2.86	2.2	2.55	3.4
26	Fe	57	31	0.014	0.131	(1.4)	(2.6)	9.36		
28	Ni	59		0.42	3.08	4.57	5.20	7.3	10.9	

[a] See footnote a in Table I.

TABLE V. Energy levels and ratios in odd-Z, even-N isotones.[a] Energies are given in Mev.

Z	Element	A	N	E_1	E_2	E_3	E_4	E_2/E_1	E_3/E_1	E_4/E_1	E_5/E_1
5	B	11	6	2.14	4.46	5.03	6.76	2.08	2.35	3.16	
7	N	13		2.369$^+$	3.511$^-$	3.558$^+$		1.50[b]			
7	N	15	8	5.28	5.31	6.33	7.16	1.00	1.20	1.36	
9	F	17		0.536	3.10	3.86	4.35	5.78	7.20	8.11	
								1.24[b]	1.40[b]	1.53[b]	
11	Na	23	12	0.439	2.07	2.10	2.37	4.72	4.79	5.41	
13	Al	25		0.45	0.95	1.81	1.94	2.1	4.9	4.3	5.6
15	P	31	16	0.44	1.02	1.74	2.25	2.3	3.95	5.1	
17	Cl	33		0.76$^+$	1.89$^+$	2.84$^-$	4.22$^-$	2.5[b]	3.7	5.5	
35	Br	83	48	0.17	0.37	1.1		2.2	6.5		
37	Rb	85		0.15	0.54			3.6			
57	La	139	82	0.163	0.184	0.8	1.05	1.13	4.91	6.44	
59	Pr	141		0.145	0.315	1.05		2.17	7.24		

[a] See footnote a in Table I.

corresponding ratios. From Table II covering 6 groups of odd-even isotopes, only Cl^{33}, Cl^{35} show the regularity; however, the data on Cl^{35} are uncertain. From Table III for 10 groups of even-even isotones, three cases, namely Be^{10}, C^{12}; Ne^{22}, Mg^{24}; and Ba^{138}, Ce^{140} show a proximity in the ratio E_2/E_1 within about 10 percent; but in the case of Ne^{22}, Mg^{24}, the values of E_1, E_2 themselves are so different in the two nuclei that the close proximity in the ratio E_2/E_1 may perhaps be regarded as accidental. The seven pairs of even-odd isotones in Table IV do not seem to show any regularity in the ratios E_m/E_n. In Table V for 6 pairs of odd-even isotones, the pair P^{31}, Cl^{33} shows an equality in the ratios but very different values in the E_m themselves. The pair Na^{23}, Al^{25} shows 4 approximately equal ratios (4.72; 4.32), (5.41; 5.58), (6.13; 6.00), and (6.84; 6.88); however, the levels in Na^{23} have not been given in a β-decay scheme.

From these tables one may conclude that from the purely empirical point of view, the interesting regularity found by Redlich for even-even isotopes has not been found as a rule in the five tables. It must be emphasized, however, that the data used in the comparison in these tables are in many cases uncertain in the sense that there may be as yet unobserved levels between the known ones.

Systematics of Photoneutron Reactions*

R. NATHANS AND J. HALPERN
University of Pennsylvania, Philadelphia, Pennsylvania
(Received October 28, 1953)

Properties of the giant dipole resonances for (γ,n) reactions have been measured for 14 singly-isotopic elements distributed throughout the range of s values. Systematics are reported for the behavior of the integrated cross sections, the energies at which the dipole resonances attain a maximum cross section, the values of the cross sections at these energies, and the widths of the resonances. Anomalously narrow widths are reported for elements with neutron numbers in the vicinity of the magic numbers.

INTRODUCTION

EARLY experimental studies[1–5] of the absorption by nuclei of photons with energies in the range from 5 Mev upwards have shown that the absorption process exhibits a giant resonance in the energy region about 20 Mev for all elements investigated, and a considerable amount of recent work has substantiated this conclusion.[6] Theoretical investigations of photonuclear processes have established that the photon absorption is predominantly dipole in nature.[7,8] One of the fundamental predictions of the theories arises from the application and extension of the sum rules for dipole absorption to absorption by nuclei, and in fact a measurement of the total integrated cross section for dipole absorption could yield a value for the percent of exchange in the neutron-proton interaction.

Experimental techniques, however, have not yet reached the state where such comparison with theory can be made with profit. Difficulties arise from the bremsstrahlung nature of the photons used, from the lack of certainty that one has measured all partial reactions resulting from the absorption process, and from lack of knowledge of any tails on the absorption curve above the giant resonance and what fraction of any tail arises from dipole absorption. On the other hand, a detailed study of the parameters of the giant dipole resonance itself and of the dependence of these parameters on atomic number can yield direct information concerning nuclear structure and is less exacting in experimental requirements, especially if the assumption is made that the excitation function for a photoneutron reaction is identical except in magnitude with that for total photon absorption over the giant dipole resonance.

With this in mind, we have made a study of the photoneutron cross sections of 14 singly-isotopic elements from threshold to 24 Mev using betatron bremsstrahlung and direct neutron detection. The practical advantages of direct neutron detection over residual activity measurements in obtaining precise yield curves are so great as to outweigh any ambiguities arising from the onset of $(\gamma,2n)$ or (γ,pn) reactions. During the course of this study there appeared a similar work by Montalbetti, Katz, and Goldenberg[9] in which many of the elements herein investigated were measured. The apparatus used for the work of this paper had a signal-to-background ratio an order of magnitude larger than that used by Montalbetti *et al.* and consequently comparatively thinner samples could be employed. Preliminary results of this work have recently been published.[10–12]

APPARATUS AND PROCEDURE

The general arrangement of the apparatus is shown in Fig. 1. The details of construction as well as the significant performance data have been presented in previous publications.[13,14] The only modification for the present study was the use of four enriched BF_3 counters imbedded symmetrically at 13.5 cm from the beam axis to enhance the yields near threshold and reduce the exposure time for a given element to reasonable limits. The samples, whose neutron yields are measured as the betatron is run at successively increasing energy in half-million volt steps from threshold to 25 Mev, are situated in the center of the paraffin house at 296-cm distance from the betatron target. At this distance the collimated betatron beam has a diameter of 1.03 cm and an intensity of 3.9 r/min at 20-Mev betatron energy. Some samples were in powder form and were packed into aluminum cylinders with walls 0.030 in. thick and end caps 0.007 in. thick. Identical blank cylinders permitted background determinations for these elements.

* Supported in part by the U. S. Air Research and Development Command and the joint program of the U. S. Office of Naval Research and the U. S. Atomic Energy Commission.
[1] G. C. Baldwin and G. S. Klaiber, Phys. Rev. 70, 259 (1946).
[2] J. L. Lawson and M. L. Perlman, Phys. Rev. 74, 1190 (1948).
[3] M. L. Perlman and G. Freidlander, Phys. Rev. 74, 442 (1948).
[4] G. C. Baldwin and G. S. Klaiber, Phys. Rev. 73, 1156 (1948).
[5] J. McElhinney, Hanson, Becker, Duffield, and Diven, Phys. Rev. 75, 542 (1949).
[6] We shall refer to individual papers that pertain to the results of this paper in subsequent sections. A relatively complete bibliography of papers on photonuclear reactions is given in the paper by L. Eyges, Phys. Rev. 86, 325 (1952).
[7] M. Goldhaber and E. Teller, Phys. Rev. 74, 1046 (1948).
[8] J. S. Levinger and H. A. Bethe, Phys. Rev. 78, 115 (1950).
[9] Montalbetti, Katz, and Goldenberg, Phys. Rev. 91, 659 (1953).
[10] Halpern, Nathans, and Mann, Phys. Rev. 88, 679 (1952).
[11] Halpern, Mann, and Nathans, Phys. Rev. 88, 958 (1952).
[12] R. Nathans and J. Halpern, Phys. Rev. 92, 207 (1953).
[13] Halpern, Mann, and Nathans, Rev. Sci. Instr. 23, 678 (1952).
[14] Sher, Halpern, and Mann, Phys. Rev. 84, 387 (1951).

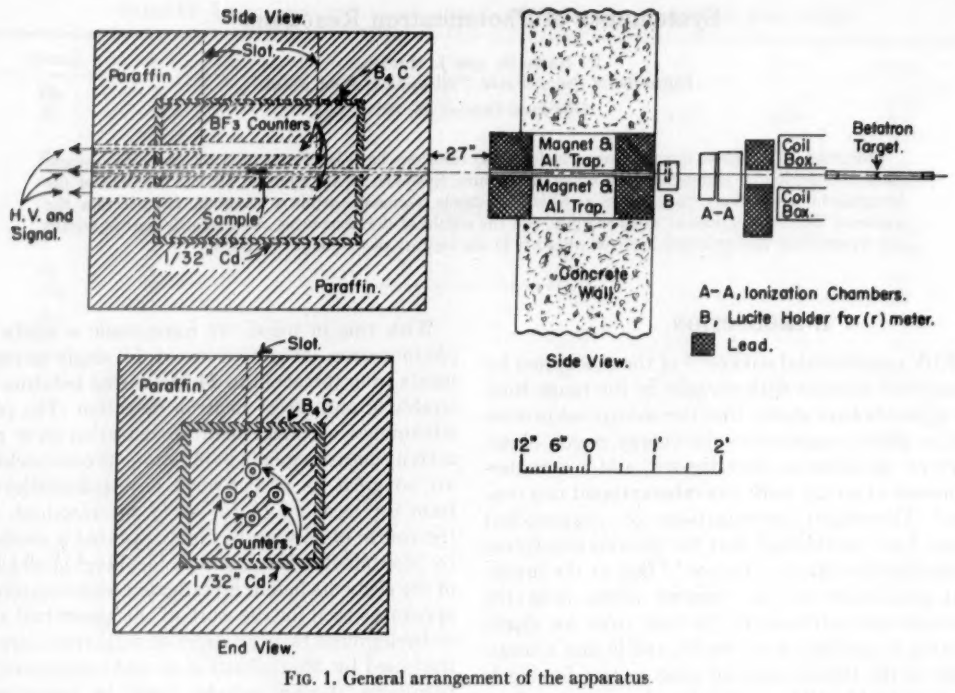

FIG. 1. General arrangement of the apparatus.

With the paraffin house modified to contain four BF_3 counters, it was necessary to establish the dependence of counting efficiency on the energy of the neutrons leaving the sample for each of the counters. Details of this calibration have also been presented previously.[13] Within the errors involved in the calibration, the efficiency of neutron detection was in all cases independent of neutron energy. Because of variations in the BF_3 counters themselves, the absolute efficiency of the four counting channels varied somewhat as determined by a standard radium-beryllium source inserted in the paraffin house at the sample position. The efficiencies so determined were 0.611 percent, 0.553 percent, 0.447 percent, and 0.591 percent, respectively. The four channels were operated from a single high-voltage supply, while their outputs were fed into two amplifying channels, each taking two counters. Data from the two channels were independently recorded and examined for consistency.

Samples were not of sufficient thickness to warrant correction for absorption of the x-ray beam in passing through them, as was demonstrated by runs in which a given element was irradiated using two samples identical in all respects except thickness. In all cases, the yields were identical when normalized to the same thickness. A more serious problem that could arise from thick samples is the possibility of x-ray scattering into the paraffin house producing a (γ,n) reaction in the natural deuterium which is present to three parts in twenty thousand in the hydrogen of the paraffin. Absence of any such difficulty was demonstrated by equality of background with and without samples at energies below the sample thresholds.

Background arose from two sources, that of cosmic-ray origin and that arising from photoneutrons produced in the betatron target and elsewhere leaking through the paraffin house shielding. Each component of the background was separately determined so that for runs near threshold of some elements, where the background is primarily of cosmic-ray origin, corrections could be made for difference in exposure times. Figure 2 shows the values of the two background components as determined from summing the counts for the four channels.

Procedure on a run for a given element consisted in determining neutron yields at various betatron energies for a given number of roentgens of exposure as measured by a 100r Victoreen thimble imbedded in a Lucite cylinder 8 cm in diameter located 3 ft from the betatron target. Each yield was taken to a statistical accuracy of 1 percent except the first three points near threshold, where the accuracy was always better than 3 percent. The entire run was repeated at least once, and internal consistency was within the statistical error. After each run, the threshold and yield at 14.5 Mev for a standard bismuth sample were measured to insure stability of the energy scale. All such determinations indicated no energy shift of the betatron greater than 0.1 Mev. Details of the energy control and calibration have appeared in a previous publication.[14] Excitation func-

tions were constructed from the yield data using the bremsstrahlung distributions as calculated at 1-Mev intervals and modified for absorption in the doughnut wall, the ionization chamber, and the Lucite block.[15]

RESULTS

Figure 3 shows the results of a typical yield curve for a sample of 1.81 g/cm² of rhodium, with the background drawn in for comparison. For economy of figures, the yield curves for the remaining elements are not presented. Furthermore, intercomparison of yield curves from different laboratories is sometimes misleading inasmuch as such curves are the peculiar property of the special arrangement of monitoring apparatus in the x-ray beam and the modification of the bremsstrahlung distribution thereby produced. In constructing excitation functions from yields, this effect is of course taken into account. Cross-section data are presented in Fig. 4 for 12 of 14 elements investigated. The curves for bismuth and tantalum have already been published.[10] Latest results of the Saskatchewan group[9] are drawn for comparison.

The parameters of the giant resonances as taken from these figures have been presented in tabular and graphical form in a preliminary account of this work.[12] Also included were the yields at 22 Mev for comparison with the measurements of Price and Kerst.[16]

In Table I, which presents the data of this paper in more complete form, the absolute values of the cross sections and yields have been modified somewhat from

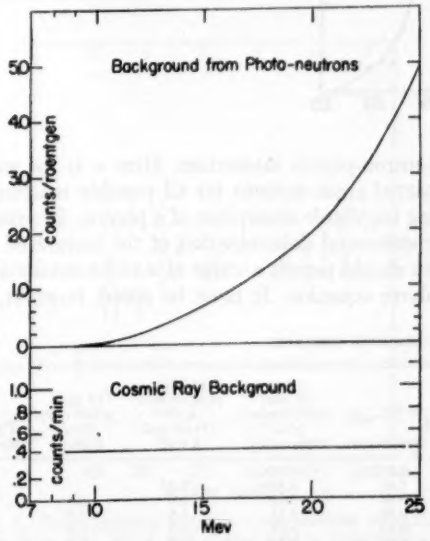

FIG. 2. The upper curve shows the background signal from photoneutrons produced in and around the betatron as a function of betatron energy. The lower curve shows the background component from cosmic rays.

[15] Johns, Katz, Douglas, and Haslam, Phys. Rev. **80**, 1062 (1950).

[16] G. A. Price and D. W. Kerst, Phys. Rev. **77**, 806 (1950).

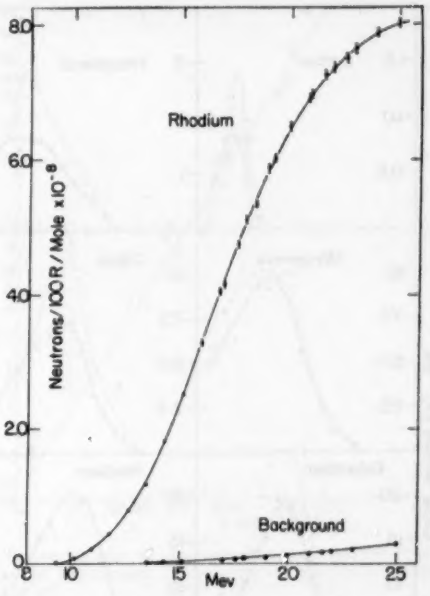

FIG. 3. Neutron yield curve for rhodium. The uncertainty on each point represents statistical error in the evaluation of the yield at each energy. Shown also is the background for comparison.

those given in reference 12. The 22-Mev yields herein given are 10 percent higher to conform to the monitoring arrangement of Price and Kerst; the absolute cross sections are 10 percent lower as a result of improved measurements of the beam area. In the case of bismuth and tantalum, however, absolute values are 40 percent and 8 percent higher, respectively, because of a previous calculational error.

McDaniel, Walker, and Stearns,[17] using the $Li^7(p,\gamma)B^8$ reaction as a radiation source and boron trifluoride proportional counters for neutron detection, have measured absolute cross sections at 17 Mev for some of the elements listed. Corresponding values from our data are tabulated for a rather stringent comparison, as will be discussed in detail below.

DISCUSSION

The parameters listed in Table I which are of special interest in a study of systematic trends in photoneutron reactions are the integrated cross section, the energy at which the dipole absorption resonance attains a maximum cross section, the value of the cross section at this energy, and the narrowness of the resonance as designated by the width in Mev at half-maximum. Each of these is separately considered below.

Integrated Cross Section

The sum rules for dipole absorption as applied to nuclei by Levinger and Bethe[8] give for the integrated

[17] McDaniel, Walker, and Stearns, Phys. Rev. **80**, 807 (1950).

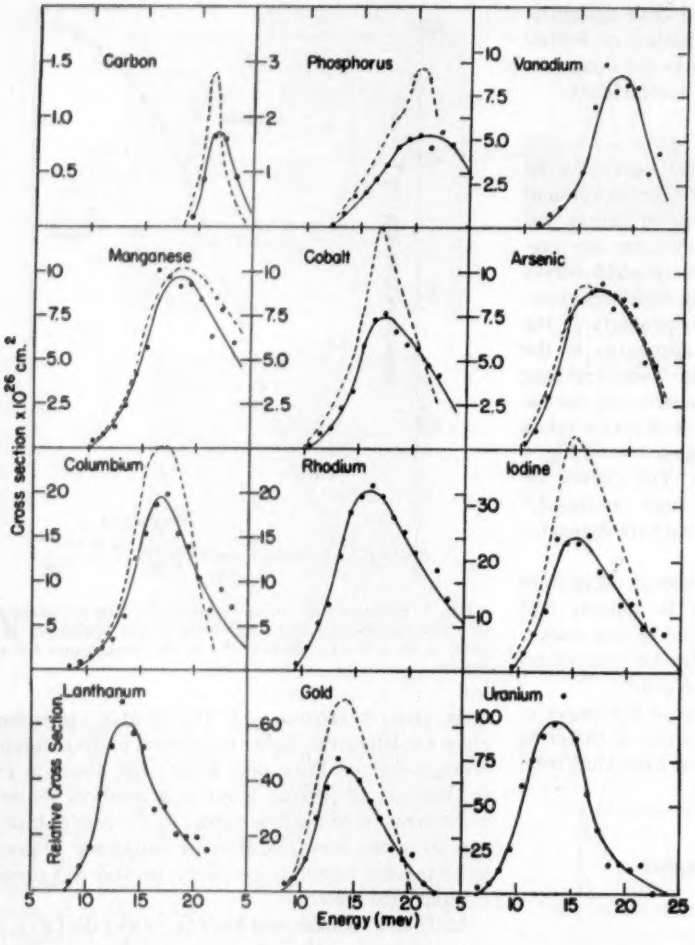

FIG. 4. Excitation functions for 12 of the 14 elements here considered. The dashed lines show the results of Montalbetti *et al.*

cross section for photon absorption:

$$\int_0^\infty \sigma dE = 0.06\frac{NZ}{A}(1+0.8x),$$

where x is the fraction of attractive exchange force in the neutron-proton interaction. Here σ is the sum of the partial cross sections for all possible reactions involving the dipole absorption of a photon. In principle, an experimental determination of the integrated cross section should permit a value of x to be obtained from the above equation. It must be noted, however, that

TABLE I. Summary of data on photoneutron reactions.

Element	Target thickness g/cm²	Thresholds (γ,n) Mev	Thresholds $(\gamma,2n)$ Mev	Thresholds (γ,pn) Mev	E_{σ_m} Mev	Half-width Mev	σ_m ×10²⁶ cm²	$\int_0^{35\text{ Mev}}\sigma dE$ Mev-barns	22-Mev yield/mole-r ×10⁻⁶ (this paper)	22-Mev yield/mole-r ×10⁻⁶ (Price and Kerst)	σ17 Mev ×10²⁶ cm² (this paper)	σ ×10²⁶ cm² (McDaniel)
$_6C^{13}$	12.80	18.70	32.60	27.41	22.0	3.0	0.86	0.027	0.028			
$_{15}P^{31}$	4.41	12.05	24.50	17.90	21.5	10.2	1.67	1.61	0.389	0.33		
$_{23}V^{51}$	2.68	11.15	19.88	18.80	18.7	5.8	8.69	0.56	2.26	1.6	6.8	3.3
$_{25}Mn^{55}$	1.57	10.00	19.40	17.72	18.4	8.8	9.69	0.88	3.15	1.9	9.0	4.0
$_{27}Co^{59}$	2.59	10.25	19.67	17.48	17.3	8.4	7.45	0.63	2.51	2.3	7.4	4.8
$_{33}As^{75}$	1.34	10.10	17.42[a]	16.82[a]	17.3	9.0	9.03	0.80	3.73	3.9	8.5	7.0
$_{41}Cb^{93}$	1.36	8.70	17.88[a]	14.08[a]	17.0	6.8	19.5	1.46	6.67	5.8		
$_{45}Rh^{103}$	1.81	9.35	17.47[a]	15.41[a]	16.5	8.9	20.5	1.94	9.00			
$_{53}I^{127}$	1.23	9.10	16.72	15.29	15.5	8.3	24.3	2.04	11.2	11.0	21.0	18.0
$_{57}La^{139}$	...	8.80	14.25[a]	14.90[a]	13.8	5.7	...	...	...	...	...	...
$_{73}Ta^{181}$	0.468	7.55	13.84[a]	13.47[a]	15.1	7.9	39.7	3.43	21.0	19.0	34.0	25.0
$_{79}Au^{197}$	0.455	7.90	13.71[a]	12.94[a]	13.9	6.9	45.6	3.19	22.4	19.0		
$_{83}Bi^{209}$	0.434	7.40	13.30[a]	12.68[a]	13.2	4.1	63.0	4.08	25.0	25.0	20.0	24.0
$_{92}U^{238}$	0.548	5.97	12.18[a]	13.34[a]	13.8	6.6	98.0	7.15	57.5	51.0	48.0	52.0

[a] Computed from mass formula.

the computed value of x is very sensitive to experimental errors in $\int\sigma dE$. For instance, with $x=0.5$, a 10 percent error in $\int\sigma dE$ leads to a 35 percent error in x. Uncertainties in $\int\sigma dE$ arise from several causes: errors in the measurement of the excitation function for a given partial reaction, neglect of some of the partial reactions, or failure to include contributions of all energy photons to a given partial cross section. For the case of the (γ,n) partial cross section where neutrons are counted, an additional error concerns lack of knowledge of the neutron multiplicity arising mainly from $(\gamma,2n)$ reactions.

Figure 5 shows the systematics of our total neutron emission cross-section measurements integrated to 25 Mev. Here $\int\sigma dE/(NZ/A)$ is plotted against A. Lines for $x=1$ and $x=0$ are shown. For elements with high Z where partial reactions involving emission of charged particles can safely be neglected, the largest contributions to the integrated cross section are those from the (γ,n) and $(\gamma,2n)$ reactions. For these elements the neutron multiplicity might be expected to decrease the values plotted by 20 percent whereas the results of Jones and Terwilliger[18] would indicate the values should be increased by the same amount because of neglect of contributions to the integrated cross sections from photons above 25 Mev. Furthermore, the magnitude of the (γ,γ) process can contribute a like amount to the integrated cross section.[19] Although these uncertainties preclude a reliable determination of x from the presently available photonuclear data, nevertheless it should be noted that the experimental integrated cross

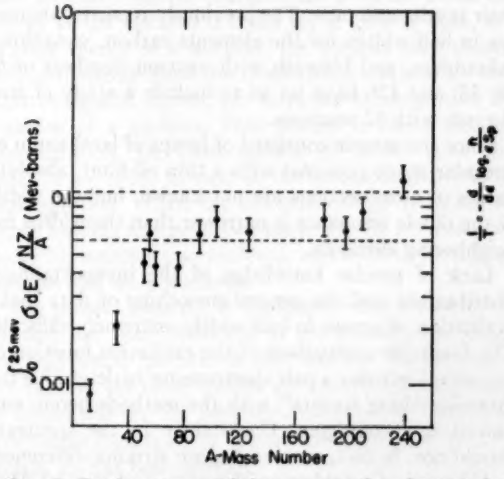

FIG. 5. Total neutron emission cross sections integrated to 25 Mev divided by NZ/A, and plotted against mass number. The straight lines indicate the results to be expected from calculation of the total integrated cross sections for dipole absorption from the theory of Levinger and Bethe for zero and 100 percent exchange force.

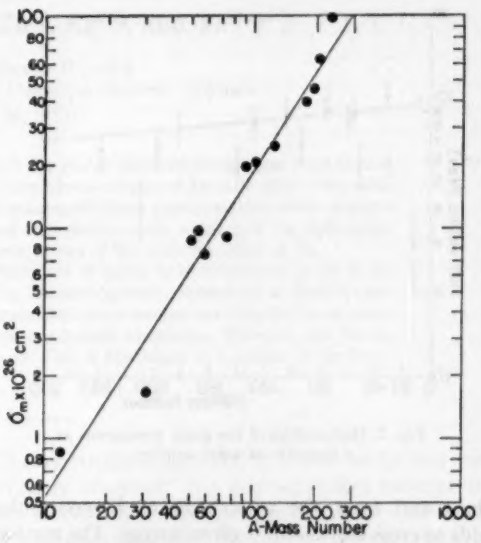

FIG. 6. Log-log plot of the maximum cross section vs A. The best straight line through the points gives a dependence on mass number of A^1.

sections for the heavy elements are consistent with the predictions of the sum rules.

Uranium, with a total neutron integrated cross section of 7.1 Mev-barns is of course a special case because of the added neutron multiplicity resulting from photofission. Duffield and Huizenga[20] have reported separate measurements of the (γ,n) and $(\gamma,$ fission) integrated cross sections with values of 2.6 Mev-barns and 1.2 Mev-barns, respectively. With these values and the assumption that the number of neutrons emitted per fission is 2.5, we compute the $(\gamma,2n)$ contribution to be 0.75 Mev-barns, and thus the total photon absorption $\int_0^{25\,Mev}\sigma dE$ to be 4.55 Mev-barns in excellent agreement with the sum rules for 50 percent charge exchange.

For light elements, neutron emission represents only a small contribution to the total photon absorption cross sections, and for $A<75$ the points of Fig. 5 fall below the line $x=0$ as might be expected.

There are still insufficient data, however, to explain the low integrated cross sections for some of these elements as exemplified by the data for carbon. The (γ,n) integrated cross section of 0.027 Mev-barns plus that for (γ,p) of 0.063 Mev-barns[21] together represent only 50 percent of the sum rule predictions for $x=0$. Should the (γ,p) excitation function exhibit as striking a tail as the (γ,n) results of Jones and Terwilliger[18] indicate, then no discrepancies exist.

We have not as yet discussed the uncertainties in the integrated cross sections arising from possible errors in our measurements. These can arise from systematic errors which may occur in determining absolute yield

[18] L. W. Jones and K. M. Terwilliger, Phys. Rev. **91**, 699 (1953).
[19] Mary Beth Stearns, Phys. Rev. **87**, 706 (1950).
[20] R. B. Duffield and J. R. Huizenga, Phys. Rev. **89**, 1042 (1953).
[21] J. Halpern and A. K. Mann, Phys. Rev. **83**, 370 (1951).

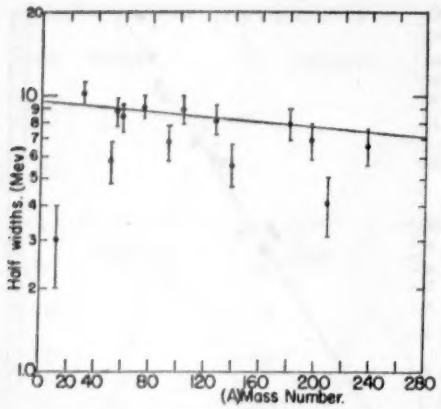

FIG. 7. Half-widths of the giant resonances as a function of mass number.

values and from the conversion of bremsstrahlung yields to cross sections at a given energy. The most significant systematic error in the determination of absolute yields arises from calibration of the efficiency of the detection system using a standard radium-beryllium source whose neutron output is known to perhaps 15 percent. All other errors should be negligibly small. The yield measured at a given maximum bremsstrahlung energy is, however, the result of contributions from photons of all energies between the threshold of the reaction and that maximum bremsstrahlung energy. To calculate the cross section at the given photon energy requires that the contributions from all photons, except these in a small energy region about the given energy, be subtracted from the measured yield. The (approximate) $1/E$ shape of the photon number spectrum in conjunction with the peaked nature of the cross section *vs* energy curve makes the sum of those contributions to be substracted a large fraction of the measured yield. For instance, in bismuth, the measured yield at 17-Mev maximum bremsstrahlung energy is 79.7 counts per r. The yield due to photons between 7.4 Mev (the threshold) and 16 Mev is 72.5 counts per r. Although the error in these counting rates is only 1 percent, errors of 25 percent in the value of a cross section at a given energy are not unlikely. From these considerations, our 17-Mev cross-sections values are in satisfactory agreement with the results of McDaniel, Walker, and Stearns.[17]

The magnitude of the possible error in the integrated cross section should be smaller than that in a cross-section value at a given energy. The reason for this is that the calculation of, say, an erroneously high value for the cross section at a given energy automatically leads to the calculation of an erroneously low cross section at the next higher energy. With a sufficient number of points to determine a smooth curve, the area under this curve is relatively insensitive to the large individual errors on the points. We estimate the uncertainty in the integrated cross sections given in this paper to be about 20 percent.

Peak Cross Section and Energy at Peak

Figure 6 shows a plot of cross-section maxima as a function of mass number, the curve drawn through the measured points showing an $A^{\frac{1}{3}}$ dependence. Considering the errors quoted above on a cross-section value at a given point, this is in good agreement with the results of Montalbetti *et al.*, who find an $A^{5/3}$ relationship. No great reliability can, however, be attached to the exact value of the exponent of A. As shown in Fig. 1 of reference 12, the energy at peak cross section varies as $38.5A^{-0.186}$ in substantial agreement again with Montalbetti *et al.*, and with the predictions of Goldhaber and Teller. With a ± 1-Mev uncertainty in the position of the peaks, the statistical uncertainty in the 0.186 exponent is calculated to be ± 0.011. This result would seem to be in contradiction to the predictions of Steinwedel, Jensen, and Jensen[22] who compute an exponent of $-\frac{1}{3}$ on the basis of a hydrodynamic nuclear model.

Widths of Giant Resonances

The widths at half-maximum of the giant resonances are plotted in Fig. 7. The gradual decrease of the widths with increasing A as indicated by the straight line drawn through the experimental points of Fig. 7 is also observed by Montalbetti *et al.*, although inspection of Fig. 4 indicates some discrepancies in shapes between their results and ours. The previously reported anomalies in half-widths for the elements carbon, vanadium, columbium, and bismuth with neutron numbers of 6, 28, 52, and 126 have let us to include a study of lanthanum with 82 neutrons.

Since the sample consisted of lumps of lanthanum of irregular shape (covered with a thin oil film), absolute values of cross sections are not known, but the width of the dipole resonance is narrower than the widths for neighboring elements.

Lack of precise knowledge of the bremsstrahlung distributions and the general smoothing of data make evaluation of errors in half-widths extremely difficult. The favorable comparison of the excitation function of copper taken using a pair spectrometer to determine the bremsstrahlung spectra[23] with the methods herein employed is encouraging. Uncertainty in the spectrum should not, in fact, much influence striking differences in behavior of neighboring elements, and the ± 1-Mev errors attributed to points in Fig. 7 should be so interpreted.

[22] Steinwedel, Jensen, and Jensen, Z. Naturforsch. **6a**, 218 (1951).
[23] V. E. Krohn and E. F. Schrader, Phys. Rev. **87**, 685 (1952).

Electrodisintegration of Cu^{63}, Zn^{64}, Ag^{109}, and Ta^{181}†*‡

KARL L. BROWN AND RICHARD WILSON§
High Energy Physics Laboratory, Stanford University, Stanford, California
(Received October 26, 1953)

The ratio of the (γ,n) photodisintegration cross section to the $(e,e'n)$ electrodisintegration cross section for the isotopes Cu^{63}, Zn^{64}, Ag^{109}, and Ta^{181} was measured for electron energies of 24 to 35 Mev. This ratio was found to decrease with energy in contrast with the Weizsäcker-Williams approximation which predicts a constant ratio. However, the Weizsäcker-Williams method does yield a result which is of the right order of magnitude for Cu, Zn, and Ag and which is within a factor of two of the observed value of Ta.

Assuming approximately one-half of the total photon absorption of nuclei to be attributed to the (γ,n) reaction, then comparison of the experimental results for Cu, Zn, and Ag with calculations of Blair is consistent with the suggestion of Bethe and Levinger that the main absorption mechanism of nuclei for photons is electric dipole with a contribution of ~6 percent electric quadrupole absorption. However, for Ta no simple correlation between experiment and theory was found. This is attributed to a failure of the Born approximation used in the Blair calculations.

I. INTRODUCTION

ELECTRONS are known or expected to interact with nuclei in the following ways: (1) They may interact with the virtual meson cloud surrounding the nucleons. This is equivalent to an interaction with the magnetic moment of the nucleus. At electron energies lower than the meson threshold this interaction appears in the form of elastic scattering of the electron corresponding to that of a square-well potential about 5-kv deep and having a width equal to the classical electron radius. (2) They are expected to interact through inverse beta decay. This process has a very low cross section of the order of 10^{-44} cm^2 and has not yet been observed. (3) The electromagnetic field of the electrons may interact with the charge of the protons. When the energy of the electron is equal to, or greater than, the binding energy of a nucleon, the nucleus may absorb sufficient energy from the bombarding electron by this electromagnetic interaction to cause disintegration by emission of a nucleon. This process is called electrodisintegration, the cross section for which is of the order of $\alpha=1/137$ of that of the corresponding photodisintegration. When the electron energy is increased to the binding energy of two nucleons, the nucleus may decay by emitting two nucleons, and so forth for higher energies and more nucleons.

The present research is concerned with the study of (3) and has been restricted to the special case where the only decay particle is one neutron. In particular the ratio of the cross section σ_{br} for the disintegration of nuclei due to the bremsstrahlung of the electrons (photodisintegration) to the electrodisintegration cross section σ_{el} has been studied.

The electrodisintegration of a few nuclei has been previously observed. The first successful attempt was made in 1939 by Collins, Waldman, and Guth[1] on Be at 1.8 Mev verifying that the electrodisintegration cross section is of the order of α times the photodisintegration cross section. Paul[2] observed electrodisintegration of deuterium at 3.8 Mev and estimated the cross section for that energy to be between 10^{-30} and 10^{-31} cm^2. For Cu^{63}, Ag^{107}, and Ag^{109}, Skaggs *et al.*[3] investigated at 16 Mev the photodisintegration cross section and the electrodisintegration cross section and found the corresponding ratio of these cross sections to be approximately 400 for all three isotopes.

Many theoretical calculations have been made to determine electrodisintegration cross sections. Weizsäcker and Williams[4] have developed a method for calculating the interaction of fast electrons using a correspondence principle argument. By use of this method the electrodisintegration cross section may be calculated provided the corresponding photodisintegration cross section is known. The validity of this method requires that the bombarding electrons are not appreciably diverted by the collision. This is equivalent to assuming that the nuclear excitation energy is small compared with the initial electron energy, which is not valid for the conditions of all electrodisintegration experiments thus far performed including the present one. There are other assumptions made by the Weizsäcker-Williams method which also tend to make it invalid. (1) It neglects the component of the field in the direction of motion of the electron. (2) It completely omits the contribution of the scaler potential. This can be important in the case of quadrupole transitions as can be seen from the calculations of

† The research reported in this document was supported jointly by the U. S. Navy (Office of Naval Research) and the U. S. Atomic Energy Commission.
* This material was presented in part at the December 29–30, 1952 meeting of the American Physical Society in Pasadena, California.
‡ This report based on a dissertation submitted for the Ph.D. degree at Stanford University by Karl L. Brown.
§ Now at Clarendon Laboratory, Oxford, England.

[1] Collins, Waldman, and Guth, Phys. Rev. **56**, 876 (1939).
[2] W. Paul, Naturwiss. **36**, 31 (1949).
[3] Skaggs, Laughlin, Hanson, and Orlin, Phys. Rev. **73**, 420 (1948).
[4] E. J. Williams, Kgl. Danske Videnskab. Selskab, Mat.-fys. Medd. **13**, 4 (1935).

Blair[5] and others. More rigorous calculations of electrodisintegration have been made using multipole expansions of the electromagnetic field of the electron. Dipole cross sections have been calculated by Bethe and Peierls,[6] and Peters and Richman;[7] whereas Wick,[8] Sneddon and Touschek,[9] and Blair[5] have included the electric quadrupole case. Recently Guth and his collaborators[10] have developed a method to calculate transitions higher than electric quadrupole and have included electric dipole-quadrupole interference terms. In this paper we shall refer to the calculations of Blair, which are in agreement with the other authors (except for a numerical error in Sneddon's quadrupole calculation) but which are presented in a form which is convenient for our experimental conditions. In particular, Blair calculates the ratio of the cross section σ_{br} for the photodisintegration of nuclei due to the thin-target bremsstrahlung of the electrons to the electrodisintegration cross section σ_{el} of the same nuclei. We have added to Blair's results, with his approval, the corrections to the bremsstrahlung formula due to atomic screening and due to bremsstrahlung by orbital electrons. No atomic screening corrections are necessary for the calculation of σ_{el} because the principal contribution comes from large momentum transfers.

II. THEORY

It should be pointed out that σ_{br} as defined by Blair and as used here is a rather peculiar kind of cross section since it depends upon the properties of the target material preceding the particular nucleus which is undergoing photodisintegration. It is defined as follows:

$$\sigma_{br}(k,E_0)=\frac{N_0 t_{eff}}{A_r}\sigma_{\gamma,n}(k)\phi(E_0,k), \tag{1}$$

where $\sigma_{\gamma,n}(k)$ = the photodisintegration cross section for a nucleus of atomic number Z and mass A, $\phi(E_0,k)$ = the "thin target" cross section for production of bremsstrahlung in a material of atomic number Z_r, and mass A_r, t_{eff} = the thickness in g/cm² of the material, Z_r producing the bremsstrahlung, N_0 = Avogadro's number, E_0 = total energy of the bombarding electrons, and k = nuclear excitation energy. Because of the fact that σ_{br} depends upon t_{eff}, Z_r, and A_r, a more general quantity F is defined which essentially eliminates them from the discussion.[11] The quantity F is defined as

$$F(k,E_0)=\left(\frac{\sigma_{br}}{\sigma_{el}}\right)\left[\frac{A_r}{Z_r(Z_r+\delta)r_0^2 N_0 t_{eff}}\right], \tag{2}$$

where $r_0=e^2/m_0c^2$ and δ is a factor which determines the magnitude of the contribution of orbital electrons to the production of bremsstrahlung. Throughout the remainder of this work it will be assumed that $\delta=1$. It follows that

$$F(k,E_0)=\frac{\alpha\sigma_{n,\gamma}(k)\phi(E_0,k)/\bar{\phi}}{\sigma_{el}(k,E_0)}, \tag{3}$$

where $\bar{\phi}=Z_r(Z_r+\delta)r_0^2\alpha$ and $\alpha=e^2/\hbar c$.

Blair calculated both σ_{br} and σ_{el} in the Born approximation assuming a compound-nucleus model.

σ_{br} was evaluated for the electric dipole case by the standard method of calculating the transition probability per unit time in terms of the incident photon intensity and the nuclear electric dipole matrix element. Dividing the transition probability by the incident electron flux yielded the cross section $(\sigma_{br})_{E.D.}$. The matrix element was *not* evaluated.

σ_{el} was evaluated by calculating the transition probability per unit time and hence the cross section in terms of the matrix element of the perturbing Hamiltonian. The electromagnetic effect of the electrons on the nucleus was represented by a multipole expansion of the Møller potentials which are equivalent to the use of plane-wave solutions for both the incoming and outgoing electrons. The perturbing Hamiltonian for the electric dipole case was then determined by calculating the energy of interaction of the electric dipole approximation of the Møller potentials with the protons in the nucleus. Evaluation of the Hamiltonian matrix element involved the same electric dipole matrix element as occurred in the photodisintegration case. Hence, the matrix element cancelled out when the ratio of σ_{br}/σ_{el} was taken. A similar calculation was made for the magnetic dipole and electric quadrupole cases.

In all of these calculations the photon intensity was evaluated using the Bethe-Heitler[12] extreme relativistic formula for bremsstrahlung including ½ the atomic screening correction $C(\gamma)$ and adding the contribution of the orbital electrons to bremsstrahlung production by replacing Z_r^2 by $Z_r(Z_r+1)$. The final results are expressed by the following equation:

$$F_T(k,E_0)=(\sigma_{br}/\sigma_{el})(g/t_{eff})$$
$$=\frac{2\pi(E/E_0)[E/E_0+E_0/E-\frac{4}{3}]\times[2\ln(2E_0E/\mu k)-1-2C(\gamma)]}{[1+(E/E_0)^2][\ln(2E_0E/\mu k)]+D}, \tag{4}$$

[5] J. S. Blair (private communication, July 11, 1952); "Summary of Calculations on Electron Disintegration of Nuclei," Department of Physics, University of Illinois, 1948 (unpublished); Phys. Rev. **75**, 907 (1949).

[6] H. Bethe and R. Peierls, Proc. Roy. Soc. (London) **148**, 146 (1935).

[7] B. Peters and C. Richman, Phys. Rev. **59**, 804 (1941).

[8] G. C. Wick, Ricerca sci. **11**, 49 (1940).

[9] I. N. Sneddon and B. F. Touschek, Proc. Roy. Soc. (London) **A193**, 344 (1948).

[10] Thie, Mullin, and Guth, Phys. Rev. **87**, 962 (1952).

[11] In general it is not convenient to eliminate the Z_r dependence in F which arises from the atomic screening correction inherent in $\phi(E_0,k)$.

[12] H. Bethe and W. Heitler, Proc. Roy. Soc. (London) **A146**, 93 (1934).

where $g=A_r/[Z_r(Z_r+1)r_0^2N_0]$; E_0= total energy of incident electron; E= total energy of scattered electron; $\mu=m_0c^2$; $k=E_0-E$= nuclear excitation energy; $C(\gamma)$ =atomic screening term; $D=-2E/E_0$ for electric dipole excitation, $=0$ for magnetic dipole excitation, $\cong 8E^2/3k^2$ for electric quadrupole excitation.

III. EXPERIMENTAL TECHNIQUE

It must be noted that $F_T(k,E_0)$ evaluates the ratio of the two cross sections for a particular excitation energy k. Experimentally, this is a quantity which is very difficult to measure; however, a quantity

$$F_{\exp}(Z,E_0) = \frac{g}{t_{\text{eff}}} \int_0^{E_0-\mu} \sigma_{\text{br}}(k,E_0)dk \Big/ \int_0^{E_0-\mu} \sigma_{\text{el}}(k,E_0)dk \quad (5)$$

is easily measured and is, in fact, a reasonable approximation of the theoretically defined quantity $F_T(k,E_0)$, provided k is chosen as described below. It should also be pointed out that $F_{\exp}$ as defined above cannot be calculated unless the matrix elements (which dropped out in Blair's calculation) are evaluated. However, two observations help to reconcile this difficulty.

(1) F_T is a slowly varying function of k.

(2) The principal contribution of (γ,n) cross sections has been experimentally observed to occur over a relatively small photon energy range. (This is discussed in Sec. VI.) Thus, for any given isotope there is an effective photon absorption energy k_0. Assuming $\sigma_{\text{el}}(k,E_0)$ to have a similar behavior, it is to be expected that

$$F_{\exp} \simeq F_T(k_0,E_0) = \frac{g}{t_{\text{eff}}} \frac{\sigma_{\text{br}}(k_0,E_0)}{\sigma_{\text{el}}(k_0,E_0)}. \quad (6)$$

Therefore, the following procedure has been adopted in this experiment. F_T was averaged over the values of $k<(E_0-\mu)$ for which the (γ,n) cross section is finite, and it is this quantity which is compared with $F_{\exp}$. This averaging is done by using the experimental results quoted in Sec. VI as follows:

$$\bar{F}_T = \int_0^{E_0-\mu} F\sigma_{\gamma,n}(k,E_0)dk \Big/ \int_0^{E_0-\mu} \sigma_{\gamma,n}(k,E_0)dk. \quad (7)$$

It would be ideal if the (γ,n) cross sections were known for each of the different types of excitation, i.e., electric dipole, magnetic dipole, and electric quadrupole. There are, however, no data available to do this. The above procedure is most likely to introduce the greatest error in the quadrupole case as it is expected that the largest contribution to the (γ,n) cross section is from electric dipole absorption.[13] Assuming that the error introduced by the above procedure is small compared to the difference between $\bar{F}_T$ for the different types of excitation, then a comparison of $F_{\exp}$ with the theoretical $\bar{F}_T$'s should show the relative importance to photodisintegration and to electrodisintegration of each type of excitation process.

The experiment was one of the "stacked foil" type in which an electron beam passed successively through a thin foil of the element being studied, a copper radiator to produce the bremsstrahlung, and a second thin foil. The resulting foil radioactivities were measured with thin-walled Geiger counters, and from the two observed activities w_1 and w_2 it can be shown that, with the aid of the simplifying assumptions stated below, $F_{\exp}$ is given by

$$F_{\exp} = \left[\frac{(x_1/x_2)w_2-w_1}{w_1-k_2w_2}\right]\left(\frac{g}{t_{\text{eff}}}\right), \quad (8)$$

where

$$k_2 = (hx_1^2)/2x_2t_{\text{eff}},$$

$$k \cong \frac{Z(Z+1)A_r}{Z_r(Z_r+1)A},$$

$$t_{\text{eff}} = t+[x_1+(x_2/2)]h,$$

and x_1= thickness of first foil in g/cm^2, x_2= thickness of second foil in g/cm^2, t= thickness of copper radiator in g/cm^2. A and Z are the atomic weight and atomic number of the foils and the subscript r refers to the copper radiator.

This equation makes the following assumptions:

(1) The electron beam current is not reduced in traversing the foils and radiator.

(2) The energy of the incident electrons is not reduced.

(3) The bremsstrahlung produced is neither absorbed nor scattered in traversing the remaining distance in the foils and radiator.

(4) There is no backward production of bremsstrahlung.

(5) Multiple scattering effects may be neglected.

(6) There is no gamma contamination in the initial electron beam.

(7) The foil and radiator thicknesses are perfectly uniform.

(8) The only radioactivity observed in the two foils is that due to the (γ,n) and the $(e,e'n)$ reactions.

(9) The efficiency in counting the first foil is exactly equal to that of counting the second foil.

As none of these assumptions can be exactly satisfied, experimental corrections were made when necessary and these will be discussed later.

By inspection of the equation for F_T it can be seen that the optimum difference between the three types of excitation occurs at $E_0 \cong 2k_0$, where k_0 is the effective absorption energy for a (γ,n) reaction. k_0 is in the range of 14–18 Mev for all of the isotopes studied, which

[13] See for example, J. M. Blatt and V. F. Weisskopf, *Theoretical Nuclear Physics* (John Wiley and Sons, Inc., New York, 1952), p. 656.

means that 28–36 Mev is the optimum initial electron energy. The experiment was performed over an energy range 24–34 Mev. The lower energy was determined by the uncertainty in the experimental corrections due to energy loss of the electrons between the first and second foils. The upper limit was determined by energy capabilities of the electron linear accelerator. It would be interesting to extend these experiments to both a higher and lower energy if the present limitations could be overcome.[14] A lower energy would give more information about what part of the excitation curve has the maximum magnetic dipole and electric quadrupole contributions; whereas, a higher energy would enable the electric quadrupole and magnetic dipole contributions to be separated. This can be seen by observing that in general the difference $F_T(\text{E.D.})-F_T(\text{E.Q.})$ increases as E_0 increases; whereas, $F_T(\text{E.D.})-F_T(\text{M.D.})$ increases for $E_0 \rightarrow 2k$, but decreases for $E_0 > 2k$. It should be noted at this point that if the Weizsäcker-Williams approximation is used for both the bremsstrahlung formula and for representing the electromagnetic field of the electron, F_T is approximately $8\pi/3$ independent of E_0 and k. This has been shown by Blair.[5] Also it should be observed that $F_T \rightarrow 8\pi/3$ as $k \rightarrow 0$ for dipole absorption but is equal to zero for electric quadrupole absorption.

IV. EXPERIMENTAL ARRANGEMENT

The source of electrons for this experiment was a 35-Mev linear accelerator constructed by Post[15] and Shiren. This machine is pulsed 60 times per second, producing 10^8–10^9 electrons per pulse in a variable energy range of 10–35 Mev. The beam pulse length is about one microsecond.

A one-mil aluminum window was placed at the end of the accelerator so that the foils could be inserted in the target area without disturbing the accelerator vacuum. Beyond this window a wedge magnet bent the electron beam through a 12° angle into the target area. (See Fig. 1.) This magnet selected electrons of the desired energy from the energy spectrum and removed the gamma-ray contamination resulting from electrons striking the sides of the accelerator, the aluminum window, and the magnet chamber. The energy interval was defined to within one or two percent by collimating slits before and after the magnet. The first collimating slit of brass, 1/10 in. wide, was situated at the end of the accelerator and served as a mount for the one-mil aluminum window. The second slit, also 1/10 in. wide, was placed 40 inches beyond the analyzing magnet and was made of carbon to minimize electron scattering and gamma background. The second collimating slit and the analyzing magnet were positioned with respect to the first slit so as to make the horizontal energy focal point of the magnet coincide as nearly as possible with the second slit, thus maximizing the beam intensity. The magnification of the electron optical system was approximately two. The calculations for this system follow the methods of Camac.[16]

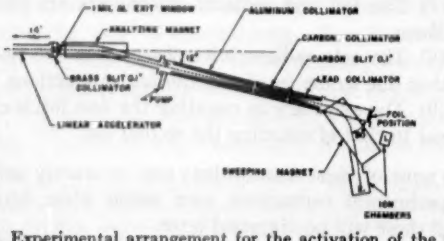

FIG. 1. Experimental arrangement for the activation of the Cu, Zn, Ag, and Ta foils.

Preceding the second slit (see Fig. 1) is a tapered collimator of aluminum designed to allow only those electrons coming from the desired direction to enter the second slit. Beyond the carbon slit is a tapered lead collimator, the purpose of which is to absorb the scattered electrons and gamma rays which are not traveling in the direction of the main electron beam defined by the brass and carbon slits.

Radiographs of the beam made at distances between 0 in. and 12 in. from the end of the lead collimator showed a readily explainable structure. By comparing the two radiographs, the slit image was observed to diverge at the rate to be expected from both the multiple scattering in the accelerator aluminum window and the analyzing magnet's focal properties. On either side of the slit image (main beam) there are bands which correspond geometrically to the electrons scattered at small angles from the aluminum collimators. A third radiograph was exposed at a position 12 in. away from the lead collimator with the electron beam deflected away from the film by a clearing field (magnet No. 2 in Fig. 1). The deflection occurred between the lead collimator and the film. Hence, the electron beam passed through the collimators and slits in a normal fashion but was not allowed to strike the film. The blackening of the film was, then, due entirely to gamma contamination which is normally present within the electron beam and clearly showed that most of the gamma contamination was in the "scatter bands." This fact was used to advantage to reduce the effective gamma background and will be discussed in Sec. V.

The fact that the central part of the beam was mid-way between the two "scatter bands" (on the second radiograph) demonstrated that the wedge magnet was correctly positioned. For first-order theory it can be shown that a slight error in magnet position would have no effect on the energy resolution, but it would shift the central beam relative to the scatter bands and would alter the energy calibration of the machine.

[14] Recently experiments have been performed at lower energies for Cu^{63}. See Scott, Hanson, and Kurst, Bull. Am. Phys. Soc. (New York Meeting) **29**, No. 1 (1954), Abstract JA2.

[15] Richard Freeman Post, Ph.D. dissertation, Department of Physics, Stanford University, June 1952 (unpublished).

[16] M. Camac, Rev. Sci. Instr. **22**, 197 (1951).

Energy Calibration

The beam was shown to have an energy spread of about three percent by taking a radiograph of the beam after it had passed through the collimators and had been deflected by the clearing field magnet. This is quite adequate for the experiment, as F_{exp} is a slowly varying function of energy. The beam energy was calibrated at 18.7 Mev by observing the threshold of the $C^{12}(\gamma,n)C^{11}$ reaction which is known from isotope mass data.[17] The calibration had an internal consistency of three percent which again is adequate for this experiment. The energy calibration was then extrapolated to 35 Mev using the *B-H* curves of the magnet.

Bombardment and Counting Procedure

The experimental procedure was as follows: The two foils and the copper radiator were placed in the vacuum chamber of the second magnet at a position approximately 12 in. from the carbon slit (immediately after the second magnet—see Fig. 1) and were bombarded for a definite period of time after which the foils were removed and inserted in Geiger counters. For fast counting rates, counting was delayed for at least one or two minutes after insertion of the samples in the counters to obviate an effect observed with argon alcohol-quenched counters whereby the counting rate is low by about three percent for the first minute. In the case of zinc a one-hour delay was imposed to allow some unwanted short-lived activity resulting from (γ,p) and (γ,pn) reactions to decay. The tantalum was allowed a 2–2½-hour delay to allow decay of activity resulting from a slight copper content in the aluminum foil holders. This was necessary because of the low tantalum counting rates. To cancel out the difference in efficiency of the two Geiger counters the samples were counted a second time interchanging the samples with respect to the Geiger counters and averaging the two counting rates after making a correction on the second count for the decay of the samples. The usual counter corrections for dead time and background were made.

In order to reduce errors due to spurious counting, the Geiger counters were operated with a multivibrator-quench unit, giving an electronically controlled dead time.

V. EXPERIMENTAL CORRECTIONS

Gamma-Ray Background

In spite of attempts to achieve a clean electron beam, a serious gamma background problem existed. Though the number of gammas in the beam was small compared to the electrons, the photodisintegration cross section is approximately 400 times as great as the electrodisintegration cross section. This gamma background was assessed by carrying out a second bombardment identical to the above except that the second magnet between the collimators and foils was energized, thus deflecting the electron beam away from the foils. Any induced activity in the foils which is of the correct half-life must, therefore, be due to the gamma contamination present in the initial electron beam. When this activity is normalized to the same incident electron beam as a regular bombardment, the background activity may be subtracted from the regular activity thus correcting for the gamma contamination.

The normalization to the same incident beam is achieved by monitoring both bombardments with ionization chambers as shown in Fig. 1. Chamber number one monitors the direct beam and chamber number two, the deflected beam. The ratio of the two chambers is determined by making a series of short runs while the electron beam current is steady—alternating with second magnet off then on (time on = time off), etc. By integrating the current collected in each chamber for equal time, the ratio is given by which the gamma background run may be normalized with the regular runs. To avoid ion recombination effects in the chambers as a result of the intense peak currents of the microsecond pulses, the ion chambers could not be used to monitor the beam directly but were used to monitor part of the scattered beam. As a result it was found that the internal consistency of the normalization procedure was good to only about ten percent. Since the gamma background was found to be of the order of twelve to twenty percent, the background correction has an uncertainty of about two percent.

As was expected, this background was found to depend rather critically upon the collimator alignment and was also found to increase with energy. Background bombardments were alternated with regular bombardments.

Correction for Foil Irregularities

The foils were cut from a large sheet of chemically pure metal with a die of diameter 1¼ in. Immediately around the 1¼-in. hole, several $\frac{3}{16}$-in. diameter pieces of foil were cut to check on the foil uniformity. These were weighed to 1/100 mg, and the results indicated that the copper, zinc, and silver foils were uniform to ± 1 percent and the tantalum to ± 2 percent. Since a large number of foils was used, the effect averages out in the final result; moreover, by pairing the foils so that in alternate runs their positions are interchanged, the error in F due to the nonuniformity can be shown to be reduced to less than ± 0.2 percent in all cases.

Corrections Due to Multiple Scattering

The electrons are incident normally upon the first foil. Yet they are multiply scattered in the first foil, radiator, and second foil resulting in an increase in path length or effective thickness of the foils and radiator. A correction factor must be made for this

[17] H. A. Bethe, *Elementary Nuclear Theory* (John Wiley and Sons, Inc., New York, 1947), p. 124.

effect. Using the methods of Yang[18] it is shown that this correction should have the form

$$1-k(21/E)^2,$$

where $k=0.020$, 0.017, 0.022, and 0.022 for copper, zinc, silver, and tantalum, respectively.

A second multiple-scattering correction arises as a result of the high gamma background. It has been mentioned previously that a large fraction of the gamma background is contained in the scatter bands of the beam. This fact was used to advantage to reduce the effective background by placing apertures over the Geiger counters in such a way as to shield the counters from the scatter-band activity of the foils. However, this leads to a second difficulty—fortunately a minor one. The beam is about 0.2 mm broader when striking the second foil than it was when striking the first foil as a result of multiple scattering in foil and radiator. Due to the aperture on the counters, this could and does lead to a slight reduction in efficiency of counting the second foil's activity. This effect is estimated to yield a correction factor of $1+[0.005(21/E)]$.

Corrections Due to Other Activities

Since the bombardments are performed at a high incident electron energy, reactions other than (γ,n) are possible. Also where there is more than one isotope in the element being bombarded, competing (γ,n) reactions of different isotopes may cause trouble. This is especially true in the case of silver. It is possible to discriminate against competing reactions in each case by an appropriate choice of the irradiation, delay before counting, and counting time. Moreover, such activities are not in themselves expected to have values of F far removed from the value of F of the desired reaction. Hence, the actual correction to F_{exp} will be much less than the proportion of the undesired activity present. Calculation shows that for our conditions no significant correction is needed except in the case of silver where the $Ag^{107}(\gamma,n)Ag^{106}$ 24.5-minute activity competes with the desired $Ag^{109}(\gamma,n)Ag^{108}$ 2.3-minute activity. By observing the ratio of the activities in the two silver foils as a function of time, it was verified that the necessary correction for the $Ag^{107}(\gamma,n)Ag^{106}$ contamination was $+1.01\pm0.005$, independent of energy. Experimental decay curves for each element were plotted and analyzed to show the expected background reactions; in every case but silver the conclusion was confirmed that the experimental correction necessary was less than ±0.5 percent.

Correction for Activity in Foil Holders

The target foils were mounted in aluminum holders to facilitate a reproducible geometry in both the bombardment and counting. The electron beam is not entirely localized in the foil area and some scattered electrons and gamma rays bombard the target holder. In the case of copper, zinc, and tantalum the holders were an aluminum alloy containing about 4-percent copper. The activity induced in the aluminum has a six to seven second half-life and is not observable after a two-minute delay between bombarding and counting. However, the copper contamination has a ten-minute half-life and is troublesome. For the tantalum runs a two-hour delay allowed the holder's copper activity to decay, but for copper and zinc a correction was made by bombarding and counting blank holders. This led to a small correction factor of the order of 0.5 percent. In the case of silver where it was important to count as soon as possible after bombarding, it was found necessary to make the foil holders out of pure 2S aluminum, thus eliminating all but the foil activity and the aluminum six to seven second activity.

Activity from Backscattered Electrons and Gamma Rays

The electron beam passes through the foils and then emerges upon a polystyrene block. The beam loses energy by ionization in this block without much scattering. There may still be some electrons or gamma rays backscattered from the walls of the second magnet chamber of such an energy that they can induce activity in the foils. An upper limit to this may be obtained by placing foils on the extreme edges of the polystyrene foil mount. Only scattered electrons can reach here. Since the backscattered intensity is certainly nondirectional this is an upper limit to the backscattered intensity. The correction is about 1 percent and is shown in the table of results.

Corrections Due to Electron and Gamma-Ray Degradation

Ionization and radiative losses of the electrons combined with pair production and Compton effect losses of the gamma rays in the foils and radiator require a modification of the Bethe-Heitler[12] thin target bremsstrahlung spectrum.

Eyges[19] has calculated a thick-target spectrum by expanding the equations for an electron-initiated shower in powers of the radiator thickness, retaining only the first-order terms. One of the authors[20] has extended this calculation (using a different approach) to include the effects of electron ionization loss and electron energy loss due to radiation of low-energy quanta. Thus, the gamma-ray spectrum inducing activity in the foils will not be that predicted by the Bethe-Heitler equation, nor will the electron-induced activity be exactly that expected from monoenergetic electrons.

Wilson has shown that the equivalent thick-target bremsstrahlung cross section may be expressed to first

[18] C. N. Yang, Phys. Rev. 84, 599 (1951).

[19] L. Eyges, Phys. Rev. 81, 981 (1951).

[20] R. Wilson, Proc. Roy. Soc. (London) A66, 638 (1953).

order in the form

$$\phi'(E_0,k,t)=\phi(E_0-\tfrac{1}{2}\bar{\Delta},\,k)$$
$$\times\left[1-\frac{Nt}{2A}\left(\int_{E_0-k-\mu}^{E_0-\mu}\phi(E_0,k')dk'+\sigma(k)\right)\right], \quad (9)$$

where $\phi(E_0,k)$ is the Bethe-Heitler cross section for the production of a quantum of energy k by an electron of total incident energy E_0; Nt/A is the number of target nuclei per cm^2; $\bar{\Delta}$ is the average of small energy losses of an electron in traversing a radiator of thickness t and may be expressed in the form

$$\bar{\Delta}=I+\frac{Nt}{A}\int_0^{E_0-k-\mu}k'\phi(E_0,k')dk', \quad (10)$$

where I is the ionization loss which may be taken from the calculations of Halpern and Hall.[21]

$\sigma(k)$ is the cross section for loss of gammas of energy k due to pair production and Compton effect. The integral term in the equation for ϕ' arises from the loss of "effective" electrons by large radiative transfers; these can never again radiate a quantum of energy k.

In order to apply these corrections to this experiment, it is necessary to average

$$[\phi(E_0,k)-\phi'(E_0,k,t)]/\phi(E_0,k) \quad (11)$$

over the values of $k<E_0-\mu$ for which the (γ,n) cross section is finite. The errors due to uncertainty in the shape of this cross section curve have been estimated and included as probable errors of the correction.

Thus far only the gamma induced activity has been discussed. A similar correction is necessary for the electron induced activity. Since the results of this experiment show that F is a slowly varying function of energy, this correction may be made by assuming that the electrons can be considered as a spectrum of "virtual quanta" as in the Weizsäcker-Williams approximation. The modified electron spectrum as a result of degradation has the form

$$\phi'(E_0,k,t)_{el}$$
$$=\phi(E_0-\bar{\Delta},\,k)_{el}\left[1-\frac{Nt}{A}\int_{E_0-k-\mu}^{E_0-\mu}\phi(E_0,k')_{el}dk'\right] \quad (12)$$

which differs from the gamma spectrum correction case by the omission of $\sigma(k)$. The factor $\frac{1}{2}$ is also omitted since this is a first-order effect resulting directly from the electrons. The quantity

$$[\phi(E_0,k)_{el}-\phi'(E_0,k,t)_{el}]/\phi(E_0,k)_{el} \quad (13)$$

averaged over k thus determines the magnitude of the electron degradation correction.

The combination of these two effects amounts to a correction of from three to ten percent in F which becomes smaller as the energy of the bombarding electrons is increased. These corrections are shown in the table of results.

[21] O. Halpern and H. Hall, Phys. Rev. **73**, 477 (1948).

VI. ACTIVATION CURVES FOR PHOTONUCLEAR (γ,n) REACTIONS

Although a knowledge of the absolute (γ,n) cross sections is not required for this experiment, the relative shape of the cross section as a function of photon energy k is required in order (1) to average F_T over $\sigma_{\gamma,n}(k)$ so that a comparison with F_{exp} may be made and (2) to evaluate the electron and gamma degradation corrections to F_{exp}. Each of the isotopes studied will be discussed separately.

Several experiments have been performed on the photodisintegration of copper. The excitation curve as a function of photon energy for the $Cu^{63}(\gamma,n)Cu^{62}$ reaction has been studied by several investigators.[22–27] The peak absorption energy k_{max} as reported by these investigators is 22, 17.5, 18, 17.5, and 17.5 Mev, respectively; however, the authors differ about the shape of the excitation curve above k_{max}; i.e., whether or not there is a high-energy tail. Strauch,[28] Marshall,[29] and Koch *et al.*[30] have measured the effective excitation energy by absorption techniques. Strauch finds 18 Mev; Marshall reports 17.3 by Compton effect and 21.0 by pair production; and Koch *et al.* find 17.2 Mev. For the purposes of this experiment, an effective energy k_0 of 18.0±0.5 Mev is used. The excitation curve of Katz and Cameron is used with the restriction that there is an uncertainty about the high-energy tail. Katz and Cameron indicate the cross section to be essentially zero above 21 Mev; whereas, Newkirk's results indicate a tail extending to about 30 Mev. With these limits an error is assigned to the degradation corrections and the averaging of F_T.

There are far less data available on the excitation curve of the other elements, but the above results for copper, give some idea as to the reliability of such measurements. For the $Zn^{64}(\gamma,n)Zn^{63}$ reaction, results of Katz and Cameron,[24] Strauch,[28] and Marshall[29] are available. From these results it seems likely that the shape of the excitation curve is similar to copper. The effective absorption energy as determined by Strauch is 19 Mev. Marshall gives 16.6 via Compton effect and 20.0 via pair production. The peak of the Katz and Cameron excitation curve is at 18.7 Mev with the tail having the same behavior as copper. Corrections similar to copper are therefore used for zinc.

[22] G. C. Baldwin and G. S. Klaiber, Phys. Rev. **73**, 1156 (1948).
[23] B. C. Diven and G. M. Almy, Phys. Rev. **80**, 407 (1950).
[24] L. Katz and A. G. W. Cameron, Can. J. Phys. **29**, 518 (1951).
[25] P. R. Byerly and W. E. Stephens, Phys. Rev. **83**, 54 (1951).
[26] L. I. Newkirk, Phys. Rev. **86**, 249 (1952).
[27] V. E. Krohn and E. F. Shrader, Phys. Rev. **87**, 685 (1952).
[28] K. Strauch, Phys. Rev. **81**, 973 (1951).
[29] L. Marshall, Phys. Rev. **83**, 345 (1951).
[30] Koch, McElhinney, and Cunningham, Phys. Rev. **81**, 318 (1951).

TABLE I. Experimental results.

Element	F_{exp} (with standard deviation)	Multiple scattering path increases	Multiple scattering affecting counting efficiency	Other activities	Backscatter	Electron degradation (with standard deviation)	Gamma degradation (with standard deviation)	Total correction factor	F_{exp} (corrected) (with probable error)	Electron energy, E_0 (Mev)
Copper	8.11±0.30	0.985	1.004	1 ±0.005	1.01±0.005	1.063±0.021	1.036±0.012	1.108	8.99±0.24	24.5
	7.49±0.23	0.988	1.004	1 ±0.005	1.01±0.005	1.049±0.016	1.031±0.010	1.082	8.10±0.20	27.2
	7.05±0.20	0.990	1.003	1 ±0.005	1.01±0.005	1.027±0.009	1.024±0.008	1.054	7.44±0.16	30.8
	7.28±0.34	0.992	1.003	1 ±0.005	1.01±0.005	1.019±0.002	1.018±0.002	1.042	7.58±0.24	33.7
	6.62±0.18	0.993	1.003	1 ±0.005	1.01±0.005	1.015±0.002	1.015±0.002	1.036	6.85±0.13	35.3
Zinc	8.09±0.20	0.987	1.004	1 ±0.005	1.01±0.005	1.056±0.019	1.030±0.010	1.087	8.78±0.20	24.5
	7.26±0.12	0.991	1.004	1 ±0.005	1.01±0.005	1.028±0.009	1.022±0.007	1.055	7.66±0.11	29.2
	7.33±0.20	0.993	1.003	1 ±0.005	1.01±0.005	1.017±0.002	1.014±0.002	1.037	7.60±0.15	33.8
Silver	6.93±0.12	0.984	1.004	1.01±0.005	1.01±0.005	1.056±0.019	1.029±0.010	1.093	7.58±0.15	24.5
	7.04±0.07	0.987	1.004	1.01±0.005	1.01±0.005	1.035±0.012	1.025±0.008	1.071	7.54±0.10	27.8
	6.59±0.18	0.990	1.003	1.01±0.005	1.01±0.005	1.025±0.003	1.021±0.003	1.059	6.97±0.13	30.8
	6.01±0.14	0.991	1.003	1.01±0.005	1.01±0.005	1.018±0.002	1.018±0.002	1.050	6.31±0.10	33.7
Tantalum	5.93±0.33	0.983	1.004	1 ±0.005	1.01±0.005	1.043±0.008	1.018±0.003	1.058	6.27±0.24	24.0
	5.12±0.25	0.989	1.004	1 ±0.005	1.01±0.005	1.027±0.003	1.015±0.002	1.045	5.35±0.18	29.6
	5.10±0.17	0.991	1.003	1 ±0.005	1.01±0.005	1.019±0.002	1.014±0.001	1.037	5.29±0.12	33.7

For the $Ag^{109}(\gamma,n)Ag^{108}$ reaction, there seem to be only the data of Diven and Almy[23] available. These data show a peak excitation energy of 16 Mev with a pronounced dropoff of the tail at 20 Mev. However, the uncertainty in their results in this region (20–22 Mev) necessitates an introduction of a large estimated probable error to the degradation correction at low energies.

For $Ta^{181}(\gamma,n)Ta^{180}$ the effective excitation energy is lower. Strauch[28] reports a value of 19 Mev, but believes that it is high. This belief is verified by Katz and Cameron who find a peak excitation energy of only 13.9 Mev with the excitation curve dropping to zero around 20–22 Mev. The Katz and Cameron results are used for this experiment.[24]

The copper, zinc, silver, and tantalum excitation curves used in this experiment are summarized in Fig. 2.

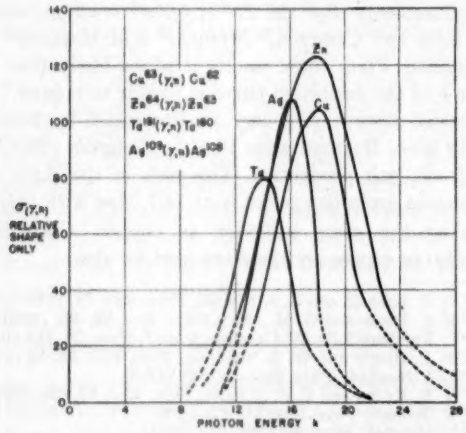

FIG. 2. Photoneutron excitation curves showing the effective photon absorption energy k_0 adopted for this experiment.

It should be emphasized that the curves in this graph indicate only the relative shape, and no inference of relative values of the cross sections for the different elements should be made from them.

VII. RESULTS

The results of this experiment are shown in Table I and in Figs. 3–6. The first column of Table I shows the results obtained from reducing the raw counting data using the formula for F_{exp}. The standard deviation shown with this value of F_{exp} is obtained from the internal consistency of a series of runs at each energy. These include the errors due to foil irregularities, counting statistics, errors of alignment in bombarding and counting geometries, and uncertainty in the gamma

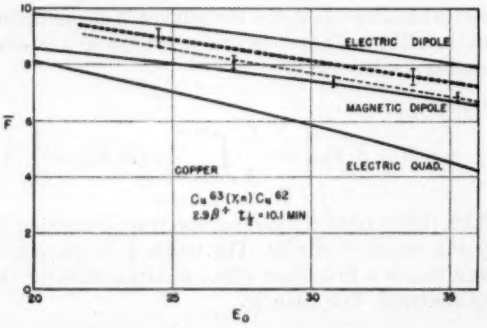

FIG. 3. $\bar{F}_T$ and F_{exp} as a function of initial electron energy E_0 (total energy in Mev). The dashed curves correspond to an effective value of F which assumes the (γ,n) cross section to be 88 percent electric dipole excitation and 12 percent electric quadrupole. The heavy dashed curve assumes the effective excitation energy of the quadrupole cross section to correspond with that of the electric dipole cross section, whereas the light dashed curve assumes the effective quadrupole excitation energy to be 4 Mev lower than that of the electric dipole cross section.

background measurements. A total of 32 copper, 21 zinc, 35 silver, and 17 tantalum activations were carried out, making an average of six for each element at a given energy. Two gamma background runs were made for every three regular runs.

The copper radiator was 1/60 of a radiation length thick, and the foils were approximately 1/340, 1/720, 1/300, and 1/600 radiation length thick for copper, zinc, silver, and tantalum, respectively. With this size radiator, it was found that the ratio of the observed activity in foil two to foil one was of the order of two.

The last column in Table I shows the experimental value of F after the various corrections have been made. The in between columns indicate the size of each correction. The gamma background and foil holder activity corrections are not shown here as they were subtracted directly from the counting data before evaluating F_{exp} in column four.

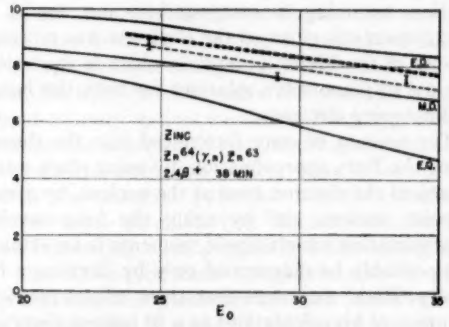

FIG. 4. $\bar{F}_T$ and F_{exp} as a function of initial electron energy E_0 (total energy in Mev). The dashed curves correspond to an effective value of F which assumes the (γ,n) cross section to be 88 percent electric dipole excitation and 12 percent electric quadrupole. The heavy dashed curve assumes the effective excitation energy of the quadrupole cross section to correspond with that of the electric dipole cross section, whereas the light dashed curve assumes the effective quadrupole excitation energy to be 4 Mev lower than that of the electric dipole cross section.

It is the corrected values of F_{exp} with their probable error which are shown in Figs. 3, 4, 5, and 6 as the experimental points. The theoretical curves are those obtained by averaging F_T over the respective (γ,n) cross sections to obtain what has been defined as $\bar{F}_T$.

VIII. DISCUSSION

There are several conclusions which may be drawn from these results.

(1) As has been stated previously, if the photodisintegration cross section is known, the Weizsäcker-Williams method may be used to approximate the electrodisintegration cross section. This method predicts a theoretical value of $F=8\pi/3$ independent of E_0 and k and hence independent of E_0 and Z. By observing Figs. 3–6 it is seen that the Weizsäcker-Williams approximation underestimates the electrodisintegration cross section in comparison with the photodisintegration, but that it yields a result which is within a factor of two of the observed value for tantalum and agrees more closely as Z and E_0 decrease. For copper, zinc, and silver the Weizsäcker-Williams value agrees with the experimental results within 10–15 percent.

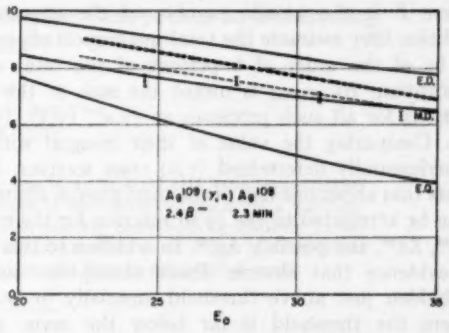

FIG. 5. $\bar{F}_T$ and F_{exp} as a function of initial electron energy E_0 (total energy in Mev). The dashed curves correspond to an effective value of F which assumes the (γ,n) cross section to be 88 percent electric dipole excitation and 12 percent electric quadrupole. The heavy dashed curve assumes the effective excitation energy of the quadrupole cross section to correspond with that of the electric dipole cross section, whereas the light dashed curve assumes the effective quadrupole excitation energy to be 4 Mev lower than that of the electric dipole cross section.

(2) Levinger and Bethe[21] suggest that the main absorption mechanism of nuclei for photons is electric dipole absorption. Using the so-called "sum rules," these authors calculate the integrated photonuclear cross section for dipole absorption to be

$$\int_0^\infty \sigma_{total}(k)dk \cong 0.044Z \text{ Mev barns}, \qquad (14)$$

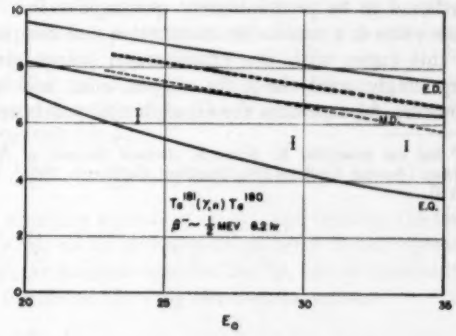

FIG. 6. $\bar{F}_T$ and F_{exp} as a function of initial electron energy E_0 (total energy in Mev). The dashed curves correspond to an effective value of F which assumes the (γ,n) cross section to be 88 percent electric dipole excitation and 12 percent electric quadrupole. The heavy dashed curve assumes the effective excitation energy of the quadrupole cross section to correspond with that of the electric dipole cross section, whereas the light dashed curve assumes the effective quadrupole excitation energy to be 4 Mev lower than that of the electric dipole cross section.

[21] J. S. Levinger and H. A. Bethe, Phys. Rev. 78, 115 (1950).

where Z is the atomic number of the element. In addition they estimate the total quadrupole absorption to be of the order of 6 percent of the total dipole absorption. By σ_{total} is meant the sum of the cross sections for all such processes as (γ,n), (γ,p), $(\gamma,2n)$, etc. Comparing the value of their integral with the experimentally determined (γ,n) cross sections, it appears that about one-half of the total photon absorption may be attributed to the (γ,n) reaction for the case of Cu^{63}, Zn^{64}, and possibly Ag^{109}. In addition to this there is evidence that electric dipole absorption may be forbidden just above threshold especially in isotopes where the threshold is far below the main dipole absorption peak,[22] whereas electric quadrupole absorption may occur under these conditions. For example, the data of Krohn and Shrader[27] show two peaks—at 13 and 17 Mev; we suggest that the lower energy peak may be due to the quadrupole excitation and the higher energy peak, to dipole excitation.

This suggests that the electric quadrupole contribution to photonuclear absorption is predominately to the (γ,n) reaction. It is expected, therefore, that about 12 percent of the total (γ,n) cross section is due to electric quadrupole excitation. From this and from the definition of F, it follows that the effective value of F would be

$$F_{eff}=(F_{\text{E.D.}})(F_{\text{E.Q.}})/(0.12F_{\text{E.D.}})+(0.88F_{\text{E.Q.}}). \quad (15)$$

The dashed curves in Figs. 3–6 correspond to the F_{eff} evaluated by this equation. The heavy dashed curve having the larger value of F_{eff} assumes that the effective excitation energy for the quadrupole cross section corresponds to that of the electric dipole, whereas the lower curve (light dash) assumes the effective quadrupole excitation to be ~4 Mev lower than the dipole peak. Inasmuch as the excitation near threshold is predicted to be predominately quadrupole, this lower peak value is a reasonable assumption and comparison of this curve with the experimental points gives a surprisingly good check for copper, zinc, and silver. However, for tantalum the experimental points are low and the question arises as to whether this is a failure of the Blair theory[5] or whether the electric quadrupole excitation becomes more important for higher Z elements. There is no evidence at the present time to indicate that the latter should be the case; thus, a discussion of the Blair theory is appropriate. It should be pointed out beforehand that no mention has been made of the contribution of magnetic dipole excitation. The magnetic dipole cross section is expected to be small compared to the electric dipole cross section but may be comparable to the electric quadrupole cross section.[13] However, by inspection of F_{eff}, which was obtained by a weighted averaging of electric dipole and quadrupole effects, it is seen that F_{eff} is insensitive to the addition of any reasonable contribution of magnetic dipole excitation for all elements studied except tantalum, and therefore it does not influence the results for Cu, Zn, and Ag.

Blair's calculation was made in the Born approximation assuming a compound-nucleus model. The electromagnetic effect of the electrons was represented by use of the Møller potentials which is equivalent to the use of plane wave solutions for both the incoming and outgoing electrons.

The amount of error introduced into the theory by using the Born approximation, by using plane waves to represent the electron even at the nucleus, by assuming a point nucleus, and by using the long-wavelength approximation for multipole moments is uncertain and can probably be determined only by devising a better theory. Blair[5] estimates that these effects restrict the accuracy of his calculations to a 10 percent theory. The Born approximation is expected to be better for low Z elements and this may well account for the fairly good agreement of experiment with theory for copper, zinc, and silver and the disagreement for tantalum.

ACKNOWLEDGMENT

The authors are indebted to Professor W. K. H. Panofsky for his valuable discussions and suggestions which have so greatly contributed to the completion of this research. Generous assistance during the latter phases of the experimental work was given by Arthur Berman.

[13] See for example, K. Strauch, *Annual Reviews of Nuclear Science* (Annual Reviews Inc., Stanford, California, 1953), Vol. 2, p. 110.

Higher-Order Potential Effects in the Radiative Correction to Scattering of Slow Electrons*†

M. H. MITTLEMAN
Columbia University, New York, New York
(Received September 28, 1953)

The radiative correction to the scattering of low-energy electrons by an external field has been calculated in first Born approximation in the external field. For strong fields or slow electrons this is not a valid approximation. With the assumption that only low-energy virtual photons contribute significantly to the effect, the radiative correction to the scattering of slow electrons is calculated to all orders of the external field. There is no change in the fractional radiative correction from the Born approximation result.

THE radiative correction to the scattering of low-energy electrons has been calculated in first Born approximation in both the radiation field and the external Coulomb potential. The approximation in the radiation field represents the first term in an expansion in powers of the small electrodynamic coupling constant α; however, the approximation in the external potential represents an expansion in powers of $Z\alpha c/v$, where Z is the nuclear charge and v the velocity of the electron. For heavy nuclei or slow electrons this is large compared to unity so that successive Born approximations cannot be expected to give meaningful results.

The radiative correction to first order in α and all orders in the external potential will be calculated using the usual nonrelativistic Hamiltonian for an electron interacting with a quantized electromagnetic field. The Bloch-Nordsieck[1] transformation is used closely following the procedure of Pauli and Fierz[2] to obtain the equation of motion for the state vector[3]

$$[\nabla^2+k_0^2+U(r)-2m\textstyle\sum_{k\lambda}N_{k\lambda}k]\Psi = -[\mathbf{q}\cdot\nabla U(r)+\tfrac{1}{2}(\mathbf{q}\cdot\nabla)^2U(r)]\Psi, \quad (1)$$

where

$$k_0^2=2mE, \quad \mathbf{q}=m^{-1}\textstyle\sum_{k\lambda}(2\pi\alpha/k^3\Omega)^{\frac{1}{2}}\mathbf{e}_{k\lambda}Q_{k\lambda},$$

with $\mathbf{e}_{k\lambda}$ the polarization vector, Ω the normalization volume for the field, and $Q_{k\lambda}$ the "position" coordinate for the $k\lambda$ mode of the field. $N_{k\lambda}$ is the occupation number operator of the $k\lambda$ mode and $U(r)=-2mV(r)$ with $V(r)$ the scattering potential.

The amplitude for the radiationless scattering of the electron is

$$f=f_0-(1/4\pi)q_0^2I(k), \quad (2)$$

where

$$I(k)=\int d^3r\psi_f(\mathbf{r})\nabla U(r)\cdot\int d^3r'K_{k_1}(\mathbf{r}',\mathbf{r})\nabla U(r)\psi_i(\mathbf{r}') -\tfrac{1}{2}\int d^3r\psi_f(\mathbf{r})\nabla^2U(r)\psi_i(\mathbf{r}), \quad (2a)$$

f_0 is the exact scattering amplitude for the potential $V(r)$ neglecting radiative effects, and

$$q_0^2=(2\alpha/3\pi)m^{-2}\int_{k_m}^{k}dk/k.$$

$K_{k_1}(\mathbf{r},\mathbf{r}')$ is the outgoing-wave Green's function satisfying

$$[\nabla^2+k_1^2+U(r)]K_{k_1}(\mathbf{r},\mathbf{r}')=\delta(\mathbf{r}-\mathbf{r}'), \quad (3)$$

with $k_1^2=k_0^2-2mk$. ψ_i and ψ_f are the initial and final wave functions satisfying the homogeneous equation. The upper and lower cutoffs in the momentum integral in q_0^2 have been used to avoid the divergencies. The divergency at the low end will cancel against the corresponding infrared catastrophe in the one quantum bremsstrahlung cross section, while the high energy cutoff will be determined so that the Born approximation limit for the result from this method agrees with the result of the low energy limit of the covariant Born approximation calculation.

In using the Bloch-Nordsieck approximation to obtain (1), the recoil of the electron has been neglected. This implies that the contribution from high energy virtual photons is unimportant. Then as a consistent assumption $I(k)$ is replaced by $I(0)$, i.e., in $I(k)$, K_{k_1} is replaced by K_{k_0}. The integral $I(0)$ can then be evaluated in terms of f_0. This is accomplished by using the equation for ψ_i,

$$[\nabla^2+k_0^2+U(r)]\psi_i=0. \quad (4)$$

Then applying a gradient to this and treating the term $[\nabla U(r)]\psi_i$ as an inhomogeneous term in the equation for $\nabla\psi_i$, an integral equation for $\nabla\psi_i$ can be constructed with the aid of (3). $I(0)$ can then be written

$$I(0)=\int d^3r\psi_f(\mathbf{r})\nabla U(r)\cdot(i\mathbf{k}_0-\nabla)\psi_i(\mathbf{r}) -\tfrac{1}{2}\int d^3r\psi_f(\mathbf{r})\nabla^2U(r)\psi_i(\mathbf{r}). \quad (5)$$

A similar procedure is repeated on the first term, and then using the fact that

$$\lim_{r'\to\infty}K_{k_0}(\mathbf{r},\mathbf{r}')=-(1/4\pi r')\exp(i\mathbf{k}_0\cdot\mathbf{r}')\psi_f(\mathbf{r}) \quad (6)$$

* Supported in part by the U. S. Atomic Energy Commission.
† Part of a thesis submitted in partial fulfillment of the requirements for a Ph.D. at Massachusetts Institute of Technology.
[1] F. Bloch and A. Nordsieck, Phys. Rev. 52, 54 (1937).
[2] W. Pauli and M. Fierz, Nuovo cimento 15, 167 (1938).
[3] Units of $\hbar=c=1$ have been used.

one gets

$$I(0)=4\pi \lim_{r\to\infty} r \exp(-ikr)(i\mathbf{k}_0\cdot\nabla+k_0^2)\psi_i(\mathbf{r}). \quad (7)$$

Then using the assymptotic form of ψ_i and substituting back into (2), the elastic scattering cross section is

$$\sigma=|f|^2=\sigma_0(1-q_0^2\Delta\mathbf{k}^2), \quad (8)$$

where

$$\Delta\mathbf{k}=\mathbf{k}_f-\mathbf{k}_0 \quad \text{and} \quad \sigma_0=|f_0|^2.$$

The one-quantum bremsstrahlung cross section is obtained from (1), the operator $\mathbf{q}\cdot\nabla U(r)$ being the one which causes the emission. Upon summing over all directions of emission and all energies of the photon up to a maximum ΔW, this cross section becomes

$$\sigma_1=q_0'^2\left|(1/4\pi)\int\psi_1(\mathbf{r})\nabla U(r)\psi_i(\mathbf{r})d^3r\right|^2, \quad (9)$$

where

$$q_0'^2=(2\alpha/3\pi)m^{-2}\int_{k_m}^{\Delta W}dk/k,$$

and ψ_1 is the final state with wave vector k_1. Since the limit $\Delta W\to 0$ is contemplated, k_1 can be replaced by k_0 so that ψ_1 is replaced by ψ_f. The integral in (9) can then be evaluated by the method used in obtaining (7). The result is

$$(1/4\pi)\int\psi_f(\mathbf{r})\nabla U(r)\psi_i(\mathbf{r})d^3r=i\Delta\mathbf{k}f_0, \quad (10)$$

giving

$$\sigma_1=\sigma_0 q_0'^2\Delta\mathbf{k}^2. \quad (11)$$

It should be pointed out here that the method of evaluation of the integral (10) applies only for potentials which vanish at infinity faster than the Coulomb potential. Indeed the integral of (10) has been evaluated directly for the Coulomb field using Coulomb wave functions.[4] The result is

$$\sigma_1=\sigma_0 q_0'^2\Delta\mathbf{k}^2(\chi/\sinh\chi)^2, \quad (12)$$

where $\chi=\pi Z\alpha c/v$. Equation (12) can be applied only in the complete absence of screening (i.e., never).

Clearly the difference arises from the long-distance behavior of the Coulomb field. In the integral of (10), attention has been focused upon photons of zero energy. These have their greatest probability of emission when the electron undergoes weak scatterings, i.e., in the region where the scattering field is small. Therefore, this region may be expected to contribute strongly in the integral. However, this is precisely the region which has been eliminated by considering a potential which goes to zero faster than the Coulomb potential. Therefore it is not surprising that there is no continuous transition of the value of the integral in the limit of the field approaching a Coulomb field.

Combining (8) and (11) the infrared catastrophe disappears and the resultant cross section is

$$\sigma=\sigma_0[1-(2\alpha/3\pi)(\Delta\mathbf{k}/m)^2\ln(\kappa/\Delta W)]. \quad (13)$$

Thus the inclusion of higher-order potential effects in the radiative correction changes the over-all cross section from the Born approximation result, but it does not change the fractional radiative correction.

The author wishes to thank Professor H. Feshbach for suggesting the problem and for his constant aid and encouragement.

[4] A. Sommerfeld, *Wellenmechanik* (Ungar Publishing Company, New York, 1947), p. 501.

Isotopic Spin and Odd-Odd $N=Z$ Nuclei*

S. A. Moszkowski† and D. C. Peaslee
Columbia University, New York, New York

(Received October 29, 1953)

The lowest-lying states of isotopic spin $T=0$ and $T=1$ are surveyed for odd-odd nuclei with $N=Z$ by considering β-decay schemes and Coulomb energy differences. For $A\geq 26$ the lowest $T=0$ and $T=1$ states appear to be very close together. The analysis permits certain predictions regarding the decay schemes of of these nuclei. Further experimental information is needed on the higher members of this series, from Sc^{42} to Cu^{58}. Predicted β-decay schemes for some corresponding $Z=N+2$ nuclei are also summarized.

I. INTRODUCTION

INTEREST in isotopic spin[1] as a relatively valid quantum number, at least for light nuclei, has been stimulated recently by the experimental evidence for associated selection rules in nuclear reactions.[2] The odd-odd $N=Z$ nuclei are especially favorable subjects for the study of isotopic spin, since they alone have more than one T value among their low-lying states. A striking affirmation of this fact has been the recent experimental discovery[3] of a 1.4-second ground state in Cl^{34}, which must be interpreted[4] as indicating that this nucleus has $T=1$ in its ground state. This is contrary to the usual expectation that the ground state has the minimum T value possible, in this case $T=0$.

It thus becomes an intriguing question to determine the relation between the lowest $T=0$ and $T=1$ states for all light odd-odd $N=Z$ nuclei and look for a systematic behavior. The present note attempts to survey the possibilities in this regard. The stable nuclei of this category—Li^6, B^{10}, N^{14},—have been well explored.[5]

We therefore consider mainly the unstable examples: F^{18}, Na^{22}, Al^{26}, P^{30}, Cl^{34}, and K^{38}. The uncertain cases V^{46}, Mn^{50}, Co^{54}, and Cu^{58} are also mentioned.

In Sec. II, likely assignments of spin and isotopic spin for odd-odd ground states are made on the basis of β-decay schemes and ft values; in Sec. III we study the energies of the lowest $T=0$ and $T=1$ states in odd-odd nuclei as function of mass number. In Sec. IV the previous considerations are employed to make tentative predictions regarding energies and decay schemes of some odd-odd excited states; these are extended in Sec. V to the β decay of the analogous even-even nuclei with $Z=N+2$.

II. BETA-DECAY SCHEMES AND ft VALUES

The odd-odd nuclei above N^{14} are all unstable, going by positron decay to an even-even nucleus with $T=1$, $J=0$ in its ground state and $T=1$, $J=2$ (generally) in its first excited state. If allowed beta-decay occurs to either of these states, we can make use of the selection rules involved to assign quantum numbers to the odd-odd ground state. There is no parity change in allowed transitions, and in addition the Fermi matrix element has selection rules $\Delta J=\Delta T=0$, the Gamow-Teller matrix element has selection rules $\Delta J=\Delta T=0,\ \pm 1$ (no $J=0\rightarrow 0$ and of course beta-decay is incompatible with $T=0\rightarrow 0$ in any case).

The introduction of one more rule about nuclear levels allows the assignment of unique T, J values to the odd-odd ground states. This rule is that for odd-odd $N=Z$ nuclei with neutrons and protons in equivalent orbits, the lowest-lying $T=0$ levels have odd J, while $T=1$ levels have even J. This rule is strictly true for j-j coupling states of lowest seniority; and even in L-S coupling there are many more low-lying states in accord with the rule than in violation of it. Some empirical evidence in support of a general principle of this sort follows from the $J=0-2-4$ and $0-2-2$ level sequences in many even-even nuclei with $T=0$.

The above rules may be summarized in the statement that

$$|\Delta J|=|\Delta T|=0 \text{ or } 1 \qquad (1)$$

for allowed beta-transitions between odd-odd and even-even nuclei where neutrons and protons occupy equivalent orbits. The half-lives are given by[6]

$$\log ft=3.7-\log|M|^2, \qquad (2)$$

where $|M|^2$ is a nuclear matrix element which includes statistical factors. We may argue that $|M|^2$ will generally be a maximum for $\Delta J=\Delta T=0$ transitions, because the two states will be exactly similar and have perfectly overlapping wave functions. For the other case, $|\Delta J|=|\Delta T|=1$ the overlap of nuclear wave

* Work supported by the research program of the U. S. Atomic Energy Commission.

† Now at University of California in Los Angeles, California.

[1] E. P. Wigner, Phys. Rev. **51**, 106 (1937); R. K. Adair, Phys. Rev. **87** 1041 (1952).

[2] We do not discuss the less restrictive condition of isotopic parity or charge symmetry of nuclear forces [N. M. Kroll and L. L. Foldy, Phys. Rev. **88**, 1177 (1952)], because charge independence or isotopic spin conservation seems to be at least approximately valid from the equivalence of n-p and p-p scattering at low energies and the equivalent energy levels in the $T=1$ triads at $A=6$, 10 and 14.

[3] W. Arber and P. Stähelin, Helv. Phys. Acta **26**, 433 (1953).

[4] D. C. Peaslee, *Nuovo cimento* **10**, 1349 (1953); O. Kofoed-Hansen and A. Winther (unpublished). The latter authors also suggest a reduction in the $T=1$ and $T=0$ spacing of odd-odd $N=Z$ nuclei as A increases. See also, O. Kofoed-Hansen, Phys. Rev. **92**, 1075 (1953) and P. Stähelin, Phys. Rev. **92**, 1076 (1953).

[5] D. R. Inglis, Revs. Modern Phys. **25**, 390 (1953).

[6] A. Winther, Physica **18**, 1079 (1952). In accordance with the evidence that the Fermi and Gamow-Teller coupling constants are equal, we write $|M|^2=|\int 1|^2+|\int \sigma|^2$.

TABLE I. Ground states of odd-odd $N=Z$ nuclei.

Parent nucleus	Beta-decay final state	log ft	$\|M\|^2$	T	J, parity
F^{18}	0+	3.6	1.3	0	1+
Na^{22}	2+	7.4	$\ll 1$	0	3+
Al^{26}	0+	3.5[a]	1.5	1 (or 0)	0+ (or 1+)
P^{30}	0+	4.9	$\ll 1$	0	1+
Cl^{34}	0+	3.4	2	1	0+
K^{38}	2+	5.0	$\ll 1$	0	3+
Sc^{42}	...	...	...	...	...
V^{46}	(0+)	≥ 3.4	≤ 2	...	...
Mn^{50}	(0+)	≥ 3.4	≤ 2	...	...
Co^{54}	(0+)	≥ 3.5	≤ 1.6	...	...
Cu^{58}	(0+)	≥ 4.7	$\ll 1$	(0)	(1+)

[a] Using β^+ maximum energy of 3.3 Mev [L. Katz (private communication)].

functions may be poor and $|M|^2$ may be considerably reduced. Using these principles, we obtain Table I.

For all the nuclei in Table I a $\Delta T=0$ transition with perfect overlap has $|M|^2=|\int 1|^2=2(|\int \sigma|^2=0)$, regardless of whether there is L-S or j-j coupling. This expectation is borne out by the measurement on Cl^{34} and the known $\Delta T=0$ transitions in C^{10} and O^{14}. It is the basis for the probable assignment of Al^{26}. For $\Delta T=1$ transitions, $|M|^2=|\int \sigma|^2=2(|\int 1|^2=0)$ in these same nuclei only for perfect L-S coupling; the value of $|M|^2=1.3$ for F^{18} suggests that L-S coupling is predominant but not without some j-j admixture. We therefore take $|M|^2<2$ to mean $|\Delta J|=|\Delta T|=1$ for this transition; this same assignment is made to all cases with $|M|^2 \ll 1$. An unequivocal value of J comes from considering decay schemes.[7]

The case of Al^{26} is of considerable interest in that it probably resembles Cl^{34} in having a $T=1$ ground state; this "ground state" may be isomeric (see Sec. IV).

III. ENERGIES OF LOWEST $T=0$ AND $T=1$ STATES

It is also of interest to study the energies of the lowest $T=0$ and lowest $T=1$ states in odd-odd $N=Z$ nuclei as function of mass number. All energies are taken for neutral atoms relative to the ground state of the neighboring even-even $N=Z-2$ isobar. Energies of odd-odd ground states (and the lowest $T=0$ state in Cl^{34}) are taken from decay schemes.[7] Energies of lowest $T=1$ states in the lightest nuclei are obtained from a survey of the excited states.[8] The results of this investigation are shown in Fig. 1. The energy $E_{T=1}$ of the lowest $T=1$, $J=0$ state in an odd-odd nucleus, relative to the ground state of the neighboring $N=Z+2$ isobar, can also be estimated from the formula for neutral atoms

$$E_{T=1}=0.60(A-2)A^{-\frac{1}{3}}-0.78 \text{ Mev}. \quad (3)$$

Here the nucleus is assumed to be a uniformly charged sphere of radius $R=1.4\times10^{-13}A^{\frac{1}{3}}$ cm. Figure 1 shows agreement to within a few tenths of an Mev between empirical results and Eq. (3). The experimental values of $E_{T=1}$ seem to increase with A slightly faster than formula (3) indicates; this is probably due to the neglect of exchange terms[9] in (3).

For $A \leq 22$, the odd-odd ground state lies far below the calculated energy for the $T=1$ state. The resulting assignment $T=0$ for ground state of these nuclei is, of course, in agreement with considerations from decay schemes (Sec. II). The ground states of Al^{26}, P^{30}, Cl^{34}, and K^{38} are close to the calculated [Eq. (3)] energies for $T=1$ states. Definite assignments of T for these cases have, however, been made by a study of decay schemes in Sec. II. The situation for the heavier nuclei is still uncertain experimentally.

IV. SOME PREDICTED EXCITED STATES OF ODD-ODD $N=Z$ NUCLEI

On the basis of the above consideration, it is possible to make some tentative predictions regarding level schemes and energies of some odd-odd $N=Z$ nuclei. We consider here only the fairly well established cases F^{18}, Na^{22}, Al^{26}, P^{30}, and K^{38}. In all of these cases except Al^{26}, the ground state appears to have $T=0$, as was pointed out above. The position of the lowest $T=1$ state, at excitation energy $E_{T=1}-E_{T=0}$ can be estimated crudely on the basis of the theoretical formula [Eq. (3)]. Perhaps slightly better estimates of $E_{T=1}$ can be made for these nuclei by adjusting the theoretical curve slightly to conform with experimentally known values of this energy for Li^6, B^{10}, N^{14}, Al^{26}, and Cl^{34}. This gives excitation energies 1.1, 0.8, 0.5, and 0.1 Mev (accurate to, say, 0.2 Mev), for the lowest $T=1$ state of F^{18}, Na^{22}, P^{30}, and K^{38}, respectively.

On the basis of these estimates, the following tentative predictions[10] regarding decay schemes can be made:

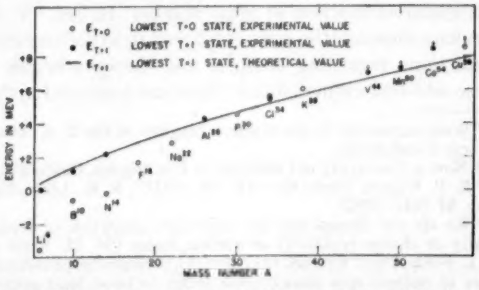

FIG. 1. Energies (neutral atom) of lowest $T=0$ and $T=1$ states in odd-odd $N=Z$ nuclei, relative to ground state of neighboring even-even $N=Z+2$ isobar.

[7] Decay schemes except Cl^{34} (references 3, 4) taken from R. W. King, Ph.D. Dissertation, Washington University, St. Louis, Missouri, 1952 (unpublished), and Hollander, Perlman, and Seaborg, Revs. Modern Phys. **25**, 469 (1953).

[8] Li^6, B^{10}, and N^{14} from F. Ajzenberg and T. Lauritsen, Revs. Modern Phys. **24**, 321 (1952).

[9] See L. N. Cooper and E. M. Henley, Phys. Rev. **92**, 801 (1953).

[10] *Note added in proof.*—Experimental investigations of some of these cases have already been made [P. Stähelin, Helv. Phys. Acta **26**, 691 (1953)]. The results are in general agreement with the remarks of this section.

F^{18}

The lowest $T=1$, $J=0+$ state probably occurs at about 1.1 Mev above the $T=0$, $J=1+$ ground state and is expected to decay to this ground state by $M1$ radiation of very short half-life. The known excited state at 1.050 Mev is produced by a $Ne^{20}(d,\alpha)$ reaction[9] and accordingly must have $T=0$ (See Adair, reference 1). Thus, the 1.050-Mev state and the lowest $T=1$ state in F^{18} appear to be distinct but close together.

Na^{22}

The $T=1$, $J=0$ state probably occurs at about 0.8 Mev above the $T=0$, $J=3$ ground state. The decay of the $T=1$ state depends on whether there is a $T=0$, $J=1$ state below it. If there is, the decay will go to the Na^{22} ground state by an $M1-E2$ cascade of very short half-life. If there is not, the $T=1$ state will decay principally to the Na^{22} ground state by $M3$ radiation with partial half-life of 10^{-2} to 1 second; in addition, it should some of the time decay instead to the Ne^{22} ground state by positron emission of $E_{max}=2.5$ Mev, $\log ft=3.4$, partial half-life = 10 sec.

P^{30}

The $T=1$ state probably occurs at about 0.5 Mev above the $T=0$, $J=1$ ground state and is expected to decay to the ground state by $M1$ radiation of very short half-life.

K^{38}

In this nucleus the $T=0$ and $T=1$ states are very close together, probably within 0.2 Mev of each other. Although the $T=0$, $J=3^+$ level seems likely to be the lower one, this is not entirely certain. In any case, if there is no intervening $J=1^+$ level between the 0^+ and 3^+ levels, there will be only a relatively small probability of a connecting $M3$ transition between them. For the most part these two states will undergo independent β decay, regardless of their exact order. The $T=1$ state will decay directly to the A^{38} ground state with a maximum energy of about 5 Mev and a half-life of about 0.5 sec.

Al^{26}

It is tempting to speculate at this point that Al^{26} may resemble K^{38} in having two lowest levels that undergo independent β decay. At present there is no known exception to the rule[11] that the J of an odd-odd $N=Z$ nucleus obeys j-j coupling near the close of a subshell. Thus the best estimate for the lowest $T=0$ state in Al^{26} appears to be $J=5^+$. Regardless of their exact order, two such lowest states would undergo independent beta decay. The Al^{26} "ground" state (probably $T=1$, $J=0^+$) decays to the ground state of Mg^{26} in about 6 sec. A $T=0$, $J=5^+$ state would decay to the first excited state of Mg^{26} ($J=2^+$, $E_{ex}=1.87$ Mev) with a half-life on the order of 10^4-10^6 years. If the second excited state of Mg^{26} ($E_{ex}=2.97$ Mev) has $J=4^+$, an allowed decay can occur with a half-life on the order of a day to a month. This decay would be about half K capture and half positron emission.

[11] R. W. King and D. C. Peaslee, Phys. Rev. **90**, 1001 (1953).

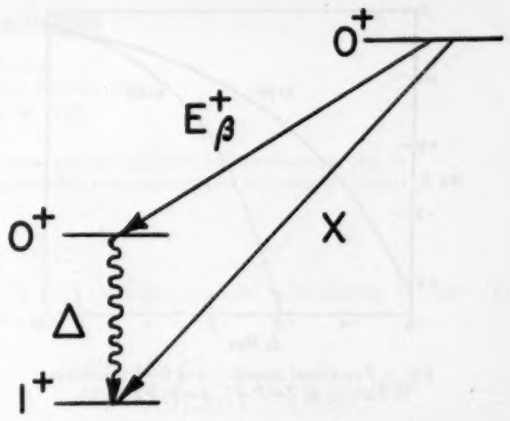

FIG. 2. General decay scheme for $Z=N+2$, $A=4n+2$ nuclei.

The above discussion suggests that it is possible to make predictions regarding the quantum numbers and decay schemes of the lowest lying states in odd-odd $N=Z$ nuclei. Naturally it would be of great interest to obtain more detailed experimental information on the decay schemes of other odd-odd $N=Z$ nuclei such as Sc^{42}, V^{46}, Mn^{50}, Co^{54} and Cu^{58}. These nuclei can all be produced by (p,n) reactions on stable targets.

V. DECAY SCHEMES OF SOME $Z=N+2$ NUCLEI

The odd-odd $N=Z$ nuclei discussed above appear as daughter products in the positron decay of nuclei with $A=4n+2$, $Z=N+2$. Experimental production of this series appears possible for $A\leq 42$. All members of the series should be particle stable by at least 5 Mev, including Ne^{18} and Ti^{42}. They can be formed by (He^3,n) on abundant target nuclei of the α-particle type (with the exception of Ca^{38}) in reactions with Q values close to zero. They are also formed (except for Ti^{42}) from the same abundant α-particle nuclei by $(\gamma,2n)$ reactions with thresholds on the order of 30 Mev. It may therefore be of interest to extend the predictions of the previous section to include the β decay schemes of these nuclei.

The $Z=N+2$ nuclei of this series are even-even with ground states $T=1$, $J=0$, from which they make superallowed transitions with $\log ft\approx 3.4$ to the corresponding states in the $N=Z$ nuclei. There will be in addition a branch of fractional intensity x (Fig. 2) to the $T=0$, $J=1$ state of the daughter nucleus. This transition has an ft value different from that for the $0-0$ transition by a factor ranging from about 2 to $\frac{1}{8}$, to judge by corresponding decays from F^{18} and P^{30} (corrected by a factor $3=2J_f+1$ for the $0\rightarrow 1$ transition). For three cases (Ne^{18}, S^{30}, Ti^{42}) the situation is already

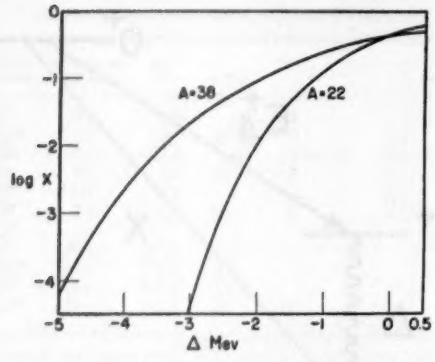

FIG. 3. Fractional intensity x of $0-1$ transition in β decay of $Z=N+2$, $A=4n+2$ nuclei.

defined by present information. The values of Δ in Fig. 2 are 1.1, 0.3 and ~ 0 Mev, respectively, where the last is an extrapolation from all known $A=4n+2$ nuclei. Using for the Coulomb energies formula (3) adjusted to fit the experimental points of Fig. 1, we obtain the results in Table II. Here E_{β^+} is the estimated energy of the $0-0$ transition, $E_\gamma=|\Delta|$ the energy of the connecting γ ray between 0^+ and 1^+ states of the final nucleus. The total half-life t and fractional intensity $x(0\leq x\leq 1)$ of the $0-1$ branch were obtained from the values of the f function for β^+ decay.[12]

For the four remaining cases we do not know the separation Δ of the 1^+ and 0^+ states in the daughter nucleus. Δ is certainly negative for $A=26$, 34 and very likely negative for $A=38$; for $A=22$ it is less certain but still probably negative. Although the negative Δ militates against the $0-1$ transition, measurement of the associated γ energy could provide valuable information about the 1^+-3^+ spacing of these particularly simple levels. The half-lives are the same order of magnitude as indicated in Table II. The fractional intensity in the $0-1$ β transition is shown in Fig. 3 as a function of Δ for $A=22$ and $A=38$. These curves are uncertain by a factor of order 2 because of uncertainty in the nuclear matrix elements.

TABLE II. Decay-scheme parameters.

Parent nucleus	E_{β^+} (Mev)	t (sec)	E_γ (Mev)	x
Ne^{18}	2.2	2	1.1	0.9
S^{30}	4.0	1.5	0.3	0.2
Ti^{42}	5.5	0.2	~ 0	~ 0.6

Comparison with the spacings in these same nuclei of the $J=0$, $J=2$ levels known from β decay suggests that $|\Delta|\lesssim 2$ Mev in this region. Observation of the weak $0-1$ β transition with the following γ ray does not then appear to be beyond the range of experimental feasibility.

In cases where the two lowest $N=Z$ states are $J=0^+$ and 3^+ ($A=38$, 34, probably 22) the γ decay from the 1^+ level will comprise an interesting competition between 1^+-0^+ (pure $M1$) and 1^+-3^+ (pure $E2$).

[12] E. Feenberg and G. Trigg, Revs. Modern Phys. 22, 399 (1950).

Čerenkov Radiation

KATSUMI TANAKA
Argonne National Laboratory, Lemont, Illinois
(Received August 10, 1953)

Čerenkov radiation is investigated for the following cases: charged particles and neutrons moving in isotropic crystals; charged particles moving in an arbitrary direction with respect to the optic axis in uniaxial crystals.

GINSBURG[1,2] investigated Čerenkov radiation of uniaxial crystals when an electron moves either along or perpendicular to the optic axis, using the Hamilton method in electrodynamics of anisotropic media.

Using Ginsburg's formalism, we obtain for the energy radiated by the particle within an angle range ϕ, $\phi+d\phi$, and per unit path length:[3]

$$\frac{dH_i}{dl}=\frac{(2\pi)^6}{v_0^2c^2 2\pi}\int_0^{2\pi}\int_{\beta n_{\lambda i}>1}(\mathbf{j}_k\cdot\mathbf{a}_{\lambda i})^2 w_{\lambda i}\times n_{\lambda i}^2(\theta_0,\phi)dw_{\lambda i}d\phi\cdots, \quad (1)$$

where ϕ and θ_0 determine the relative orientation of the propagation vector $\mathbf{k}_\lambda$ and the uniform velocity of the particle $\mathbf{v}_0$, ϕ is the angle the projection of $\mathbf{k}_\lambda$ on the XZ plane makes with the X axis, $\mathbf{a}_{\lambda i}$ is the component of the properly normalized vectors of electric field strength, $\mathbf{j}_k$ is the Fourier component of the charge density, and $n_{\lambda i}$ is the index of refraction.[4] The i index corresponds to two directions of polarization, the angle θ_0 is given by

$$\cos\theta_{0i}=\frac{c}{n_{\lambda i}v_0}=\frac{1}{n_{\lambda i}\beta}, \quad (2)$$

and $w_{\lambda i}$ is given by

$$w_{\lambda i}^2=\frac{k_\lambda^2c^2}{n_{\lambda i}^2}=c^2\{(\mathbf{k}_\lambda^2\cdot\mathbf{a}_{\lambda i}^2)-(\mathbf{k}_\lambda\mathbf{a}_{\lambda i})^2\}. \quad (3)$$

In isotropic crystals, let $\mathbf{a}_{\lambda 1}$ be in the plane determined by $\mathbf{v}_0$ and $\mathbf{k}_\lambda$. Integrating (1) with respect to ϕ,

$$\frac{dH_1}{dl}=\frac{(2\pi)^6}{v_0^2c^2}\int_{\beta n_\lambda>1}\mathbf{j}_k^2\left(1-\frac{1}{n_\lambda^2(w)\beta^2}\right)wdw, \quad (4)$$

$$dH_2/dl=0.$$

For charged particles,

$$\mathbf{j}_k=\frac{1}{(2\pi)^3}\int_{-\infty}^{\infty}\mathbf{j}(r)e^{-i\mathbf{k}_\lambda\cdot\mathbf{r}}d\mathbf{r}=\frac{e\mathbf{v}_0}{(2\pi)^3}, \quad (5)$$

as $\mathbf{k}\cdot\mathbf{r}\ll 1$ over the particle. Substituting (5) into (4), we get

$$\frac{dH_1}{dl}=\frac{e^2}{c^2}\int_{\beta n_\lambda>1}\left(1-\frac{1}{n_\lambda^2(w)\beta^2}\right)wdw, \quad (6)$$

which is the Frank and Tamm formula[5] giving the total energy radiated by a charged particle through the surface of a cylinder per unit length, the axis of which coincides with the line of motion of the particle. For neutrons,

$$\mathbf{j}_k=\frac{1}{(2\pi)^3}\int_{-\infty}^{\infty}\mathbf{j}(r)e^{-i\mathbf{k}\cdot\mathbf{r}}d\mathbf{r}=\frac{c}{(2\pi)^3}\int_{-\infty}^{\infty}\nabla\times\mathbf{m}(r)e^{-i\mathbf{k}\cdot\mathbf{r}}d\mathbf{r}=\frac{c}{(2\pi)^3}M\times\mathbf{k}, \quad (7)$$

where M is the magnetic moment of the neutron.

Putting (7) into (4), assuming neutrons are oriented randomly in space, we find:[6]

$$\frac{dH_1}{dl}=\frac{M^2}{3v^2}\int_{\beta n_\lambda>1}\frac{w^3n_\lambda^2}{c^2}\left(1-\frac{1}{n_\lambda^2(w)\beta^2}\right)wdw. \quad (8)$$

This distribution depends on two extra powers of frequency compared to that of charged particles.

Comparing (6) and (8), the ratio of $dH/dwdl$ for neutrons to that of charged particles is of the order 10^{-17} for the visible region.

With reference to Fig. 1, we choose the electron velocity vector $\mathbf{v}_0$ so that it determines the YZ plane. The optic axis is taken along the Z direction. Indices o and e refer to the ordinary and extraordinary rays, respectively.

$$\epsilon_o=\epsilon_x=\epsilon_y, \quad \epsilon_e=\epsilon_z.$$

[1] V. L. Ginsburg, J. Phys. (U.S.S.R.) **3**, 95 (1940).
[2] V. L. Ginsburg, J. Phys. (U.S.S.R.) **3**, 101 (1940).
[3] The reader is referred to references 1 and 2 for the method of calculation.
[4] The results of a special case are given by K. Tanaka, University of California Radiation Laboratory Report UCRL-1286, May 1951 (unpublished).
[5] I. Tamm, J. Phys. (U.S.S.R.) **1**, 439 (1939).
[6] An alternative calculation obtained by expanding the field variables of Maxwell's equation in four-dimensional Fourier series and expressing the Poynting vector in terms of the generalized current density was reported at the Cambridge Meeting of the American Physical Society, January, 1953, by K. Tanaka [Phys. Rev. **90**, 358 (1953)]. The results agree with those of the present paper.

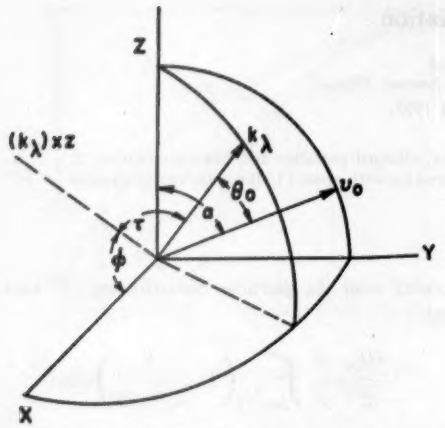

FIG. 1. Relation between the optic axis Z, propagation vector $\mathbf{k}$, and electron velocity vector $\mathbf{v}$.

The results of a calculation for $n_{\lambda_t}^2$ and $(2\pi)^6(\mathbf{j}_k\cdot\mathbf{a}_{\lambda_t})^2 = e^2(\mathbf{v}_o\cdot\mathbf{a}_{\lambda_t})^2$ that are to be substituted into Eq. (1) are as follows:

$$n_{\lambda_o}^2=\epsilon_o, \tag{9a}$$

$$n_{\lambda_e}^2=\frac{\epsilon_e\epsilon_o}{\epsilon_o\cos^2\phi+\epsilon_e\sin^2\phi+(\epsilon_o-\epsilon_e)\sin^2\phi\sin^2\tau}, \tag{9b}$$

where

$$\sin\tau=\frac{\cos\theta_i\sin\alpha\pm\sin\phi\cos\alpha(\sin^2\alpha-\cos^2\theta_i+\cos^2\alpha\sin^2\phi)^{\frac{1}{2}}}{\sin^2\alpha+\cos^2\alpha\sin^2\phi}, \tag{10}$$

$$\cos\theta_0=1/\epsilon_o^{\frac{1}{2}}\beta, \tag{11a}$$

$$\cos\theta_e=(Q/R)^{\frac{1}{2}}, \tag{11b}$$

$$Q=\frac{1}{(\epsilon_o-\epsilon_e)^2\sin^4\phi}\{\beta^2\epsilon_e\epsilon_o e(d\sin^2\alpha+\epsilon_o\cos^2\alpha\sin^2\phi)$$
$$+(\epsilon_o-\epsilon_e)\sin^2\phi(\epsilon_o\sin^2\phi\cos^2\alpha-d\sin^2\alpha)$$
$$+2(\epsilon_o-\epsilon_e)[\epsilon_e\epsilon_o(d\sin^2\alpha+\epsilon_o\cos^2\alpha\sin^2\phi)]^{\frac{1}{2}}$$
$$\times\beta\cos\alpha\sin\alpha\sin^2\phi\},$$

$$R=\left(\frac{\beta^2\epsilon_e\epsilon_o}{\epsilon_o-\epsilon_e}\right)^2\frac{e^2}{\sin^4\phi}-2(\sin^2\alpha-\sin^2\phi\cos^2\alpha)$$
$$\times\frac{\beta^2\epsilon_e\epsilon_o}{(\epsilon_o-\epsilon_e\sin^2\phi)}+1,$$

$$d=\epsilon_o\cos^2\phi+\epsilon_e\sin^2\phi,$$

$$e=\sin^2\alpha+\cos^2\alpha\sin^2\phi.$$

$$(\mathbf{v}_0\cdot\mathbf{a}_{\lambda_0})^2=v_0^2\,\frac{\cos^2\phi\sin^2\alpha(1-\sin^2\tau)}{\epsilon_0(\cos^2\phi+\sin^2\tau\sin^2\phi)} \tag{12a}$$

$$(\mathbf{v}_0\cdot\mathbf{a}_{\lambda_e})^2=N/D, \tag{12b}$$

where

$$N=v_0^2\{(-\sin^2\alpha\sin^2\phi+\cos^2\alpha\sin^4\phi)\sin^4\tau$$
$$+(\sin^2\phi\sin^2\alpha+2\cos^4\alpha\sin^2\phi)\sin^2\tau+\cos^6\alpha$$
$$\pm2(\epsilon_o/\epsilon_e)\sin\alpha\cos\alpha(\cos^2\phi+\sin^2\tau\sin^2\phi)$$
$$\times\sin\tau[\sin^2\phi(1-\sin^2\tau)]^{\frac{1}{2}}\},$$

$$D=\epsilon_o\left\{\left(\sin^2\phi+\frac{\epsilon_o}{\epsilon_e}\cos^2\phi\right)-\left(1-\frac{\epsilon_o}{\epsilon_e}\right)\sin^2\phi\sin^2\tau\right\}$$
$$\times\{\cos^2\phi+\sin^2\tau\sin^2\phi\},$$

and $\sin\tau$ is given by (10).

One may easily find Ginsburg's results when the charged particle is traveling along and perpendicular to the optic axis, by taking the angle which determines the position of the velocity $\alpha=0$ and $\alpha=\pi/2$.

The author is indebted to Professor Robert Serber for helpful discussions and Dr. E. J. Hellund for his interest.

Total Cross Sections of Rare Earths for Fast Neutrons*

A. Okazaki, S. E. Darden, and R. B. Walton
University of Wisconsin, Madison, Wisconsin
(Received October 28, 1953)

The total neutron cross sections averaged over resonances have been measured for Nd, Sm, Er, Yb, and Hf as functions of neutron energy from 0.06 to 3 Mev. The cross-section curves have shapes which change gradually with atomic weight and are in agreement with the values predicted by the theory of Feshbach, Porter, and Weisskopf.

TOTAL fast neutron cross sections averaged over resonances of many medium and heavy elements have been measured as functions of neutron energy.[1–3] Although the cross sections of neighboring elements exhibit similarities, there are changes in the shape of the cross-section curves of elements widely separated in atomic weight.[4] Feshbach, Porter, and Weisskopf[5] have proposed a theory based on a single-particle interaction which has been successful in reproducing the slow variations in the cross sections. The present article presents the measured total cross sections of Nd, Sm, Er, Yb, and Hf. These elements, which are in the rare earth portion of the periodic table, were not investigated previously because samples of size sufficient for total cross-section determinations had not been available.

Total cross sections were measured by means of transmission experiments in which the scattering samples were placed midway between the neutron source and detector. Neutrons were produced by bombarding lithium and tritium targets with protons from the Wisconsin electrostatic generator. The lithium targets, which were used for the production of neutrons with energies less than 1 Mev, were prepared by evaporating lithium on a tantalum backing. For higher energies a tritium target in which the tritium was adsorbed in a thin layer of zirconium evaporated on a wolfram disk was used.

The averaging of the total cross sections over resonances was accomplished experimentally through the use of a neutron beam having an energy spread which was large compared with the level spacing in the nuclei being investigated. Such a beam was produced with thick targets which also had the advantage of large neutron yields. The target thickness, which is the energy loss of protons in the target, was measured by the rise method at the threshold of the reactions.[6] Most of the measurements in which Li targets were used were made with targets 120-kev thick for protons near the threshold energy. Sm and Yb measurements below 600 kev were done with a 40-kev Li target. A 120-kev thick T target was used in the higher energy measurements.

The scattering samples of Nd, Er, and Hf were in the form of metallic cylinders about 1 inch in diameter. Sm and Yb were available only in the form of the oxides Sm_2O_3 and Yb_2O_3. Before being sealed in brass cans of 1-in. inside diameter and $\frac{1}{32}$-in. walls, the oxides were heated to red heat in a platinum crucible to drive off adsorbed water and CO_2.

In the case of the rare-earth oxides, transmission measurements include the effects of scattering from the O nuclei. Subtraction of the O cross section was done experimentally by measuring transmissions of SnO_2 samples containing the same number of oxygen nuclei per cm² as was present in the rare-earth oxides. Similarly the cross section of Sn was subtracted using metallic cylinders of Sn containing the same number of Sn nuclei per cm² as was in the SnO_2 samples. The cross section σ of the rare earths was then calculated by use of the relation

$$e^{-N\sigma}=T(s)T(\mathrm{Sn})/T(\mathrm{SnO_2}),$$

where N is the number of rare-earth nuclei per cm², and $T(s)$, $T(SnO_2)$, and $T(Sn)$ are the transmissions of the rare-earth oxide sample, SnO_2, and Sn, respectively.

A check for proper subtraction of the O cross section was made by measuring the cross sections of Sm and Yb with a thin target over the large resonance in O which occurs for neutrons of 440-kev energy.[7] The absence of a peak in the cross sections at this energy indicated that the number of O nuclei not properly subtracted was less than 2 percent of the number of rare-earth nuclei.

Neutrons were detected with a recoil counter, which was filled with 27 atmos of He for measurements with neutrons above 1 Mev in energy and with approximately 7 atmos of H for lower-energy neutrons. Measurements were made in the forward direction with respect to the incident proton beam with the exception of those below 150-kev neutron energy, which were made at an angle of 115 deg. In the forward direction, the solid angles subtended at the source and detector by the samples

* Work supported by the U. S. Atomic Energy Commission and the Wisconsin Alumni Research Foundation.
[1] Miller, Adair, Bockelman, and Darden, Phys. Rev. **88**, 83 (1952).
[2] Walt, Becker, Okazaki, and Fields, Phys. Rev. **89**, 1271 (1953).
[3] N. Nereson and S. Darden, Phys. Rev. **89**, 775 (1953).
[4] H. H. Barschall, Phys. Rev. **86**, 431 (1952).
[5] Feshbach, Porter, and Weisskopf, Phys. Rev. **90**, 166 (1953).
[6] R. F. Taschek and A. Hemmendinger, Phys. Rev. **74**, 373 (1948).
[7] Adair, Barschall, Bockelman, and Sala, Phys. Rev. **75**, 1124 (1949).

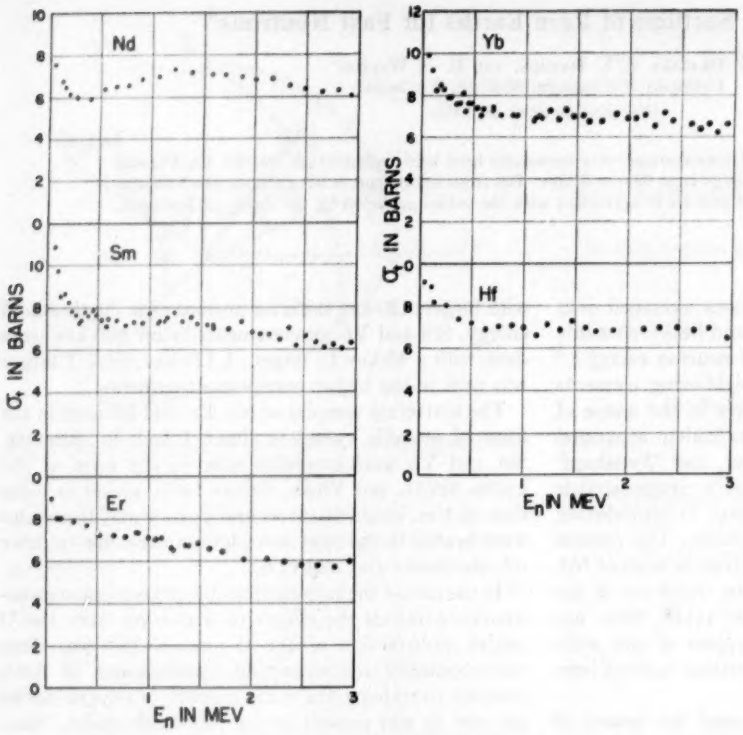

FIG. 1. Total cross sections of Nd, Sm, Er, Yb, and Hf.

were less than 0.016 sterad while at 115 deg the solid angles were less than 0.031 sterad.

Figure 1 shows the total cross sections of Nd, Sm, Er, Yb, and Hf plotted as functions of neutron energy. The uncertainties in the cross sections arising from the statistical errors in the number of neutron counts are in most cases less than 3 percent. The results have not been corrected for the effect of neutrons scattered by the samples into the detector; consequently, the cross sections are probably too small. Previous measurements at this laboratory indicate that for the geometry used in this experiment, the correction to the cross section of Bi for neutrons of 3-Mev energy is of the order of 4 percent. Since the forward scattering and, hence, the amount of inscattering increases with energy and atomic weight, it is expected that the corrections to the present measurements are less than 4 percent.

The average total cross section divided by the geometrical area of the nucleus is plotted as a function of neutron energy and atomic weight in the upper half of Fig. 2. The nuclear radius R was calculated assuming that it is given by

$$R=1.45\times 10^{-13}A^{\frac{1}{3}}\text{ cm},$$

where A is the atomic weight. To illustrate the gradual variation in the shape of the cross-section curve, a smooth surface was drawn through the experimental curves, most of which were obtained earlier at this laboratory.[1,2] The present results, which are plotted between atomic weights 144 and 179, fit smoothly on the surface.

Feshbach, Porter, and Weisskopf have calculated total cross sections on the assumption that the interaction of the neutron with the nucleus is described by a

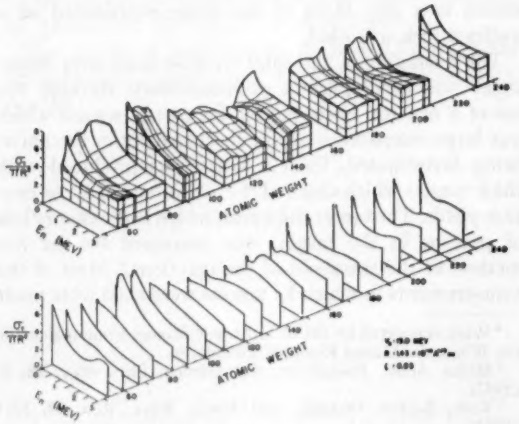

FIG. 2. Total neutron cross section as a function of neutron energy and atomic weight. The upper part of the figure is a plot of the experimental values. The lower half is a plot of the cross sections calculated by Feshbach, Porter, and Weisskopf using the constants indicated.

complex potential of the form

$$V=-V_0(1+i\zeta) \quad \text{for} \quad r<R,$$
$$V=0 \quad \text{for} \quad r>R,$$

where $V_0=19$ Mev and $\zeta=0.05$. Comparison of the measured cross sections with the calculated values shown in the lower part of Fig. 2 shows that the gradual change in cross section is reproduced by this theory. In the region investigated in this experiment the broad maximum at 1-Mev energy, evident in the Nd curve, slowly disappears with increasing atomic weight, a behavior which is predicted by the theory.

We wish to thank Dr. F. H. Spedding, Mr. David Dennison, and Dr. Jack Powell of the Ames Laboratory of the U. S. Atomic Energy Commission, Iowa State College, for their interest in this work and for their efforts in preparing the pure Nd and Er metal cylinders and the Sm and Yb oxides used in this experiment.

PHYSICAL REVIEW VOLUME 93, NUMBER 3 FEBRUARY 1, 1954

Inelastic Scattering of Protons and Neutrons by Deuterons

R. M. Frank and J. L. Gammel
University of California, Los Alamos Scientific Laboratory, Los Alamos, New Mexico

(Received September 11, 1953)

If it is assumed that the range of nuclear forces is small compared to the size of the deuteron and the wavelength of the incoming particle ("zero-range" approximation) and something like the impulse approximation is used, a connection between the cross sections for elastic and inelastic p-d or n-d scattering is derived.

The results of this simple theory are compared with available experimental data, and the agreement between the two is much better than the crude assumptions of the theory merit.

An interesting consequence of the theory is that the connection between the elastic and inelastic scattering cross sections is independent of the properties of the two-body forces. The elastic scattering cross section depends hardly at all on the exchange properties of the two-body n-p potential (provided it gives the binding energy of the deuteron correctly) and the n-n potential, and the connection suggests that the same is true of the inelastic scattering cross section. This is in disagreement with more elaborate calculations of Bransden and Burhop.

I. THE BORN APPROXIMATION FOR THE INELASTIC SCATTERING CROSS SECTION

A FORMULATION of the Born approximation for the inelastic scattering cross section has been given in several papers.[1,2] The initial and final states are the following:

Initial State. A neutron (say) is incident on a deuteron. The wave vector of the neutron is $\mathbf{k}$:

$$\mathbf{k}=\frac{M}{\hbar}\mathbf{v}, \quad k^2=\frac{4}{3}\frac{M}{\hbar^2}E, \tag{1}$$

where $\mathbf{v}$ is the velocity of the neutron in the center of mass system and E is the kinetic energy of *both* particles in the center-of-mass system.

Final State. A neutron is ejected with wave vector $\mathbf{k}'$ (the "scattered" neutron). A deuteron remains in an excited (continuum) state described by a wave vector $\mathbf{k}''$:

$$\mathbf{k}'=\frac{M}{\hbar}\mathbf{v}', \quad k'^2=\frac{4}{3}\frac{M}{\hbar^2}E',$$
$$\mathbf{k}''=\frac{M}{\hbar}\mathbf{v}'', \quad k''^2=\frac{M}{\hbar^2}E'', \tag{2}$$

where $\mathbf{v}'$ and E' have the same meaning as $\mathbf{v}$ and E, $\mathbf{v}''$ is the velocity of the neutron (say) belonging to the deuteron in the center-of-mass system of the two particles forming the deuteron, and E'' is the excitation energy of the deuteron. Thus, with the usual definition,

$$\alpha^2=\frac{M}{\hbar^2}E_b, \tag{3}$$

where E_b is the binding energy of the deuteron, conservation of energy

$$E'+E''=E-E_b \tag{4}$$

gives

$$k'^2+(4/3)k''^2=k^2-(4/3)\alpha^2. \tag{5}$$

The differential cross section for the scattering process corresponding to a transition from this initial to this final state is [reference 1, Eq. (13b)]:

$$d\sigma=\frac{1}{4}\frac{1}{(2\pi)^5}\frac{4M^2}{3\hbar^2}\frac{k'}{k}|M|^2d\Omega'd\mathbf{k}'', \tag{6}$$

or, equivalently [reference 2, after Eq. (51)],

$$d\sigma=\frac{1}{4}\frac{1}{(2\pi)^5}\frac{4M^2}{3\hbar^2}\frac{1}{kk'}$$
$$\times\delta(k'-[k^2-(4/3)k''^2-(4/3)\alpha^2]^{\frac{1}{2}})|M|^2d\mathbf{k}'d\mathbf{k}'', \tag{7}$$

[1] R. L. Gluckstern and H. A. Bethe, Phys. Rev. **81**, 761 (1951).
[2] Ta-You Wu and Julius Ashkin, Phys. Rev. **73**, 986 (1948).

where [reference 1, Eq. (25)]

$$M=\{(1-P_{13})\psi_f\chi_f, [V_{nn}(13)+V_{np}(12)]\psi\chi_i\}. \quad (8)$$

Whereas for elastic scattering Eq. (8) leads to three kinds of integrals,[3] it now leads to six kinds of integrals, because the deuteron wave function which appears in ψ_f depends on the direction of $\mathbf{k}''$. These integrals are

$$J_1^+=\int \varphi_{\mathbf{k}''}(23)f'(1)U(13)\varphi(23)f(1)d\tau_1d\tau_2d\tau_3,$$

$$J_2^+=\int \varphi_{\mathbf{k}''}(13)f'(2)U(13)\varphi(23)f(1)d\tau_1d\tau_2d\tau_3, \quad (9)$$

$$J_3^+=\int \varphi_{\mathbf{k}''}(23)f'(1)U(13)\varphi(12)f(3)d\tau_1d\tau_2d\tau_3,$$

and three more, J_1^-, J_2^-, and J_3^-, obtained by reversing the argument of $\varphi_{\mathbf{k}''}$; for example,

$$J_3^-=\int \varphi_{\mathbf{k}''}(31)f'(2)U(13)\varphi(23)f(1)d\tau_1d\tau_2d\tau_3. \quad (10)$$

Performing the spin sums in Eq. (8) and defining α_+ to be the coefficient of J_1^+, etc., as in reference 3, Eq. (9) and Eq. (10), we find for $S=3/2$, triplet continuum states:

$$\begin{aligned}
\alpha_+&={}^3V_{nn}^-,\\
\alpha_-&=\tfrac{1}{2}{}^3V_{np}^+ +\tfrac{1}{2}{}^3V_{np}^-,\\
\beta_+&=-\tfrac{1}{2}{}^3V_{np}^+ +\tfrac{1}{2}{}^3V_{np}^-,\\
\beta_-&=-\tfrac{1}{2}{}^3V_{np}^+ -\tfrac{1}{2}{}^3V_{np}^-,\\
\gamma_+&=-{}^3V_{nn}^-,\\
\gamma_-&=\tfrac{1}{2}{}^3V_{np}^+ -\tfrac{1}{2}{}^3V_{np}^-;
\end{aligned} \quad (11)$$

for $S=1/2$, triplet continuum states:

$$\begin{aligned}
\alpha_+&=\tfrac{3}{4}{}^1V_{nn}^+ +\tfrac{1}{4}{}^3V_{nn}^-,\\
\alpha_-&=\tfrac{1}{8}{}^3V_{np}^+ +\tfrac{1}{8}{}^3V_{np}^- +\tfrac{3}{8}{}^1V_{np}^+ +\tfrac{3}{8}{}^1V_{np}^-,\\
\beta_+&=\tfrac{1}{4}{}^3V_{np}^+ -\tfrac{1}{4}{}^3V_{np}^-,\\
\beta_-&=\tfrac{1}{4}{}^3V_{np}^+ +\tfrac{1}{4}{}^3V_{np}^-,\\
\gamma_+&=\tfrac{3}{4}{}^1V_{nn}^+ -\tfrac{1}{4}{}^3V_{nn}^-,\\
\gamma_-&=\tfrac{1}{8}{}^3V_{np}^+ -\tfrac{1}{8}{}^3V_{np}^- +\tfrac{3}{8}{}^1V_{np}^+ -\tfrac{3}{8}{}^1V_{np}^-;
\end{aligned} \quad (12)$$

for $S=1/2$, singlet continuum states:

$$\begin{aligned}
\alpha_+&=-\frac{\sqrt{3}}{4}({}^1V_{nn}^+ -{}^3V_{nn}^-),\\
\alpha_-&=\frac{\sqrt{3}}{8}(-{}^3V_{np}^+ -{}^3V_{np}^- +{}^1V_{np}^+ +{}^1V_{np}^-),\\
\beta_+&=-\frac{\sqrt{3}}{4}({}^1V_{np}^+ -{}^1V_{np}^-),\\
\beta_-&=-\frac{\sqrt{3}}{4}({}^1V_{np}^+ +{}^1V_{np}^-),\\
\gamma_+&=-\frac{\sqrt{3}}{4}({}^1V_{nn}^+ +{}^3V_{nn}^-),\\
\gamma_-&=\frac{\sqrt{3}}{8}(-{}^3V_{np}^+ +{}^3V_{np}^- +{}^1V_{np}^+ -{}^1V_{np}^-),
\end{aligned} \quad (13)$$

and [compare reference 1, Eq. (31)]

$$|M|^2=\tfrac{2}{3}|M(S=3/2)|^2+\tfrac{1}{3}|M(S=1/2,\text{ triplet states})|^2 +\tfrac{1}{3}|M(S=1/2,\text{ singlet states})|^2. \quad (14)$$

Equations (11) and (12) can be compared with Eqs. (9) and (10) of reference 3. Were the deuteron wave function in ψ_f the ground-state wave function, interchanging the particles in its argument would make no difference, so that for elastic scattering $J_1^+=J_1^-$, for example. In fact, comparing the two sets of equations, we see that

$$\alpha=\alpha_++\alpha_-, \quad (15)$$

for example, where α is given by Eq. (9) of reference 3.

II. COORDINATE SYSTEM

If 1 is the "incoming" neutron (say) and 2 and 3 are the proton and neutron in the deuteron, respectively, we use

$$\mathbf{r}_3-\mathbf{r}_2=\mathbf{r}, \quad -\mathbf{r}_1+\tfrac{1}{2}(\mathbf{r}_2+\mathbf{r}_3)=\mathbf{q}. \quad (16)$$

III. CONTINUUM STATES OF THE DEUTERON

In the following, we use zero-range potentials for the two-body potentials. As explained in reference 3, it is not necessary to think of this as a strict zero-range approximation. It is perhaps better to imagine that is an approximate way of evaluating the integrals in Eq. (9) in which it is assumed that the range of the two-body nuclear forces is short compared to the size of the deuteron and the wavelength of the incident particle, and then it does not seem such a crude way of proceeding.

Consistent with this approximation, we take for the

[3] R. S. Christian and J. L. Gammel, Phys. Rev. **91**, 100 (1953). We follow the notation of this paper in the following.

wave function of the ground state of the deuteron

$$\varphi(r)=\left(\frac{\alpha}{2\pi}\right)^{\frac{1}{2}}\frac{\exp(-\alpha r)}{r}, \tag{17}$$

and for the triplet continuum states[4]

$$\varphi_{\mathbf{k}''}(r)=\exp(i\mathbf{k}''\cdot\mathbf{r})+\frac{\{\exp(2i\delta_0(k''))\}-1}{2ik''}\frac{\exp(ik''r)}{r}. \tag{18}$$

Equations (17) and (18) indicate that the wave functions reach their asymptotic form at once. The condition that $\varphi_{f''}$ and φ be orthogonal requires that

$$k''\cot\delta_0=-\alpha, \tag{19}$$

as may be calculated from Eqs. (17) and (18) by setting

$$\int\varphi\varphi_{\mathbf{k}''}d\mathbf{r}=0. \tag{20}$$

A further assumption contained in Eq. (18) is that in a two body n-p collision only the S-state interaction is important and no interaction takes place in states with $l\gtrsim 1$. This is known to be very nearly the case, especially for low energies.

It should be noted that we are not making the usual assumption that the wave functions for continuum states of the deuteron are plane waves.

IV. THE ZERO RANGE APPROXIMATION

With these coordinates and wave functions, we find

$$J_1^+=\int\varphi_{\mathbf{k}''}^*(\mathbf{r})\exp(-i\mathbf{k}'\cdot\mathbf{q})\times U(|\mathbf{q}+\tfrac{1}{2}\mathbf{r}|)\varphi(r)\exp(i\mathbf{k}\cdot\mathbf{q})d\mathbf{r}d\mathbf{q},$$

$$J_2^+=\int\varphi_{\mathbf{k}''}^*(\mathbf{q}+\tfrac{1}{2}\mathbf{r})\exp[-i\mathbf{k}'\cdot(-\tfrac{1}{2}\mathbf{q}+\tfrac{3}{4}\mathbf{r})]\times U(|\mathbf{q}+\tfrac{1}{2}\mathbf{r}|)\varphi(r)\exp(i\mathbf{k}\cdot\mathbf{q})d\mathbf{r}d\mathbf{q}, \tag{21}$$

$$J_3^+=\int\varphi_{\mathbf{k}''}^*(\mathbf{r})\exp(-i\mathbf{k}'\cdot\mathbf{q})U(|\mathbf{q}+\tfrac{1}{2}\mathbf{r}|)\times\varphi(|\mathbf{q}-\tfrac{1}{2}\mathbf{r}|)\exp(-i\mathbf{k}\cdot(\tfrac{1}{2}\mathbf{q}+\tfrac{3}{4}\mathbf{r}))d\mathbf{r}d\mathbf{q}.$$

The sign of the argument of $\varphi_{\mathbf{k}''}$ is changed for J_1^-, J_2^-, J_3^-. With a zero-range potential,

$$U(|\mathbf{q}+\tfrac{1}{2}\mathbf{r}|)=U_0\delta(|\mathbf{q}+\tfrac{1}{2}\mathbf{r}|), \tag{22}$$

integration over $\mathbf{r}$ gives

$$\mathbf{r}=-2\mathbf{q}, \tag{23}$$

so that

$$J_1^+=\frac{4\pi}{3}r_0^3U_0\int\varphi_{\mathbf{k}''}^*(-2\mathbf{q})\times\exp(-i\mathbf{k}'\cdot\mathbf{q})\varphi(2q)\exp(i\mathbf{k}\cdot\mathbf{q})d\mathbf{q},$$

$$J_2^+=\frac{4\pi}{3}r_0^3U_0\varphi_{\mathbf{k}''}(r_0)\int\exp(2i\mathbf{k}'\cdot\mathbf{q})\varphi(2q)\exp(i\mathbf{k}\cdot\mathbf{q})d\mathbf{q},$$

$$J_3^+=\frac{4\pi}{3}r_0^3U_0\int\varphi_{\mathbf{k}''}^*(-2\mathbf{q})\times\exp(-i\mathbf{k}'\cdot\mathbf{q})\varphi(2q)\exp(i\mathbf{k}\cdot\mathbf{q})d\mathbf{q}.$$

Since

$$\lim_{r_0\to 0}r_0^2U_0 \tag{24}$$

is finite,

$$\lim_{r_0\to 0}r_0^3U_0 \tag{25}$$

vanishes, and J_1^+ and J_3^+ vanish. But

$$\lim_{r_0\to 0}r_0^3\varphi_{\mathbf{k}''}(r_0)U_0=\lim_{r_0\to 0}r_0\varphi_{\mathbf{k}''}(r_0)\lim_{r_0\to 0}(r_0^2U_0)=\frac{\{\exp 2i\delta_0(k'')\}-1}{2ik''}\lim_{r_0\to 0}r_0^2U_0. \tag{26}$$

This is independent of the direction of $\mathbf{k}''$, so that in this approximation

$$J_2^+=J_2^-=J_2=\frac{4\pi}{3}\frac{\{\exp 2i\delta_0(k'')\}-1}{2ik''}\cdot\lim_{r_0\to 0}r_0^2U_0\times\int\exp(2i\mathbf{k}'\cdot\mathbf{q})\varphi(2q)\exp(i\mathbf{k}\cdot\mathbf{q})d\mathbf{q}, \tag{27}$$

and all other integrals vanish.

For elastic scattering, instead of Eq. (27) we find, in the same way,

$$J_2=\frac{4\pi}{3}\left(\frac{\alpha}{2\pi}\right)^{\frac{1}{2}}\lim_{r_0\to 0}r_0^2U_0\times\int\exp(2i\mathbf{k}'\cdot\mathbf{q})\varphi(2q)\exp(i\mathbf{k}\cdot\mathbf{q})d\mathbf{q}. \tag{28}$$

Using Eqs. (11), (12), (13), and (14), we find for the

---

[4] Very accurate continuum wave functions for the deuteron may be obtained for a Yukawa potential in this same way. For the ground state a well-known approximation is [see for example G. F. Chew, Phys. Rev. 74, 809 (1948)]

$$\varphi=\left(\frac{\alpha\beta(\alpha+\beta)}{2\pi(\beta-\alpha)^2}\right)^{\frac{1}{2}}\frac{\{\exp(-\alpha r)\}-\{\exp(-\beta r)\}}{r}.$$

For the approximate continuum wave function,

$$\varphi_{\mathbf{k}''}(r)=\exp(i\mathbf{k}''\cdot\mathbf{q})+\frac{\{\exp(2i\delta_0(k''))\}-1}{2ik''r}(\{\exp(2ik''r)\}-\{\exp(-\beta r)\}),$$

Eqs. (19) and (20) lead to

$$k''\cot\delta_0(k'')\left[\frac{1}{\alpha^2+k''^2}-\frac{1}{\beta^2+k''^2}\right]=\frac{1}{\alpha+\beta}-\frac{1}{2\beta}+\frac{\beta}{\beta^2+k''^2}-\frac{\alpha}{\alpha^2+k''^2},$$

which corresponds to a scattering length of 5.26×10^{-13} cm as compared to the accepted value $5.29\pm0.04\times10^{-13}$ cm. For the 90-Mev n-p scattering it gives a ^3S phase shift of 54° as compared to the accepted value $60°\pm5°$.

inelastic scattering

$$|M|^2=\tfrac{3}{8}|J_2|^2+\tfrac{1}{12}|J_2|^2+\tfrac{1}{4}({}^1V_{np}{}^+)^2|J_2(\text{singlet})|^2, \quad (29)$$

and for the elastic scattering

$$|M|^2=\tfrac{3}{4}|J_2|^2. \quad (30)$$

V. CONNECTION BETWEEN THE INELASTIC AND ELASTIC SCATTERING CROSS SECTIONS

Equations (27) and (28) are very much alike. The $\mathbf{k}''$s which appear in them are different, because in Eq. (28) (elastic scattering)

$$|\mathbf{k}'|=|\mathbf{k}|,$$

whereas for Eq. (27) (inelastic scattering), Eq. (5) applies. However, following the procedures of the impulse approximation,[5] we overlook this, so that

$$\frac{J_2(\text{inelastic})}{J_2(\text{elastic})}=\left(\frac{2\pi}{\alpha}\right)^{\frac{1}{2}}\frac{\{\exp(2i\delta_0(k''))\}-1}{2ik''}, \quad (31)$$

and

$$\frac{|J_2(\text{inelastic})|^2}{|J_2(\text{elastic})|^2}=\frac{2\pi}{\alpha}\frac{\sin^2\delta_0(k'')}{(k'')^2}. \quad (32)$$

Then Eqs. (29) and (30) and Eq. (6) and the corresponding equation for elastic scattering give

$$d\sigma_{\text{in}}=\sigma_{\text{el}}\frac{2\pi}{\alpha}\frac{k'}{k}\sin^2\delta_0(k'')\frac{4\pi}{(2\pi)^3}dk''d\Omega'. \quad (33)$$

σ_{el} depends on the angle between $\mathbf{k}'$ and $\mathbf{k}$. The last 4π in the numerator comes from $d\mathbf{k}''=4\pi k''^2dk''$, and the $1/(2\pi)^3$ comes from the fact that the cross section for elastic scattering has a $1/(2\pi)^2$ instead of the $1/(2\pi)^5$ in Eq. (6). Sometimes a $1/(2\pi)^{\frac{1}{2}}$ is put in front of Eq. (18) to make the equations corresponding to Eq. (6) the same for elastic and inelastic scattering; but, however we do it, we have the $1/(2\pi)^3$ at the end.

Still following the ideas of the impulse approximation, we proceed as follows.[6] To calculate an inelastic cross section we put the *experimental n-d* angular distribution into Eq. (33) and values of $\sin^2\delta_0(k'')$ calculated from

$$\sin^2\delta_0(k'')=\frac{k''^2}{[k''\cot\delta_0(k'')]^2+k''^2} \quad (34)$$

and

$$k''\cot\delta_0(k'')=-\frac{1}{a}+\frac{1}{2}r_0(k'')^2, \quad (35)$$

where we use the best values of the scattering lengths and effective range. Of course, in view of Eq. (29), part of the time we use the triplet scattering length and effective range and, part of the time, the singlet scattering length and effective range. Equation (33) written more fully, with Eq. (29) taken into account becomes

$$d\sigma_{\text{in}}=\frac{\sigma_{\text{el}}}{\pi\alpha}\frac{k'}{k}k''^2\left\{\frac{1}{(k''\cot\delta)^2_{\text{triplet}}+k''^2}+\frac{({}^1V_{np}{}^+)^2}{3}\frac{1}{(k''\cot\delta)^2_{\text{singlet}}+k''^2}\right\}dk''d\Omega', \quad (36a)$$

or alternately, according to Eq. (7),

$$d\sigma_{\text{in}}=\frac{\sigma_{\text{el}}}{4\pi^2\alpha}\frac{1}{kk'}\left\{\quad\right\}\times\delta(k'-[k^2-(4/3)k''^2-(4/3)\alpha^2]^{\frac{1}{2}})d\mathbf{k}'d\mathbf{k}''. \quad (36b)$$

VI. EMISSION OF NEUTRONS AND PROTONS IN *n-d* INELASTIC SCATTERING

In *n-d* inelastic scattering, two neutrons (a "scattered" neutron and a neutron "ejected" from the deuteron) appear and one proton (a proton "ejected" from the deuteron).

The wave-number vectors of these particles are as follows:

"scattered" neutron: $\mathbf{k}'$, (37a)

"ejected" neutron: $\mathbf{S}_n=-\frac{1}{2}\mathbf{k}'+\mathbf{k}''$, (37b)

"ejected" proton: $\mathbf{S}_p=-\frac{1}{2}\mathbf{k}'-\mathbf{k}''$. (37c)

$\mathbf{k}''$ may be eliminated from $d\sigma_{\text{in}}$, Eq. (36b), by the use of one of Eqs. (37b) or (37c).

If we want the energy and angular distribution of the "scattered" neutron ($d\sigma_{\text{scatt}}$), we express Eq. (36b) in terms of $\mathbf{k}'$ and $\mathbf{S}_n$ (say) and integrate out the directions of $\mathbf{S}_n$. [The magnitude of $\mathbf{S}_n$ is fixed by Eq. (37b) and Eq. (5).] This is easy to do since it is equivalent to putting k'' and dk'' from Eq. (5) into Eq. (36a), which gives the energy and angular distribution of the "scattered" neutrons at once.

Graphs of $d\sigma_{\text{scattered}}$ as functions of E_n, the energy of the scattered neutron in the laboratory system, and θ_n, the angle through which it is scattered, are presented in Fig. 1.[7]

[5] G. F. Chew and G. C. Wick, Phys. Rev. **85**, 636 (1952).

[6] Gluckstern and Bethe (reference 1, p. 770) also replace terms occurring in a result calculated in Born approximation by observed values wherever possible.

[7] Transformation to the laboratory system is accomplished as follows. First, we express Eq. (36a) in terms of energies by using Eqs. (1)–(5). We find

$$d\sigma=\frac{1}{2\pi}\frac{\sigma_{\text{el}}}{\sqrt{E_b}}\frac{\sqrt{E'}}{\sqrt{E_{\text{lab}}}}(E_{\text{lab}}-\tfrac{3}{4}E'-\tfrac{3}{4}E_b)^{\frac{1}{2}}\times\left\{\frac{1}{D_{\text{triplet}}}+\frac{({}^1V_{np}{}^+)^2}{3}\frac{1}{D_{\text{singlet}}}\right\}dE'd\Omega',$$

where

$$D=\frac{\hbar^2}{M}[(k''\cot\delta)^2+k''^2]$$

and E_{lab} is the energy of the incident particle in the laboratory system. This may be expressed in terms of laboratory energies

If we want the energy and angular distribution of the "ejected" neutron ($d\sigma_{\text{ejected}}$), we express Eq. (36b) in terms of $\mathbf{k}'$ and $\mathbf{S}_n$ and integrate out the directions of $\mathbf{k}'$ [the magnitude of $\mathbf{k}'$ is fixed by Eq. (37b) and Eq. (5)]. This time there is no easy way to do the calculation. The procedure for carrying it through is described in reference 2, paragraph C, p. 996.

Let E_n be the energy of the ejected neutron and θ_n the angle it makes with $\mathbf{k}$ (both measured in the laboratory system). The wave-number vector of the ejected neutron in the laboratory system is

$$\mathbf{p}_n = \mathbf{S}_n + \tfrac{1}{2}\mathbf{k}, \tag{38}$$

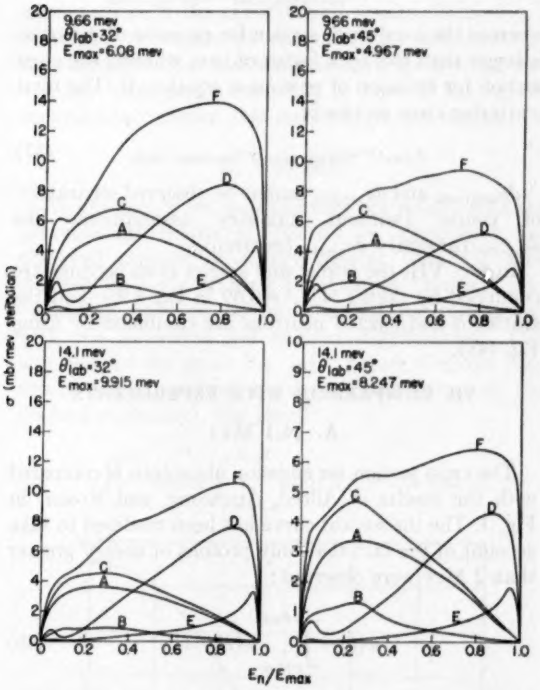

FIG. 1. Energy distributions of inelastically scattered particles at two angles. The contributions of triplet deuteron continuum states to the cross sections for emission of protons and scattering of neutrons are labeled *A* and *D*, respectively. The corresponding curves for singlet deuteron continuum states are labeled *B* and *E*. The cross sections for emission of protons and neutrons are labeled *C* and *F*, respectively.

and angles by using

$$\cos(k',k) = \frac{2\sqrt{E_n}\cos\theta_n - \sqrt{E_0}}{2(E_n + \frac{1}{4}E_0 - \sqrt{E_0 E_n}\cos\theta_n)^{\frac{1}{2}}},$$

$$E' = \tfrac{4}{3}[E_n + \tfrac{1}{4}E_0 - (E_0 E_n)^{\frac{1}{2}}\cos\theta_n],$$

and

$$dE' d\cos(\mathbf{k}',\mathbf{k}) = |J|\, dE_n d\cos\theta_n,$$

where E_0 is $4E_{\text{lab}}/9$ and J is the Jacobian of the transformation:

$$J = \frac{3}{2}\left(\frac{3}{2}\frac{E_n}{E'}\right)^{\frac{1}{2}}.$$

Numerically, with the energies in Mev,

$$D_{\text{triplet}} = 1.431 \ \ + 0.455(E_{\text{lab}} - 1.5E' - 1.5E_0) + 0.00782(\quad)^2,$$
$$D_{\text{singlet}} = 0.0743 + 0.743(\qquad\qquad) + 0.0195\ (\quad)^2.$$

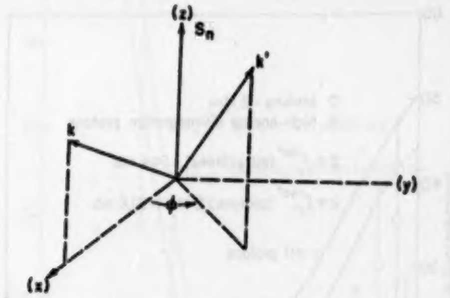

FIG. 2. Coordinate system to which $\mathbf{k}'$ is referred in performing the integrations to obtain angular and energy distributions of ejected particles.

so that

$$p_n^2 = (2M/\hbar^2)E_n. \tag{39}$$

In integrating out the directions of $\mathbf{k}'$, we refer to $\mathbf{S}_n$ as polar axis ($\mu = \cos\mathbf{k}', \mathbf{S}_n$), the azimuth, φ, being measured from the plane of $\mathbf{k}$ and $\mathbf{S}_n$ (see Fig. 2). The angle between $\mathbf{k}'$, $\mathbf{k}$ which appears in σ_{el} in Eq. (36b) must be expressed in terms of variables appropriate to this reference system.

$$\cos(\mathbf{k}',\mathbf{k}) = \sin(\mathbf{k},\mathbf{S}_n)(1-\mu^2)^{\frac{1}{2}}\cos\varphi + \mu\cos(\mathbf{k},\mathbf{S}_n) \equiv y. \tag{40}$$

Actually, Eq. (37b) and Eq. (5) leave two values of k' possible:

$$k_+' = \tfrac{2}{3}[-S_n\mu + (S_n^2\mu^2 - 4S_n^2 + 3k^2 - 4\alpha^2)^{\frac{1}{2}}], \tag{41a}$$

$$k_-' = \tfrac{2}{3}[-S_n\mu - (S_n^2\mu^2 - 4S_n^2 + 3k^2 - 4\alpha^2)^{\frac{1}{2}}]. \tag{41b}$$

Only real positive values of k_+' and k_-' are permitted. This restricts the allowed values of μ for a given S_n. For

$$0 \leqq S_n^2 \leqq \tfrac{3}{4}k^2 - \alpha^2,$$

k_+' is real and positive for all μ. k_-' is negative for all μ and thus is excluded. For

$$\tfrac{3}{4}k^2 - \alpha^2 < S_n^2 \leqq k^2 - (4/3)\alpha^2,$$

both k_+' and k_-' are real and positive when

$$-1 \leqq \mu \leqq -2\left(1 - \frac{3}{4}\frac{k^2}{S_n^2} + \frac{\alpha^2}{S_n^2}\right)^{\frac{1}{2}} \equiv -\nu$$

and are either complex or negative when $\mu > -\nu$. For

$$S_n^2 > k^2 - (4/3)\alpha^2,$$

both k_+' and k_-' are complex for all μ, and this region is excluded. (This is an obvious consequence of conservation of energy.)

Any function $f(k')$ of k' labeled $f^+(k')$ or $f^-(k')$ means $f(k_+')$ or $f(k_-')$ in the following. Let

$$I = \frac{\sigma_{\text{el}}(y)}{4\pi^2\alpha}\frac{1}{(k''\cot\delta)^2 + k''^2}, \tag{42}$$

where $k''\cot\delta$ is given by Eq. (35) expressed in terms

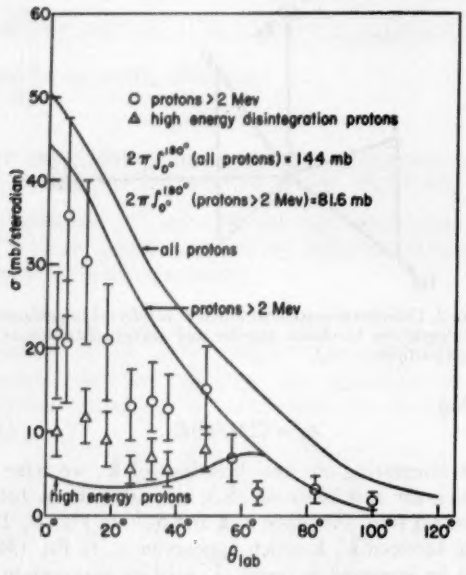
○ protons > 2 Mev
△ high energy disintegration protons
$2\pi\int_{0^\circ}^{180^\circ}$ (all protons) = 144 mb
$2\pi\int_{0^\circ}^{180^\circ}$ (protons > 2 Mev) = 81.6 mb
all protons
protons > 2 Mev
high energy protons
σ (mb/steradian)
θ_{lab}

FIG. 3. Angular distribution of disintegration protons from 14.1-Mev inelastic *n-d* scattering.

of $\mathbf{k}'$ and S_n through Eq. (37b). Then Eqs. (55) and (56) of reference 2 become

$$d\sigma_{\text{ejected}}=\frac{M}{\hbar^2}\frac{p_n}{k}I(E_n,\theta_n)dE_n d\Omega_n. \tag{43}$$

For

$$0<S_n^2<\tfrac{3}{4}k^2-\alpha,$$

$$I(E_n,\theta_n)=\frac{3}{2}\int_0^{2\pi}d\varphi\int_{-1}^{1}d\mu \times\frac{k_+'^2}{(3k^2-4\alpha^2-4S_n^2+S_n^2\mu^2)^{\frac{1}{2}}}I^+. \tag{44a}$$

For

$$\tfrac{3}{4}k^2-\alpha^2<S_n^2<k^2-(4/3)\alpha^2,$$

$$I(E_n,\theta_n)=\frac{3}{2}\int_0^{2\pi}d\varphi\int_{-1}^{-\nu}d\mu\frac{k_+'^2}{(3k^2-4\alpha^2-4S_n^2+S_n^2\mu^2)^{\frac{1}{2}}}I^+ +\frac{3}{2}\int_0^{2\pi}d\varphi\int_{-1}^{-\nu}d\mu\frac{k_-'^2}{(3k^2-4\alpha^2-4S_n^2+S_n^2\mu^2)^{\frac{1}{2}}}I^-. \tag{44b}$$

Graphs of $d\sigma_{\text{ejected}}$ as a function of E_n and θ_n are presented in Fig. 1. It can be seen that the energy and angular distribution of the ejected neutron and ejected proton are the same in the present theory because Eq. (36b) depends only on the magnitude of $\mathbf{k}''$, so that expressing (36b) in terms of k' and S_n or k' and S_p give the same result.

The cross section for the emission of neutrons is composed of two parts:

$$d\sigma_n=d\sigma_{\text{scattered}}+d\sigma_{\text{ejected}}. \tag{45}$$

The total cross section for the scattered neutrons obtained by integrating $d\sigma_{\text{scattered}}$ over E_n and θ_n must be the same as the total cross section for the ejected neutrons because every time a neutron is scattered one is ejected. That we must get this result follows on a moment's reflection. We have integrated Eq. (36b), expressed in terms of $\mathbf{k}'$ and $\mathbf{S}_n$, in only two different orders, so that we ought to get the same result from them. This requirement serves as a useful check on the numerical work.

Since two neutrons appear in the final state,

$$\sigma_{\text{inelastic, total}}=\tfrac{1}{2}(\sigma_{\text{scattered, total}}+\sigma_{\text{ejected, total}}) =\sigma_{\text{scattered, total}}=\sigma_{\text{ejected, total}}, \tag{46}$$

whereas the total cross section for emission of neutrons is larger than this by a factor of two, whereas the cross section for emission of protons is equal to it. The total scattering cross section is

$$\sigma_{\text{total}}=\sigma_{\text{elastic total}}+\sigma_{\text{inelastic total}}. \tag{47}$$

$d\sigma_{\text{scattered}}$ and $d\sigma_{\text{ejected}}$ cannot be observed separately, of course [without auxiliary assumptions like $d\sigma_{\text{ejected}}(\text{proton})=d\sigma_{\text{ejected}}(\text{neutron})$].

In Sec. VII, the triplet and singlet cross sections are combined by taking ${}^1V_{np}{}^+=0.69$ in Eq. (36), and the scattered and ejected neutrons are combined by using Eq. (45).

VII. COMPARISON WITH EXPERIMENTS

A. 14.1 Mev

The cross section for emission of protons is compared with the results of Allred, Armstong, and Rosen[8] in Fig. 3. The theoretical curve has been modified to take account of the fact that only protons of energy greater than 2 Mev were observed:

$$\sigma(\theta)=\int_{2\text{ Mev}}^{E_{\max}}\sigma(E,\theta)dE. \tag{48}$$

Allred, Armstrong, and Rosen also observed high-energy disintegration protons (protons whose range in the emulsion is greater than the range in the emulsion of deuterons elastically scattered at the same angle). Figure 4 shows $E_p(\theta_{\text{lab}})$, the energy of a proton whose range in the emulsion is the same as the range in the emulsion of a deuteron elastically scattered at the same angle, as a function of θ_{lab}. Then the cross section for emission of high-energy disintegration protons is

$$\sigma(\theta)=\int_{E_p(\theta)}^{E_{\max}}\sigma(E,\theta)dE. \tag{49}$$

The total cross section at 14.1 Mev has been measured with precision by the transmission method, and is 802 mb.[9] It is extremely doubtful that the total cross

[8] Allred, Armstrong, and Rosen, Phys. Rev. **91**, 90 (1953).
[9] Poss, Salant, Snow, and Yuan, Phys. Rev. **87**, 116 (1952).

section for elastic scattering is greater than 650 mb.[3] This leaves 150 mb for the total cross section for emission of protons. Allred, Armstrong, and Rosen observed 57±13 mb for the total cross section for emission of protons of energy greater than 2 Mev. This work was undertaken partly in order to determine whether the cross section for emission of protons of energy less than 2 Mev could be sufficiently large to explain the difference between 150 mb and 57±13 mb. This appears to be the case. We find 144 mb for the total cross section for emission of protons and 80 mb for the cross section for emission of protons of energy greater than 2 Mev.

On the whole the theoretical results seem in good agreement with the experimental results. From Fig. 3 it might be concluded that the theoretical energy distributions have too many low-energy protons and too few high-energy ones, but in view of the experimental uncertainties, this conclusion is not certain.

B. 9.66 Mev

At this energy we may compare our results with the experimental results of Juanita H. Gammel.[10] She observed protons of energy greater than 1.3 Mev emitted in *p-d* scattering (the names "proton" and "neutron" have to be interchanged for comparison with the calculated *n-d* angular distributions). This was allowed for as in Eq. (48). Figure 5 shows that theory and experiment are in excellent agreement (no doubt fortuitously). She found

$$\int_{20°}^{130°} \sin\theta d\theta \int_{1.3\ \mathrm{Mev}}^{E_{\max}} dE\sigma(E,\theta) = 114\ \mathrm{mb},$$

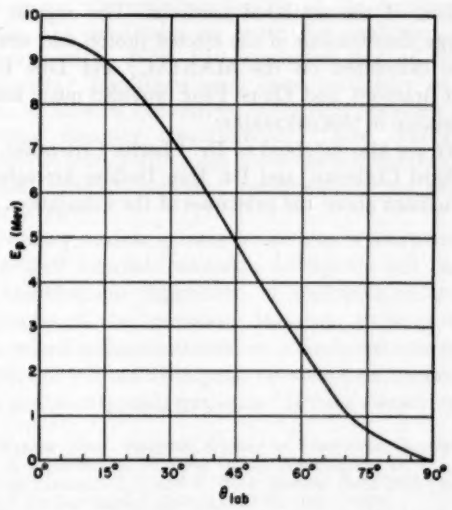

FIG. 4. The energy of a proton having the same range in the emulsion as a deuteron elastically scattered at the same angle as a function of the laboratory angle (14.1-Mev *n-d* scattering).

[10] Juanita H. Gammel (to be published).

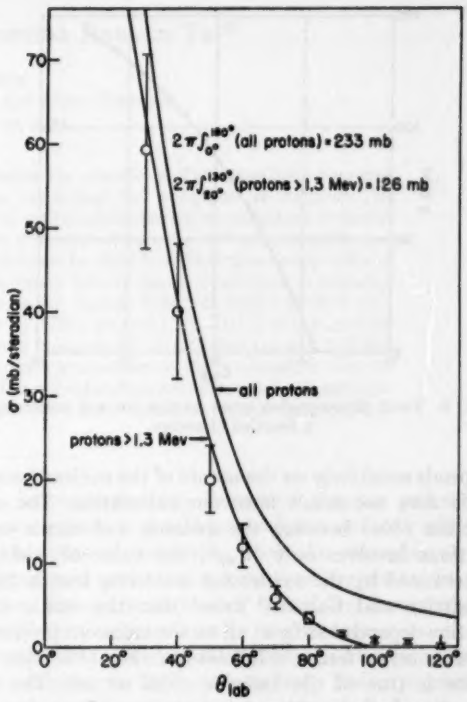

FIG. 5. Angular distribution of protons emitted in 9.66-Mev inelastic *p-d* scattering.

and we find 126 mb for the same quantity. It is interesting to note that the total cross section for emission of protons is more than twice this, or 233 mb. About one-half of the protons have an energy less than 1.3 Mev.

Coulomb effects were neglected in the calculation. They might be taken into account approximately by use of the following as a Coulomb penetration factor:

$$C_0(k+\tfrac{1}{2}k)C_0(|\mathbf{k}'+\tfrac{1}{2}\mathbf{k}'+\mathbf{k}''|); \qquad (50)$$

that is, we use the relative momenta of the two protons in the initial and final states. Here, as usual,

$$C_0 = 2\pi\eta/[\exp(2\pi\eta)-1], \quad \eta = e^2/\hbar v_{\text{relative}}. \qquad (51)$$

For the initial state,

$$\tfrac{1}{2}k = Mv_{\text{relative}}/\hbar; \qquad (52)$$

and for the final state,

$$|\tfrac{1}{2}\mathbf{k}'+\mathbf{k}''| = Mv_{\text{relative}}/\hbar. \qquad (53)$$

C. Total Cross Section

A graph of the *n-d* inelastic cross section is presented in Fig. 6.

VIII. DISCUSSION

Bransden and Burhop have presented some calculations which show that the inelastic cross section

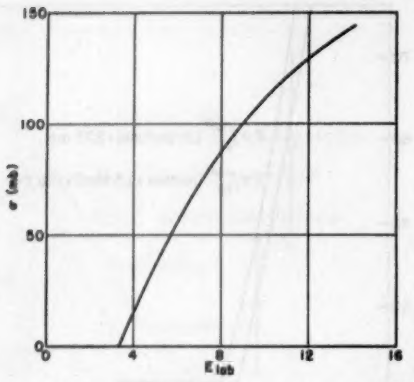

FIG. 6. Total disintegration cross section for n-d scattering as a function of energy.

depends sensitively on the nature of the nuclear forces.[11] This does not result from our calculation. The connection (36a) between the inelastic and elastic cross sections involves only ${}^1V_{np}{}^+$, the value of which is determined by the singlet n-p scattering length. Since Christian and Gammel[3] found that the elastic cross section depends hardly at all on the unknown properties of the nuclear forces, it follows from Eq. (36a) that the same is true of the inelastic cross section. The discrepancy between this result and that of Bransden and Burhop arises partly perhaps from the crudeness of our theory, but the problem should be studied more carefully if possible.

Another point of interest is the following. Use of plane-wave wave functions for the continuum states of the deuteron in calculating the integrals (the J's) would have made them all vanish. One is led to believe, first, that the nonplane-wave parts of the deuteron-continuum states should make the most important contribution to the inelastic cross section even in calculations better than the one made here, and, second, that it is doubtful that the use of plane wave-continuum wave functions could give a better approximation to the total scattering cross section than the inelastic scattering cross section as is sometimes stated (one would hardly want to get zero for the total scattering cross section, especially after calculating a nonzero elastic scattering cross section as Christian and Gammel did using the same zero-range approximation used here).

It might not be out of place to point out one further motivation for carrying through such a long calculation based on such doubtful premises as the zero-range approximation, the impulse approximation, and the replacement of quantities calculated in the Born approximation by exact quantities.

The "phase shifts" which occur in an analysis of n-d elastic scattering at energies greater than 3.342 Mev must be complex numbers since inelastic scattering also takes place. We have developed a method of calculating complex phase shifts for which it is necessary to know the absorption from each partial wave by inelastic scattering. Since the connection Eq. (36a) between the inelastic and elastic cross sections is independent of the angle between $\mathbf{k}$ and $\mathbf{k}'$ and of the direction of $\mathbf{k}''$, the ratio $\sigma_{\text{in},l}/\sigma_{\text{el},l}$ is independent of l (l is the angular momentum of the partial wave) and is equal to $\sigma_{\text{in}}/\sigma_{\text{el}}$. This makes it simple to compute $\sigma_{\text{in},l}$ when σ_{in}, σ_{el}, and $\sigma_{\text{el},l}$ are known.

Thus the calculation was carried out partly in order to determine whether such a simple relation as Eq. (36a) could be in agreement with experimental evidence at low energies.

IX. ACKNOWLEDGMENTS

We are greatly indebted to Chester Kazek for his assistance in calculating the angular and energy distributions of the scattered neutrons. The angular and energy distributions of the ejected proton and neutron were calculated on the MANIAC; and Lois Cook, Don Bradford, and Elaine Felix provided much needed assistance in this calculation.

We are also indebted to Dr. Charles Critchfield, Dr. Richard Christian, and Dr. Don Dodder for valuable discussions about the principles of the calculation.

[11] B. H. Bransden and E. H. S. Burhop, Proc. Phys. Soc. (London) A63, 1337 (1950).

Angular Correlations of Gamma Rays in Ta^{181}

F. K. McGowan
Oak Ridge National Laboratory, Oak Ridge, Tennessee
(Received October 19, 1953)

The directional angular correlation of three different gamma-ray cascades in Ta^{181} have been measured with a fast delayed-coincidence scintillation spectrometer employing NaI phosphors as detectors. An interpretation of the results, in combination with measured K-shell internal-conversion coefficients, indicates that an unambiguous assignment of the angular momenta of three excited states in Ta^{181} and a classification of the gamma rays are possible. The spin sequences are as follows: for the 132-480 kev gamma-ray cascade $5/2(E2)9/2(E2+M1)7/2$ with δ_{480}, the square root of the intensity ratio of electric quadrupole to magnetic dipole radiation, equal to -1.25; for the 132–345 kev gamma-ray cascade $5/2(E2)9/2(E2+M1)9/2$ with $\delta_{345}=1.0\pm0.2$; and for the 345–135 kev gamma-ray cascade $9/2(E2+M1)9/2(E2+M1)7/2$ with $\delta_{345}=0.95\pm0.10$ and $\delta_{135}=0.5\pm0.05$. The observed angular correlation functions for the 132–480 kev and 132–345 kev cascades indicate an appreciable attenuation by perturbing interactions in the intermediate state of the nucleus by its surroundings, even in the liquid state. For polycrystalline hafnium metal and hafnium compounds, the attenuation coefficients are smaller than the "hard core" values for a static electric quadrupole interaction.

I. INTRODUCTION

THE radiations from the decay of Hf^{181} have been studied by many investigators.[1] In spite of the numerous activities produced by neutron-irradiated Hf, the general features of the decay scheme of Hf^{181} given originally by Chu and Wiedenbeck[2] are probably correct.[3] Several different sets of spins have been assigned the excited states in Ta^{181} on the basis of relative gamma-ray intensities, lifetimes, K/L ratios, and internal-conversion electron data.[4–6] It is apparent that the data and assignments are not all consistent. In the level assignments by Goldhaber and Sunyar[5] and Fan,[6] nearly all the spins ($d_{5/2}$, $d_{3/2}$, and $s_{1/2}$) predicted by the nuclear shell model were included. As we shall see from the interpretation of the results in this paper, the primitive version of the nuclear-shell model has practically no value for predicting level assignments in Ta^{181}. Fan concluded that all of the gamma-ray transitions were pure multipoles on the basis of internal conversion coefficients obtained from electron intensity measurements. These conclusions are not in accord with some recent measurements of the K-shell internal-conversion coefficients of the gamma rays in Ta^{181}.[7]

In many nuclear gamma transitions, a measurement of K-shell internal-conversion coefficients will permit an unambiguous assignment of multipole order and character of the transition. However, in some cases of a mixed multipole transition, a measured conversion coefficient will not distinguish between a parity-favored or a parity-unfavored transition.[7] If these measurements are supplemented by directional angular correlation measurements, it should be possible to infer, in addition to the spins of the states, both the character of the gamma rays and relative parity of the states. In this paper, the application of a fast delayed coincidence scintillation spectrometer to the measurement of the directional angular correlation of three different gamma-ray cascades in Ta^{181} is described. The experimental measurements and results are presented. Finally, an interpretation of the results, in combination with the K-shell internal-conversion coefficients,[7] is discussed.

II. APPARATUS

For the detection of the radiations, scintillation detectors consisting of thallium-activated sodium iodide crystals mounted on RCA type 5819 photomultiplier tubes were used. The lateral sides and front face of the crystals were covered with 30 mg/cm² of MgO and 0.010 in. of Al.[8] Fluorothene source holders with 0.025-in. wall thickness were located at the intersection of the axes of the cylindrical crystals at a distance of 7 cm from the front face of each crystal. The delayed coincidence scintillation spectrometer which uses the fast-slow coincidence method has been described previously.[7] The windows of the differential pulse-height analyzers of the coincidence spectrometer in the angular correlation apparatus are always set to include only the full-energy pulse spectrum peak of the gamma ray. Most of the data in these experiments were recorded automatically at 90°, 135°, 180°, 225°, and 270°. The time for the collection of a fixed number of coincidence counts was printed on a paper tape by a printing timer, but the angular positions were changed manually.

III. EXPERIMENTAL MEASUREMENTS AND RESULTS

Sources of Hf^{181} were prepared from samples of Hf metal and HfO_2 irradiated with pile neutrons for four

[1] *Nuclear Data*, National Bureau of Standards Circular 499 (U. S. Government Printing Office, Washington, D. C., 1950) and Supplements 1, 2, and 3. "New Nuclear Data 1952 Cumulation," Nuclear Science Abstracts 6, No. 24B (1952).
[2] K. Chu and M. Wiedenbeck, Phys. Rev. 75, 226 (1949).
[3] A. Hedgran and S. Thulin, Phys. Rev. 81, 1072 (1951).
[4] W. C. Barber, Phys. Rev. 80, 332 (1950).
[5] M. Goldhaber and A. W. Sunyar, Phys. Rev. 83, 906 (1951).
[6] Chang-Yun Fan, Phys. Rev. 87, 252 (1952).
[7] F. K. McGowan, Phys. Rev. 93, 163 (1954).
[8] C. J. Borkowski, Rev. Sci. Instr. 24, 1046 (1953).

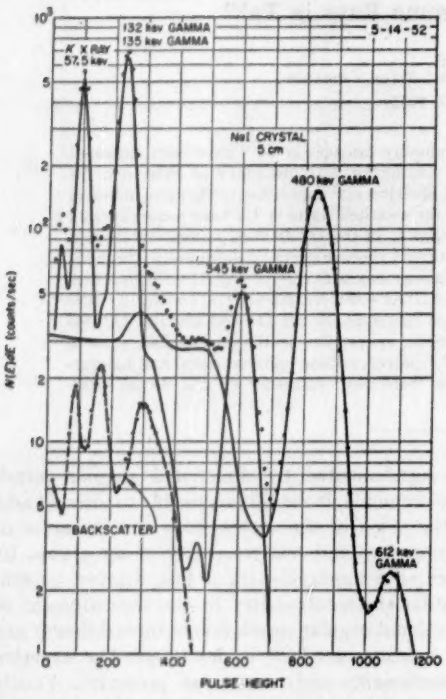

FIG. 1. A differential pulse height spectrum of the gamma radiation from $Hf^{181} \rightarrow Ta^{181}$.

weeks. The sample of HfO_2 was enriched in Hf^{180} (93.96 percent).[9] With this enrichment, the intensity of the 342-kev gamma ray of Hf^{175} in the source relative to the 345-kev gamma ray of Hf^{181} is about 4 percent. With sources of normal Hf, the intensity of the 342-kev gamma ray is equal to the 345-kev gamma-ray intensity three weeks after the end of the irradiation. A differential pulse-height spectrum of the gamma radiation from $Hf^{181} \rightarrow Ta^{181}$ is shown in Fig. 1.

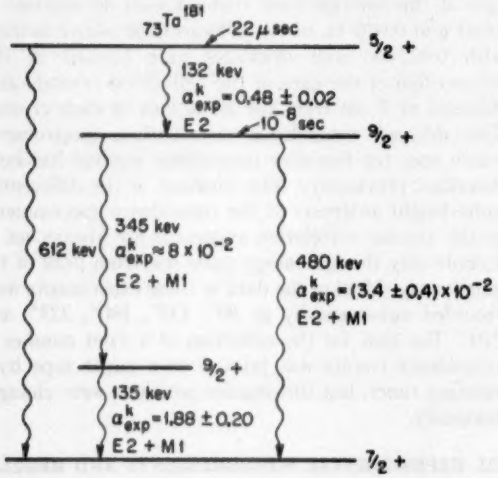

FIG. 2. Decay scheme of Ta^{181} with the spin assignments of the excited states and the character of the gamma rays.

[9] Obtained from the Isotopes Division of the Oak Ridge National Laboratory.

A. 132–480 kev Cascade

Since the intermediate state of this cascade (see Fig. 2) is metastable with a half-life of 10^{-8} sec, the initial experiments were devoted to measurements of the anisotropy, $A' = [C(\pi)/C(\pi/2)] - 1$, as a function of the chemical and physical state of the source, where $C(\pi)$ and $C(\pi/2)$ are the coincidence counting rates at $\theta = \pi$, and $\pi/2$, respectively. For this cascade, sources prepared from normal Hf may be used because coincidences from the Hf^{175} gamma-ray cascades are not detected under the conditions for which the data were collected. Since a resolving time, $2\tau_0$, of 0.18 μsec was used, the measurements represent the anisotropy of the integral angular correlation, i.e., all of the 480-kev gamma rays are detected with equal probability with regard to the time of emission of the gamma ray. In Table I, the anisotropy, A', of the 132–480 kev gamma cascade in Ta^{181} with different sources of Hf^{181} is summarized. Since Hf is a rather difficult element to work with from the standpoint of chemistry, only a few compounds were studied. The largest anisotropy found is exhibited by solution sources of Hf metal and HfO_2 taken up in concentrated HF as a solvent. Unless otherwise specified, this type of source was used in all experiments to be discussed in this paper.

A series of experiments was performed to measure the coefficients A_2 and A_4 of the terms in the expansion of the correlation function in Legendre polynomials for the 132–480 kev gamma-ray cascade. These measurements included both the integral and differential directional angular correlation, i.e., directional angular correlation as a function of the time of emission of the 480-kev transition. The operating conditions and the angular correlation coefficients, corrected for finite angular resolution,[10] are tabulated in Table II. The true coincidence counting rate for this cascade was of the order of 3 counts per sec while the random rate is about 15 percent and 1 percent of this for $2\tau_0 = 0.18$ μsec and 1.32×10^{-8} sec, respectively. From the results in Table II the anisotropy in the angular correlation of the 132–340 kev gamma-ray cascade is independent of the emission time of the 480-kev transition to within ±3.2 percent.

B. 132–345 kev Cascade

To obtain the experimental angular correlation function for the 132–345 kev gamma-ray cascade, the coincidences were collected at a time delay of 10^{-8} sec, which is sufficient to resolve all prompt coincidences due to the 345–135 kev gamma-ray cascade. Only sources of Hf^{181} prepared from irradiated samples of HfO_2

[10] M. E. Rose, Phys. Rev. **91**, 610 (1953).

enriched in Hf^{180} were used in these measurements. The window of one differential pulse height analyzer, which accepted only the full-energy pulse-spectrum peak of the 345-kev gamma ray, also accepted a small portion of the Compton recoil electron pulse distribution from the 480-kev gamma ray. Thus, the data collected represented a composite correlation function of the 132–480 kev and 132–345 kev gamma-ray cascades. The contribution from the 132–480 kev gamma-ray cascade was removed from the composite data by a direct measurement of the 132–480 kev gamma-gamma correlation at the same time delay and by a determination of the number of counts in the window of the

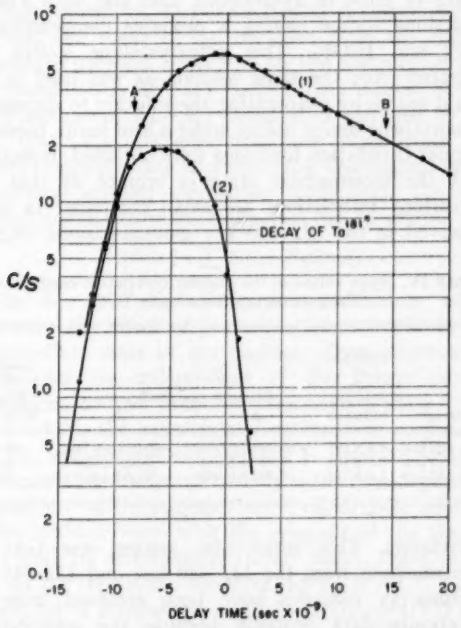

FIG. 3. Curve (1) is the number of coincidences as a function of the time delay obtained between the 132-kev and 480-kev gamma rays of Ta^{181} which represents the decay of Ta^{181*} (10^{-9} sec). Curve (2) is a time-resolution curve for prompt events obtained between annihilation gamma rays from Na^{22}.

analyzer from the 480-kev transition. A procedure for constructing the shape and intensity of the Compton recoil electron pulse distribution of the 480-kev gamma radiation from a differential pulse-height spectrum of the 512-kev gamma radiation from Sr^{85} has been described previously.[7] In this way and with a knowledge of the window width, the number of counts in the window from the 480-kev transition was obtained by (a) an integration of the differential pulse-height spectrum over the width of the window used in the angular correlation measurements and (b) a direct measurement of the counts in window with a source of Sr^{85} corrected for the difference in the intensities of the two Compton distributions.[7] Good agreement was

TABLE I. Effect of chemical and physical state of Hf sources on the angular correlation of the 132-480 kev gamma-ray cascade.

Sample	Solvent	Form of the source	Anisotropy $A'=\frac{C(\pi)}{C(\pi/2)}-1$
Hf metal		Polycrystalline Hf	$-(0.06\pm0.01)$
Hf metal	27*N* HF	0.10 ml of solution	$-(0.38\pm0.01)$
Hf metal	27*N* HF	0.10 ml of solution plus 0.10 ml $HClO_4\cdot 2H_2O$	$-(0.38\pm0.02)$
Hf metal	27*N* HF	Above source 24 hr after preparation	$-(0.31\pm0.02)$
Hf metal	27*N* HF	Above source 48 hr after preparation	$-(0.26\pm0.02)$
Hf metal	27*N* HF	Above source 21 days after preparation	$-(0.22\pm0.02)$
Hf metal	0.27*N* HF	0.10 ml of solution	$-(0.32\pm0.02)$
HfF_4	12*N* HCl	0.10 ml solution of $HfOCl_2$	$-(0.28\pm0.01)$
Hf metal		Hf extracted into a benzene layer containing TTA	$-(0.12\pm0.01)$
$Hf(OH)_4$	8*N* HNO_3	Gelatinous	$-(0.10\pm0.01)$
$Hf(OH)_4$		Dry	$-(0.09\pm0.01)$
$Hf(NO_3)_4$	8*N* HNO_3	0.02 ml of solution	$-(0.19\pm0.02)$
HfO_2	27*N* HF	0.02 ml of solution	$-(0.38\pm0.01)$
HfO_2		Polycrystalline HfF_4 and $HfOF_2$	$-(0.08\pm0.01)$

obtained between the two measurements. The composite coincidence rate was of the order of 1 count per sec while the random rate was about 3 percent of this. The contribution from the 132–480 kev cascade to the composite coincidence rate was between 20 and 30 percent of this. The results from the measurements are given in Table II.

C. 345–135 kev Cascade

In order to get a measurement of the angular correlation function of the 345–135 kev gamma-ray cascade, the following set of experiments was performed. At a time delay *A* of Fig. 3, coincidences were collected resulting from the 132–480 kev, 132–345 kev, and

TABLE II. Directional angular correlation coefficients for the 132–480 kev and 132-345 kev gamma cascades in Ta^{181}.

Cascade	Operating conditions	A_2	A_4
132–480 kev	$2\tau_0=0.18$ μsec	−0.2789	−0.0565
132–480 kev	$2\tau_0=0.18$ μsec	−0.2747	−0.0554
132–480 kev	$2\tau_0=0.18$ μsec	−0.2820	−0.0587
132–480 kev	$2\tau_0=0.18$ μsec	−0.2747	−0.0554
132–480 kev	$2\tau_0=1.32\times10^{-9}$ sec; time delay $=6\times10^{-9}$ sec	−0.2765	−0.0700
132–480 kev	$2\tau_0=1.32\times10^{-9}$ sec; time delay $=6\times10^{-9}$ sec	−0.2622	−0.0524
132–480 kev	$2\tau_0=1.40\times10^{-9}$ sec; time delay $=10^{-8}$ sec	−0.2866	−0.0487
132–480 kev	$2\tau_0=1.40\times10^{-9}$ sec; time delay $=10^{-8}$ sec	−0.2787	−0.0664
132–480 kev	$2\tau_0=1.40\times10^{-9}$ sec; time delay $=10^{-8}$ sec	−0.3061	−0.0623
132–345 kev	$2\tau_0=1.40\times10^{-9}$ sec; time delay $=10^{-8}$ sec	0.1306	0.0045
132–345 kev	$2\tau_0=1.40\times10^{-9}$ sec; time delay $=10^{-8}$ sec	0.1081	0.0529
132–345 kev	$2\tau_0=1.40\times10^{-9}$ sec; time delay $=10^{-8}$ sec	0.0909	0.0303

345–135 kev gamma-ray cascades. Since the observed angular correlation functions for the 132–480 kev and 132–345 kev gamma-ray cascades are independent of the time of emission of the 480- and 345-kev transitions, their effect in the composite correlation function was was removed by a direct measurement. That is, the coincidence rates for the 132–480 kev and 132–345 kev gamma-ray cascades were measured at a time delay B. At this time delay, these coincidence rates are equal to the contributions of the 132–480 kev and 132–345 kev cascades to the coincidence rates at time delay A. A determination of the time delays A and B used in these measurements was obtained from a measurement of time resolution curves for both prompt and delayed events. For instance, these latter experiments involved a measurement of a shift of 6×10^{-10} sec of the centroids of two time resolution curves to within $\pm5\times10^{-11}$ sec. In Fig. 3, curve (1), the number of coincidences are plotted as a function of the delay time obtained with a source of Hf^{181}. This delayed-coincidence resolution curve was recorded with the window of one analyzer accepting only the full-energy pulse spectrum peak of the 132-kev gamma ray and the window of the other analyzer accepting only the full-energy pulse spectrum peak of the 480-kev gamma ray. Without a change in the apparatus, a resolution curve for prompt events (curve 2) was obtained between annihilation gamma rays from a source of Na^{22}. However, in the angular correlation measurements the window of one analyzer included only the full-energy pulse spectrum peak of the 345-kev gamma ray. A second time resolution curve for prompt events with the window set for pulses corresponding to 345 kev was taken (not shown in Fig. 3). This curve was shifted 6×10^{-10} sec towards positive time delays with respect to curve (2) of Fig. 3. Thus, a delayed coincidence resolution curve of 132–480 kev and 132–345 kev coincidences with the window of the analyzer on the full-energy pulse spectrum peak of the 345-kev gamma ray would be shifted a like amount. In the angular correlation measurements the time delays A and B corresponded to -7.7 and 15.4×10^{-9} sec, respectively.

In addition to the contribution from the 132–480 kev and 132–345 kev gamma-ray cascades, there was another source of coincidences at a time delay of -7.7×10^{-9} sec which was not present at a time delay of 15.4×10^{-9} sec arising from the Compton scattering of the 480-kev gamma ray between the detectors. This effect was small because the position and width of the windows of the analyzers discriminated almost completely against such a source of coincidences. However, this source of coincidences was measured directly using the 512-kev gamma ray from Sr^{85}. The coincidence rate was an isotropic 10 percent effect and was removed from the composite data.

To check the influence of perturbing interactions in the intermediate state by extranuclear fields on the angular correlation of the 345–135 kev gamma-ray cascade, the measurements were taken with a solution source of HfO_2 in hydrofluoric acid and with a polycrystalline source having a probable composition of HfF_4 and $HfOF_2$. This polycrystalline source was prepared from the same solution as was used in the liquid source by evaporating the solution to dryness in a fluorothene source holder under a heat lamp. Identical angular correlation functions were obtained, indicating that the intermediate state is prompt or that the perturbing interactions are small compared to those observed in the 132–480 kev gamma-gamma angular correlation. This result also assures one that the contributions from the 132–480 kev and 132–345 kev gamma-ray cascades have been removed from the composite data properly because the contributions from these two cascades are quite different for liquid and polycrystalline sources (see Table I). The angular correlation coefficients, corrected for finite angular resolution,[10] for the 345–135 kev gamma-ray cascade are tabulated in Table III. The contribution of the 132–480 kev and 132–345 kev coincidences to the composite coincidence rates was about 20 percent, where the composite rates were of the order of 1.5 counts per sec.

TABLE III. Directional angular correlation coefficients for the 345–135 kev gamma-ray cascade in Ta^{181}.

Form of the source	Experimental Coefficients A_2	A_4
$Hf^{181}O_2$ in 27N HF as a solvent	0.2003	−0.0343
$Hf^{181}O_2$ in 27N HF as a solvent	0.2292	−0.0541
Polycrystalline HfF_4 and $HfOF_2$	0.2010	−0.0962
Polycrystalline HfF_4 and $HfOF_2$	0.2196	−0.0712
$Hf^{181}O_2$ in 27N HF as a solvent	0.1908	−0.0547
Polycrystalline HfF_4 and $HfOF_2$	0.1710	−0.0086

TABLE IV. Mean values of the angular correlation coefficients for the gamma-ray cascades in Ta^{181}.

Cascade	Number of coincidences collected	Experimental coefficients A_2	A_4	Anisotropy $A=\frac{W(\pi)}{W(\pi/2)}-1$
132–480 kev	4.3×10^6	$-(0.280\pm0.004)$	$-(0.058\pm0.003)$	−0.408
132–345 kev	6.8×10^5	0.110 ± 0.012	0.029 ± 0.014	0.192
345–135 kev	1.6×10^6	0.202 ± 0.009	$-(0.053\pm0.014)$	0.295

IV. INTERPRETATION OF RESULTS

In Table IV the directional angular correlation coefficients for the gamma-ray cascades in Ta^{181} are summarized. An analysis of these results, in combination with the measured K-shell internal conversion coefficients[7] shown in Fig. 2, indicates that an unambiguous assignment of the angular momenta of these excited states in Ta^{181} and a classification of these

gamma rays are possible. Many spin sequences must be considered in the analysis and for completeness those that are excluded by the experimental results are enumerated. In the case of the 132–480 kev gamma-ray cascade, none of the following spin sequences fit experiment: $j\pm2(E2+M3)j=7/2$, $7/2\pm1(Q+D)\times7/2$; j or $j\pm1(Q+D)j=7/2$, $7/2\pm1(Q+D)7/2$; j, $j\pm1$, or $j\pm2(E2)j=7/2$, $7/2\pm1(Q+D)7/2$, except the decay sequence $5/2(E2)9/2(E2+M1)7/2$. In this notation $j_1=j$, $j\pm1$, or $j\pm2$ and all combinations are considered. The unperturbed angular correlation coefficients,[11] A_2 and A_4, are shown in Fig. 4 as a function of $|\delta_2|$, where δ_2^2 is the ratio of squares of the reduced matrix elements and is defined as the intensity ratio (in this case) of quadrupole to dipole radiation in the 480-kev transition. The experimental values of A_2 and A_4 and the value of δ_{480} obtained from the K-shell internal-conversion coefficient on the assumption that the transition is $E2+M1$ radiation are plotted in Fig. 4. A mixture of $E1+M2$ radiation is excluded by the fact that $(A_4)_{\text{exp}}$ is larger than the unperturbed A_4. These results indicate an appreciable attenuation in the directional angular correlation coefficients. The perturbed angular correlation function can be written as

$$W(\theta)=1+\sum_\nu G_{\nu j}A_\nu P_\nu(\cos\theta),$$

where $G_{\nu j}$ are the attenuation coefficients which represent the effect of perturbing interactions in the intermediate state of the nucleus. These attenuation coefficients are independent of the nature of the transitions to and from the intermediate state.[12] For $\delta_{480}=-1.25$, the experimental attenuation coefficients are $G_{2,9/2}=0.63$ and $G_{4,9/2}=0.60$. If these attenuation coefficients are attributed entirely to the time-dependent interaction[13] of the nuclear electric quadrupole moment of the 480-kev state with the gradient of the electric field from its surroundings (liquid state), these values are not too consistent. However, for $\delta_{480}=-1.7$, a consistent set of attenuation coefficients, $G_{2,9/2}=0.735$ and $G_{4,9/2}=0.497$, is obtained. This leads to $\alpha^K(480\text{ kev})=2.8\times10^{-2}$, which is still in fair agreement with the measured value.

From this consistent set of attenuation coefficients for $\delta_{480}=-1.7$, one may make an estimate of the electric quadrupole interaction energy.[13] For $\tau_N=1.5\times10^{-8}$ sec, and if the correlation time τ_e is taken to be 10^{-11} sec, then $eQ(\partial^2V/\partial z'^2)/h$ is 1949 Mc/sec. If the electric quadrupole moment of the 480-kev state in Ta^{181} is comparable to the ground-state quadrupole moment of 6×10^{-24} cm^2, which is one of the largest quadrupole moments known, than this quadrupole interaction is probably by no means unreasonably large.

Since many spin sequences are already excluded by the 132–480 kev angular correlation function, only two

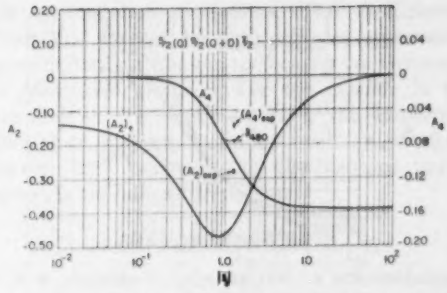

FIG. 4. Unperturbed angular correlation coefficients as a function of $|\delta_2|$ for the decay sequence $5/2(Q)9/2(Q+D)7/2$. The curve labelled $(A_2)_+$ corresponds to taking δ_2 positive. *Note added in proof.*—The curve labelled $(A_2)_+$ should read $(A_2)_-$ and corresponds to taking δ_2 negative. The change of sign is due to a misprint in Eq. (70c) of a prepublication copy of the paper referred to in reference 11.

spin sequences need be considered in the analysis of the 132–345 kev angular correlation data. These are $5/2(E2)9/2(Q+D)9/2$ and $5/2(E2)9/2(Q+D)\times7/2$. The sign of the coefficient $(A_4)_{\text{exp}}$ immediately excludes the latter spin sequence. The unperturbed angular correlation coefficients, A_2 and A_4, as a function of $|\delta_2|$ are shown in Fig. 5. The attenuation coefficients determined from the 132–480 kev angular correlation data should, of course, be the same in the 132–345 kev angular correlation and are used in the analysis to determine δ_{345}. Unperturbed experimental coefficients, $(A_\nu)_{\text{exp}}/G_{\nu,9/2}$, for $\delta_{480}=-1.25$ are plotted in Fig. 5. From the value of $(A_2)_{\text{exp}}/G_{2,9/2}$, one finds $\delta_{345}=0.93$. If the consistent set of attenuation coefficients corresponding to $\delta_{480}=-1.7$ is used, δ_{345} is equal to 1.08. A final value for δ_{345} determined from the 132–345 kev angular correlation data is 1.0 ± 0.2. This value is in good agreement with the absolute value of δ_{345} obtained from the K-shell internal-conversion coefficient on the assumption that the transition is $E2+M1$ radiation.

Although $\alpha^K{}_{\text{exp}}(135\text{ kev})$ indicates that the transition is predominantly $M1$, the uncertainty in the measurement does not exclude a small admixture of $E2$ radiation. However, the presence of a $P_4(\cos\theta)$ term in the

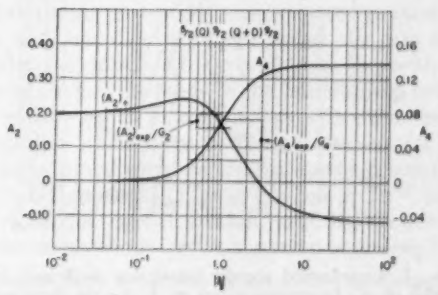

FIG. 5. Unperturbed angular correlation coefficients as a function of $|\delta_2|$ for the decay sequence $5/2(Q)9/2(Q+D)9/2$. The curve labelled $(A_2)_+$ corresponds to taking δ_2 positive.

[11] L. C. Biedenharn and M. E. Rose, Revs. Modern Phys. **25**, 729 (1953).
[12] Kurt Alder, Helv. Phys. Acta **25**, 235 (1952).
[13] A. Abragam and R. V. Pound, Phys. Rev. **92**, 936 (1953).

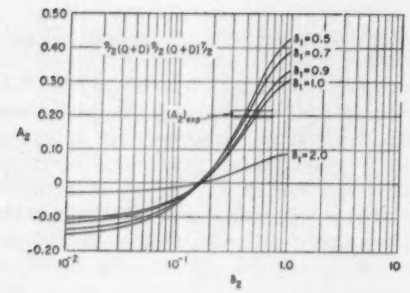

FIG. 6. Unperturbed angular correlation coefficient A_2 as a function of δ_2 for various values of δ_1 for the decay sequence $9/2(Q+D)9/2(Q+D)7/2$.

observed angular correlation function of the 345–135 kev gamma-ray cascade requires an admixture of $E2$ radiation. This is the first correlation which has been observed in which each transition is a mixture of electric and magnetic multipole radiation. An explicit form of the directional angular correlation function for a mixed-mixed gamma-ray cascade has been derived by Rose.[14] A computation of the angular correlation coefficients for a mixed-mixed gamma-ray cascade for all possible values of δ_1 and δ_2 and many possible spin sequences is quite tedious. However, in this case of the 345–135 kev gamma-ray cascade the coefficient A_4 is independent of the sign of δ_1 and δ_2 and $\alpha^K{}_{exp}$(135 kev) restricts $|\delta_2|\leq 0.5$. As a result many of the possible spin sequences, j, $j\pm1(Q+D)j=7/2$, $7/2\pm1(Q+D)\times 7/2$, that need be considered are excluded by examining the sign of the coefficient A_4. Only the spin sequence $9/2(E2+M1)9/2(E2+M1)7/2$ fits experiment. The angular correlation coefficients, A_2 and A_4, are shown as a function of δ_1 and δ_2 in Figs. 6 and 7, respectively. From the 345–135 kev angular correlation another independent determination of δ_{345} is obtained which is in good agreement with the value from the analysis of the 132–345 kev angular correlation data.

A summary of the interpretations obtained from the analysis of the angular correlation results, in combination with the measured K-shell internal-conversion coefficients, is given in Table V.

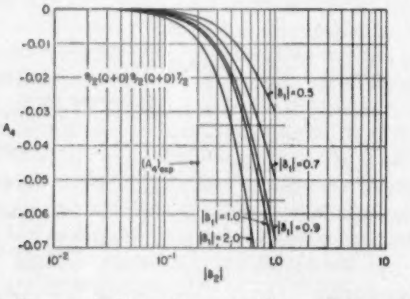

FIG. 7. Unperturbed angular correlation coefficient A_4 as a function of $|\delta_2|$ for various values of $|\delta_1|$ for the decay sequence $9/2(Q+D1)9/2(Q+D)7/2$.

[14] M. E. Rose, following paper [Phys. Rev. **93**, 477 (1954)].

Since we know within limits the unperturbed angular correlation function for the 132–480 kev gamma-ray cascade, it is of interest to examine the magnitude of the anisotropies quoted in Table I for polycrystalline Hf metal and polycrystalline HfF_4 and $HfOF_2$. The unperturbed an isotropy for $\delta_{480}=-1.25$ and -1.70 is -0.6092 and -0.5622, respectively. The "hard core" limits[13] of the attenuation coefficients for a static quadrupole interaction with an electric field having axial symmetry and with no degeneracies would lead to predicted anisotropies of -0.1335 and -0.1185 for $\delta_{480}=-1.25$ and -1.70, respectively. Taking into account the finite angular resolution of the detectors, these values become -0.1212 and -0.1069 which may be compared directly with anisotropies A' (not corrected for finite angular resolution) in Table I. The experimental values are definitely smaller than the "hard core" limit, which is a lower limit because the G_ν(lim) can be larger than $1/(2\nu+1)$ when there are degeneracies or when there are fields of lower than axial symmetry.[13]

TABLE V. Spin assignments of the excited states and character of the gamma-rays in Ta^{181}.

Cascade	Spin sequence	δ_γ
132–480 kev	$5/2(E2)9/2(E2+M1)7/2$	$\delta_{480}=-1.25^{+0.29}_{-0.22}$
132–345 kev	$5/2(E2)9/2(E2+M1)9/2$	$\delta_{345}=1.0\pm0.2$
345–135 kev	$9/2(E2+M1)9/2(E2+M1)7/2$	$\delta_{345}=0.95\pm0.1$ $\delta_{135}=0.50\pm0.05$

V. CONCLUSIONS

The ambiguity[7] that existed in the classification of the 345-kev and 480-kev gamma rays of Ta^{181} from the measured K-shell internal-conversion coefficients has been removed by the directional angular correlation measurements. Although several of the gamma rays are mixed multipoles and only perturbed angular correlation functions were observed for cascades via the 10^{-8} sec intermediate state, it appears that there exists an unambiguous assignment of the spins and relative parties of the excited states in Ta^{181}. This spin sequence is certainly different from those suggested by Goldhaber and Sunyar,[5] Goldhaber and Hill,[15] and Fan[6] in terms of the nuclear shell model. At least for Ta^{181}, the shell model could be very misleading if one considered only spin sequences covered by the shell model in the interpretation of the results presented above.

The $\log_{10}$ (ft) value of the beta transition from $_{72}Hf^{181}$ to the 22-μsec state in Ta^{181} is 7.2.[16] An assignment of $p_{3/2}$ for the ground state of $_{72}Hf^{181}$ is inferred by the nuclear-shell model which has met with considerable

[15] M. Goldhaber and R. D. Hill, Revs. Modern Phys. **24**, 179 (1952).

[16] A. M. Feingold, Revs. Modern Phys. **23**, 10 (1951).

success for ground state assignments. This assignment is consistent with a first forbidden transition as suggested by the $\log_{10}(ft)$ value.

The observed angular correlation functions for the cascades via the 10^{-8} sec intermediate state indicate an appreciable attenuation by perturbing interactions in the intermediate state of the nucleus by its surroundings even in the liquid state. Also, the measured anisotropy of the 132–480 kev angular correlation for polycrystalline Hf metal and Hf compounds indicates that the attenuation coefficients are smaller than the "hard core" values for a static electric quadrupole interaction.

Since the expected unperturbed angular correlation functions are known with fair certainty, the cascades 132–480 kev and 132–345 kev provide a good case in which to study the influence of electric and magnetic fields on angular correlations. The coefficients of $P_2(\cos\vartheta)$ and $P_4(\cos\vartheta)$ for both cascades are reasonably large so that all attenuation coefficients can be measured with reasonable precision. For the cascade in Cd^{111}, which follows the decay of In^{111}, the unperturbed coefficient of $P_4(\cos\vartheta)$ is rather small ($A_4=-0.001$). However, Hf^{181} possesses the disadvantage that Hf compounds are difficult to prepare.

ACKNOWLEDGMENTS

It is a pleasure for the author to acknowledge his appreciation to B. H. Ketelle of the Chemistry Division for preparing some of the compounds used in these experiments and to Dr. M. E. Rose for several stimulating discussions concerning the interpretation of the results.

PHYSICAL REVIEW VOLUME 93, NUMBER 3 FEBRUARY 1, 1954

Mixed Gamma-Mixed Gamma Angular Correlation

M. E. Rose
Oak Ridge National Laboratory, Oak Ridge, Tennessee
(Received October 19, 1953)

The γ-γ correlation in which both radiations are mixed, with arbitrary admixture ratios, is discussed.

RECENT experimental evidence indicates that the occurrence of mixed γ radiation (E_L+M_{L+1} or M_L+E_{L+1}) is not uncommon.[1] There are also several cases in which the intensity ratio δ^2 of 2^{L+1} pole to 2^L pole is of order unity (δ^2 neither $\ll 1$ nor $\gg 1$). Therefore it should not be surprising if a γ-γ cascade occurs in which both radiations are mixed. Indeed, the 345–135 kev cascade in Ta^{181} appears to be such a case[2] (both radiations $E2+M1$) and for both $\delta^2\sim 1$. For this reason it seems worth while to give the correlation function applicable in such cases.

The general theory of angular correlation covers the case of an arbitrary γ-γ cascade, and the required correlation function can be obtained from the general formula given by several authors.[3] For the cascade $j_1(L_1,L_1')j(L_2,L_2')j_2$ with δ_i^2 equal to the intensity ratio of $2^{L_i'}$ to 2^{L_i} poles, the correlation function is

$$W(\vartheta)=\sum_\nu P_\nu(\cos\vartheta)\{F_\nu(L_1j_1j)+\delta_1^2F_\nu(L_1'j_1j)$$
$$+2\delta_1(-)^{j_1-j-1}[(2j+1)(2L_1+1)(2L_1'+1)]^{\frac{1}{2}}G_\nu(L_1L_1'j_1j)\}$$
$$\times\{F_\nu(L_2j_2j)+\delta_2^2F_\nu(L_2'j_2j)+2\delta_2(-)^{j_2-j-1}$$
$$\times[(2j+1)(2L_2+1)(2L_2'+1)]^{\frac{1}{2}}G_\nu(L_2L_2'j_2j)\}. \quad (1)$$

The normalization is to $\langle W(\vartheta)\rangle_{\text{Av}}=(1+\delta_1^2)(1+\delta_2^2)$. In practice $L_1'=L_1+1$ and $L_2'=L_2+1$. The coefficients F_ν and G_ν are defined in BR [Eqs. (69b) and (70d)] and are tabulated in Tables I and II of that reference. Of course, when spin coupling is present the correlation function is modified in the usual way by inserting attenuation factors Q_ν which are independent of the properties of the emitted radiations.[4]

The presence of two adjustable intensity ratios (the signs of δ_1 and δ_2 may be $\pm$) makes the case under consideration somewhat overly flexible. However, it is quite likely that the study of the mixed-mixed correlation will be useful in conjunction with other experimental data which serve to fix one of the δ's (or δ^2's). For example, there may be internal conversion data for one of the transitions or, as in the case of Ta^{181}, one of the radiations participates in another cascade the correlation for which can be measured separately.[2]

[1] The evidence has been summarized by R. M. Steffen, Indiana Conference on Nuclear Spectroscopy and the Shell Model (unpublished).

[2] F. K. McGowan, preceding paper [Phys. Rev. **93**, 471 (1954)].

[3] For small admixture ratios the explicit correlation function was given by S. P. Lloyd, Phys, Rev. **83**, 716 (1951). For the more general case one obtains the desired result by using, for example, Eq. (64) in L. C. Biedenharn and M. E. Rose, Revs. Modern Phys. **25**, 729 (1953), referred to as BR. We use the notation of this reference. Further references to the general formulation are to be found in that paper.

[4] K. Alder, Helv. Phys. Acta **25**, 235 (1952); A. Abragam and R. V. Pound, Phys. Rev. **92**, 936 (1953). These authors denote the attenuation coefficients by G_ν.

Annihilation of Positrons in Condensed Materials*

T. A. Pond†
Palmer Physical Laboratory, Princeton University, Princeton, New Jersey
(Received October 9, 1953)

Approximately ½ percent fewer positrons are found to annihilate with emission of two photons in amorphous solids and benzene than do so in metals. Fused quartz shows the same effect when compared with crystalline quartz. Assuming, with Bell and Graham, that this defect is due to triplet positronium in the amorphous materials, the mean life of triplet positronium against three-photon annihilation in the various materials is found to be approximately that observed in gases. Addition of a free radical to the benzene partially quenches the difference between pure benzene and metals. High-purity crystalline germanium is found to be similar to crystalline quartz.

BELL and Graham[1] find that, while the annihilation of positrons in all types of solids is predominantly two-photon, the mean lives of approximately 30 percent of those stopped in amorphous solids are an order of magnitude longer than the remainder, or of those stopped in crystalline or metallic solids (all of the order of 10^{-10} sec). They suggest that the anomalously rapid annihilation in the latter cases is due to the formation of positronium before the positrons are thermalized. The slow component in amorphous materials they attribute to collision-induced two-photon annihilations of triplet positronium. If this is correct, three-photon annihilation will occur in a fraction of the slow component given by the ratio of its observed lifetime to the lifetime of triplet positronium in the solid against three-photon annihilation. Thus in Teflon,[1] using the free-space triplet mean life, 1.4×10^{-7} sec,[2,3] 0.8 percent of the positrons should annihilate with three photons.

The apparatus shown in Fig. 1 was used to detect this effect by comparing the two-photon annihilation rates in an amorphous solid and a material in which the slow component is absent. The small-diameter source (~0.2-mC Na^{22}) was mounted between aluminum or plastic foils of about 75-percent positron-transmission. The source was enclosed by identical sandwiches of the two substances under comparison, each layer thick enough to stop the positrons. The two NaI(Tl) scintillators were mounted on 1-inch Lucite light-pipes. This, combined with the sharp collimation of the beam to one of the crystals, made the system relatively insensitive to positron range differences. Reversing the sandwiches thus changed the stopping material without appreciably altering the geometry or the effects of positron range and γ-ray scattering. The coincidence circuit gave a resolving time of 3×10^{-7} sec. The high stability required was obtained by careful electronic regulation and very frequent reversals of the sandwiches. A directly measured correction for the annihilations in the source itself was applied to all data.

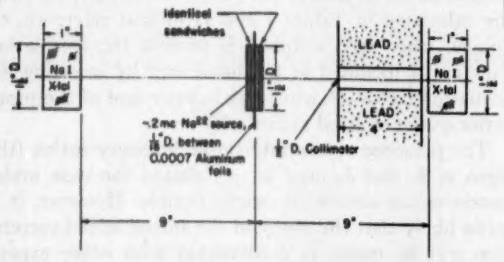

FIG. 1. Apparatus for comparing the two-photon annihilation rates of positrons in different materials.

The results of various comparisons of two-photon annihilation rates are shown in Table I. The consistency of the various comparable triads of ratios is within the probable errors, which were computed from the scatter in the many individual determinations. The quartz data agree with the observation of a slow component only in the fused-quartz lifetime.[1] Comparison of duraluminum, magnesium, Polystyrene, and Teflon shows consistent defects in the two-photon rates in the latter two amorphous solids. These effects cannot be attributed to density or Z differences. This possibility was further eliminated by placing sufficient aluminum to stop the positrons between the source and the sandwiches. Reversal of the sandwiches then showed no effect outside of statistics. Sandwiches of copper and duraluminum annihilators gave a two-photon coincidence-rate ratio, Cu to Al, of 0.9994 $\pm$0.0010. The effect is in the direction that would be produced by annihilation in flight and is ⅓ the estimated size.[4] Since this was by far the greatest range of Z compared, no correction is made in the other data for this effect.

The slow-component fractions and lifetimes of reference 1 can be combined with these data to give the mean life of triplet positronium against three-photon

* This work was supported by the U. S. Atomic Energy Commission and the Higgins Scientific Trust Fund. Some of these results were reported at the 1953 Washington Meeting, American Physical Society [Phys. Rev. 91, 455 (1953)].
† Present address: Department of Physics, Washington University, St. Louis 5, Missouri.
[1] R. E. Bell and R. L. Graham, Phys. Rev. 90, 644 (1953).
[2] A. Ore and J. L. Powell, Phys. Rev. 75, 1696 (1949).
[3] M. Deutsch, Phys. Rev. 82, 455 (1951).
[4] H. A. Bethe, Proc. Roy. Soc. (London) 150, 129 (1935).

TABLE I. Ratio of two-photon coincidence rates in various pairs of materials. Densities (g/cm³): Teflon 2.14, Polystyrene 1.18, magnesium 1.74, duraluminum 2.90.

0.050-in. Duraluminum/0.050-in. Teflon = 1.0055 ± 0.0008	0.070-in. Magnesium/0.050-in. Teflon = 1.0064 ± 0.0009	0.050-in. Duraluminum/0.070-in. Magnesium = 0.9997 ± 0.0010
0.050-in. Duraluminum/0.125-in. Polystyrene = 1.0056 ± 0.0011	0.070-in. Magnesium/0.125-in. Polystyrene = 1.0058 ± 0.0006	
0.050-in. Teflon/0.125-in. Polystyrene = 1.0007 ± 0.0008		
0.070-in. Crystal quartz/0.060-in. Fused quartz = 1.0058 ± 0.0012	0.060-in. Duraluminum/0.060-in. Fused quartz = 1.0057 ± 0.0009	0.060-in. Duraluminum/0.070-in. Crystal quartz = 1.0007 ± 0.0008

annihilation in the amorphous materials: Teflon, $(1.7\pm0.8)\times10^{-7}$ sec; Polystyrene, $(1.5\pm0.7)\times10^{-7}$ sec; fused quartz, $(0.9\pm0.5)\times10^{-7}$ sec. The proximity of these values to the free-space triplet lifetime seems fortuitous, since considerable corrections for the polarizability of the materials and for possible compressive effects of the lattices would be required before a meaningful comparison could be made.

Samples of crystalline germanium of 45 ohm-cm resistivity[5] were compared with copper. The coincidence-rate ratio, Cu to Ge, was 0.9991±0.0009. If exchanges with the conduction electrons were to cause the observed absence of an effect due to thermal positronium comparable to that found in amorphous materials, the destruction cross section by these electrons, as estimated from the resistivity,[6] would have to exceed 10^{-12} cm². Thus it is more probable that this absence places germanium in the class with crystalline sulfur and quartz.[1]

Annihilations in benzene were studied using sandwiches of thin-windowed (0.0006-in. Al) cells, each $\frac{1}{8}$ in. thick. Two-photon coincidence rates in pure benzene, and in benzene in which the free radical, diphenyl picryl hydrazyl (DPH), had been dissolved, were compared. The energy required to invert the unpaired electron in DPH has been shown to be negligible compared to thermal energies.[7] The results are the open circled points in Fig. 2. The point at DPH concentration 5.1 mg/cm³ of benzene is at the limit of solubility of DPH. The boxed point is the ratio of the two-photon coincidence rate in magnesium to that in pure benzene: 1.0072±0.0008. This is taken to be the ratio of infinitely concentrated DPH in benzene to pure benzene. This interpretation is supported by a measurement of the coincidence-rate ratio of magnesium to the 3.40 mg DPH/cm³ of benzene sample: 1.0044 ±0.0012. The difference between the magnesium comparisons of pure and 3.40 mg DPH/cm³ benzene is then equal, within statistical uncertainty, to the directly determined coincidence-rate ratio for the 3.40 mg DPH/cm³ to pure benzene: 1.0033±0.0011. Assuming thermal triplet positronium of mean life 2×10^{-9} sec, the calculated curve of Fig. 2 corresponds to a destruction cross section of 1.1×10^{-17} cm², or an electron-exchange cross section of 4.4×10^{-17} cm².

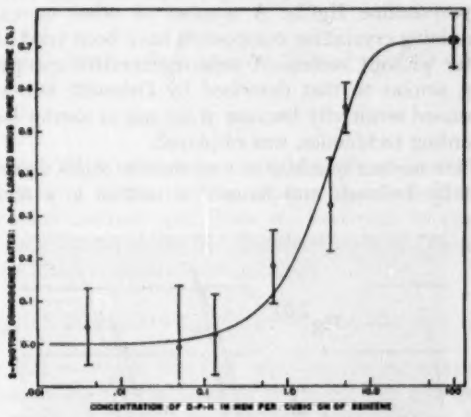

FIG. 2. Percent excess of two-photon annihilations in solutions of diphenyl picryl hydrazyl in benzene over those in pure benzene (circled points). The boxed point is the ratio of magnesium to pure benzene.

This is close to the value found for exchange in nitric oxide.[8]

These results are consistent with the hypothesis of Bell and Graham. In particular, the work with DPH seems to give direct evidence for the presence of triplet positronium in benzene.

It is a pleasure to thank R. H. Dicke for valuable discussions.

[5] S. M. Christian, Radio Corporation of America Laboratories, Princeton, New Jersey, kindly supplied the germanium.

[6] W. Shockley, *Electrons and Holes in Semiconductors* (D. Van Nostrand Company, Inc., New York, 1950), p. 246.

[7] Hutchison, Pastor, and Kowalsky, J. Chem. Phys. **20**, 534 (1952).

[8] M. Deutsch, Massachusetts Institute of Technology Laboratory of Nuclear Science and Engineering Quarterly Progress Report, August 31, 1951 (unpublished).

Nuclear Quadrupole Resonance of Hg^{201}†

H. G. Dehmelt, H. G. Robinson,* and Walter Gordy
Department of Physics, Duke University, Durham, North Carolina
(Received October 16, 1953)

Five nuclear quadrupole resonance lines have been observed in polycrystalline $HgCl_2$. From their frequencies, the magnitudes of the quadrupole coupling constants $eQq_{zz}(Hg^{201}) = 720$ Mc/sec and $eQq_{zz}(Cl^{35}) = 44.3$ Mc/sec were evaluated. Comparison of the Cl^{35} coupling constant in $HgCl_2$ with that known for the free Cl atom from atomic beam experiments facilitates the discussion of the molecular structure. A quadrupole coupling constant of 1000 Mc/sec per p electron in the $6s6p$ configuration of free Hg is deduced from the Hg^{201} coupling in $HgCl_2$. This value can be directly compared with the coupling of the $6s6p$, $^3P_2$ HgI term, $eQq_{zz}(Hg^{201}, p_z) = 780$ Mc/sec, which is equivalent to the value of the quadrupole parameter $B = 0.27 \times 10^{-2}$ cm^{-1} known from optical hfs investigations. Whereas a standard analysis of the hfs of the $^3P_2$ term had given $Q(Hg^{201}) = 0.5 \times 10^{-24}$ cm^2, a discrepant value $Q(Hg^{201}) = 0.2 \times 10^{-24}$ cm^2 was obtained from the $^1P_1$ term. Our results yield a value 0.6×10^{-24} cm^2, in fair agreement with the larger value found for the $^3P_2$ term.

FIVE rf magnetic absorption lines caused by nuclear quadrupole resonance of the mercury isotope Hg^{201} occurring with its natural abundance of 13.2 percent and the chlorine isotopes $Cl^{35,37}$ have been observed in polycrystalline $HgCl_2$. A number of other mercury-containing crystalline compounds have been tried also, so far without success. A superregenerative spectrometer, similar to that described by Dehmelt[1] but with increased sensitivity because of the use of narrow-band recording techniques, was employed.

Pure nuclear quadrupole resonance in solids detected first by Dehmelt and Kruger[2] is treated in a review article by Dehmelt.[3] No previous detection of such resonance for Hg^{201} has been reported, although a theoretical prediction of the Hg^{201} resonance frequency in $HgCl_2$ was published by Bassompierre[4] after our measurements on this substance had been made. His predicted frequency, 230 Mc/sec, is appreciably lower than the actual frequency, 360 Mc/sec, observed in the present work (see Fig. 1). Bassompierre mentions the unpublished observations of two Cl^{35} lines at 22.26 and 22.07 Mc/sec by Buyle-Bodin and Monfils. These independent observations are in essential agreement with our measurements of the Cl^{35} frequencies.

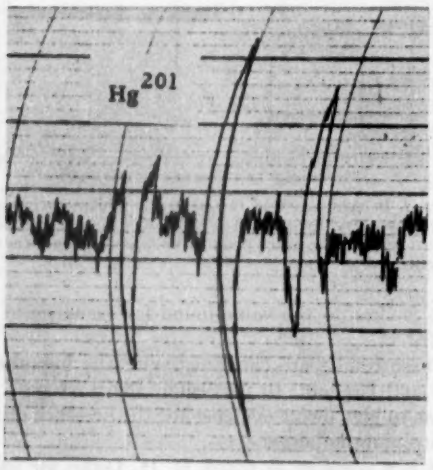

FIG. 1. Recording of the Hg^{201} nuclear quadrupole resonance line at 354 207±60 kc/sec in $HgCl_2$ at room temperature. Besides the strong main line in the center, two strong and two weaker super-regeneration satellites appear on the recording; the distance between the lines is equal to the quench frequency of 200 kc/sec. Capacitive frequency modulation and detection of the second harmonic of the modulation frequency with a time constant of about 0.15 sec were used.

The frequencies of the lines observed in $HgCl_2$ are given in Table I. They have been assigned on the assumption that only one line is expected per isotope and lattice site, as the spin of the Hg^{201} isotope as well as that of the Cl isotope is $\frac{3}{2}$. The known quadrupole moment ratio of the Cl isotopes served to identify the Cl lines. Distinct, nearly linear, Cl−Hg−Cl molecules are discernible in the crystal.[5] However, the two Cl atoms do not have identical surroundings in the lattice. This explains the occurrence of two closely spaced lines for each Cl isotope.

For further interpretation of the experimental results, we shall make the assumption that the $HgCl_2$ crystal is made up of essentially separate Cl−Hg−Cl molecules. The justification is provided by the smallness of the heat of evaporation, 14 kcal/mole, as compared with the heat of formation of the molecule from the elements, about 110 kcal/mole, and by the fact that the Cl coupling is almost identical to that found[6] for Cl in gaseous CH_3HgCl (eQq for $Cl^{35} = -42$ Mc/sec). Furthermore, the observed coupling in solid $HgCl_2$ (44 Mc/sec) is that expected for free $HgCl_2$ from the relation of the number of unbalanced p electrons to the electronegativity difference of the bonded atoms.[7]

† The work has been supported by a contract with the Ordnance Corps, Department of the U. S. Army.
* National Science Foundation Fellow.
[1] H. G. Dehmelt, Z. Physik **130**, 356 (1951).
[2] H. G. Dehmelt and H. Kruger, Z. Physik **129**, 401 (1951).
[3] H. G. Dehmelt, Am. J. Phys. (to be published); see also R. V. Pound, Phys. Rev. **79**, 685 (1950).
[4] M. A. Bassompierre, Compt. rend. **236**, 596 (1953).
[5] C28 type, *Strukturbericht* (Akademische Verlagsgesellschaft M.B.H., Leipzig, 1937), Vol. III, p. 23.
[6] W. Gordy and J. Sheridan, J. Chem. Phys. (to be published).
[7] W. Gordy, J. Chem. Phys. **19**, 792 (1951).

The treatment of the electronic structure of the molecule which will yield information on the nuclear quadrupole moment of Hg^{201} is facilitated by the following: the nuclear quadrupole coupling constant per unbalanced atomic p electron for the free Cl^{35} atom is known from atomic beam experiments[8] to be -109.746 Mc/sec, and the Cl^{35} coupling of -44.3 Mc/sec found in $HgCl_2$ can be compared with it. To describe the structure of the molecule, we assign a localized molecular orbital occupied by two electrons with antiparallel spins to each of the two Hg—Cl bonds. These molecular orbitals can be expressed approximately as

$$\Psi_{HgCl}=a(1/\sqrt{2})(s\pm p_z)_{Hg}\mp b(p_z)_{Cl}. \quad (1)$$

The $(s\pm p_z)_{Hg}$ denotes a hybrid consisting of equal parts of normalized real atomic $6s$ and $6p$ eigenfunctions of the mercury atom; $(p_z)_{Cl}$ is a corresponding Cl $3p$ eigenfunction. The a and b are positive real numbers; and the upper signs hold for one bond, the lower ones for the other bond. One should expect Ψ_{HgCl} to represent the true molecular orbital best in the immediate neighborhood of the nuclei. Fortunately, the quantities we are interested in, namely, the gradients of the electric fields at the sites of the nuclei, are mainly determined by the parts of the molecular electron cloud near to the nuclei, where the approximation is best. If we try to normalize Ψ_{HgCl}, we get

$$1=\int \Psi_{HgCl}^2 dV=a^2+b^2+2ab \times\left[\mp\int (1/\sqrt{2})(s\pm p_z)_{Hg}(p_z)_{Cl}dV\right], \quad (2)$$

where the factor in brackets, the "overlap integral," is a positive quantity and may have a value as large as 0.5. However, the approximation of the true molecular orbital by atomic orbitals is necessarily rather crude in the overlap region. The experimental evidence for elemental molecules like Cl_2 [9] and Br_2,[10] of which the quadrupole couplings agree within 1 percent with the couplings found by atomic beam methods for the free chlorine[8] and bromine[11] atoms, does not support the thinning out of the electron cloud around the nuclei which would be demanded by normalization in this form. Taking away electronic charge from the neighborhood of the nuclei in order to build up a concentration of charge in the overlap region of the bonding orbitals should result in an increase in the molecular quadrupole coupling over that in the free atoms, which is observed for neither Cl_2 nor Br_2.

For the reasons given above, we assume the normalizing conditions, $a^2+b^2=1$, to apply for the present purposes. Now b^2 is connected with the expression for

[8] V. Jaccarino and J. G. King, Phys. Rev. **83**, 471 (1951).
[9] R. Livingston, J. Chem. Phys. **19**, 803 (1951).
[10] H. G. Dehmelt, Z. Physik **130**, 480 (1951).
[11] J. G. King and V. Jaccarino (private communication).

TABLE I. Nuclear quadrupole resonance frequencies in $HgCl_2$.

Isotope	Lattice site	Temperature °C	Frequency of resonance lines kc/sec	Line width kc/sec	Frequency ratio of Cl isotopes
Hg^{201}		-186 ±4	361 966 ±40	75	
		26.1±0.5	354 207 ±60	50	
Cl^{35}	I	30 ±0.5	22 230.3±0.8	1	1.26887
Cl^{37}			17 519.7±0.9		±0.0001
Cl^{35}	II	30 ±0.5	22 050.5±0.7	1	1.2688
Cl^{37}			17 378.9±1		±0.0001

the contribution of *one* bonding electron to the molecular field gradient at the Cl nucleus:

$$q_{zz}(\text{Cl, bond})=\int \Psi_{HgCl}^2 r_{Cl}^{-5}(3z_{Cl}^2-r_{Cl}^2)dV. \quad (3)$$

Here r_{Cl}, z_{Cl} are the coordinates of one bonding electron with respect to the Cl nucleus as origin. Approximately, we obtain from (1) and (3)

$$q_{zz}(\text{Cl, bond})\approx b^2\int (p_z)_{Cl}^2 r_{Cl}^{-5}(3z_{Cl}^2-r_{Cl}^2)dV \quad (4)$$

$$=b^2 q_{zz}(\text{Cl, } p_z),$$

where $q_{zz}(\text{Cl, } p_z)$ stands for the field gradient caused by an atomic p electron in the substate $m_l=0$ and with decoupled electron spin. Now we have still to relate the contribution of *one* bonding electron, q_{zz}(Cl, bond), to the total molecular field gradient:

$$q_{zz}(\text{Cl, molecule})=2q_{zz}(\text{Cl, bond})-2q_{zz}(\text{Cl, } p_z). \quad (5)$$

The factor two of the first term on the right arises because there are two bonding electrons. The last term is a result of the four nonbonding p electrons on the Cl atom. By combining Eqs. (4) and (5) we get

$$eQq_{zz}(Cl^{35}, \text{molecule})/eQq_{zz}(Cl^{35}, p_z)=2(b^2-1). \quad (6)$$

With the molecular Cl^{35} coupling observed here, -44 Mc/sec, and the atomic beam value of -110 Mc/sec, Eq. (6) yields $b^2=0.8$. Effects of possible sp hybridization of the Cl orbitals have been neglected here in view of the rather approximate nature of the whole analysis. Also any reduction of the molecular field gradient against that in the neutral Cl atom, because of an excess negative charge on the Cl atom, has been considered negligible.

Now we shall relate the field gradient per unbalanced p electron in the $6s6p$ configuration of neutral Hg, for which optical hfs data are available, with that in the $HgCl_2$ molecule. The contribution of one electron in the one Hg—Cl bond is given by

$$q_{zz}(\text{Hg, bond})=\int \Psi_{HgCl}^2 r_{Hg}^{-5}(3z_{Hg}^2-r_{Hg}^2)dV. \quad (7)$$

This yields, approximately,

$$q_{zz}(\text{Hg, bond}) \approx (a^2/2)q_{zz}(\text{Hg}, p_z). \quad (8)$$

The meaning of the symbols corresponds to the meaning of those used in the Cl formulas. The molecular field gradient is simply four times as large since there are two electrons in each of the two bonds and no nonbonding electrons on the Hg atom,

$$q_{zz}(\text{Hg, molecule}) = 2a^2 q_{zz}(\text{Hg}, p_z). \quad (9)$$

With the value of b^2, 0.8, obtained from the Cl coupling, the normalization $a^2+b^2=1$ gives $a^2=0.2$. This value of a^2 suggests that the bonding creates an electronic charge deficit of $1.2e$ on the Hg atom, so that it is essentially ionized to Hg^+. In terms of the valence bond resonance concepts, the contributing structures

TABLE II. Values for quadrupole coupling and quadrupole moment of Hg^{201}.

Experimental method	State of $6s6p$ configuration of Hg atom	Measured[a] coupling eQq_{zz} Mc/sec	Coupling per unbalanced p-electron $eQq_{zz}(p_z)$ Mc/sec	Quadrupole moment Q 10^{-24} cm^2
Optical atomic hfs	$^3P_2$	390	780	0.5
	$^1P_1$	168	312	0.2
Nuclear quadrupole resonance	bonded in $HgCl_2$	720	1000	0.6

[a] The optical hfs values given in this column are the B values of references 12 and 15 converted with the help of the formula given in footnote 14. While these couplings depend upon the term for which they are obtained, the $eQq_{zz}(p_z)$ values calculated from them should be the same; this, however, is not the case.

would be

Cl^-Hg^+-Cl	40 percent
$Cl-Hg^+Cl^-$	40 percent
$Cl^-Hg^{++}Cl^-$	20 percent.

Since the fine structure doublet separation of the $6p$ electron of HgII (Hg^+) is considerably larger than that in the $6s6p$ configuration of neutral HgI, we have to correct for this positive charge. It is $\Delta\nu(6p, \text{HgII}) = 9322$ cm^{-1}, whereas $\Delta\nu(6p, \text{HgI})$, after correction for spin-orbit interaction of unlike electrons, is 5622 cm^{-1}.[12] Therefore, we assume a fractional increase of $(9322/5622)-1=0.66$ per positive elementary charge on the Hg atom. Applying this correction, we obtain

$$\begin{aligned} q_{zz}(\text{Hg, molecule}) &= (2a^2[1+0.66\times 4(0.5-a^2)])q_{zz}(\text{HgI}, p_z) \\ &= 0.72 q_{zz}(\text{Hg}, p_z). \end{aligned} \quad (10)$$

[12] H. Schuler and T. Schmidt, Z. Physik **99**, 285 (1936).

[Note that q_{zz}(Hg, molecule) is not particularly sensitive to variation of a^2.] With the measured Hg^{201} coupling in $HgCl_2$, $eQq_{zz}(Hg^{201}, \text{molecule}) = 720$ Mc/sec, Eq. (10) yields for the atomic coupling constant per p electron in the $6s6p$ configuration of HgI,

$$eQ^{201}q_{zz}(\text{HgI}, p_z) = 1000 \text{ Mc/sec}.$$

This is expected to be equal to the quadrupole coupling measured for the $^3P_2$ state of the $6s6p$ configuration which is independent of the type of coupling between the two electrons.[13] The value $B=0.27\times 10^{-3}$ cm^{-1} for the quadrupole hfs parameter obtained from optical hfs measurements then is equivalent[14] to

$$eQ^{201}q_{zz}(\text{HgI}, p_z) = 780 \text{ Mc/sec}.$$

This value, when q_{zz}(HgI, p_z) is calculated from the doublet separation and small relativistic corrections are applied, leads[12] to

$$Q(Hg^{201}) = 0.5\times 10^{-24} \text{ cm}^2,$$

whereas our results indicate that

$$Q(Hg^{201}) = 0.6\times 10^{-24} \text{ cm}^2.$$

Recently the optical hfs of the $^1P_1$ term also has been investigated.[15] Its analysis is somewhat more complicated because the type of coupling between the two electrons enters into it. The calculations give

$$Q(Hg^{201}) = 0.2\times 10^{-24} \text{ cm}^2.$$

Our result favors the value obtained from the $^3P_2$ term. The difference between the optical value of 0.5 and our value of 0.6, however, cannot be considered significant. The various results are summarized in Table II.

Murakawa and Suwa report significant differences between the ratios of the magnetic hfs parameters A of the Hg^{199} and Hg^{201} isotopes depending upon the term for which they are measured. Since only the magnetic moment of the Hg^{199} isotope is known from nuclear magnetic resonance measurements, an experiment is under way to determine the Hg^{201} magnetic moment from the Zeeman effect of the nuclear quadrupole resonance line.

[13] H. Kopfermann, *Kernmomente* (Akademische Verlagsgesellschaft, Leipzig, 1940), Sec. 13.

[14] The hfs parameter B and the atomic quadrupole coupling constant for the aligned state $m_J=J$ are related in this way:

$$eQq_{zz}(m_J=J) = (8/3)B\cdot I(2I-1)\cdot J(2J-1).$$

In the discussion of p bonds, it is convenient to use the atomic coupling for a p electron with decoupled electron spin in the substate $m_l=0$ instead of $m_l=1$ which is double the latter one. Further, it can be shown that the coupling constants for a $p_{\frac{1}{2}}(m_J=J=\frac{1}{2})$ electron and a $p(m_l=l=1)$ electron with decoupled spin are the same.

[15] K. Murakawa and S. Suwa, J. Phys. Soc. Japan **5**, 429 (1950).

Cross Sections for the Reactions D(d,p)T, D(d,n)He³, T(d,n)He⁴, and He³(d,p)He⁴ below 120 kev*

W. R. Arnold,† J. A. Phillips, G. A. Sawyer, E. J. Stovall, Jr., and J. L. Tuck
Los Alamos Scientific Laboratory, University of California, Los Alamos, New Mexico

(Received August 31, 1953)

These cross sections were measured by the process of passing a deuteron beam into a thin gas target contained behind a thin window of evaporated silicon monoxide. The energy loss in the window was measured by a deceleration technique. Charged particles from the reactions were observed at 90° in the laboratory system with proportional counters. Some results are as follows: for the reaction D(d,p)T, by use of the angular distribution reported by Wenzel and Whaling, the total cross section σ is 15.4 mb with a probable error of 3.2 percent at 100-kev incident deuteron energy; $\sigma=0.629$ mb±5 percent at 25 kev. For the reaction D(d,n)He³, $\sigma=15.2$ mb±3.2 percent at 100 kev; $\sigma=0.592$ mb±5 percent at 25 kev. The sum of these two cross sections follows a Gamow function below 50 kev. For the reaction T(d,n)He⁴, isotropy in the center-of-mass system being assumed, σ shows a peak value of 4.95 barns±2.8 percent at 107 kev; at 40 kev, $\sigma=0.72$ barn±3.2 percent; at 19 kev, $\sigma=0.045$ barn±5 percent; below 19 kev, σ follows a Gamow function. For the reaction He³(d,p)He⁴ with isotropy assumed, $\sigma=16$ mb±3 percent at 93 kev; $\sigma=0.124$ mb±5 percent at 36 kev; and σ follows a Gamow relation below 100 kev.

INTRODUCTION

A DETERMINATION of the reaction cross sections for the reactions D(d,p)T, D(d,n)He³, T(d,n)He⁴, and He³(d,p)He⁴ at deuteron bombarding energies below 120 kev was considered to be of general interest. At the time this investigation was started in the fall of 1950, the D(d,p)T cross section was known below 100-kev deuteron bombarding energy from thick target measurements[1] by use of an uncertain value for the stopping power of heavy ice and from a brief advance report of results using a thin target method.[2] The cross section for the neutron branch depended upon the same measurements and upon the branching ratio measurements of Pepper,[3] McNeill, Thonemann and Price,[4] and McNeill and Keyser.[5] Recently, the reaction cross section and angular distribution for D(d,p)T have been reported on more fully by Moffatt, Roaf, and Sanders,[6] who provide independent data, and by Wenzel and Whaling,[7] whose work was carried out in coordination with the present work.

The cross section for the reaction T(d,n)He⁴ has been measured previously[8] but the results were not entirely consistent with measurements at higher energies.[9] Several measurements of the cross section for the reaction He³(d,p)He⁴ have been made,[10] but no measurement at deuteron energies below 100 kev was known to the authors.

The measurement of these cross sections presented several problems which are peculiar to the low-energy range. These may be summarized as follows:

(1) σ is a steep function of energy. At 20 kev, a 100-v change in energy causes a 2 percent change in cross section for T(d,n)He⁴, while at 10 kev, 100 v of change cause a 6 percent change in cross section.

(2) The stopping power of most substances passes through a maximum in the region of 50- to 100-kev deuteron energy so that, combined with (1) above, even monatomic layers of contamination on targets can introduce significant error.

(3) At the time when these considerations arose (1950), the stopping power for likely target materials was certainly not known to within ±20 percent at these low energies.

(4) The cross sections for the charge-exchange reactions

$$D^+ + X^0 \rightarrow D^0 + X^+$$

and

$$D^0 + X^0 \rightarrow D^- + X^+$$

become large when the velocity of the beam deuteron approaches the velocity of an orbital electron, which is the energy range of the present experiment. The charge-exchange cross section approximates molecular dimensions (10^{-16} cm²). Thus the beam current measurement can be complicated by exchange with the normally negligible residual gas in high vacuums.

When this experiment was being planned, it seemed that thick target methods were ruled out by (3), since

* Work performed under the auspices of the U. S. Atomic Energy Commission.

† Now at Schlumberger Oil Well Prospecting Company, Ridgefield, Connecticut.

[1] Bretscher, French, and Seidl, Phys. Rev. **73**, 815 (1948).

[2] Sanders, Moffatt, and Roaf, Phys. Rev. **77**, 754 (1950).

[3] T. P. Pepper, Can. J. Research **27A**, 143 (1949).

[4] McNeill, Thonemann, and Price, Nature **166**, 28 (1950).

[5] K. G. McNeill and G. M. Keyser, Phys. Rev. **81**, 602 (1951).

[6] Moffatt, Roaf, and Sanders, Proc. Roy. Soc. (London) **A212**, 220 (1952).

[7] W. Wenzel and W. Whaling, Phys. Rev. **88**, 1149 (1952).

[8] E. Bretscher and A. P. French, Phys. Rev. **75**, 1154 (1949); D. L. Allan and M. J. Poole, Proc. Roy. Soc. (London) **A204**, 500 (1951).

[9] T. W. Bonner, Proc. Harwell Nuclear Physics Conf. (September, 1950); Argo, Taschek, Agnew, Hemmindinger, and Leland, Phys. Rev. **87**, 612 (1952).

[10] Baker, Holloway, King, and Schreiber, U. S. Atomic Energy Commission Declassified Report No. 2189, 1948 (unpublished); J. Hatton and G. Preston, Nature **164**, 143 (1949); Lillie, Bonner, and Conner, Phys. Rev. **86**, 630 (1952); Yarnell, Lovberg, Stratton, and Stratton, Phys. Rev. **88**, 158 (1952).

in such cases

$$\sigma=(dY/dE)\cdot(dE/dx).$$

On the other hand, thin targets could be made so that the error introduced by an uncertainty in dE/dx by, say, 20 percent introduced an inappreciable error. This result called for a target density in the region of 10^{-5} g/cm², and, in such a case, we obtain the cross section

$$\sigma=N/(n_1n_2l\Omega),$$

where N = number of disintegrations, n_1 = number of bombarding particles from the beam current, n_2 = target density in particles/cm², l = beam-path length in the target, and Ω = the counting system solid angle. Although it was perfectly possible to obtain films of, say, tritiated ice or tritiated zirconium of sufficient thinness, the problem of estimating n_2 in such films seemed unattractive for an absolute experiment, and, in addition, backscattering of particles from the support which such films require was a further complication.

A thin target consisting of several centimeters of path in gas at 1-mm pressure seemed ideal for precise determination of n_2 and l, n_2 being defined by the readily measurable gas composition, pressure, and temperature and l being large enough for direct measurement.

Such gas targets are commonly operated by admitting the beam through an aperture from the high-vacuum region and disposing of the outflowing gas by a fast differential pumping system. However, at the low energies reason (4) rules against this: the pressure in the antechamber, combined with the large charge-exchange cross section, makes the beam current measurement untrustworthy. Moffatt, Roaf, and Sanders[6] avoided this difficulty by abandoning measurement of beam current and measuring beam power calorimetrically.

The solution adopted here was to interpose a thin window between the gas target and the high vacuum. The problem then became one of knowing the energy loss in this window with sufficient accuracy and correcting for the scattering and straggling in the beam produced by the window.

Although in principle it was possible to correct for any degree of scattering and straggling, such corrections impaired the reliability of the results, and in designing this experiment our aim was to keep the total magnitude of such corrections below the planned probable error of 6 percent. The requirement that the scattering correction be less than 6 percent proved equivalent to the requirement that half the beam be included within an angle of 5°, or, for 20-kev deuterons in window material with an atomic number in the region of 13(Al), a thickness of 10 μg/cm². The straggling correction depended on the curvature of the σ *vs* E curve and was most serious at the lowest energies. We found, for example, from the measured σ *vs* E curve for $T(d,n)He^4$ that at 20 kev, if $\Delta\sigma$ is the error, $\Delta\sigma/\sigma=0.4\delta(E)/E$, where $\delta(E)$ is the root-mean-square deviation in the straggling. Hence $\delta(E)$ must be <3 kev for a correction <6 percent.

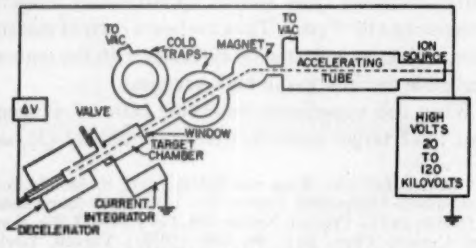

FIG. 1. Cross-section apparatus.

It proved possible to develop windows fulfilling these requirements. They consisted of evaporated films of SiO, of thickness about 7 μg/cm² (not known precisely), with capability to withstand 1-mm gas pressure on a diameter of 8 mm, of substantial durability under bombardment by 1 μa of deuterons, and with sufficient constancy in thickness. A characteristic film has a mean energy loss of 5 kev at 30 kev, straggling of ±0.4 kev, and average scattering angle of 5°. The films have been discussed elsewhere.[11]

The beam current was determined by measurement of the charge accumulated by the target chamber and window as a whole. The beam-defining apertures and guard rings were maintained in a high vacuum so that the guard rings could be effective and the charge exchange small.

Other considerations taken into account in the experiment were:

(1) Error in the target density, n_2, produced by (*a*) Temperature differences between manometer and target chamber; (*b*) Local change of gas density produced by heating which resulted from passage of the beam or from contact with the hot window. This effect might be detected by an apparent change of σ with a change in beam current. None was found.

(2) Repassage of beam particles through the target volume caused by backscattering in the rear of the the chamber. This effect turned out to be negligible on account of the combination of steep fall-off of σ with E and the small angle subtended by the target volume from the rear of the chamber.

EXPERIMENTAL PROCEDURE

Accelerator

The high voltage, supplied by a conventional Cockcroft-Walton voltage doubler, was fed through a surge resistor to a box containing the probe and focus voltage supplies. The center of the two-gap accelerating tube was tied through surge resistors to the half-voltage point.

The apparatus is shown schematically in Figs. 1 and 2.

The high voltage was measured by means of a series

[11] G. A. Sawyer, Rev. Sci. Instr. 23, 604 (1952).

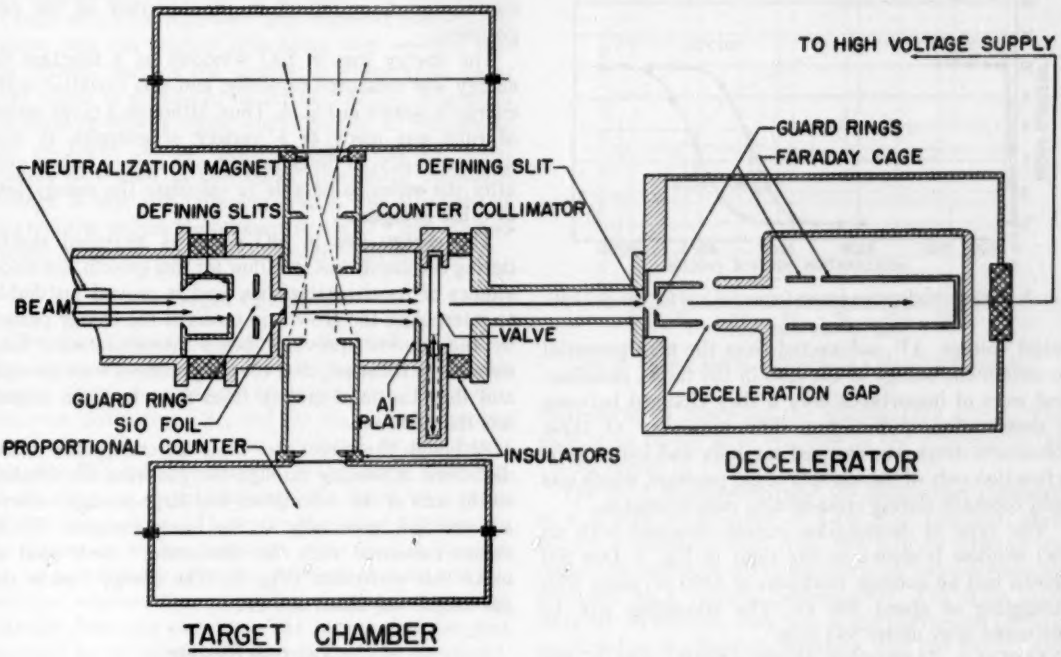

FIG. 2. Target chamber and decelerator for the measurement of low-energy cross sections.

of 30 high-voltage resistors (Shallcross Type 505) of 5 megohms each, rated at 7.5 kv each. The total resistance of the resistors was measured in the Los Alamos Standards Laboratory and fell well within the 0.1 percent accuracy specified by the manufacturer. A type *K* potentiometer measured the potential drop across a 1000-ohm standard resistor at the bottom of the stack. The high-resistance stack was checked for linearity and corona by applying twice the working gradient. No deviation exceeding 0.05 percent was found.

The top of the high-voltage measuring stack was connected to the anode of the ion source (which had the potential closest to that of the ions). The ions started out at a potential slightly below this, and the necessary correction will be discussed under "Energy of Beam in Target."

The ripple on the high voltage, when all parts of the apparatus were functioning, was calculated to be 1 v/kv and checked by measurement to be of this order.

The high voltage was held constant manually, and it was possible to hold the drifts in the high voltage to less than 50 v.

The rf-ion source was copied from the Oxford source.[12] This ion source with plasma focusing and magnetic excitation yielded more than 90 percent of the total beam as D^+.

[12] Thonemann, Moffat, Roaf, and Sanders, Proc. Phys. Soc. (London) **61**, 483 (1948).

Energy of Beam in Target

The energy of the ion beam in the target chamber differed from the energy represented by the high-voltage measurement by (a) a small-voltage drop (~100 v) between the ion-source anode and the ion plasma in the ion source, (b) a much larger loss of energy (~5 kev) in the thin window of the target chamber, and (c) an energy loss of the order of 300 ev in the target gas. A decelerator was used to measure the energy of the ions after they passed through the window and, hence, to measure (a) and (b), whereas (c) was evaluated by a separate measurement of dE/dx in the target gas.

A gate valve at the rear of the target chamber could be opened when the chamber was evacuated to allow the beam, degraded in energy by the thin window, to pass into the decelerating gap of the decelerator of Fig. 2. The accelerator high voltage conveniently provided the main deceleration potential. Since the deuterons of the beam had lost some energy, this voltage was too high and had to be reduced an amount ΔV equal to the amount of energy lost in the film before the deuterons were able to reach the collector of the decelerator.

In operation, deceleration curves such as those in Fig. 3 were obtained. The "no-foil" curve shows that the energy spread of the beam was about 100 ev, and the average energy of the ions about 100 ev below the high-voltage reading. Since these amounts were included in the deceleration curve which was obtained with an SiO window in place, they were included in the differ-

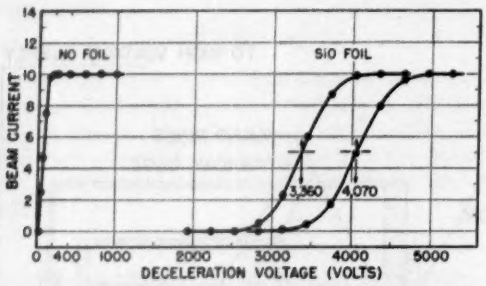

FIG. 3. Typical deceleration curves for no foil and for two SiO foils.

ential voltage, ΔV, subtracted from the high potential to obtain the energy of the ions in the target chamber, and were of importance only if they changed between a deceleration and a run. The constancy of these ion-source drops was checked carefully and found to be a function only of the ion-source gas pressure, which was held constant during cross-section measurements.

The type of deceleration curves obtained with an SiO window is shown to the right in Fig. 3. One foil shown had an average thickness of 3360 ev, along with straggling of about 500 ev. The straggling will be discussed later under SiO foils.

During a deceleration of the positive ions in the measurement of the thickness of a foil, any negative ions caused by charge exchange in the window would, of course, be accelerated. Thus, when the voltage of the decelerator was such as to collect no positive ions, the reading on the electrometer would be an indication of the number of negative ions. The small negative current observed was assumed constant throughout the deceleration since there was no change in the electrometer reading as the deceleration voltage was varied (except when positive ions were being collected).

Although charge equilibrium would be expected to have been reached in the window, there was a possibility that the negative ions did not have the same energy distribution as the positives. We removed this doubt by running the machine at low incident voltages, reversing the polarity of the voltage supply in the decelerator, and decelerating the negative ions. When corrections were made for the biasing voltages on the guard rings, the loss of energy resulting from passage of both positive and negative ions through the foil was found to be the same.

The decelerator received and measured the energy of only that part of the beam within a cone of semiangle 0.8°. The more widely singly-scattered particles had on the average less energy both from having traversed more window thickness and from nuclear scattering through a larger angle. At 25-kev deuteron energy and with an SiO window having a mean energy loss of 5 kev, these effects amounted to 15 and 20 ev, respectively, at a scattering angle of 6° and were thus not serious. However, at lower energies, they became serious and contributed to a fall-off in the accuracy of the experiment.

The energy loss in SiO windows as a function of energy was measured carefully, and this variation with energy is shown in Fig. 4. Thus, although a given series of runs was made at a variety of energies, it was necessary only to decelerate at one energy before and after the series to be able to calculate the energy loss at other energies.

The energy loss in SiO windows increased slowly during bombardment: to allow for this growth, we made studies of its characteristics, and it proved justifiable to interpolate the growth in terms of the charge passed by the window, provided beam intensities were held reasonably constant, that the gas pressures were normal, and that the total growth from start to finish stayed less than 500 ev.

Although the target was thin, the energy loss of the deuterons in passing through the gas from the window to the axis of the collimators was large enough to need a correction, especially at the lower energies. dE/dx values measured with the decelerator[13] were used to make this correction (Fig. 5). The energy loss in the gas target was about 300 ev.

Vacuum System

After passing through the probe channel of the ion source, the beam passed through two focusing gaps used to obtain the desired diffuse beam on the target-chamber window. It then proceeded through two accelerating gaps to an analyzing magnet which deflected the desired mass-2 beam through 30°. The operating pressure in this part of the system ran at about 12×10^{-6} mm Hg. The beam then passed through an 8-in. section of $\frac{3}{4}$-in. diameter tubing held at liquid

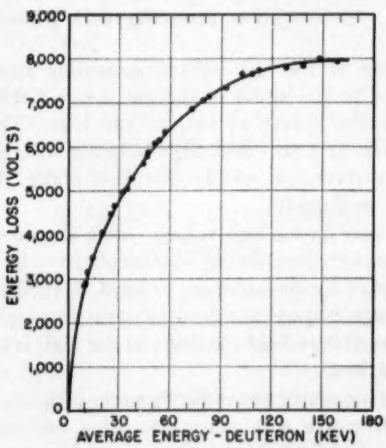

FIG. 4. Energy loss as a function of energy for a typical SiO foil. The curve shown is the average of many SiO foils normalized to a typical energy-loss scale.

[13] J. A. Phillips, Phys. Rev. **90**, 532 (1953).

air temperatures and with $\frac{3}{8}$-in. diameter diaphragms at each end. This liquid-air trap removed condensable vapors near the window. The beam then emerged into the "clean" part of the apparatus where great pains were taken to eliminate, as far as possible, sources of condensable vapors which would lead to an increase in the thickness of the target-chamber window. Lead gaskets were used in this region instead of Neoprene O-rings. A side arm pumping system was also used at this point to reduce the pressure to 4×10^{-6} mm Hg and thereby reduce the amount of beam neutralization.

Target Chamber

The target chamber is shown in detail in Fig. 2. The beam entered at the left through the deflecting magnet (used to measure neutralization), the 5-mm diameter collimating hole, and the electron-suppressing guard ring. The beam then impinged on the 8-mm diameter SiO entrance window of the target chamber. At the right the target chamber was closed by a vane-type valve which could be opened to admit the beam to the decelerator. Glass insulators were used to insulate the target chamber from the accelerator tube and decelerator whereas thin mica rings insulated the target chamber from the counters. The target chamber was insulated so the beam current to it could be measured.

Target Atoms

Since a gas target was used, the calculation of the number of target atoms per cubic centimeter depended upon measurement of pressure, temperature, and purity.

A. Pressure

Measurement of pressure was complicated by the requirement that condensable vapors in the target chamber be kept to an absolute minimum, for reasons that will be discussed below under "Purity." This condition ruled out the use of oil or mercury manometers in direct contact with the tritium gas in the target chamber. Instead, a Consolidated Engineering Company micromanometer was used to measure tritium gas pressure. The micromanometer was not absolute and had to be calibrated with a fluid manometer.

The micromanometer has a diaphragm which is deformed by the pressure to be measured, changing the capacity between the diaphragm and a fixed plate. This capacity is in one arm of a capacity bridge which may be balanced by placing a standard variable condenser in another arm and adjusting to balance. This micromanometer was designed originally to work over the pressure range 1–100μ, and modification of the bridge was required for the pressure range 1–1000μ. As ordinarily used, the manometer was found to be subject to zero shifts and temperature effects. It proved necessary to follow a strict procedure in applying pressures to the gauge to eliminate the zero shifts and to control the temperature of the gauge to 0.1°C by a thermostat to eliminate the temperature effects. The measuring bridge gave readings of the pressure in the 1000-μ region to 1 part in 1000.

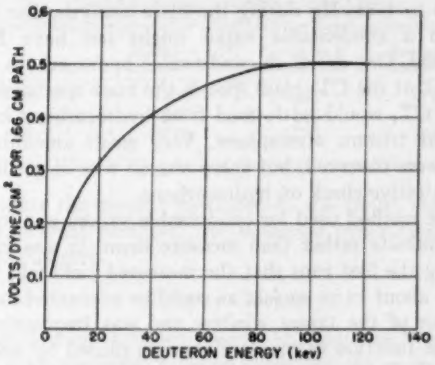

FIG. 5. Energy loss in hydrogen as a function of energy.

The fluid manometer used for calibration consisted of a U-tube constructed of 1-cm bore precision glass tubing. Collimated light from two sources striking the respective menisci were viewed through two microscopes mounted on a vertical cathetometer. The cross hairs were set on the first dark line of the diffraction pattern produced at the fluid-air interface, and the setting was very reproducible. The calibration of the gauge was checked periodically throughout the series of runs and did not vary by more than ±0.3 percent throughout. It was necessary to calibrate at the end of a day's running so that the manometer vapor introduced into the gauge during calibration could be pumped out overnight. Analytical quality butyl phthalate was used as the manometer fluid, and, as a precaution against errors of composition, its density was measured over a range of temperatures with a standardized pycnometer.

B. Temperature

Two measurements were made: (1) the temperature of the target chamber body as read by a thermometer, and (2) the temperature difference between the gas and the chamber body as measured by a fine wire thermocouple in the gas. Use of the thermocouple was discontinued after no temperature difference was observed between gas and chamber body.

C. Purity

Attainment of purity proved to be one of the major difficulties in the experiment. Tritium was supplied from a small uranium reservoir and after use was collected into another uranium trap. About one-third of the gas from each filling was taken as a sample for analysis. The tritium gas was analyzed on a mass spectrometer before and after use. However, the gas sample was collected at about 800 to 1000 dynes/cm² (about $\frac{3}{4}$-mm Hg) and then compressed by a Toeppler

pump to 1 cm Hg during the mass analysis. For this reason a condensable vapor might not have been detected. One check on condensable hydrocarbons was to look at the CT_4 mass spot in the mass spectrometer since CT_4 would be formed from hydrocarbons in an ionized tritium atmosphere. Very small amounts of CT_4 were observed, but there was no way of getting a quantitative check on hydrocarbons.

The method used for condensable vapors was to try to eliminate rather than measure them. It was found during the first runs that the measured yield fell, with time, about twice as fast as could be accounted for by growth of the target window and was frequently an erratic function of pressure changes caused by adding or removing part of the tritium. The difficulty was apparently caused by an increase in the partial pressure of oil vapors which started building up the moment the target chamber was isolated. Such a rise in pressure could be noted on the Consolidated gauge and was much worse immediately after calibration (which involved exposing the systems to fluid vapors).

The pressure rise was reduced to less than 0.3 dyne/cm^2 min at pressures of less than 5 dynes/cm^2 in the target chamber by pumping at least overnight after calibration. Although this rate of rise extrapolates to predict a 2 percent drop/hr in cross section, the drop actually observed was in almost all cases less, indicating that vapor reached an equilibrium pressure.

The gas entered the target as 99.5 percent tritium plus 0.5 percent hydrogen, and the mass analysis after running was usually about 96 percent T, 2 percent H, 2 percent N. The absence of oxygen to go with the nitrogen indicated that air had entered the chamber during the run instead of during handling of the sample and that the oxygen had been converted to T_2O in the ionized target gas. The T_2O could not be measured on the mass spectrometer because of background difficulties. However, water vapor (T_2O) was not a cause of error since the number of tritium atoms per unit pressure is the same as for T_2 gas. The increase in hydrogen was undoubtedly the result of exchange of tritium with hydrogen in hydrocarbons on the chamber walls. At very low deuteron energies (below 20 kev), the rate of hydrogen contamination of the tritium was greatly increased, possibly because of widely scattered beam particles striking the Gelva (polyvinyl acetate) used to anchor the collimator slits in the collimator tube. This was one of several factors which decreased the accuracy of the very low energy measurements.

Thin SiO Window

The foil window at the entrance to the target chamber served to contain the target gas and to admit the deuteron beam to the target chamber.

The SiO windows used in the experiment were 5–10 μg/cm^2 (about 300 atoms thick) and were made by evaporating SiO onto a thin Zapon backing which was later removed by bombarding the film in the ion beam of the accelerator. The SiO films have been discussed more fully elsewhere.[11] The windows were glued to their holders with dextrose. In the early stages of this work much difficulty was experienced with windows rupturing when exposed to the beam under vacuum conditions, for example, during a deceleration. The rupturing was completely overcome by having a supply of electrons ($\sim$1 μa) available from a small tungsten filament during deceleration operations. With gas in the chamber, no auxiliary electron supply was required.

Electrons were removed from the window both by being pushed out by the beam and by charge exchange. When the window became charged in this way, the beam was decelerated in approaching it. Thus dE/dx was changed, as was the energy loss. By measuring this change in stopping power, and referring to Fig. 4, it was possible to estimate the potential reached by the window with the electron supply cut off. In one such case the potential was calculated to be 2 kv. The rupturing was attributable to electrostatic forces.

The scattering and straggling in these films which depended on the nature of the film had a bearing on the interpretation of the results of this experiment. For if the observed straggling of, say, 300 ev in a film of stopping power 3.5 kev were the result of variations in thickness, it would follow that the least scattered deuterons would have come from the thin parts of the film and on the average would have had more energy than the more widely scattered deuterons. Since the decelerator on which the energy measurements are based accepted only a narrow pencil of deuterons (estimated semiangle 0.8°), a systematic overestimate of the mean deuteron energy could have arisen. There were two independent reasons for believing that such did not occur.

The films were prepared by evaporating SiO from a tungsten coiled filament onto a Zapon film about 15 cm away in vacuum. Knowledge of the actual density of the films, in SiO atoms/cm^2, was based only on the geometry of the evaporation of a weighed amount of SiO and on weighing extensive films deposited on mica sheets. These methods agreed to 20 percent and gave an estimated surface density of $1.4\pm0.2\times10^{17}$ SiO molecules/cm^2.

The following types of film can be identified:

(1) Pure SiO films, prepared by washing off the Zapon backing. These are tiresome to prepare.

(2) SiO films in which the Zapon backing had been largely driven off by deuteron bombardment.

(3) SiO films of either of the above types, in which appreciable ($\sim$500 ev) growth had occurred presumably because of the deposition of carbon films from the residual gas.

When decelerator current was plotted against energy for films of type (1), a Gaussian distribution was obtained; in fact, the data appeared as straight lines

when plotted on probability paper. These films showed an essentially constant relation between energy loss ΔE and straggling S, where S is defined as the interval which includes half the current on either side of the peak of the Gaussian distribution.

Films of type (1) gave the data shown in Table I (30-kev incident deuterons). If the film were uniform, and if the straggling arose from the fluctuations in the number of interactions N, then

$$S/\Delta E=0.674N^{\frac{1}{2}}/N,$$

and $N=(0.674\Delta E/S)^2$. This equation gives for the three films above, $N=181$, 158, 153, and the energy per interaction $\epsilon=39$, 33, 31 ev, respectively.

Such consistent behavior suggests that the films were uniform. Films of type (2) are believed to retain a skeleton of decomposed Zapon, which contributes one-third of the total stopping power. These films were similar to type (1) films in their relation between stopping power and straggling. Type (3) films showed a larger $S/\Delta E$, suggesting that the matter deposited under bombardment in vacuum took place nonuniformly. Preferential deposition of this kind has been observed on electron microscope preparations.

Nonuniform carbon deposition has, however, negligible effect on the angular distribution since, for Rutherford scattering, the probability of scattering at θ into $d\theta$ is

$$P(\theta)d\theta=\frac{2Ne^4Z^2z^2}{E^2}\frac{d\theta}{\theta^3},$$

and most of the scattering is due to Si, the highest Z component. Secondly, an energy analysis of the scattered deuterons has been made by Wenzel (private communication) on a type (2) film using a double focusing spectrometer. Most of the intensity in such an analysis can be identified as due to Rutherford scattering from the Si and O components with only a minor contribution from carbon and an extremely faint trace from tungsten.

Scattering in these films was essentially plural for the least scattered one-third and single for the remainder. A calculation of the scattering in one of these films, by use of the theory of Molière, and a Fermi-Thomas screening model for Si gave a calculated scattering of 40 percent of the observed scattering; and this is all that can be expected, considering the modest resolving power of the scattering measurements (1.2°) and the uncertainty in density and composition of the films.

Beam Measurement

In the design of this experiment, all particles incident upon the thin window passed through target gas which was visible from the proportional counters. Thus the whole target chamber could be made a Faraday cup, and the chamber was insulated for this purpose. To translate the current measured to the target chamber into incident particles, the following precautions had to be observed.

TABLE I. Energy straggling in SiO films.

	Energy at ½ intensity, ev	Energy at ¼ intensity, ev	Energy at ⅛ intensity, ev
Film I	7450	7080	6740
Film II	5420	5140	4870
Film III	5020	4770	4500

A. Stray Currents

Conduction between target chamber and ground was made negligible by good insulation. An appreciable electron current was found from electrons knocked out of the window by the incoming beam and was suppressed by a negatively charged electrode between window and beam defining slit. The potential required to suppress the current was proportional to the energy of the incoming beam; 1 v of suppression per kilovolt of beam energy reduced it to zero. Deuterons scattered from the window or through the window from the interior of the target chamber were not suppressed and, by calculation, should have been quite negligible.

Undesired parts of the incoming beam were removed by the 5-mm defining slit, the edges of which were sharp enough so that there should have been no appreciable scattering at these energies. Another source of spurious charge was the selective collection of ions produced by the beam in the residual gas of the vacuum outside the window. The target chamber was held 10 to 16 v positive with respect to ground by the current integrator and hence could have collected negative ions from this region. However, the electron suppression electrode was 100 to 150 v negative and could have collected positive residual gas ions from the same regions so that the positive current to it gave an indication of the error from this source. The error was quite negligible.

B. Corrections for Neutralized Deuterons in the Beam

A fraction of the beam incident on the target was neutral because of charge exchange with the residual gas between the analyzer magnet and the target chamber and gave reactions although not registering as charge. These reactions were estimated by the following procedure. The incident beam was adjusted until it was as steady as possible, and three runs were made. The first and third were made with both charged and neutral particles entering the target whereas the second was made with the charged particles being deflected by a neutralization magnet placed directly in front of the SiO window so that only neutrals entered the target. From the data for these three runs the percentage of neutrals was calculated. The accuracy of the measurement of the percentage of neutrals was only 10 percent, but, since the neutral beam was, at most, 5 percent of the charged beam, there was an uncertainty

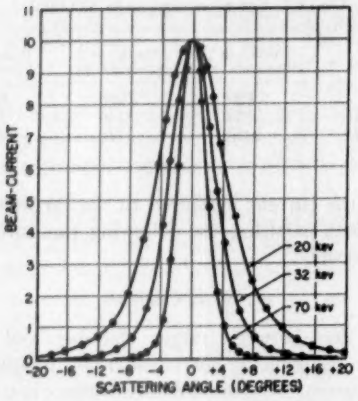

Fig. 6. Scattering in a typical SiO foil.

of less than ±0.5 percent in the total number of incident particles. At the lower energies, some negatively charged deuterons were produced; and these, if numerous, could have produced an error in the beam current measurement since the method used to detect neutrals did not indicate the presence of negatives. Measurements of the positive-neutral-negative ion proportion as a function of energy, made in another apparatus, show that the energies do not go low enough in these correction measurements for the negative ions to reach significant proportions.

C. Beam Contamination

For most of the data the mass-2 beam spot was used, and contamination of the D^+ ions with H_2^+ had to be considered. However, as discussed previously, the ion source used produced over 10 times as many atomic ions as molecular ions, and, since the deuterium used contained less than 1 percent hydrogen, the H_2^+ should have been less than 0.1 percent of the mass-2 beam. A check was made by the comparison of cross sections obtained with mass-2 and mass-4 beam; these checked within the statistical error of 1.5 percent.

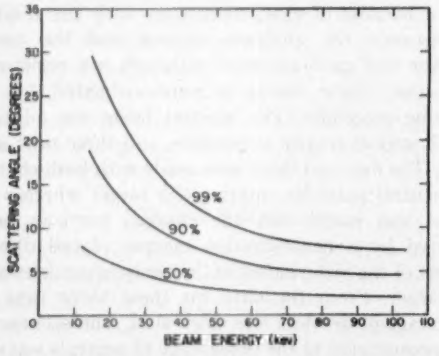

Fig. 7. Semiangle of the cones which include 50, 90, and 99 percent, respectively, of the total beam transmitted by a typical SiO window, as a function of energy.

D. Current Integrator

The current integrator used has been described elsewhere.[12] It was not absolute and so was calibrated with a potentiometer and a standard resistor. Calibrations had an internal consistency of 0.3 percent. The absolute accuracy appears to be 0.5 percent for currents above 0.04 μa.

Counters

The counters were 2 in. in diameter and 6 in. long, with a 2-mil central wire, and were operated in the proportional region. Two counters were used simultaneously (with separate amplifiers and scalers) for the purpose of detecting and correcting for possible asymmetry in the primary beam. For one counter, the geometry was sensitive to such displacements. Both counters were used throughout the experiments, although the counts observed in the two channels turned out to be the same, within statistics, so that the double counter precautions were not needed.

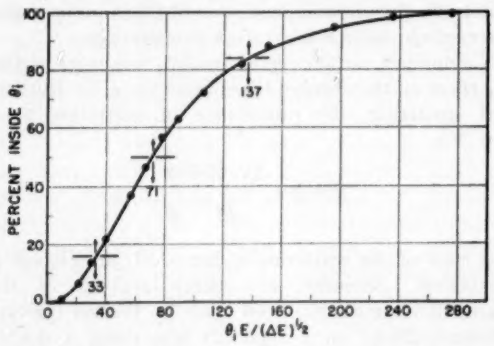

Fig. 8. Percent of beam included inside angle θ.

The counter window thicknesses and gas pressures were adjusted to give optimum discrimination for the wanted particles in each case and are given under the separate headings.

Counter pulses from each counter were recorded separately with a Los Alamos Model 101 amplifier and a Model 750 scaler. At a counting rate of 1000/sec, counting losses caused by the insensitive time of the amplifier after a pulse amounted to 0.2 percent. Accordingly, counting rates were always kept below 1000/sec.

Solid Angle and Path Length

The length of the paths of the deuterons in the target volume and the solid angle of acceptance of the counters at different points along the path varied with the inclination and orientation of the beam path. It was first necessary to know the angular distribution of the beam as scattered by the window. This was measured by building an apparatus in which an arm with a small

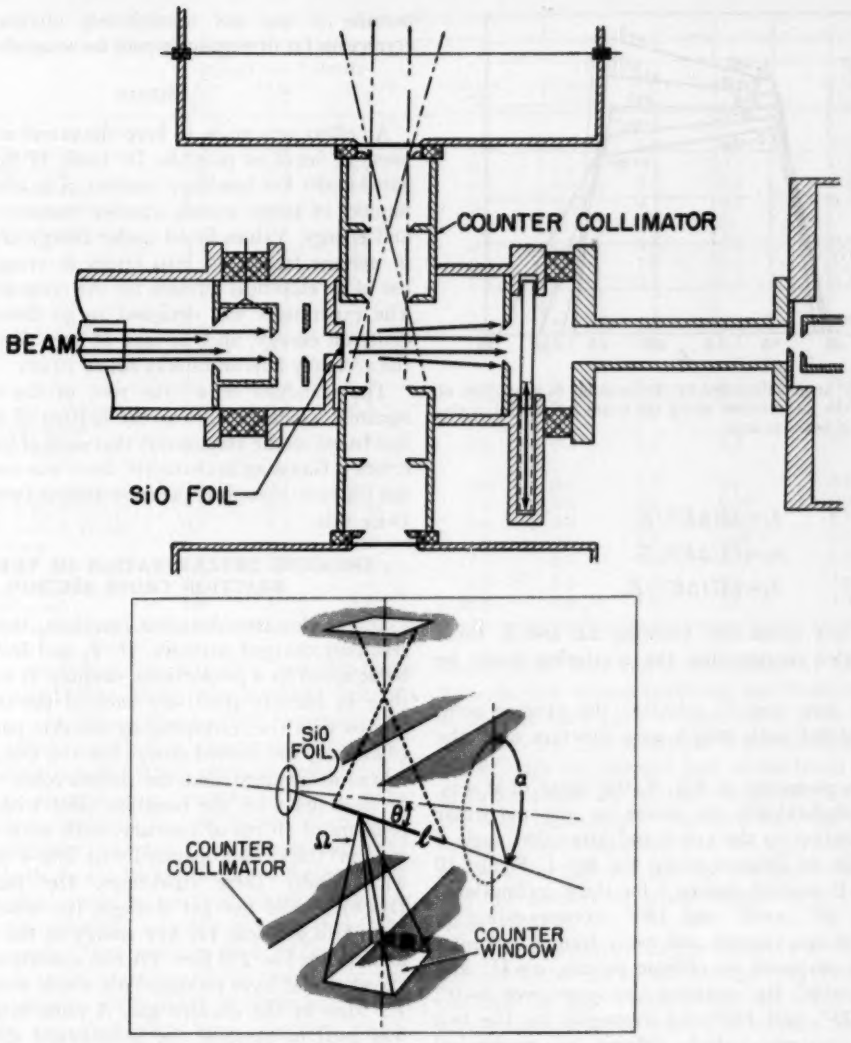

FIG. 9. Schematic diagram of target chamber showing geometry.

shielded Faraday cup rotated about the center of the window as an axis. The current collected by this cup as a function of scattering angle θ gave data of the type shown in Fig. 6. A series of such curves taken at various energies was translated into curves showing how the percentage of beam current included inside a given angle varies with energy (Fig. 7).

In these measurements, the angular resolving power was of the order of 1.2°, and an unscattered beam would have had an angular half-width of 1.1° at half-maximum.

For application of these scattering measurements to the solid-angle correction, it was necessary to construct a universal curve from which the divergence produced by windows of differing thicknesses could be read off at various energies.

It was found experimentally that the data could be well represented by a universal curve (Fig. 8) in which intensity was plotted against $(E/\Delta E^1)\theta$, where ΔE is the energy loss in the film measured at a standard 30-kev energy, and, therefore, a measure of the film's thickness and E was the average deuteron energy in the window.

In application of the universal scattering curve to the correction, for counter solid angle, the approximation was made that the distribution could be represented by scattering at three angles, θ_1, θ_2, and θ_3, each containing one-third of the total beam (this approximation was considerably better than needed to keep within the desired accuracy). From the curve in Fig. 8, one

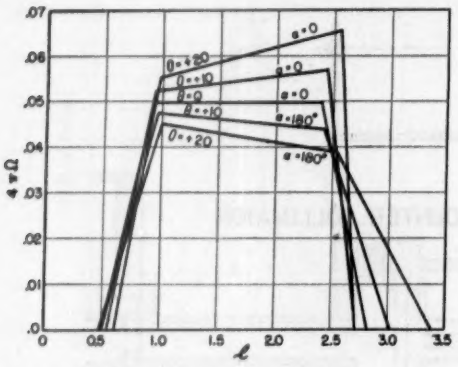

FIG. 10. Solid angle subtended by the counters as a function of distance from the SiO window along the beam for several angles of inclination of beam to axis.

finds that

$$\theta_1 = 33(\Delta E)^{\frac{1}{2}}/E,$$
$$\theta_2 = 71(\Delta E)^{\frac{1}{2}}/E,$$
$$\theta_3 = 137(\Delta E)^{\frac{1}{2}}/E.$$

Thus for any given run, knowing ΔE and E, three average angles representing the scattering could be calculated.

The next step was to calculate the average solid angle and target path length as a function of θ, the divergence.

Using the geometry of Fig. 9, the value of Ω was calculated algebraically for points on any particular ray of inclination to the axis θ and azimuthal angle α as a function of distance along the ray l. Figure 10 shows such Ω plotted against l for three inclinations: $\theta=0°$, 10°, 20°; $\alpha=0°$ and 180° (corresponding to going toward one counter and away from it). Similar curves were prepared for oblique pencils, $\alpha=45°$ and 135° and $\alpha=90°$. By summing the areas over $\alpha=0°$, 45°, 90°, 135°, and 180° and averaging for the two counter-slit systems (which differed by mechanical tolerances), an average value of Ωl was obtained for a given value of θ. Figure 11 shows the resulting Ωl averages as a function of θ.

It turned out that this geometrical factor Ωl is insensitive to θ over the range zero to 30°, varying only 2 percent. At $\theta=32°$, Ωl jumped by nearly 10 percent, and this occurred when particles passed inside the counter-slit system. In these experiments few particles were scattered out to $\theta=32°$. From Fig. 7, at 20 kev we see that in one particular case 99 percent of the beam lay within $\theta=25°$ for beam energy 20 kev.

These linear approximations to nonlinear functions used in calculating the effect of scattering were more than sufficiently accurate since the whole correction to Ωl because of the scattering was only 1 percent, and the uncertainty in Ωl because of other factors was larger. The corrections are included in this report mainly because it was not immediately obvious that the correction for divergence would be so small.

Errors

An effort was made to keep the errors in the experiment as small as possible. In Table II the errors are listed under five headings: number of incident particles, number of target atoms, number counted, solid angle, and energy. Values listed under energy are the errors in voltage translated into errors in cross section by use of an empirical formula for the cross-section curve. The experiment was designed to go down to 20-kev deuteron energy, and, as may be seen from the table, the accuracy falls off rapidly below 20 kev.

The standard error (the root of the sum of the squares) which appears at the bottom of each column was based on the assumption that each of the individual errors is Gaussian in character. Such was most probably not the case; therefore, the error assigned was arbitrarily twice this.

ABSOLUTE DETERMINATION OF THE D(d,p)T REACTION CROSS SECTION

In the deuteron-deuteron reactions, there are three resultant charged particles, H, T, and He^3, which can be detected by a proportional counter. It was necessary then to identify positively each of the counter pulse groups with the corresponding reaction particle and to count only the desired group. For the D(d,p)T branch, it was determined that the tritons could conveniently be detected with the counters filled with argon to a pressure of 10 cm of mercury, with mica windows 1.5 mg/cm² thick, and operated with 550 v on the center wire. Under these conditions, He^3 particles from D(d,n)He^3 did not get through the window, protons from D(d,p)T lost 120 kev energy in the counter gas, and tritons lost 270 kev. Tritium contamination in the target would have produced α's which would have lost 1.9 Mev in the counter gas. A pulse-height analyzer was used to examine the pulse-height distribution of the counters. The tritons were well resolved from the protons. The protons were poorly resolved from the

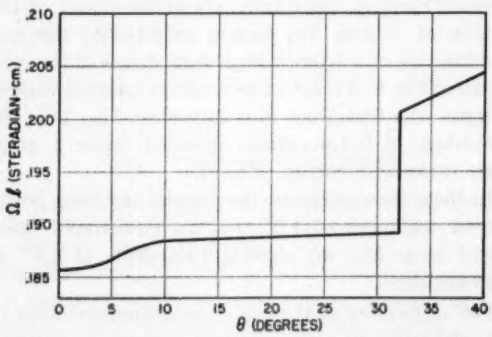

FIG. 11. Product of solid angle subtended by the counters and beam path length as a function of scattering angle.

TABLE II. Errors.

	$D(d,p)T$ and $D(d,n)He^3$			$T(d,n)He^4$				$He^3(d,p)He^4$	
	25 kev (%)	50 kev (%)	100 kev (%)	10 kev (%)	25 kev (%)	50 kev (%)	100 kev (%)	40 kev (%)	80 kev (%)
1. Number of incident particles									
a. Current integrator	0.5	0.5	0.5	0.5	0.5	0.5	0.5	0.5	0.5
b. Neutralized beam	0.3	0.1	0.1	0.5	0.3	0.1	0.1	0.2	0.1
c. Secondary particles	0.3	0.3	0.3	0.3	0.3	0.3	0.3	0.3	0.3
d. Beam contamination	0.1	0.1	0.1	0.1	0.1	0.1	0.1	0.1	0.1
2. Number of target atoms									
a. Pressure	0.5	0.5	0.5	0.5	0.5	0.5	0.5	0.5	0.5
b. Gas purity	1.0	1.0	1.0	2.0	1.0	1.0	1.0	1.0	1.0
c. Temperature	0.1	0.1	0.1	0.1	0.1	0.1	0.1	0.1	0.1
3. Number counted									
a. Efficiency of counters	0.2	0.2	0.2	0.2	0.2	0.2	0.2	0.2	0.2
b. Statistics	1.7	0.7	0.8	0.5	0.2	0.1	0.1	1.7	0.4
4. Solid angle									
a. Beam not central	0.3	0.3	0.3	0.3	0.3	0.3	0.3	0.3	0.3
b. Measurement of slit system	0.3	0.3	0.3	0.3	0.3	0.3	0.3	0.3	0.3
c. Error in calculation approximations	0.2	0.2	0.2	0.5	0.2	0.2	0.2	0.2	0.2
5. Energy									
a. High-voltage measurement	0.4	0.2	0.1	0.6	0.4	0.3	0.1	0.6	0.4
b. Variation in high voltage	0.4	0.2	0.04	1.6	0.4	0.2	0.03	0.2	0.1
c. Spread in particle energy	0.3	0.1	0.03	0.4	0.3	0.1	0.02	0.1	0.1
d. Film thickness	0.6	0.3	0.07	3.0	0.7	0.3	0.05	0.3	0.2
e. Energy loss in gas	0.7	0.3	0.05	3.0	0.7	0.3	0.05	0.4	0.2
Standard error	2.5	1.6	1.6	5.3	1.8	1.5	1.4	2.4	1.5
Assigned error	5.0	3.2	3.2	10.6	3.6	3.0	2.8	4.8	3.0

noise. A very small counting rate of α particles from $T(d,n)He^4$ showed that there was a slight tritium contamination. At these bombarding energies the protons and tritons came off in almost opposite directions. Since the top and bottom counters were located opposite each other, it was possible to count these pairs of reaction particles in coincidence when both particles entered the counters. Coincidences did occur and gave a check on the identification of the particles.

The one other reaction particle which could be detected in the counters was the neutron from the $D(d,n)He^3$ branch. This neutron had an energy of 2.47 Mev and could cause recoils in the gas of the counters. To measure the number of these recoils, the counters were provided with brass shutters which could be drawn across the counter windows to prevent any charged particles from entering the counter. It was found that 0.3 percent of the pulses assigned to the tritons were from neutron recoils, and the number of tritons detected was so corrected.

The target gas, deuterium, was supplied from a small uranium reservoir, from which it was admitted to the target by careful heating. The pressure in the target was controlled by means of needle valves. A sample of gas was taken from the target before running for analysis on a mass spectrometer to obtain the initial purity. Another sample was taken and analyzed at the completion of a half-day of running to obtain the final purity. The variation in purity was then interpolated linearly with bombardment time.

Before and after each series of runs, the thickness of the window was measured with the decelerator at a high voltage of E_0. Then, with deuterium gas in the target, runs were made at a series of different high voltages, but always beginning and finishing with runs at E_0. At each high voltage three runs were made, first with the total analyzed beam entering the target, second with the charged part of the beam deflected so as to determine the neutral component, and third with the total beam again. For each run, the time, target pressure, and temperature at the beginning and end of the run, the high voltage, the integrated beam current, and the number of triton counts from each counter were recorded.

The mean energy in the target was calculated for any particular run by subtracting from the high voltage one-half the gas thickness and the window thickness at the energy of the run. The window thickness was computed from the thickness at E_0, interpolated for the midtime of the run, by means of the thickness *vs* energy curve of Fig. 4.

The density of the target nuclei, in number per cubic centimeter, was calculated by the equation

$$N_t = CmN_0PT_0/V_0P_0T,$$

where C = the purity of the deuterium gas, m is the number of atoms per molecule (2 for deuterium), N_0 = Avogadro's number, P and T are the pressure and absolute temperature of the gas, and V_0 is the molar volume at pressure P_0 and temperature T_0. The number of incident deuterons was calculated by the relation:

$$n_i = q/[e(1-\nu)],$$

where q is the integrated beam current in coulombs, e is the electronic charge in coulombs, and ν is the fraction of the total beam that is neutral. The differential

TABLE III. Cross sections derived from smoothed curves.

Deuteron energy (kev)	D(d,p)T (millibarns)	D(d,n)He³ (millibarns)	T(d,n)He⁴ (barns)	He³(d,p)He⁴ (millibarns)
7.5			0.000275[a]	
9.0			0.000939[a]	
13.0	0.0352	0.0329	0.00780[a]	
19.0	0.213	0.200	0.0448[a]	
22.0	0.391	0.367	0.0859	
25.0	0.629	0.592	0.144	
30.0	1.14	1.08	0.278	
33.0	1.54	1.46	0.394	
36.0	1.98	1.88	0.519	0.124
40.0	2.56	2.43	0.723	0.258
46.0	3.58	3.42	1.11	0.605
53.0	4.98	4.78	1.62	1.28
60.0	6.50	6.25	2.18	2.32
67.0	8.14	7.86	2.82	3.84
73.0	9.59	9.30	3.36	5.65
80.0	11.2	10.9	3.93	8.45
93.0	13.9	13.6	4.74	16.2
100.0	15.4	15.2	4.90	
107.0	16.5	16.6	4.95	
110.0	17.1	17.0	4.95	
113.0	17.5	17.4	4.94	
120.0			4.70	

[a] Derived from extrapolated Gamow curve.

reaction cross section at 90° was then calculated by the equation

$$(d\sigma/d\omega)_{90°}=Y/(N_t n_t w),$$

where Y is the total number of triton counts in both counters and w is the average geometry of counting for the two counters in steradian-cm. Finally the total cross section was computed by the formula

$$\sigma_{\text{total}}=4\pi g h(E)(d\sigma/d\omega)_{90°},$$

where g is the correction factor to the counter solid angle for motion of the center of mass, and $h(E)$ is the correction factor for the angular anisotropy of the reaction products in the laboratory system. The correction g was applied although its maximum value was only 1.02. The factor $h(E)$ has the form

$$h(E)=\frac{1}{1+\frac{1}{2}C_2+\frac{3}{8}C_4+[(3/2)C_2+(30/8)C_4]p^2},$$

where C_2 and C_4 are experimentally determined coefficients in the Legendre polynomial expansion of the anisotropy, taken from Wenzel and Whaling,[7] and

$$p^2=\cos^2\theta=3E/(8000+E),$$

where θ is the center-of-mass angle that corresponds to 90° in the laboratory system and E is the energy in kev.

Values of the total cross section as a function of energy for the reaction D(d,p)T are given in Table III. A plot of the total cross section as a function of energy for the reaction D(d,p)T is shown in Fig. 12. The lowest energy at which the cross section was measured was determined by a balance between the low yield and the growth of the SiO windows, i.e., the longer running time required to obtain a sufficient number of counts caused greater uncertainty in the determination of the energy loss in the SiO window.

THE D(d,n)He³ CROSS SECTION

Although the D(d,n)He³ reaction can be detected by counting either neutrons or He³ particles, the latter can be counted with higher precision because of their charge. The He³ particles have a range in air of only 0.4 cm; therefore, thin counter windows made of Zapon, of 0.1-cm air equivalent, were used. The counters were filled with an argon-CO_2 mixture to a pressure of 3 cm of mercury. The He³ particles and the tritons from the D(d,p)T reaction were well separated from each other in pulse height and from noise. The He³ particles were stopped in the counter gas whereas the tritons passed through the counter volume. This provided a test of the identification of the pulses, for the He³ particles gave not only the larger pulses but their pulse heights were not appreciably changed by small changes in counter gas pressure whereas the triton pulses were almost proportional to the pressure. No coincidences should occur between the tritons in one counter and He³ particles in the other, and none was observed.

The thin Zapon windows had a serious disadvantage in that it was impossible to make them gas-tight, and the deuterium gas in the target chamber quickly became contaminated with argon. At the higher bombarding energies the deuterons in the beam were scattered by the argon with enough energy to penetrate the counter windows. These deuterons gave a large number of small pulses, and pile-up of these pulses occurred which rendered the counters inoperable when the argon contamination became high. An absolute determination of the cross section was attempted at a few energies, but, because of the uncertainty in the knowledge of the target gas composition and difficulties in counting, the accuracy was poor.

A better procedure was found to be to measure the 90°

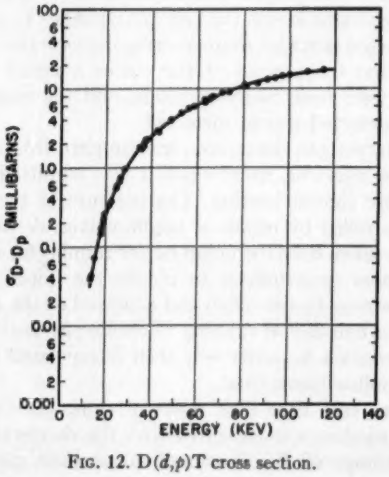

FIG. 12. D(d,p)T cross section.

yields for the two reactions D(d,p)T and D(d,n)He^3 by counting tritons and He^3 particles simultaneously and combining this ratio with the previously determined D(d,p)T cross section to give that for D(d,n)He^3 branch.

Such a procedure had the advantage that since the ratio is essentially independent of target gas parity and density, a constant stream of target gas could be used, which swept out argon contamination and reduced scattering to acceptable limits. The D(d,n)He^3 cross section derived from this ratio, assuming similar angular distributions for the two branches, is given in Table III.‡

The results are shown in Fig. 13. Each point plotted represents the average of about five experimental determinations. The ratio at 20 kev is 0.94 and it increases with increasing energy to a value of 0.99 at 100 kev. The D(d,n)He^3 cross section, derived from this ratio and the measured D(d,p)T cross section, is presented in Table III, as is the total cross section.

The resulting total cross section is shown on a Gamow plot in Fig. 14. If the finite height of the Coulomb

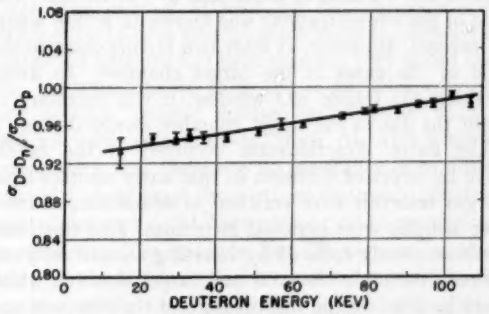

FIG. 13. Ratio 90° yield D(d,n)He^3/D(d,p)T vs energy.

barrier is allowed for,[14] this introduces a departure from the zero energy slope (44.4 kev$^{\frac{1}{2}}$) amounting to 0.2 percent at 10 kev and 7.2 percent at 100 kev. The best straight line was drawn through the experimental points, with a slope of 45.8, i.e.,

$$\sigma=\frac{2.88\times10^2}{E}\exp(45.8E^{-\frac{1}{2}})\text{ barns},$$

with E in kev.

THE ABSOLUTE DETERMINATION OF THE T(d,n)He^4 CROSS SECTION

Tritium gas was used as the target. It was supplied from a small uranium reservoir and after use was collected into another uranium trap. About one-third of the gas for each filling was taken as a sample for analysis. Analyses were made on a mass spectrometer before and after use.

‡ *Note Added in Proof.*—Eliot, Roaf, and Shaw, [Proc. Roy. Soc. (London) **A216**, 57 (1953)], report markedly differing angular distributions for the two branches, based on observations at two angles, 90°±15°, and 125°±15°.

[14] H. Bethe, Revs. Modern Phys. **9**, 163 (1937).

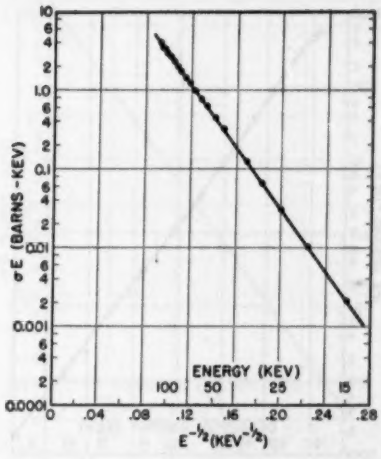

FIG. 14. Gamow plot of total $d-$D cross section.

The number of reactions taking place was determined by counting the α particles resulting from the reaction. The counters were filled with argon gas to a pressure of 10 cm of mercury and were operated with 550 v on the center wire. The counter windows were of mica 1.5 mg/cm^2 thick. The α-particle pulses were so much larger than pulses from anything else that the background was negiligible.

The experimental procedure was the same as in the case of the D(d,p)T reaction. The calculation of the total cross section differed only in that it was assumed that the α particles were given off isotropically in the center-of-mass system, as based on the results of Bretscher and French,[8] so that

$$\sigma=4\pi(d\sigma/d\omega)_{90°}.$$

The experimental results for this cross section are listed in Table III and are shown in Fig. 15 with a smooth curve drawn through most of the points. The peak of the cross-section curve, around 107 kev,

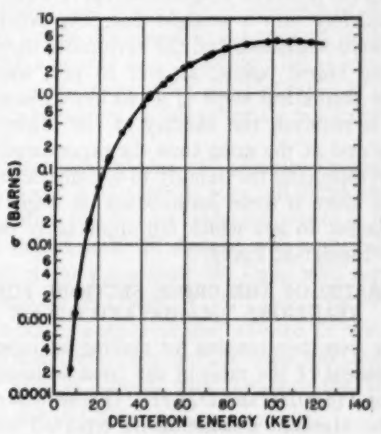

FIG. 15. T(d,n)He^4 cross section.

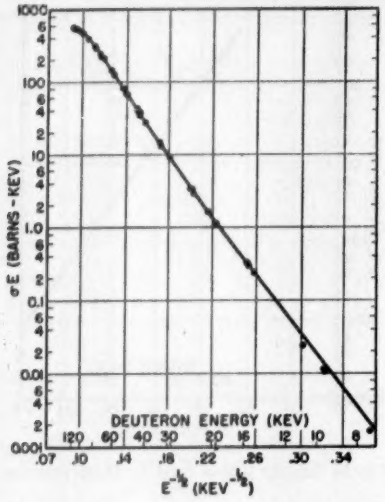

FIG. 16. Gamow plot of cross section $T(d,n)He^4$.

is quite broad. The accuracy in selecting the peak energy is somewhat limited because of the high-voltage limitations of the equipment. The smooth curve lies above the experimental points at the energies 7, 9, and 11 kev because failure of the counter collimating system and excess production of condensable vapor gave good reason to expect that the experimental value of the cross sections at these energies might be low.

A Gamow plot of the results is given in Fig. 16. Since angular anisotropy has not been detected, it is reasonable to assume an S-wave interaction which leads to a cross section with a dependence on energy, at energies remote from the resonance, of the form

$$\sigma=(A/E)\exp(-2\pi e^2/hv)=(A/E)\exp(-44.40E^{-\frac{1}{2}}),$$

where e is the electronic charge and v is the relative velocity of the nuclei and the deuteron energy E is expressed in kev. When $\log E\sigma$ is plotted against $E^{-\frac{1}{2}}$ (Fig. 16), the points lie on a smooth curve which merges asymptotically into a straight line. The points below 16 kev were neglected, and the asymptote through the remaining lowest points, 20 and 16 kev, was drawn with the theoretical slope of 44.40 $kev^{\frac{1}{2}}$. Since, as the energy is reduced, the validity of the theory should improve and at the same time the experimental errors increase, especially the liability to systematic error, it is felt that there is some justification for neglecting the values below 16 kev which fall appreciably below the Gamow theoretical curve.

THE RATIO OF THE CROSS SECTIONS FOR THE REACTIONS $T(d,n)He^4$ AND $D(d,p)T$

There were two reasons for making an independent measurement of the ratio of the cross sections for the reactions $T(d,n)He^4$ and $D(d,p)T$: (1) the ratio obtained from the absolute measurements reported here is in rather serious disagreement with previous measurements;[1] (2) the ratio measurement provided a test of the internal consistency of the separate cross-section measurements.

In this experiment the α particles from the $T(d,n)He^4$ reaction and the tritons from the $D(d,p)T$ reaction were counted simultaneously, by use of a known mixture of tritium and deuterium gas as a target. The ratio of the counting rates for these two particles, when corrected for the concentrations of the gases in the mixture, gave the ratio of the cross sections directly. This measurement, as in the previous ratio experiment, was independent of the beam current and pressure and temperature of the target gas.

For obtaining the comparable counting rate required for minimum error from the two reactions, it was necessary to have a gas mixture containing a relatively small proportion of tritium since the cross section of tritium is about 350 times larger than the deuterium cross section. A gas mixture was prepared by mixing accurately known volumes of the two gases in the ratio of 400 volumes of deuterium to 1 of tritium. The ratio of gas concentrations was known to within about 0.5 percent. However, at least two factors changed the ratio of the gases in the target chamber. To avoid breaking the fragile SiO window, it was necessary to admit the gas to the target chamber slowly through a needle valve. Fractionation occurred in the needle valve by selective diffusion so that early samples from the gas reservoir were enriched in deuterium, whereas later samples were enriched in tritium. This fractionation was greatly reduced by inserting a small reservoir between the main reservoir and target chamber which could be filled to the full pressure of the reservoir and then emptied completely through the needle valve into the target chamber. Also, the SiO windows in the target chamber had small leaks into the high vacuum, and fractionation occurred at these leaks because deuterium leaked through more readily than tritium. Because of this, the gas in the target chamber was progressively enriched in tritium. These fractionation effects reduced the accuracy of the ratio measurement.

Both the α particles from the $T(d,n)He^4$ reaction and

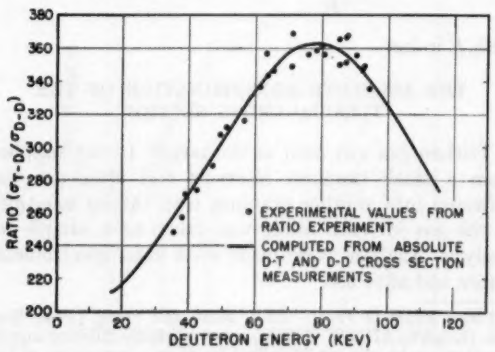
RATIO (σT-D/σD-D)
DEUTERON ENERGY (KEV)
EXPERIMENTAL VALUES FROM RATIO EXPERIMENT
COMPUTED FROM ABSOLUTE D-T AND D-D CROSS SECTION MEASUREMENTS

FIG. 17. Ratio 90° yield $[D(d,n)He^3]$/90° yield $[D(d,p)T]$ vs energy.

the tritons from the D(d,p)T reaction were counted simultaneously. The counters had mica windows, 1.5 mg/cm² thick, and were filled with argon to a pressure of 10 cm of mercury. There was good separation in pulse height between the α pulses and triton pulses and from background.

The experimental values for the ratios are shown by circles in Fig. 17. The smooth curve is the result of dividing the experimental values of the cross section of the T(d,n)He⁴ reaction by those of the D(d,p)T reaction reported here. The agreement between the measured ratio and the ratio of the absolute measurements is within 1.5 percent.

THE CROSS SECTION FOR THE REACTION He³(d,p)He⁴

For this experiment, pure He³ gas was used in the target chamber at a pressure of 1 mm of mercury, supplied from a glass flask through a needle valve. Samples of the gas were analyzed with the mass spectrometer, as in the case of deuterium and tritium above. The number of reactions was determined by counting the 14-Mev protons resulting from the reaction because if α particles had been counted, they would have been indistinguishable from the α particles resulting from possible tritium contamination. The counter windows used were 0.035-in. thick Al. The windows were so thick that there was no possibility of confusion in the identification of the particles since only penetrating particles such as 14-Mev protons could get through the windows. The protons lost 90 percent of their energy in the windows and were then stopped in the counters, which were filled to 1 atmos with argon. The experimental procedure and the treatment of data are similar to that reported above. In calculating

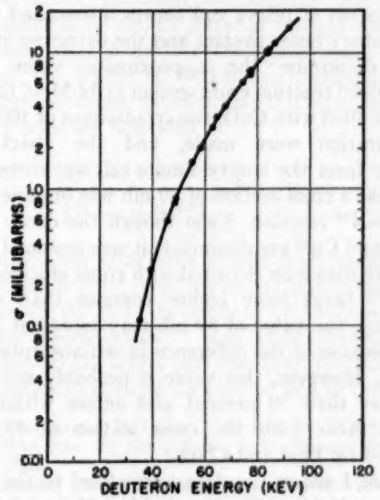

FIG. 18. He³(d,p)He⁴ cross section.

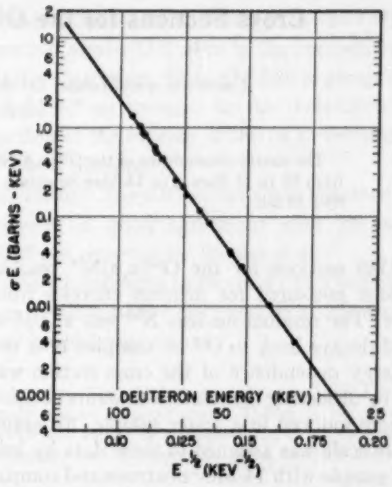

FIG. 19. Gamow plot of D(He³,p)He⁴ cross section.

the total cross sections from the measured differential cross sections at 90° the angular distribution was assumed to be isotropic in this energy region.[10]

A plot of the cross section as a function of the energy of the incident deuteron is shown in Fig. 18 and the results tabulated in Table III. The lowest energy at which the cross section was measured was fixed by the background, which became objectionable at low counting rates, whereas the highest energy was the maximum available energy of the accelerator used.

A Gamow plot of the data (Fig. 19) is linear with a slope of 91.0 kev$^{\frac{1}{2}}$. The simple penetrability gives a slope of 88.80, within 2.5 percent of the experimental value.

Although nuclear cross sections conventionally refer to interactions between bare nuclei, laboratory measurements such as these refer to interactions in which at least one of the partners is a neutral atom (or part of a molecule). This verges on significance at these energies, for an energy E in the lab system is equivalent to $E+Ze^2/\bar{r}$ ($\bar{r}$ is the effective radius of the electron cloud) in the conventional system. $Ze^2/\bar{r}$ amounts to 26 ev for H or 87 ev for He. Expressed as a correction to the cross section, this amounts to -2.6 percent for $\sigma_T(d,n)$He⁴ at 10 kev and -2.7 percent for σD(He³,p)He⁴ at 35 kev. The data presented in this paper do not include this correction.

The authors acknowledge with pleasure the assistance of E. Fermi and R. L. Garwin, who called the problems to our attention and had an important share in formulating the experiment; H. Agnew, who contributed to the design of the apparatus; W. Ogle, who suggested the deceleration technique; J. H. Coon, who designed the gas handling apparatus and advised in that field; B. B. McInteer, who provided the mass spectrographic analyses; and W. Jones, who prepared the tritium-deuterium gas mixture.

Cross Sections for the $O^{16}(n,p)N^{16}$ Reaction from 12 to 18 Mev*

H. C. MARTIN
University of California, Los Alamos Scientific Laboratory, Los Alamos, New Mexico

(Received September 11, 1953)

The energy dependence of the $O^{16}(n,p)N^{16}$ reaction cross section has been determined for neutron energies from 12 to 18 Mev. For 14-Mev neutrons, the absolute value of the reaction cross section was found to be 89±30 mb.

CROSS sections for the $O^{16}(n,p)N^{16}$ reaction have been measured for neutron energies from 12 to 18 Mev. The residual nucleus N^{16} has a 7.35-sec half-life and decays back to O^{16} by complex beta emission;[1] the energy dependence of the cross section was determined by observing the relative amounts of this activity that were induced in a water sample. An approximate absolute scale was assigned to these data by irradiating a CuO sample with 14-Mev neutrons and comparing the N^{16} activity from the $O^{16}(n,p)N^{16}$ reaction to the 9.9-min Cu^{62} activity from the $Cu^{63}(n,2n)Cu^{62}$ reaction, which has a known cross section of 0.51±0.04 barn.[2]

Monoergic neutrons were made by bombarding a 3-cm-long tritium gas target with deuterons from a 2.5-Mev electrostatic accelerator. The target was filled to a pressure of 25-cm Hg. With a deuteron energy of 1.80 Mev at the center of the gas target, the energy of the neutrons from the $T(d,n)He^4$ reaction varied from 18.0 Mev at an angle of 0° with respect to the deuteron beam to 12.4 Mev at an angle of 150°.[3]

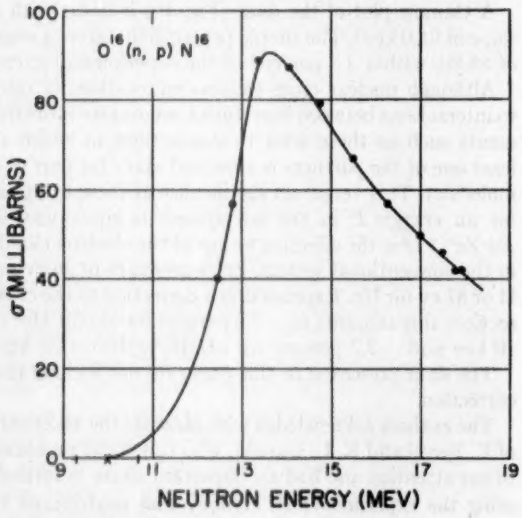

FIG. 1. Cross section for the $O^{16}(n,p)N^{16}$ reaction.

Irradiations of 40-sec duration were made on a 5-g water sample successively placed at 15° angular intervals at a distance of 9 cm from the neutron source. The water sample was contained in a Lucite cell. At least four irradiations of the sample were made at each position, and the relative intensity of each irradiation was determined by measuring the integrated beam current. Deuteron beams of approximately three μa were used; during each irradiation the variation in beam current was held to within ±3 percent.

A ½-mm thick × 4-cm diameter stilbene crystal mounted in a Lucite holder on a 5819 photomultiplier was used to detect the N^{16} activity. When the scintillator was placed near the neutron source following an irradiation, the background counting rate due to activities induced in the materials of the gas target assembly was very large, and it was necessary to remove the water sample from the vicinity of the source for counting. Therefore, the detector was placed on the floor 8 ft below the neutron source, and an arrangement was used which allowed the irradiated sample to slide down a rod into position near the scintillator. Pulses from the photomultiplier were fed to a preamplifier, amplifier, and scaler; the register pulse from the scaler was fed to one pen of a dual-pen Brush recorder, and timing pulses were fed to the other pen. The timing sequence for irradiating and counting the sample was controlled by a system of relays and timers interlocked with the accelerator's beam shutter and the detecting system.

To determine the approximate value of the $O^{16}(n,p)N^{16}$ reaction cross section at 14 Mev, the Lucite cell was filled with CuO, two irradiations of 100 and 200 sec duration were made, and the "background" activity from the empty Lucite cell was measured. In each case a cross section of 89 mb was obtained for the $O^{16}(n,p)N^{16}$ reaction. Even though the decay schemes of N^{16} and Cu^{62} are dissimilar, it was assumed that the two activities were detected with equal efficiency. Since the N^{16} betas have higher energies than the Cu^{62} positrons, the value of 89 mb may represent an upper limit because of the difference in self-absorption in the sample. However, this value is probably not in error by more than 30 percent and agrees within experimental error with the cross section of 49±25 mb reported by Paul and Clark.[4]

Figure 1 shows the data normalized to the value of 89 mb at 14 Mev. The threshold of 10.0±0.7 Mev was

* Work done under the auspices of the U. S. Atomic Energy Commission.

[1] Bleuler, Scherrer, Walter, and Zunti, Helv. Phys. Acta **20**, 96 (1947).

[2] Stuart G. Forbes, Phys. Rev. **88**, 1309 (1952).

[3] Hanson, Taschek, and Williams, Revs. Modern Phys. **21**, 635 (1949).

[4] E. B. Paul and R. L. Clark, Can. J. Phys. **31**, 267 (1953).

TABLE I. Laboratory differential cross sections for neutrons from the $T(d,n)He^4$ reaction for a deuteron energy of 1.80 Mev.

θ_{lab}	0°	30°	60°	90°	120°	150°
$\sigma(\theta_{lab})$ mb/sterad	22.5	18.8	12.5	9.5	8.8	9.7

determined from the reported reaction Q value of 9.4 Mev.[5] Neutron energy spreads vary from ±0.2 Mev at a mean energy of 18 Mev to nearly ±1 Mev from 12 to 15 Mev. In correcting the observed activities for the angular distribution of the $T(d,n)He^4$ neutrons, the laboratory differential cross sections shown in Table I were used.[3,6] Relative errors in these values are about ±10 percent.[7]

A possible cause of the decrease in the $O^{16}(n,p)N^{16}$ cross section above 13.5 Mev is the competitive effect of inelastic scattering. Since O^{16} has a group of levels near 13 Mev,[8] an increase in the inelastic-scattering cross section at the expense of the (n,p) reaction at this energy seems plausible.

A half-life of 7.38±0.05 seconds was obtained for the N^{16} activity, in good agreement with the value of 7.35±0.05 sec reported by Bleuler *et al.*[1]

The writer is indebted to Dr. R. F. Taschek and other members of the 2.5-Mev electrostatic accelerator group for many helpful suggestions.

[5] Hornyak, Lauritsen, Morrison, and Fowler, Revs. Modern Phys. **22**, 291 (1950).

[6] T. F. Stratton and G. D. Freier, Phys. Rev. **88**, 261 (1952).

[7] *Note added in proof.*—Recent measurements by S. J. Bame of this laboratory have shown that the angular distribution of the neutrons from the $T(d,n)He^4$ reaction given in Table I is probably too strongly peaked at small angles. Hence, in Fig. 1, the cross section at 18 Mev should be increased from 40 mb to about 60 mb.

[8] F. Ajzenberg and T. Lauritsen, Revs. Modern Phys. **24**, 321 (1952).

PHYSICAL REVIEW VOLUME 93, NUMBER 3 FEBRUARY 1, 1954

Range Distribution of Alpha Particles Following the Decays of Li^8 and B^8

F. C. GILBERT
Radiation Laboratory, Department of Physics, University of California, Berkeley, California

(Received October 2, 1953)

The range distributions of the alpha particles resulting from the decays of Li^8 and B^8 nuclei in nuclear track emulsion have been determined and compared. The range distribution from the decay of Li^8 nuclei is found to be similar to that measured by previous investigators and, within statistical error, the range distribution from the decay of B^8 nuclei is the same as that found from Li^8 nuclei.

IN recent experiments[1] designed to analyze the high-energy disintegration products produced by 375-Mev alpha particles bombarding beryllium, a large number of B^8 and Li^8 hammer tracks (note Fig. 1) were found in the nuclear track emulsions used as detectors. Dr. Walter H. Barkas has suggested that by analyzing the range distribution of the alpha tracks resulting from the reactions

$$\left.\begin{aligned} B^8 &\rightarrow \epsilon^+ + Be^{8*} \\ Li^8 &\rightarrow \epsilon^- + Be^{8*} \end{aligned}\right\} Be^{8*} \rightarrow 2He^4, \quad (1), (2)$$

the energy level structures arising from these mirror processes in the short-lived Be^8 nuclei may be compared. Although the Be^8 from the decay of Li^8 has been studied by many investigators,[2-4] additional measurements were taken on the alpha particles from reaction (2) as a means of calibration of the method and in the hope of improving the statistics over previous investigations. The alpha-particle range distribution from reaction (1) was studied for the purposes of (*a*) checking the similarity of the two mirror nuclei, Li^8 and B^8, and (*b*) searching for a possible new level in the excited Be^8 nucleus.

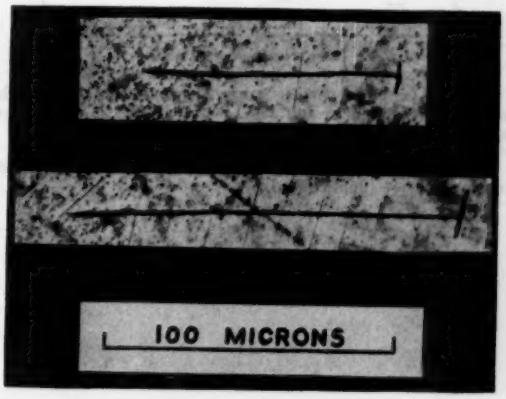

FIG. 1. Photomicrographs of tracks of Li^8 and B^8 nuclei: (top) a 28-Mev Li^8 track, (bottom) a 66-Mev B^8 track.

[1] W. H. Barkas and H. Tyren, Phys. Rev. **89**, 1 (1953); W. H. Barkas, Phys. Rev. **89**, 1019 (1953); R. W. Deutsch, Phys. Rev. **90**, 499 (1953).

[2] F. Ajzenberg and T. Lauritsen, Revs. Modern Phys. **24**, 336 (1952).

[3] C. M. Class and S. S. Hanna, Phys. Rev. **89**, 877 (1953).

[4] D. St P. Bunbury, Phys. Rev. **90**, 1121 (1953).

The probability of a second level is enhanced for reaction (1) because of the slightly greater energy (~1 Mev) available in the B^8 nucleus as compared to the Li^8 nucleus.

The B^8 tracks could be differentiated from the Li^8 tracks by the differences in range and in grain density for a given radius of curvature in the cyclotron magnetic field. Owing to the short range of the Li^8 or B^8 tracks penetrating the emulsion, in about one-third of the decays one of the alpha tracks left the emulsion before the end of its range. In these cases the range of the remaining alpha particle was measured from the end of the B^8 or Li^8 track. In the events in which both alpha particles remained in the emulsion, the two ranges were averaged. The later cases provided a means for estimating the errors involved in the measurement of the alpha ranges. Since the two alpha particles come apart with equal energies in their center-of-mass system, the difference in their measured ranges gives an estimate of the errors due to range straggle, recoil of the Be^8 nucleus from the beta decay, indeterminacy of the end points, and human error. In this manner the standard deviation in the measurement of individual alpha ranges was estimated to be about 0.5 micron. The alpha energies as a function of range were determined from a range-energy relation for C-2 emulsions worked out by Wilkins.[5]

The alpha ranges from 100 B^8 disintegrations and 257 Li^8 disintegrations, normalized to 100 for comparison, are shown in Fig. 2. No significant difference is

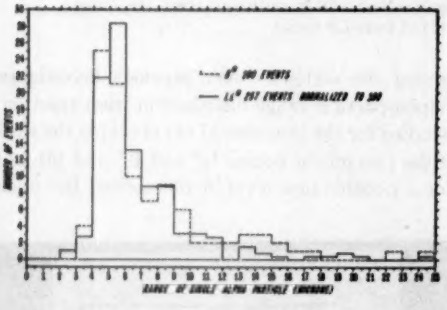

FIG. 2. The alpha-particle range distributions following the decays of 100 B^8 nuclei and 257 Li^8 nuclei. The 257 Li^8 events have been normalized to 100 for comparison.

[5] J. J. Wilkins, Harwell Atomic Energy Research Establishment Report G/R 664 (unpublished).

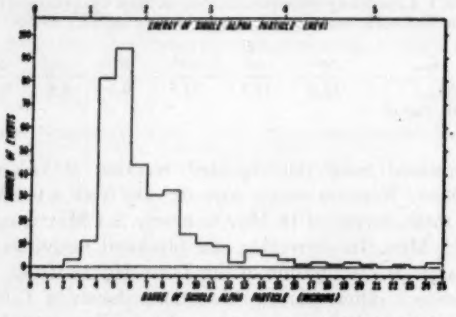

FIG. 3. The combined alpha-particle range distribution following the decay of 357 Be^8 nuclei.

detectable; in particular, no additional long-range alpha particles were found following the decay of B^8. The Li^8 distribution is similar to that found by previous investigators.[2–4]

The combined 357 events shown in Fig. 3 have a maximum at about $E_\alpha = 1.5$ Mev and a width at half-maximum, $\Delta E_\alpha = \approx 0.7$ Mev. Near resonance the distribution may be fitted by a single resonance theory due to Wheeler[6] as modified for the alpha penetrability by Bonner *et al.*,[7] where $E_0 = 2.9$ Mev, $\Gamma = 1.2$ Mev, and J, the angular momentum of the excited state of Be^8, is 2. Roughly 15 percent of the decays, principally the higher-energy alpha particles, are not included by this resonance and must be explained by the presence of higher levels in the Be^8 nucleus. It is to be noted that the data may be fitted satisfactorily over the entire energy range of this experiment by the single resonance theory if J is chosen to be 4 in agreement with the analysis by Bonner *et al.*[7]

The presence of the longer-range alpha particles, 15 to 25 microns, from the decay of B^8, and the similarity of the B^8 and Li^8 distributions, suggest that the B^8 beta decay leads to the same energy levels in Be^8 as does the Li^8 beta decay. This is in essential agreement with the interpretation of the positron spectrum of B^8 as measured by Alvarez.[8]

I am particularly indebted to Dr. Walter H. Barkas for his invaluable guidance and to Mrs. Doreen Hornback for having made many of the measurements that were necessary for this experiment.

[6] J. A. Wheeler, Phys. Rev. **59**, 27 (1941).
[7] Bonner, Evans, Malich, and Risser, Phys. Rev. **73**, 885 (1948).
[8] L. Alvarez, Phys. Rev. **80**, 519 (1950).

Radioactive Si^{31}†

W. S. LYON AND J. J. MANNING
Analytical Chemistry Division, Oak Ridge National Laboratory, Oak Ridge, Tennessee
(Received October 19, 1953)

One gamma ray of energy 1.26 Mev is found to accompany 0.07 percent of the disintegrations of Si^{31}. The thermal neutron atomic activation cross section for the reaction $Si^{30}(n,\gamma)Si^{31}$ is observed to be 2.9 ± 0.3 millibarns.

SILICON-31 (2.6 hr) has been reported as a pure negatron emitter with no accompanying gamma transition.[1] Recently, however, Cobb[2] has reported 3 gamma rays of energies 0.17, 0.52, and ~1 Mev. In addition workers at this laboratory have observed electromagnetic radiation from Si ampoules which have been irradiated in the Oak Ridge National Laboratory graphite reactor. Consequently, a careful examination of the gamma spectrum of Si^{31} seemed indicated.

Spectroscopically pure elemental silicon was irradiated in the Oak Ridge National Laboratory graphite reactor for one week, removed, and the silicon metal volatilized off by treatment with HF and HNO_3. The total activity of the residue was less than 100 counts/min as measured on a Geiger counter, a further evidence of the high purity of the metal.

A portion of the active Si was examined on a calibrated NaI(Tl) scintillation gamma-ray spectrometer. One photopeak corresponding to a gamma ray of 1.26 Mev was observed. The decay of this photopeak was followed and found to be identical with the Si^{31} beta decay. The area beneath this photopeak when multiplied by the appropriate efficiency factor (obtained from an experimentally determined graph of γ energy *versus* efficiency) yielded the number of γ transitions.

An absorption curve of the Si^{31} beta particles was made using aluminum absorbers. Extrapolation of this curve yielded the absolute disintegration rate of the source. The counter used was a Tracerlab T.G.2 Geiger counter; the geometry of the counter was determined using National Bureau of Standards P^{32} as the standard. These data indicated that 0.07 percent of the Si^{31} decay proceeds through the 1.26-Mev γ. No evidence was observed for any lower-energy γ rays.

The thermal neutron activation cross section for the reaction $Si^{30}(n,\gamma)Si^{31}$ was also measured. In these experiments ~10 mg weighed portions of Si were irradiated in the Oak Ridge National Laboratory graphite reactor together with weighed amounts of an alloy containing a known amount of manganese. Irradiation times varied from 4 to 7 minutes. The amount of Si^{31} activity produced was obtained by Geiger counting as described above; the neutron flux was calculated from the Mn^{56} activity produced as measured on a calibrated high-pressure ionization chamber. These data indicate the atomic activation cross section to be 2.9 ± 0.3 millibarns. Seren *et al.*,[3] have previously reported 4.8 ± 1.0 millibarns.

The authors are indebted to G. W. Leddicotte who suggested this investigation and to H. A. Mahlman who assisted in some of the work.

† Work performed under contract to U. S. Atomic Energy Commission.

[1] K. Way *et al.*, *Nuclear Data*, National Bureau of Standards Circular 499 (U. S. Government Printing Office, Washington, D. C., 1950), and Supplements 1, 2, 3 (1951).

[2] P. G. Cobb, Purdue University Progress Report II, June, 1952 (unpublished).

[3] Seren, Friedlander, and Turkel, Phys. Rev. 72, 888 (1947).

Elastic Scattering of Electrons by the Coulomb Field of Nuclei Using Born Approximations

VACHASPATI
Institute for Theoretical Physics, Copenhagen, Denmark, and Physical Research Laboratory, Ahmedabad, India
(Received August 27, 1953)

Calculations including the second Born cross section for the elastic scattering of electrons by nuclei are performed taking a model for which the matrix elements are particularly simple. The potential corresponding to this model is a mixture of an attractive Coulomb and a repulsive Yukawa potential of range $1/B$ and relative strength C. The density is given by

$$\rho=-(C-1)\delta^3(\mathbf{r})+\frac{CB^2}{4\pi}\frac{e^{-Br}}{r}.$$

Since the scattering is fairly insensitive to the details of the nuclear model, one can use the calculations made here to find scattering cross sections on different models by suitably choosing B and C. This is done here for the uniform density model and the results are compared with the phase-shift calculations of Acheson for 15- to 35-Mev electrons. A fairly close agreement with his results is obtained up to medium elements ($Z\lesssim 50$).

I. INTRODUCTION

AMONG the elementary particles one feels that one is most familiar with the electrons. Their scattering can therefore form a good means of getting information about some features of the nucleus without the uncertainties inherent in employing other particles. This problem has been considered by several authors[1,2] in recent years, who have calculated the scattering cross sections at various energies assuming that the nucleus is a sphere of uniform charge density (uniform model). The most extensive calculations on this basis are those of Acheson,[2] who has also used another model in which the whole charge is spread over a thin shell at the surface of the sphere (shell model). He has pointed out the interesting fact that, in general, the most important phase shift obtained from the uniform model at a given energy and Z is also given by the shell model using a radius about three fourths that of the uniform model. This observation can, in fact, be shown to hold quite generally,[3] two models giving about the same scattering cross section for moderate energies so long as the second moment of their density distribution is the same.

This insensitivity to the details of the nuclear model can be utilized in calculating the electron scattering cross sections taking a simple model with some open parameters which can later be adjusted to yield results for any other model. Calculations by the Born approximation are particularly suitable because the results can be expressed in an algebraic form. One may think of an apparent difficulty here. While the equivalence of two models is valid for $k_0R_0\lesssim 1$, the convergence of the Born approximations improves with increasing energy of the incident electron ($\mathbf{k}_0$ is the wave vector of the incident electron and R_0 is the nuclear radius). This shows that our calculations are valid only for some intermediate energies. However, this is not a serious drawback; in fact, the Born approximations calculated on the basis of our model[4] are in fair agreement with Acheson's[2] results with the uniform model for 20- to 35-Mev electrons up to medium elements ($Z\lesssim 50$). (See Table X.)

In our calculations we have chosen a model for which the plane-wave matrix element is particularly simple; in fact, it appears to be the most natural choice, as will be clear later. It involves two parameters, B and C, which can be adjusted so as to give a good fit for practically any one-parameter model.[5] The potential to which this model corresponds is a combination of an attractive Coulomb and a repulsive Yukawa potential, C representing the relative strength and $1/B$ the range of the latter [see (IV.1)]. The corresponding charge density is given by

$$\rho=-(C-1)\delta^3(\mathbf{r})+\frac{CB^2}{4\pi}\frac{e^{-Br}}{r}. \tag{I.1}$$

Since $C>1$, the first term represents a negative charge center and the second a positive charge distribution whose density increases towards the center.[6] A good fit with the uniform model is obtained if C is put equal to 7/4. The above expression for ρ then represents a nucleus with $\frac{3}{4}Ze$ negative charge at the center and $(7/4)Ze$ positive charge outside.

Apart from looking at our model as a tool for the calculation of scattering from other models, one may also consider it in its own right. The experiments so far made are unable to decide between different models.

[1] M. E. Rose, Phys. Rev. **73**, 279 (1948); **82**, 389 (1951); L. R. B. Elton, Proc. Phys. Soc. (London) **A63**, 1115 (1950); **65**, 481 (1952); G. Parzen, Phys. Rev. **80**, 261, 355 (1950).

[2] L. K. Acheson, Phys. Rev. **82**, 488 (1951).

[3] See Rose, reference 1; H. Feshbach, Phys. Rev. **84**, 1206 (1951).

[4] There are two open parameters in our model which give it more flexibility and a greater range of validity than $k_0R_0\lesssim 1$, since this is roughly equivalent to considering two terms in the expansion of $\sin(kr)$ instead of just one. See (III.10).

[5] This has been explicitly examined in the cases of uniform, shell, and exponential models. See (III.11), (III.12), and (III.13) for proper values of B and C for these models.

[6] The proposal of a repulsive core for nucleon-nucleon forces has been made by Jastrow and by Lévy. R. Jastrow, Phys. Rev. **81**, 165 (1951); M. M. Lévy, **86**, 806 (1952); **88**, 725 (1952).

It will require experiments at higher energies where $k_0R_0 \gg 1$ for the differences in models to be effective. However, the experiments[7] of Lyman, Hanson, and Scott at 15.7 Mev already indicate that a greater concentration of the charge towards the center is required than was hitherto supposed. It is worth while observing that our model fulfills this requirement.

II. THEORY OF BORN APPROXIMATIONS

The Dirac equation for an electron moving in the potential[8] ZeV of a fixed center of force is

$$[E-i(\boldsymbol{\alpha}\cdot\text{grad})+m\beta]\psi=-Ze^2V\psi, \qquad \text{(II.1)}$$

where E is the energy of the electron, m its rest mass, Ze the charge of the nucleus, and $\boldsymbol{\alpha}$ and β are the well known Dirac matrices. We shall throughout put $\hbar=1$, $c=1$.

Operating on both sides by

$$D=E+i(\boldsymbol{\alpha}\cdot\text{grad})-m\beta, \qquad \text{(II.2)}$$

we get

$$(\nabla^2+k_0^2)\psi=-Ze^2DV\psi, \qquad \text{(II.3)}$$

where

$$k_0^2=E^2-m^2. \qquad \text{(II.4)}$$

Equation (3) can be solved as a power series in Ze^2. We write

$$\psi=\psi_0+\psi_1+\psi_2+\cdots \qquad \text{(II.5)}$$

and solve (3) by iteration. Using for ψ_0 the plane wave solution,

$$\psi_0=u^s(\mathbf{k}_0)\cdot\exp(i\mathbf{k}_0\cdot\mathbf{x}), \qquad \text{(II.6)}$$

as representing the incident electron, $u^s(\mathbf{k}_0)$ being the Dirac amplitude, and s denoting the spin state of the electron, it is shown in Appendix I that we get

$$\psi_1=Ze^2(A_1/r)\exp(ik_0r) \qquad \text{(II.7a)}$$

and

$$\psi_2=(Ze^2)^2(A_2/r)\exp(ik_0r), \qquad \text{(II.7b)}$$

where

$$A_1=(1/4\pi)(\mathbf{k}_1|V|\mathbf{k}_0)(E-\boldsymbol{\alpha}\cdot\mathbf{k}_1-m\beta)u^s(\mathbf{k}_0), \qquad \text{(II.8a)}$$

$$A_2=-\{1/[4\pi(2\pi)^3]\}(E-\boldsymbol{\alpha}\cdot\mathbf{k}_1-m\beta)\times\int_C\frac{(\mathbf{k}_1|V|\mathbf{k})(E-\boldsymbol{\alpha}\cdot\mathbf{k}-m\beta)(\mathbf{k}|V|\mathbf{k}_0)}{k_0^2-k^2}d^3ku^s(\mathbf{k}_0). \qquad \text{(II.8b)}$$

The vector $\mathbf{k}_1$ denotes the momentum of the scattered electron ($|\mathbf{k}_1|=k_0$) and

$$(\mathbf{k}_1|V|\mathbf{k}_0)=\int\exp(-i\mathbf{k}_1\mathbf{x})V(\mathbf{x})\exp(i\mathbf{k}_0\mathbf{x})d^3x. \qquad \text{(II.9)}$$

$(\mathbf{k}_1|V|\mathbf{k}_0)$ is a function of $(\mathbf{k}_1-\mathbf{k}_0)$ and is symmetrical between $\mathbf{k}_0$ and $\mathbf{k}_1$:

$$(\mathbf{k}_1|V|\mathbf{k}_0)=(\mathbf{k}_0|V|\mathbf{k}_1). \qquad \text{(II.10)}$$

[7] Lyman, Hanson, and Scott, Phys. Rev. **84**, 626 (1951).
[8] We shall from now on refer to V as the "potential."

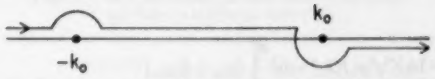

FIG. 1. Contour of integration C for the integral in Eq. (II.8b).

The integration in (8b) is to be performed in the complex plane as shown in Fig. 1.

In (8b), the $(E-m\beta)$ in the integrand can be take outside the integral sign. Observing that the integral

$$\int\frac{(\mathbf{k}_1|V|\mathbf{k})(\boldsymbol{\alpha}\cdot\mathbf{k})(\mathbf{k}|V|\mathbf{k}_0)}{k_0^2-k^2}d^3k$$

is symmetrical between $\mathbf{k}_0$ and $\mathbf{k}_1$ (see 10), it is easy to see that it must be proportional to $\boldsymbol{\alpha}\cdot(\mathbf{k}_0+\mathbf{k}_1)$. Hence, we can write (8b) as

$$A_2=(E-\boldsymbol{\alpha}\cdot\mathbf{k}_1-m\beta)[a_2(E-m\beta)-a_3\boldsymbol{\alpha}\cdot(\mathbf{k}_0+\mathbf{k}_1)]u^s(\mathbf{k}_0), \qquad \text{(II.11)}$$

where a_2 and a_3 are complex numbers given by

$$a_2=-\frac{1}{4\pi(2\pi)^3}\int_C\frac{(\mathbf{k}_1|V|\mathbf{k})(\mathbf{k}|V|\mathbf{k}_0)}{k_0^2-k^2}d^3k \qquad \text{(II.12a)}$$

and

$$a_3=-\frac{1}{4\pi(2\pi)^3}\frac{1}{(\mathbf{n},\mathbf{k}_0+\mathbf{k}_1)}\times\int_C\frac{(\mathbf{k}_1|V|\mathbf{k})(\mathbf{n}\cdot\mathbf{k})(\mathbf{k}|V|\mathbf{k}_0)}{k_0^2-k^2}d^3k. \qquad \text{(II.12b)}$$

In view of the remarks just made, a_3 is independent of the arbitrary vector $\mathbf{n}$.

From (7) and (8)

$$\psi_1+\psi_2=(Ze^2A/r)\exp(ik_0r) \qquad \text{(II.13)}$$

$$A=A_1+Ze^2A_2. \qquad \text{(II.14)}$$

Using (11) for A_2, we get

$$A=(E-\boldsymbol{\alpha}\cdot\mathbf{k}_1-m\beta)(a_1+Ze^2M)u^s(\mathbf{k}_0) \qquad \text{(II.15)}$$

where

$$a_1=\frac{1}{4\pi}\cdot(\mathbf{k}_1|V|\mathbf{k}_0) \qquad \text{(II.16)}$$

and

$$M=a_2(E-m\beta)-a_3(\boldsymbol{\alpha},\mathbf{k}_0+\mathbf{k}_1). \qquad \text{(II.17)}$$

Taking the absolute square of Ze^2A, summing over the spin directions of the scattered electron, and averaging over that of the incident electron, we obtain, as shown in Appendix II, the differential scattering cross section:

$$\frac{d\phi}{d\Omega}=\frac{d\phi_1}{d\Omega}+\frac{d\phi_2}{d\Omega}, \qquad \text{(II.18)}$$

with

$$\frac{d\phi_1}{d\Omega}=4Z^2e^4|a_1|^2k_0^2\cos^2\frac{\theta}{2}\left(1+\frac{m^2}{k_0^2}\sec^2\frac{\theta}{2}\right) \qquad \text{(II.19a)}$$

and

$$\frac{d\phi_2}{d\Omega}=16Z^2e^4a_1Ek_0^2\cos^2\frac{\theta}{2}\left[(a_{2r}+\tfrac{1}{2}a_{2r})+\frac{m^2}{k_0^2}a_{2r}\sec^2\frac{\theta}{2}\right]. \quad \text{(II.19b)}$$

Here, a_{2r} and a_{3r} are the real parts of a_2 and a_3. These are obtained if, instead of integrating along the contour C in (12), one takes the principal values of these integrals, i.e.,

$$a_{2r}=-\frac{1}{4\pi(2\pi)^3}\mathrm{P}\int\frac{(\mathbf{k}_1|V|\mathbf{k})(\mathbf{k}|V|\mathbf{k}_0)}{k_0^2-k^2}d^3k, \quad \text{(II.20a)}$$

$$a_{3r}=-\frac{1}{4\pi(2\pi)^3}\frac{1}{(\mathbf{n},\mathbf{k}_0+\mathbf{k}_1)}\times\mathrm{P}\int\frac{(\mathbf{k}_1|V|\mathbf{k})(\mathbf{n}\cdot\mathbf{k})(\mathbf{k}|V|\mathbf{k}_0)}{k_0^2-k^2}d^3k, \quad \text{(II.20b)}$$

P standing here for the principal value. a_1 is already defined in (16).

III. THE MATRIX ELEMENTS

The Coulomb potential V caused by a charge density ρ is given by

$$V(\mathbf{x})=\int\frac{\rho'}{|\mathbf{x}-\mathbf{x}'|}d^3x',$$

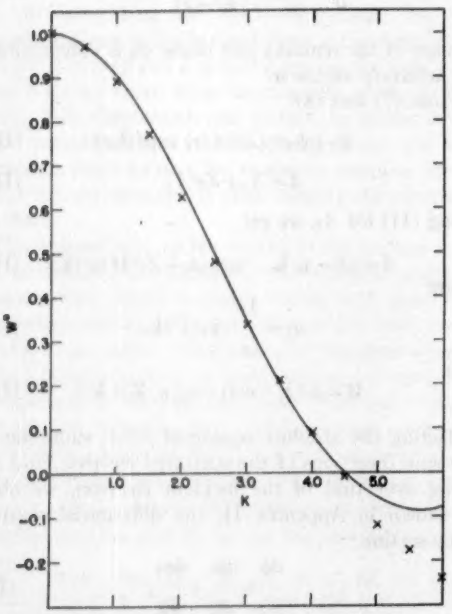

FIG. 2. Comparison of the exact and approximate matrix element for the uniform model. The crosses indicate the value of $1-(1.75K^3/14.8+K^3)$ which we have used as matrix element for the second order Born cross-section calculation. (See Table I.)

where $\rho'=\rho(x')$. To avoid unnecessary complications which arise in the case of Coulomb field, we introduce a cut-off factor, $\exp(-\lambda|\mathbf{x}-\mathbf{x}'|)$. Eventually we shall put $\lambda=0$. Thus

$$V(\mathbf{x})=\lim_{\lambda\to0}\int\frac{\rho'}{|\mathbf{x}-\mathbf{x}'|}\exp(-\lambda|\mathbf{x}-\mathbf{x}'|)d^3x'.$$

For a spherically symmetrical charge distribution,

$$V(\mathbf{x})=\lim_{\lambda\to0}\int\rho'r'^2dr'\int\frac{\exp(-\lambda|\mathbf{x}-\mathbf{x}'|)}{|\mathbf{x}-\mathbf{x}'|}d\Omega'.$$

Now

$$\lim_{\lambda\to0}\int\frac{\exp(-\lambda|\mathbf{x}-\mathbf{x}'|)}{|\mathbf{x}-\mathbf{x}'|}d\Omega'=4\pi\cdot\lim_{\lambda\to0}\begin{cases}\exp(-\lambda r)/r & \text{for } r\geq r'\\ \exp(-\lambda r')/r' & \text{for } r<r'\end{cases} \quad (|\mathbf{x}|=r).$$

Therefore

$$V(r)=\frac{4\pi}{r}\lim_{\lambda\to0}\left[\exp(-\lambda r)\int_0^r\rho'r'^2dr'+r\int_r^\infty\rho'r'\exp(-\lambda r')dr'\right]. \quad \text{(III.1)}$$

Using this in (II.9), and writing $\mathbf{p}$ for the momentum transfer,

$$\mathbf{p}=\mathbf{k}_1-\mathbf{k}_0, \quad p=|\mathbf{p}| \quad \text{(III.2)}$$

we get

$$(\mathbf{k}_1|V|\mathbf{k}_0)=\int V(r)\exp(-i\mathbf{p}\cdot\mathbf{x})d^3x$$

$$=\frac{4\pi}{p}\int_0^\infty rV\sin(pr)dr$$

$$=\frac{(4\pi)^2}{p}\int_0^\infty\sin(pr)dr\cdot\left[\exp(-\lambda r)\int_0^r\rho'r'^2dr'+r\int_r^\infty\rho'r'\exp(-\lambda r')dr'\right].$$

We normalize ρ to unity:

$$\int\rho d^3x=4\pi\int_0^\infty\rho r^2dr=1, \quad \text{(III.3)}$$

and employ

$$\int_0^\infty\sin(pr)\exp(-\lambda r)dr=p/(\lambda^2+p^2).$$

We then get

$$a_1=\frac{1}{4\pi}(\mathbf{k}_1|V|\mathbf{k}_0)=\frac{1}{p^2}-\frac{1}{p}\int_0^\infty f\sin(pr)dr, \quad \text{(III.4)}$$

where

$$f/(4\pi)=f(r)/(4\pi)=\int_r^\infty \rho' r'^2 dr' - r\int_r^\infty \rho' r' dr'. \quad \text{(III.5)}$$

It is to be noted that the function f is independent of p and depends only on the density distribution.

Simplification of the Matrix Elements

The first term in (4) is just the one due to a point charge, and the second can be considered as due to deviations from it. The function f is appreciable only within the region $r \lesssim R_0$, R_0 being the effective radius of the nucleus. We can therefore expand $\sin(pr)$ and get

$$a_1 = 1/p^2 - C_1 + C_2 p^2 - \cdots, \quad \text{(III.6)}$$

where

$$C_1 = \int_0^\infty r f dr, \quad \text{(III.7a)}$$

$$C_2 = (1/6)\int_0^\infty r^3 f dr, \text{ etc.} \quad \text{(III.7b)}$$

We can, in the first instance, neglect C_2, C_3, etc., so that

$$a_1 = 1/p^2 - C_1. \quad \text{(III.8)}$$

The expression (8) for the matrix element shows that two models will give the same scattering cross section provided that C_1 has the same value for both of them.

Our Matrix Element

If we take (8) for the matrix element and insert it in the integrals (II.20a, b) to calculate the second Born cross section, we notice at once that they diverge for high momenta. This shows that the expression (8) is not suited for working out the higher Born approximations.

However, we can introduce a "damping" term in (8) and write

$$a_1 = \frac{1}{p^2} - \frac{C}{B^2+p^2}, \quad \text{(III.9)}$$

where B and C are constants. If we expand the second term in increasing powers of p^2, we get

$$a_1 = 1/p^2 - (C/B^2)(1 - p^2/B^2) + \cdots, \quad \text{(III.10)}$$

and we see that C/B^2 corresponds to C_1 and C/B^4 to C_2. Knowing C_1 and C_2 for one kind of density distribution, they can be used to fix B and C in (9), and we can expect the two models to yield the same scattering cross section for a fairly large range of energies.[9] However, actual calculation shows that B and C can be much better found empirically by making a direct comparison of the matrix element (9) with that of another model without making an expansion in power series of p^2/B^2 utilizing (7).[10] In this way we get the following values of B and C for different models:

Uniform model ($\rho=\rho_0$ for $r \lesssim R_0$ and zero otherwise):

$$(BR_0)^2 = 14.8, \quad C = 1.75; \quad \text{(III.11)}$$

Shell model [$\rho = \rho_0 \delta(r - R_s)$]:

$$(BR_s)^2 = 7.4, \quad C = 1.75; \quad \text{(III.12)}$$

Exponential model [$\rho = \rho_0 \exp(-r/R_e)$]:

$$(BR_e)^2 = 2, \quad C = 1.1. \quad \text{(III.13)}$$

The close fit between the matrix elements of the uniform and our models with B and C given by (11) is illustrated by Table I and Fig. 2. W there is defined as $p^2 a_1 = (p^2/4\pi)(\mathbf{k}_1|V|\mathbf{k}_0)$. The difference between our W and W^{uniform} is within less than 4 percent for K not greater than 4.5 ($K = pR_0$).[11]

The ratio of the first Born approximation cross section for the uniform model to the Mott cross section is shown in Fig. 3.

TABLE I. Matrix elements and first-order cross section on uniform model.[a]

K	Our W	W^u	$d\phi_1{}^u/d\phi_c$
0.0	1	1	1
0.5	0.9709	0.9752	0.9511
1.0	0.8892	0.9035	0.8163
1.5	0.7691	0.7923	0.6278
2.0	0.6277	0.6531	0.4265
2.5	0.4804	0.4995	0.2495
3.0	0.3382	0.3457	0.1195
3.5	0.2075	0.2048	0.0419
4.0	0.0909	0.0871	0.0076
4.5	−0.0111	−0.0001	0.0000
5.0	−0.1195	−0.0571	0.0033
5.5	−0.1751	−0.0830	0.0069
6.0	−0.2402	−0.0839	0.0070

[a] $K = pR_0 = 2k_0 R_0 s$, $s = \sin(\theta/2)$; R_0 is the nuclear radius on the uniform model. $W = (\rho^0/4\pi)(\mathbf{k}_1|V|\mathbf{k}_0)$; $W^u = (3/K^3)(\sin K - K\cos K)$; our $W = 1 - Cp^2/(B^2+p^2) = 1 - CK^2/[(BR_0)^2 + K^2]$, with $C = 1.75$ and $(BR_0)^2 = 14.8$. $d\phi_1{}^u/d\phi_c = (W^u)^2$ is the differential cross section in units of the Mott cross section for a point charge. Notice the close agreement between $(W^u)^2$ and our W for $K \lesssim 4.5$. See Figs. 2 and 3.

IV. POTENTIAL AND CHARGE DENSITY

Since the Fourier transform of $\exp(-\lambda r)/r$ is $4\pi/(\lambda^2+p^2)$, the matrix element (III.9) that describes our model corresponds to a potential:

$$V = 1/r - (C/r)\exp(-Br), \quad \text{(IV.1)}$$

which, as already remarked in the introduction, is a mixture of an attractive Coulomb and a repulsive Yukawa potential. The difference between this and the Coulomb potential of a point charge is illustrated in

[9] This is an improvement over Feshbach's (see reference 3) criterion as it considers two terms in the expansion of $\sin(pr)$ while Feshbach considers only one. See also Rose (1948), reference 1, and reference 4 above.

[10] If one writes $C/B^2 = C_1$ and $C/B^4 = C_2$ and uses C_1 and C_2 obtained from the uniform model, one gets $(BR_0)^2 = 20$, $C = 3$. These are much less satisfactory than the empirically found values (III.11).

[11] For $Z = 79$ and $\theta = 180°$, $K = 4.3$ at 50 Mev.

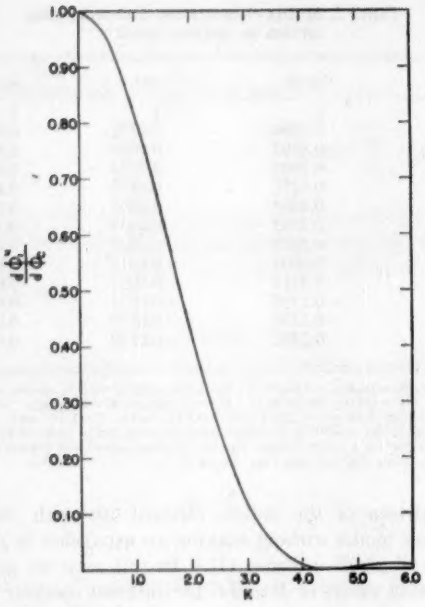

FIG. 3. Ratio of first Born approximation cross section for the uniform model to the Mott cross section. (See Table I.)

Table II and Fig. 4. It is appreciable for $Br \lesssim 2$, which corresponds to a distance of about one half the nuclear radius.[12]

It is interesting to see what the charge distribution is which gives (1) as the potential. This can be readily found by using Poisson's equation:

$$\rho = -(1/4\pi)\nabla^2 V.$$

Inserting (1) for V, we get

$$\rho = -(C-1)\delta^3(\mathbf{r}) + CB^2/(4\pi r)\exp(-Br). \quad \text{(IV.2)}$$

TABLE II. Comparison of our potential and the Coulomb potential.[a]

Br	$V/\left(\frac{1}{r}\right)$	V/B	V^c/B
0.0	−0.75	$-\infty$	$+\infty$
0.2	−0.433	−2.164	5.000
0.4	−0.173	−0.433	2.500
0.6	0.040	0.660	1.667
0.8	0.214	0.267	1.250
1.0	0.356	0.356	1.000
1.2	0.473	0.394	0.833
1.4	0.568	0.406	0.714
1.6	0.647	0.404	0.625
1.8	0.711	0.395	0.556
2.0	0.763	0.382	0.500
2.4	0.841	0.351	0.417
2.8	0.894	0.319	0.357
3.2	0.929	0.290	0.313

[a] $V/\left(\frac{1}{r}\right) = 1 - C\exp(-Br)$ with $C = 1.75$; consequently, $V/B = (Br)^{-1} \times [1 - C\exp(-Br)]$. $V^c = 1/r$. See Fig. 4.

[12] This is based on the correlation (III.11) between the two models.

This is the distribution (I.1) mentioned in the introduction where we have already discussed its significance. It may be remarked that the presence of C does not affect the normalization (III.3) of ρ, as can be directly verified from (2).

V. THE SECOND BORN CROSS SECTION

It is a simple matter to find the first Born cross section (II.19a) for any model when its matrix element is known. The second-order cross section (II.19b) requires the calculation of a_{2r} and a_{3r}. This is done for our model in Appendix III. We find

$$\tfrac{1}{2}a_{2r} = (1/w)(-CX_1 + C^2X_2), \quad \text{(V.1)}$$

$$a_{3r} = (1/w)(Y_0 - CY_1 + C^2Y_2), \quad \text{(V.2)}$$

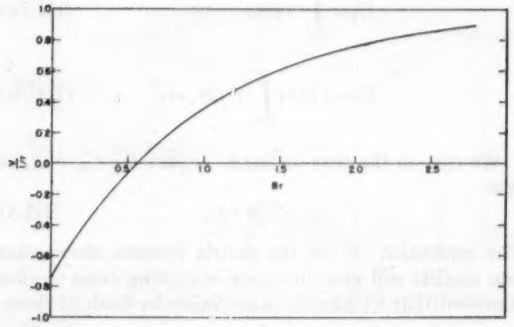

FIG. 4. Ratio of auxiliary potential (IV.1) to Coulomb potential. $V = (1 - Ce^{-Br})/r$, $BR_0 = 3.85$ (R_0 = nuclear radius on uniform charge density model), $C = 1.75$.

where

$$w = 8k_0^3(1-s^2),$$

$$X_1 = [(1-s^2)\xi^2/(1+s^2\xi^2)]\cdot\tan^{-1}(1/\xi), \quad \text{(V.3a)}$$

$$X_2 = [(1-s^2)\xi^2/(2s\eta)]\cdot\tan^{-1}(s\xi/(2\eta)), \quad \text{(V.3b)}$$

$$Y_0 = \pi(1-s)/(2s), \quad \text{(V.4a)}$$

$$Y_1 = \pi(1-s)/s - (2/s)\cot^{-1}(s\xi) + \frac{2+(1+s^2)\xi^2}{1+s^2\xi}\cot^{-1}\xi, \quad \text{(V.4b)}$$

$$Y_2 = \pi(1-s)/(2s) + [(2+\xi^2)/(2s\eta)]\cdot\tan^{-1}(s\xi/2\eta) + \cot^{-1}\xi - (1/s)\cot^{-1}(s\xi/2), \quad \text{(V.4c)}$$

$$s = \sin(\theta/2), \quad \xi = 2k_0/B, \quad \eta = (1+\xi^2+s^2\xi^4/4)^{\frac{1}{2}}.$$

Substituting these values of a_{2r} and a_{3r} in (II.19b), we find after some simplifications,

$$\frac{d\phi_2}{d\Omega} = 2Z^3e^6a_1(E/k_0)\{CR_1 + (C-1)^2R_2 + C(C-1)R_3 + C(m^2/k_0^2)[N_1 + (C-1)N_2]\}, \quad \text{(V.5)}$$

TABLE III. $100T_1$. See (V.12) and (V.6a).[a]

θ in degrees \ ξ	0.2	0.4	0.6	0.8	1.0	1.2	1.4	1.6	1.8	2.0
30	0.4605	0.4327	0.3947	0.3522	0.3078	0.2640	0.2219	0.1826	0.1464	0.1136
45	0.6107	0.5510	0.4719	0.3860	0.3016	0.2235	0.1545	0.0952	0.0457	0.0053
60	0.7237	0.6239	0.4960	0.3643	0.2428	0.1395	0.0557	−0.0091	−0.0569	−0.0912
90	0.8694	0.6794	0.4542	0.2473	0.0820	−0.0368	−0.1150	−0.1621	−0.1860	−0.1951
120	0.9447	0.6731	0.3505	0.1259	−0.0485	−0.1547	−0.2109	−0.2341	−0.2341	−0.2255
150	0.979	0.650	0.309	0.046	−0.126	−0.217	−0.257	−0.261	−0.251	−0.227
θ in degrees \ ξ	2.2	2.4	2.6	2.8	3.0	3.2	3.4	3.6	3.8	4.0
30	0.0841	0.0578	0.0351	0.0151	−0.0020	−0.0167	−0.0291	−0.0394	−0.0480	−0.0548
45	−0.0270	−0.0521	−0.0713	−0.0854	−0.0953	−0.1020	−0.1060	−0.1079	−0.1082	−0.1072
60	−0.1144	−0.1290	−0.1369	−0.1401	−0.1400	−0.1374	−0.1331	−0.1277	−0.1216	−0.1154
90	−0.1939	−0.1870	−0.1765	−0.1647	−0.1522	−0.1398	−0.1276	−0.1164	−0.1061	−0.0968
120	−0.2094	−0.1917	−0.1730	−0.1553	−0.1365	−0.1229	−0.1102	−0.0981	−0.0880	−0.0789
150	−0.208	−0.185	−0.164	−0.143	−0.126	−0.112	−0.0968	−0.0863	−0.0758	−0.0674

[a] For $\xi=0$, $T_1=T_3=\pi\epsilon^3 s/(1+s)$ (see Table IV). $\xi=2k_0/B$. See Figs. 5(a), (b).

where

$$R_1=(2/s)\cot^{-1}(s\xi)-(1/s)\cot^{-1}(\tfrac{1}{2}s\xi)-\frac{1+(2-s^2)\xi^2}{1+s^2\xi^2}\cot^{-1}\xi+\frac{2+(2-s^2)\xi^2}{2s\eta}\tan^{-1}(s\xi/2\eta), \quad \text{(V.6a)}$$

$$R_2=\pi(1-s)/(2s), \quad \text{(V.6b)}$$

$$R_3=\cot^{-1}\xi-(1/s)\cot^{-1}(\tfrac{1}{2}s\xi)+\frac{2+(2-s^2)\xi^2}{2s\eta}\tan^{-1}(s\xi/2\eta), \quad \text{(V.6c)}$$

$$N_1=(\xi^2/(s\eta))\tan^{-1}(s\xi/2\eta)-\frac{2\xi^2}{1+s^2\xi^2}\cot^{-1}\xi, \quad \text{(V.6d)}$$

$$N_2=(\xi^2/(s\eta))\tan^{-1}(s\xi/2\eta). \quad \text{(V.6e)}$$

In the relativistic region in which we are interested, we can neglect the terms proportional to (m^2/k_0^2), so that (5) simplifies to

$$d\phi_2/d\Omega=2Z^3e^6a_1[CR_1+(C-1)^2R_2+C(C-1)R_3]. \quad \text{(V.7)}$$

Born Cross Sections in Units of Mott Cross Section

It is simpler to express our cross sections in terms of the Mott cross section for scattering by a point charge. The latter is given by

$$d\phi_c/d\Omega=4Z^2e^4(k_0^2/p^4)\cos^2(\theta/2)\cdot[1+(m^2/k_0^2)\sec^2(\theta/2)]. \quad \text{(V.8)}$$

Hence we can write the first-order cross section (II.19a) as

$$d\phi_1/d\phi_c=p^4a_1^2=W^2 \quad \text{(V.9)}$$

$$W=p^2a_1=(p^2/(4\pi))(\mathbf{k}_1|V|\mathbf{k}_0); \quad \text{(V.10)}$$

$$p=2k_0s, \quad s=\sin(\theta/2).$$

TABLE IV. $100T_2$. See (V.12) and (V.6b).[a]

θ	30°	45°	60°	90°	120°	150°	180°
$100T_2$	0.4715	0.6347	0.7644	0.9498	1.064	1.127	1.1465

[a] $T_3=\pi\epsilon^3 s/(1+s)$, $s=\sin(\theta/2)$. Both T_1 and $-T_3$ reduce to T_2 for $\xi=0$. See Fig. 6.

TABLE V. $-100T_3$. See (V.12) and (V.6c).[a]

θ in degrees \ ξ	0.2	0.4	0.6	0.8	1.0	1.2	1.4	1.6	1.8	2.0
30	0.4713	0.4696	0.4659	0.4593	0.4507	0.4403	0.4286	0.4158	0.4024	0.3885
45	0.6341	0.6305	0.6220	0.6083	0.5898	0.5679	0.5434	0.5173	0.4905	0.4635
60	0.7634	0.7573	0.7429	0.7197	0.6891	0.6531	0.6139	0.5730	0.5320	0.4919
90	0.9480	0.9356	0.9073	0.8628	0.8052	0.7397	0.6714	0.6041	0.5397	0.4802
120	1.061	1.043	1.001	0.9361	0.8552	0.7656	0.6761	0.5912	0.5123	0.4445
150	1.124	1.103	1.050	0.9705	0.8736	0.7684	0.6673	0.5726	0.4905	0.4168
θ in degrees \ ξ	2.2	2.4	2.6	2.8	3.0	3.2	3.4	3.6	3.8	4.0
30	0.3745	0.3604	0.3463	0.3324	0.3187	0.3054	0.2923	0.2797	0.2674	0.2555
45	0.4368	0.4106	0.3854	0.3612	0.3380	0.3161	0.2954	0.2760	0.2577	0.2407
60	0.4532	0.4167	0.3824	0.3505	0.3211	0.2939	0.2692	0.2465	0.2259	0.2071
90	0.4259	0.3776	0.3344	0.2965	0.2630	0.2337	0.2081	0.1856	0.1660	0.1489
120	0.3838	0.3328	0.2883	0.2503	0.2180	0.1901	0.1669	0.1467	0.1295	0.1148
150	0.3558	0.3031	0.2589	0.223	0.192	0.166	0.145	0.126	0.112	0.0989

[a] For $\xi=0$, $T_3=-T_1=-\pi\epsilon^3 s/(1+s)$. See Table IV and Figs. 7(a), (b).

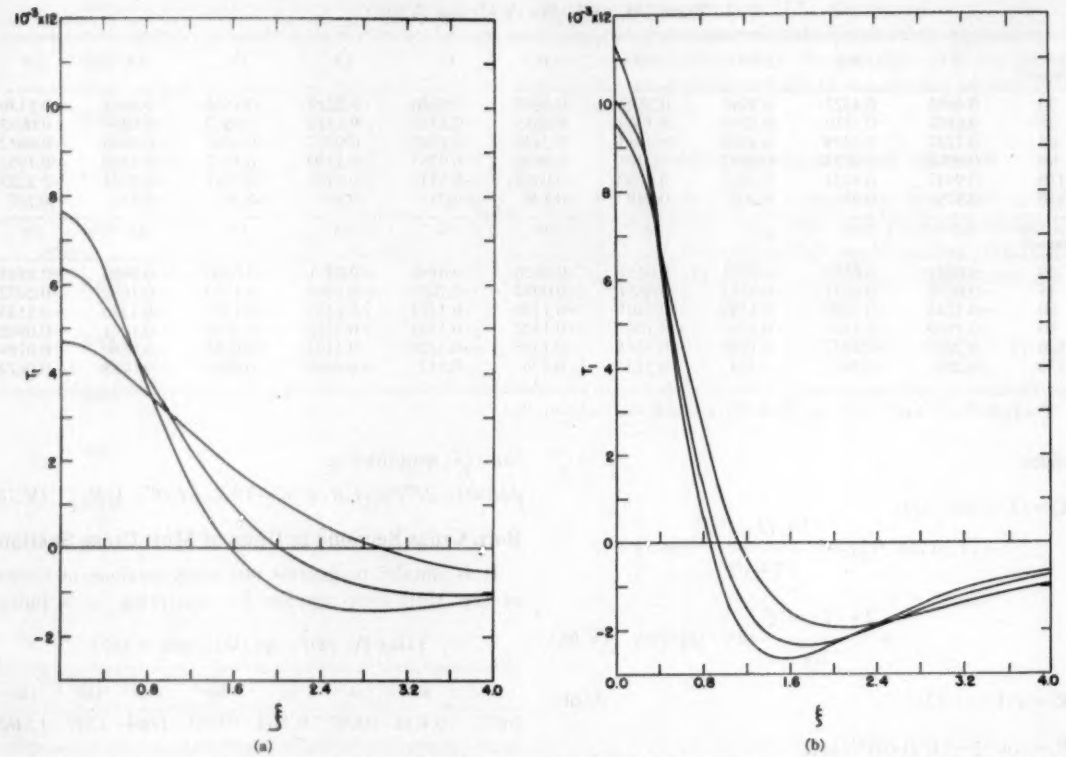

FIG. 5. (a) T_1 as function of ξ for $\theta=30°, 45°, 60°$ [see Table III and (V.12)]. (b) T_1 as function of ξ for $\theta=90°, 120°, 150°$ [see Table III and (V.12)].

If we neglect $(m^2/k_0^2)\sec^2(\theta/2)$ as compared to 1 in (8), we can also write (V.7) in the form

$$d\phi_2/d\phi_e = Ze^2[2s^2/(1-s^2)](p^2a_1) \times[CR_1+(C-1)^2R_2+C(C-1)R_3] = ZW[CT_1+(C-1)^2T_2+C(C-1)T_3], \quad \text{(V.11)}$$

where W is defined by (10) and

$$T_i = e^2R_i\cdot[2s^2/(1-s^2)] \quad (i=1, 2, 3). \quad \text{(V.12)}$$

Denoting by P the expression in the square brackets in (11),

$$P=CT_1+(C-1)^2T_2+C(C-1)T_3, \quad \text{(V.13)}$$

we can write

$$d\phi_2/d\phi_e = ZWP. \quad \text{(V.14)}$$

VI. HOW TO FIND THE SCATTERING CROSS SECTION FOR A GIVEN MODEL

From the tables and curves that we have plotted, scattering cross sections at different angles and energies can be found for practically any one-parameter model. How this can be done is explained below. The quantities relating to this model are denoted by a superscript x in this section.

(1) Find $W^x=(p^2/(4\pi))\cdot(\mathbf{k}_1|V^x|\mathbf{k}_0)$ and use it in (V.9) to find out the first Born cross section.

(2) Adjust B and C empirically so that our $W=1-Cp^2/(B^2+p^2)$ lies close to W^x for as wide a range of p as possible. If W^x vanishes at some point, it may be a useful hint to arrange our W also to vanish at that point.

(3) Having found B, $\xi=2k_0/B$ is known for the energy at which one wishes to find the cross section. Corresponding to this ξ, the values of T_1, T_2, and T_3 can be found from Tables III, IV, and V or from Figs. 5(a), 5(b), 6, 7(a) and 7(b). Multiplying them respectively by C, $(C-1)^2$ and $C(C-1)$ and adding, we get P in (V.14).

Knowing W^x and P, $d\phi_2/d\phi_e$ in (V.14) is now known for the element in question. [Notice that it is good to use W^x in (V.14) in order to avoid an extra unnecessary error by using our W instead.] Adding this to $d\phi_1/d\phi_e$ found in step (1), we know the whole cross section $d\phi/d\phi_e$.

The Uniform Model

For comparison with the uniform density model, the values of $(BR_0)^2$ and C are given by (III.11). The values of ξ for various elements and energies are given

TABLE VI. ξ for various elements at different energies.[a]

Z	A \ ε(Mev)	15	20	25	30	35	50	75	100
13	27	0.172	0.229	0.287	0.344	0.401	0.573	0.860	1.146
29	63	0.228	0.304	0.380	0.456	0.532	0.760	1.140	1.521
50	120	0.283	0.377	0.471	0.565	0.660	0.942	1.414	1.885
79	197	0.334	0.445	0.556	0.667	0.778	1.112	1.668	2.223
92	238	0.355	0.474	0.592	0.710	0.829	1.184	1.776	2.368

[a] $\xi = 2k_0/B$, where $1/B$ is the characteristic length in our model. It can be correlated with the nuclear radius R_0 by comparing the matrix elements of our model with those of the uniform density model. See (III.11). This gives $(BR_0)^2 = 14.8$. Writing $R_0 = r_0 A^{\frac{1}{3}}$ and using $r_0 = 1.45 \times 10^{-13}$ cm, which is the value used by Acheson[2] in his calculations, we get $2k_0R_0 = 1.47 \times 10^{-2} \epsilon A^{\frac{1}{3}}$, where ϵ is the energy of the electron in Mev. This gives

$$\xi = 2k_0R_0/(BR_0) = 3.82 \times 10^{-2} \epsilon A^{\frac{1}{3}}.$$

It may be remarked here that recent experiments indicate a lower value for r_0 ($\simeq 1.2 \times 10^{-13}$ cm). The values of the ξ will then be proportionately smaller.

in Table VI. We have also tabulated P for this case[13] (Table VII and Figs. 8a, b, c). Using the values of W^{α} given in Table I (or Fig. 2) we have also tabulated $(100/Z)d\phi_2/d\phi_e$ (Table VIII; see also Figs. 9(a), 9(b)). When this is taken together with the first Born cross section given in Table I and plotted in Fig. 3, we readily get the whole cross section for a given element, energy, and angle.

Table XI gives the ratio of the second to the first Born cross section.

VII. EXPANSION OF P IN POWERS OF ξ

P involves only elementary functions whose expansions in power series are well known. If one makes

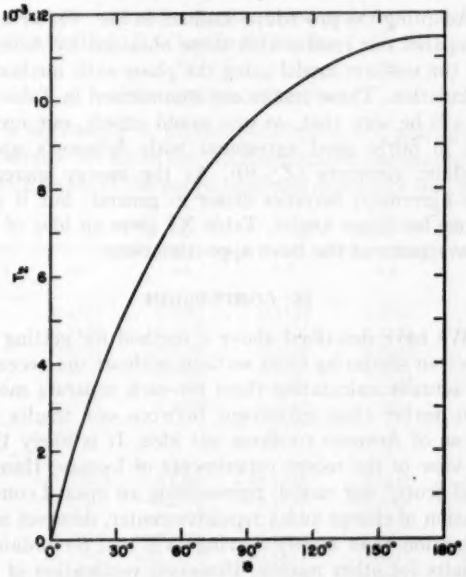

FIG. 6. T_1 as function of θ [see Table IV and (V.12)].

[13] See also Sec. VII.

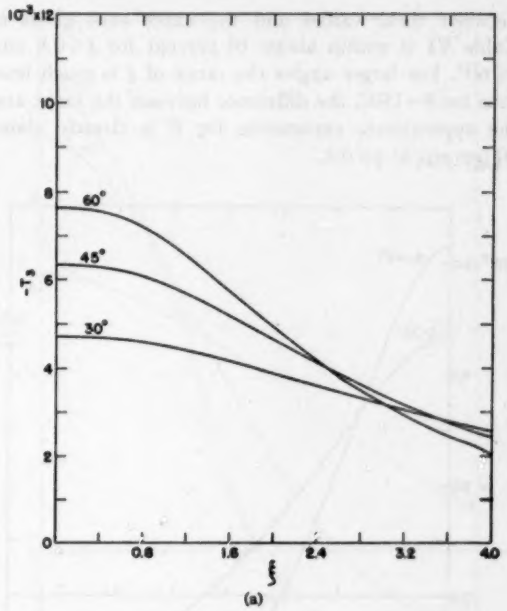

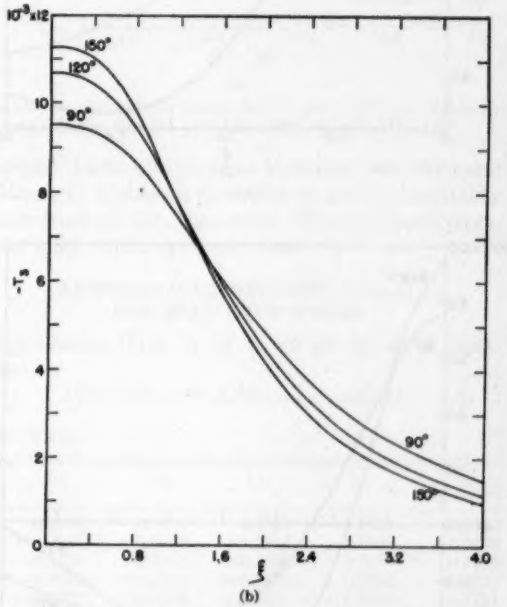

FIG. 7. (a) T_1 as function of ξ for $\theta = 30°$, 45°, 60° [see Table V and (V.12)]. (b) T_1 as function of ξ for $\theta = 90°$, 120°, 150° [see Table V and (V.12)].

these expansions, one obtains, up to terms in ξ^3,

$$P = [\pi e^2 s/(1+s)] \cdot [1 - 2Cs(1+s)\xi^2 \times \{1 - (1/3\pi)(4+C)\xi\}]. \quad \text{(VII.1)}$$

The numerical values of P obtained from this expression are given in Table IX. It will be seen that the agreement

between these values and the exact ones given in Table VI is within about 10 percent for $\xi \lesssim 0.8$ and $\theta \lesssim 60°$. For larger angles the range of ξ is much less; thus for $\theta = 150°$, the difference between the exact and the approximate expressions for P is already about 40 percent at $\xi = 0.4$.

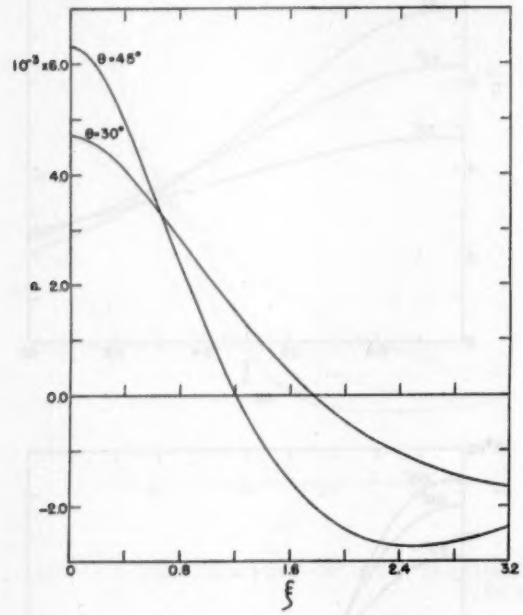

(a)

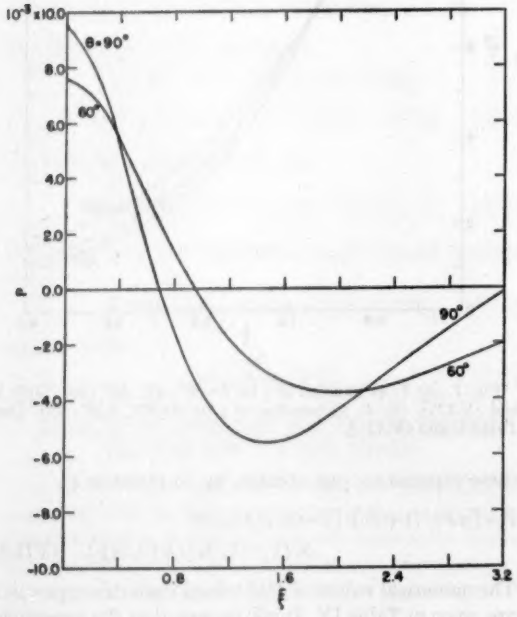

(b)

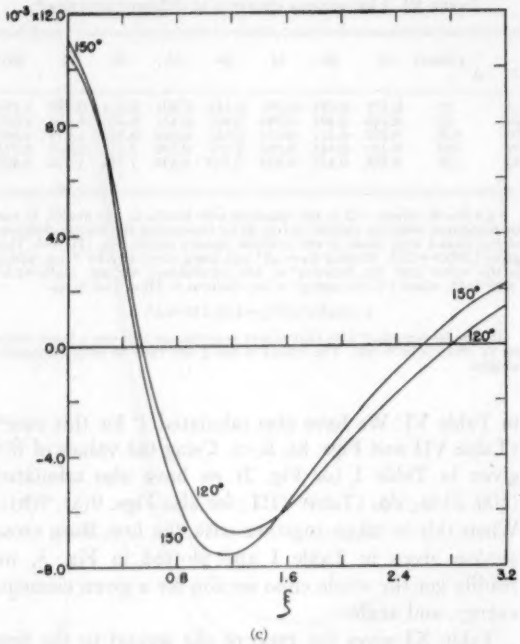

(c)

FIG. 8. (a) P as a function of ξ for the uniform model; $\theta = 30°$, 45° [see Table VI and (V.13)]. (b) P as a function of ξ for the uniform model; $\theta = 60°$, 90° [see Table VI and (V.13)]. (c) P as a function of ξ for the uniform model; $\theta = 120°$, 150° [see Table VI and (V.13)].

VIII. COMPARISON WITH ACHESON'S RESULTS FOR THE UNIFORM MODEL

Adopting the procedure outlined in Sec. VI, we have compared our results with those obtained by Acheson for the uniform model using the phase-shift method of calculation. These results are summarized in Table X. It will be seen that, as one would expect, our results are in fairly good agreement with Acheson's up to medium elements ($Z \lesssim 50$). As the energy increases the agreement becomes closer in general; but it gets worse for larger angles. Table XI gives an idea of the convergence of the Born approximations.

IX. CONCLUSION

We have described above a method for getting the electron scattering cross sections without the necessity of actually calculating them for each separate model. The rather close agreement between our results and those of Acheson confirms our idea. It is likely that, in view of the recent experiments of Lyman, Hanson, and Scott,[7] our model, representing an inward concentration of charge and a repulsive center, deserves more attention than merely serving as a tool for obtaining results for other models. However, verification of this will require work at energies higher than those at which experiments so far have been performed.

Incidentally, it appears that Born approximations

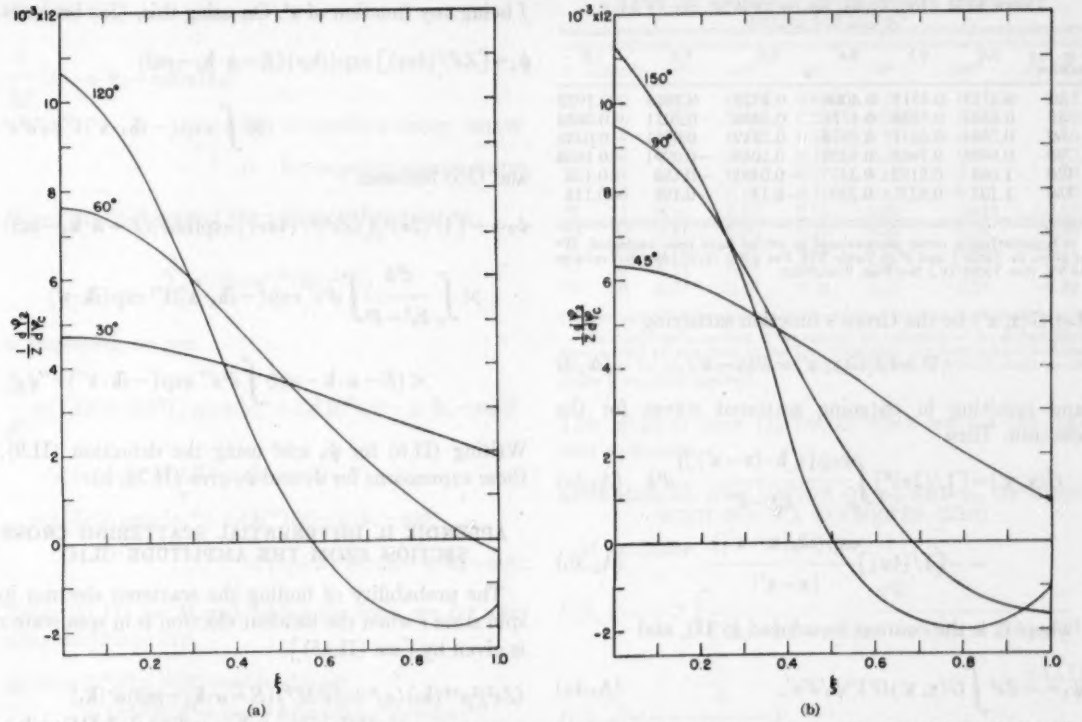

FIG. 9. (a) Second-order Born cross section, in units of Mott cross section, for the uniform model; $\theta=30°$, 60°, 120° [see Table IX and (V.14)]. (b) Second-order Born cross section in units of Mott cross section for the uniform model; $\theta=45°$, 90°, 120°.

are actually not so bad as they are reputed to be.[14] In fact, they seem to provide fairly accurate results so long as one does not expect too much from them (validity for high Z or low energies; see Table XI).

ACKNOWLEDGMENTS

It is impossible to express sufficiently my gratitude to Professor W. Kohn for the innumerable discussions I had with him and the suggestions and assistance that he provided. I wish also to thank Professor Niels Bohr and Professor C. Møller for extending to me the hospitality of the Institute for Theoretical Physics, Copenhagen, where most of this work was done.

APPENDIX I. EXPRESSIONS (II.7a,b) FOR SCATTERED WAVES

Introducing (II.5) in (II.3), we get the set of equations:

$$(\nabla^2+k_0^2)\psi_n=-Ze^2DV\psi_{n-1} \quad (n\geqslant 1). \qquad (A_1.1)$$

TABLE VII. $100P$. See (V.13).

θ in degrees \ ξ	0.2	0.4	0.6	0.8	1.0	1.2	1.4	1.6	1.8	2.0
30	0.4525	0.4061	0.3445	0.2786	0.2122	0.1492	0.0911	0.0391	−0.0067	−0.0460
45	0.5934	0.4938	0.3664	0.2340	0.1106	0.0027	−0.0859	−0.1554	−0.2068	−0.2420
60	0.6945	0.5280	0.3230	0.1228	−0.0496	−0.1833	−0.2783	−0.3380	−0.3679	−0.3752
90	0.8113	0.4953	0.1383	−0.1654	−0.3790	−0.5008	−0.5481	−0.5421	−0.4996	−0.4375
120	0.8587	0.4071	−0.0598	−0.4096	−0.6089	−0.6771	−0.6579	−0.5871	−0.4835	−0.3793
150	0.8715	0.3242	−0.2042	−0.5600	−0.7347	−0.7536	−0.6926	−0.5747	−0.4484	−0.3116
θ in degrees \ ξ	2.2	2.4	2.6	2.8	3.0	3.2	3.4	3.6	3.8	4.0
30	−0.0791	−0.1063	−0.1278	−0.1447	−0.1566	−0.1648	−0.1694	−0.1707	−0.1697	−0.1661
45	−0.2636	−0.2731	−0.2736	−0.2664	−0.2535	−0.2363	−0.2162	−0.1940	−0.1706	−0.1465
60	−0.3651	−0.3172	−0.3115	−0.2752	−0.2365	−0.1963	−0.1564	−0.1171	−0.0792	−0.0439
90	−0.3640	−0.2886	−0.2137	−0.1431	−0.0772	−0.0171	0.0378	0.0869	0.1307	0.1695
120	−0.2716	−0.1735	−0.0824	−0.0015	0.0738	0.1340	0.1866	0.2346	0.2746	0.3100
150	−0.1979	−0.0881	0.0063	0.0905	0.162	0.221	0.274	0.318	0.3537	0.3852

[a] For $\xi=0$, $P=T_2=xe^{2s}/(1+s)$, $s=\sin(\theta/2)$. See Figs. 8(a), (b), (c).

[14] R. Jost and A. Pais, Phys. Rev. 82, 840 (1951).

TABLE VIII. $(100/Z)(d\phi_2/d\phi_e) = 100W^*P$. See (V.14).*

θ in degrees \ ξ	0.0	0.2	0.4	0.6	0.8	1.0
30	0.4715	0.4511	0.4008	0.3322	0.2613	0.1922
45	0.6347	0.5826	0.4775	0.3386	0.2031	0.0884
60	0.7644	0.6837	0.4974	0.2819	0.0961	−0.0336
90	0.9498	0.7868	0.4389	0.1049	−0.0991	−0.1634
120	1.064	0.8192	0.339	−0.0391	−0.184	−0.152
150	1.127	0.823	0.259	−0.12	−0.198	−0.111

* Nonrelativistic terms proportional to m^2/k_0^2 have been neglected. W^* is given in Table I and P in Table VII. For $\xi = 0$, $(1/Z)(d\phi_2/d\phi_e)$ reduces to T_2. (See Table IV.) See Figs. 9(a), 9(b).

Let $G(\mathbf{x}, \mathbf{x}')$ be the Green's function satisfying

$$(\nabla^2 + k_0^2)G(\mathbf{x}, \mathbf{x}') = \delta^3(\mathbf{x}-\mathbf{x}') \qquad (A_1.2)$$

and resulting in outgoing scattered waves for the electron. Then

$$G(\mathbf{x}, \mathbf{x}') = [1/(2\pi)^3]\int_C \frac{\exp\{i[\mathbf{k}\cdot(\mathbf{x}-\mathbf{x}')]\}}{k_0^2 - k^2} d^3k \qquad (A_1.3a)$$

$$= -[1/(4\pi)]\frac{\exp(ik_0|\mathbf{x}-\mathbf{x}'|)}{|\mathbf{x}-\mathbf{x}'|} \qquad (A_1.3b)$$

(where C is the contour mentioned in II), and

$$\psi_1 = -Ze^2\int G(\mathbf{x}, \mathbf{x}')D'V'\psi_0' d^3x', \qquad (A_1.4a)$$

$$\psi_2 = (Ze^2)^2\int G(\mathbf{x}, \mathbf{x}')D'V'G(\mathbf{x}', \mathbf{x}'') \times D''V''\psi_0'' d^3x' d^3x''. \qquad (A_1.4b)$$

Inserting (3b) in (4a), we get, for large distances r,

$$\psi_1 = [Ze^2/(4\pi r)]\exp(ik_0 r) \times \int \exp(-i\mathbf{k}_1\cdot\mathbf{x}')D'V'\psi_0' d^3x', \qquad (A_1.5a)$$

where

$$\mathbf{k}_1 = k_0(\mathbf{r}/r).$$

In (4b), we introduce (3b) for $G(\mathbf{x}, \mathbf{x}')$ and (3a) for $G(\mathbf{x}', \mathbf{x}'')$. In this way we get, for large r,

$$\psi_2 = -[(Ze^2)^2/\{(4\pi)(2\pi)^3\}]\cdot(1/r)\exp(ik_0 r)\int_C \frac{d^3k}{k_0^2 - k^2} \times \int d^3x' \exp(-i\mathbf{k}_1\cdot\mathbf{x}')D'V' \exp(i\mathbf{k}\cdot\mathbf{x}') \times \int d^3x'' \exp(-i\mathbf{k}\cdot\mathbf{x}'')D''V''\psi_0''. \qquad (A_1.5b)$$

These expressions can be simplified by observing that

$$\int \exp(-i\mathbf{k}_1\cdot\mathbf{x}')D'f(\mathbf{x}')d^3x' = (E - \boldsymbol{\alpha}\cdot\mathbf{k}_1 - m\beta)\int \exp(-i\mathbf{k}_1\cdot\mathbf{x}')f(\mathbf{x}')d^3x',$$

f being any function of $\mathbf{x}'$. On using this, (5a) becomes

$$\psi_1 = [Ze^2/(4\pi r)]\exp(ik_0 r)(E - \boldsymbol{\alpha}\cdot\mathbf{k}_1 - m\beta) \times \int \exp(-i\mathbf{k}_1\cdot\mathbf{x}')V'\psi_0' d^3x'$$

and (5b) becomes

$$\psi_2 = -[1/(2\pi)^3][(Ze^2)^2/(4\pi r)]\exp(ik_0 r)(E - \boldsymbol{\alpha}\cdot\mathbf{k}_1 - m\beta) \times \int_C \frac{d^3k}{k_0^2 - k^2}\int d^3x' \exp(-i\mathbf{k}_1\cdot\mathbf{x}')V' \exp(i\mathbf{k}\cdot\mathbf{x}') \times (E - \boldsymbol{\alpha}\cdot\mathbf{k} - m\beta)\int d^3x'' \exp(-i\mathbf{k}\cdot\mathbf{x}'')V''\psi_0''.$$

Writing (II.6) for ψ_0 and using the definition (II.9), these expressions for ψ_1 and ψ_2 give (II.7a, b).

APPENDIX II. DIFFERENTIAL SCATTERING CROSS SECTION FROM THE AMPLITUDE (II.14)

The probability of finding the scattered electron in spin state r when the incident electron is in spin state s is given by [see (II.15)]

$$(Ze^2)^2 u^{r*}(\mathbf{k}_0)(a_1^* + Ze^2M^*)(E - \boldsymbol{\alpha}\cdot\mathbf{k}_1 - m\beta)u^r(\mathbf{k}_1) \times u^{r*}(\mathbf{k}_1)(E - \boldsymbol{\alpha}\cdot\mathbf{k}_1 - m\beta)(a_1 + Ze^2M)u^s(\mathbf{k}_0).$$

Averaging over the spin directions of the incident electron and summing over those of the scattered electron, we get the scattering cross section

$$\frac{d\phi}{d\Omega} = \frac{1}{2}\sum_{r,s=1,2}(\text{the above expression}),$$

where we denote the positive energy states by 1, 2 and the negative energy states by 3, 4.

The summation over the spin states can be performed in the usual way by introducing the well-known projection operator,

$$[1/(2E)](E - \boldsymbol{\alpha}\cdot\mathbf{k}_0 - m\beta),$$

TABLE IX. $100P$ from the approximate expression (VII.1).*

θ in degrees \ ξ	0.2	0.4	0.6	0.8	1.0
30	0.4526	0.4065	0.3488	0.2953	0.2619
45	0.5934	0.4925	0.3665	0.2496	0.1765
60	0.6939	0.5217	0.3065	0.1070	−0.0179
90	0.8089	0.4644	0.0340	−0.3651	−0.6147
120	0.8526	0.3359	−0.3098	−0.9083	−1.283
150	0.8637	0.2210	−0.5823	−1.327	−1.792

* Comparing these values of P with those given in Table VI, one sees that for angles less than or equal to 60° and $\xi \lesssim 0.8$, the agreement is within about 10 percent. For larger angles the range of ξ is much less; thus, for 150° and $\xi = 0.4$, the difference is about 40 percent. $P = T_2$ for $\xi = 0$.

so that

$$\frac{1}{2E}(E-\boldsymbol{\alpha}\cdot\mathbf{k}_0-m\beta)u(\mathbf{k}_0)$$
$$=\begin{cases} u(\mathbf{k}_0) & \text{for positive energy states} \\ 0 & \text{for negative energy states.}\end{cases}$$

When this is done and the orthogonality relation,

$$\sum_{r=1}^{4} u^r{}_i(\mathbf{k}_0)u^r{}_j{}^*(\mathbf{k}_0)=\delta_{ij},$$

is employed, we get

$$\frac{d\phi}{d\Omega}=[(Ze^2)^2/(8E^2)]\,\mathrm{spur}\,(a_1{}^*+Ze^2M^*)(E-\boldsymbol{\alpha}\cdot\mathbf{k}_1-m\beta)^3$$
$$\times(a_1+Ze^2M)(E-\boldsymbol{\alpha}\cdot\mathbf{k}_0-m\beta)$$
$$=\tfrac{1}{2}(Ze^2)^2\,\mathrm{spur}\,(a_1{}^*+Ze^2M^*)(E-\boldsymbol{\alpha}\cdot\mathbf{k}_1-m\beta)$$
$$\times(a_1+Ze^2M)(E-\boldsymbol{\alpha}\cdot\mathbf{k}_0-m\beta).$$

Using (II.17) for M and taking the spur, we get after some simplifications,

$$d\phi/d\Omega=2Z^2e^4|a_1|^2(E^2+m^2+k_0{}^2\cos\theta)$$
$$+2Z^3e^6E(E^2+3m^2+k_0{}^2\cos\theta)(a_1{}^*a_2+a_1a_2{}^*)$$
$$+2k_0{}^3(1+\cos\theta)(a_1{}^*a_3+a_1a_3{}^*)$$
$$+\text{terms of order } Z^4e^8 \text{ which we neglect.}$$

TABLE X. Comparison of our cross sections with Acheson's results.[a,b]

Z	ϵ(Mev)	30°	60°	90°	120°	150°
13	20	0.977	0.943	0.892	0.850	0.823
		(0.99)	(0.95)	(0.90)	(0.86)	(0.82)
13	30	0.964	0.893	0.794	0.712	0.665
		(0.98)	(0.90)	(0.80)	(0.71)	(0.65)
29	15	0.953	0.887	0.819	0.769	0.744
		(0.98)	(0.93)	(0.87)	(0.82)	(0.79)
29	20	0.947	0.850	0.755	0.680	0.646
		(0.98)	(0.90)	(0.80)	(0.71)	(0.65)
29	25	0.933	0.805	0.679	0.577	0.526
		(0.95)	(0.85)	(0.71)	(0.60)	(0.51)
29	30	0.917	0.756	0.596	0.473	0.394
		(0.95)	(0.80)	(0.60)	(0.46)	(0.37)
29	35	0.898	0.700	0.509	0.370	0.288
		(0.92)	(0.73)	(0.52)	(0.34)	(0.22)
50	20	0.918	0.708	0.557	0.449	0.409
		(0.95)	(0.81)	(0.64)	(0.49)	(0.40)
50	30	0.868	0.578	0.364	0.242	0.166
		(0.91)	(0.62)	(0.37)	(0.20)	(0.125)
79	20	0.915	0.522	0.317	0.206	0.159
		(0.98)	(0.69)	(0.40)	(0.236)	(0.16)
79	30	0.839	0.382	0.197	0.064	0.032
		(0.925)	(0.44)	(0.12)	(0.038)	(0.12)

[a] The numerical values of the cross section given above are based on the correlation (III.11) between our model and the uniform model. The point charge cross section $d\sigma_s/d\Omega$ used by Acheson in his work is taken as the unit; therefore, the values of the first and the second cross sections given in Tables I and VIII have first to be multiplied by $d\phi_s/d\sigma_s$ before the above table can be obtained.

[b] Acheson's values of the cross sections are given in parentheses. They were obtained from the curves that he has plotted in his paper.

TABLE XI. $d\phi_2/d\phi_1$ for various elements at different energies and angles.[a]

Z	ϵ(Mev)	30°	45°	60°	90°	120°	150°
13	20	0.059	0.076	0.089	0.10	0.11	0.11
13	30	0.055	0.069	0.078	0.086	0.082	0.085
29	15	0.13	0.17	0.20	0.23	0.25	0.26
29	20	0.13	0.16	0.19	0.21	0.21	0.22
29	25	0.12	0.15	0.17	0.17	0.16	0.15
29	30	0.12	0.14	0.15	0.13	0.10	0.05
29	35	0.11	0.13	0.13	0.09	0.032	−0.034
50	20	0.21	0.26	0.29	0.30	0.28	0.26
50	30	0.18	0.21	0.20	0.12	0.053	−0.12
79	20	0.32	0.39	0.41	0.38	0.29	0.17
79	30	0.27	0.27	0.24	0.23	−0.25	−0.49

[a] This table gives an idea of the relative contribution of the second Born cross section as compared to the first. Note that the Born approximations are better for higher energies, as one would expect. The dependence on angles is not quite apparent.

This gives at once (II.19a, b) when we use the fact that a_1 is real.

APPENDIX III. EVALUATION OF a_{2r} AND a_{3r} OF (II.20) WITH MATRIX ELEMENTS (III.9)

If we define

$$I_1(\lambda,\mu)=-\mathrm{P}\int\frac{d^3k}{[(\mathbf{k}_0-\mathbf{k})^2+\lambda^2](k_0{}^2-k^2)[(\mathbf{k}_1-\mathbf{k})^2+\mu^2]}, \quad (A_3.1)$$

$$I_2(\lambda,\mu)=-\frac{1}{\mathbf{n}\cdot(\mathbf{k}_0+\mathbf{k}_1)}\mathrm{P}$$
$$\times\int\frac{(\mathbf{n}\cdot\mathbf{k})d^3k}{[(\mathbf{k}_0-\mathbf{k})^2+\lambda^2](k_0{}^2-k^2)[(\mathbf{k}_1-\mathbf{k})^2+\mu^2]}, \quad (A_3.2)$$

we can write a_{2r} and a_{3r} as follows, where we insert the expressions (III.9) for the matrix elements:

$$a_{2r}=[4\pi/(2\pi)^3][I_1(0,0)-C\{I_1(0,B)+I_1(B,0)\}$$
$$+C^2I_1(B,B)], \quad (A_3.4)$$

$$a_{3r}=[4\pi/(2\pi)^3][I_2(0,0)-C\{I_2(0,B)+I_2(B,0)\}$$
$$+C^2I_2(B,B)]. \quad (A_3.5)$$

The technique of evaluating $I_{1,2}(\lambda,\mu)$ is given by Dalitz.[15] He has given $I_{1,2}(0,0)$ and $I_{1,2}(B,B)$ in his paper. The calculation of $I_{1,2}(0,B)+I_{1,2}(B,0)$ is straightforward. The final results are

$$I_1(0,0)=0,$$
$$I_1(0,B)=I_1(B,0)=\pi^2X_1/[4k_0{}^3(1-s^2)],$$
$$I_1(B,B)=\pi^2X_2/[2k_0{}^3(1-s^2)],$$
$$I_2(0,0)=\pi^2Y_0/[4k_0{}^3(1-s^2)],$$
$$\tfrac{1}{2}(I_2(0,B)+I_2(B,0))=\pi^2Y_1/[8k_0{}^3(1-s^2)],$$
$$I_2(B,B)=\pi^2Y_2/[4k_0{}^3(1-s^2)].$$

X_1, X_2 and Y_0, Y_1, Y_2 are defined in (V.3,4); $s=\sin(\theta/2)$.

When these expressions are used in (4) and (5), one gets the results mentioned in (V.1, 2).

[15] R. H. Dalitz, Proc. Roy. Soc. (London) **A206**, 509 (1951).

Experimental Studies of (p,t) Reactions

B. L. COHEN AND T. H. HANDLEY
Oak Ridge National Laboratory, Oak Ridge, Tennessee
(Received July 20, 1953; revised manuscript received October 28, 1953)

Several (p,t) reactions in heavy nuclei are studied by measuring excitation functions and angular distributions. While the data are not sufficiently extensive to justify general conclusions, they seem to indicate that: (1) a "pick-up" process is important only when the target nucleus contains two loosely bound neutrons; and (2) the inherent probability for the emission of tritons in the breakup of a compound nucleus is not much (if any) less than for the emission of neutrons or protons.

INTRODUCTION

OF the several new types of nuclear reactions that first became accessible to study with the entrance of proton accelerators into the 20-Mev energy region, one of the most interesting is the (p,t) reaction on various nuclei. In the first place, there is the question of whether the reaction can proceed by a "pick-up" process such as operates in (p,d) reactions. In accordance with the reciprocity theorem, such a process must be important in at least some cases if we are to accept the evidence of Kundu and Pool[1] that (t,p) reactions proceed by double neutron stripping. In the second place, if the reaction goes only by a compound nucleus interaction, there is the question of how well the statistical theory of nuclear reactions[2] can predict its cross section. An implicit assumption of that theory is that, aside from energy and Coulomb barrier considerations, all particles are emitted with equal probability; however, it would seem that there should be a greater inherent probability for emission of a simple particle like a neutron or proton than of a complex, loosely bound structure such as a triton (cf. the "many-body" theory of alpha decay[3,4]).

In this paper, we present the results of experimental studies of (p,t) reactions carried out with the internal, circulating beam of the Oak Ridge National Laboratory 86-in. cyclotron. While the results are not as complete and clear-cut as one would prefer, they give indications of the answers to the foregoing questions.

The data obtained, shown in Figs. 1–5, consist of excitation functions for (p,t) reactions on beryllium-9 and iron-54 and angular distributions of tritons from (p,t) reactions on beryllium, niobium, and palladium. Due to the extreme experimental difficulties, it is not considered feasible to carry the work further at this time.

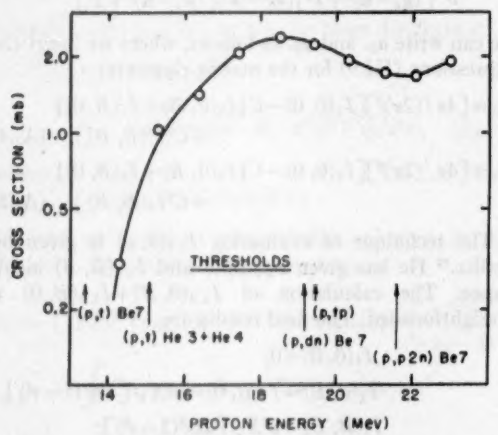

FIG. 1. Excitation function for $Be^9(p,t)Be^7$. Two other runs are in substantial agreement with these data; they are not shown because, in one case, the incident proton energy was not sufficiently homogeneous and, in the other, counting statistics were considerably poorer than in this run. Due to a calibration error, the ordinates should be multiplied by five. For example, the absolute cross section at 22 Mev is 9.0 mb.

EXPERIMENTAL METHODS

Excitation Functions

The excitation functions were measured by the stacked-foil method, modified for use with an internal cyclotron beam as described in detail elsewhere.[5] The beryllium foil was counted with a scintillation spectrometer set on the 480-kv peak. In one run, chemical purification was used. The iron was processed radiochemically after the bombardment and counted under an end-window Geiger counter with a 5-mg/cm² silver foil interposed to remove the Fe^{55} x-rays. Absolute decay rates were determined for beryllium with a Geiger counter which has been calibrated for gamma sensitivity[5a] and for iron by absolute beta-counting techniques. Absolute cross sections were determined by comparing with the known cross section for the (p,n) reaction in copper; the probable errors in the absolute cross sections shown in Figs. 1 and 2 are about 30 percent.

Angular Distributions

The general method of measuring angular distributions of nuclear reactions products with the internal,

[1] D. N. Kundu and M. L. Pool, Phys. Rev. **73**, 22 (1948).
[2] J. M. Blatt and V. F. Weisskopf, *Theoretical Nuclear Physics* (John Wiley and Sons, Inc., New York, 1952).
[3] H. A. Bethe, Revs. Modern Phys. **9**, 161 (1937).
[4] B. L. Cohen, Phys. Rev. **80**, 105 (1950).
[5] Cohen, Newman, Charpie, and Handley, (to be published).
[5a] *Note added in proof.*—New measurements have recently been made by counting with a scintillation spectrometer set on the 480-kv gamma peak and comparing with a well-assayed Be^7 source.

circulating cyclotron beam has been described in detail elsewhere;[6] only the most pertinent details will be discussed here. The target assembly consists essentially of a thin target of the element being studied at the center of a 3½-in. radius semicircular detector holder. The tritons are detected by the 1.6-hr activity of Co^{61} which they induce in cobalt metal foil by the (t,p) reaction. The cobalt foil is prepared[7] by electroplating from a $CoCl_2$-boric acid solution onto a stainless steel plate; the cobalt is then easily peeled off.

In the case of beryllium, the variation of triton energy with angle due to center-of-mass motion is corrected

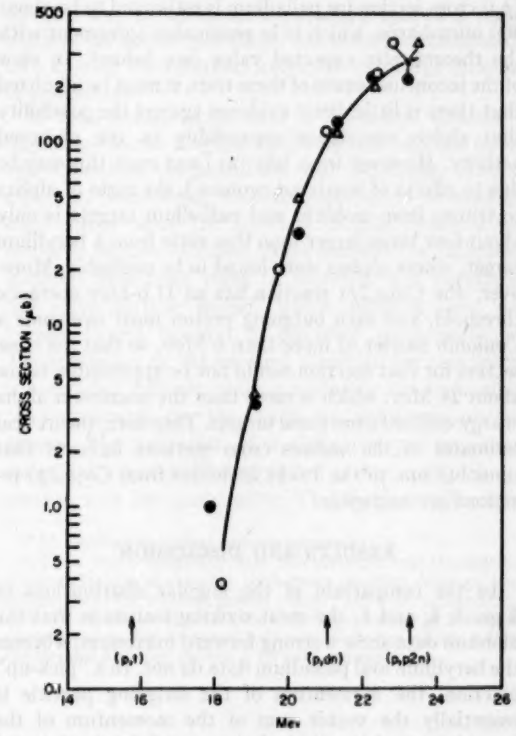

FIG. 2. Excitation function for $Fe^{54}(p,t)Fe^{52}$. The arrows show the thresholds for production of Fe^{52} by various reactions.

for by covering the detectors with a stepped absorber to reduce the long-range groups (those coming from reactions which leave Be^7 in its ground state or 470-kev excited state) to the same energy at each angle, and completely to absorb all lower-energy triton groups. For niobium and palladium, no effort was made to distinguish between the various triton groups.

All parts of the target assembly which are exposed to the cyclotron beam are covered with carbon; this minimizes or eliminates backgrounds of tritons,

[6] B. L. Cohen and R. V. Neidigh, Rev. Sci. Instr. (to be published).

[7] O. Sissman and C. D. Bopp, Oak Ridge National Laboratory Report ORNL-299 (unpublished).

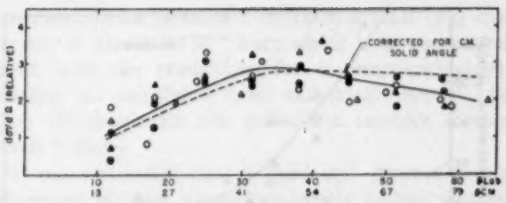

FIG. 3. Angular distribution of tritons from $Be^9(p,t)Be^7$. Only tritons from reactions in which Be^7 is left in its ground or first excited states are counted.

neutrons, deuterons, and alpha particles, since (p,t), (p,n), (p,d), and (p,α) reactions have very high thresholds in carbon-12. The target is bombarded for 1½ hr with about 10 μa of 22-Mev protons, after which the cobalt foils are removed, processed chemically to remove all elements except cobalt, and then counted under end-window Geiger counters with 70-mg/cm² aluminum absorbers interposed. The chemical processing eliminates the products of (n,α) and $(\alpha,2n)$ reactions on cobalt which have half-lives comparable with that of Co^{61} and at the same time eliminates activities from impurities. Counting under an absorber removes the 9-hr internal conversion activity of Co^{58}, which is produced in great abundance by elastically scattered protons, and strongly absorbs the 70-day Co^{58} activity which is the principle source of background. The most serious background difficulty is at the 20° position for the palladium target where the counting rates for the 70-day, the 9-hr grow-in of the 70-day, and the cosmic-ray background are initially greater than the 1.6-hr Co^{61} activity by ratios of 10, 2, and 3, respectively. At larger angles, only cosmic-ray background interferes, but even this presents a problem because it is at all times considerably larger than the 1.6-hr counting rate. It is therefore necessary to place each cobalt sample under a separate counter and use automatic recording over at least a 24-hr period. In almost every case, the activity remaining after background has been subtracted indicates a half-life between 1.3 and 2.0 hr. with 1.6 hr representing a fair average. However, due to the errors introduced by subtracting the large background, the uncertainties in individual points in Figs. 3–5 are about 40 percent.

To check whether the 1.6-hr activity could be due to proton or neutron induced activities on impurities (in spite of the original purity of the foils and the rather exhaustive chemical processing), one of the detecting foils was covered with a 100 mg/cm² absorber during the bombardment. In every case, the 1.6-hr activity was removed. Since the angular distributions of both elastically and inelastically scattered protons and of deuterons from (p,d) reactions exhibit strong maxima in the forward direction, the possibility that the 1.6-hr activities are induced by either deuterons or protons would seem to be excluded by the fact that the results for beryllium and palladium, Figs. 3 and 5, showed no

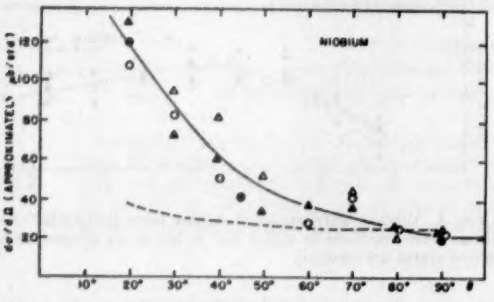

FIG. 4. Angular distribution of tritons from $Nb^{93}(p,t)Nb^{91}$. All triton groups are included. The dashed line is the line through the palladium data of Fig. 5.

forward peak; and even the forward rise for niobium, Fig. 4, was much too slow. Alpha particles could cause difficulty, however, expecially since the $(\alpha,2p)$ reaction on cobalt also produces Co^{61}. Three types of tests were made which indicate that, for beryllium at least, this reaction is a negligible contributor:

(a) Determinations were made of the 3.4-hr Cu^{61} activity in some of the foils. This activity is produced by $(\alpha,2n)$ on cobalt, which should have a cross section much larger than $(\alpha,2p)$. The corrected activity of Cu^{61} was found to be only twice that of Co^{61}.

(b) A rough excitation function for the detecting reaction was obtained by covering several cobalt foils at the same angle with different thicknesses of absorber. Three thick-target relative yields of 6.5, 2.5, and $\gtrsim$0.5 must be due either to tritons of 8.0 to 4.5, 6.6 to 2.5, and 5.0 to 0 Mev, or to alpha particles of 18 to 10, 13 to 0, and 4 to 0 Mev.[8] Since the $(\alpha,2p)$ energetic threshold is 11.6 Mev and proton emission is through a Coulomb barrier of 6 Mev, it hardly seems possible that thick target yields of this reaction should decrease by only a factor of 2.6 from 18 to 13 Mev. On the other hand, these yields agree roughly with what might be expected for the (t,p) reaction.

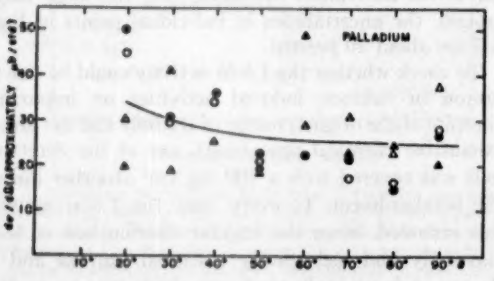

FIG. 5. Angular distribution of tritons from (p,t) reactions on palladium. All triton groups from all palladium isotopes are included.

[8] The spread in energies is due to the finite thickness of the beryllium target.

(c) By estimating the (t,p) absolute cross section from Kundu's work,[9] the cross section for the (p,t) reaction can be calculated from angular distribution data. The results agree roughly with the measured $Be(p,t)$ cross section, Fig. 1.

For niobium and palladium, test (a) indicated the relative yields of Cu^{61} and Co^{61} to be in the ratio of about 8 to 1 at large angles (there was difficulty at small angles because Cu^{61} is produced by elastically scattered protons on the nickel impurity). Test (b) could not be performed because the tritons are not monoenergetic. With regard to test (c), the total (p,t) cross section for palladium is estimated to be about 300 microbarns, which is in reasonable agreement with the theoretically expected value (see below). In view of the inconclusiveness of these tests, it must be admitted that there is little direct evidence against the possibility that alphas contribute appreciably to the observed activity. However from test (a) [and even this may be due to effects of scattered protons], the ratio of alphas to tritons from niobium and palladium targets is only about four times larger than that ratio from a beryllium target, where alphas were found to be negligible. Moreover, the $Co(\alpha,2p)$ reaction has an 11.6-Mev energetic threshold, and each outgoing proton must overcome a Coulomb barrier of more than 6 Mev, so that the cross section for that reaction would not be appreciable below about 24 Mev, which is more than the maximum alpha energy emitted from these targets. Therefore, theoretical estimates of the various cross sections indicate that contributions to the 1.6-hr activities from $Co(\alpha,2p)$ reactions are negligible.

RESULTS AND DISCUSSION

In the comparison of the angular distributions of Figs. 3, 4, and 5, the most striking feature is that the niobium data show a strong forward maximum, whereas the beryllium and palladium data do not. In a "pick-up" reaction, the momentum of the outgoing particle is essentially the vector sum of the momentum of the incoming particle, which is large and in the forward direction, and the momentum of the particles that are picked up, which have no strongly preferred direction. The angular distribution of the outgoing particles is therefore characterized by a strong maximum in the forward direction or at a relatively small angle. A compound nucleus interaction could, of course, also give a strong forward maximum in special cases of resonance reactions. However, the tritons that are detected in the experiments on niobium or palladium come from reactions in which the final nucleus is left in all states of excitation up to several Mev. Furthermore, the incident proton energies are inhomogeneous by about 1 Mev, and the compound nucleus excitation is about 30 Mev, so that a very large number of compound states are

[9] D. N. Kundu and M. L. Pool, Phys. Rev. **82**, 772 (1951).

involved. The observed angular distributions are therefore averages over a tremendous number of resonant reactions, which fact precludes the possibility that strongly nonisotropic angular distributions can be observed unless there is some strongly systematic reason for it. Goldhaber[10] has suggested that there may be some such reason connected with the rather large spin of niobium (9/2). However, incident orbital angular momentum waves up to $l=7$ are important in formation of the compound nucleus so that the range of compound-nucleus spins that can be formed in the bombardment of niobium is not much larger than in the bombardment of palladium. Moreover, there is no obvious way in which an unpolarized spin of a target nucleus, no matter how large, can introduce complexity into angular distributions averaged over large numbers of resonances.

It thus seems likely that a "pick-up" process is important in the niobium (p,t) reaction but not in the (p,t) reactions on palladium and beryllium. This is especially interesting from the standpoint of nuclear-shell theory since the niobium nucleus contains two neutrons outside of closed shells whereas the palladium isotopes have from eight to fourteen. For beryllium, the alpha-particle model, which predicts only one loosely bound neutron is probably most pertinent. The minimum in the forward direction for beryllium[11] is somewhat difficult, though certainly not impossible, to understand on the basis of compound-nucleus theory. The indication of a slight forward maximum for palladium could be interpreted as due to a "pick-up" process with low probability. The absolute differential cross section for palladium indicates a total (p,t) cross section of about 3×10^{-4} barn which is in good agreement with the predictions for a compound-nucleus reaction as calculated from statistical theory[2] [the (p,t) thresholds for the palladium isotopes average about 7 Mev].

If our conclusion that a "pick-up" process is only important in cases where two loosely bound neutrons are available is correct, the (p,t) reaction on Fe^{54} should proceed by a pure compound-nucleus interaction since the Fe^{54} nucleus contains 28 neutrons. A comparison of the data from Fig. 2 with the predictions of the statistical theory of nuclear reactions indicates that the theoretical values are too small by about a factor of two. Since most predictions from statistical theory in this mass region are too small by factors of from 2 to 10,[12] this result indicates that the inherent probability of triton emission is not a great deal lower than for neutron or proton emission. This conclusion is consistent with the absolute cross-section determination from the palladium angular distribution.

In summary, although the data are not sufficiently extensive to justify definite conclusions, they seem to indicate the following answers to the two questions posed in the introduction:

(1) The "pick-up" process is significant in (p,t) reactions only in cases where the target nucleus contains two loosely bound neutrons (outside of closed shells).

(2) The inherent probability for triton emission in compound-nucleus decay is not much, if any, lower (i.e., less than an order magnitude) than for neutrons or protons.

The authors would like to acknowledge the assistance of A. Timnick (Michigan State College) in some of the chemical separations and the many helpful suggestions, discussions, and comments of K. Boyer (Los Alamos), J. L. Fowler, and R. A. Charpie.

[10] M. Goldhaber (private communication).

[11] There was a possibility that the minimum was the result of a miscalculation of absorber thicknesses resulting from an overestimation of the incident proton energy; however, separate runs with the absorbers calculated for an incident energy 1½ Mev lower (open points in Fig. 3) caused only a small change. (Runs without the stepped absorber showed a forward maximum.)

[12] E. B. Paul and R. L. Clark, Can. J. Phys. 31, 267 (1953).

Internal Bremsstrahlung and Ionization Accompanying Beta Decay*

F. BOEHM† AND C. S. WU
Columbia University, New York, New York
(Received October 7, 1953)

Internal bremsstrahlung spectra from S^{35} and Pm^{147} have been investigated with the NaI scintillation spectrometer. Both the absolute cross section of production and the energy distribution agree with theoretical predictions. The theoretical internal bremsstrahlung spectrum of RaE was calculated by using both the observed forbidden β spectrum and an allowed β distribution. No significant differences in shape were found in these two cases except in the absolute cross section of production.

The ionization accompanying beta decay was studied in the case of RaE and also in Pm^{147} by measuring the characteristic x-rays in an NaI scintillation counter as well as in a proportional counter spectrometer. Both K and L radiations were observed, and their absolute cross sections were compared with the theoretical calculations of Migdal, Feinberg, and Levinger. Because of the approximate nature of the theoretical calculations, the agreement between the theoretical and experimental results is considered satisfactory.

I. INTRODUCTION

THE process of β decay is accompanied by various secondary effects which have been subjects of investigations for the last two decades. One of these secondary effects is the interaction of the nuclear beta particle with the radiation field of the nucleus causing the emission of internal bremsstrahlung (continuous x-rays). Another secondary effect is the perturbation of the atomic electrons resulting from either the sudden change of nuclear charge or simply the direct collision between the beta particle and the inner electrons. This perturbation induces electronic excitation to an unoccupied discrete level or ionization to the continuum. The hole in the inner electron shell thus created will be immediately filled up by an electron from the outer shell or from the continuum. Characteristic x-rays or Auger electrons will be emitted as a result. Additional secondary effects which are expected as the result of beta decay are the annihilation of the electron-positron on the atomic core and pair creation during β decay. However, we shall concern ourselves here only with the the production of inner bremsstrahlung and the ionization of the atom.

II. INTERNAL BREMSSTRAHLUNG

1. Introduction

The probability of emission of the internal bremsstrahlung and the shape of the bremsstrahlung spectrum have been investigated both experimentally and theoretically in various laboratories. The more recent experimental investigations are by Wu;[1] by Stahel and Guillessen[2] with the ionization chamber method; by Novey,[3] and by Bolgiano, Madansky, and Rasetti[4] with a NaI scintillation spectrometer. The β-radioactive substances used in these investigations were P^{32}, Y^{91}, and RaE^{210}. Investigations on electron-capture processes were made by Maeder and Preiswerk,[5] by Bell *et al.*,[6] and also by Anderson and his co-workers.[7] Calculations on the internal bremsstrahlung spectrum were first made by Knipp and Uhlenbeck[8] and by Bloch[9] for allowed β transitions with a polar vector interaction. Chang and Falkoff[10] and Madansky[11] extended these calculations to first and second forbidden β transitions and different types of interactions. (Allowed: scalar or tensor, first forbidden; scalar or tensor ($\Delta I=2$, yes), second forbidden; scalar.) Their results indicate that both the ratio of γ intensity to β intensity and the shape of the bremsstrahlung spectrum are almost the same for forbidden transitions as for allowed transitions, irrespective of the types of interactions. The production of internal bremsstrahlung due to the electron-capture process was first theoretically investigated by Morrison and Schiff.[12]

Furthermore, in evaluating the production of internal bremsstrahlung, one usually treats the over-all process in two steps:

$$N_0 \xrightarrow{(1)} P+\nu+e' \xrightarrow{(2)} P+\nu+e+\gamma(k),$$

where (1) represents the transition from initial to intermediate state with the transformation of the nucleon and the creation of a pair of light particles and (2) represents the transition of the electron from the intermediate state to the final state with the simultaneous emission of a light quantum of energy k.

The joint probability of the over-all process of emission of a quantum of energy k can be calculated with the

* This work was partially supported by the U. S. Atomic Energy Commission.
† Boese Postdoctoral Fellow of Columbia University (1952–1953), presently at California Institute of Technology, Pasadena, California.
[1] C. S. Wu, Phys. Rev. **59**, 481 (1941); references to earlier papers given here.
[2] E. Stahel and J. Guillessen, J. phys. radium **1**, 12 (1940).
[3] T. B. Novey, Phys. Rev. **89**, 672 (1953).
[4] Bolgiano, Madansky, and Rasetti, Phys. Rev. **89**, 679 (1953); L. Madansky and F. Rasetti, Phys. Rev. **83**, 187 (1951).
[5] D. Maeder and P. Preiswerk, Phys. Rev. **84**, 595 (1951).
[6] Bell, Tauch, and Cassidy, Science **115**, 12 (1952).
[7] Anderson, Wheeler, and Watson, Phys. Rev. **87**, 668 (1952).
[8] J. K. Knipp and G. E. Uhlenbeck, Physica **3**, 425 (1946).
[9] F. Bloch, Phys. Rev. **50**, 272 (1936).
[10] C. S. Wang Chang and D. L. Falkoff, Phys. Rev. **76**, 365 (1949).
[11] Madansky, Lipps, Bolgiano, and Berlin, Phys. Rev. **84**, 596 (1951).
[12] P. Morrison and L. Schiff, Phys. Rev. **85**, 24 (1940).

rigorous second-order perturbation method. However, Knipp and Uhlenbeck introduced an alternate method in which the joint probability for the over-all process was simply the product of the probabilities of all the steps. This simplification could be justified if the two processes were independent of each other. Although there is no basis for assuming these processes as independent, the result obtained with this simple approach for the allowed β transition turns out to be exactly the same as that from the more rigorous second-order perturbation method. Therefore, the acceptance of its use for the allowed transition invoked no arguments.

However, the question was then raised as to the validity of the application of this simple method to forbidden transitions. It was pointed out by Morrison and Schiff[12] that the close agreement between the calculations by second-order and by first-order perturbation methods for allowed transitions results from the fact that the electron-neutrino coupling does not depend explicitly on the momenta of these particles. This is certainly not true in forbidden cases. Chang and Falkoff[10] carried out calculations with both the second-order perturbation method and the simple method for first and second forbidden transitions of scalar interactions. They found that, although the results from these two methods are not exactly the same, the close agreement between them justifies the adoption of the simple method. Under the assumption of independence of these two processes, the probability for the emission of a γ quantum with energy k can be expressed[8,9] as

$$S(k)=\int dW_e P(W_e)\Phi(W_e, k),$$

where $P(W_e)dW_e$ is the distribution of the β spectrum and $\Phi(W_e, k)$ is the probability of an electron coming from the nucleus with energy W_e. The function $\Phi(W_e, k)$ was calculated to be

$$\Phi(W_e, k)=\frac{\alpha p_e}{\pi p_e k}\left\{\frac{W_e^2+W_e^2}{W_e p_e}\ln(W_e+p_e)-2\right\},$$

where "W_e and W_e" and "p_e and p_e" are the energies and momenta of the electron before and after the emission of the photon k. It can be seen that one obvious advantage of using the simple expression is that one may use the experimentally measured β spectrum for $P(W_e)dW_e$, thereby avoiding the difficulty of dealing with the lack of uniqueness in the type of interaction in β decay. This is particularly so in the case of RaE. The β spectrum of RaE has an unique forbidden shape with a great excess of low-energy electrons. The only reasonable theoretical fitting to the observed spectrum was attempted by Petschek and Marshak[13] by using a mixture of interactions (tensor and pseudoscalar). However, no calculations using this particular mixture of interactions have been made for the internal bremsstrahlung. By applying the simple method, one could use the observed β spectrum of RaE. Nevertheless, it is interesting to examine how sensitive the shape of the bremsstrahlung is to changes in the distribution of the β-particle energy in the case of RaE by calculating its spectrum, assuming first the observed β spectrum, then an allowed spectrum. The result of this comparison is shown in Fig. 1 on an absolute scale. Both curves 1 and 2 are normalized per β disintegration. It is interesting to note that the difference in shape of these two curves is rather insignificant. However, the absolute probabilities in the low-energy region of these two calculations do differ from one another by a factor of 1.3 with the higher cross section for the curve with allowed β distribution. This is quite understandable since the measured β spectrum has an excess of electrons with energy less than 0.2 Mev, which contribute less in the production of internal bremsstrahlung.

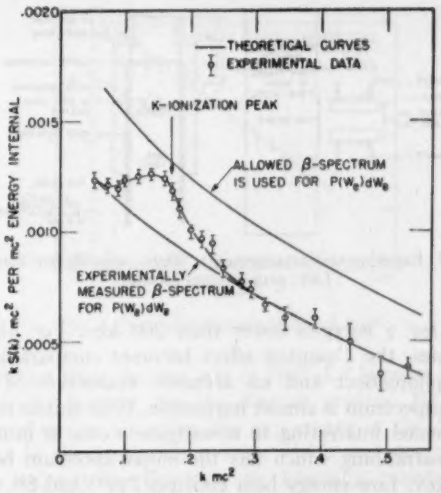

FIG. 1. Internal bremsstrahlung and K-ionization radiation from RaE (measured on the NaI scintillation spectrometer).

The advantage of a NaI scintillation spectrometer over the ionization chamber method in the investigation of the internal bremsstrahlung is not merely its high detecting efficiency but also the fact that it yields information on its energy distribution. Wu[1] and Stahel and Guillessen[2] found good agreement between their measured total yields of bremsstrahlung and those predicted by the theory by the ionization method. Novey[3] and Bolgiano *et al.*[4] further confirmed the good agreement with the theory of the shape of the bremsstrahlung spectrum at the low-energy region using a NaI spectrometer. Unfortunately, the analysis of a continuous γ spectrum in a crystal can be carried out only as long as the photoeffect dominates over all other interactions in the crystal. This is approximately

[13] A. G. Petschek and R. E. Marshak, Phys. Rev. **85**, 698 (1952); C. S. Wu, Physica **18**, 989 (1952).

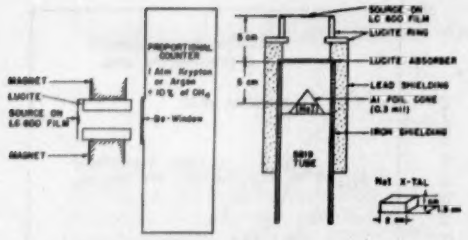

FIG. 2. Experimental arrangements. Right: scintillation counter. Left: proportional counter.

true for γ energies lower than 200 kev. For higher energies, the Compton effect becomes comparable to the photoeffect and an accurate evaluation of the photospectrum is almost impossible. With this in mind, it seemed interesting to investigate a case of internal bremsstrahlung which has the entire spectrum below 200 kev. Low-energy beta emitters Pm^{147} and S^{35} were chosen because they both yield simple beta spectra with upper energy limits of 227 and 167 kev, respectively and emit no nuclear gamma radiations.

2. Experimental Arrangement

Figure 2 shows the experimental arrangement of the scintillation counter apparatus. The NaI crystal is in optical contact with the photocathode of a 5819 photomultiplier. The crystal is covered with a 200-$\mu g/cm^2$ Al foil. The pulses are amplified by a linear amplifier, and the pulse distributions is analyzed with a single-channel differential pulse-height analyzer. The β particles are absorbed in a Lucite absorber whose thickness is adjusted according to the maximum energy of the β spectrum. The absorber is always placed halfway between the crystal and the source. The amount of external bremsstrahlung which could reach the detector under this geometrical arrangement is not more than 10 percent compared with that of the internal bremsstrahlung. In order to avoid the production of external bremsstrahlung and the excitation of characteristic lead radiation, no lead collimator was used. The sources used were prepared by evaporation of an aqueous solution of the radioactive chemicals on an LC 600 film of a thickness of about $50 \mu g/cm^2$. The thickness of the source itself was of the order of 50 $\mu g/cm^2$, and the intensity of the source was of the order of 0.1 to 1 mC.

3. Calibration and Correction

The energy calibration of the scintillation spectrometer was carried out with gamma or x-rays of Cd^{109}, Cs^{137}, and Tl^{204}. With the dimensions of the crystal used (2.0 cm×1.5 cm×1.0 cm), its detecting efficiency is practically 100 percent throughout [in the energy region investigated (below 200 kev)]. The absorption of γ rays in the Lucite absorbers and the thin Al reflector is corrected with known coefficients of absorption. Another correction for the shifting of pulses to lower energy regions due to the escape of iodine K x-rays from the crystal following photoelectric interaction near the surface was estimated [3] and applied. A small resolution correction similar to that used by Palmer and Laslett[14] (which takes into account the energy dependence of the half-width of the Gaussian distribution of a monochromatic photoline) was applied to the measured spectrum. However, the channel width of the analyzer was always set several times smaller than the line width of the Gaussian distribution.

In order to compare the absolute cross section for bremsstrahlung production with the theoretical prediction, the absolute intensity of the β source and the efficiency factor of the detector system must be known. The first quantity was measured in a large cylindrical vacuum chamber (the Columbia solenoid spectrometer) using a G-M counter with a thin Formvar window of a thickness of 0.03 mg/cm^2. A suitable antiscattering baffle-system was put in to exclude electrons scattered from the wall. Several measurements were made with varying distances between the source and the detector to insure square distance relation. The efficiency factor of the NaI detector or the proportional counter (including the solid angle subtended) was estimated with the help of a Cd^{109} source which was calibrated in terms of an absolute number of disintegrations per second by measuring the conversion electrons in the mentioned vacuum chamber and G-M counter system and assuming 0.8 K-conversion electron and 1.5 K quanta per disintegration.

4. Results and Conclusion

After all the corrections were applied, the spectrum of the internal bremsstrahlung was plotted with $kS(k)$ *vs* energy to avoid an abrupt rise at the low-energy end. Figures 1, 3, and 4 represent the experimental results of RaE, S^{35} and Pm^{147}. In calculating $S(k)$, the allowed β spectrum was used for S^{35} and Pm^{147}, but the observed β spectrum was substituted for RaE. Because of the uncertainties involved in the calibration of the β source

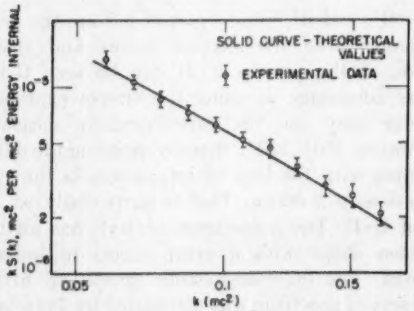

FIG. 3. Internal bremsstrahlung of S^{35}.

[14] J. P. Palmer and L. J. Laslett, U. S. Atomic Energy Commission Report AECU-1220, (March 14, 1951) (unpublished).

and in the detector efficiency, the emphasis is put on comparing the energy distribution of the internal bremsstrahlung rather than the absolute yields. The absolute yield may have an error of the order of 20 percent. Nevertheless, both of these factors agree rather satisfactorily with the theoretical predictions. Recently, Renard[15] investigated the internal bremsstrahlung from P^{32} in an energy region of 3–30 kev in a proportional counter and also obtained good accord with the theory. The excellent agreement between the theory and the experimental findings may imply that the simplification (first-order perturbation) and approximation (Z independent) introduced in the theoretical calculations have very little effect on the distribution or yield of the bremsstrahlung.

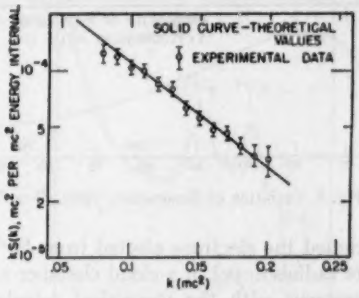

FIG. 4. Internal bremsstrahlung of Pm^{147}.

III. EXCITATION AND IONIZATION OF THE ATOM

1. Introduction

The excitation and ionization processes of the atomic core often accompany the β decay of a nucleus. As the nuclear charge suddenly changes from Z to $Z\pm1$ and the β particle passes through the atom in a β-decay process, the atomic core may suffer two kinds of perturbations. One is the direct collision with the nuclear β particle. This is analogous to the excitation and ionization of an atom by an external fast electron. The other is a "shaking" effect caused by the sudden change of nuclear charge. Because the time taken for the fast β particle to pass through the atom is much shorter than the period of revolution of the orbital electrons, the atomic core has very little time to make adiabatic readjustments (shrinkage for β^- decay and expansion for β^+ decay) but mostly undergoes nonadiabatic transition, that is, excitation or ionization.

The probability of the ionization of the atom due to β decay was first investigated theoretically by Feinberg[16] and Migdal.[17] Their estimate showed the dominating role played by the shaking process and the insignificant contribution from the direct collision. Therefore, on the basis of the sudden change of nuclear charge alone, they calculated the probability of ionization of K, L, and M electrons in β decay. The K ionization is given as $(2\times0.32)/Z^2$, whereas the L ionization is given as $6.8/Z^2$. Later, Levinger[18] independently studied this problem and reached general agreement with Feinberg and Migdal on the probability of ionization of K-shell electrons ($0.65/Z^2$) but differed on the results for L-shell electrons ($2.1/Z^2$). Recently, Schwartz[19] took up the calculation of the probability of ionization resulting from β decay and his L-shell ionization yield is in agreement with that of Levinger. Winther[20] also carried out a detailed calculation of the ionization effect for the case of $He^6\rightarrow Li^6$ because of its particular interest for the β-recoil studies. He also pointed out in his paper the importance of the Auger effect in the ionization process which was not taken into account in Feinberg or Migdal's calculation. Serber and Snyder[21] calculated the average excitation energy of the atom for β decay. Their expression for an average excitation energy per closed electronic shell compared favorably for the K shell with Levinger's evaluation.

In Feinberg and Migdal's original calculations of the ionization probability, three approximations were used: (1) no screening corrections for Coulomb wave functions, (2) nonrelativistic treatment, and (3) sudden change of nuclear charge. Levinger first calculated the correction resulting from the screening effect by applying Hartree wave functions for Hg and found that for heavy atoms the screening effects cause an appreciable increase in the ionization probability following β decay. For K electrons, the factor is 1.4 while it is 3 or 4 for L electrons. He also estimated the errors introduced by the other two approximations and found that the use of the nonrelativistic wave functions lead to an underestimation of the ionization probability by a factor of 2. Also, the approximation of sudden perturabtion calculation should not be very accurate for a heavy atom with low energy β decay.

To detect the ionization process caused by β decay, one could either

(1) detect the orbital electrons ejected during electron-capture or the β^+ decay process,

(2) observe the characteristic x-rays emitted in filling the holes in the K or L shells, or

(3) measure the Auger electrons emitted in competition with the x-ray emission.

Bruner,[22] with the aid of a magnetic spectrometer, has applied the first method to Sc^{44}, a radioactive isotope which decays by β^+ emission and electron capture process as well as by emission of nuclear gamma rays. However, the calculated yield of ionization based on the number of electrons detected is much too high to be reconciled with the theory. Recently, Porter and

[15] G. Renard, J. phys. radium **14**, 361 (1953).
[16] E. L. Feinberg, J. Phys. (U.S.S.R.) **4**, 423 (1941).
[17] A. Migdal, J. Phys. (U.S.S.R.) **4**, 449 (1941).
[18] J. S. Levinger, Phys. Rev. **90**, 11 (1953).
[19] H. M. Schwartz, J. Chem. Phys. **21**, 45 (1953).
[20] A. Winther, Kgl. Danske Videnskab. Selskab, Mat.-fys. Medd. **27**, 2 (1952).
[21] R. Serber and H. S. Snyder, Phys. Rev. **87**, 152 (1952).
[22] J. A. Bruner, Phys. Rev. **84**, 282 (1951).

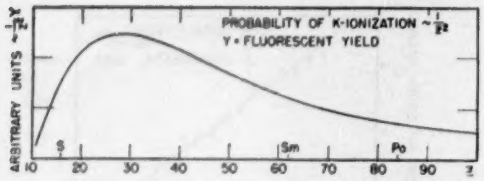

Fig. 5. Variation of fluorescence yield/Z^3 *vs* Z.

Hotz[23] studied the electrons ejected from Fe^{55} (a pure K-capture radioisotope) in a cloud chamber and found good agreement with the theoretical calculations by Primakoff and Porter.[24]

The method employed in the investigation of the ionization of the atom due to β^- decay as reported in this paper is based on the detection of the characteristic x-rays by a proportional counter or scintillation counter spectrometer. In order to rule out the characteristic x-rays from other effects, a radioactive substance with no nuclear gamma radiation or electron capture is preferred. The substances used in our investigation are RaE and Pm^{147}, whose simple decay schemes are well established. The β decay of Pm^{147} is particularly suited for this investigation. Since the cross section for ionization varies with $1/Z^2$, one would therefore at first suggest the use of β^- radioactive light nuclei. However, the fluorescence yield of the atom decreases rapidly with decreasing Z. One therefore must make a compromise between these two effects. Furthermore, the energy of the characteristic x-radiations of a light atom is low and would require the detection of a weak line on a high background of low-energy internal bremsstrahlung. Figure 5 gives the curve showing the variation of the product of ionization probability times fluorescence yield for K-shell electrons *versus* atomic number Z.

In the curves showing the continuous internal bremsstrahlung of RaE by Novey[3] and Madansky and Rasetti,[4] an unmistakable peaking could be interpreted as an evidence of the ionization of the atom by β decay. Nevertheless, a similar peak of the same energy is shown also on the bremsstrahlung curve of P^{32}. This suggests that at least a great portion of that peak is likely to be the result of the fluorescence radiation of lead excited by external electrons on the lead shielding and not the result of ionization caused by the sudden change of nuclear charge.

2. Experimental Arrangement

A proportional counter and a scintillation counter spectrometer were used for the measurement of the characteristic radiations. Figure 1 shows the experimental arrangement of the counter setup. The proportional counter is filled with a mixture of one atmosphere of Kr and 7 cm of methane. The counter window consists of a 10-mil Be foil. The scintillation counter is the same one used for the internal bremsstrahlung. The electrons are bent away with a strong permanent magnet. All metal parts are carefully shielded with lucite in order to avoid the production of any external characteristic radiation. The Pm^{147} was a carrier-free fission product from Oak Ridge National Laboratory. The extremely thin source was deposited on a 50μg/cm^2 LC 600 film. The thickness of a source must be carefully considered as any small amount of carrier would produce a fluorescent radiation which may be mistaken as due to the ionization effect under investigation. The amount of characteristic radiation produced in the source by electron bombardment could be estimated[25] from the total ionization by electrons of an energy equivalent to the mean energy of the β spectrum. It is found that the carrier free 0.1-mC Pm^{147} source of an amount ~10 μg/cm^2 would produce $\sim 6\times10^{-7}$ K ionization and 5×10^{-5} L ionization per beta decay. As we shall see, the K ionization is several orders of magnitude smaller than the actually measured ionization probability.

The RaE was first separated from polonium and was then separated from RaD be the dithiazone method. The purity of RaE can easily be assured by checking the absence of the 46.5-kev gamma line of RaD and also by following the half-life. If the separation of RaE from RaD were not complete, a faint L x-ray from such a RaE source due to the remaining RaD could easily be mistaken as the L radiation of RaE due to the ionization effect. The RaE separation was actually carried out with only 2μg of Bi carrier. Nevertheless, the source prepared is quite visible, probably because of impurities from the reagents used. The source thickness is no more than 100μg/cm^2. The fluorescence yield estimated[25] from this thickness of the source is 1.5×10^{-6} K ionization and 1.5×10^{-4} L ionization per β decay per 100μg/cm^2. The K ionization again is at least two orders of magnitude smaller than the value found in the experiment.

The energy calibration of the proportional counter was effected with the x and gamma radiation of Cd^{109},

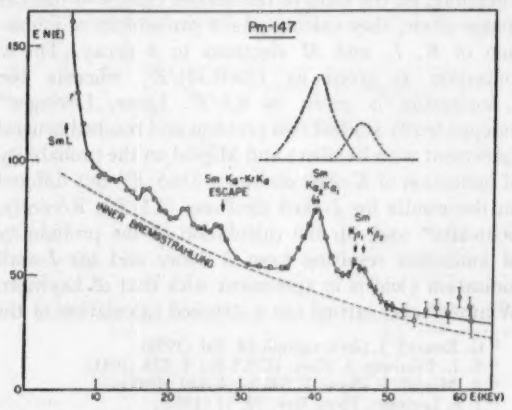

Fig. 6. K ionization radiations from Pm^{147}.

[23] F. T. Porter and H. P. Hotz, Phys. Rev. **89**, 938 (1953).
[24] H. Primakoff and F. T. Porter, Phys. Rev. **89**, 930 (1953).
[25] E. H. S. Burhop, Proc. Cambridge Phil. Soc. **36**, 47 (1940).

Cs^{137}, and RaD. The total effeciency calibration was established with a Cd^{109} source of known strength.

3. Results

The experimental results for Pm^{147} are shown in Figs. 6 and 7. Figure 6 exhibits the region of the K x-rays with the K_α, K_β, and escape peak distinctly shown. Two small peaks appeared between 15 and 25 kev, which may be due to some impurities. Figure 7 shows the photon spectrum in the L-energy region and a pronounced L peak of 5.6 kev is present.

The results on RaE are shown in Figs. 1 and 8. The K x-ray region of Fig. 1 was measured with the scintillation spectrometer. The K peak is pronounced, but the line profile is poor because of the broad resolution and high bremsstrahlung background. Figure 8 shows the peak due to L radiation as measured with a proportional counter. L_α and L_β are resolved.

The probabilities of the ionization processes were found by absolute measurements of the source strength and by calibrating the instrument with a calibrated Cd^{109} source as described in Sec. A.

The values for the fluorescent yield used for correction of the Auger effect are taken from Burhop's new book on *The Auger Effect*.[26] The K-shell fluorescence yield for Pm^{147} is 0.90 and 0.94 for RaE. The L fluorescence yield is 0.19 for Pm^{147} and 0.47 for RaE.

The results are summarized in Table I. The second column lists the experimental results on the probabilities of K- and L-shell ionization as calculated from the results of our investigations. The third column gives the probabilities as calculated from the formula of Migdal or Feinberg. The numerical values for the K shells are generally

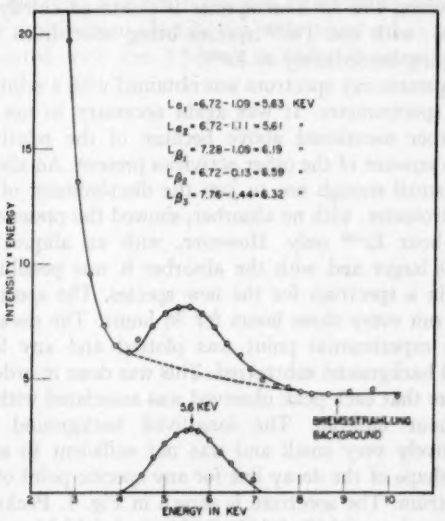

FIG. 7. L ionization radiations from Pm^{147}.

[26] E. H. S. Burhop, *The Auger Effect*, Cambridge Monographs on Physics (Cambridge University Press, Cambridge, 1952).

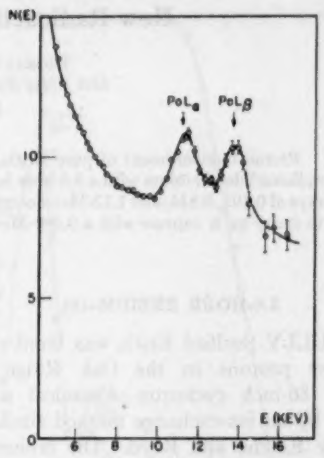

FIG. 8. L ionization radiations from RaE.

smaller than those found in experiments. Levinger applied a screening correction to the Coulomb field of the nucleus and obtained a larger probability of ionization as shown in the fourth column. However, neither relativistic correction nor direct collision was ever taken into account in the theoretical calculations. A preliminary estimate of the relativistic correction made by Levinger gave an increase of a factor of 2 for the K-shell ionization. As for the nonadiabatic approximation, the calculation may be close enough for the case of

TABLE I. Absolute probabilities for K- and L-shell ionization.

		Experimental results	Migdal or Feinberg	Levinger
Pm^{147}	K	$(3.85\pm0.5)\times10^{-4}$	1.64×10^{-4}	2.36×10^{-4}
	L	$(2.05\pm0.3)\times10^{-3}$	1.77×10^{-3}	1.9×10^{-3}
RaE	K	$(1.2\pm0.5)\times10^{-4}$	0.95×10^{-4}	1.28×10^{-4}
	L	$(0.6\pm0.3)\times10^{-3}$	1.01×10^{-3}	1.04×10^{-3}

RaE, but in the case of Pm^{147}, the average energy of the β distribution (62 kev) is comparable to the K-binding energy of Pm^{147} (45 kev). In other words, the β particles travel with a velocity comparable to that of the inner orbital electrons. Obviously, this is no longer a completely nonadiabatic case. One should therefore expect that the ionization probability would be less than that calculated from the sudden change of charge effect.

In view of the approximate nature of the theoretical calculations and the uncertainties involved in the experimental determinations, the agreement as shown in Table I is at least of the right order of magnitude.

ACKNOWLEDGMENT

The authors wish to express their thanks to Dr. E. Nagel and Dr. L. Lidofsky for their valuable cooperation throughout the investigation and to Professor W. W. Havens, Jr., for his constant interest in the experiment.

New Radioactive Nuclides of the Rare Earths

THOMAS H. HANDLEY AND ELMER L. OLSON
Oak Ridge National Laboratory, Oak Ridge, Tennessee
(Received October 5, 1953)

Proton bombardment of pure Er_2O_3, followed by ion-exchange separation, has yielded an unreported radionuclide of erbium with a 3.6-hour half-life. It is assigned to Er^{161} and decays by K capture with gamma rays of 0.195, 0.824, and 1.12-Mev energy. Its daughter, 2.5-hour Ho^{161}, was also identified and was observed to decay by K capture with a 0.090-Mev gamma ray.

3.6-HOUR ERBIUM-161

CAREFULLY purified Er_2O_3 was bombarded with 24-Mev protons in the Oak Ridge National Laboratory 86-inch cyclotron. Chemical separations were made by an ion-exchange method similar to that reported by Ketelle and Boyd.[1] The erbium fraction contained the following species: 10.5-hour Er^{165} and 75-minute[2] Er^{163}, formed by (p,n) and $(p,3n)$, respectively; and also 9.4-day Er^{169} and 7.5-hour Er^{171} formed by secondary (n,γ) reactions. Another activity of relatively low intensity was found by counting with a GM tube through an absorber consisting of a "sandwich" of 1700 mg/cm² aluminum, 2000 mg/cm² lead, and 200 mg/cm² aluminum. It was necessary to use this absorber because of the low intensity of this activity relative to others present. This 3.6-hour activity was not observed as a product of proton bombardment of holmium, and it was not observed as a product of (n,γ) reaction on erbium. This would eliminate all mass numbers higher than 161 for its assignment. The lowest mass number it could have is 160, since no lighter mass could be produced by bombarding erbium with 24-Mev photons. It could be formed by either $Er^{162}(p,pn)Er^{161}$ or $Er^{162}(p,2n)Tm^{161}$. In the last case, the thulium activity would be short-lived, with immediate decay to Er^{161}.

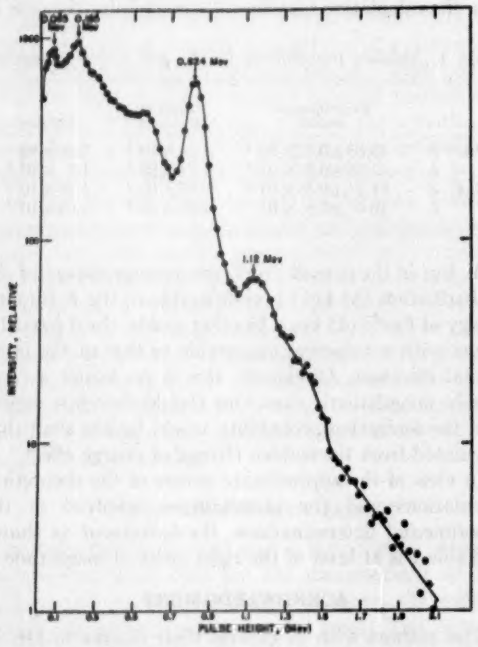

FIG. 1. Gamma-ray spectrum of 3.6-hour erbium-161.

To further clarify the mass assignment and method of production, the following experiments were performed. With appropriate absorbers the incident proton-beam energy was reduced to 20.5 and 17 Mev in separate experiments. The relative amount of the 3.6-hour activity was reduced by approximately one-half. Since it is shown elsewhere[3] that the threshold for $(p,3n)$ reactions in this region is 19 Mev for masses near the line of stability and, since this species is produced from Er^{162}, five mass units below the line of stability, it is expected that the threshold for a $(p,3n)$ reaction would be even higher (calculations from the empirical mass formula show it to be 4 Mev higher). Therefore, the 3.6-hour species is produced chiefly by $(p,2n)$, with the Tm^{161} species being short-lived and decaying immediately to Er^{161}.

A gamma-ray spectrum was obtained with a scintillation spectrometer. It was again necessary to use the absorber mentioned above because of the relatively large amount of the other activities present. An aliquot just small enough not to jam the discriminator of the spectrometer, with no absorber, showed the presence of 10.5-hour Er^{165} only. However, with an aliquot ten times larger and with the absorber it was possible to obtain a spectrum for the new species. The spectrum was run every three hours for 36 hours. The decay of each experimental point was plotted and any long-lived background subtracted. This was done in order to assure that each peak observed was associated with the 3.6-hour half-life. The long-lived background was relatively very small and was not sufficient to affect the shape of the decay line for any specific point of the spectrum. The spectrum is shown in Fig. 1. Peaks are observed at 0.065, 0.195, 0.824, and 1.12 Mev. The energy region below 0.10 Mev is distorted because of

[1] B. H. Ketelle and G. E. Boyd, J. Am. Chem. Soc. **69**, 2800 (1947).
[2] T. H. Handley and E. L. Olson, Phys. Rev. **92**, 1260 (1953).
[3] See reference 2.

the absorber used. Therefore, the spectrum in this region cannot be differentiated. It is unlikely, however, that the peaks at 0.195, 0.824, and 1.120 Mev are affected, energy-wise, by the absorber. The 0.195-Mev peak may be due to 180° scattering from more energetic radiation. The annihilation peak was not observed, and positrons, if present, constitute a very small fraction of the decay. Although the x-ray peak was not actually observed, it may be assumed that Er^{161} decays by *K* capture, since the annihilation peak was not observed. While plotting the decay of the experimental points, it was noted that an activity grew in, at the low-energy region of the spectrum. This activity appeared to have a half-life of >1 hour and <3.6 hour, and it would, of course, be a holmium activity. In order to determine the characteristics of this species, further bombardments and separations were necessary, as explained in the following section.

2.5-HOUR HOLMIUM-161

Erbium oxide was bombarded with 24-Mev protons and chemical separations were made immediately. A second separation of the erbium fraction was made five hours later. This elapsed time enabled the daughter species to grow in. Holmium carrier was added for the second separation. Decay of the holmium fraction of the second separation was followed, and a half-life of 2.5 hours was observed. The gamma-ray spectrum for this 2.5-hour holmium activity is shown in Fig. 2. Peaks are observed at 0.043 and 0.090 Mev. The 0.043-Mev peak is the x-ray peak; thus the isotope decays by *K* capture. There is also some evidence of a low intensity peak in the neighborhood of 0.17 Mev. The spectrum was run every two hours for 14 hours in order positively to identify the peaks observed as being associated with the 2.5-hour half-life. If other more

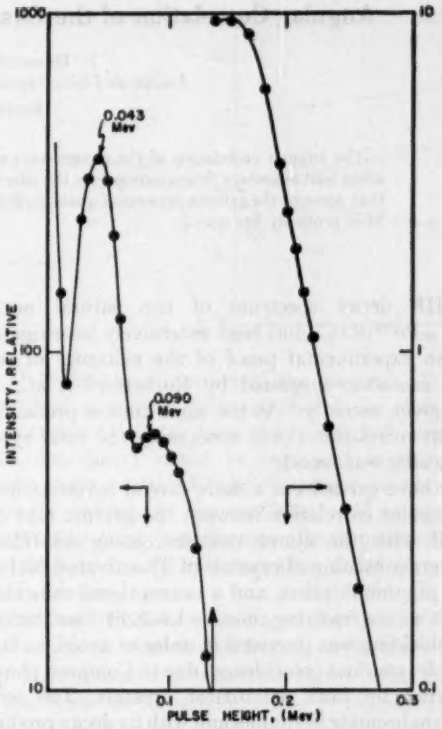

FIG. 2. Gamma-ray spectrum of 2.5-hour holmium-161.

energetic radiations were present they constituted a small fraction of the decay scheme. Positrons are also excluded, since the annihilation peak was not observed. The 2.5-hour species was also observed as a product of proton bombardment of dysprosium. This activity is assigned a mass of 161 because it is the daughter of 3.6-hour Er^{161}.

Angular Correlation of the Cascade γ Rays from the Decay of $_{84}Po^{214}$

F. DEMICHELIS AND R. MALVANO
Istituto di Fisica Sperimentale del Politecnico, Turin, Italy
(Received June 8, 1953)

The angular correlation of the gamma rays accompanying the decay of $_{84}Po^{214}$(RaC') has been obtained using lead absorbers to separate partly the effects due to the several cascades involved. The results indicate that some of the gamma rays are of quadrupole character and that the excited state of $_{84}Po^{214}$(RaC') at 0.608 Mev probably has spin 2.

THE decay spectrum of the natural nuclide $_{84}Po^{214}$(RaC') has been extensively investigated,[1] and an experimental proof of the existence of some γ-ray cascades, suggested by Rutherford *et al.*,[2] has been given recently.[3] At the same time a preliminary angular-correlation curve concerning the total system of cascades was found.[4]

We have carried out a more careful investigation of the angular correlation between the gamma rays connected with the above cascades, using scintillation counters consisting of crystals of Tl-activated NaI and 1P21 photomultipliers, and a conventional coincidence circuit with a resolving time $\tau = 1.6_2 \times 10^{-7}$ sec. Suitable lead shielding was provided in order to avoid, as far as possible, spurious coincidences due to Compton photons scattered by both scintillator crystals. The source (radium bromide in equilibrium with its decay products) had an activity of about 20 microcuries and was contained in an extremely small glass container.

In order to test our apparatus we measured the angular correlation given by a $_{27}Co^{60}$ source of about the same intensity, the same volume, and the same geometrical arrangement; we obtained results agreeing, within experimental errors, with the results given in previous works.[5]

We have made measurements for $\theta = 90°$, 120°, 150°, 180°, and for three values of lead thickness: $x = 1$ mm, $x = 4$ mm, $x = 7$ mm, because, as we shall see below, it is possible in this way to determine the contribution of the different cascades to the total angular correlation. The experimental points plotted in Fig. 1, with their probable errors, represent $\epsilon(\theta) = (N_\theta/N_{90°}) - 1$, where N_θ and $N_{90°}$ are the true coincidence rates at the angles θ and 90°, respectively, and the three sets of experimental points correspond to the three lead thicknesses previously indicated.

The angular correlations $\epsilon = \epsilon(\theta)$ indicated by the three sets of experimental points are significantly different from each other, and this fact indicates that the various cascades, whose characteristics have been studied in a previous work,[3] must belong to at least two different types; in effect, the existence of only one type of cascade would give rise to an angular correlation completely unaffected by absorption. Besides, we recall that from the previous experimental investigations[1] it was concluded that the complicated γ-decay spectrum from $_{84}Po^{214}$ consists entirely of dipole and quadrupole transitions of various energies from 0.6 to 2.4 Mev.

According to the foregoing paragraphs, the general behavior of the angular correlation ought to be explained with the following relation:

$$\epsilon(\theta) = \sum_i \alpha_i a_{i1} \cos^2\theta + \sum_i \alpha_i a_{i2} \cos^4\theta,$$

where a_{i1} and a_{i2} are the coefficients of the angular correlation relative to each type of cascade and

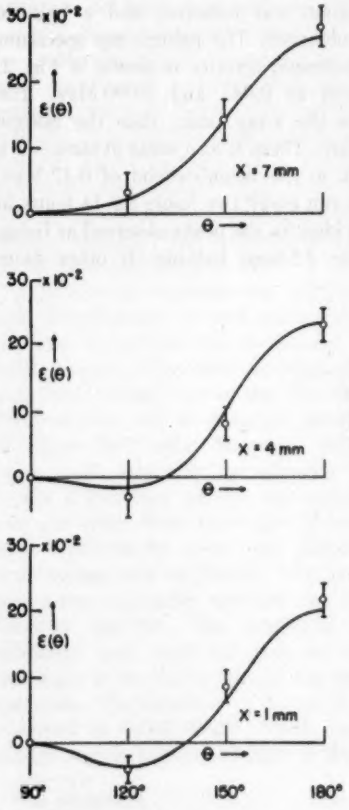

FIG. 1. Gamma-gamma angular correlation of Po^{214} for various thicknesses x of lead absorber.

[1] C. D. Ellis and G. H. Aston, Proc. Roy. Soc. (London) **A129**, 180 (1930); C. D. Ellis, Proc. Roy. Soc. (London) **A143**, 350 (1935); G. D. Latyshev, Revs. Modern Phys. **19**, 132 (1947).
[2] Rutherford, Lewis, and Bowden, Proc. Roy. Soc. (London) **A142**, 347 (1933).
[3] F. Demichelis and R. Malvano, Nuovo cimento **10**, 405 (1953).
[4] F. Demichelis and R. Malvano, Nuovo cimento **9**, 1106 (1952).
[5] E. L. Brady and M. Deutsch, Phys. Rev. **78**, 558 (1950).

$\alpha_i = N_{i,90°}/\sum N_{i,90°}$ is the relative contribution of the ith cascade to the coincidence rate at 90°. The qualitative behavior of the angular correlation $\epsilon = \epsilon(\theta)$ for $x = 1$ mm suggests that $\sum_i \alpha_i a_{i1}$ must be negative while $\sum_i \alpha_i a_{i2}$ is positive and much smaller; on the other hand, the absorption behavior indicates that the first sum must increase with lead thickness, while the second must decrease.

Following the data given in Hamilton's work,[6] and assuming that the ground state reached by different cascades has zero angular momentum, we made a systematic trial of possible combinations. Limiting ourselves first of all to two types of cascades, we found that the only coefficients that could fit both our data and reasonable values for the relative intensities of the different cascades are the following ones:

$$(1)\quad a_{11} = 3/7, \qquad a_{12} = 0,$$
$$(2)\quad a_{21} = -15/13, \quad a_{22} = 16/13.$$

With the foregoing values of the coefficients we draw the solid-line curves of Fig. 1, while the intensities α_1 and α_2, obtained with a least-squares method, are given in Fig. 2. In Fig. 2 the broken lines are obtained according to the relative intensities suggested by the level scheme proposed by Surugue,[7] where the cascades of type (1) and (2) would consist, respectively, of the γ rays

$$(1)\quad 1.120 \text{ Mev}, 1.761 \text{ Mev},$$
$$(2)\quad \begin{cases} 0.608 \text{ Mev}, 1.235 \text{ Mev}, \\ 0.608 \text{ Mev}, 2.090 \text{ Mev}. \end{cases}$$

From the above results we may draw the following tentative conclusions:

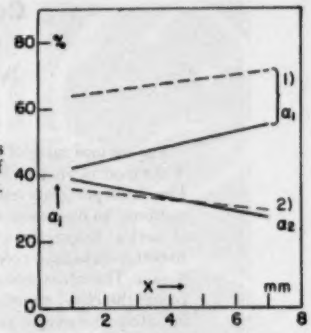

FIG. 2. The coefficients α_1 and α_2 as functions of thickness x of lead absorber.

(a) While the intensities of the cascades (2) are in very good agreement with our results, the intensity of the cascade (1) is far from the theoretical prediction. This discrepancy could be explained in two ways: Either there is a third type of cascade, of very small intensity indeed, or the coefficient 3/7 is about 30 percent too great; interference effects produced by a mixed (magnetic-electric) transition could give rise to such a lowering.[8]

(b) The 0.608-Mev γ ray is probably not an electric-dipole but an electric-quadrupole transition; if this fact is true and this transition occurs from the first excited state to the ground state, it follows that the former must be a 2+ level in accordance with recent theoretical work on even-even nuclei.[9]

We want to express our deep gratitude to Professor E. Perucca for his constant interest and his stimulating help.

[6] D. R. Hamilton, Phys. Rev. **58**, 122 (1940).
[7] J. Surugue, J. phys. radium (8), **7**, 145 (1946).
[8] D. S. Ling and D. L. Falkoff, Phys. Rev. **74**, 1224 (1948).
[9] G. Scharff-Goldhaber, Physica **18**, 1105 (1952).

Cosmic-Ray Nuclear Interactions in Gases*

W. W. BROWN†
Department of Physics, Duke University, Durham, North Carolina
(Received August 14, 1953)

The natural rates of occurrence, in the gases He, N, Ne, and A, of nuclear interactions of the cosmic ray N component in which more than 8 Mev are given to charged secondary particles, have been measured. The rates per gram atom of the four gases are in about the same ratio as their geometric nuclear cross sections. An integrated flux of N rays of 6.0×10^{-3} cm^{-2} sec^{-1} would produce the observed rates of occurrence of nuclear interactions if the cross section were geometric. The rates in argon, measured at sea level and 10 600-ft elevation, correspond to an absorption mean free path in air of 132 ± 4 g cm^{-2} for the total flux of N rays. The interactions, 2783 in total, were observed in the gas of a cloud chamber filled to 5 atmos pressure. Inside the cloud chamber was placed a system of wires forming an ionization chamber. An expansion was initiated whenever a pulse from the ionization chamber corresponding to an energy release of more than 8 Mev (1.5 Po alpha) occurred. Fast reduction of the high voltage after electron collection was over permitted track formation on the positive ions. Of the nuclear interactions produced in argon about 20 percent are produced by charged particles at the higher elevation, and about 15 percent at sea level.

I. INTRODUCTION

THE present report is of an experiment in which the relative cross sections for nuclear interaction that the elements helium, nitrogen, neon, and argon present to the N component of cosmic rays are measured. The method employed is to count the number of cosmic-ray nuclear interactions occurring, over a measured time interval, in the gas of a cloud chamber successively filled with these atoms. The relative rates of occurrence of nuclear interactions in the gases may then be compared with the relative geometric cross sections of their nuclei. Rather than use random expansions, which would make the experiment prohibitively long, a detector, offering relatively little experimental bias, was placed inside the chamber to act as a triggering device. The details of the detecting system, experimental results, and corrections applied to them are described below.

II. EXPERIMENTAL ARRANGEMENT

The cloud chamber, of the expansion type with rubber diaphragm, was designed to operate at pressures up to 75 lb in.$^{-2}$. It has a useful area, as viewed by the camera, of 10 in.$\times$10 in. and an illuminated depth of 8 in.

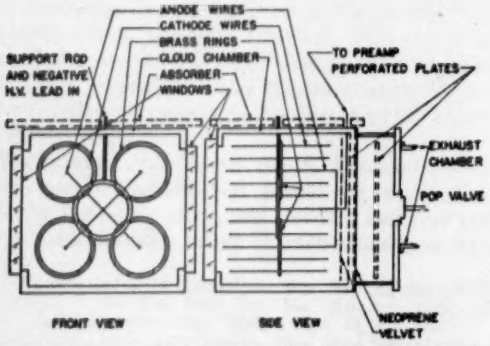

FIG. 1. Two perpendicular sections showing the location of the ionization chamber assembly inside the cloud chamber.

Five ionization chambers are mounted inside the cloud chamber (Fig. 1). Each ionization chamber consists of eight parallel and equally spaced cathode wires $\frac{1}{16}$-in. diameter$\times$8-in. length held at their midpoints by a thin 4-in. diameter brass ring and all equidistant from and parallel to a similar central anode wire. The cathodes of the five chambers are tied together and the whole system supported by the high-voltage lead passing through the cloud chamber roof. The anodes, also in parallel, are connected to the amplifying system through another insulated lead passing through the cloud chamber roof.

TABLE I. Conditions of operation of the cloud chamber and the numbers of photographs, sensitive times, and numbers of nuclear interactions involving one or more charged particles observed under these conditions.

Atmospheric depth, g cm^{-2}	700	700	700	700	700	700	1032
Gas	A	A	A	Ne	N	He	A
Pressure, lb in.$^{-2}$	71	71	71	71	60	72	74
Temp. °C	19	19	19	21	18	20	17
Brass above chamber, in.	0	0.25	0.75	0	0	0	0
No. of photographs	2713	431	1026	104	2156	832	1948
Operating time, min	30 548	5017	11 665	1415	17 006	12 802	57 900
Dead time per picture, min	8.43	8.43	8.43	8.43	4.95	8.43	8.43
Sensitive time, min	7680	1382	3005	537	6345	5780	41 500
No. of nuclear interactions	1112	179	379	67	439	106	501

The amplified pulse resulting from collection at the anode of the electrons produced by a charged particle traversing the sensitive volume serves to trigger the cloud-chamber expansion if it is larger than a prescribed size. It also initiates the reduction of the high negative voltage of the cathode (1 to 1.5 kilovolts) to zero or a slightly positive value by electronic means. The voltage reduction is rapid enough so that the positive ions along the path of the particle are not appreciably moved. The small displacement given to them is somewhat compensated when the cathode is allowed to

* Assisted by the joint program of the U. S. Office of Naval Research and the U. S. Atomic Energy Commission.
† Now at the University of California, Berkeley, California.

go positive during cutoff. Droplet formation on these ions thus permits observation of the track of a pulse producing particle.

Isoamyl alcohol was used as the cloud chamber vapor because it does not capture electrons easily and so does not interfere with the operation of the ionization chamber. With this vapor an expansion ratio of 1.15 is required for track formation in the monatomic gases and 1.25 in nitrogen.

The operational details of the cloud chamber and control system have been published elsewhere.[1]

The high-voltage input lead was made tubular so that through it a polonium-alpha source on the end of a thin wire could be manually inserted into or retracted from the central ionization chamber. Pulses generated by this source were used to calibrate a discriminator

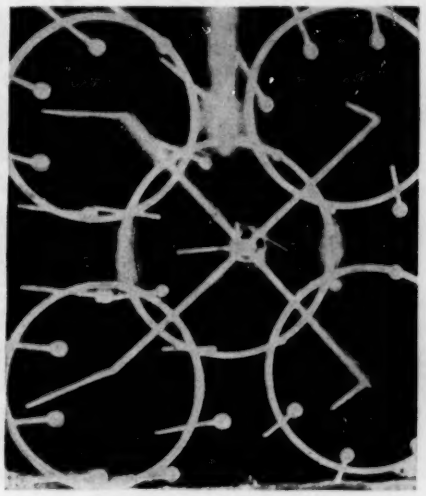

FIG. 2. A neutral particle interacts with a helium nucleus to produce two charged secondary particles in the central ionization chamber just above the anode (10 600-ft elevation).

circuit that allowed pulses greater than a given size to pass from the amplifier to the control circuit. Throughout the experiment only pulses greater than 1.5 times a polonium-alpha pulse were permitted to trigger the chamber. This minimum corresponds to an energy release of 8 Mev by ionization in the gas of the chamber.

Stereo photographs were taken at an angular separation of 12 degrees between the two optic axes.

III. EXPERIMENTAL PROCEDURE AND RESULTS

The cloud chamber was operated at sea level for 5 months and at 10 600-ft elevation (White Mountain, California) for 3 months. At the higher altitude the chamber was filled successively with argon, neon,[2]

[1] Lewis, Brown, Seevers, and Hones, Rev. Sci. Instr. 22, 259 (1951).

[2] Thirty cubic feet of high purity neon were donated by the Linde Air Products Company for use in this part of the experiment.

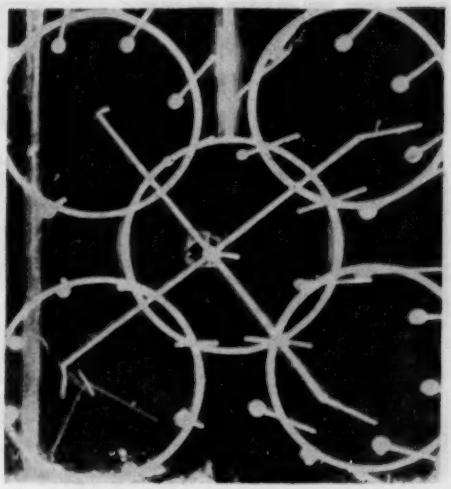

FIG. 3. An interaction of a neutral particle with a nitrogen nucleus in which four charged secondaries are produced in the lower left ionization chamber (10 600-ft elevation).

helium, and nitrogen. At sea level the operation was carried out only with an argon filling. During part of the argon run at high altitude, layers of brass absorber were placed immediately above the cloud chamber. The operating conditions throughout the experiment together with the numbers of photographs taken and numbers of nuclear interactions observed in each gas are summarized in Table I. The sensitive time in each case is the difference between the total operating time

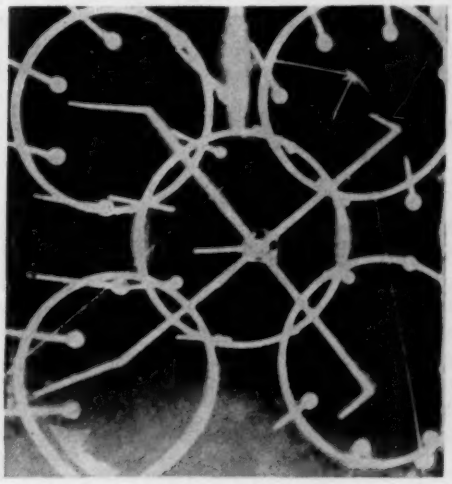

FIG. 4. Seven charged secondary particles are produced in the upper right ionization chamber by the interaction of a neutral particle with a neon nucleus. The whisp of droplets pointing toward the anode are from negative ions formed as some of the electrons heading toward the anode are captured (10 600-ft elevation).

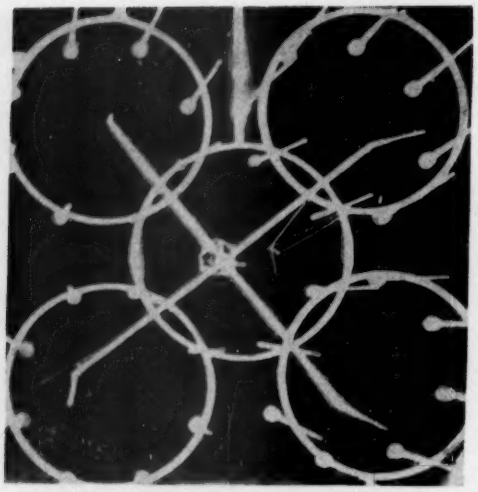

FIG. 5. In the original photograph six charged particles can be distinguished in the nuclear interaction with an argon nucleus in the upper right ionization chamber. One of the lightly ionizing particles lies in the upper hemisphere and may be the primary particle. One of the secondary particles interacts with another argon nucleus in the central ionization chamber to produce four heavily ionizing particles (10 600-ft elevation).

and the product of the chamber dead time and the number of photographs taken.

Of the total of 9210 cloud chamber expansions occurring in the experiment, 30 percent were triggered by nuclear interactions in the gas, 22 percent by nuclear interactions in solid material, 7 percent by extensive air showers, and 41 percent by spurious pulses arising from lightning and other causes. Figures 2, 3, and 4 are examples of nuclear interactions occurring in the gases helium, nitrogen, and neon, respectively, and Figs. 5, 6, and 7 are examples of interactions in argon.

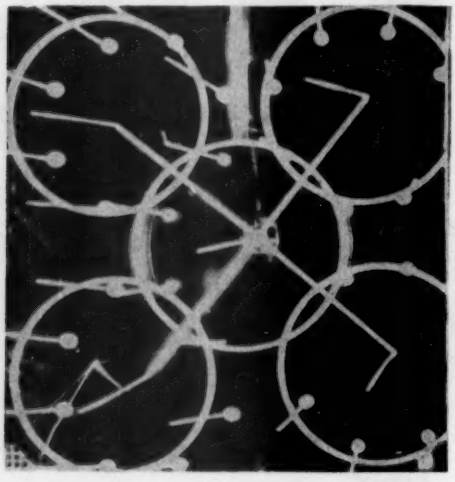

FIG. 6. In this nuclear interaction in argon in the lower left-hand chamber, 13 nearly minimum ionizing particles are involved. Three of these lie in the upper hemisphere. Of the ten moving downward, seven lie in a narrow cone. The thick whisp of droplets is from capture of some of the electrons on their way to the anode (sea level).

IV. ALTITUDE VARIATION

From the data of Table I the ratio of the rate of occurrence of nuclear interactions in argon at 10 600-ft elevation to that at sea level at the same gas pressure is 12.5 ± 1.0. This corresponds to an absorption mean free path in air, for the total flux of N radiation, of 132 ± 4 g cm^{-2}, in fair agreement with the value 138 g cm^{-2} obtained from the altitude variation of burst rates in thin-walled ionization chambers.[3]

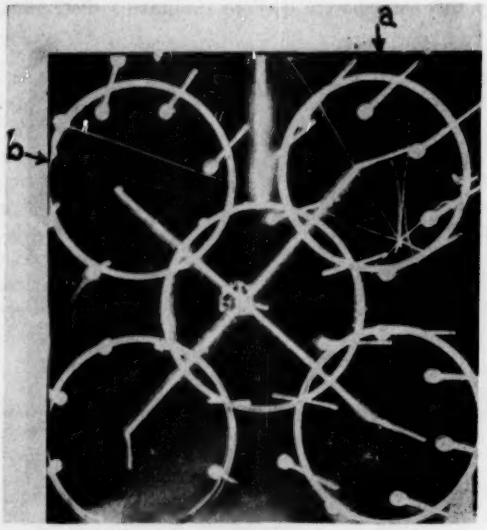

FIG. 7. A nuclear interaction in argon in which 12 charged particles are involved. Four of them are nearly minimum ionizing. Of these, particle (a) is probably the primary. The apparent deviation in the direction of particle (b) as it passes near the anode of the upper left chamber is just the result of motion of the positive ions in the intense electric field that exists near the anode before being cut off (10 600-ft elevation).

V. SIZE OF THE INTERACTIONS

The numbers of nuclear interactions occurring in each of the four gases studied are listed in Table II according to the total number of charged particles observed in each interaction irrespective of their being primary or secondary particles. All tracks longer than 2 mm were counted. No direction could be assigned to groups of ions covering dimensions smaller than this.

There is a general decrease in the size of the interactions, as far as numbers of charged particles are concerned, with the size of the target nucleus. Though lightly ionizing particles are included in the above table, this result is qualitatively in agreement with the

[3] B. Rossi, Revs. Modern Phys. 20, 537 (1948).

conclusion, from sandwich emulsion work,[4] that nuclear interactions (stars) generated in the oxygen and smaller nuclei of the emulsion have less than 6 heavily ionizing prongs.

VI. ANGULAR DISTRIBUTIONS OF THE PRIMARY AND SECONDARY PARTICLES

The zenith angles of the trajectories of the charged particles involved in each nuclear interaction occurring in the gas were measured as follows. The cloud chamber photographs were reprojected through an optical system identical with that of the camera onto a screen that could be set in any direction and was provided with scales such that when the two images of a given track were brought into conjunction the zenith angle of the track could be read directly to within 1 or 2 degrees. So that the accuracy of measurement would be kept within these limits, the zenith angles of only those particles having a range greater than 5 mm were measured.

Since the direction of motion of the more lightly ionizing particles, some of which may be initiating

TABLE II. Numbers of nuclear interactions observed to occur in the gases A, Ne, N, and He, classified according to the number of charged particles associated with each interaction.

Gas	Elevation, feet	Absorber above cloud chamber, in. brass	Number of charged particles 1	2	3	4	5	6	7	8	9	10	>10
A	10 600	0	179	214	235	159	127	75	46	25	17	14	21
A	10 600	0.25	22	32	46	27	25	12	6	2	3	2	2
A	10 600	0.75	45	94	77	69	43	14	14	8	9	2	4
A	s.l.	0	100	89	107	81	46	28	20	10	8	5	7
Ne	10 600	0	1	14	24	10	10	4	3	1			
N	10 600	0	80	99	141	96	21	2					
He	10 600	0	102	4									

particles, could not be determined, they were regarded, for the purposes of the above measurement, as emanating from the points of origin of the nuclear interactions.

In all of the observed interactions produced in the gas and involving only one charged particle of range greater than 2 mm, the particle both started and terminated in the gas. The end representing the point of origin of such an interaction could often be distinguished by the presence of a glob of ionization, probably attributable to the recoil nucleus, whereas at the terminus distinguishing features were an increase in ionization (widening of the track) or small deviations of the direction of motion of the particle.

The distribution in zenith angle of the trajectories of the charged particles involved in nuclear interactions in argon at high altitude and at sea level are shown in Fig. 8. The distributions of particles having ionization less than twice minimum (lightly ionizing particles) and those greater than twice minimum (heavily ionizing particles) have been plotted separately. The data

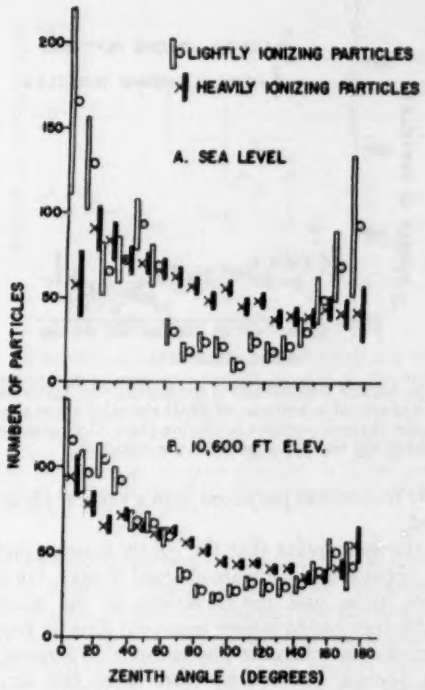

FIG. 8. Zenith-angle distributions of the lightly (<2 times minimum) and heavily (>2 times minimum) ionizing particles associated with nuclear interactions in argon at sea level and 10 600-ft elevation. Ordinates are proportional to the numbers of particles per steradian. All curves have been normalized to the same area. Zero-zenith angle corresponds to the vertically downward direction.

from all of the argon runs at high altitude have been combined. All curves have been normalized to the same area for purposes of comparison.

The heavily ionizing particles show a preference for the downward (zenith angles less than 90°) over the upward hemisphere to about the same degree at both altitudes. At both altitudes the distribution of the lightly ionizing particles can be separated into two groups, one concentrated in the upward and one in the downward direction. The former group may be interpreted as consisting, in part at least, of initiating particles belonging to the charged N radiation arriving from the atmosphere above the apparatus. The latter group are the high-energy protons and charged mesons that have been produced in the nuclear interactions in the argon. At sea level, where the collimating effect of the atmosphere has had more influence, the interacting charged N radiation arriving from the vertical is seen from Fig. 8*A* to be about 6 times the intensity of the horizontal, lightly ionizing particles, whereas at 10 600-ft elevation this ratio is only 2. This is in qualitative agreement with the results of photographic plate work[5] in which the distribution of the zenith angle of star-

[4] J. B. Harding, Nature **163**, 440 (1949).

[5] R. H. Brown *et al.*, Phil. Mag. **40**, 862 (1949).

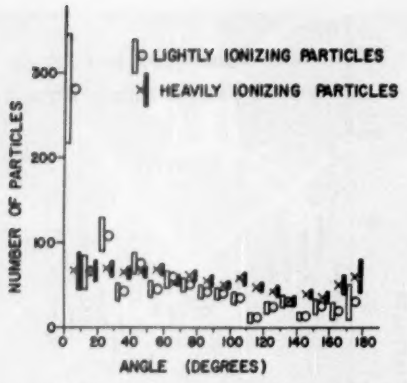

FIG. 9. Angular distributions of the heavily and lightly ionizing particles produced in argon at 10 600-ft elevation about the direction of the charged particles producing them. Ordinates are proportional to the number of particles per steradian.

particle trajectories projected onto a vertical plane were studied.

On the assumption that the lightly ionizing particles in the upper hemisphere are charged N rays, the angles between them and the directions of the secondary particles they produce were measured directly from the projected cloud chamber photographs. Whenever, in a single nuclear interaction, there were two or more lightly ionizing particles in the upper hemisphere that showed no distinguishable difference in ionization, the one nearest the vertical was selected as the N ray. The angular distributions of the heavily and lightly ionizing secondary particles are given in Fig. 9 for the interactions occurring in argon at 10 600-ft elevation. The collimation of the lightly ionizing secondaries about the direction of the particle assumed to be the initiator is further evidence favoring this assumption. The heavily ionizing secondaries show a less pronounced preference to move in the direction of the primary particle.

VII. RATIO OF THE NUMBERS OF CHARGED AND NEUTRAL N RAYS

In the argon high-altitude runs in which no absorber was above the cloud chamber, there was a total of 236 nuclear interactions in which one or more lightly ionizing particles lie in the upper hemisphere. If these are produced by charged N rays and the remaining 876 interactions, observed during the same runs, by neutral N rays, their ratio, 0.27 ± 0.02, may be taken as a measure of the ratio of the number of charged to neutral N rays arriving at this elevation. It will be the true ratio only if the charged and neutral N rays have the same average cross section for the production of the observed nuclear interactions. The charged fraction is favored in this analysis because the neutral N rays may be expected to send some lightly ionizing secondaries in the upward direction that would be classed incorrectly as charged primary particles.

At sea level the observed ratio is 0.18 ± 0.02. The lower value is consistent with the atmospheric absorption of the charged N component being more rapid than the neutral part because of ionization loss.

The observed ratios are those which occur in a region separated from the atmosphere by heavy walls ($\frac{1}{2}$ inch of brass or $1\frac{1}{4}$ inches of glass) and may be expected to be somewhat different from the natural ratio.

VIII. ABSORPTION OF THE N RADIATION

Before reaching the gas in the sensitive volume of the cloud chamber, the N radiation must pass through the $\frac{1}{2}$-inch brass roof. To investigate the influence of the roof on the number of nuclear interactions observed, the cloud chamber was run with additional layers of brass above it as indicated in Fig. 1. The rates of occurrence of nuclear interactions in argon at 10 600-ft elevation calculated from the observed data listed in Table I are plotted in Fig. 10 as a function of the total absorber thickness (roof plus added brass) separating the N radiation from the contained gas. Also plotted in Fig. 10 are the observed rates subdivided into two groups, one including all interactions involving more than one charged particle and the other all interactions involving only one charged particle. If an exponential variation is assumed, extrapolation of the latter two curves to zero roof thickness gives the result that the true rates of occurrence of nuclear interactions involving only one or more than one charged particle are 1.34 ± 0.20 and 1.06 ± 0.06 times greater, respectively, than the rates observed under the normal $\frac{1}{2}$-inch brass roof.

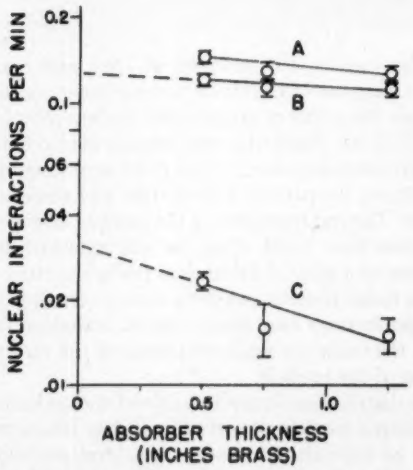

FIG. 10. Dependence of the rate of occurrence of nuclear interactions in argon at 10 600-ft elevation on the amount of absorber between the atmosphere and the interior of the cloud chamber: A, all interactions; B, interactions involving more than one charged particle; C, interactions involving only one charged particle.

IX. EFFICIENCY OF THE IONIZATION CHAMBER

By means of the projection system already described, the geometric location of the point of origin of each nuclear interaction occurring in the gas was determined. The coordinates measured were the distances of each point of origin from (i) the vertical plane containing the five end points of the ionization chamber anodes nearest the camera (see Fig. 1) and from (ii) the central anode wire of the ionization chamber within which the interaction originated.

The length of each ionization chamber was divided into ten equal intervals, and the numbers of origin coordinates, defined by (i) above, falling in each interval were counted. The full-line histogram in Fig. 11 is the distribution of the interaction origins among these intervals for all of the observed interactions occurring in the monatomic gases argon, neon, and helium at sea level and high altitude combined. This included the 2344 interactions listed in Table I plus 83 others that occurred during runs for which the sensitive time was not measured. A total of 806 interactions occurs in the front half of the ionization chamber assembly while 1621 occur in the rear half. The front half of the ionization chamber is therefore $806/1621=0.50\pm0.02$ as efficient as the rear. A similar plot for the nuclear interactions occurring in nitrogen (broken-line histogram of Fig. 11) gives the result that the front half of the ionization chamber is 0.39 ± 0.04 as efficient as the rear half when filled with this gas.

The volume of each ionization chamber was divided into 10 radial intervals coaxial with the anode wire. The radii of the cylinders defining the intervals were so chosen as to make the volumes of the intervals equal. The number of radial coordinates, defined by (ii) above, falling in each interval were counted for the nuclear

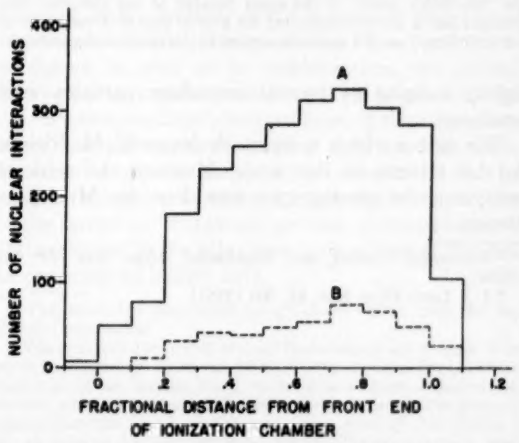

FIG. 11. The distribution of the points of origin of the nuclear interactions along the length of the ionization chamber assembly. Ordinates are numbers of interactions occurring per tenth of the chamber length. *A*, for interactions occurring in helium, neon, and argon at sea level and 10 600 ft combined; *B*, for interactions occurring in nitrogen at 10 600-ft elevation.

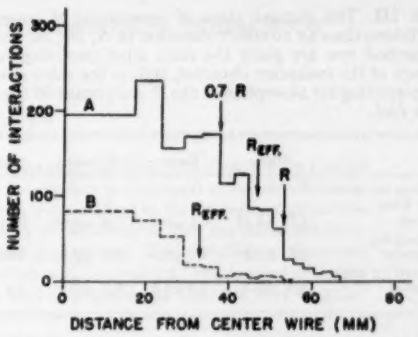

FIG. 12. Distribution of the distances of the points of origin of the nuclear interactions from the central wire of the ionization chamber in which they occurred. The radial intervals along the horizontal axis correspond to equal volume intervals in the ionization chamber. *A*, for interactions occurring in helium, neon, and argon at sea level and 10 600 ft combined; *B*, for interactions occurring in nitrogen at 10 600-ft elevation. *R* is the geometric radius of an ionization chamber. The ordinates are numbers of interactions per radial interval.

interactions in argon, neon, and helium, occurring in the more sensitive region (0.5 to 1.0 of the geometric length) of each ionization chamber. The distribution of the points of origin in the radial intervals is given by the full-line histogram of Fig. 12 for all five ionization chambers combined. Out to 0.71 of the geometric radius, *R*, the distribution is nearly uniform as would be expected if the ionization chambers were highly efficient in this region. Beyond this radius the distribution gradually drops to zero. An effective radius may be defined as $0.71R+r$, where rf is the area under the histogram beyond $0.71R$ and f is the average frequency of occurrence of nuclear interactions per radial interval from zero to $0.71R$. The efficiency of the rear part of the ionization chamber, defined as the detected fraction of the nuclear interactions occurring within its geometric boundaries, is $[(0.71R+r)/R]^2$. From Fig. 12 a value of $[(47.1\pm0.5)/53]^2=0.79\pm0.02$ is obtained. The efficiency of the complete ionization chamber assembly is thus $0.79(0.50+1)/2=0.59\pm0.014$ when filled with a monatomic gas.

The broken-line histogram of Fig. 12 is the radial distribution of points of origin of the nuclear interactions in nitrogen. Calculations similar to those above give 33.0 ± 0.6 mm as the effective radius and 0.27 ± 0.01 as the over-all efficiency of the ionization chamber when filled with this gas. The lower efficiency is caused by the higher percentage of electron capturing impurities in the nitrogen used.

X. NATURAL RATE OF OCCURRENCE OF COSMIC-RAY NUCLEAR INTERACTIONS

The observed rates of occurrence of nuclear interactions in the four gases at 10 600-ft elevation calculated from the data of Table I for which there was no absorber above the cloud chamber are given in the first row of Table III. The rates have been multiplied by

TABLE III. The natural rates of occurrence of cosmic-ray nuclear interactions at 10 600-ft elevation in A, Ne, N, and He. In the second row are given the rates after correcting for the inefficiency of the ionization chamber, and, in the third row after further correcting for absorption of the N component in the cloud chamber roof.

	Argon	Neon	Nitrogen	Helium
Interactions per gram atom per hour:				
Observed	4.75 ±0.14	4.1 ±0.5	1.34 ±0.06	0.60 ±0.06
Corrected for inefficiency	8.0 ±0.3	7.0 ±0.9	5.0 ±0.3	1.02 ±0.10
Corrected for roof absorption	8.9 ±0.6	7.4 ±1.0	5.5 ±0.5	1.4 ±0.3

appropriate factors so that they apply to the same number of atoms (one gram atom) of each gas. In this calculation the rates are assumed to be proportional to the quotient of the absolute pressure and temperature. The geometric volume of the ionization chamber assembly used is 9.1±0.2 liters. In the second row the rates have been corrected for the inefficiency of the ionization chamber (see Sec. 9). In the third row a further correction has been applied for losses in the cloud chamber roof (see Sec. 8). In this last correction the fractions of the interactions involving one and more than one charged particle (see Table II) have been increased by factors of 1.34±0.20 and 1.06±0.06, respectively.

The corrected rates of occurrence of nuclear interactions are plotted in Fig. 8 as a function of the two-thirds power of the mass number, A. The correction for losses in the cloud chamber roof is questionable because it was investigated only for the one gas, argon, it involves a considerable extrapolation, and it neglects the existence of any transition effect in the roof. The rates have been plotted both with and without this correction. Irrespective of its application, however, the general conclusion is that the rate of occurrence of cosmic-ray nuclear interactions shows no great departure from being proportional to $A^{\frac{1}{2}}$. The relative cross sections that the atoms present for nuclear interaction to the cosmic-ray N component are therefore nearly the same as their relative geometric nuclear cross sections.

For an incoming integrated flux of N radiation of 6.0×10^{-3} particle cm^{-2} sec^{-1}, the expected rate of occurrence of nuclear interactions per gram atom of an element would be that given by the straight line in Fig. 13 if the cross section for interaction were truly geometric. This flux is somewhat higher than estimates of the N-component flux that can be made from measurements of the number of stars cm^{-3} day^{-1} occurring in nuclear emulsions.[6,7] The higher value is to be expected since the interactions involving one and two charged particles that are omitted in emulsion studies are counted in the present work. The true flux may be still higher than the above value since interactions in which less than 8 Mev of the energy released to charged particles is dissipated within the ionization chamber are not counted. This omitted group would be made up partly of interactions of some of the low-energy neutrons and protons and partly of interactions of high-energy neutrons and protons in which only

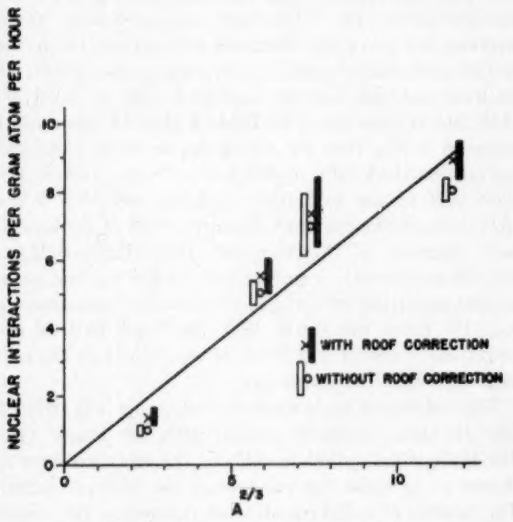

FIG. 13. The rate of occurrence of cosmic-ray nuclear interactions at 10 600 ft per gram atom of an element as a function of the two-thirds power of the mass number of the element. The straight line is the rate expected for a total flux of N radiation of 6.0×10^{-3} cm^{-2} sec^{-1} if the cross section for interaction is geometric.

lightly ionizing or neutral secondary particles were produced.

The author wishes to thank Professor W. M. Nielson for his interest in this work. Much of the work of analyzing the photographs was done by Mrs. Jane Brown.

[6] Bernardini, Cortini, and Manfredini, Phys. Rev. 79, 952 (1950).
[7] J. J. Lord, Phys. Rev. 81, 901 (1951).

Emulsion Studies of Cosmic-Ray Stars Produced in Metal Foils*

IAN G. BARBOUR
Kalamazoo College, Kalamazoo, Michigan
(Received September 1, 1953)

A method is described in which cosmic-ray induced disintegration of nuclei of several elements are studied with metal foils sandwiched between nuclear emulsions placed face-to-face and exposed at balloon altitudes. The range distributions of low-energy particles are obtained from tracks ending in the emulsion. Calculation of the probabilities of detecting star particles permits conversion of the observed star size distributions to the real size distributions, whose variation with atomic number is presented. The variation, with atomic weight, of the cross-sections for the production of stars of various sizes is analyzed. The number of tracks per star corresponding to protons in the energy range 25–100 Mev is obtained and found to vary approximately as the nuclear radius.

I. INTRODUCTION

THE interaction of a high-energy particle with a nucleus appears to be characterized by three major processes: (1) high-energy inelastic processes in which new particles are created (e.g., π-meson production in the collision of an incident nucleon with one or more nucleons in the target nucleus); (2) a "knock-on" process or "nuclear cascade" in which particles of moderate energy are ejected; (3) a final process in which any particles, associated with these interactions, whose energies have degraded until they cannot escape from the nucleus, contribute to the excitation of the whole nucleus and its "evaporation" of low-energy particles. Insight into the operation of all three types of interaction may be expected from investigation of how various characteristics of nuclear disintegrations depend on the atomic number of the target nucleus. Because photographic emulsions include a variety of elements, it is often impossible to ascribe with certainty to the disintegration of the nucleus of a particular element an individual event observed in an ordinary emulsion;[1] knowledge of how star characteristics vary with the atomic number of the nucleus is thus also of importance in interpreting existing data on stars in emulsions, as well as in understanding the nuclear interaction processes themselves. This paper will: (a) describe an experiment designed to study disintegrations in various elements; (b) present data on size distributions and cross-sections; and (c) analyze the data on particles ejected at moderate energies and their relation to the second or "knock-on" process mentioned above. Data relevant to the other two types of interaction will be presented at a later date.

* This work has been aided by a Cottrell Grant from the Research Corporation.

[1] The principal exceptions are: (a) there exist stars of more than seven heavy prongs which can be attributed to Ag or Br; (b) there exist stars of less than six heavy prongs *plus* a minimum-ionization shower, which have been attributed by some authors to the group of lighter elements [see L. S. Osborne, Phys. Rev. **81**, 238 (1951)]; (c) an attempt has been made to differentiate certain stars from the capture of negative π mesons on the basis of the presence of Auger electrons or of α particles of energy less than the potential barrier for bromine [see Menon, Muirhead, and Rochat, Phil. Mag. **41**, 583 (1950)]; (d) Harding [Phil. Mag. **40**, 530 (1949)] has shown that stars with recoil fragments are mostly due the disintegration of Ag or Br.

The comparison of stars in ordinary emulsions with those occurring in emulsions "loaded" with transparent salts does not allow an unambiguous interpretation of each observed event and requires exceptionally good statistics if the differences are to be reliable. Harding[2] attempted to avoid this difficulty by studying stars produced in alternated layers of pure gelatin and standard emulsion; this method is valuable but can be used to study stars produced only in a certain group of light elements. In our initial attempt to introduce small but visible particles of metal within the emulsion, we found that quantities in excess of about 2 percent by volume interfere with the scanning of the plates. In the method finally adopted after having overcome a number of practical difficulties, thin foils of various metals were "sandwiched" between pairs of plates placed face-to-face; the procedure has been briefly described and preliminary results communicated.[3] More recently Hodgson[4] has reported analysis of stars from the disintegration of nuclei of a lead plate in contact with a single photographic emulsion. Some results of an experiment using the "sandwich" method have also been reported by Setti and Merlin.[5]

II. EXPERIMENTAL PROCEDURE

1. Preparation and Exposure

Six metal foils with thicknesses as follows were used in this investigation: Au (51μ); Pt (25μ); Sn (36μ); Cu (43μ); Ni (23μ); and Al (51μ). Ilford G5 200μ emulsions, 2 in.×4 in., were employed. Although more accurate energy measurements at low energies and better discrimination between alpha particles and protons could have been obtained with less sensitive emulsions, such as C2, it seemed desirable to use "minimum ionization" plates in order to record the star particles of higher energy. It was found in preliminary experiments that, even under the maximum pressure which could be applied safely without breaking the glass backing of the plates, the foils would not lie flat

[2] J. B. Harding, Nature **163**, 440 (1949).
[3] I. Barbour and L. Greene, Phys. Rev. **79**, 406 (1950); I. Barbour, Phys. Rev. **82**, 280 (1951).
[4] P. E. Hodgson, Phil. Mag. **42**, 92 (1951).
[5] R. Setti and M. Merlin, Nuovo cimento **8**, 504 (1951).

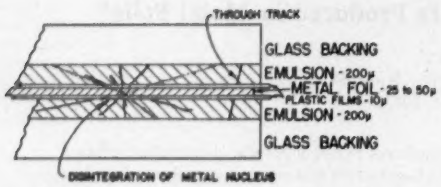

FIG. 1. Cross-sectional diagram of emulsion "sandwich" showing how tracks from the disintegration of a metal nucleus are recorded in the emulsion on either side of the foil. A "through" track is also depicted for comparison.

enough to insure good contact; for if the two emulsion surfaces are more than about 100μ apart during exposure, the particles from disintegrations in the foil may have diverged so much before striking the emulsion that a substantial fraction will be located in the emulsion outside the microscope field-of-view and will be missed during scanning of the plates. It was found desirable therefore to give each foil a preliminary treatment by heating to its annealing temperature in a furnace to render it malleable and then subjecting it to a pressure of $\sim$1 ton/in.^{2} between two very flat steel surfaces. The foils thus flattened were placed between 10μ sheets of cellophane to prevent interaction of the metal atoms with those of the emulsion, and included between pairs of photographic plates as indicated in Fig. 1.

Each such "sandwich" was then placed between two $\frac{3}{16}$-inch aluminum plates which, when fitted into a yoke containing setscrews, could be clamped together to insure good contact and prevent the plates from slipping during exposure. The corners of one of the aluminum plates as well as those of the foil had been cut off to allow a system of registration dots to be imprinted on each pair of emulsions in order to facilitate realignment after development; these registration marks were imprinted[6] by interposing a $\frac{1}{32}$-inch Pb plate drilled with 100μ holes between the sandwich and a distant x-ray source.

A small gondola containing these plate assemblies was attached to a "Skyhook" balloon load-line 40 feet from any other apparatus, and was flown[7] at 55° N geomagnetic latitude for six hours at 93 000 feet. After removal of the foils, the plates were developed by the familiar "two-temperature" method. Each pair of "matching" plates was then in turn placed emulsion-to-emulsion on the microscope stage for re-alignment.

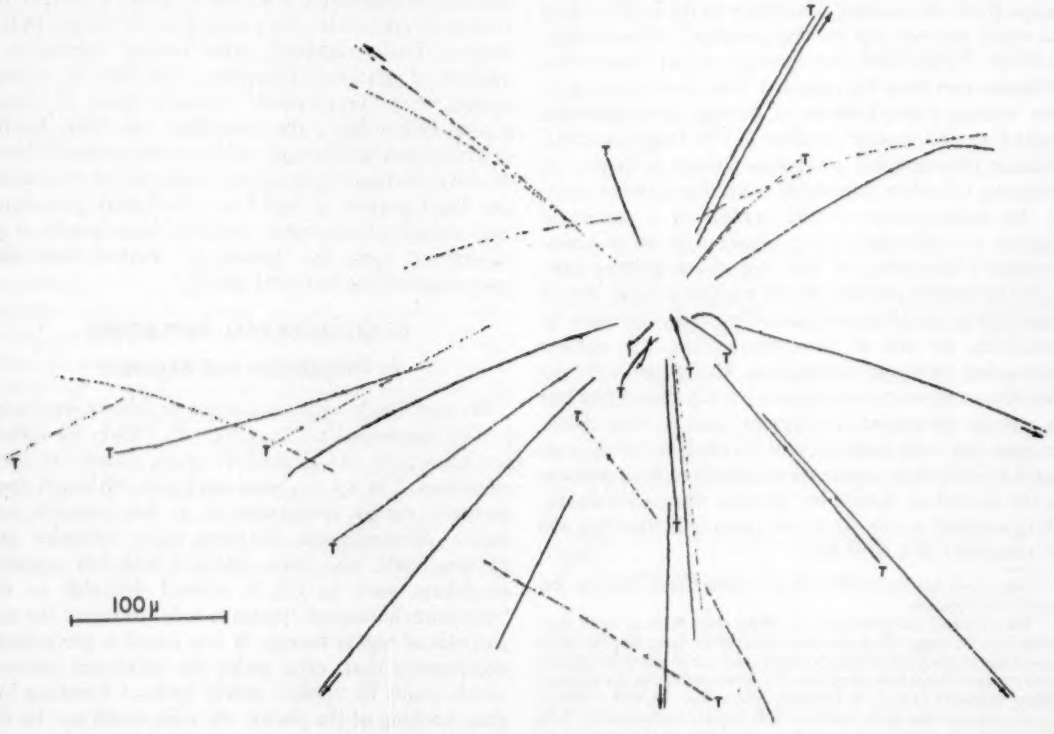

FIG. 2. Microprojection tracing of 24 tracks from the disintegration of a gold nucleus. Tracks marked "*T*" were found in the top plate, others in the bottom plate. Arrows indicate tracks continuing in the emulsion beyond the limits of the tracing. Several matching "through" tracks not associated with the star are also present.

[6] I. Barbour, Phys. Rev. 78, 518 (1950).
[7] Arranged through the kindness of the U. S. Office of Naval Research and General Mills, Inc.

The x-ray dots allowed approximate reconstruction of the original relative orientation of the two plates; exact realignment was achieved by painstakingly touching the top plate at appropriate points with a micrometer-screw adjustment until the "matching" segments of high-energy "through" tracks in all portions of the plates were aligned to within a few microns (except where distorted at the plate edges). Weights were then placed on the top plate to hold the two emulsions in close contact and in this position each pair of plates was cemented together for scanning.

2. Scanning

The two juxtaposed emulsion layers of each pair of plates were scanned at a magnification of 200×. A typical foil star and "through" tracks are shown in Fig. 2. Scanning for tracks from the disintegration of foil nuclei is accomplished in two ways simultaneously: (a) positively, the scanner looks in the double emulsion for groups of three or more tracks which appear to diverge from a common center between the emulsion surfaces, and (b) negatively, he can, for each and every track observed in the emulsion, look for a continuation in the "matching" plate which would eliminate that track from consideration as a possible member of a foil star. (An occasional cosmic-ray particle stopping in the foil will, of course, leave a track in one emulsion only, but the scanner will at least have been alerted to look for a possible foil star.) The use of two emulsions thus appears to have several advantages over foil experiments using only one plate: (1) there is twice the probability of detecting a particle from a foil star; (2) fewer foil stars will be missed since every single track observed can be examined and the majority rejected as "through" tracks by method (b) above; (3) cases of the random crossing of 2 or 3 "through" tracks, which on one plate might erroneously be interpreted as due to a foil star, can be eliminated; (4) the probability of missing a particle from an observed foil star is, as shown below, almost independent of the point within the foil at which the star occurs, since the increased detection-probability for tracks in the plate nearer the disintegrating nucleus is compensated for by the decreased detection-probability in the further plate.

After the plates had been scanned, each event of interest was examined under 450× magnification (using a 30× objective of large working distance to observe through the glass backing of the top plate), and an approximate scale drawing was made of each foil star and all the tracks in its neighborhood, by use of an eyepiece protractor. Finally each pair of plates was separated and both halves of every foil star were examined under oil, to search for tracks which might have been missed at lower magnification and to obtain for each track data such as grain density, horizontal and vertical projection of track length, and distance from the point of entering the emulsion to the star "center."

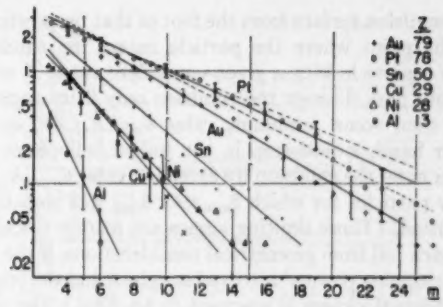

FIG. 3. Observed star-size distributions: relative number of stars observed, per target nucleus, with m or more observed prongs (excluding min ionization tracks) per star, plotted against m for various foils.

III. FOIL STAR DATA AND DETECTION PROBABILITIES

1. Observed Size Distributions

The uncorrected integral star-size distributions observed are shown in Fig. 3, where for each foil the number of stars observed with m or more observed prongs per target nucleus is plotted logarithmically against m. Throughout this analysis, "minimum ionization" tracks of grain density <1.5 times minimum have not been included in describing star size. Typical statistical probable errors are indicated in the graph, as well as limits for the best straight-line fit from which were found constants of a distribution of the form $M(m)=M_0e^{-\lambda m}$. (The low experimental values for stars of $m\leqslant 5$ can be attributed to inefficiency in detecting small stars; although this error due to missing small stars has been estimated by having a second observer rescan sample areas with very great care, the data must be considered less reliable with respect to small stars than large ones. This error of completely missing stars should not be confused with failure to detect additional particles produced in observed stars, an effect for which correction can be made rather rigorously, as discussed in the ensuing paragraphs.)

2. Observed and Real Range Distributions

For each particle observed to stop in the emulsion, an equivalent total range R in emulsion was calculated from the relative stopping power of foil, cellophane, and emulsion, using the various angle and distance data on each track. The real production spectrum was obtained from the observed number of prongs of equivalent range R by dividing by $S(R)$, the probability that a prong of equivalent range R will be detected as a track stopping in the emulsion, calculated for each foil as follows. Consider for the moment one emulsion, and assume that these stopping particles are emitted isotropically. Let f be the distance of the star center from the emulsion surface, θ the original dip angle of a track measured from the line through the star center perpendicular to the emulsion surface, and $r=f\tan\theta$ the distance along

the emulsion surface from the foot of that perpendicular to the point where the particle enters the emulsion. Now a particle with a given equivalent range R will in general pass through the emulsion only if its angle θ is less than some minimum value $\theta_{min}(R,f,Z)$; on the other hand, it will stop in the foil or cellophane and never enter the emulsion if θ exceeds a value $\theta_{max}(R,f,Z)$. Only particles for which $\theta_{min}<\theta<\theta_{max}$ will stop in the emulsion. (These limiting angles are readily calculable for each foil from geometrical considerations, if the relative stopping powers[8] involved are given and the original emulsion thickness is assumed to be 200μ.) The probability of detecting a particle of equivalent range R as a track stopping in the emulsion is then given by

$$S_f(R)=\int_{\theta_{min}}^{\theta_{max}} D(f\tan\theta)\cdot\tfrac{1}{2}\sin\theta d\theta, \qquad (1)$$

where $D(f\tan\theta)$ is the scanning efficiency or probability of actually observing a track which enters the emulsion at a distance $r=f\tan\theta$ from the foot of the perpendicular through the star center.

The scanning efficiency $D(r)$ depends on the magnification and care used in examining the region in which the star is located. To obtain an analytic expression for the above integral, we have assumed $D(r)=1$ for $r<100\mu$, thereafter dropping uniformly to zero at $r=250\mu$, which is about the greatest distance at which a particle is likely to be detected at our magnification.[9] Such an assumption for $D(r)$ is consistent with the experimental data. Figure 4, for instance, shows for a sampling from Pt, the curve of the theoretical distribution-in-r (the number of tracks which would be expected to enter the emulsion at a distance r from the perpendicular through the star center, calculated on the basis of isotropy and averaged over the various f values or depths in the foil, with allowance for particles stopped in the foil as found below); experimental points are plotted for the number of tracks actually observed in various intervals of r. The decrease in experimental values as compared with the theoretical curve for $r>100\mu$ is consistent with the assumed scanning efficiency function, $D(r)$.

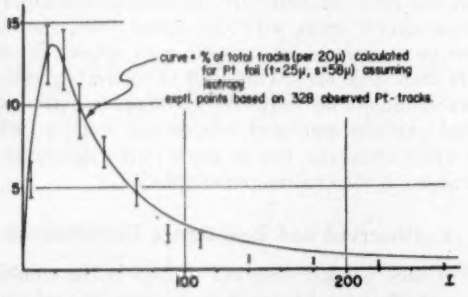

FIG. 4. Number of tracks from Pt-stars observed to enter emulsion at a distance r from the star "center," per 20μ interval of r. (r is measured along the emulsion surface from the point at which a track enters the emulsion to the line perpendicular to the emulsion surface through the star center.) The theoretical curve (assuming 100 percent scanning efficiency) allows for tracks stopping in the foil (see text).

The average probability $S(R)$ of detecting a particle of equivalent range R as a track stopping in the emulsion can thus be obtained for each foil by evaluating the expression in Eq. (1) and then integrating numerically over f, the various depths in the foil at which the star could occur, for both plates. Taking the observed number of prongs of equivalent range R and dividing by the probability function $S(R)$, one can now obtain the real range distribution $\nu(R)$, as given in Fig. 5 for several foils. Stopped particles from a sampling of emulsion stars of 8 or more prongs are the basis for the spectrum of "Ag+Br" (weighted again by an appropriate probability function which for tracks both beginning and ending in the emulsion is readily calculated from geometric considerations). The preponderance of short prongs in the lighter elements is attributable to their lower barrier.

3. Total Detection Probabilities

The total probability $P(R)$ of detecting a particle of equivalent range R (i.e., observing it as a particle stopping in the emulsion or passing through it) is calculated in an analgous way for each foil, with the lower limit in Eq. (1) replaced by zero since here particles passing through the emulsion are to be included. The resulting total probability for two plates is almost independent of f, the distance of the star center from one emulsion surface. [Because the increased probability of detection in the plate nearer the star center is almost exactly compensated for by the decreased probability in the opposite emulsion, the same $P(R)$ values can be used for all stars in a given foil, simplifying the calculations greatly.] Now for each foil $P(R)$ is found to be constant (to within 2 percent) above $R\cong 250\mu$ [essentially because the integral in Eq. (1) is insensitive to $\theta_{max}(R,f)$ once the scanning efficiency $D(f\tan\theta)$ has dropped to zero; in other words, particles of long range are lost by stoppage in the foil only at angles where they would in any case have escaped detection beyond the limits of the field-of-view]. This limiting value of $P(R)$, which we may call P_∞, the probability of detecting an energetic particle, is determined largely by the average solid angle which the fields-of-view of the two emulsion surfaces subtend from the star center and to a lesser extent by the loss of scanning efficiency $D(r)$

[8] H. Yagoda, *Radioactive Measurements with Nuclear Emulsions* (John Wiley and Sons, Inc., New York, 1949).

[9] Although the radius of the field of view in scanning was 250μ, a *greater* region around each star was examined by placing the star center successively at various points on the periphery of the field-of-view. On the other hand, the region which can be examined effectively under oil is considerably *smaller*. There is also evidence (see Fig. 4) that some steep tracks, mostly of low grain density, are missed. The assumed scanning efficiency function $D(r)$ represents a reasonable compromise of these factors.

near the edges of the field of view; P_∞ has values of 0.7 to 0.8 for the various foil thicknesses used. At the other extreme, $P(R)$ of course approaches zero as $R \to 0$, due to losses in the foil.

The total detection probability P for all particles is

$$P = \int_0^\infty P(R)\nu(R)dR \Big/ \int_0^\infty \nu(R)dR, \qquad (2)$$

where, as before, $\nu(R)$ is the real range distribution. This can most conveniently be expressed in the form $P = P_\infty/(1+C/L)$, where L is the total number of observed tracks and C, the number of additional particles missed because of stoppage in the foil at angles where they might otherwise have been detected, is given by

$$C = \int_0^{250} \nu(R)[P_\infty - P(R)]dR. \qquad (3)$$

Only the portion of the range distribution below 250μ is needed here, as above that value $P(R) \cong P_\infty$; the correction C/L amounts to 3 to 5 percent in the various foils. [Actually the π/p ratio[10] and the fraction of particles observed to stop in the emulsion do vary somewhat with star size, so that a separate range distribution $\nu(R)$ and correction C should be worked out for groups of stars of different sizes in each foil; we are justified, however, in using an average value of P for stars of all sizes since C is in any case a small correction to P_∞.]

IV. CONVERSION FROM OBSERVED TO REAL SIZE DISTRIBUTIONS

Having obtained for each foil the over-all detection probability P, the observed size distribution $M(m)$ can be used to calculate the real size distribution, $N(n)$ (the original distribution as produced at the nucleus), where m and n are the number of observed and real prongs respectively. Assume that the real integral distribution of stars of n or more prongs is given by $N = N_0 e^{-\xi n}$, giving a real differential distribution $N'(n) = \xi N_0 e^{-\xi n}$ stars of n prongs. If the probability of observing an individual track is P, then the probability[11] that an n prong star will be observed as an m prong star is given by

$$p(n,m) = \frac{n!}{m!(n-m)!} P^m (1-P)^{n-m}. \qquad (4)$$

Now the total number of m-prong stars to be expected will be $M'(m) = \sum_n p(n,m)N'(n)$. Substituting the values of $p(n,m)$ and $N'(n)$ above, the resulting sum may be evaluated analytically if summed over values of n from m to infinity [a procedure which is justified, despite the obvious upper limit to n set by the size of the nucleus disintegrating, because $p(n,m)$ is small for $n \gg m$, and also $N'(n)$ drops to a negligible value as n approaches its actual upper limit]. When the sum is evaluated, the resulting observed differential distribution $M'(m)$ is found to be exponential, giving an expression for the observed integral distribution to be expected of the form $M(m) = M_0 e^{-\lambda m}$, where the constants are functions of the original parameters ξ, N_0, and P. In practice, however, instead of calculating the *observed* distribution to be expected from a given *real* distribution, one's objective is just the reverse. The constants of the real integral distribution, in terms of those observed, are found to be: $\xi = \ln[Pe^\lambda + (1-P)]$ and $N_0 = (M_0\lambda/\xi) \times [1-(1-P)e^{-\xi}]$. For $P > 0.7$, the former expression differs only slightly from the value $\xi = \lambda P$ which would hold if all n prong stars were to be observed as stars of exactly nP prongs, rather that the correct probability spread around this value given by Eq. (4) above.

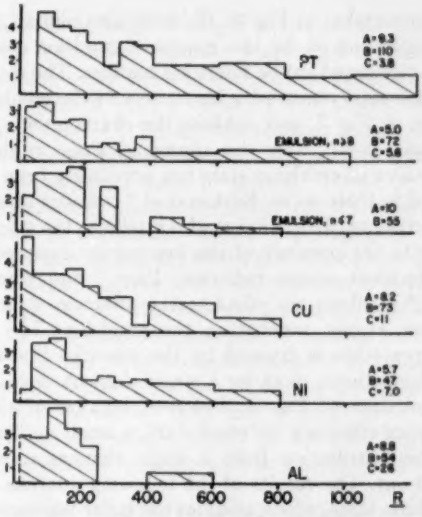

FIG. 5. Range distributions $\nu(R)$ of particles observed to stop in the emulsion for various foils. Number of particles of equivalent emulsion range R, per interval of 50μ in R, corrected as indicated in the text for detection probability and for the portion of the trajectory of each particle in the foil. (To compare the number of particles *per star*, divide the ordinates by the factor A; to compare number of particles *per target nucleus*, divide by $B(\times 10^{23})$; to compare number of particles *per real star track*, divide by C.)

V. REAL SIZE DISTRIBUTIONS

The value of the exponent ξ of the real size distribution, calculated for each foil from the exponent λ of the observed distribution (Fig. 3) and the detection probability P (Sec. III–3 above) by the conversion formulas just developed (Sec. IV), is plotted[12] as a function of the

[10] See also D. Perkins, Phil. Mag. 41, 138 (1950).

[11] See also reference 4 above.

[12] Probable errors shown represent the extreme slopes of distributions drawn at the limits of statistical probable errors of individual points, as illustrated for Pt in Fig. 3. With respect to both foil star data and the emulsion star analysis discussed below, the values for *lighter* elements are more uncertain than those for heavier elements because estimation of the scanning inefficiency for 3-, 4-, or 5-prong stars results in a greater uncertainty for small nuclei. Failure to detect very small stars originating in either the foil or the emulsion would result in an under estimation of the value of ξ for elements of low atomic number.

atomic number in Fig. 6. We have also plotted points corresponding to the two groups of emulsion constituents, calculated in the following manner. The distribution for stars observed with centers in the emulsion is shown in Fig. 7, and exhibits the characteristic break at about $n=7$. Now this change of slope in the distributions of emulsion stars has previously been interpreted in three ways. Barton *et al.*[13] consider this effect as fortuitous. Bernadini *et al.*[14] attribute the change of slope to the presence of the low-energy component in the incident cosmic-radiation. Page,[15] and Birnbaum *et al.*[16] attribute the effect to the presence of elements of low atomic number in the emulsion. The latter interpretation is favored by the essential linearity of our logarithmic plots for a *single* element, such as the Pt-foil data of Fig. 3; however, because of the low scanning efficiency for small stars, a small nonlinearity in the distribution from a single element cannot be ruled out. The results of the following analysis of the emulsion stars, which assumes the latter interpretation, are consistent with the foil star data [see Fig. 8]. The emulsion contains a group of heavy elements (Ag and Br) of average atomic weight 94, and a light group (chiefly C, N, O) of average atomic weight 14. If then ξ_1 and ξ_2 are the slopes of the two portions of the curve in Fig. 7, and we assume that portion 2 and its extrapolation is contributed by the group of heavy elements, then the slope of the star distribution contributed by the group of light elements is calculated to be $\xi_L \cong K(\xi_1-\xi_2)(K-1)$, where $K=e^{7(\xi_1-\xi_2)}$. The values obtained in this way for the heavy and light emulsion groups, on the basis of our data, as well as those calculated by this same method from the emulsion star

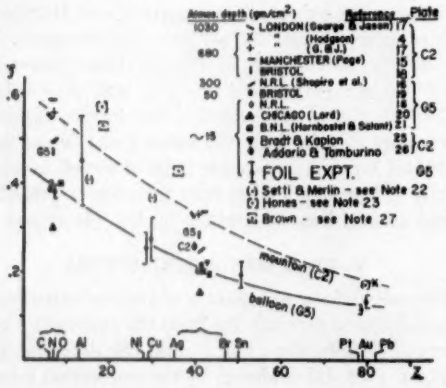

FIG. 6. Exponent, ξ, of real star size distributions, plotted as a function of atomic number. Values obtained from the data of other observers by the method described in the text are shown for comparison. (References given as indicated, in footnotes.)

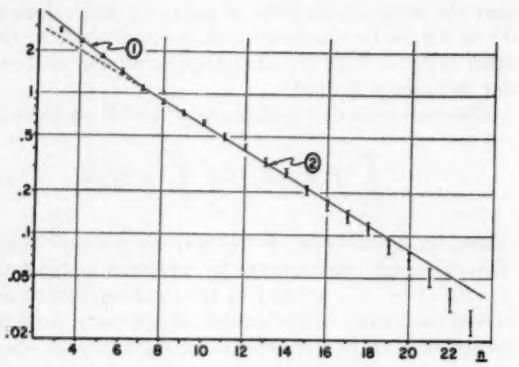

FIG. 7. Relative integral star-size distribution for stars with centers in the emulsion (number of emulsion stars of n or more prongs).

data given by a number of other observers,[16–27] are plotted in Fig. 6.

Hodgson's value[4] obtained with a Pb plate is also given in this graph. We have calculated very rough values shown in brackets from the data of Setti and Merlin.[22] Harding's gelatin-layer data[2] yield $\xi \sim 0.9$ for the C–N–O group; this value is higher than the other data, but is based on a small number of stars. Data obtained on cloud-chamber stars by Hones[23] using argon at sea level and by Brown[27] at mountain altitudes are the basis of other values plotted in Fig. 6. In general, the effect of the difference in the incident energy spectrum at balloon and mountain altitudes is clearly reflected in the graph.[24] Results at cyclotron energies give even higher values for the slope of the star-size distributions. Bernadini's data[28] yields a value ~0.8 for emulsion stars produced by 385-Mev protons; cloud chamber measurements by Bøggild and Tenney[29] with

[13] Barton, George, and Jason, Proc. Phys. Soc. (London) **A64**, 175 (1951).
[14] Bernadini, Cortini, and Manfredini, Phys. Rev. **79**, 952 (1950).
[15] N. Page, Proc. Phys. Soc. (London) **A63**, 250 (1950).
[16] Birnbaum, Shapiro, Stiller, and O'Dell, Phys. Rev. **86**, 86 (1952).
[17] E. George and A. Jason, Proc. Phys. Soc. **A62**, 243 (1949).
[18] Brown, Camerini, Fowler, Heitler, King, and Powell, Phil. Mag. **40**, 862 (1949).
[19] Camerini, Davies, Fowler, Franzinetti, Muirhead, Lock, Perkins, and Hekutieli, Phil. Mag. **42**, 1241 (1951).
[20] J. Lord, Phys. Rev. **81**, 901 (1951).
[21] J. Hornbostel and E. O. Salant, quoted in reference 16.
[22] Reference 5. G5 emulsions at 4450 m. Their method of converting from observed to real distribution does not appear to us valid; we have instead used their observed data together with very rough estimates of their detection probabilities to obtain by the method of Sec. IV the three very approximate values plotted in brackets.
[23] E. Hones, Phys. Rev. **83**, 1263 (1951) and private communication. Cloud chamber stars in argon at sea level; triggering was with built-in ionization chamber.
[24] The points on the graph representing C2 data are invariably somewhat higher than those from G5 data under the same conditions. This may be attributed to the insensitivity of C2 emulsions to the high energy particles occurring more frequently in large stars (see references 18 and 19), resulting in a steeper size-frequency distribution in C2.
[25] H. Bradt and M. Kaplon, Phys. Rev. **78**, 680 (1950).
[26] M. Addario and S. Tamburino, Phys. Rev. **76**, 983 (1949).
[27] F. Brown (private communication and Princeton University thesis). Cloud ion-chamber data at mountain altitude (700 g/cm²). Probable errors quoted are ~10 percent; singly charged particles of ~2.5 minimum ionization were recorded.
[28] Bernadini, Booth, and Lindebaum, Phys. Rev. **80**, 905 (1950).
[29] J. Bøggild and F. Tenney, Phys. Rev. **84**, 1070 (1951).

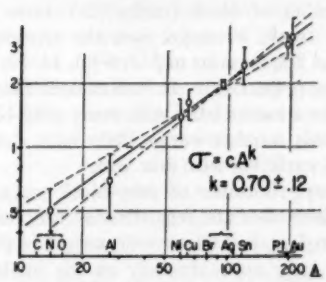

FIG. 8. Number of stars (per target nucleus) with 4 of more real prongs, plotted against the atomic weight of the target. The derivation of the points representing the emulsion constitutents is explained in the text.

190-Mev neutrons give values around 0.9 for krypton and oxygen, whereas for 90-Mev neutrons in alcohol and water vapor, Horning's data[30] would give a value of about 1.2.

VI. STAR-PRODUCTION CROSS SECTIONS

From the values of N_0 and ξ, calculated for the real star size distributions of each element, the star-production cross sections may be computed. The relative integral cross sections for all stars of four or more real prongs are shown in Fig. 8. (Probable errors include uncertainty in ξ, as well as statistical errors in number of stars observed.) Values for stars in the emulsion were obtained as follows. The ratio of the observed number of emulsion stars of $n \geqslant 3$ to the number of stars of three or more prongs attributable to Ag and Br is found by extrapolation of curve 2, Fig. 7. Averaging our value of this ratio with that obtainable from the star populations of other observers (see values quoted in reference 16) gives an average of $\sim 1.43 \pm 0.1$ for this ratio. Using the chemical analysis of the emulsion as supplied by the manufacturer, the cross sections for stars of $n \geqslant 4$ in the light and heavy emulsion groups can be calculated, and is plotted also in Fig. 8. If the observed exponential size distributions (*e.g.*, straight-line curves in Fig. 3) are assumed to hold down to the smallest stars, the cross sections for stars of $n \geqslant 1$ as a function of atomic weight would fall on a line of somewhat less steep slope ($\sim A^{\frac{1}{3}}$). This would involve a rather great extrapolation beyond the smallest stars observable in our foil experiments ($m=3$ or $n=4$). Even for emulsion stars, scanning efficiency for $n \leqslant 3$ is low, and most observers do not quote results for $n=1$ or 2 because of the ambiguity in interpreting such events.[31]

Although comparison with experiments of other observers where different energy spectra are involved may be of little value, it might be noted that Brown[27] finds for cloud ion chamber stars size distributions varying uniformly down to the smallest stars, and also finds for stars of $n \geqslant 2$ a variation with atomic weight less rapid than $A^{\frac{1}{3}}$. These cross sections should not in any case be interpreted as total interaction cross sections, which would have to include "stars" of zero-prongs and other processes whereby the star-producing radiation is absorbed.[32] Other experimeters[33] have reported results consistent with a geometric cross section for the total absorption of the star-production radiation under lead, air, ice, etc. Experiments on the production of bursts in ionization chambers of various wall materials[34] and the study of stars produced in emulsions with gelatin layers[3] have also shown an approximately geometrical variation. Blau and Oliver[35] have more recently exposed gelatin layers to 300-Mev neutrons and find evidence for some nuclear transparency.

VII. THE GRAY-BLACK TRACKS

1. Experimental Results

In the preceding sections we have been considering all particles except shower particles (<1.5 min). We turn now to the analysis of a particular group of particles, the "gray-black" tracks of density from 3 to 7 times minimum ionization, corresponding to protons of energy from 25 to 100 Mev. Every foil star track (except those making an angle of more than 60° with the emulsion surface) was grain-counted, and those with corrected grain counts falling near the boundaries of the above interval were rechecked. Calibration was established by grain counts on very long mesons coming to rest in the emulsion. The average number of gray-black tracks per star (corrected for detection efficiency) is shown for various elements and star sizes in Table I. Here, as throughout, star size refers to the number of prongs with >1.5 min ionization. The data for Ag+Br

TABLE I. Values for the average number of gray-black tracks per star, classified according to star size (vertical columns) and target material (horizontal lines).

m (obs. prongs) / *n* (real prongs)	3–4	3–5 / 5–7	6–9 / 8–13	10–13 / 14–19	14–20 / 20–30	All stars
Emulsion	1.2 ±0.3	1.2 ±0.2	3.1 ±0.6	3.8 ±0.7	6.8 ±0.8	2.0 ±0.2
Pt		1.2 ±0.2	3.4 +0.6	4.9 ±0.8	6.2 ±0.7	2.9 ±0.2
Ag and Br			3.1 ±0.6	3.8 ±0.7	6.8 ±0.8	(2.1 ±0.3)
Cu		1.9 ±0.4	2.5 ±0.5	6.4 ±1.6		1.9 ±0.3
Ni		1.7 ±0.4	3.0 ±0.7	5.7 ±1.7	7.1 ±3.2	2.0 ±0.3
Al		1.2 ±0.5	3.5 ±2.5			1.4 ±0.4
C, N, O	(1.2)	(1.3)				(1.2)
Average	(1.2)	1.3	2.9	4.6	6.4	

[30] W. Horning, Phys. Rev. **75**, 378 (1949).

[31] C. Lees *et al.* [Lees, Morrison, Muirhead, Rosser, Phil. Mag. **44**, 304 (1953)] have recently reported comparison of "diluted" and normal emulsions, bombarded with 120-Mev protons. Using "along the track" scanning, they find many more stars of 0, 1, and 2 outgoing particles attribtable to heavy than to light elements at these low energies.

[32] There is also low-energy secondary radiation present which will be effective in producing stars in the light elements but not in the heavier elements with higher Coulomb barriers. A low-energy neutron may produce a star of 3 or 4 particles in a light nucleus because of the low binding energy for alpha particles.

[33] D. George, Nature **162**, 333 (1948); J. Harding and J. Lattimore, Nature **163**, 319 (1949); and reference 17 above.

[34] H. Lewis, Phys. Rev. **78**, 483 (1950).

[35] M. Blau and A. Oliver, Phys. Rev. **87**, 182 (1952).

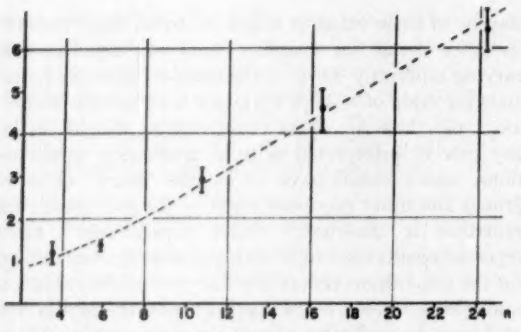

FIG. 9. Number of gray-black tracks per star, averaged over all stars of a given size in all the foils, as a function of star size. n is the number of real tracks with ionization >1.5 min.

were obtained from large stars in the emulsion (top line).[36]

It can be seen that the number of gray-black tracks per star increases with star size, indicating the increase in excitation energy accompanying the process which gives rise to more knock-ons, as discussed below. There is little variation with Z in the number of gray-black tracks per star *for stars of a given size* (vertical columns); the variation in the values averaged for all stars in a given element (last column) arises primarily from the varying distributions of the star population among the star size groups for various elements. The number of gray-black tracks per star of a given size (average for all elements weighted as inverse square of prob. errors, as shown in the bottom line of Table I) is plotted against star size in Fig. 9. Comparable values by Brown *et al.*[18] for "grey" tracks are uniformly ~25 percent lower; however, their "grey" tracks refer to a slightly different energy interval (1.5 to 5 times min) and were obtained at mountain altitudes. The mountain data of Bernadini *et al.*[14] for protons in the interval 80–300 Mev would give a curve about 50 percent lower. At cyclotron energies (400 Mev), Bernadini, Booth, and Lindebaum[37] report an average of 0.35 tracks (per star) in their "sparse-black" group (3 to 6 times minimum, corresponding to 30–100 Mev protons) and a mean of 3.3 prongs per star.[38]

[36] It was found that the ratio of the number of gray-black tracks per star for *all* stars to that for *large* stars only ($m \geq 6$ or $\sim n \geq 8$) in Pt, Cu, and Ni was almost constant (~1.3). If we assume that this same ratio applies for Ag+Br, the number of gray-black prongs for *all* Ag+Br stars can be estimated as shown in brackets in Table I. The calculation for the light emulsion elements is less reliable; the large Ag+Br star data were first extrapolated to small Ag+Br stars on the basis of the corresponding ratios in the foils, and the fraction of small stars attributable to the light elements obtained from the cross sections (Fig. 8) and emulsion composition. This permitted an estimate to be made of the number of gray-black tracks per star attributable to C, N, and O.

[37] Bernadini, Booth, and Lindebnaum, Phys. Rev. **88**, 1017 (1952).

[38] The resulting point would fall about 40 percent below our curve, and their energy interval is nearly the same as ours. However, the situation differs in that the total available energy is constant, so that the more energy escapes in fast protons, the less there is available for evaporation prongs.

The number of *black* tracks (>7 times min) per gray-black track, averaged over the elements, is 3.4, 2.7, 2.6, and 2.8, for stars of 5–7, 8–13, 14–19, and 20–30 real prongs, respectively. It is thus seen that about $2\frac{3}{4}$ black tracks are associated with every gray-black track, and that this number varies little with Z and shows only slight variation with star size.

The average number of gray-black tracks per star averaged over all stars, regardless of size, from a given foil is plotted against the atomic weight in Fig. 10, and is seen to vary approximately as the nuclear radius. While here, as throughout this section, the absolute values are subject to considerable error, the relative values must be considered fairly reliable; since the same scanning and grain-counting techniques were used in all cases, errors due to failure to detect fast particles, or in calibrating grain-counts, tend to effect all foil values approximately equally.

2. Theory and Discussion

Since the gray-black group includes protons only of energies greater than 25 Mev it can contain relatively few evaporation particles. Although the separation is not clear-cut, especially for lighter nuclei (e.g., the Fermi energies ~20 Mev), it is clear that we are dealing primarily with particles ejected at energies higher than those for which evaporation theory can account. Our data also show that the gray-black group has a much greater anisotropy than the tracks of density corresponding to protons of $E<25$ Mev, which also indicates that their origin is not in an evaporation process.

Since we are dealing in the cosmic radiation with particles whose de Broglie wavelength is less than that of the nuclei involved, a semiclassical approach to the theoretical consideration of the origin of these fast protons can be expected to be fairly satisfactory. In this approach, a high-energy nucleon is considered as interacting independently with a single nucleon in the nucleus with the same cross section as a free nucleon-nucleon interaction; each particle from such a collision can in turn collide with other nuclei, or escape from the nucleus. (When any nucleon has insufficient energy to escape, it is considered as contributing to the excitation of the whole nucleus and the subsequent "evaporation.") Goldberger[39] has calculated by the Monte Carlo method

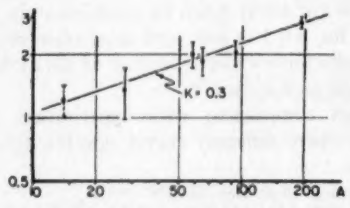

FIG. 10. Average number of gray-black tracks per star (averaged over all stars regardless of size from a given foil) plotted against the atomic weight of the target.

[39] M. Goldberger, Phys. Rev. **74**, 1268 (1948).

the effect of the exclusion principle for the nucleon-nucleon collisions resulting when 90-Mev neutrons are incident on such a Fermi gas of nucleons and finds a reduction of the effective cross-section in the ratio of 1 to $(1-7E_F/5E_i)$, where E_F is the Fermi energy and E_i is the energy of the incident neutron. A similar calculation was carried out at 400 Mev by Bernadini *et al.*[37]

According to this model, the mean free path, λ, of a proton in nuclear matter is given by the average proton-nucleon cross sections, namely,[40]

$$1/\lambda = 3F[Z\sigma_{pp} + (A-Z)\sigma_{pn}]/4\pi R^3, \qquad (5)$$

where R is the nuclear radius and F the factor taking into account the effect of the exclusion principle. A similar expression holds for an incident neutron. As a first approximation, λ will not be a function of Z, provided we assume: (a) the density of nuclear matter is constant (as indicated in scattering experiments, such as those of DeJuren and Knable;[41] (b) the effect which the small variation in the A/Z ratio has on the average nucleon-nucleon scattering cross section (averaged over protons and neutrons in the nucleus) can be neglected; and (c) the variation of F with A can be neglected. The last assumption seems justified since the Fermi momentum turns out to be independent of Z, except for a small shift due to the variation in the A/Z ratio; in any case, at these higher energies the exclusion principle, which operates chiefly in forbidding small momentum-transfers, plays a less significant role except in the final stages of any given internal nucleonic cascade. With these assumptions the mean-free-path in the nuclear matter of various elements is a function of energy only.

On this basis one would anticipate that the number of fast protons ejected would increase with nuclear size faster than the nuclear radius, because of cascade action within the nucleus. However, for larger nuclei it is more difficult for a proton of moderate energy to escape. (Thus for 90-Mev incident neutrons Hadley and York[42] find for the production of protons of greater than 20 Mev in C, Cu, and Pb cross sections of 0.41, 0.31, and 0.24 times the respective inelastic cross sections. This decrease they interpret as due to the increased difficulty for a proton to leave the larger nuclei.) For incident neutrons of average energy 300 Mev, Blau, Oliver, and Smith,[43] using stratified emulsions, find that the number of protons of greater than 60 Mev ejected per star in the light and heavy nuclei is approximately the same, indicating the smaller percentage of protons in the larger nuclei which can escape at these energies. At higher energies the effect of cascade action would be expected to predominate, as reflected in the variation of gray-black tracks in our experiment.

For a more detailed treatment, a Goldberger-type analysis of a group of cascades in nuclei of various sizes can be made. Since the mean free path in nuclear matter is, as shown above, in first approximation independent of the nuclear radius, the same diagrams can be used for several elements by redrawing the surface of the nucleus for smaller and smaller nuclei. This has been carried out on a 2-dimensional analysis (of the sort developed by Bernadini *et al.*[37]) for a few interactions by Lindenbaum,[44] but the small number of cases analyzed gives an inconclusive result. The assumptions of the Goldberger model would in any case be very dubious for nuclei as small as $A=14$, since no allowance is made for the alpha-particle structure of the light elements or for the depletion of the nucleus during the cascade, which represents a significant change in the case of small nuclei.

VIII. CONCLUSION

The foil sandwich method described appears to be a valuable tool in studying nuclear disintegrations. Data have been presented on the variation of star size distributions and cross sections with the atomic number of the target nucleus. In addition, the particles of moderate energy attributed to a "knock-on" process were analyzed. The low-energy spectra, excitation energies, "temperatures," and α/p ratios associated with the "evaporation" process, and their variation with atomic number, will be presented and compared with theory upon completion of analysis of low-sensitivity plates which permit more accurate grain counts at low energies and better differentiation between protons and alpha particles. At the other extreme of energy, the foil sandwich method appears to be of limited value in studying very high-energy processes such as meson production, because the detection efficiency for shower particles is low. (Minimum ionization tracks which pass steeply through the emulsion are difficult to detect, whereas those at glancing angles strike the emulsion far from the star center.) A series of foil experiments at cyclotron energies is to be undertaken; use of monoenergetic incident particles permits a more adequate comparison with the theory of the Z dependence of evaporation and knock-on processes than is possible with the variety of particles and energies present in the cosmic radiation. Bombardment with a neutron beam will also permit a much higher star density to be recorded because of the relative absence of the spurious unrelated tracks which determine the maximum exposure allowable in the cosmic-ray sandwich experiments.

The assistance of Mr. Lawrence Greene and Mr. Richard Wilson in analyzing the plates is gratefully acknowledged. The following students also participated in the project: H. Martinek, D. Orr, M. Meux, J. Bailey, M. Jones, and M. Reed.

[40] See, e.g., Fernbach, Serber, and Taylor, Phys. Rev. **75**, 1352 (1949).
[41] J. DeJuren and N. Knable, Phys. Rev. **77**, 606 (1950).
[42] J. Hadley and H. York, Phys. Rev. **80**, 345 (1950).
[43] We are indebted to Dr. Blau for a prepublication copy of this forthcoming paper.
[44] S. Lindenbaum (private communication).

Cosmic Radiation in the Trapped Orbits of a Solar Magnetic Dipole Field*

S. B. TREIMAN
Palmer Physical Laboratory, Princeton University, Princeton, New Jersey
(Received October 21, 1953)

One of the well-known consequences which would follow from the existence of an appreciable solar magnetic dipole field is a diurnal variation in cosmic-ray intensity at intermediate latitudes on the earth. For the purpose of calculating the expected diurnal effect, it is first necessary to determine the extent to which the bounded orbits of the solar field are filled by the mechanism which has been discussed by Kane, Shanley, and Wheeler: namely, the scattering of cosmic-ray particles into bounded orbits as a result of magnetic deflection in the earth's field. A calculation of this effect is carried out here along the lines indicated by Kane, Shanley, and Wheeler but with several modifications. A solar dipole moment of 6.5×10^{33} gauss-cm^3, which is implied by the latitude cutoff at the earth, is adopted for the calculations. The cosmic-ray intensity in the trapped orbits is found to be appreciably smaller than indicated in the earlier calculations. Correspondingly, it is expected that the diurnal effect at the earth will be larger than the currently accepted theoretical values. The apparent experimental absence of the effect, although not conclusive, casts doubt on the existence of a solar dipole field as large as 6.5×10^{33} gauss-cm^3. The present work also provides an estimate of the average time which a cosmic-ray particle would spend in the trapping region. The value 5000 years, previously given, is revised downward by an order of magnitude.

I. INTRODUCTION

DIRECT measurements, based on the observation of Zeeman splitting of solar-spectrum lines, have lead to inconclusive results in the attempt to establish the existence and magnitude of a general solar magnetic field. The early work of Hale and co-workers[1] pointed to a general field of a dipole character with a value of ~50 gauss at the pole. Although some of Hale's observers failed to detect any Zeeman splitting whatever, Cowling[2] and Blackett[3] have argued in favor of Hale's interpretation of his measurements in terms of a dipole field. Thiessen,[4] in 1945, also obtained evidence for a field of ~50 guss at the pole, but in more recent measurements he has failed to find any field as large as 5 gauss.[5] In a set of measurements made between 1940 and 1947, Babcock[6] found fields between 6 and 60 gauss in 18 cases, whereas the remaining 24 cases gave no measureable fields or slightly negative values for the polar field. Measurements carried out in recent years give an upper limit of at most several gauss for the magnetic field.[7]

Further, a theoretical difficulty connected with direct measurements has been pointed out by Alfvén.[8] He argues that the presence of turbulent magnetic fields on the surface of the sun makes it impossible to reach any conclusions about a general solar field on the basis of Zeeman-effect measurements.

An independent approach to the question of a possible solar dipole field consists in studying the effects which such a field would have on the cosmic radiation. The most obvious effect would be to set a lower limit to the magnetic rigidity of particles which can arrive at the earth from infinity. The existence of a cutoff in the primary cosmic-ray spectrum at the earth—as deduced from the occurrence of a "knee" in the latitude effect at high altitudes—was first reported definitely by Cosyns[9] in 1936. Recent measurements have clearly established the location of the "knee" at 58°.[10,11] The corresponding cutoff rigidity in the cosmic-ray spectrum at the earth is 1.5 Bv; and if this is interpreted in terms of a solar dipole field, it leads to a dipole moment of 6.5×10^{33} gauss-cm^3.

No other reasonable interpretation of the cutoff has been put forward. However, the most conclusive test of the solar dipole hypothesis will be given when it becomes possible to determine the cutoff rigidity separately for primary particles of different charge.[10] If it should prove to be that the cutoff rigidity is independent of charge, the case for a solar dipole field would be greatly strengthened.

As a second consequence of a solar dipole field, one expects a diurnal effect in cosmic-ray intensity at the earth. Particles whose magnetic rigidity lies between the solar-imposed cutoff and value $(1+2^{\frac{1}{2}})^2$ times this limit can arrive in the vicinity of the earth only over a limited cone of directions. The further deflection of these particles in the short-scale field of the earth will give rise to a pattern of allowed directions at the earth which, however complicated, has a fixed relation to the earth-sun line. As the earth rotates on its axis, the cosmic-ray intensity will consequently vary at a fixed geographic location. If the intensity within the forbidden cones were indeed zero, the resulting diurnal

* Supported by the joint program of the U. S. Atomic Energy Commission and the U. S. Office of Naval Research.
[1] Hale, Seares, Van Maanen, and Ellerman, Astrophys. J. **47**, 206 (1918).
[2] T. G. Cowling, Monthly Notices Roy. Astron. Soc. **105**, 166 (1945).
[3] P. M. S. Blackett, Phil. Mag. **40**, 125 (1949).
[4] G. Thiessen, Ann. astrophys. **9**, 101 (1946).
[5] G. Thiessen, Z. Astrophys. **26**, 16 (1949).
[6] H. D. Babcock, Publs. Astron. Soc. Pacific **60**, 244 (1948).
[7] H. Von Kluber, Monthly Notices Roy. Astron. Soc. **111**, 2 (1951); G. Thiessen, Nature **169**, 147 (1952).
[8] H. Alfvén, Nature **168**, 1036 (1951).
[9] M. G. E. Cosyns, Nature **137**, 616 (1936).
[10] J. A. Van Allen and S. F. Singer, Nature **170**, 62 (1952).
[11] Neher, Peterson, and Stern, Phys. Rev. **90**, 655 (1953).

variation on the earth would be very substantial. However, as was first pointed out by Alfvén,[12] particles which approach the earth from allowed directions may be scattered by deflection in the earth's field into the "forbidden" cone. These particles will then find themselves on bounded orbits in the field of the solar dipole and will be removed from the trapping region only by scattering at the earth into unbounded orbits which lead off to infinity or by collisions with bodies in the solar system. The cosmic-ray intensity in the trapping region is therefore determined by the competition between absorption and net scattering.

The details of this process have been very thoroughly discussed by Kane, Shanley, and Wheeler.[13] They found that the intensity in the forbidden directions is appreciable in comparison with that in the allowed directions. The diurnal effect at the earth was therefore expected to be small. It was calculated by Dwight[14] and more recently by Singer[15] and by Dawton and Elliot.[16] In all cases the calculations have been based on the results of KSW.

The calculated magnitude of the diurnal effect (~2–3 percent at 56° for a solar dipole moment of 6.5×10^{33} gauss-cm^3) was not thought to be inconsistent with the apparent experimental absence of the effect.[16–18]

The purpose of the present work is to consider anew the question of the filling of trapped orbits by the mechanism discussed above. Some of the results obtained by KSW require modification. In the present calculations it is found that the intensities in the trapped orbits are smaller than was indicated by KSW. As a result, the diurnal effect at the earth is expected to be larger than the currently accepted theoretical values, although the discrepancy with experiment is still not entirely conclusive. A second change in the results of KSW has to do with the average time which particles spend in the trapping region. The figure 5000 years, given by KSW as representing a typical value of the lifetime, is revised downward by an order of magnitude in the present calculations. A knowledge of this lifetime is important in connection with certain neglections which are made in the calculations (e.g., neglect of collisions with interplanetary dust) and is of some interest in connection with certain theories on the origin of cosmic rays.[19]

II. DISCUSSION OF THE TRAPPING PROCESS

In accordance with the model which we wish to consider, it is assumed that the dominant magnetic field within the solar system is due to a solar dipole whose moment is taken to be 6.5×10^{33} gauss-cm^3. On a scale of solar-system distances the earth's field is relatively important only over a small region of space. It is treated therefore as an essentially point-like center which scatters particles from one to another of the static trajectories in the field of the solar dipole; in particular, it will scatter particles from unbounded orbits into trapped orbits, and *vice versa*. At the same time, absorption of the trapped particles will occur in collisions with the sun, the earth, and other objects in the solar system.

The possibility that planets other than the earth (e.g., Mars and Venus) have appreciable magnetic moments and thus contribute to the filling of trapped orbits cannot be ruled out. We nevertheless neglect this possibility. We likewise neglect several other effects which might conceivably contribute to the filling of trapped orbits, e.g., direct production of cosmic radiation in the vicinity of the sun, albedo radiation leaving the earth and other bodies in the solar system and going directly into trapped orbits, scattering in the magnetic fields carried by ionized beams of particles from the sun, etc.

For a particle of charge e and momentum p, which moves in the field of the solar dipole M_s, there exists an integral of motion γ (Stoermer's angular momentum parameter) given by

$$-(r/R)\cos\lambda\cos x+(R/r)\cos^2\lambda=-2\gamma, \qquad (1)$$

where R is the so-called characteristic radius:

$$R=(eM_s/cp)^{\frac{1}{2}}. \qquad (2)$$

Here λ and r are, respectively, the latitude of the particle (relative to the magnetic equator) and its radial distance from the dipole; x is the angle between the velocity vector and the "directrix," a reference vector perpendicular to the meridian plane and pointing east (where we assume that the solar dipole points south). The quantity cp/e is called the magnetic rigidity. It will be assumed that the earth lies in the plane of the sun's magnetic equator so that the coordinates at the earth are $r=r_e$, $\lambda=0°$.

From Eq. (1), one finds that the "allowed" region in the meridian plane ("allowed" regions are characterized by the requirement $|\cos x|\leq1$) splits up into two parts when $\gamma<-1$, the outer part extending to infinity, the inner part being insulated from infinity by forbidden regions. This leads to the result that particles of characteristic radius R, which come from infinity, can arrive in the vicinity of the earth at angle x only if

$$R/r_e\leq1+(1+\cos x)^{\frac{1}{2}}. \qquad (3)$$

Thus, a complete cutoff is imposed by the solar dipole when $R/r_e>1+2^{\frac{1}{2}}$, whereas all directions of arrival are allowed when $R/r_e<1$. Stated another way, particles of characteristic radius R can arrive from infinity only

[12] H. Alfvén, Phys. Rev. **72**, 88 (1947).
[13] Kane, Shanley, and Wheeler, Revs. Modern Phys. **21**, 51 (1949). This paper will hereafter be referred to as KSW.
[14] K. Dwight, Phys. Rev. **78**, 40 (1950).
[15] S. F. Singer, Nature **170**, 63 (1952).
[16] D. I. Dawton and H. Elliot, J. Atmos. Terr. Phys. **3**, 217 (1953).
[17] T. A. Bergstralh and C. A. Schroeder, Phys. Rev. **81**, 244 (1951).
[18] M. A. Pomerantz and G. W. McClure, Phys. Rev. **86**, 536 (1952).
[19] H. Alfvén, Phys. Rev. **77**, 375 (1950).

over the cone of angles between $x=0$ and $x=\bar{x}$, where

$$\cos\bar{x}=-2(R/r_e)+(R/r_e)^2. \quad (4)$$

Over this range of directions, particles arrive with full intensity. For $x>\bar{x}$, on the other hand, the solar field imposes a cutoff at the earth, and the intensity would drop to zero except for the fact that trapped orbits (orbits which lie within the inner allowed region) are to some extent filled by scattering at the earth, i.e., a particle approaching the earth along an unbounded orbit may suffer a deflection Δx such that its new value of γ is less than -1. In this case the particle finds itself in a trapped orbit, provided $R/r_e>1$. Conversely, trapped particles approaching the earth may be scattered into unbounded orbits and go off to infinity.

Trapped particles, whose rigidity and angular-momentum parameter lie within specified intervals, will wander about in more or less complicated orbits and in the course of time approach indefinitely close to every point in space consistent with the conservation equation (1). From Liouville's Theorem, it then follows that the intensity is constant throughout this volume of space. In general, the intensity I at any point in the trapping region will depend on R and x but not on azimuth about the directrix.

Consider the group of trapped particles whose characteristic radius and angular momentum parameter lie, respectively, in the specified intervals dR and $d\gamma$. The number of such particles per unit volume of space is given by

$$2\pi(I/v)d(\cos x)dR=2\pi(I/v)(2R/r\cos\lambda)d\gamma dR, \quad (5)$$

where v is the particle velocity and where we have used the equation

$$d(\cos x)=(2R/r\cos\lambda)d\gamma, \quad (6)$$

which follows from Eq. (1). The total number N of trapped particles of the given class is now obtained by integrating this expression over the total volume of the trapping region. The result is

$$N=4\pi(I/v)R^2dRd\gamma(2\pi)g(\gamma), \quad (7)$$

where

$$g(\gamma)=R^{-2}\int_{\text{bounded area}} r dr d\lambda.$$

The integral g represents the area in a meridian plane of the trapping region in units of R^2. One finds for the area the expression

$$g(\gamma)=-2-2\gamma\int_0^{\pi/2}[(\gamma^2+\cos^2\lambda)^{\frac{1}{2}}-(\gamma^2-\cos^2\lambda)^{\frac{1}{2}}]d\lambda/\cos^2\lambda. \quad (8)$$

This expression differs from the one given by KSW, and the resulting correction in their estimate of the mean lifetime of trapped particles turns out to be quite large. The integral has been evaluated numerically for several values of γ; results are given in Table I.

TABLE I. Values of $g(\gamma)$-area of trapping region in meridian plane, in units of R^2.

$-\gamma$	1.0	1.1	1.2	1.414	$\gg 1$
$g(\gamma)$	0.223	0.106	0.0667	0.0313	$4/35\gamma^4$

III. ABSORPTION CROSS SECTIONS

Absorption of trapped particles, of specified R and γ, will in general occur in collisions with the sun, the earth, and the moon, and also in collisions with Mars and Venus whenever the latter are accessible to particles of the given class. For the bodies which are assumed to have no magnetic field, the absorption cross sections simply correspond to the geometrical cross sections. For example, when Mars is accessible to particles for which R and γ lie in the specified intervals dR and $d\gamma$, losses will occur at the rate

$$(\pi a_M^2)2\pi I d(\cos x)dR=(\pi a_M^2)4\pi I(R/r_M)d\gamma dR, \quad (9)$$

where a_M is the radius of Mars and r_M is the radius of its orbit. Thus Mars, when it can absorb earth-accessible particles, has the same effect as a fictitious planet located in the earth's orbit with a cross section

$$(r_e/r_M)\pi a_M^2=2.42\times10^{17}\text{ cm}^2. \quad (10)$$

In the same way, we define for Venus the effective cross section

$$(r_e/r_V)\pi a_V^2=17.25\times10^{17}\text{ cm}^2. \quad (11)$$

The cross section for the moon is simply

$$\pi a^2_{\text{Moon}}=0.95\times10^{17}\text{ cm}^2. \quad (12)$$

The conditions under which Mars and Venus can be reached by earth-accessible particles are discussed by KSW. It turns out that Venus can bring its large cross section to bear only for a small fraction of the particles of interest to us here.

As for the earth, it cannot absorb with its full geometrical cross section particles of rigidity less than 60 Bev. Because of the earth's own dipole field, the allowed cone of arrival at a given latitude on the earth's surface fills a solid angle which depends on the rigidity and the latitude and which is in general less than 2π. The absorption cross section thus depends on the rigidity, and it can be represented by the expression

$$(\pi a_e^2)F, \quad (13)$$

where F is an *accessibility factor* which has been computed by KSW. It rises from the value zero (for zero rigidity) to the value one (for rigidity=60 Bev).

This brief discussion of the absorption by the planets has been given for the sake of completeness. As it turns out—and this represents an important correction in the results of KSW—the main absorber of trapped

particles is the sun. Its effective cross section depends on the magnetic rigidity, but it is always many times larger than the sum of the planetary cross sections. In subsequent calculations, therefore, we neglect the absorption of trapped particles by the planets.

The capture rate at the sun of particles for which γ and R lie within the specified intervals $d\gamma$ and dR is given by

$$\int \text{flux}\cdot\text{direction cos}\cdot d(\text{surface}) = 2\pi a_s^2 I d\gamma dR \times \int_0^\pi \sin\phi d\phi \int_0^\pi \sin x d(\cos x) d(\sin\lambda)/d\gamma, \quad (14)$$

where a_s is the sun's radius and ϕ is the azimuthal angle about the directrix (direction cos$=\sin x \sin\phi$). For the case of interest, here, where $a_s \ll R$ and $\gamma \lesssim -1$, one finds, from Eq. (1),

$$d(\sin\lambda)/d\gamma \simeq a_s/R. \quad (15)$$

The capture rate is therefore[19a]

$$4\pi(\pi a_s^2/2)(a_s/R) I d\gamma dR. \quad (16)$$

The equivalent cross section σ_s of a fictitious absorber located on the earth's orbit is obtained by equating the above expression with the expression

$$2\pi\sigma_s I d(\cos x) dR = 2\pi\sigma_s (2R/r_e) I d\gamma dR. \quad (17)$$

This leads to the result

$$\sigma_s = (\pi a_s^2/2)(a_s/r_e)(r_e/R)^2 = 3.54\times 10^{19}\times (r_e/R)^2 \text{ cm}^2. \quad (18)$$

IV. TIME OF CIRCULATION OF TRAPPED PARTICLES

Particles are lost from the trapping region both by absorption (mainly at the sun) and by scattering (at the earth) into unbounded orbits. Any discussion of the average time which a particle spends in the trapping region must take into account both of these effects. Indeed, for any single case the lifetime inside the trapping region can only be found by a detailed computation of the individual orbit. A simpler approach, which leads to an estimate of the average behavior for particles of a given class (specified R and γ), consists in the following.

Suppose that the trapped orbits are filled to their equilibrium intensity and that the scattering into the trapping region suddenly ceases (i.e., assume that the intensity of particles approaching the earth from infinity suddenly vanishes). A measure of the mean lifetime T is then given by the expression

$$T = -N/(dN/dt), \quad (19)$$

where N is the number of particles of the given class in the trapping region [Eq. (7)] and $-dN/dt$ is the rate of loss of these particles due to absorption and outscattering.

Assume for the moment that scattering at the earth is negligible, so that losses occur only by absorption. The rate of loss is given by

$$-dN/dt = 2\pi\sigma(2R/r_e) I d\gamma dR, \quad (20)$$

where σ is the sum of the absorption cross sections. From Eqs. (7), (19), and (20) we then find for the lifetime due to absorption only

$$T_{\text{abs}} = 2\pi(r_e/c)R^2 g(\gamma)/\sigma. \quad (21)$$

The absorption lifetime depends on the parameters R and γ; i.e., it depends on the magnetic rigidity and the angle x which the particles make with respect to the directrix at the earth [x is uniquely specified by R and γ accordinging to Eq. (1)]. Values of the absorption lifetime are given in Table II for several choices of x and R.

TABLE II. Absorption mean lifetime, in units of 100 years, for various values of the characteristic radius R and angle of inclination x at the earth's orbit.

cos$x$ \ R/r_e	2.414	2.000	1.000
1.0	47.2	...	...
0.0	13.6	22.2	...
−1.0	6.62	5.24	1.39

When the effect of scattering is taken into account, the definition of lifetime according to Eq. (19) becomes ambiguous. In each passage near the earth, a given particle may be scattered into an unbounded orbit, or it may be scattered back into the trapping region. The out-scattering cross section depends on the parameters R and γ. If a particle is scattered back into the trapping region, its value of γ will in general be changed, so that in each successive passage near the earth the probability of outscattering is changed. Any attempt to follow the course of these successive scatterings would be equivalent to the prohibitive task of computing individual orbits. An additional difficulty is that the scattering cross section diverges for small angles of scatter. Thus, the out-scattering cross section diverges for those particles which require only a small deflection to go into unbounded orbits (these are the particles for which $\gamma \approx -1$). For such particles, the mean lifetime, as defined by Eq. (19), becomes very small; but the quasi-ergodic hypothesis, and the treatment of the earth's field as a point scattering center, are approximations which are then no longer valid.

Despite these difficulties, it is relatively easy to set a lower limit to the out-scattering cross section for par-

[19a] An extra factor of one-half has been inserted into expression (16) in order to take into account, in an approximate manner, the effect of the sun's shadow in reducing the opening of the allowed cone at the sun. This estimate is based on curves given in the following references: T. H. Johnson, Revs. Modern Phys. **10**, 193 (1938); R. A. Alpher, J. Geophys. Research **55**, 437 (1950). See also Fig. 5 of reference 13.

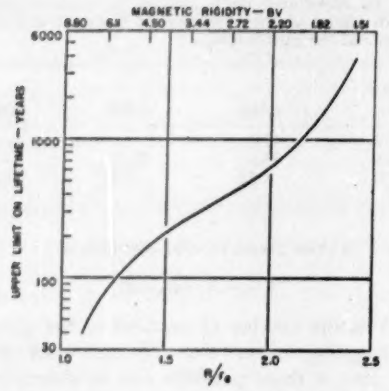

FIG. 1. Upper limit on lifetime in trapped orbits as a function of magnetic rigidity.

ticles of given magnetic rigidity and thereby obtain an *upper* limit on the lifetime as defined by Eq. (19). According to KSW, the differential cross section for scattering through an angle θ can be approximated by the expression

$$d\sigma_{sc}/d\Omega = (\pi/32)(eM_e/cp)[(\sin\tfrac{1}{2}\theta)^{-3}+2] - (1/4\pi)\pi a_e^2 F, \quad (22)$$

where M_e is the earth's dipole moment and F is the accessibility factor defined in connection with Eq. (13). For the cases of interest to us, the second term is small compared to the first, and it will be neglected in subsequent calculations. Suppose now that a trapped particle approaches the earth at an angle x_0 with respect to the directrix and suppose that its direction of motion after the scattering is specified by the angles x and ϕ, where ϕ is the azimuthal angle about the directrix, relative to the azimuth before scattering. The angle of scattering θ can be expressed in terms of x_0, x, and ϕ. The total out-scattering cross section is then given by

$$\sigma_{sc}(x_0,R) = \int (d\sigma_{sc}/d\Omega)d\phi \sin x dx, \quad (23)$$

where the integration is carried out over all values of ϕ and over values of x between $x=0$ and $x=\bar{x}(R)$ [see Eq. (4)]. This is the range of x for which particles of characteristic radius R are unbounded.

Because of the term $(\sin\frac{1}{2}\theta)^{-3}$ which appears in Eq. (22), it is clear that σ_{sc} takes on its minimum value when $x_0=\pi$. Our procedure for setting an upper limit on the lifetime consists then in the following. Equation (21) is modified by including σ_{sc} in addition to σ (absorption) in the denominator. The scattering cross section depends on x_0 and R, or, alternatively, on γ and R. Since in fact γ varies in successive approaches to the earth, we obtain an upper limit on the lifetime, for any choice of R, by choosing that value of γ which maximizes T. The term $g(\gamma)$ in Eq. (21) favors small values of $|\gamma|$, whereas σ_{sc} favors large values ($|\gamma|$ has its largest value when $x_0=\pi$, which, as we have seen, minimizes σ_{sc}). Since the evlauation of σ_{sc} is simple only in the special case $x_0=\pi$, we obtain an upper limit on T, which is larger than could be obtained by the maximization procedure, by simply assigning to g its maximum possible value 0.223 and to σ_{sc} its minimum value (which corresponds to $x_0=\pi$).

For the case $x_0=\pi$ we have

$$\sin\tfrac{1}{2}\theta = [(1+\cos x)/2]^{\frac{1}{2}}. \quad (24)$$

From Eqs. (22) and (23)—neglecting the second term on the right-hand side of Eq. (22)—we then obtain the result

$$\sigma_{sc}(x_0=\pi;R) = 4\pi(\pi/32)(eM_e/cp) \times[2\sqrt{2}(1+\cos\bar{x})^{-\frac{1}{2}}-(1+\cos\bar{x})], \quad (25)$$

where $\cos\bar{x}$ is related to R by Eq. (4).

The upper limit on the lifetime is plotted as a function of R/r_e in Fig. 1. It is seen to depend fairly strongly on the magnetic rigidity, but in all cases the upper limit on T is smaller than the figure 5000 years given by KSW as representing the order of magnitude of the lifetime for a typical case. Indeed, taking into account the fact that the present calculations provide only an upper limit, it seems more reasonable to take the lifetime for a typical case to be of the order of a few hundred years. Our neglect of losses due to collisions with interplanetary dust thus becomes even more easily justifiable than it was in the calculations of KSW.

V. EQUILIBRIUM INTENSITIES OF TRAPPED PARTICLES

Under equilibrium conditions, the intensities of trapped particles are determined by the competition between absorption and scattering. The appropriate mathematical technique for handling this problem has been given by KSW. In general, the intensity I depends on the magnetic rigidity and the angle of inclination x at the earth's orbit, but it is independent of the azimuthal angle about the earth's directrix. When $x<\bar{x}$ [see Eq. (4)], the intensity has the standard value I_0 associated with particles of the given rigidity at great distances from the solar system. For inclinations between $\bar{x}$ and π, on the other hand, the intensity has a lower value, which it is now our purpose to determine.

Consider the particles of a given magnetic rigidity. When the losses from a fixed solid angle element $d\Omega_1$, at $x=x_1$, balance the gains from all other solid angle elements $d\Omega_2$, then the intensity $I(x)$ at the earth's orbit satisfies the integral equation

$$\int_2 d\Omega_2 I(x_2)(d\sigma_{sc}/d\Omega)_{21} = I(x_1)\left[\sigma+\int_2 d\Omega_2(d\sigma_{sc}/d\Omega)_{12}\right], \quad (26)$$

for x_1 between $\bar{x}$ and π. Insofar as we shall consider

absorption only by the sun, $\sigma=\sigma_s$ is independent of x, as can be seen from Eq. (18). The cross section for scattering from direction 2 to direction 1, $(d\sigma_{sc}/d\Omega)_{21}$, is of course equal to the cross section for scattering in the reverse direction.

The integral equation is transformed to a more convenient form by expanding I into a series of Legendre polynomials:

$$I(x)=\sum C_L P_L(\cos x). \tag{27}$$

From the law of addition of associated Legendre functions, KSW shows that the integral equation now reduces to the equation

$$\sum S_L C_L P_L(\cos x)+\sigma \sum C_L P_L(\cos x)=0 \tag{28}$$

for $x>\bar{x}$. The scattering coefficient S_L is defined by

$$S_L=2\pi\int_0^\pi [1-P_L(\cos\theta)](d\sigma_{sc}/d\Omega)\sin\theta d\theta. \tag{29}$$

Neglecting the second term on the right-hand side of Eq. (22), we find for the scattering coefficients

$$S_L=\begin{cases}0, & L=0\\ (2L+1)(\pi^2/4)(eM_s/cp), & L>0.\end{cases} \tag{29'}$$

Equation (28) is of course supplemented by the equation

$$\sum C_L P_L(\cos x)=I_0 \tag{30}$$

for $x<\bar{x}$.

Consider now the quantity

$$J=2\sum S_L C_L^2/(2L+1)+\sigma\int_{\bar{x}}^\pi I^2(x)\sin x dx. \tag{31}$$

Suppose that I is given the variation $\delta I(x)$ for $x>\bar{x}$, whereas $\delta I(x)=0$ for $x<\bar{x}$. This will produce the variation

$$\delta J=2\int_{\bar{x}}^\pi [\sum S_L C_L P_L(\cos x)+\sigma I(x)]\delta I(x)\sin x dx. \tag{32}$$

We have made use here of the equation

$$\delta C_L=\tfrac{1}{2}(2L+1)\int_{\bar{x}}^\pi P_L(\cos x)\delta I(x)\sin x dx. \tag{33}$$

By virtue of Eq. (28), the expression in brackets in Eq. (32) vanishes for the true solution $I(x)$, i.e., J takes on a stationary value for the true solution. Thus, by representing $I(x)$ as an empirical function with a certain number of adjustable parameters and adjusting the parameters to give J a stationary value, we obtain the best approximation to the exact solution which is attainable with a function of the given form.

An additional result which proves to be useful is the following. Multiplying through by $I(x)$ in Eq. (28), integrating over x from $\bar{x}$ to π, and making use of the equation

$$2C_L/(2L+1)=\int_{\bar{x}}^\pi I P_L\sin x dx+I_0\int_0^{\bar{x}} P_L\sin x dx, \tag{34}$$

we find that

$$\sigma I_0\int_{\bar{x}}^\pi I\sin x dx = 2\sum S_L C_L^2/(2L+1)+\sigma\int_{\bar{x}}^\pi I^2\sin x dx. \tag{35}$$

The right-hand side is just the quantity J, which takes on a stationary value.

For the trial function we adopt the expression, used by KSW,

$$I/I_0=\begin{cases}1-K_2(y-\bar{y})^2-K_3(y-\bar{y})^3, & y<\bar{y}\\ 1, & y>\bar{y},\end{cases} \tag{36}$$

where $\bar{y}=\cos\bar{x}$, $y=\cos x$. The magnetic rigidity determines the value of $\bar{y}$, in accordance with Eq. (4). Solutions were obtained for the four cases: $\bar{y}=0.9$, 0.5, 0.0, -0.5. The requirement that J be stationary with respect to variations in K_2 and K_3 leads to the best choice of these parameters for each case. For $\bar{y}=0.9$, the Legendre coefficients C_L higher than the third were negligible. With decreasing $\bar{y}$, however, it is necessary to include additional coefficients in evaluating J. Thus, for $\bar{y}=-0.5$ it was necessary to evaluate twelve terms to obtain sufficiently accurate results. The adequacy of the solutions was tested by means of Eq. (35), which holds only for the exact solution. In every case the two sides of Eq. (35) agreed to within three significant figures for the adjusted trial solution.

The calculated intensity given by Eq. (36) reaches a minimum value for some negative value of $\cos x$ and then rises again as $\cos x$ further decreases to -1. This latter behavior is anomalous, since the intensity is expected to decrease continuously as $\cos x$ decreases. The situation would presumably be improved by using more adjustable parameters in the trial solution. In any case, we arbitrarily cut off the rise in $I(x)$ beyond the minimum (dotted lines in Fig. 2). The results of the computations are shown in Fig. 2, where the intensity in the trapped orbits is plotted against $\cos x$ for four different magnetic rigidities. The value 6.5×10^{25} gauss-cm^3 was taken for the solar dipole moment. The best choices of the parameters K_2 and K_3 are given in Table III.

One additional point requires mentioning. It is obvious on physical grounds that, as $\cos\bar{x}$ approaches very

TABLE III. Values of the parameters K_2 and K_3.

$\cos\bar{x}$	K_2	K_3
0.9	0.239	0.109
0.5	0.328	0.186
0.0	0.712	0.601
−0.5	3.20	5.40

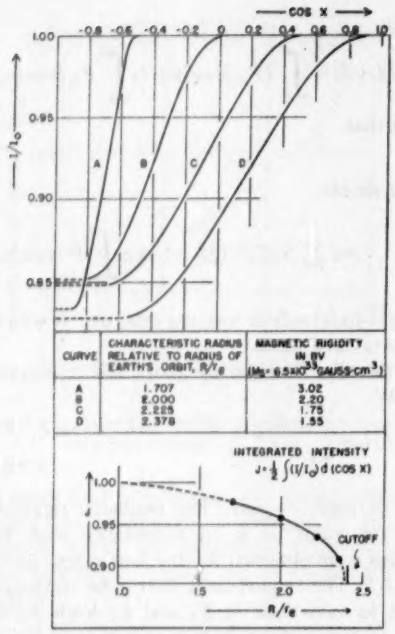

FIG. 2. Intensity of trapped particles at the earth's orbit, relative to the standard intensity at infinity, as a function of the angle of inclination with respect to the earth's directrix. The lower diagram gives the omnidirectional flux at the earth's orbit, relative to the standard value at infinity, as a function of magnetic rigidity.

close to unity (i.e., as the magnetic rigidity approaches the absolute cut-off value imposed by the solar dipole), the intensity in the trapped orbits must approach zero. This sharp drop in intensity has not yet occurred, however, for $\cos\chi = 0.9$.

VI. DISCUSSION

Kane, Shanley, and Wheeler have computed the intensities in trapped orbits for two choices of the solar dipole moment: $M_s = 1.0\times10^{24}$ and 4.2×10^{25} gauss-cm³. One can interpolate from their curves to find the results appropriate to a dipole moment 6.5×10^{25} gauss-cm³. One finds that the intensities reported here are appreciably smaller. To this extent, calculations of the diurnal effect based on the results of KSW require modification. Dwight's work[14] was based on a cosmic-ray differential spectrum of the form $I_0 \approx (cp/e)^{-2.75}$. The exponent in this spectrum, over the latitude-sensitive range of magnetic rigidities, is now believed to be closer to -2.1,[20,21] so that, as pointed out by Singer,[15] Dwight's results lead to an over-estimate of the diurnal effect. According to the calculations of Singer,[15] which were based on the curves of KSW, the maximum variation in intensity over a diurnal cycle is ~2.5 percent for $\lambda = 56°$ and $M_s = 6.5\times10^{25}$ gauss-cm³. A similar estimate is given by Dawton and Elliot.[16] In the light of the present results, this figure must be revised upwards to perhaps 7 or 8 percent.

The recent measurements of Dawton and Elliot[16] (18 day-night balloon flights at $\lambda = 57°$) have failed to confirm the existence of a regular diurnal effect larger than 1.4 percent, although irregular variations of the order of 6 percent are frequently found. Other observers have likewise failed to detect a diurnal effect of the kind we are discussing here.[17,18] However, because of the large, irregular intensity variations in the low-energy part of the primary spectrum,[11,16,22] one cannot conclude with complete certainty that the experimental results are inconsistent with the 7 or 8 percent diurnal variation which would be expected on the basis of a solar dipole moment of 6.5×10^{25} gauss-cm³.

Nevertheless, it should be noted that for this value of the dipole moment a larger diurnal effect is predicted for latitudes somewhat above 56–57°, where the detailed experiments have to date not been carried out. The calculations indicate that at $\lambda = 60°$ the effect should be about 12 percent.[23] It should be possible to reach a definite experimental decision about an effect of this size.

In addition to the experimental difficulties connected with the large, irregular intensity variations, one might attempt to explain away the discrepancies between experiment and theory by supposing that the trapped orbits are filled to an even larger extent than reported here, by additional mechanisms which have not been considered in the present work. Some examples of possible such mechanisms have been mentioned briefly at the beginning of Sec. II.

To take one example, large increases in cosmic-ray intensity at the earth are occasionally observed at times of large solar flares.[24] The increases are most pronounced at the low-energy end of the cosmic-ray spectrum. It is clear from the magnitude of the effect and the close correlation with solar disturbances that cosmic radiation is being produced on or near the sun at these times. Many of the particles which are involved in this effect would certainly go into trapped orbits if the solar moment were as large as 6.5×10^{25} gauss-cm³.

These large increases in cosmic-ray intensity are of course infrequent (only four such events have been reported over a period of many years). However, it has recently been found that the smaller but more common solar flares are often accompanied by (small) cosmic-ray intensity increases.[25] It does not appear unreasonable then to suppose that production of low-energy cosmic radiation on or near the sun is sufficiently significant so that it would contribute appreciably to the filling of trapped orbits in a solar dipole field. This suggestion, however, meets with two difficulties. (1) It

[20] Winckler, Stix, Dwight, and Sabin, Phys. Rev. **79**, 656 (1950).
[21] J. A. Van Allen and S. F. Singer, Phys. Rev. **78**, 819 (1950).
[22] Simpson, Fonger, and Wilcox, Phys. Rev. **85**, 366 (1952).
[23] Firor, Jory, and Treiman, following paper [Phys. Rev. **93**, 551 (1954)].
[24] Forbush, Stinchcomb, and Schein, Phys. Rev. **79**, 501 (1950).
[25] J. Firor, Phys. Rev. (to be published).

would be expected that particles with rigidities below the solar-imposed cutoff would be involved. There is no obvious reason why such particles would not be able to reach the earth as easily as particles of slightly higher rigidity. If sufficiently abundant, they would destroy the latitude cutoff at the earth. The other mechanisms mentioned at the beginning of Sec. II also meet with this difficulty. (2) Certain characteristics of the cosmic-ray effects associated with solar flares point to the fact that the new particles approach the earth preferentially along the earth-sun line.[25] On the basis of this observation, an argument has been made that the solar dipole moment cannot be larger than about 5×10^{32} gauss-cm^3.[26]

[26] S. B. Treiman, Phys. Rev. (to be published).

VII. SUMMARY AND ACKNOWLEDGMENTS

The cosmic-ray evidence on the question of a possible solar dipole field can be briefly summarized as follows. The latitude cutoff at the earth, if interpreted in terms of a solar magnetic dipole, implies a dipole moment of 6.5×10^{32} gauss-cm^3; the apparent absence of a diurnal effect, although not yet conclusive, at least suggests an upper limit on the dipole moment which is somewhat smaller than the above value; the characteristics of the cosmic-ray intensity increases associated with solar flares imply a much smaller upper limit on the dipole moment.

It is a pleasure to thank Professor John A. Wheeler for many informative discussions.

PHYSICAL REVIEW VOLUME 93, NUMBER 3 FEBRUARY 1, 1954

Solar Magnetic Moment and Diurnal Variation in Cosmic-Ray Intensity*

J. Firor and F. Jory, *Institute for Nuclear Studies, University of Chicago, Chicago, Illinois*

AND

S. B. Treiman, *Palmer Physical Laboratory, Princeton University, Princeton, New Jersey*

(Received October 21, 1953)

The expected diurnal variation in cosmic-ray intensity at geomagnetic latitude 60° has been calculated assuming a solar magnetic dipole moment of 6.5×10^{32} gauss-cm^3. The calculation is based on new estimates of the intensity of cosmic radiation in the trapped orbits of the solar dipole field. The method of Dwight is followed, but with an important modification. The magnitude of the expected diurnal variation turns out to be about 12 percent.

I. INTRODUCTION

THE existence of a "knee" in the cosmic-ray latitude effect at high altitudes implies, as is well known, a cutoff in the primary spectrum of cosmic radiation incident on the earth. Recent measurements have clearly established the location of the knee at $\lambda=58°$.[1,2] In terms of magnetic rigidity, the corresponding cutoff is 1.5 Bv. As first pointed out by Janossy, this cutoff can most easily be understood if one assumes the existence of a solar magnetic dipole, which would deflect away from the earth particles of rigidity below the cutoff. If the knee at 58° is explained in this way, the solar dipole moment must have the value 6.5×10^{32} gauss-cm^3.

Although no other detailed explanation of the cutoff has been put forward, doubt has been cast on the existence of a solar moment of this magnitude. Direct measutements, based on the observation of Zeeman-splitting of solar spectrum lines, have in recent years set an upper limit on the dipole moment which is one order of magnitude smaller than the above value;[3] and the diurnal effect in cosmic-ray intensity at intermediate latitudes on the earth, which would be expected on the basis of a solar dipole moment of the above magnitude, has not been found experimentally.[4–6]

The apparent experimental absence of the diurnal effect, however, has not generally been considered as conclusive evidence against a solar dipole moment of 6.5×10^{32} gauss-cm^3. The theoretically expected effect for this dipole moment, according to the calculations of Singer[7] and of Dawton and Elliot,[6] is 2–3 percent at $\lambda=56°$, whereas the extensive experimental measurements of Dawton and Elliot set an upper limit of 1.4 percent for the diurnal variation. Because of the frequent occurrence of large (5–10 percent), irregular intensity variations,[2,6,8] which might well mask a

* Assisted by the Office of Scientific Research, Air Research and Development Command, U. S. Air Force.

[1] J. A. Van Allen and S. F. Singer, Nature **170**, 62 (1952).

[2] Neher, Peterson, and Stern, Phys. Rev. **90**, 655 (1953).

[3] For a summary, see H. Van Kluber, Monthly Notices Roy. Astron. Soc. **112**, 540 (1952).

[4] T. A. Bergstralh and C. A. Schroeder, Phys. Rev. **81**, 244 (1951).

[5] M. A. Pomerantz and G. W. McClure, Phys. Rev. **86**, 536 (1952).

[6] D. I. Dawton and H. Elliot, J. Atm. and Terrest. Phys. **3**, 217 (1953).

[7] S. F. Singer, Nature **170**, 63 (1952).

[8] Simpson, Fonger, and Wilcox, Phys. Rev. **85**, 366 (1952).

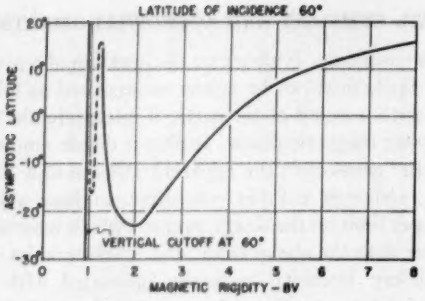

FIG. 1. Latitude of asymptotic velocity vector as a function of magnetic rigidity for particles which arrive vertically at the earth at magnetic latitude 60°.

small diurnal effect, the discrepancy between theory and experiment has not hitherto appeared to be serious. More recently, however, several important modifications have been introduced into the theory of the diurnal effect,[9] and it has been indicated that the magnitude of the effect at 56° should be more nearly 7–8 percent for the case of a solar dipole moment of 6.5×10^{33} gauss-cm^3. It seems unlikely that an effect of this size could have escaped detection.

In the present paper we present detailed results on the predicted diurnal effect at $\lambda=60°$ (see Fig. 3). At this latitude the effect is even larger than at 56°. The maximum intensity variation over a diurnal cycle is expected to be about 12 percent. A decision as to whether or not an effect of this magnitude exists can surely be made experimentally.

II. OUTLINE OF THE THEORY

The calculation of the diurnal effect due to a solar dipole field comes in two parts.

(1) The effect of the solar field is to establish a cone of directions ("allowed" cone) in which particles of given magnetic rigidity can arrive in the vicinity of the earth from infinity. The cosmic-ray intensity in the "forbidden" directions would be zero except for the fact that particles which approach the earth from allowed directions may be scattered by the earth's field into the forbidden directions. The intensity in the forbidden cone is thus determined by the competition between this scattering effect and the effect of absorption of the "trapped" particles in collisions with the sun, the earth, and other objects in the solar system. In calculations dealing with this process, the earth's field is treated as a point-like center which scatters particles from one to another of the static trajectories in the field of the solar dipole. The calculations lead to an estimate of the intensity in the forbidden directions, expressed as a function of magnetic rigidity and angle of inclination with respect to the earth's "directrix," a reference vector tangent to the earth's orbit.

[9] S. B. Treiman, preceding paper, Phys. Rev. **93**, 544 (1954).

(2) In the second part of the theory of the diurnal effect, one takes into account the details of the short-scale deflection in the field of the earth's dipole. The resulting pattern of forbidden cones at the earth has a fixed relation to the earth-sun line. The reduced intensity in the forbidden directions (relative to the full intensity in the allowed directions) gives rise to a diurnal effect at a fixed geographic location on the earth as the earth rotates on its axis.

A thorough discussion of part (1) of the theory was given by Kane, Shanley, and Wheeler.[10] They found that the intensity in the forbidden directions is appreciable in comparison with that in the allowed directions. The diurnal effect at the earth was therefore expected to be small. Recently, however, several corrections have been made in this part of the theory, and it has been found that the intensity in the forbidden directions is considerably smaller than indicated in the earlier results.[9]

An excellent discussion of part (2) of the theory is given by Dwight.[11] In his numerical work he proceeds from the results of Kane, Shanley, and Wheeler and assumes a cosmic-ray differential spectrum of the form $(cp/e)^{-2.75}$, where (cp/e) is the magnetic rigidity. The more recent calculations of Singer[7] and of Dawton and Elliot[6] are likewise based on the results of Kane, Shanley, and Wheeler; but a more realistic primary spectrum has been adopted and several improvements made in the approximations which are involved in the calculations.

In the present work we assume a primary spectrum of the form $(cp/e)^{-2.0}$, which is consistent with the results of a number of recent investigations,[12] and we proceed from the new results on the trapped-orbit

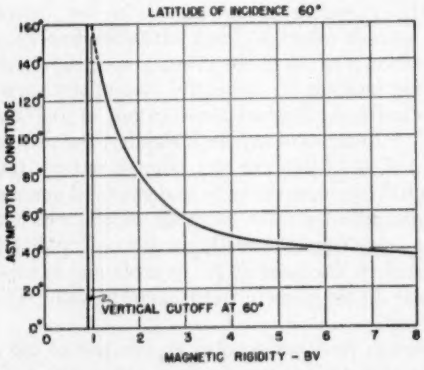

FIG. 2. Longitude of asymptotic velocity vector as a function of magnetic rigidity for particles which arrive vertically at the earth at magnetic latitude 60°.

[10] Kane, Shanley, and Wheeler, Revs. Modern Phys. **21**, 51 (1949).

[11] K. Dwight, Phys. Rev. **78**, 40 (1950).

[12] J. A. Van Allen and S. F. Singer, Phys. Rev. **78**, 819 (1950); Winckler, Stix, Dwight, and Sabin, Phys. Rev. **79**, 656 (1950); M. L. Vidale and M. Schein, Nuovo cimento **8**, 774 (1951); H. V. Neher, Phys. Rev. **83**, 649 (1951).

intensities.[9] We specifically assume a solar dipole moment of 6.5×10^{33} gauss-cm^3 and carry out the calculations for the diurnal effect of vertically-incident cosmic radiation at magnetic latitude 60°. It is assumed that the earth's dipole is perpendicular to the plane of the solar magnetic equator. The latitude 60° is believed to be near the optimum location for the diurnal effect because of a solar dipole moment of the above magnitude.

The procedure which is followed in the present work is similar to that which has been followed in previous calculations (in particular, see reference 11). We therefore omit all discussion of the details, except for several points wherein we have introduced modifications in the procedure.

The basic curves of the present calculations are shown in Figs. 1 and 2, which give respectively, the latitude and longitude of the "asymptotic velocity vector" as a function of magnetic rigidity for particles which arrive vertically at the earth at latitude 60°. (The definition of asymptotic velocity vector is given in reference 11.) These curves were constructed from data provided in the following sources: calculated trajectories given by Stoermer,[13] interpolation from the curves of Dwight,[11] and orbits obtained in the terrella experiments of Malmfors.[14]

The present calculations differ from earlier work in the following respects.

(1) As a matter of convenience, we imagine that the intensity in the allowed directions is zero and that the intensity in the forbidden directions is equal to the difference between the full intensity and actual intensity in these directions. In this way we calculate directly the *defect* in cosmic-ray intensity as a function of local time. This procedure somewhat simplifies the computations.

(2) In previous work, the dependence of trapped-particle intensity on the angle of inclination with respect to the earth's directrix has not been taken into account in detail. Instead, it has been the practice to assume that the trapped orbits are uniformly filled to an average intensity (averaged over the angle of inclination). We instead take into account this dependence on the angle of inclination as well as the dependence on magnetic rigidity (see Fig. 2 in reference 9). As it turns out, this refinement has a large effect on the final diurnal curve.

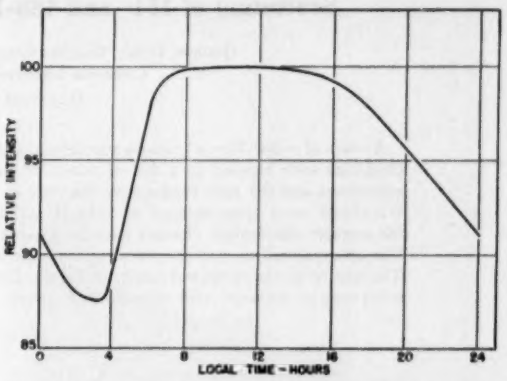

FIG. 3. Diurnal variation of vertically-incident cosmic-ray intensity at magnetic latitude 60°, a solar dipole moment of 6.5×10^{33} gauss-cm^3 being assumed.

III. SUMMARY AND ACKNOWLEDGMENTS

The final result of the calculations is shown in Fig. 3, where we plot the vertical cosmic-ray intensity at latitude 60° as a function of local solar time, on the assumption of a solar dipole moment of 6.5×10^{33} gauss-cm^3 and a primary differential spectrum of the form $(cp/e)^{-2.0}$. The magnitude of the variation in intensity over a diurnal cycle is about 12 percent, an effect which is considerably larger than previous calculations have indicated. This difference results in part from the recent improvements which have been made in the estimate of trapped-orbit intensities[9] and in part from the refinement which has been introduced in the present work and which has been discussed in the preceding paragraph.

We wish to express our thanks to Professor J. A. Simpson for his kind assistance and encouragement. One of us (SBT) wishes especially to thank Professor Simpson for the many courtesies extended to him during the course of an extended visit in the summer of 1953 at the Institute for Nuclear Studies, University of Chicago.

[13] C. Stoermer, Astrophys. Norv. **2**, 1 (1937).
[14] K. G. Malmfors, Arkiv Mat. Astron. Fysik **30A**, No. 12 (1944); **32A**, No. 8 (1945).

Scattering of 151- and 188-Mev Positive Pions by Protons*

GEORGE HOMA, GERSON GOLDHABER,† AND LEON M. LEDERMAN
Columbia University, New York, New York

(Received October 1, 1953)

A beam of ~200-Mev π^+ mesons was defined inside the vacuum chamber of the Nevis Cyclotron. Nuclear emulsions were exposed to a flux of about 10^4 mesons/cm². The plates were scanned for pion-hydrogen scatterings and 103 such events were observed in two interaction energies, 151±7 Mev and 188±8 Mev. We obtain total cross sections of 152±31 and 159±34×10^{-27} cm², respectively. The data suggest that the angular distribution changes from backwards peaked to almost symmetric over this energy interval. Our observations are not in agreement with the hypothesis of a $P_{\frac{3}{2}}$-wave resonance in this energy region. The best fit to the combined results includes a D-wave contribution of $-5.4°$, although satisfactory agreement may be obtained with only S and P waves.

I. INTRODUCTION

PION-NUCLEON scattering experiments[1–3] have demonstrated a very strong increase of cross section with meson energy. Studies have been carried out with positive pions up to 135 Mev and negative pions up to 220 Mev.[1] The fruitful partial wave analyses of the angular distributions in the three possible scattering processes: $\pi^-+p\rightarrow\pi^-+p$, $\pi^-+p\rightarrow\pi^0+n$, $\pi^++p\rightarrow\pi^++p$, have demonstrated a strong p-state interaction between pion and proton. The possibility that the coupling is strong enough to produce a resonance in the meson-nucleon interaction has recently been discussed.[4] The Chicago experiments do not extend far enough in energy to support this hypothesis.[5] This experiment was designed to yield some data on the π^+ hydrogen scattering in the region of the suspected resonance. Positive mesons in this energy region are not conveniently studied by the techniques which have recently been employed at Columbia and Chicago. These have made use of external meson beams. The focusing action of the cyclotron fringing field is effective only for negative mesons which are produced roughly in the forward direction, and positive mesons produced in the backward direction with respect to the proton beam. The velocity of the center of mass in the production process results in a large decrease in the yield of high-energy positive mesons. At Nevis, external π^- beams up to 160 Mev are obtained with good flux, whereas the highest usable π^+ beam reaches 85 Mev. In this experiment, use was made of the forward-produced positive mesons which are deflected into the cyclotron from the target. Photographic emulsions were used to detect these particles. The technique of using the hydrogen content of the emulsion as the scatterer had already been used with external beams[6] and was employed here.

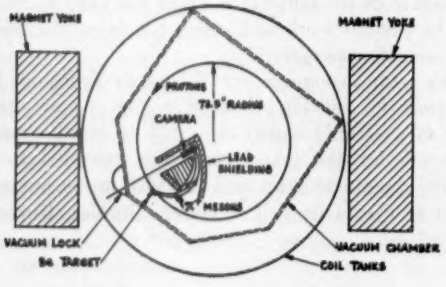

FIG. 1. Plan view of internal exposure.

II. EXPERIMENTAL PROCEDURE

Positive pions produced by the 385-Mev proton beam in a beryllium target are focused at 180° by the cyclotron magnet. In the energy region of interest, 150–200 Mev, the focusing point is about one-third the distance from the cyclotron center along a radius to the target (see Figs. 1 and 2). The dispersion in this region is about 6 Mev per inch of radial displacement. The problem was to obtain good exposures of Ilford G-5 emulsions to these high-energy mesons, with minimum

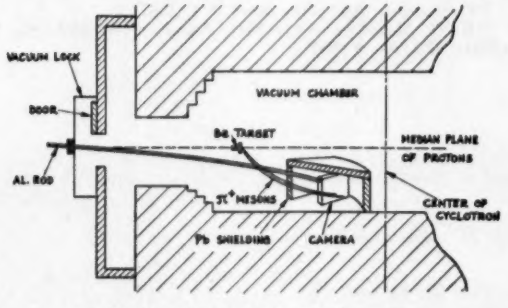

FIG. 2. Elevation view of internal exposure.

* This research was supported by the joint program of the U. S. Office of Naval Research and the U. S. Atomic Energy Commission.

† Now at the Physics Department, University of California, Berkeley, California.

[1] Anderson, Fermi, Martin, and Nagle, Phys. Rev. **91**, 155 (1953).

[2] Bodansky, Sachs, and Steinberger, Phys. Rev. **90**, 996 (1953).

[3] J. P. Perry and C. E. Angell, Phys. Rev. **91**, 1289 (1953).

[4] K. A. Brueckner, Phys. Rev. **86**, 106 (1952).

[5] Martin, Fermi, and Nagle [Phys. Rev. **91**, 467 (1953)] have recently reported results for 169- and 192-Mev π^- scattering.

[6] G. Goldhaber, Phys. Rev. **89**, 1187 (1953).

TABLE I. Typical energy evaluation from proton range calibration.

Proton Steps	R_p[a] μ	R_p(Cu)[b] g/cm²	T(Cu)[c] g/cm²	E_p[d] Mev	E_π[e] Mev
1	7700	3.06	0.64	52.1±1	205.7±3
2	5900	2.31	1.49	52.8±1	207.7±3
3	4700	1.83	1.92	52.5±1	206.8±3
4	3400	1.32	2.35	51.9±1	205.2±3
5	2400	0.935	2.78	52.2±1	206.0±3

Result: 206±1 Mev. Result from position in magnetic field: 208±3 Mev.
[a] Residual range of protons in emulsion, R_p (see Fig. 4).
[b] Equivalent range in Cu. R_p(Cu).
[c] Thickness of Cu absorber steps on camera cover T(Cu).
[d] Proton energy incident on camera E_p.
[e] Meson energy incident on camera (of same momentum) E_π. The mesons incident on the emulsions have to penetrate the camera cover 0.2 in. of Cu and their energy is thus reduced by ≈7 Mev.

background, and to scan these plates for π^+-H scattering events. The exposures were carried out in a vacuum-tight camera which was introduced into the cyclotron chamber through a vacuum lock at the end of a long rod. In this manner the emulsions were kept at normal pressure and humidity conditions during the exposure.

The camera, in its final position, rested upon the lower cyclotron pole face, the plane of the emulsions vertical and the long edge facing the meson beam. The camera was mounted in a 2-in. thick brass block which provided extra shielding and which adjusted the tilt of the emulsion so as to receive the beam perpendicular to the long edge. The assembly was pushed into a predetermined position within a mass of lead-shielding bricks which were strategically disposed on the magnet face. Two curved channels defined the meson trajectories; one at 165 Mev and one at 205 Mev. In spite of about 1 ton of lead shielding, it was discovered that to avoid blackening the plates the exposures had to be of the order of 3–5 seconds. After a particular shielding arrangement had been installed, it was found that continuous operation of the cyclotron for several hours would produce radioactivity in the lead bricks. This added serious background in the 10–20 minutes during which the camera was being pushed in and out of the vacuum chamber. Exposures were therefore carried out only after a shutdown of the cyclotron for several days and with a fresh "inner lining" of lead bricks. In this way, plates were obtained having track densities of $\sim 10^4$ mesons/cm² with acceptable background. Ilford G-5 600μ and 400μ plates were used.

III. ENERGY CALIBRATION

The scattering cross sections are known to vary greatly with energy of the meson. This made necessary a rather precise determination of the interaction energy. Three independent methods were employed to this end.

(1) The location of the emulsions relative to the proton target in the magnetic field of the cyclotron was used to compute the momentum of the particles incident upon the camera. The exposures resulted in a quite parallel flux of particles in the proper direction. Thus no important contribution could be made by mesons either scattering in the collimator or originating outside of the target. The average value of the cyclotron field over the trajectory was 17 300 gauss. Particles traversing the higher-energy channel had a maximum momentum of 318 Mev/c. This corresponds to a pion kinetic energy of 208 Mev. Ten plates were exposed simultaneously across the 2.5-in. channel breadth. The energy interval over the high-energy channel was 2.5 in. ×6 Mev/inch = 15 Mev. Similarly, the low-energy channel was centered about 165 Mev.

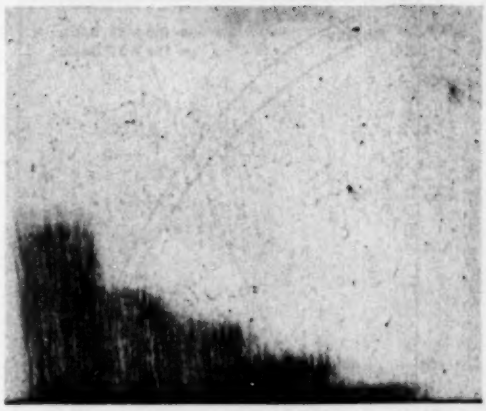

FIG. 3. Proton range curve in nuclear emulsion exposed to 318-Mev/c particles. The longest step is actually 8 mm in length. The steps correspond to increasing thicknesses of brass absorber.

(2) The selected momentum of 318 Mev/c corresponds to a proton energy of 52 Mev. Protons of this energy are made far more copiously than the mesons and had to be prevented from reaching the emulsion. A 0.20-in. brass cover plate was used to stop the protons. A series of five grooves were milled in the lower half-inch of the cover plate in order to obtain a range curve of the incident protons. Where the grooves were deep enough, the heavily ionizing protons were able to reach and blacken the emulsion. Correspondingly, each nuclear track plate then had a series of steps indicating the residual range of the protons incident upon it. This range was converted to proton momentum incident upon the cover plate. The energy of the pions was obtained by assuming them to have the same momentum as the protons. Figure 3 is an enlargement of a nuclear emulsion exposed to 318±5 Mev/c particles. The parallelism and monochromaticity of the protons is additional evidence in favor of the validity of the geometry. Table I presents an analysis of the proton range curve in a typical plate. The results obtained by this method are in excellent agreement with the energy as determined from position in the magnetic field.

The incident meson energy is reduced by its ionization loss in the 0.20-in. brass cover plate and by one-half the loss in traversing the emulsion (average lengths

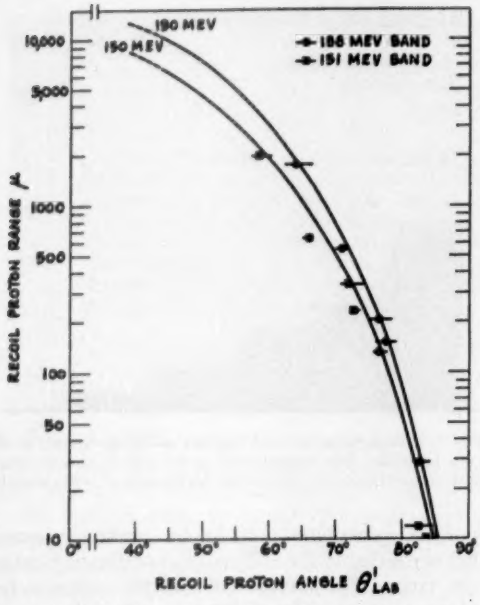

FIG. 4. Range-angle correlation for recoil protons in $\pi+p$ collisions.

were 4000μ). The resulting interaction energies were 151±7 Mev for the low-energy exposure, 188±8 Mev for the high-energy exposure.

(3) In the π^+ hydrogen collisions, it occasionally happened that the recoil proton stopped in the emulsion. This was used to recalculate the meson energy. The results are given in Fig. 4 where the observed cases are plotted on a curve of proton range *vs* proton recoil angle.

The proton recoil angles plotted are the "best fit" values of the experimental θ and φ measurements to the angular correlation curve (Fig. 6), where θ and φ are the proton recoil and meson scattering angles, respectively. The extremities of the angular uncertainty shown in Fig. 4 correspond to the measured values of θ and φ. As can be seen from the curves, the energy determinations are extremely sensitive to errors in proton recoil angle. The present method can only be considered as a confirmation of the previously described techniques.

IV. SCANNING PROCEDURE

The presence of a comparatively large background of proton tracks ruled out the possibility of employing area scanning with any assurance of good scanning efficiency. Instead, the far more laborious method of track scanning was adopted. In this technique, the scanner selects a track satisfying ionization and directional criteria and follows it under 10×45 (oil) or 10×90 (oil) magnification until it either leaves the plate or interacts. Essentially 100 percent efficiency for the detection of all types of events should be obtained with this method. All scatterings through angles greater than 1° were recorded. Figure 5 gives the frequency per meter of track in projected angle intervals less than 30°. These results were used to obtain good statistics on relative efficiency among the various scanners. To the extent that nuclear effects are small below 15°, this also constitutes a comparison with a known (Rutherford) cross section and an order of magnitude check on the over-all scanning efficiency. The agreement with Coulomb scattering begins above 7°. However, hydrogen collisions are associated with heavily ionizing recoil proton tracks and are much more prominent than small angle elastic scatterings.

The observed events were categorized as stops in flight, elastic scatterings, one-prong ("inelastic") scatterings, one-prong stars and stars of two to nine prongs. The one-prong events were all considered as possible hydrogen events and subjected to the detailed measurements described below. An additional measure of relative efficiency compared the ratio of all types of meson interactions resulting in one black prong to observed path length and to the number of stars with two or more prongs. These comparisons, together with the elastic scattering data, led to the conclusion that the track scanning, especially on plates of high background, were not necessarily 100 percent efficient. We

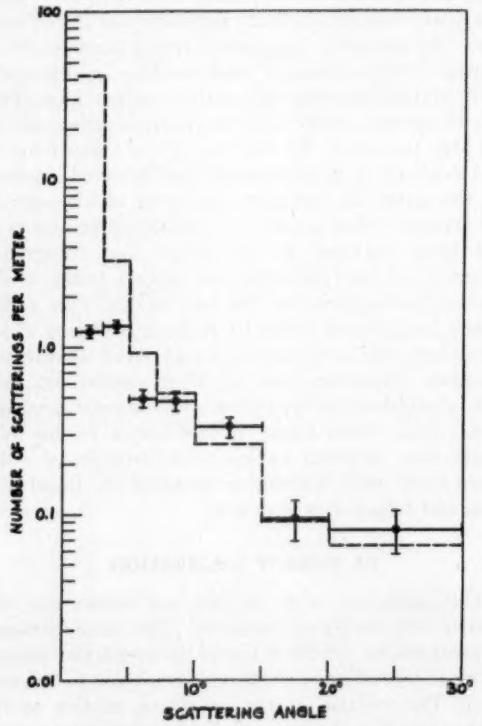

FIG. 5. Elastic scatterings of high-energy pions in nuclear emulsion. Projected angles of scattering are given. The dashed curve is the projected angular distribution due to Rutherford scattering averaged over the emulsion contents.

estimated that an over-all variation of 12 percent existed in the efficiency for finding one-prong events. Since this is always a negative effect, a correction of half this amount was made to the data and the uncertainty in the scanning efficiency was taken as ±10 percent.

V. THE IDENTIFICATION OF π^++H SCATTERING EVENTS

Because of energy and momentum conservation in the π^++H scattering interaction, such events can be identified on the basis of the two criteria:

1. Coplanarity of the three prongs π, π', and p.
2. Angular correlation between the scattered meson (π') and the recoil proton (p).

An additional confirmation is obtained from the range-angle correlation for those recoil protons which end in the emulsions (Fig. 4). All events with one proton prong found in the course of the scanning were carefully examined for possible associated scattered mesons. These events with one proton and a scattered meson were measured. Measurements were made of the two projected angles (in the plane of the emulsion) $\alpha_{\pi'}$ and α_p, the three dip angles β_π, $\beta_{\pi'}$, and β_p, and the range of the recoil proton R_p.

The details of the analysis are presented in Figs. 6, 7, and 8 for those events found in 173 meters of track scanning. The quantity $F=\tan\beta_{\pi'}\sin\alpha_p-\tan\beta_p\sin\alpha_{\pi'}-\tan\beta_\pi\sin(\alpha_{\pi'}-\alpha_p)$ is proportional to the volume of a pyramid formed by the center of the event and 3 points unit distance along each of the 3 vectors π, π', and p. F was computed for all events as a measure of the coplanarity where $F\to 0$ corresponds to coplanarity. Figures 6 and 7 give the angular correlation curves between meson scattering angle φ_{lab} and proton recoil angle θ_{lab} which follow from the kinematics of $\pi-P$ scattering. All events with $F/\Delta F\leq 2.5$ are called "coplanar" and are given in Fig. 6, where ΔF is the rms error in F based on the various individual measuring errors. All other events are called "noncoplanar" and for clarity are given separately in Fig. 7. In Fig. 8 we plot[7] $F/\Delta F$ *vs* $\Theta/\Delta\Theta$ where $\Theta=(\delta\theta^2+\delta\varphi^2)^{\frac{1}{2}}$ is the deviation from the angular correlation curve (Figs. 6 and 7) and $\Delta\Theta$ is again the rms error due to measurements.

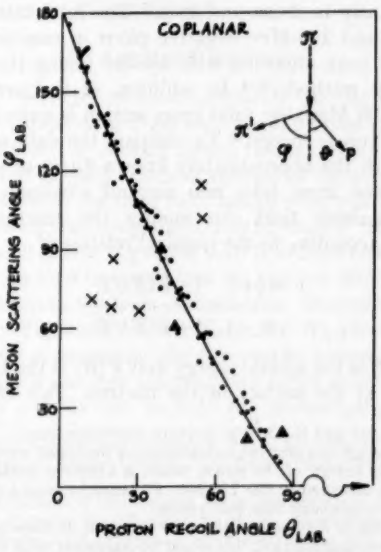

FIG. 6. Angular correlation relating the meson scattering angle and the proton recoil angle. The triangles represent "doubtful" cases. The crosses represent events which satisfied coplanarity requirements but are excluded because of lack of correlation. The dots represent π-p collisions.

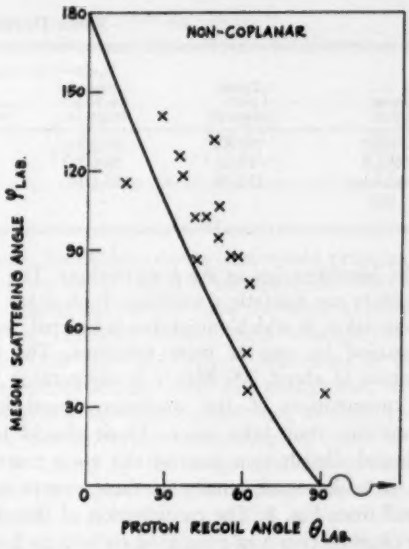

FIG. 7. Distribution of noncoplanar events about the angular correlation curve. Events having a proton emitted backwards are not included.

Of the 104 events on Fig. 8, 75 events lie in the circle of radius 1.75 in units of the rms measuring errors, 4 events lie between the radii 1.75, and 2.5 and 25 events lie outside the radius 2.5. These events are classified as "sure" $\pi+p$ events, "doubtful" $\pi+p$ events and "not" $\pi+p$ events, respectively, and are represented by different symbols in Figs. 6, 7, and 8.

An additional check on the identification of hydrogen scatterings was made by grain-counting all scattered mesons of sufficient length ($>400\mu$). The ratio of grain densities of the incident and scattered meson is related to the angle of scattering. At these energies, this is not a sensitive test unless the tracks are very long. One event, satisfying all other criteria, was discarded by this test. All other measurable cases were consistent

[7] Figures 6, 7, and 8 do not include events in which the proton goes in the backward direction ($\alpha_p>90°$) or events in which the projection on the plane of the emulsion of π' and p are both on the same side of π (i.e., the signs of $\alpha_{\pi'}$ and α_p are equal). Such events can be excluded on visual inspection from being possible $\pi-p$ scattering events.

TABLE II. Evaluation of total cross section.

Energy Mev	Total path (meters)	Path corrected for 10± 10% $\mu+e$	No. of nuclear interactions	Path obtained from $\lambda=31.7$ cm	No. of $\pi+p$ obs. events	No. of events corrected	Cross section $\times10^{-27}$ cm^2
151±7	95.34	85±8.5	260	82.5±9.0	41	43	152±31
188±8	77.44	70±7.0	225	71.0±8.0	34	38	159±34
Combined 168	172.78	155±16	485	153.5±17	75	81	155±24

with the identification as $\pi+p$ scatterings. The "not" $\pi+p$ events are inelastic scatterings from other nuclei in the emulsion, in which one proton is emitted, possibly accompanied by one or more neutrons. The meson momentum of about 300 Mev/c is comparable to the Fermi momentum of the nucleons. Quasi-elastic[8,9] collisions can thus take place. These should have a very broad distribution around the $\pi+p$ correlation curve. A background density of these events may be obtained from Fig. 8. The contribution of this density to the cross section was computed to be 1 to 2 events. It is interesting to note that in previous work[6] at $E_\pi=75$ Mev ($P_\pi=165$ Mev/c, which would give an even broader distribution) no evidence was seen for quasi-elastic scattering. (At that energy the π^+-p cross section is also considerably smaller.) Similarly, with negative pions at $E_\pi=135$ Mev,[10] no evidence for quasi-elastic scattering was seen in emulsions. Here again the π^-+p cross section is much smaller and presumably π^-+"N" quasi-elastic scattering occurs.

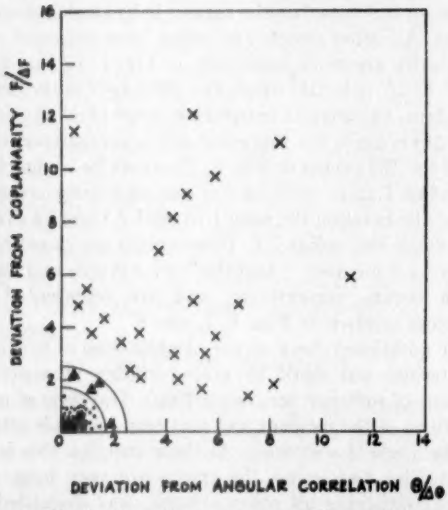

FIG. 8. Distribution of one-prong events in correlation space. The dots represent "sure" hydrogen collisions. The triangles represent doubtful cases. The crosses represent background. Only events which were observed in the 173 meters of track scanning are included here.

[8] Cladis, Hess, and Moyer, Phys. Rev. **87**, 425 (1952).
[9] P. A. Wolff, Phys. Rev. **87**, 434 (1952).
[10] G. Goldhaber and S. Goldhaber, Phys. Rev. **91**, 467 (1953).

VI. ANALYSIS OF DATA

A. Total Cross Sections

A total of 173 meters of track was recorded for the determination of the total cross sections. We have observed 535 nuclear interactions of all kinds, including 75 which were classified as certain hydrogen events. See Table II.

External meson beams are known to contain contaminations of muons and electrons. The electrons are very probably made in the cyclotron target by conversion of π^0 γ rays. The insensitivity of the mu "tail" in range curves to geometry[11] is evidence that most of the muons originate near the target. Thus it seems reasonable to assume that similar contaminations are present in internal fluxes.[12] Using the data on mu and electron contaminations in the external π^- (forward-produced) beams we have estimated that the internal flux is 90±10 percent pions.

An independent evaluation of the pion flux is made by considering the total reaction cross section (stars, stops, inelastic scattering) observed in these plates and recalling that muons and electrons do not contribute significantly to these processes.[13] The total interaction of 135- and 210-Mev negative pions in emulsions has recently been observed with similar (along the track) scanning methods.[10,14] In addition, it is known that above 100 Mev, the total cross section is quite insensitive to meson energy.[15] To compare the data obtained here with the approximately known fluxes of negative pions, one must take into account Coulomb effects. The Coulomb field can modify the reaction cross section according to the classical relation:[16]

$$\frac{\sigma(+)}{\sigma(-)}=\frac{1-V(R)/E}{1+V(R)/E},$$

where E is the kinetic energy and $V(R)$ is the Coulomb barrier at the surface of the nucleus. This effect has

[11] H. Loar and R. Durbin (private communication).
[12] Although the electron contamination decreases strongly with increasing energy of the meson beam, a 4-percent contamination has been observed in the 135-Mev π^- beam by means of a cloud chamber containing thin lead plates.
[13] A total of 8 stops in flight were observed. If these are all due to positron annihilation, this would be consistent with a 3 percent contamination.
[14] A. H. Morrish, Phys. Rev. **90**, 674 (1953).
[15] R. L. Martin, Phys. Rev. **87**, 1052 (1952); Chedester, Isaacs, Sachs, and Steinberger, Phys. Rev. **81**, 918 (1951).
[16] J. M. Blatt and V. F. Weisskopf, *Theoretical Nuclear Physics* (John Wiley and Sons, Inc., New York, 1952), p. 346.

TABLE III. Differential cross sections of π^+ mesons on protons (10^{-27} cm²/sterad).[a]

Lab. energy Mev	Cm. Angular interval 8–30°	30–60°	60–90°	90–120°	120–150°	150–180°
151±7	10.3±4.2	8.3±2.3	8.7±2.5	6.1±1.6	20 ±3.2	39±8
188±8	21.5±6.5	9.0±2.6	9.8±2.2	12 ±2.7	14.8±3.5	24±7
168±30	15.2±3.5	8.5±1.6	9.1±2.0	8.6±1.4	17.6±2.2	32±5.1

[a] The errors shown are probable errors arising from statistics only.

been observed in a direct comparison of π^+ and π^- meson reactions at 60 Mev and at 110 Mev.[17] For emulsions at 170 Mev this is a 10-percent effect. Accordingly, the mean free path for all nonelastic processes of references 10 and 13 was increased by 10 percent. This gave a result of 31.7±3.3 cm of emulsion. The total number of nuclear events observed in this experiment included 75 hydrogen scatterings, whereas the hydrogen contribution to the π^- experiments was only of the order of $\frac{1}{3}$ as much.[1] Thus we used 485 events (Table II) to make the comparison.[18] The flux obtained by this method is then 485×0.317=153.5 meters. This is in (fortuitously) excellent agreement with the estimate of 10-percent beam contamination. Table II contains a breakdown in the two energy intervals. The corrections to the observed number of hydrogen events include a subtraction due to background (Sec. V, 2 events), and an addition (6 events) due to scanning efficiency (Sec. IV). In the evaluation of the error, we have included the statistical standard deviation, and the contributions to possible systematic errors from the flux, scanning efficiency, doubtful and background events, and the small uncertainty in the density of hydrogen in the emulsion.[19]

B. Angular Distribution

There were 103 events acceptable for the angular distribution. Some of these were found by area scanning in the vicinity of selected meson tracks. Most of these were found in track scanning outside of the prescribed region in which the total path length was counted.

For meson scattering angles greater than 5° the range of the recoil proton is greater than 10μ. Thus essentially no bias can be introduced into the angular distribution by the various methods of detection. The results are plotted in Fig. 9 and listed in Table III. We also include the results of averaging the two energy intervals. The errors shown are only the probable errors arising from statistics and do not include the normalization uncertainty. Systematic errors here would presumably be due only to the inclusion of background events (quasi-elastic scatterings) which have the same kinematics as free $\pi+P$ collision. Recent data obtained at lower energies (135 Mev) on inelastic scattering in C, Pb,[20] and emulsion[10] indicate that this background would, if present in any significant proportion, increase the ratio of backward to forward scattering. A cutoff at small angles is forced by the range of recoil protons. We have set 10μ as the minimum acceptable range. This corresponds to a meson scattering angle of 5° in the laboratory system and 8° in the cm system. Coulomb contributions are expected to be negligible above 15° although interference effects may be contributing to the 8–30° interval. These probably act to depress this point slightly.[2]

VII. DISCUSSION

Figure 10 summarizes recent determinations of the π^+ total cross section as a function of meson energy. Data are included from Chicago,[1] Columbia,[2] Rochester,[3] and from a diffusion cloud chamber study at Brookhaven.[21,22] One of the most interesting questions raised by these data is that of the detection of nucleon structure. A feature of strong-coupling pseudoscalar meson theory is the existence of isobaric levels having definite angular momentum and isotopic spin assignments. The specific level presumed to be responsible for the scattering at these energies is the $J=\frac{3}{2}$, $I=\frac{3}{2}$ level. The phenomenological introduction of such a

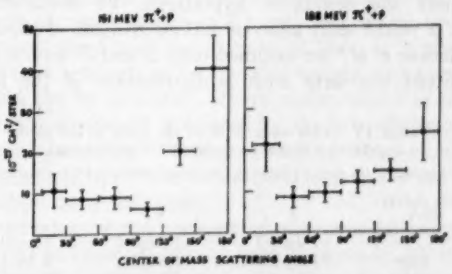

FIG. 9. Differential cross sections of 151- and 188-Mev pions in hydrogen. The uncertainties are the probable errors due to statistics only.

[17] Byfield, Kessler, and Lederman, Phys. Rev. **86**, 17 (1952); Aarons, Ashkin, Feiner, Gorman, and Smith, Phys. Rev. **90**, 342 (1953).

[18] The weakness of this method lies in the uncertain efficiency of the π^- scanning for the detection of very small events, principally stops-in-flight. These are either absorptions with neutron emission or charge exchange scatterings. In both cases, the corresponding events with positive mesons are associated with heavily ionizing prongs and are more easily detected. Stops constitute about 10 percent of the reaction cross section in the π^- work.

[19] Goldhaber, Bielk, Frankl, and Goldhaber, Rev. Sci. Instr. (to be published).

[20] J. Kessler and L. M. Lederman (to be published).

[21] Fowler, Lea, Shephard, Shutt, Thorndike, and Wittemore, Phys. Rev. **92**, 832 (1953).

[22] S. Lindenbaum and L. C. L. Yuan have recently obtained a value of 48 mb at 340 Mev. This confirms the decrease at higher energies suggested by Fig. 10.

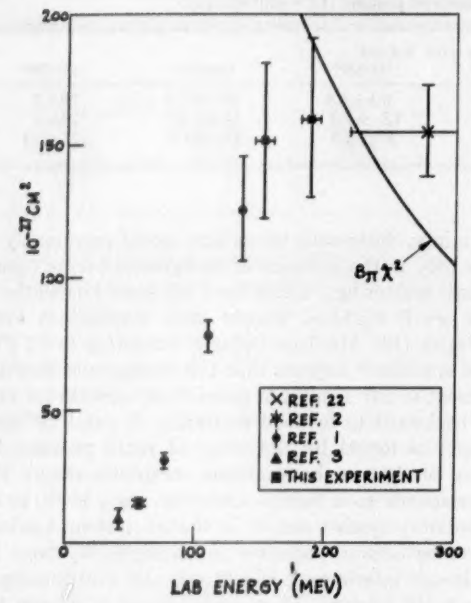

FIG. 10. Variation of total cross section of π^+ mesons with energy. Recent results from Brookhaven [S. Lindenbaum and L. Yuan (private communication)] indicate a cross section of 48±9 mb at 340 Mev.

resonance at $E\sim200$ Mev has been successful in fitting the lower-energy pion-nucleon scattering[4] and the photomeson production data.[23] In addition, recent results[24] at higher photon energies have shown a very rapid decrease in cross section above 320 Mev, again suggesting a resonance in the meson-nucleon interaction.

The most direct evidence for the resonance must come from the π^+ scattering data since only this experiment involves a pure $I=\frac{3}{2}$ state. Although Fig. 10 clearly shows the provisional nature of the results in the resonance region, the present experiment tends not to support the resonance hypothesis. To demonstrate this, a phase shift analysis has been made. Following Anderson *et al.*[1] we assumed only S and P waves, and so fitted the data with a distribution of the form $a+b\cos\theta+c\cos^2\theta$. This is given in Table IV. The result of combining the data for the two energy intervals is also given. The equations relating the three phase shifts, α_3, α_{33}, and α_{31},[25] to the three parameters a, b, and c are transcendental. Graphical[26] and numerical investigations of these equations show that there exist sets of a, b, c's for which solutions do not exist. Angular distributions which yield such sets are presumably inconsistent with the assumption of only S and P wave contributions to the scattering. In the present experiment, the distributions given in Table IV fall in this category. However, the errors are large and it is always possible to obtain solutions by varying the a, b, and c coefficients within the experimental uncertainties. The results of such variations corresponding to the Fermi-type solutions[1] are given in Table V. The least squares sum,

$$M=\sum_i^6\left(\frac{\delta i}{\mathrm{PE}_i}\right)^2,$$

where δ_i are the deviations of the phase-shift results from the observed points and PE_i are the probable errors, is also given. In each case, an attempt, by no means exhaustive, was made to minimize M. Large but difficult to compute uncertainties go with these phase shifts.

TABLE IV. Least-squares fit of the data to the form $d\sigma/d\Omega=a+b\cos\theta+c\cos^2\theta\times10^{-27}$ cm^2/sterad.

Lab. energy Mev	a	b	c
78[a]	1.9±0.3	−1.7±0.4	1.6±0.9
110[a]	3.6±0.7	−4.8±0.8	7.5±1.9
135[a]	3.9±2.3	−7.1±2.8	18 ±6.8
151	6.2±2.4	−7.7±2.6	19 ±5.0
188	10 ±3.5	−4.1±2.0	8.7±2.8
Combined $E=168$	7.7±2.0	−6.1±2.1	14.6±3.2

[a] See reference 1.

We have investigated the effect on the α's of a small D-wave contribution. It has been theoretically noted[27] that D-wave scattering should accompany the large P scattering as a nucleon recoil effect. Choosing the largest D phase shift,[27] the $D_{\frac{3}{2}}$,[3] and keeping only interference terms (we assume α_{31} small here), results in a $\cos^3\theta$ term with coefficient $12\lambda^3\sin\alpha_{33}\sin d_{53}\cos(d_{53}-\alpha_{33})$. The data very much require this term and hence d_{53} to be negative with respect to α_{33}, in agreement with theory. One such solution for $\bar{E}=168$ Mev (combined data) is given in Table V. It is interesting to note that the α_3 phase shift has been strongly decreased by the $-5.4°$ of D wave. All of the distributions in Table V "fit" the observations. However, the fact that the actual experimental values at 168 Mev seem to require D waves (not outside of experimental errors) raises the question of the existence of any *a priori* theoretical prejudice against this conclusion. On the other hand, a reinterpretation of the lower energy data on the basis of a small negative D wave could lead to a simpler S-wave energy dependence.

Table V shows that the α_{33} phase shift is of the order of 40–55° over this energy interval. Thus, at least up to 190 Mev, no evidence for a resonance is observed. To re-enforce this conclusion we note that for a resonant interaction in the $P_{\frac{3}{2}}$ state, the total cross section would have to be at least $8\pi\lambda^2$. This is just inside of the

[23] K. A. Brueckner and K. M. Watson, Phys. Rev. **86**, 923 (1952).
[24] Walker, Oakley, and Tollestrup, Phys. Rev. **89**, 1301 (1953).
[25] We use the notation of reference 1.
[26] J. Ashkin and S. H. Vosko, Phys. Rev. **91**, 1248 (1953).
[27] E. M. Henley and M. Ruderman, Phys. Rev. **90**, 719 (1953).

experimental errors. However, any additional states contributing to the scattering would add to the total cross section. The angular distributions are qualitatively different from a pure $P_{\frac{3}{2}}$ state $(1+3\cos^2\theta)$. In fact, if one assumes α_{33} near 90°, then, independent of any normalization, the angular distribution at 188 Mev would imply an even-wave contribution of at least 40 mb.[28] Thus the total cross section would have to be larger than 240 mb. No such argument may be made against a possible α_{31} resonance. The experimental momentum dependence of the α_{33} phase shift suggests a leveling-off although an extrapolation to 90° at about 230 Mev is possible.

[28] This is obtained by forming the ratio $[\sigma(0°)+\sigma(180°)]/2[\sigma(90°)]$ as $\alpha_{33}\to 90°$. For the 188-Mev case, this is 2.1 ± 1.0 and implies $\sin^2\alpha_3>0.5$ or $\sigma_T>2.5(4\pi\lambda^2)$.

TABLE V. Phase-shift solutions.

Lab. energy Mev	Phase shifts	M
151	$\alpha_3=-30°$, $\alpha_{31}=8°$, $\alpha_{33}=45°$	12
188	$\alpha_3=-35°$, $\alpha_{31}=+0°$, $\alpha_{33}=55°$	15
Combined $\bar{E}=168$	$\alpha_3=-40°$, $\alpha_{31}=12°$, $\alpha_{33}=40°$	10
$\bar{E}=168$ and D waves	$\alpha_3=-23°$, $\alpha_{31}=-8°$, $\alpha_{33}=50°$ $d_{33}=-5.4°$	4.5

The authors wish to acknowledge the contribution of the scanners, B. Kuharetz, M. Johnson, M. Hecht, and R. Klein, to this work. D. C. Peaslee's computation group assisted greatly in the analysis of the track measurements.

PHYSICAL REVIEW VOLUME 93, NUMBER 3 FEBRUARY 1, 1954

Neutron Production by Cosmic Rays*

WILLIAM C. G. ORTEL†
Sloane Physics Laboratory, Yale University, New Haven, Connecticut

(Received September 9, 1953; revised manuscript received November 4, 1953)

An experimental study has been made of the production of neutrons in the nuclear interactions of cosmic rays. An apparatus selected events in which a nuclear interaction occurred in or near a liquid scintillation counter, with the production not only of ionizing particles but also of neutrons of a few Mev energy which were slowed to thermal energy in a paraffin moderator and detected by BF_3-filled proportional counters. Such coincidences are termed (s,n), $(s,2n)$, and so on, according to the number of *detected* neutrons. The average number, $\bar{\nu}$, of neutrons *produced* per disintegration was calculated from the observed relative numbers of (s,n) and $(s,2n)$ coincidences.

These data were obtained at Climax, Colorado, at an altitude of 11 200 ft. Analysis shows that events of the type selected in this experiment account for the production of 3×10^{-4} neutrons g^{-1} sec^{-1}, a figure which is close to the total neutron-production rate in carbon as previously measured at the same location. In these events, it is concluded that $\bar{\nu}=1.3\pm0.2$. Combination of this result with previously determined relative multiplicities yields the values $\bar{\nu}=2.2$ for production in aluminum and $\bar{\nu}=6$ for production in lead.

I. INTRODUCTION

EVIDENCE that neutrons are produced by cosmic rays in their interactions with matter was sought and found soon after the discovery of the neutron.[1] It is believed that the predominant neutron-production process must be the type of high-energy nuclear disintegration observed as a "star" in nuclear emulsion. The ionizing particles produced in stars are accessible to study since they leave tracks, or "prongs," in emulsion. It has been established[2] that in emulsion exposed at mountain altitude the mean number of prongs per star of one or more prongs is 2.2 and that many prongs represent protons of energy near 10 Mev. It is reasonable that neutrons of comparable energy and number should also be produced. Direct measurement of these neutrons is severely restricted by the low efficiency of all available neutron detectors, and the mean number, or "multiplicity," of neutrons produced in one act has remained quite uncertain.

A number of comparisons of the over-all rates of neutron and star production have been made. All these involve two extrapolations. First, some adjustment must be made to allow for the difference in the materials for which the neutron and star rates have been measured. Second, the star rate must be corrected for the disintegrations involving 2, 1, and 0 ionizing secondaries, which are events difficult or impossible to observe

* This paper is an adaptation of a dissertation presented to the Graduate School of Yale University in candidacy for the degree of Doctor of Philosophy. The work was supported in part by the joint program of the U. S. Office of Naval Research and the U. S. Atomic Energy Commission. Preliminary results were presented at the Cambridge meeting of the American Physical Society in January, 1953.

† U. S. Atomic Energy Commission Predoctoral Fellow.

[1] G. L. Locher, Phys. Rev. **44**, 779 (1933) and J. Franklin Inst. **224**, 555 (1937); L. H. Rumbaugh and G. L. Locher, Phys. Rev. **49**, 855 (1936); E. Schopper, Naturwiss. **25**, 557 (1937); E. M. Schopper and E. Schopper, Physik. Z. **40**, 22 (1939); E. Fünfer, Naturwiss. **25**, 235 (1937) and Z. Physik **111**, 351 (1938).

[2] P. E. Hodgson, Phil. Mag. **42**, 82 (1951); N. C. Barford and G. Davis, Proc. Roy. Soc. (London) **A214**, 225 (1952).

in emulsion. Montgomery and Tobey[3] made one of the best comparisons of this sort. They measured the neutron-production rate in several materials, deriving an empirical interpolation formula from which to estimate the production rate in emulsion. Two sets of star data were available to them for comparison. For each of these, they extrapolated the observed prong-number distributions to include zero-prong events and concluded that the neutron multiplicity in emulsion was 2.6 or 4.6. Recent star observations favor the smaller figure. Another figure has been published by Puppi and Dallaporta,[4] based on Yuan's[5] measurements of the neutron-production rate in the atmosphere. They estimate that the neutron multiplicity for production in air is 3.5.

A more direct measurement of the neutron multiplicity may be made by observing coincidences between a detector of neutrons and a detector of neutron-producing events. The present experiment is of this type. Several previous coincidence experiments have been reported in which boron detectors in a paraffin moderator have been used to detect neutrons. In all of these, however, arrays of Geiger counters have been used to select neutron-producing events. The efforts of the Washington University group[6] have been concentrated on neutron production by μ mesons. The Cornell group has studied neutron production in extensive air showers[7] and in events in which penetrating ionizing particles are produced.[8] Examination of the counting rates of all of these experiments indicates that the events selected were very infrequent compared to those selected in the present experiment so that the measured multiplicities are not characteristic of the most common neutron-producing processes. The Cornell experiments were designed to select quite high-energy events, and it was judged that the observed neutrons were in general the products of several simultaneous disintegrations; thus the multiplicity per disintegration was not determined.

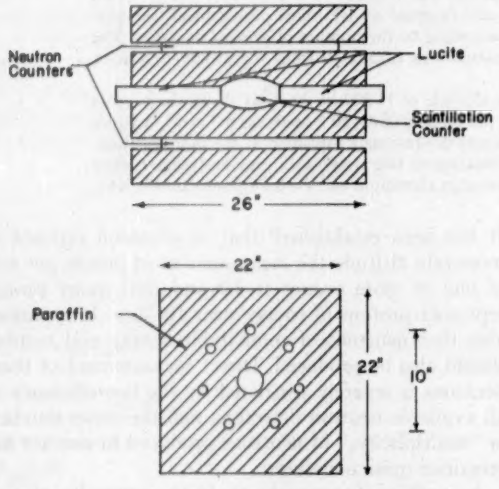

FIG. 1. Sketch of the apparatus.

The present experiment differs from previous coincidence experiments in that the most common neutron-producing events are selected, and the location of these events is specified well enough to permit knowledge of the efficiency of neutron detection. The apparatus is shown in Fig. 1. BF_3-filled proportional counters were used as neutron detectors. They were embedded in a paraffin moderator in which the neutrons would slow down from their initial energies of a few Mev to thermal energies, the range where the counters are most sensitive. A scintillation counter, consisting of 210 g of an organic liquid, was placed in the center of the moderator. A nuclear disintegration in or near this counter was detected by it if among the disintegration products there was a particle whose loss of energy by ionization in the counter exceeded 13 Mev.

Those scintillations accompanied by one or more neutron counts were selected. These coincidences will be referred to as (s,jn) events, with j standing for the number of detected neutrons. Coincidences may be attributed primarily to nuclear disintegrations in or near the scintillator. The efficiency ϵ, for detecting a neutron originating in this region, was measured with a calibrated neutron source. The multiplicity of neutron production could then be derived from the rates of (s,n) and $(s,2n)$ events.

Tongiorgi *et al.*[7] established that the extensive air showers contain neutrons and neutron-producing particles. A Geiger counter tray of sensitive area 560 cm^2 was employed to reject such showers. Since the scintillator's area was 58 cm^2, a shower of sufficient density to be detected by the scintillator would almost certainly produce a Geiger pulse. The neutron multiplicity was derived from the Geiger anticoincidence rates $(s,n,\bar{g})$ and $(s,2n,\bar{g})$.

Whenever a coincidence occurred, the scintillation pulse height and the delay time between the scintillation and the first neutron pulse were recorded. The electronic recording circuits have, for the most part, been described previously.[9] Additional circuits of conventional design were employed to note the occurrence of a second or third neutron pulse or of a Geiger pulse in prompt coincidence with a scintillation.

[3] A. R. Tobey, thesis, Yale University, 1948 (unpublished); C. G. Montgomery and A. R. Tobey, Phys. Rev. **76**, 1478 (1949); A. R. Tobey and C. G. Montgomery, Phys. Rev. **81**, 517 (1951).

[4] G. Puppi and N. Dallaporta, *Progress in Cosmic Ray Physics*, edited by J. G. Wilson (North-Holland Publishing Company, Amsterdam, 1952), p. 378.

[5] L. C. L. Yuan, Phys. Rev. **81**, 175 (1951) and **86**, 128 (1952).

[6] R. D. Sard *et al.*, Phys. Rev. **76**, 1134 (1949); A. M. Conforto and R. D. Sard, Phys. Rev. **86**, 465 (1952).

[7] V. Tongiorgi, Nuovo cimento **5**, 101, 391 (1948); Phys. Rev. **73**, 923 (1948) and **75**, 1532 (1949).

[8] Cocconi, Tongiorgi, and Widgoff, Phys. Rev. **79**, 768 (1950).

[9] W. C. G. Ortel, Rev. Sci. Instr. (to be published).

II. APPARATUS

A. Scintillation Counter

The scintillation counter is shown in Fig. 2. The scintillating material was 210 g of a solution prepared by dissolving 1 g terphenyl and 3 mg diphenylhexatriene in ⅓ l phenylcyclohexane. This liquid contains only carbon and hydrogen, being nearly identical in composition and density with paraffin. The liquid was contained in a 90 g glass cell covered with an aluminum foil reflector and a light-tight layer of tape. The photomultiplier tubes were separated from the cell by Lucite "light pipes." Since the events detected by the scintillator included disintegrations in or near it, the construction materials were chosen so that the disintegrations detected would be predominantly those of carbon nuclei. The other elements present were of quite low atomic weight and may reasonably be expected not to introduce serious error in the average neutron multiplicity.

Pulses from the two photomultipliers were added and amplified before being introduced into the coincidence circuits. For the purpose of obtaining some idea of the meaning of pulse size in terms of energy, two Geiger counters were used to select scintillations produced by ionizing particles capable of penetrating 4 in. of Pb. This amount of Pb will just be penetrated by a μ meson of energy corresponding to minimum ionization density. The arrangement of counters and the pulse-height distribution obtained are shown in Fig. 3. The pulse-height distribution expected is also shown. This was calculated with consideration of the distribution of possible path lengths through the scintillator and the distribution of possible energy losses by a minimum-ionizing particle along each path. The greater width of the observed distribution may be attributed partly to the limited energy resolution of the scintillator and partly to the possibility of spurious coincidences caused by side showers.

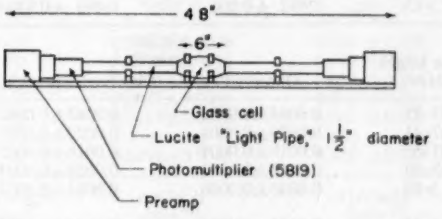

FIG. 2. Scintillator and photomultiplier assembly.

The peak of the pulse-height distribution was calculated to represent an energy loss of 8.5 Mev. All pulse-height distributions were scaled to the position of this peak. An energy value obtained in this way is not a good measure of a disintegration energy for two reasons. First, some scintillations are the result of nearby disintegrations, all of whose secondaries may not enter the counter. Second, many scintillations will be produced by heavily ionizing particles, and it is known that the light output of an organic scintillator is a function of both ionization and ionization density.

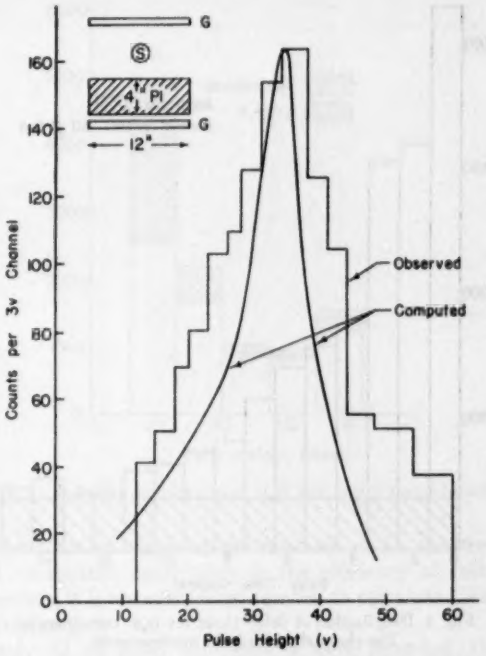

FIG. 3. Pulse-height distribution of minimum-ionizing particles.

B. Neutron Counters

The neutron counters[10] were of 1.5-in. outer diameter and 22-in. active length, with center wires of 0.002-in. diameter. They were filled to a pressure of 45 cm Hg with BF_3 enriched to 96 percent in B^{10}.[11] All counters together had a 150-v plateau starting at 2200 v when all pulses greater than 0.003 v were recorded.

The counting rate averaged 144 min^{-1} over background. The background, measured with no paraffin present but with each counter surrounded by at least 1 in. of borax, was 16 min^{-1} and may probably be attributed to radioactive contamination of the counter walls and to cosmic-ray bursts.

The efficiency of the moderator and neutron counters for detecting neutrons from a point source was measured directly. The efficiency of the apparatus is somewhat energy dependent; however, it has been shown previously[7] that the energy of neutrons produced by cosmic rays is about the same as the average energy of those from a Ra-Be source. A 5-mC source of this type was supplied by the Canadian Radium and Uranium Corporation, who state that the rate of neutron emission is

[10] The neutron counters were made and filled by the N. Wood Counter Laboratory, Chicago, Illinois.

[11] The BF_3 was furnished by the Isotopes Division, U. S. Atomic Energy Commission, Oak Ridge, Tennessee.

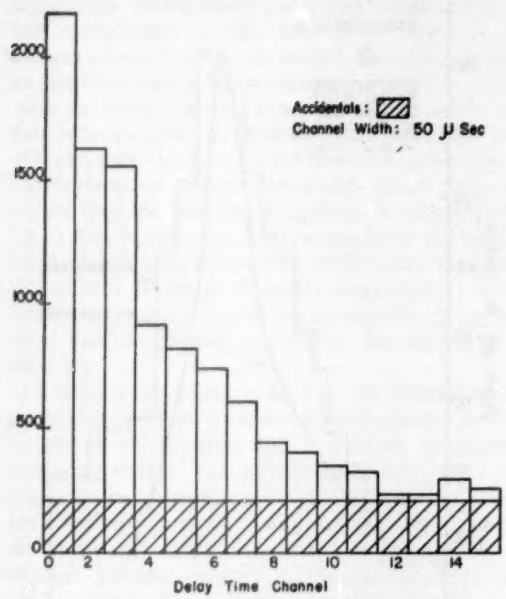

FIG. 4. Distribution of delay times for (s,n) coincidences. The channel width is 50 microseconds.

5.2×10^4 sec^{-1}, with an estimated error of ±10 percent. This figure was checked by comparing this source with two others, one calibrated by the Bureau of Standards and one by the Argonne National Laboratory. The measured efficiency for neutrons originating in the center of the scintillator was 0.050. The location of the detected disintegrations may be estimated from the previously observed range distribution of the protons from emulsion stars. Such an estimate, based on the data of Lattimore,[12] indicated that 45 percent of the detected disintegrations are within the scintillator and 90 percent are no more than 11 g cm^{-2} distant. Investigation showed that ϵ is very nearly constant over this region.

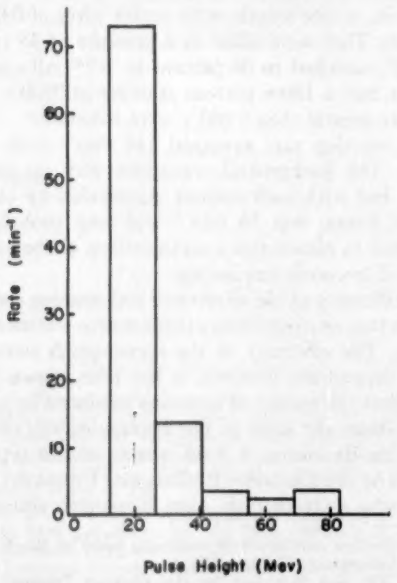

FIG. 5. Scintillation pulse-height distribution.

III. EXPERIMENTAL DATA

The equipment was operated at the Yale Cosmic Ray Laboratory at Climax, Colorado, during the autumn of 1952. The laboratory is located at 11 200-ft altitude, 51-cm Hg atmospheric pressure, magnetic latitude 48.1°N. The neutron production rate was measured there by Montgomery and Tobey[3] and found to be 13 times as great as at sea level.

TABLE I. Coincidence rates.

Pulse height (Mev)	$r(s,n)$ (min^{-1}) Observed	Observed less accidental
13–27	0.321 ±0.005	0.173 ±0.008
27–41	0.142 ±0.003	0.114 ±0.004
41–55	0.067 ±0.002	0.060 ±0.003
55–69	0.062 ±0.002	0.057 ±0.003
>69	0.100 ±0.003	0.093 ±0.004
>13	0.692 ±0.006	0.496 ±0.010

Pulse height (Mev)	$r(s,2n)$ (min^{-1}) Observed	Observed less accidental
13–27	0.0063±0.0006	0.0047±0.0007
27–41	0.0029±0.0004	0.0022±0.0005
41–55	0.0019±0.0004	0.0016±0.0005
55–69	0.0018±0.0003	0.0014±0.0004
>69	0.0046±0.0006	0.0041±0.0007
>13	0.0175±0.0011	0.0140±0.0015

Pulse height (Mev)	$r(s)$ (min^{-1})
13–27	73 ±2
27–41	13.8 ±0.3
41–55	3.53±0.06
55–69	2.11±0.05
>69	3.37±0.06
>13	96 ±3

Figure 4 shows the delay time distribution of all (s,n) coincidences. If the accidentals are subtracted, the distribution is exponential. From this distribution, the mean life of neutrons in the moderator was found to be 175 μsec, a reasonable value.

The coincidence rates (s,n) and $(s,2n)$ and the scintillation rates not selected by any coincidence requirement are given in Table I. The pulse-height distributions of these events were measured in 40 channels, and the channels were grouped into five ranges of equal voltage width. It should be recalled from the discussion of Sec. IIA that the energy values given

[12] S. Lattimore, Phil. Mag. 40, 394 (1949) and 41, 819 (1950).

for the boundaries of these pulse-height ranges are derived from a calibration in terms of the energy loss of minimum-ionizing particles and are probably underestimates by a factor of two or more for pulses due to heavily ionizing particles. The accidental (s,n) coincidence rate is distributed according to the pulse-height distribution of the total, unselected scintillations. The accidental $(s,2n)$ coincidence rate is distributed according to the distribution of (s,n) coincidences. The number of accidental $(s,2n)$ events was calculated from a measurement which indicated that there is a probability of 0.0050 ± 0.0003 that any neutron pulse will be closely followed by another. These "neutron showers" were about twice as frequent as would be expected on a random basis. The pulse-height distributions in Table I are presented graphically in Figs. 5, 6, and 7.

The Geiger tray was placed near the moderator, 4 ft center-to-center from the scintillator. The coincidence

TABLE II. True coincidence and anticoincidence rates with the Geiger counters.

Pulse height (Mev)	$r(s,n,g)$ (min^{-1})	$r(s,n,\bar{g})$ (min^{-1})
13–27	0.0044 ± 0.0006	$0.168\ \pm0.008$
27–41	0.0046 ± 0.0006	$0.109\ \pm0.004$
41–55	0.0023 ± 0.0004	$0.057\ \pm0.003$
55–69	0.0037 ± 0.0005	$0.053\ \pm0.003$
>69	0.0113 ± 0.0012	$0.082\ \pm0.005$
>13	0.0264 ± 0.0013	$0.470\ \pm0.011$
Pulse height (Mev)	**$r(s,2n,g)$ (min^{-1})**	**$r(s,2n,\bar{g})$ (min^{-1})**
13–27	—	0.0047 ± 0.0007
27–41	—	0.0022 ± 0.0005
41–55	—	0.0016 ± 0.0005
55–69	—	0.0014 ± 0.0004
>69	0.0020 ± 0.0003	0.0021 ± 0.0006
>13	0.0024 ± 0.0003	0.0115 ± 0.0009

rates, corrected for accidentals, are given in Table II. These data are included in Figs. 5, 6, and 7. The (s,g) coincidence rate of 33 ± 2 hr^{-1} agrees with the expected rate of air showers to which the present arrangement of counters is sensitive. The (s,n,g) rate of 0.026 ± 0.002 min^{-1} is small compared with the (s,n) rate of $0.496\ \pm0.006$ min^{-1}, indicating, as expected, that only a few percent of the neutrons produced by cosmic rays are produced in air showers.

The ratios of various counting rates are given in Table III. The significance of these ratios in terms of neutron multiplicity will be discussed in Sec. IV. The ratio $r(s,n)/r(s,2n)$ is significantly greater than the ratio $r(s,n,g)/r(s,2n,g)$ and indicated that, as expected, the multiplicity of neutrons in air showers is greater than the average multiplicity. In view of the uncertainty

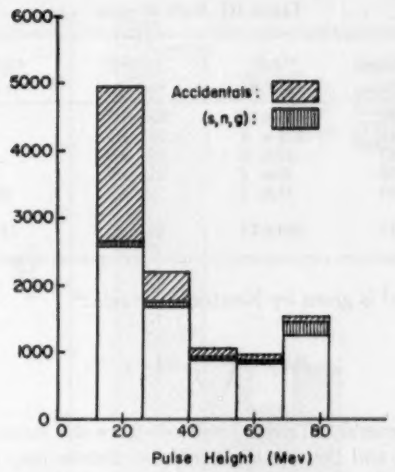

FIG. 6. Pulse-height distribution of (s,n) and (s,n,g) coincidences.

of the point of origin of the neutrons in air showers and consequent uncertainty in the efficiency of their detection, it is not considered feasible to calculate their multiplicity.

Only 23 $(s, \geqslant 3n)$ coincidences were recorded. Of these, 18 were $(s, \geqslant 3n, g)$ events. These data are not extensive enough to be of much significance. They are, however, consistent with the idea that neutrons are produced in air showers with a greater than average multiplicity.

IV. INTERPRETATION OF THE DATA IN TERMS OF MULTIPLICITY

Consider an event in which ν neutrons are produced in a disintegration near the scintillator, where the *a priori* probability of detecting a neutron is ϵ. The probability that exactly j of the neutrons will be

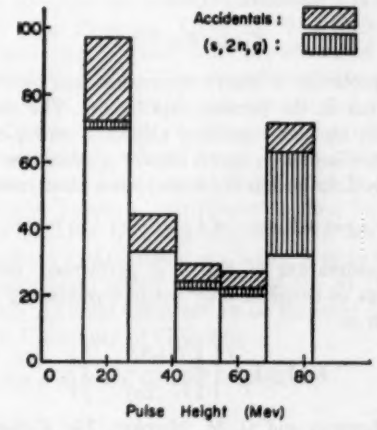

FIG. 7. Pulse-height distribution of $(s,2n)$ and $(s,2n,g)$ coincidences.

TABLE III. Ratio of rates.

Pulse height (Mev)	$\frac{r(s,\bar{g})}{r(s,n,\bar{g})}$	$\frac{r(s,n,\bar{g})}{r(s,2n,\bar{g})}$	$\frac{r(s,n,g)}{r(s,2n,g)}$
13–27	435±12	37 ±5	
27–41	127± 4	51 ±9	
41–55	62± 2	40 ±9	
55–69	39± 2	41 ±9	
>69	41± 2	39 ±7	6±1
>13	204±15	40.8±3.1	11±1

detected is given by Newton's formula:[13]

$$P_\nu(j)=\binom{\nu}{j}\epsilon^j(1-\epsilon)^{\nu-j}. \tag{1}$$

In general, all events will not have the same multiplicity, and the rate of (s,jn) coincidences may receive a contribution from any event in which j or more neutrons are produced. If the rate of those disintegrations detected by the scintillator in which ν neutrons are produced is $R(\nu)$, the rate of (s,jn) coincidences is:

$$r(s,jn)=\sum_\nu R(\nu)P_\nu(j). \tag{2}$$

The total rate, R, of detected disintegrations and the average multiplicity, $\bar{\nu}$, are

$$R=\sum_\nu R(\nu), \tag{3}$$

$$\bar{\nu}=R^{-1}\sum_\nu \nu R(\nu). \tag{4}$$

Unless the coincidence rates $r(s,jn)$ for all values of j are known, R and $\bar{\nu}$ can be computed only with some assumed form for the distribution $R(\nu)$. In the simple case that all events have the same multiplicity, ν, it may be shown that

$$\nu=1+2\left(\frac{1-\epsilon}{\epsilon}\right)\frac{r(s,2n)}{r(s,n)}. \tag{5}$$

Another manageable assumption is that $R(\nu)$ has the the form of a geometric series:

$$R(\nu)=R_0e^{-\nu/\nu_0}. \tag{6}$$

This is probably a better approximation to the true distribution in the present experiment. The stars observed[2] in nuclear emulsion exhibit a prong-number distribution which is quite closely a geometric series. With this distribution the coincidence rates reduce to

$$r(s,jn)=R_0\epsilon^je^{-j/\nu_0}[1-e^{-1/\nu_0}(1-\epsilon)]^{-(j+1)}. \tag{7}$$

If the summation of Eq. 4 is performed, excluding $\nu=0$ so as to consider only neutron-producing events, the result is

$$\bar{\nu}=1+1\Big/\left\{\epsilon\left[\frac{r(s,n)}{r(s,2n)}-1\right]\right\}. \tag{8}$$

Table IV gives the comparative results of Eqs. 5 and 8 when applied to the experimental data for all pulse sizes together after subtraction of coincidences due to air showers. These data are $r(s,n,\bar{g})/r(s,2n,\bar{g})=40.8\pm3.1$, $r(s,n,\bar{g})=0.470\pm0.006$ min^{-1}.

Comparison shows that in spite of the radical difference in the form of the assumed distributions, the calculated rate of events and the average multiplicity are not very different for the two cases.

In Table III, the ratios of various rates are given for each pulse-size group. Examination of this table leads to two conclusions. First, the neutron multiplicity of events not including air showers does not appear to be a function of pulse size. This conclusion is based on the constancy of the ratio $r(s,n,\bar{g})/r(s,2n,\bar{g})$. Second, the two ratios $r(s,n,\bar{g})/r(s,2n,\bar{g})$ and $r(s,\bar{g})/r(s,n,\bar{g})$ appear to be equal for the larger pulse sizes. This would be expected if the multiplicity distribution were a geometric series extending to zero-neutron events. If a geometric series of multiplicities is fitted to $r(s,n,\bar{g})$ and $r(s,2n,\bar{g})$ and extended to zero multiplicity, the calculated rate of disintegrations agrees with the observed rate of scintillations, for large pulses. This comparison is shown in Fig. 8. This line of argument suggests that a geometric series of multiplicities is a reasonable approximation to the true situation and that a relatively large proportion of disintegrations may have zero neutron multiplicity.

The best value of the average neutron multiplicity for neutron-producing events is judged to be $\bar{\nu}=1.5$. This value has a statistical error of ±0.05 and a further error of ±0.05 introduced by the uncertainty in ϵ.

Much recent evidence[14] favors the theory that each detected disintegration is part of a cascade of disintegrations so that the particles capable of nuclear interaction at any point are secondaries, produced in disintegrations above. Since the efficiency for neutron detection is appreciable for neutrons originating throughout a fairly large portion of the moderator, the observed events must sometimes include more than one disintegration. An estimate of the effect of cascades on the measured value of $\bar{\nu}$ was made on the basis of an oversimplified model. If a mean free path for star-producing radiation of 80 g cm^{-2} is assumed, and if it is assumed that neutrons originating within 20 g cm^{-2} of the scintillator would be detected, it may be con-

TABLE IV. Comparison of results calculated from two different assumed multiplicity distributions.

Distribution	$R(\nu\geq1)$	$\bar{\nu}$
$R(\nu)=R$	5.1 min^{-1}	1.9
$R(\nu)=R_0e^{-\nu/\nu_0}$	6.6	1.5

[13] H. Margenau and G. M. Murphey, *The Mathematics of Physics and Chemistry* (D. Van Nostrand Company, Inc., New York, 1948), p. 422.

[14] G. Thomson and P. E. Hodgson, Phil. Mag. **42**, 978 (1951); B. Rossi, *High Energy Particles* (Prentice-Hall Publishing Company, New York, 1952), p. 486.

cluded that about 25 percent of the detected events include two disintegrations. If both of these disintegrations have the same multiplicity, it may be concluded that the measured value of $\bar{\nu}$ must be corrected by the factor 0.7; thus a corrected value of $\bar{\nu}=1.1$ is obtained. This is probably an overcorrection, since, as mentioned in the previous paragraph, there is reason to believe that many disintegrations produce no neutrons, and so many cascades of more than one star will produce no more than one neutron.

It is believed that the best estimate of the corrected multiplicity is $\nu=1.3$, with an uncertainty of ± 0.2 resulting mainly from the absence of a direct experimental basis for the cascade correction.

V. DISCUSSION OF THE RESULTS

In addition to the neutron multiplicity, this experiment yields several secondary results. The star production rate in paraffin may be derived on the assumption that, as stated in Sec. IIB, 45 percent of the detected events are stars in the scintillator. Using the rate of neutron-producing events from Table IV, on the basis of a geometric series of multiplicities, the star production rate is 21 g^{-1} day^{-1}. For comparison, if Lattimore's star rates,[12] including the production rate of single fast protons as possible neutron-producing events, are extrapolated from emulsion to paraffin on the assumption that the cross section varies with atomic weight, A, as $A^{\frac{1}{3}}$, the result is 17 g^{-1} day^{-1}. The assumptions involved in this calculation make it difficult to estimate the errors.

The neutron production rate in paraffin may be derived from this experiment in two different ways. Using $\bar{\nu}=1.3$, the star production rate of 21 g^{-1} day^{-1} implies a neutron production rate of 3×10^{-4} g^{-1} sec^{-1}. This figure depends ultimately on the measured coincidence rates. The total neutron counting rate is also related to the neutron-production rate. A calculation identical to that of Montgomery and Tobey[3] indicates that the observed rate of 144 min^{-1} implies a neutron-production rate of 2.6×10^{-4} g^{-1} sec^{-1}. Both of these figures may be compared with the result of Montgomery and Tobey, 2.5×10^{-4} g^{-1} sec^{-1}, which was obtained at Climax. Again, it is difficult to estimate the errors. The calculation indicates, however, that the bulk of neutron production, as measured by Montgomery and Tobey, is the result of events of the type selected in the present coincidence experiment.

Relative production rates of neutrons in materials of different atomic weight have been measured by Montgomery and Tobey[3] and by Simpson.[15] As pointed out by Montgomery and Tobey, these rates are proportional to $\bar{\nu}\sigma/A$, where σ is the relative cross section of the material. Relative multiplicities calculated from this expression may be reduced to absolute values by the result, $\bar{\nu}=1.3$ for C, of the present experiment. For this calculation, the production rates measured by Montgomery and Tobey were used whereas values of σ were taken to be proportional to the total cross sections measured by Fox *et al.*[16] for 300-Mev neutrons. The result is $\bar{\nu}=2.2$ for production in Al and $\bar{\nu}=6$ for production in Pb. The mean atomic weight of the elements in nuclear emulsion is about the same as the atomic weight of Al. The mean neutron multiplicity in Al is comparable to the mean prong multiplicity, 2.2, of stars observed[2] in emulsion.

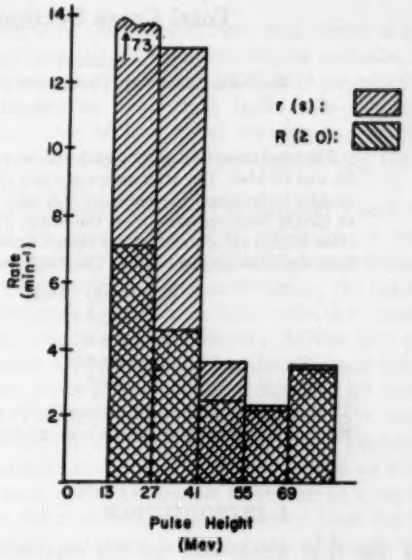

FIG. 8. Comparison of the rate of detected disintegrations, calculated from $r(s,\gamma)$ and $r(s,2n)$, with the observed scintillation rate.

This investigation was initiated following suggestions of the late Professor Carol G. Montgomery. The experiment was planned with the advice of Professor Raymond V. Adams. The experiment was performed and the data interpreted with the aid and encouragement of Professor Henry L. Kraybill, for whose constant and stimulating interest I am most grateful. The members of the Yale Cosmic Ray Group, in particular Mr. Irwin Tessman, contributed willing help to the experiment. The generous hospitality of Mr. Richard T. Hansen, Chief Observer at Climax, greatly facilitated the work there, which was carried out at the site of the High Altitude Observatory of Harvard University and the University of Colorado.

[15] J. A. Simpson, *Proceedings of the Echo Lake Cosmic Ray Symposium* (U. S. Office of Naval Research, Washington, D. C. 1949), p. 252.

[16] R. Fox *et al.*, Phys. Rev. **80**, 23 (1950).

Total Cross Section for Positive Ions in Hydrogen

STANLEY L. LEONARD* AND DONALD H. STORK
Radiation Laboratory, Department of Physics, University of California, Berkeley, California
(Received September 21, 1953)

The total cross section for positive pions in hydrogen has been measured at pion kinetic energies of 33, 44, 56, and 70 Mev. The attenuation of pions of these energies in liquid hydrogen was studied by scintillation-counter techniques. The geometry was such that pions scattered at angles greater than ±35° were counted as having been removed from the beam. Therefore, the term "total cross section" is taken to mean the cross section for all interactions except those in which the pion is scattered into an angle of less than ±35° from the pion-beam direction. The results are:

Pion energy (Mev)	Cross section (mb)
33±4.5	6.4±2.1
44±4	9.8±1.5
56±4	17.6±2.2
70±5	19.0±2.6

The energy dependence of the cross section seems to agree with the predictions of lowest-order perturbation theory for pseudoscalar mesons with gradient coupling to the nucleon.

I. INTRODUCTION

At the time when work on this experiment was begun, the total cross section for positive pions in hydrogen had been measured for pions of energies greater than 53 Mev.[1–3] It is of theoretical interest to extend these measurements to lower energies. This paper describes a determination of this cross section for 33-, 44-, 56-, and 70-Mev pions. This measurement provides a comparison with previous measurements and extends the cross-section data to energies as low as feasible for the particular method utilized. The lower energy limit resulted from the low pion beam flux and the rapid increase, with decreasing energies, of the correction required because of pion-muon decay.

Recently, cross-section measurements have been reported for pions of 37 Mev,[4] 40 Mev,[5] and 43 Mev.[6] Comparison of the results with those of this experiment shows that the agreement is satisfactory.

II. EXPERIMENTAL METHOD

In this experiment, the 340-Mev scattered deflected proton beam of the Berkeley 184-in. synchrocyclotron was brought out through the cyclotron shielding, through a 2-in. diameter collimator, into the so-called "cave" area (Fig. 1). There it passed through a pion-production target, of polyethylene or carbon, placed at the front edge of a strong magnetic field. Pions of the desired energy were deflected by the field, through about 90° in an arc of 18.5-in. radius, passed through an exit slit at the rear edge of the magnet pole faces and into a narrow hole cut through the concrete shielding that formed the side wall of the cave. In this way a beam of pions of the desired energy was produced. This beam was further defined by a thin anthracene scintillation counter placed inside the hole in the cave wall. The beam then emerged into a region outside the shielding, passed through two stilbene crystals viewed by photomultiplier tubes, and entered the liquid-hydrogen target. Upon emerging from this attenuation target, the beam passed into a large cell of liquid scintillator viewed by photomultipliers.

Pions were identified by the heights of the pulses produced in the photomultiplier tubes viewing the two stilbene crystals, in conjunction with the momentum measurement which is implicit in the magnetic selection of beam particles. By means of the electronic setup (see following), those pions that interacted with the hydrogen nuclei, and so did not reach the back counter, were counted. In addition, the total number of pions passing through both the stilbene crystals was measured. From these two numbers, plus information about the amount of hydrogen in the attenuation target, the total attenuation cross section was calculated.

Carbon targets were used to produce the beams for the 56- and 70-Mev attenuation measurements, and polyethylene was used at the other two energies. The

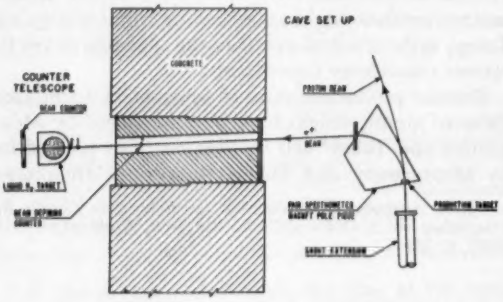

FIG. 1. Experimental arrangement.

* Now at Principia College, Elsah, Illinois.
[1] Anderson, Fermi, Nagle, and Yodh, Phys. Rev. **86**, 793 (1952); Anderson, Fermi, Martin, and Nagle, Phys. Rev. **91**, 155 (1953).
[2] Isaacs, Sachs, and Steinberger, Phys. Rev. **85**, 803 (1952).
[3] Fowler, Fowler, Shutt, Thorndike, and Whittemore, Phys. Rev. **91**, 135 (1953).
[4] C. E. Angell and J. P. Perry, Phys. Rev. **92**, 835 (1953).
[5] J. P. Perry and C. E. Angell, Phys. Rev. **91**, 1289 (1953).
[6] Weaver, Lord, and Orear, Phys. Rev. **91**, 466 (1953).

thicknesses of the polyethylene targets were chosen so that the pions due to the reaction $p+p=\pi^{+}+d$ would emerge from the target at the energy desired for the pion beam. In all cases the width of the production target was $1\frac{1}{8}$ in., the same width as the exit slit. These dimensions determined the momentum selection of the pions.

Counters 1 and 2 (Fig. 1) were placed at the approximate position where the magnetic lens consisting of the fringing field of the magnet formed an image (in the vertical plane) of the target. For the lower two pion energies, the magnetic field was varied and the twofold coincidence counting rate in counters 1 and 2 was maximized with respect to the field intensity, thus insuring that the beam particles were primarily due to the intense peak in production from polyethylene resulting from the $p+p=\pi^{+}+d$ reaction.[7]

The energy of the particles in the beam was determined by an integral range measurement, in which the threefold coincidence counting rate for counters 1 and 2 and the back counter was obtained for various thicknesses of copper placed between counter 2 and the back counter. The percentage of the beam particles that were pions was determined by a pulse-height analysis that is described below.

The intensity of the pion beam was increased over the value obtained in preliminary runs by a factor of about two by extending to the pion-production target the evacuated tube through which the protons traveled. This expedient reduced the spreading of the beam caused by multiple Coulomb scattering in the air and in the ion chamber monitor that was placed at the exit of the evacuated tube. Since the vertical dimension of the proton beam at the production target was decreased in this way, the vertical focusing of the magnet fringing field produced a smaller pion image at the counter telescope. The resulting pion-beam flux through the telescope was about two particles per second.

The beam defining counter (No. 0 in Fig. 1) was placed two feet in front of counter 1 and consisted of a $1\frac{1}{2}$-in.$\times 1\frac{1}{2}$-in.$\times\frac{1}{4}$-in. anthracene crystal viewed from one edge through a short Lucite light pipe by a single RCA 1P21 photomultiplier tube. Counter 1 was a $1\frac{1}{4}$-in.$\times 1\frac{1}{4}$-in.$\times\frac{1}{2}$-in. stilbene crystal viewed from opposite ends through short Lucite light pipes by two RCA 5819 photomultipliers. Counter 2 was very similar, a $1\frac{1}{4}$-in.$\times 1\frac{1}{4}$-in.$\times\frac{1}{4}$-in. stilbene crystal viewed on opposite ends by two RCA 5819 photomultipliers, also through short light pipes. The separation between counters 1 and 2 was $2\frac{3}{4}$ in. The back counter consisted of a disk-shaped cell, 14 in. in diameter and $\frac{1}{2}$ in. thick. The front face was made of 16-mil dural foil and the rear face of $\frac{1}{4}$-in. Lucite. This cell was filled with a solution of terphenyl (0.4 percent by weight) in phenylcyclohexane with about 15 mg of diphenylhexatriene per kilogram of solution, for the purpose of shifting the wavelength of the radiated light to a region of greater sensitivity of the 5819 photomultiplier cathode. It was viewed from the rear by ten RCA 5819 photomultiplier tubes separated by a light baffle into two groups, a central core of four tubes viewing a central 8-in. circle, and an outer ring of six tubes viewing the outer 3-in. ring of the disk.[8]

The photomultipliers used in counters 1 and 2 were selected for good pulse-height resolution in viewing stilbene crystals. Since the pulse-height resolution also depended upon light-collection efficiency, the light pipes were designed for optimum light collection consistent with the requirements of geometry. All the 5819 photomultipliers were protected from the effects of the stray magnetic fields in the cyclotron building by mumetal shields. The tubes viewing the pulse-height counters were encased in an iron box for additional shielding.

The liquid hydrogen target was placed as close to the second crystal as possible to reduce to a negligible amount the number of pions removed from the beam by multiple scattering in the crystal. Although "poor" geometry was required for the multiple Coulomb scattering, it was desirable to have the back counter as far from the target as possible in order to have fairly "good" geometry for the nuclear scattering so that as much of the total attenuation cross section was measured as possible.

The angle subtended at the second crystal by the back counter was determined in part by the fact that some beam pions decayed in flight after passing through the first crystal (some of the decay muons then passing through the second crystal) or the second crystal. It was important to make the angle subtended by the back counter large enough so that a negligible number of the decay muons passed outside the rear counter. As a compromise between the conflicting "good" and "bad" geometry requirements, the back counter was placed so that it subtended a half-angle of 35° at the center of the hydrogen target. This was the smallest angle which was still large enough to include all but a negligible fraction of the multiply scattered pions and all but a negligible fraction of the largest angle pion muon decays.

It was impossible to distinguish experimentally the true attenuation events from those pion-muon decay events occurring after counter 2 which yielded muons of such low energy that they reached the end of their range without entering the back counter. A discussion of the calculation of this correction appears later in this paper.

The electronic apparatus used in this experiment is shown schematically in Fig. 2. Pulses from the defining counter and counters 1 and 2 were amplified by means

[7] Cartwright, Richman, Whitehead, and Wilcox, Phys. Rev. 91, 677 (1953).

[8] This separation was not at all complete since the baffle extended only up to the rear face of the disk, but it would have permitted an estimate of the relative number of pions scattered into the outer ring as compared with those coming through the center section. This feature of the rear counter was not exploited in this experiment.

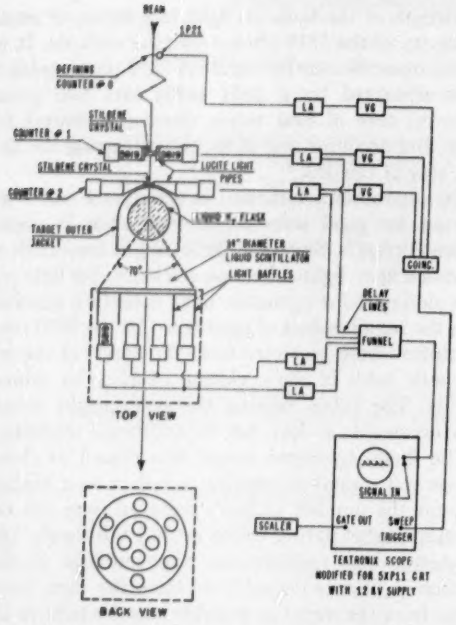

FIG. 2. Schematic diagram of electronic apparatus and counters.

of standard linear amplifiers (*LA*) and passed through gate-forming circuits (*VG*). The outputs of the gate-forming circuits were fed into a coincidence circuit of 0.5 microsecond resolving time. A threefold coincidence caused by pulses from these counters triggered the oscilloscope sweep. From the second outputs of the linear amplifiers, pulses from counters 1 and 2 and from the two sections of the back counter passed through different amounts of RG65/U delay line and were fed into a "funnel" circuit whose output was fed into the signal input of the oscilloscope. The function of this funnel circuit was to provide independent impedance matching and voltage attenuation and to funnel the pulses into one output. In this way, the four pulses from the four counting units, separated in time by means of the delay line, were displayed on the oscilloscope trace, the sweep being triggered by the threefold coincidence. These traces were photographed on continuously moving 35-mm film. The sweep time was 5 microseconds, and the pulses were separated by about 0.8 microsecond.

In order to insure that the pulses in the two pulse-height counters were not too short for effective feedback in the linear amplifiers, the pulses were lengthened by a simple $R-C$ network not shown in the diagram and then clipped to 0.25 microsecond in length by shorted clipping lines. The individual voltage attenuation at the input of the funnel circuit made it possible to adjust the heights of the pulses for photographic convenience at the start of any run without tampering with the gains of the amplifiers or the voltages on the phototubes. The latter two variables could thus be adjusted for optimum performance of the phototubes, amplifiers, and gates.

The oscilloscope was equipped with a gating circuit that provided a gate pulse whenever the sweep was triggered. This gate output was fed into a scaler, which therefore registered the total number of sweeps. A record was kept of the number of sweeps photographed on each section of film. An ion chamber placed in the primary proton beam served to monitor the integrated proton beam flux.

The liquid hydrogen target used in this experiment (Fig. 3) was one designed by Mr. John Garrison for experiments on proton-proton scattering. The hydrogen flask was a circular cylinder with axis perpendicular to the beam, and about 5.6 in. in diameter. The thickness of hydrogen in the beam direction was 1.00 gram/cm². A liquid nitrogen jacket cooled the target, several heat shields reduced radiant heat transfer, and an insulation vacuum of less than 10^{-2} micron provided good heat insulation.

For this experiment a new outer jacket was designed and constructed. This jacket is shown in Fig. 3. The beam entered the target through a hole in the jacket 3 in. in diameter, covered with a 7.5-mil aluminum foil. The exit window was covered with 10-mil aluminum foil and was 9 in. in diameter. This diameter was such that when the back counter was set to subtend a half-angle of 35° at the center of the hydrogen flask, the

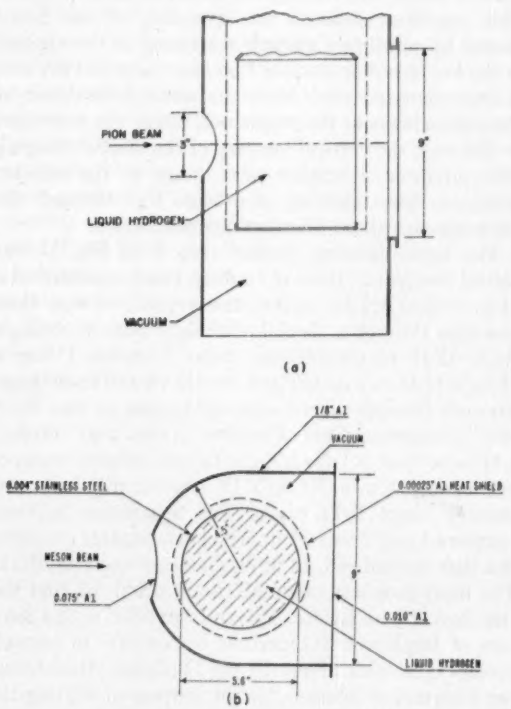

FIG. 3. Sketch of liquid hydrogen target. (a) Side-view cross section; (b) top-view cross section.

angles subtended at the second crystal by the back counter and by the exit window were the same.

The pulses from counters 1 and 2 and from both sections of the back counter were displayed on the screen of a 5XP11A cathode-ray tube using a 12-kv power supply. These pulses were photographed on continuously moving Kodak Linagraph Pan 35-mm film by means of a General Radio camera with a $f/1.5$ lens. The speed with which the film was moved through the camera was adjusted to keep the spacing between sweeps great enough for ease in subsequent reading of the processed film. A set of small neon lamps was mounted around the rim of the cathode-ray tube face and inside the light shield which enclosed the camera lens and oscilloscope face. The lights were controlled from outside the shield and were used to mark the film to identify which portions were exposed under a given set of conditions. After processing, the film was examined with the aid of a Recordak film reader. The pulse heights and separations between pulses could then be measured on an arbitrary scale by means of a grid placed in the focal plane of the film reader. The height of the pulses could be read to an accuracy of about one part in thirty, and the separation between pulses could be determined to about one part in twenty. The latter corresponded to a time resolution of about 0.04 microsecond.

III. DETERMINATION OF THE CROSS SECTION

In order to determine the attenuation cross section, it was necessary to know the thickness of the target in grams/cm², the total flux of pions through the target, and the number of pions that failed to reach the back counter. The target thickness was 1.00 g/cm².

In order to find the flux of pions, it was only necessary to determine the fraction of the sweeps initiated by pions since the total number of traces photographed on each section of film was registered on the scaler connected to the gate output of the oscilloscope. For the purpose of accomplishing this, pulse-height measurements were made on all traces in a group of samples of the film. These pulse heights were then plotted in the following way: a set of coordinate axes was laid out with the abscissa representing the pulse height in counter 1 and the ordinate representing the pulse height in counter 2. Each trace was represented by a dot whose coordinates indicated the pulse heights in the two counters. The distribution of the dots then represented the pulse-height distribution for the counters. A typical diagram representing the data at the lowest pion energy is given in Fig. 4. It is seen that most of the dots cluster in a rather limited region; these represent the pions. From this diagram one can set up criteria for classifying the particle responsible for a given trace on the oscilloscope. The criteria actually used are shown on the diagram, all dots inside the indicated polygon being ascribed to beam pions. From this diagram the fraction of beam particles that fulfilled the criteria was determined. From this fraction and the total number of sweeps, the number of pions traversing the target was computed. It is seen from this diagram that the pulse-height resolution in counter 1 is about 1.5 times as good as that in counter 2. This ratio is what one expects if the resolution width is due primarily to the statistics of electron emission at the photocathodes of the photomultiplier tubes, since about twice as much energy is lost in the first crystal as in the second.

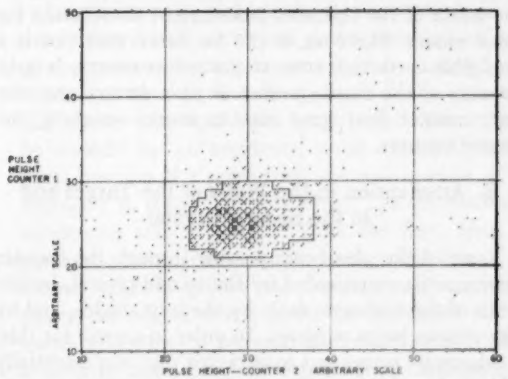

FIG. 4. "Three-dimensional" plot of pulses from counters 1 and 2 on all sweeps in a group of samples of film, for the case of 33-Mev pions. Criteria for identifying pions are shown.

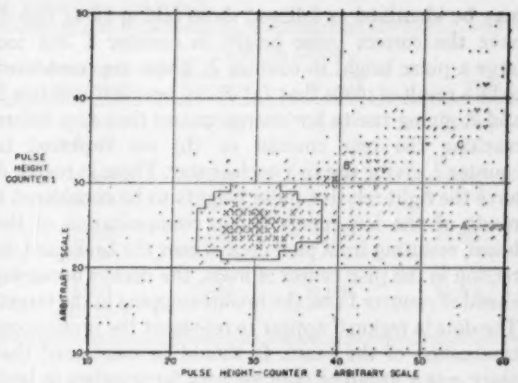

FIG. 5. "Three-dimensional" plot of pulses from counters 1 and 2 on all sweeps for which the pulses from the back counter were missing for the case of 33-Mev pions.

The number of attenuated pions, N_{att}, was determined in the following way: all of the film exposed with the liquid hydrogen target in place was scanned for sweeps on which appeared pulses from counters 1 and 2 alone. The heights of the two pulses on each of these sweeps were measured. These were then plotted in the "three-dimensional" type of diagram described above. The diagram for the lowest energy measurement is shown in Fig. 5. The pulse-height criteria for pion identification were applied, and the number of such anticoincidence events initiated by pions was determined.

It is believed that the other groups of dots in Fig. 5

may be identified as follows: those falling along line A have the correct pulse height in counter 1 but too large a pulse height in counter 2. These are considered to be a result of pions that (a) decay between counters 1 and 2, giving rise to low energy muons that stop before reaching the rear counter or (b) are captured in counter 2, giving rise to a nuclear star. Those in region B have the right relative pulse heights to be considered a result of the low-energy muon contamination of the beam, resulting from pion decays near the backward direction in the pion center of mass, the decays occurring ahead of counter 1 and the muons stopping in the target. The dots in region C appear to represent the proton contamination of the beam. It should be mentioned that there was a group of dots for very large pulses in both counters which could not be shown on this diagram; this group also represented protons.

Then, if N_b is the total number of pions passing through the target, ρt the thickness of the target in grams/cm², A the atomic weight of the target hydrogen, and A_0 Avogadro's number, one can write an expression for the attenuation cross section

$$\sigma=\frac{N_{att}}{N_b\rho t A_0/A}=\frac{N_{att}}{5.98N_b}\times10^{-23}\text{ cm}^2.$$

The last relation makes use of the fact that the target thickness was 1.00 gram/cm² and that the attenuation fraction was very small compared to unity.

IV. CORRECTIONS

A. Pion Decay Giving Rise to Spurious Events

It is apparent that beam pions that decayed after passing through counter 1 and at least most of the way through counter 2 were indistinguishable from any other beam pions. Some of the muons from these decay events had such low energy in the laboratory that they reached the end of their range before being detected in the back counter. Such events were indistinguishable from the true attenuations of the pion beam. Therefore, it was necessary to correct for these false attenuations on a theoretical basis, by use of the lifetime and dynamics of the decay process. At the lowest energy (33 Mev), the correction is a very significant one, the number of false attenuations being about 0.53 percent of the total flux and the number of true attenuations being about 0.36 percent of the total pion flux. At 44 Mev, the correction was about 0.1 percent of the total flux, and it was negligibly small at the two higher energies.

Because of the asymmetry of the liquid-hydrogen target with respect to the beam direction, it was inconvenient to calculate the correction for spurious events by means of any analytic expressions. For this reason it was decided that the correction could most reliably be determined by means of a Monte Carlo calculation that simulated the actual random processes involved in the experimental situation. Such a calculation is exact within the limits determined by the statistics involved and can be carried to any desired degree of precision, the accuracy of the results being limited only by the uncertainty in the initial data used for the calculation (such as the value of $\tau=2.54\times10^{-8}$ sec used for the pion mean life).[9] Because of the relatively large statistical uncertainties caused by the low counting rate in this experiment, coupled with the large target-out subtraction (Sec. V. B below), it is necessary only that the muon-decay correction be known to an accuracy of 15 percent at the lowest energy. At the higher energies the required accuracy was smaller still.

To calculate this correction to 15 percent, it was necessary to consider only 600 decay events in the counter telescope. These were assumed to be isotropically distributed in the pion center of mass, and consideration had to be given only to those muons coming off at large enough center-of-mass angles to have a chance of being stopped in the target. For each of these latter muons the position and the direction of decay were assigned with the aid of a table of random numbers, and its fate was then decided on the basis of knowledge of the geometry and stopping power of materials in its path. The spread in the energy of the beam pions was taken into account to first approximation and introduced only a very small uncertainty (less than 5 percent) into the correction.

It was the magnitude of this correction and its rapidly increasing importance as the pion energy was reduced that set the lower practical limit on the pion energies used in the experiment.

In addition to the above considerations, it was necessary to take into account those muons arising from decay of beam pions ahead of counter 1. Some of these muons had such low energy that they stopped before reaching the rear counter. At all energies except the lowest (33 Mev), these muons were reliably separated from the pions by pulse height. It is possible that at the lowest energy some of these muons caused pulse heights within the limits of the pion criteria, because of the width of the Gaussian pulse-height distribution for these muons. However, it can be shown that this is a negligible correction even at the lowest energy, largely because of the small number of pion decays near the first counter that gave rise to muons reaching the second counter.

B. Attenuation in the Walls of the Target and in the Second Crystal

Some of the pion beam passing through the counter telescope was attenuated by the second crystal, by the walls of the hydrogen flask, by the heat shields, and by the various beam windows. In order to correct for this, a "dummy" target was constructed that was essentially identical to the actual target except that the hydrogen

[9] Jakobson, Schulz, and Steinberger, Phys. Rev. 81, 894 (1951).

TABLE I. Summary of data, corrections, and results.

T_π	% Pions attenuated[a] H_2	Dummy[b]	Spurious events	Net % attenuated	Correction factors Muon flux correction	Unequal H_2 path	Final σ
33±4.5 Mev	1.207 ±0.071	0.313 ±0.062	0.530 ±0.070	0.364 ±0.118	1.034	1.009	6.4±2.1 mb
44±4	0.919 ±0.061	0.247 ±0.054	0.107 ±0.026	0.565 ±0.086	1.033	1.009	9.8±1.5
56±4	1.343 ±0.094	0.329 ±0.083	0.004 ±0.003	1.010 ±0.125	1.031	1.009	17.6±2.2
70±5	1.480 ±0.132	0.388 ±0.077	0	1.092 ±0.152	1.029	1.009	19.0±2.6

[a] Corrected for accidentals.
[b] Corrected for energy difference.

was replaced by a vacuum. In the experimental run, a measurement of the total attenuation in the dummy was made in precisely the same manner as the measurement of the attenuation in the target itself. The percentage attenuated in the dummy cannot be directly subtracted from that in the hydrogen target, however. In the hydrogen target the pion beam was reduced in energy by passing through the target hydrogen and therefore passed through the rear walls, heat shield, and window of the target at a lower energy. In the dummy, the beam passed through all the material at essentially the same energy. Since the attenuation cross section for positive pions in complex nuclei is a rather steep function of the energy, the amount of attenuation in the rear half of the dummy had to be corrected for this difference in cross section before the attenuation in the dummy was subtracted from that in the hydrogen target. The correction to the correction was relatively small, however. The total "target out" or dummy correction was greatest for the 70-Mev measurement, amounting there to 6.5 mb.

C. Accidentals

In addition to the pulses from the counters, single, randomly distributed, accidental pulses appeared on many of the sweeps. These presumably were caused by the random charged-particle background in the vicinity of the counter telescope. Since an attenuation event could be masked by an accidental pulse appearing at the usual position of a pulse from the rear counter, it was necessary to correct for this effect. The distribution of accidentals was determined from the film; from the portions of the sweeps between the positions of the normal counter pulses the frequency of accidental pulses per cm of sweep could be calculated. It was found necessary to increase the observed number of attenuated pions by about 3 percent at each energy to correct for this effect. The number of pions attenuated in the dummy target was similarly corrected.

D. Muon Flux Correction

The calculated cross section must also be corrected to take into account the fact that (a) the pion beam contained a small fraction of muons of the same pulse height as the pions and (b) the flux of pions through the hydrogen target was reduced by pion decay after the first pulse-height counter.

Calculation of the muon flux correction for muons coming from the region ahead of counter 1 was based on reasonable assumptions as to the variation of pion intensity with distance from the production target and the portion of the total beam area "seen" by the counter telescope. The pion mean life used was $\tau = 2.54 \times 10^{-8}$ sec.[9] This calculation indicated a contamination of about 0.5 percent. The contribution of muons from pion decay in the region of high pion density near the production target was estimated to be negligibly small (<1 percent) on the basis of some experimental data on the number of particles passing through large ranges of Cu. These data were obtained during the integral range measurements of the pion beam energies.

The number of pion traversals was reduced by about 2 percent at each energy by decays after counter 2. Calculation of the correction for decays between the two pulse-height crystals took into account (a) the fact that many of the muons resulting from these decays did not have such a pulse height as to be confused with pions, and (b) the fact that many of the muons that would have had such a pulse height decayed at large enough laboratory angles to miss the second counter altogether.

This muon contamination was assumed to be noninteracting, and the total correction to the flux was between 3 and 3.5 percent at each energy.

V. RESULTS

The measured values for the cross section and the major corrections are given in Table I. Column 1 gives the mean energy of the pions in the target. In the second and third columns appear the attenuation percentages in the liquid hydrogen target and in the dummy target,

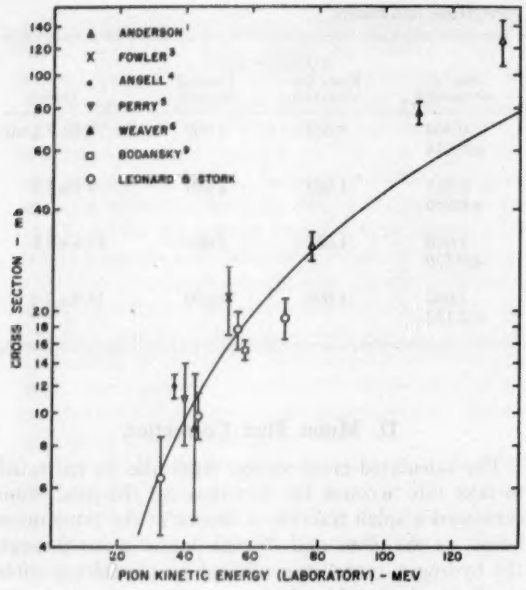

FIG. 6. Experimental values of the total cross section for positive pions in hydrogen as a function of pion energy.

corrected for accidentals. The fourth column lists the corrections for the spurious events caused by pion decay in the counter telescope. The sixth and seventh columns list the correction factors needed to account for the noninteracting muon contamination of the beam and for the fact that the length of path in hydrogen varied for pions in different parts of the beam because of the cylindrical shape of the hydrogen flask. The last column gives the corrected values for the cross section.

Since the rear counter subtended an angle of $\pm 35°$ at the center of the hydrogen target, these values for the "total cross section" refer to the cross section for all interactions except those in which a pion is scattered into an angle within $\pm 35°$ of the pion beam direction.

VI. DISCUSSION OF RESULTS

The total cross section for positive pions in hydrogen has been measured by a number of observers at a variety of energies. The results are displayed in Fig. 6, along with those obtained in this experiment. The measurements at 110 and 135 Mev are those obtained by Anderson, Fermi, Martin, and Nagle[1] from the integration of their measured angular distribution. The measurement shown at 58 Mev is that of Bodansky, Sachs, and Steinberger.[10] This value is believed by these authors to be more reliable than their earlier value, obtained in an attenuation measurement.[2] The value shown at 53 Mev is that of Fowler, Fowler, Shutt, Thorndike, and Whittemore,[3] measured by cloud-chamber techniques. The measurement at 47 Mev is a very recent one by Weaver, Lord, and Orear,[6] using nuclear emulsions. The cross section shown at 37 Mev is the most recent value obtained in an attenuation measurement reported by Angell and Perry.[4] The cross section at 40 Mev was obtained by Perry and Angell[5] by integrating their measured angular distribution. Most of these values represent the cross section for scattering of positive pions at angles larger than some limiting angle determined by the experimental apparatus used. This limiting angle is different for each of the measurements. The cross sections may be compared with little error, however, since the angular distributions of Anderson *et al.*,[1] Bodansky *et al.*,[2] and Perry and Angell[5] show that the scattering cross section at small angles is relatively small.

The curve drawn through the points represents the relation $\sigma = bp'^4/E'^2$ plotted as a function of the pion kinetic energy in the laboratory, T; E' is the center-of-mass total energy of the pion and p' is its center-of-mass momentum. The value of b has been adjusted for least squares best fit to all the data. The above energy dependence is obtained theoretically when the cross section is calculated from second-order perturbation theory, assuming a pseudoscalar pion field and using gradient coupling ($\sigma \cdot \nabla\phi$) to the nucleon. Marshak[11] has performed this calculation in the lowest order perturbation theory, using (a) the complete pseudovector coupling interaction and (b) the pseudoscalar coupling interaction. The result for the pseudovector coupling differs only slightly from the curve shown in Fig. 6. The result for pseudoscalar coupling gives an entirely different energy dependence, the cross section decreasing slightly with energy, in disagreement with the experimental results. The results of these theoretical calculations depend very strongly on the mathematical methods used to obtain them. Recent speculations[12,13] have lent support to the notion that pseudovector and pseudoscalar coupling may give results which are quite similar in this energy range. Nevertheless, the curve shown provides a fairly good fit over a large range of energies, and it seems plausible to infer that gradient coupling is predominant above 30 Mev.

VII. ACKNOWLEDGMENTS

It is a pleasure to acknowledge the advice and encouragement of Professor C. Richman. Several stimulating conversations were also held with Dr. J. Lepore. The experimental technique used in this work was first suggested by Professor H. A. Wilcox while he was at the University of California. We are indebted to Mr. John Garrison for the use of his liquid hydrogen target.

[10] Bodansky, Sachs, and Steinberger, Phys. Rev. **90**, 996 (1953).

[11] R. E. Marshak, *Meson Physics* (McGraw-Hill Book Company, Inc., New York, 1952), pp. 236–245.

[12] S. D. Drell and E. M. Henley, Phys. Rev. **88**, 1053 (1952).

[13] Brueckner, Gell-Mann, and Goldberger, Phys. Rev. **91**, 460 (1953).

The Scattering of 45-Mev Positive Pions by Hydrogen*

JAY OREAR, *Institute for Nuclear Studies, University of Chicago, Chicago, Illinois*

AND

J. J. LORD AND A. B. WEAVER, *Department of Physics, University of Washington, Seattle, Washington*

(Received October 22, 1953)

Standard Ilford G.5 plates were exposed in an improvised 46-Mev external pion beam of the Chicago cyclotron. Scatterings of the pions by the hydrogen in the emulsion were observed by scanning for recoil protons and examining the proton beginnings for an incoming and scattered pion. Energy-momentum conservation permits separation of similar looking nonhydrogen events from the pion-proton scatterings. The average pion energy in the plates was determined to be 45 ± 2 Mev from 15 events where the recoil proton stops in the emulsion. A total cross section of (12 ± 3) millibarns has been obtained from 37 pion-proton scatterings. No scatterings were observed less than 79°. Only four are less than 90°. A phase-shift analysis of the data gives $\alpha_3=-(5.7\pm1.2)°$, $\alpha_{33}=(4.4\pm1.1)°$, and $\alpha_{31}=(2.4\pm1.8)°$. Since these particular phase shifts happen to give very little Coulomb interference, these data do not determine the absolute signs of the phase shifts. Upon comparison of these results with scattering data at other energies, α_3 appears to vary as the first power of the pion momentum and α_{33} with the third power at pion energies less than 80 Mev.

I. INTRODUCTION

FOR pion energies less than 80 Mev, λ is greater than the range of nuclear forces ($r_0=1.4\times10^{-13}$ cm). Pion-proton scatterings in the low-energy region should be simpler to interpret than the higher energy scattering results. For example, in the energy region where $\lambda\gg r_0$, quantum mechanics gives for the phase shift of l-wave scattering:

$$\delta_l\propto\eta^{2l+1}, \tag{1}$$

where η is the pion momentum in units of $M_\pi c$. So far (π^+-p) angular distributions below 80 Mev have been obtained at 53,[1] 78,[2] 58,[3] and 40 Mev.[4]

The earlier scattering results[1,5] indicated that the s-wave phase shift might not behave according to Eq. (1) in the 50-Mev region. The early results of Anderson *et al.*[5] at 110 and 135 Mev gave an increase in α_3 (the s-wave phase shift) much more rapid than the first power of η, and the 53-Mev results of Fowler *et al.*[1] gave a symmetric angular distribution indicating zero s-phase shift at this energy. An explanation for such an anomalous s-wave behavior was given by Marshak[6] by postulating an attractive s-wave interaction with a strong, short-range repulsive core. This would force α_3 to change sign at some intermediate energy. However, the present experiment along with the more recent 40-Mev[4] and 58-Mev[3] results gives strong evidence that α_3 is proportional to the first power of the pion momentum at these energies. If α_3 had changed sign, there would be predominant scattering in the forward direction. In this experiment 33 scatterings were observed greater than 90° and 4 less than 90°. This is an even stronger backward scattering than observed at the higher energies.

These 37 events were fitted by an extended maximum likelihood method described in Sec. IV to give $\alpha_3=-(0.100\pm0.023)$, $\alpha_{33}=(0.077\pm0.020)$, and $\alpha_{31}=(0.042\pm0.035)$. α_{33} is the phase shift for scattering into the $P_{\frac{3}{2}}$ state and α_{31} for scattering into the $P_{\frac{1}{2}}$ state. Because $\eta<1$, states of higher angular momentum are neglected.

The resulting phase shifts happen to give a small nuclear scattering in the region 0° to 60° and thus a Coulomb interference perhaps even smaller than the pure Rutherford scattering. This makes determination of the signs of the phase shifts unfeasible for this energy region.

Details of exposure and beam analysis are given in Sec. II. As described in Sec. III the plates were area scanned under 830× magnification for single proton beginnings. Then each proton beginning was examined for an incoming and scattered pion. Three-pronged events of this type, but not due to hydrogen, were rejected on the basis of two tests: coplanarity of the three prongs, and angular correlation of the two scattering angles to satisfy energy-momentum conservation. The resulting total cross section of 12 ± 3 mb and the corresponding phase shifts are calculated in Sec. IV. The angular distribution is shown in Fig. 2.

II. EXPOSURE

The lowest-energy pions able to escape the field of the Chicago cyclotron are 29 Mev. The channel in the 12-foot iron shield closest to this escape orbit is the channel normally used for external scattered protons. This channel gives pions of 46 Mev according to an absorption curve obtained by using two scintillation counters preceding the absorber and two others following in quadruple and double coincidence. This technique of beam analysis is described in reference 2.

* Supported by the joint program of the U. S. Atomic Energy Commission and U. S. Office of Naval Research.

[1] Fowler, Fowler, Shutt, Thorndyke, and Whittemore, Phys. Rev. **86**, 1053 (1952).

[2] Anderson, Fermi, Martin, and Nagle, Phys. Rev. **91**, 155 (1953).

[3] Bodansky, Sachs, and Steinberger, Phys. Rev. **90**, 996 (1953).

[4] J. P. Perry and C. E. Angell, Phys. Rev. **91**, 1289 (1953).

[5] Anderson, Fermi, Nagle, and Yodh, Phys. Rev. **86**, 793 (1952).

[6] R. Marshak, Phys. Rev. **88**, 1208 (1952).

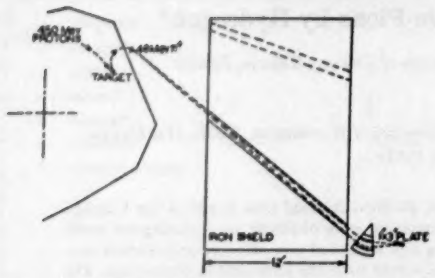

FIG. 1. Experimental setup for obtaining 46-Mev external pi-plus beam using proton channel of the Chicago cyclotron.

Of course a somewhat lower-energy pion beam of less path length could be obtained if a channel were cut as indicated by the dotted lines in Fig. 1. Analysis of the absorption curve gives a value of 81±3 percent for the pion content of the beam used. This value was independently checked by counting grain density of 73 successive tracks over a length of 600μ. The tracks cluster into two groups of grain densities: 13 tracks about an average of 250 grains and 60 tracks at 330 grains. Muon decay electrons gave a value of 177±8 grains. If the lighter tracks are assumed to be muons, this gives a value of 82±5 percent for the pion content.

The beam was carefully collimated to reduce high-energy background protons. The low-energy protons of the same momentum as the pions were filtered out by the Bakelite wall of the plate holder. In an effort to achieve parallel pion tracks the plates were exposed in the vertical plane. In the plates used, 50 percent of the tracks were parallel to within ±2°. The flux of tracks was 4.1×10^5 mesons/cm^2.

III. SCANNING

The scanning technique is exactly the same as that described by one of the authors.[7] At this energy discovery of events is easier than at 120 Mev since all recoil protons are quite heavy and the 45-Mev pions are about twice minimum ionization. Scanning efficiency is estimated to be greater than 90 percent on the basis of a double scanning. The first scanning was accomplished by scanner X whose efficiency was about 80 percent based on 30 of these (π^+-p) collisions. Scanner Z then completely rescanned this area. In no case did scanner Z fail to find an event which was found previously by scanner X. In addition certain test portions of the plate (about 20 percent of the scanned area) were scanned a third time by scanner Y and again all events were seen.

Events which occur near the surfaces of the emulsion, or are close to being straightforward or backward scatterings are somewhat more difficult to see, and are thus excluded from the cross-section calculations, with the appropriate geometrical corrections being made. The regions excluded are those within 15μ of the surfaces of the emulsion, and events where the scattering angle is less than 30° or greater than 160°.

The probability that a nonhydrogen event be counted as a pion-proton collision is very small in this case.[7]

IV. RESULTS

If L_π is the total pion path scanned, n_H the density of hydrogen in the plates, and $dN/d\omega$ the number of events per unit solid angle, then

$$\frac{d\sigma}{d\omega}=\frac{1}{L_\pi n_H}\frac{dN}{d\omega}.$$

The value $n_H=3.34\pm0.1\times10^{22}$ protons/cm^3 is specified by Ilford, where the uncertainty is that due to moisture content of the emulsion. The value $L_\pi=(1.045\pm0.040)\times10^5$ cm is based on flux determination using 1357 tracks. In Table I the region $30°<\chi<160°$ is divided into four regions of equal solid angle, $\Delta\omega=2.84$ steradians. χ is the scattering angle in the center-of-mass system. These four points of the angular distribution are shown in Fig. 2. The corresponding total cross section is 12±3 mb. The error of ±3 mb is obtained by combining the statistical error of 36 events with the uncertainty in total pion track scanned and the uncertainty of scanning efficiency (assumed to be 0.95 ±0.05).

TABLE I. Number of events in four equal units of solid angle.

Limits of χ	30° to 66°	66° to 92°	92° to 119°	119° to 160°
No. of events	0	5	10	21
$(d\sigma/d\omega)\times10^{27}$	<0.13	0.48±0.21	0.96±0.30	2.00±0.55

The following is a list of values of χ for all 37 events observed. Parentheses containing the energy (in Mev) of the incoming pion follow those events in which the recoil proton stops in the emulsion: 79.5° (47.0 Mev), 84, 84.5 (47.2), 87, 92, 97.5 (43.8), 102.5, 111, 113.5, 115(47.2), 115, 116 (49.0), 116, 117.5, 117.5, 121 (47.7), 124(48.6), 126.5, 128.5(43.3), 132, 133.5, 137, 140.5-(45.3), 142, 142.5(48.2), 143(47.8), 145, 145, 146, 148(46.5), 148, 150, 152(46.5), 158(48.1), 158, 160-(38.6), and 162.

A theoretical curve is fitted to these 36 data using a statistically efficient method which makes equal use of each scattering angle. The theoretical form for the differential cross section is given in Eq. (2) which is a close approximation including Coulomb interference when the phase shifts are small.[8]

$$f(\chi)=\lambda^2\left[\alpha_3+(2\alpha_{33}+\alpha_{31})\cos\chi-\frac{e^2}{2\hbar c\beta}\frac{1}{\sin^2\frac{1}{2}\chi}\right]^2+\lambda^2(\alpha_{33}-\alpha_{31})^2\sin^2\chi. \quad (2)$$

[7] Jay Orear, Phys. Rev. 92, 156 (1953).

[8] J. Ashkin and L. Smith, "Coulomb Interference Effects in the Scattering of Mesons by Protons," Technical Report No. 1, Carnegie Institute of Technology, Feb. 2, 1953 (unpublished).

The maximum-likelihood method was used to obtain the phase shifts and their errors. According to statistics, no other method of analysis can give the phase shifts with greater accuracy in the limit of large N.[9]

The relative probability that N events be found at N scattering angles χ_i is

$$P=\exp\left\{-n_H L_\tau \int_{30°}^{160°} f(\chi)d\omega\right\}\prod_{i=1}^{N} f(\chi_i). \quad (3)$$

The maximum-likelihood theorem states that the best values of the phase shifts are those which maximize P. The theorem also states that the standard deviation in the value of α so obtained approaches the minimum possible error:

$$[\langle(\Delta\alpha)^2\rangle_{Av}]^{\frac{1}{2}}=\left[\int f d\omega \Big/ N\int f^{-1}(\partial f/\partial\alpha)^2 d\omega\right]^{\frac{1}{2}}. \quad (4)$$

The error ellipsoid in the three-dimensional space of α_3, α_{33}, and α_{31} was calculated using expressions of the form of Eq. (4). The extreme points of this ellipsoid in the α directions were taken as the errors in the α's. These calculations were made assuming both sets of signs for the phase shifts. For repulsive s-wave the calculations gave $\alpha_3=-0.100\pm0.023$, $\alpha_{33}=0.077\pm0.020$, and $\alpha_{31}=0.042\pm0.035$. The attractive s-wave calculations gave $\alpha_3=0.133\pm0.021$, $\alpha_{33}=-0.057\pm0.020$, and $\alpha_{31}=-0.045\pm0.035$. The two curves are plotted in Fig. 2.

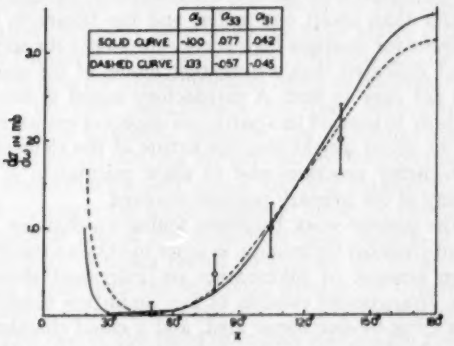

FIG. 2. $d\sigma/d\omega$ in mb/sterad corresponding to dividing the data into four equal units of solid angle. The solid curve is the best-fit theoretical form assuming repulsive s wave. The dashed curve is the best fit assuming attractive s wave.

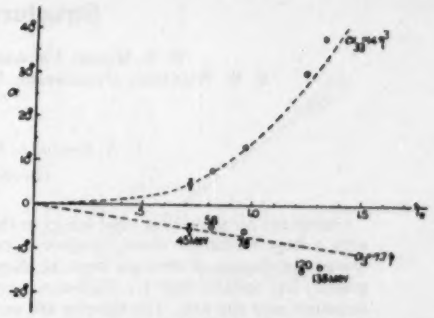

FIG. 3. α_3 and α_{33} vs η of the pion in the center-of-mass system. Present 45-Mev results are plotted along with those of 58 Mev (see reference 3), 78 Mev (see reference 2), 120 Mev (see reference 2), and 135 Mev (see reference 2).

V. CONCLUSIONS

The quantity P in Eq. (3) is proportional to the probability that the experiment turn out as it did given $f(\chi)$. In this experiment the ratio of the two P values corresponding to the two sets of phase shifts is 1.4 in favor of the repulsive s-wave. Thus whether one assumes attractive or repulsive s-wave, the probability of the experiment turning out the way it did is about the same. This is because α_{33} is close to $-1/2\alpha_3$ and according to Eq. (2) there should be almost no interference term. For this reason it is extremely difficult to determine the signs of the phase shifts from Coulomb interference in this energy region. Determination of the signs of α should be possible using this plate technique at higher energies. Preliminary results on 120-Mev π^+ tend to favor repulsive s-wave.[10]

The values of α_3 and α_{33} are plotted vs η in Fig. 3 along with the values obtained by others. It appears that for data below 80 Mev α_3 can be fitted quite well by $\alpha_3=-7.7\eta$ and α_{33} by $\alpha_{33}=14\eta^3$ in degrees. This good fit helps verify both Eq. (1) and the results of others.[3-4]

We wish to acknowledge the scanning done by Miss Irene Kubota and Mr. Paul Hodge at the University of Washington and by Mr. William LaMere at the University of Chicago. Dr. Frank Solmitz and Mr. George Backus at the University of Chicago helped with the statistical analysis and calculations. In addition we are indebted to Professor Enrico Fermi for many helpful discussions.

[9] We are indebted to Mr. George Backus at the University of Chicago for proving that the maximum-likelihood theorem may be extended to a probability function of the form in Eq. (3).

[10] Jay Orear, Bull. Am. Phys. Soc. **28**, No. 6, 14 (1953).

Structure of Air Showers*

W. E. HAZEN, *University of Michigan, Ann Arbor, Michigan*
R. W. WILLIAMS, *Massachusetts Institute of Technology, Cambridge, Massachusetts*
AND
C. A. RANDALL, JR., *Ohio University, Athens, Ohio*
(Received August 10, 1953)

Cosmic-ray air showers of total energy in the range 10^{14} to 10^{15} ev have been studied at 3260-m elevation with a large multiplate cloud chamber in combination with five thin-walled ionization chambers. The spatial distribution of electrons near the shower axis is usually a smooth function of distance with a singularity less marked than $1/r$. Evidence is presented, however, to show that some showers have a lumpy structure near the axis. The showers are very poor in high-energy electrons and photons near the axis, relative to the expectation for a single electron-photon cascade. The angular distributions of shower axes are found for various shower sizes and prove to be quite similar to those expected for single electron-photon cascades. The implications for various shower models are discussed and a fairly extensive nucleonic cascade is indicated.

I. INTRODUCTION

COSMIC-RAY events of very high energy have been studied in three stages of development: the initial interaction, which is explored with emulsion techniques;[1] the resulting cascades near their maximum development; and the residual high-energy μ mesons, which are studied in underground experiments.[2] The low absolute rate of these events limits the emulsion techniques to about 10^{13} ev, and the underground observations to about 10^{15} ev, so that the highest energy events can be studied only at their full development, where their large spatial extension increases the effective observing area; the practical energy limit at this stage has so far been about 10^{17} ev.[3,4]

The general features of these cascades near their maximum have been clarified in a number of studies, by use of counter trays and hodoscopes,[5] ionization chambers,[3,6] and cloud chambers.[7] The charged particles present are about 98-percent electrons, and the lateral distribution-in-space of these electrons largely agrees with the calculation of Molière[8] which is based on a simplified model of a pure electron-photon cascade. However, several experiments[3,7,9] have yielded evidence that the density of electrons within a meter or so of the shower axis does not show the steep rise expected from the Molière theory. This fact is not surprising since one is presumably dealing with several superposed cascades, each well past its maximum. Nevertheless, the agreement with Molière's calculations, for distances greater than about one meter, and the failure to find evidence for multiple high-energy cores near the shower axis,[7] indicated that a consistent model of the shower was not easy to find. A satisfactory model is needed, not only to unravel this particular aspect of cosmic rays, but to afford insight into the nature of the elementary high-energy processes and to allow calculation of the energy of the primary particle involved.

The present work combines ionization-chamber and cloud-chamber techniques, in order to obtain a relatively large amount of information on individual showers. The arrangement consists of five ionization chambers, in a three-by-five meter area, and a cloud chamber of 0.2 m² effective area located near the center of the ionization-chamber array. The ionization chambers afford a measure of the density of charged particles at five points in a shower, and the cloud chamber gives observations of the spatial distribution of particles in the chamber, their angular inclination, and, by means of five lead plates in the chamber, the energy of the more energetic electrons and photons. This information is available for each shower; for those showers whose axes were close enough to the apparatus one could specify the size and location of the shower.

Data will be presented on the nature of the shower near its axis, the high-energy electron-photon component of the shower, and the angular distribution of showers of a given size.

The experiments were carried out at Echo Lake, Colorado, at an altitude of 3260 m.

II. APPARATUS

The use and calibration of thin-walled pulse ionization chambers for measurement of particle density in air showers is discussed in reference 3. In the present investigation the equipment was very similar, with

* Assisted by the U. S. Office of Naval Research and the U. S. Atomic Energy Commission.

[1] Kaplan, Ritson, and Walker, Phys. Rev. **90**, 716 (1953); Lal, Pal, Peters, and Swami, Proc. Indian Acad. Sci. **36**, 75 (1952); Lord, Fainberg, and Schein, Phys. Rev. **80**, 970 (1950).

[2] Barrett, Bollinger, Cocconi, Eisenberg, and Greisen, Revs. Modern Phys. **24**, 133 (1952); George, Mac Anuff, and Sturgess, Proc. Phys. Soc. (London) **A96**, 345 (1953).

[3] R. W. Williams, Phys. Rev. **74**, 1689 (1948).

[4] Cocconi, Tongiorgi, and Greisen, Phys. Rev. **76**, 1020 (1949).

[5] K. Sitte, Phys. Rev. **87**, 344 (1952), in which other references are given.

[6] I. D. Campbell and J. R. Prescott, Proc. Phys. Soc. (London) **A65**, 258 (1952).

[7] W. E. Hazen, Phys. Rev. **85**, 455 (1952).

[8] G. Molière, *Cosmic Radiation* (Dover Publications, New York, 1946).

[9] J. M. Blatt, Phys. Rev. **75**, 1584 (1949), discusses the implications of Williams' results.

larger ionization chambers (area 0.079 m²) filled to a higher pressure, so that the available range of measurement was extended to lower particle densities. The lower limit which was set on pulse height, one millivolt (see reference 3), corresponded to 187 particles per square meter or 15 particles passing through the chamber if the shower is near the vertical.

The cloud chamber is described in reference 7. The effective area of observation was 25×80 cm (0.2 m²), and the chamber contained five lead plates, the top one ½ in. thick, the others 1 in. thick. The top of the chamber was ½ in. of dural, and material over the chamber was one inch of Celotex.

Figure 1 shows two views of the experimental arrangement: four of the ionization chambers form the symmetrical arrangement used in reference 3, but with three chambers on a circle of radius 1.27 m and the fourth at the center. The cloud chamber is as near the center of the circle as possible, and the fifth ionization chamber is out beyond the cloud chamber, 3.62 m from the center.

The ionization-chamber pulse heights were recorded photographically whenever any two of the four closely-grouped chambers simultaneously gave pulses greater than 1 millivolt (equivalent to 187 particles/m²), the resolving time for this coincidence being 20 microseconds. Since fourfold coincidences on the photographic record were ultimately required, the accidental coincidences were nil. During the first part of the experiment the same criterion (any two of the four chambers) was used to trigger the cloud chamber; however, there was appreciable loss of cloud-chamber time because of its five-minute recycling period, so that for the latter part of the experiment the selection criterion for triggering the cloud chamber was changed: the triggering event was any two of the three chambers which were closest to the cloud chamber. It was hoped in this way to eliminate from the cloud-chamber pictures some of the small distant showers which yield very little information.

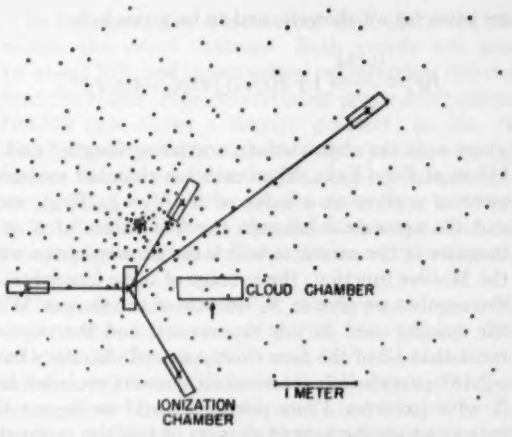

FIG. 1. Plan view of the experimental arrangement, showing the effective areas of the ionization chambers and cloud chamber. The plane of the ionization chambers is actually one meter above the central plane of the cloud chamber. The direction of photography is indicated by an arrow. The dots illustrate schematically the expected spatial distribution of electrons in a cascade whose core struck near the apparatus. For a shower of $N=10^8$ electrons each dot should represent 100 electrons.

III. DETERMINATION OF POSITION AND SIZE OF INDIVIDUAL SHOWERS

(a) Method

Reference 3 discusses the method and assumptions under which a few isolated measurements of particle density, in a shower, can be used to determine the center of the shower and the total number of particles in it. We must assume that the particle density in the shower falls off monotonically as we proceed away from the axis of the shower; then simultaneous observations at a sufficiently large number of points would allow a complete determination of the size and location of the shower and of its lateral structure in the plane of observation. Actually, we have only five density measurements available for each shower and must therefore *assume* a lateral structure function for all showers. In this way we determine whether the assumed function is consistent with all the showers we observe; if it is consistent, then the ionization chamber data give the position and size of each shower that strikes nearby and a lower limit to the size of showers that strike farther away.[10a]

We have assumed the lateral distribution function calculated by Molière and located the centers of the showers by the method of intersection of lines of constant particle-density-ratio discussed in reference 3. In agreement with previous work[3,4] the Molière distribution proves to fit the data fairly well, with certain exceptions which will be noted in Sec. IV. The accuracy of location of the axis of an individual shower varied from perhaps ±20 cm for the most favorable close-in cases to about two meters for those which struck four or five meters from the center of the circle. Showers which struck farther away than about five meters, or even less in some unfavorable cases, could not be located, and only a lower limit was assigned to their size. In order to ascertain the size of those showers whose axes can be located, we note that the particle density at a distance r from the axis of the shower is given, according to Molière, by $\rho(r)=Nf(r)$, where N is the total number of charged particles (here assumed to be all electrons) in the shower at this stage in its development, and $f(r)$ is the function describing the structure of the shower, which we assume to be

[10a] *Note added in proof.*—G. Cocconi has pointed out that the earth's field broadens the shower distribution in an E-W direction, in our case by a factor of about 1.45. Since we force a fit to a symmetrical distribution, our locations and shower sizes will have a somewhat larger error than we have here assigned to them.

the same for all showers, and to be given by[9]

$$f(r)=\frac{0.454}{r/r_1}[1+4(r/r_1)]\exp[-4(r/r_1)^4],$$

where r_1 is the characteristic scattering length,[8] and is 115 m at Echo Lake. Then each ion chamber measurement of ρ gives us a value of N, $N_A=\rho_A/f(r_A)$, etc.; and the agreement between the five values of N is a measure of the extent to which the shower agrees with the Molière function; the average of these five values is the number we give as N, the size of the shower. With the spacing used in this experiment, and the requirement that all of the four closely-spaced chambers have $\rho\geq 187$ particle/m^2, the smallest showers recorded had $N\sim 10^5$ particles. From previous work[3] we expect the rate at which the axes of showers of this size or greater arrive at a given point to be 0.05 per square meter per hour, so that we cannot expect more than about one event per week of this size in which the core passes directly through the cloud chamber, and must therefore rely mainly on observations of showers whose cores struck near rather than in the cloud chamber.

The lower limit on shower size, and therefore upper limit on rate of arrival of showers, is set by statistical fluctuations in the number of particles actually traversing the ionization chambers. With a limit corresponding to 15 particles, one expects a fractional standard deviation in the particle density of $1.04/\sqrt{15}=0.27$,[10b] and one cannot afford a larger error.

(b) Results and Discussion (the Lateral Distribution Function)

A total of 260 showers was examined, of which about 45 percent struck close enough to be analyzed; of these, 80 percent fit the Molière distribution within the rather large statistical errors. This indicates that even as close as 1 to 3 meters from the axis of a shower, the $1/r$ variation describes the density of charged particles fairly well. However, by considering a chart of the locations we have assigned to these showers, one can see that a systematic discrepancy exists. Figure 2 shows such a chart (all of the showers are shown in one sextant of the circle); the number of showers should increase steadily as one appraoches the center of the circle since the required minimum shower size goes down (see reference 9), but instead we find a blank space at the center of the circle, and another, less pronounced, around that ionization chamber on the circumference of the circle which is closest to the shower axis (labeled "A" in the figure). Clearly the showers whose axes were too close to an ionization chamber have been mislocated because the particle density at the ionization chamber was not as large as the Molière function would predict.[11] The true distribution function, therefore, must be considerably flatter, within about ½ meter of the axis, than the Molière function. This observation agrees with Blatt's analysis[9] of Williams' data,[3] and with Campbell and Prescott's sea-level results[6] on showers of about the same size. It is hard to draw a very definite conclusion from the observation since at least three questions are raised: (1) whether the Molière approximate treatment is correct even for a shower at its maximum; (2) the extent to which the shower is flattened out because it is past its maximum; (3) the number and distribution of the individual showers which presumably originate from the gamma rays from π^0-mesons and overlap to give the observed shower. The effect of "age" of the shower on the distribution near the core (that is, the extent to which an individual shower is past its maximum) has been calculated by Nishimura and Kamato[12] in an approximation similar to that of Molière; they find that the singularity at the core of a shower should go as $1/r^{2-s}$, where s, the "age" parameter, is 1 at the shower maximum and increases slowly as the shower maximum and increases slowly as the shower progresses. For a size of shower slightly smaller than the average observed in this experiment, assuming that the showers start at a depth of 100 g cm^{-2} in the atmosphere, we find that the vertical showers would have $s\approx 1.08$, while those at 40° from the vertical (where the intensity is down by more than a factor of four) have $s\approx 1.24$. The comparable numbers if we assume an initial multiplicity of 20 (i.e., it is assumed that we are observing 20 overlapping showers at once) are $s\approx 1.24$ for vertical, $s\approx 1.32$ for 35°. Thus the average value of s is probably somewhere between 1.2 and 1.3, and the strength of the singularity at the axis of the shower is accordingly reduced.

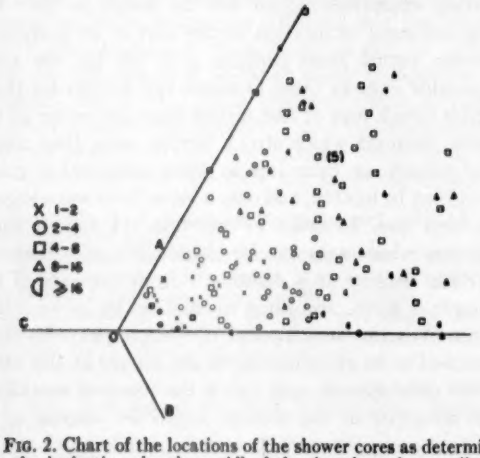

FIG. 2. Chart of the locations of the shower cores as determined by the ionization chambers. All of the data have been collected into one sextant. The size of each shower, in units of 10^5 electrons, is indicated by the legend.

[10b] The factor 1.04, which takes into account the cylindrical shape of the chambers, was incorrectly given in reference 3 as 1.5.

[11] The finite size of the ionization chamber has a similar effect; that is, it causes a mislocation of close-by showers but over a much smaller area than the one exhibited by Fig. 2.

[12] J. Nishimura and K. Kamata, Progr. Theoret. Phys. Japan 5, 899 (1950).

The effect of the spread in space and variation in size of the individual showers in a multiple-production model is hard to estimate although it seems clear that a reduction of the singularity near the axis should result. Hazen, Heineman, and Lennox[13] have applied the Fermi theory of high-energy meson production to the problem and find that the cores should be spread out over a region of 1 to 10 meters unless one assumes an unreasonably large primary energy for a shower of a given size. Such a large spacing of cores would appear to be incompatible with most of the observed showers.

Some of the showers simply do not fit the Molière function. If we define a satisfactory fit to be one in which all chambers give values of N less than 40 percent from the average, then out of 39 showers which struck close to the apparatus, 8 do not fit. This may be compared with the work of reference 3, in which the spacing of the ionization chambers was much larger and which has no bad fits out of 28 showers. Examination of the 8 cases suggests that the particle density was irregular rather than merely flattened in the middle. This interpretation is strengthened by sea level observations.[14]

To summarize, most showers seem to be regular except for some flattening within ~0.3 m of the core. The remainder of the showers appear to be "bumpy" within a meter or so of the core.

We have examined the question of the extent to which the flattening of the distribution function will cause systematic errors in our prediction of the distance of the shower axis from the cloud chamber and found the effect to be small. Also our estimate of the total size of the shower will not be much affected since the part of the shower within 1 meter of the core contributes (according to Molière) only 3 percent of the total number of electrons.

Showers that struck near the observation plane of the cloud chamber and within about one meter of either end of the chamber should display a detectable variation in particle density from one end to the other, according to the Molière distribution; the observed density should vary by nearly a factor of two even when the finiteness of detecting areas is taken into account.

There were 12 events for which such density variations were expected. Only one event shows a marked variation in density and in that case there is a maximum within the chamber, the maximum coinciding with a concentration of high-energy rays. The ion-chamber data, however, locate this particular shower axis about one meter from the peak observed in the cloud chamber. Another event, in which the axis determined by the ion chambers is 25 cm beyond the *left* end of the cloud chamber, displays a concentration of high-energy rays at the *right* end of the cloud chamber.

In two cases the ion-chamber data place the axes within the cloud chamber. Both events are small (N about 10^5), and the statistical uncertainties therefore result in rather large uncertainties in the axis position. Neither case shows a density gradient; in one, the cloud-chamber sample contains only rays of low energy, and we therefore believe the ion chamber samples give a misleading axis position; in the other, there were rays up to $E=5\times10^9$ ev in the cloud chamber, but one expects higher energies if the axis is really within the chamber.

Thus, the cloud-chamber observations generally confirm the conclusions from the ion-chamber data that the Molière distribution is too peaked near the axis and that distributions that are "bumpy" sometimes occur. However, the statistical uncertainties in the location of the axis of individual showers, particularly the smaller ones, make it desirable to use a method of analysis that includes a larger proportion of the available data. This is done in the next section.

IV. DETERMINATION OF THE NUMBER OF HIGH-ENERGY RAYS

(a) Method

The cloud chamber enables us to observe other details of the shower structure, at distances from the axis that are determined by the ion-chamber data, for example, the hardness of the energy spectrum. As a measure of the hardness of the energy spectrum we choose $R\equiv\rho(r,10^9)/\rho(r,o)$, where the second parameter in each set of parentheses is the lower limit of energy. Because of the large number of tracks in the top section of the chamber, it was essentially impossible to distinguish between photon and electron initiators for the showers produced in the lead and thus $\rho(r,10^9)$ refers to the density of electrons plus photons of energy $>10^9$ ev.

The dural top certainly has negligible effect on $\rho(r,10^9)$ but perhaps not on $\rho(r,o)$. Heineman[15] has treated the transition effect for one inch of dural numerically using the energy spectra of Richards and Nordheim[16] and the lateral distribution functions of Eyges and Fernbach.[17] He found that the electrons increase by a factor that is about two for $r<2$ or 3 meters and that decreases to 1.3 at 10 meters. Since one inch of dural constitutes only 0.3 radiation unit, we should not expect the transition effect to depart drastically from a linear dependence on thickness for smaller thicknesses; thus a linear interpolation was used to obtain the transition effect.

The energy of the photons and electrons was determined from the showers that they produced in the lead plates. The criterion for energy greater than 10^9 ev

[13] Hazen, Heineman, and Lennox, Phys. Rev. 86, 198 (1952).
[14] R. E. Heineman and W. E. Hazen, Phys. Rev. 90, 496 (1953).
[15] R. E. Heineman, Ph.D. thesis, University of Michigan, 1953 (unpublished).
[16] J. A. Richards, Jr. and L. W. Nordheim, Phys. Rev. 74, 1106 (1948).
[17] L. Eyges and S. Fernbach, Phys. Rev. 82, 23 (1951).

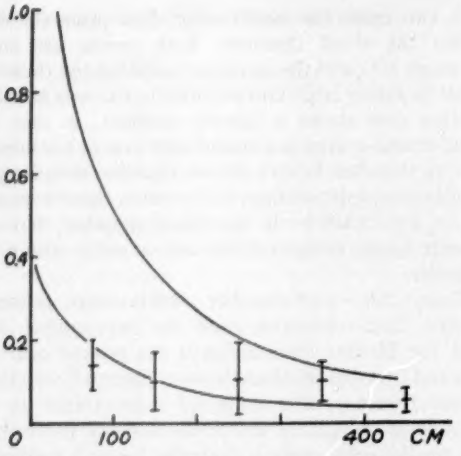

FIG. 3. The observed number of electrons and photons of energy $>10^9$ relative to the number of electrons of all energies as a function of the distance from the shower axis. The upper curve is calculated for a single-electron model with $s=1$, the lower curve with $s=1.5$.

was that a shower with a maximum of more than 10 electrons be produced. It is believed that the film-reading criteria were such that the proportion of high-energy rays was not underestimated. It is possible to overestimate the number of high-energy rays in showers entering at an angle from the front or back unless one ignores showers starting in the second and succeeding lead plates. This procedure results in a slight underestimate of the true number since a few events that actually pass through the top plate do not develop strongly until the second plate. The difficulty was minimized by the large area and close spacing of the plates, and furthermore a third photograph, taken at nearly 90°, allowed a good determination of the forward-backward angle in most cases.

(b) Results and Discussion

The results are shown in Fig. 3. The flags represent the rms deviation from the mean and probably give a good representation of the uncertainty.

The expected energy distribution was obtained by utilizing approximation A of shower theory[18] in order to determine the total number of electrons or photons with $E>10^9$ ev at a given depth and by utilizing the lateral distribution functions of Eyges and Fernbach[17] in order to determine the lateral distributions. Since most of the electrons and photons with $E>10^9$ ev have energies $<10^{10}$ ev, approximation A should be very good as long as the initiating energy $E_0>10^{11}$ ev.[18] The accuracy of the lateral distribution functions is more difficult to estimate. For electrons of all energies, we use the usual results of approximation B in order to obtain the number and the Molière distribution to obtain the spatial distribution. The former should be fairly accurate for air, and the latter agrees moderately well with experiment. The results are shown in the upper curve of Fig. 3.

We have assumed that the showers were at their maxima. If a shower is to be at its maximum and we let its origin be at 100 g/cm², there results $E_0\simeq10^{15}$ ev and $\Pi\simeq10^6$ particles, which is the size of the larger observed showers. However, the next step toward a realistic model is to assume a multiplicity in the shower initiators. One result would be a reduction in E_0 with a consequent increase in age at the observation level *if* we assume that the major contribution comes from the first generation. The predicted effect of age was investigated by using the usual results of shower theory again to determine the relative number of high energy particles and the results of Fernbach[19] to determine the lateral distribution of electrons at $s=1.5$. (The choice of $s=1.5$ is based on available calculations and not on the belief that the showers are so old.) It was assumed that the photon lateral distribution changes by the same factors as the electron distribution as s goes from 1 to 1.5. The results are presented in the lower curve of Fig. 3.

It is seen that the experimental evidence seems to favor old showers *if we assume* that the axes of the constituent showers are separated no more than about 100 cm. With $s=1.5$ and again assuming an origin at 100 g/cm², we obtain $E_0=3\times10^{11}$ ev and $\Pi=100$ electrons. Thus a multiplicity of 10 000 would be required to obtain the same shower size as before, i.e., $N=10^6$. This multiplicity is far removed from the Fermi multiplicity of ~30 that one believes to be about right since it agrees quite well with emulsion observations at lower energies. However, the showers need not be so old in order to give tolerable agreement with the observations, e.g., with $s=1.25$, $E_0\simeq10^{13}$, $\Pi\simeq5\times10^3$, and the multiplicity becomes 200. Furthermore, the expected finite angles of emission of the π^0 mesons with consequent lateral scatter in the shower axes will also reduce the predicted proportion of high-energy rays.

The next step would be to include the effect of later generations in the nuclear cascade. It seems very likely that a sizable contribution is made by cascade components that originate in later generations. Qualitatively, there are two opposing effects on s and hence on R: the over-all multiplicity is increased, thus effecting a decrease in the average energy; the origins of the individual cascade initiators are brought closer to the observation level. We might therefore expect little change in the average value of s as compared with the one-generation model. Moreover, the difficulty concerning multiplicity noted in the preceding paragraph will be ameliorated since only a few generations, with the slowly varying Fermi multiplicity at each generation, will suffice to give the required large overall multiplicity. We shall consider this model in more detail in Sec. VI.

[18] B. Rossi and K. Greisen, Revs. Modern Phys. **13**, 240 (1941).

[19] S. Fernbach, Phys. Rev. **82**, 288 (1951).

There is some indication from the data that the large showers consist of electron-cascade components that are younger on the average than for the smaller showers (as expected): the average R for $N<10^6$ is 0.10; for $N>10^6$, it is 0.16 with an uncertainty of about 0.05 in either case.

V. THE ZENITH ANGLE DISTRIBUTION

(a) Method

Previous observations of zenith angle have involved some sort of average over showers of various sizes with the weighting factor determined by the detecting system. In the present case, we can obtain zenith angle distributions for particular local shower sizes, and thus we expect to be able to place more severe restrictions on a shower model than was possible heretofore.

The projected angle as seen by one lens was determined by aligning a grid of parallel lines with the tracks in the top of part of the chamber. In the cases where the angle varied detectably from one side of the chamber to the other, the mean of the two extreme angles was used, and this was checked by a measurement of the angle at the center. The uncertainty was judged to be a few degrees in most cases and was attributable to the breadth of the distribution in angles of the individual electrons. When there were high-energy rays, the axes of their local showers provided a further check on the angle.

TABLE I. Mean projected angle as a function of shower size.

Classification of event	Number of events	Mean projected angle
Density at cloud chamber		
<500 particles/m²	197	15.5°
>500 particles/m²	69	13.1°
Shower size		
$1\times10^5<N<5\times10^5$	59	15.7°
$5\times10^5<N<10\times10^5$	50	15.2°
$10\times10^5<N(\bar{N}=24\times10^5)$	33	18.8°

It was found that most showers with a local density ≤ 200 particles/m² had such a broad distribution among the individual electrons that the angle could not be determined within 10°. These events proved to be distant hits by showers whose sizes could not be determined anyway.

The observed angles were used to renormalize the ion-chamber determination of shower size where necessary.

(b) Results and Discussion

The data were divided according to shower size into three groups with results that are partly indicated in Table I. Since the distributions for the two smaller shower ranges are indistinguishable, the data have been combined in the graph of Fig. 5 whereas Fig. 6 is a graph for the largest showers.

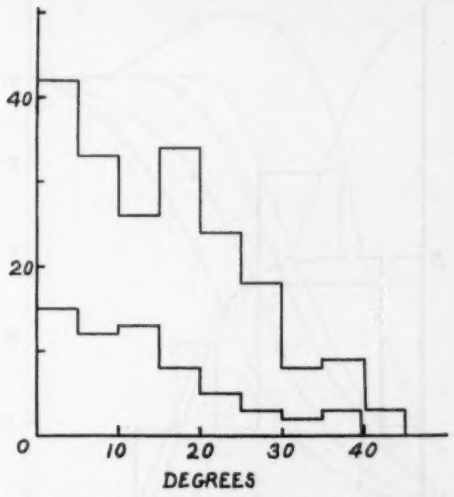

FIG. 4. The observed projected zenith-angle distributions for local densities at the cloud chamber <500 m^{-2}, higher distribution, and >500 m^{-2}, lower distribution.

The angular distributions for showers of a given local *density* determined by the cloud-chamber sample alone, are given for the sake of comparison; these data include events triggered by GM counters as well as by the ion chambers. The distributions are plotted in Fig. 4.

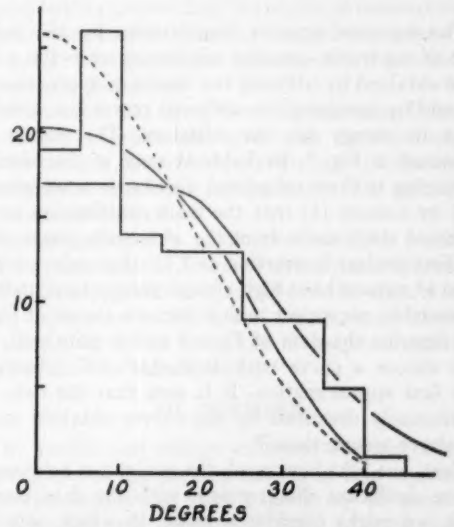

FIG. 5. The observed projected zenith-angle distribution for showers of size N between 10^5 and 10^6. The dotted curve is obtained from a nuclear cascade model and is practically independent of shower size in this range. The solid curves are for a single electron model with $\Pi=10^5$, peaked curve, and 10^6, flat-topped curve. The curves are space-angle distributions but can be compared directly with the observed distributions. They are normalized to the observed total number of events.

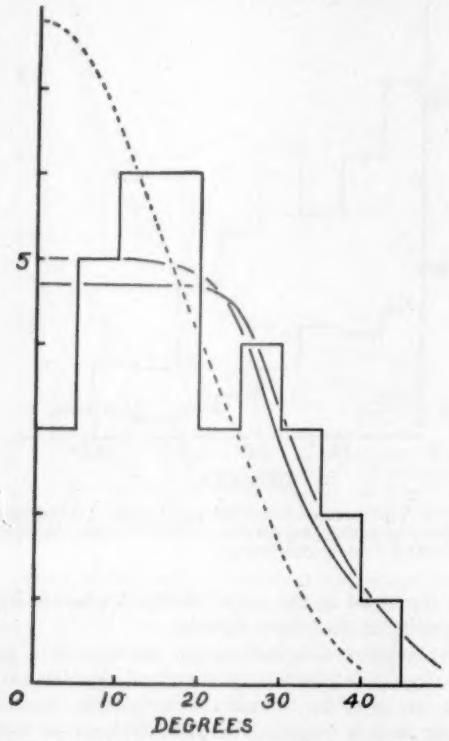

FIG. 6. Same as Fig. 5 with $N>10^6$ (average $N=2.4\times10^6$), $\Pi=10^6$ (solid curve with higher peak), and $\Pi=3\times10^5$ (solid curve with lower peak).

The expected angular distributions for the simple case of electronic cascades originating at $\sim$100 g/cm^2 were obtained by utilizing the results of approximation B[18] and by assuming two different power law distributions in energy for the initiators. The results are presented in Fig. 7. In Table II some of the numbers pertaining to these calculated distributions are given.

If we assume (1) that the main contribution to the observed electrons is from the π^0 mesons produced in the first nuclear interaction and (2) that only a few of these π^0 mesons have high enough energy to contribute appreciably, we expect to find that the curves of Fig. 7 will describe the data of Figs. 5 and 6 quite well. We then choose a curve with $\Pi(E_0,0,t,\theta)=N$ (observed) as a first approximation. It is seen that the data are satisfactorily described by the curves obtained under the above assumptions.[20]

Next, one asks how much the model can be changed before significant disagreement with the data occurs. First, we might consider a model in which only the first generation contributes appreciably. The effect of multiplicity of π^0-meson production can then be approximated by simply choosing a curve with $\Pi=N/2m$ (where m is the multiplicity of π^0 mesons) for comparison with the data. Actually, since there is no rapid variation in shape of the angular-distribution curves in these energy ranges, the mean angle may be used as a single parameter that characterizes a distribution with sufficient accuracy for the present purpose. We find that the observed angular distribution for $N=10^5$ to 10^6 is described by the calculated distributions for $\Pi=5\times10^4$ to $\Pi=7\times10^5$, where the two values of Π come from the limits on the mean angle imposed by the observed breadth in its distribution. The mean value of N was 5×10^5 and, therefore, we find that m, the multiplicity of π^0 mesons, would be in the range $\frac{1}{2}$ to 5. Similarly, for the showers with $N>10^5$, the multiplicity would be $\frac{1}{4}$ to 5, since Π from 5×10^5 to 5×10^6 agrees with the observations.

VI. EFFECT OF NUCLEAR CASCADE

An inconsistency must now be admitted: the local energies (Part IV) have indicated a high multiplicity of electron cascade initiators whereas the angular distributions have indicated low multiplicities. The difficulty, of course, probably lies in the simplicity of the assumption of a one-generation, equipartition model. It is impossible to better the situation by altering the energy spectrum of π^0 mesons since any changes that aid the explanation of the local spectrum hinder the explanation of the angular distribution. Thus it seems necessary to assume that later generations play an important role. The problem of explaining the observations is one of separating the function of energy transport from that of electron shower formation. Thus it becomes possible, in principle, to obtain (a) the penetration dictated by the angular distribution observation by utilizing the N-component cascade as the principal energy carrier and (b) the "old" average age required by the observation of the local-energy distribution by a suitable choice of the cross sections for production of secondaries.

In order to see what sort of general effect the nuclear cascade might have, a simplified model based on the following assumptions was used: (1) the multiplicity for both primary and secondary collisions is that given by Fermi, (2) all the energy is shared equally by the secondaries, (3) one-third of the secondaries are π^0

TABLE II. "Primary" energies contributing to a given local shower size and the mean zenith angle on a single electron cascade model. Π is the total number of electrons at a vertical depth of 16 units and E_0 is the primary energy.

Π	E_0/e 0°	40°	θ
3.2×10^4	4.9×10^8	1.4×10^8	13.5
1×10^5	1.32×10^8	3.4×10^8	15.0
3.2×10^5	3.8×10^8	8.5×10^8	16.0
1×10^6	1.3×10^7	2.2×10^7	17.5
3.2×10^6	3.8×10^7	6.3×10^7	19.0
1×10^7	1.5×10^8	1.8×10^8	22.0

[20] It should be noted that we are comparing space-angle calculations with projected-angle observations. J. Daudin [J. phys. et radium 6, 302 (1945)] points out that there need be no distinction when the distributions can be tolerably well represented by $\cos^n\theta$.

mesons, (4) all the other secondaries interact at the end of 100 g/cm², and (5) all the interacting secondaries have a probability of decay corresponding to π mesons.

Experimental results[1] at lower energies confirm the essential correctness of (1); (2) is certainly wrong in the assumption of equipartition and seems to be wrong in the assumption of complete inelasticity;[21] (3) is unknown at high energies but is probably not far wrong;[22] (4) is a simplification that does not affect the results greatly because of the large average number of mean free paths to the observation level; and, finally, (5) gives an admittedly rough estimate of the rate of removal of energy from the beam that produces π^0 mesons, an estimate which is too high because of elasticity and the creation of nucleon pairs.

The effect of the production of intermediate-mass particles is even more difficult to predict because of lack of knowledge of the fraction produced and lack of knowledge of how much decay energy is lost to μ mesons and how much goes to gamma rays [Bridge, Courant, de Staebler, and Rossi, Phys. Rev. **91**, 1024 (1953),

TABLE III. Detailed results from the nuclear cascade model. $N=7.3\times10^5$ electrons from the vertical for a primary proton of 1.5×10^{15}-ev energy. A single electron primary would require about one-half this energy.

Generation	1	2	3	4	5	6	7
Depth (g/cm²)	100	200	etc.				
No. of π^0 mesons	0	12	160	890	1450	550	
Contribution to electrons at 700 g/cm²	0	2.8×10^5	1.9	1.8	0.7	0.1	
No. of "N rays"	1	36	480	3160	10^4	10^4	3000
No. decaying to μ mesons	0	0	0	460	6000	9300	3000

have found evidence that at least some of these particles have gamma rays among their decay products].

The angular distribution obtained with the above model does not change appreciably with N. The results are shown in Figs. 5, 6, and 7. It is seen that the distribution is indistinguishable from that for a single electron model of low energy, *viz.*, $\Pi=3.2\times10^4$. The mean angle is, therefore, 14 degrees. Thus, this model gives an angular distribution that does not seem to agree with the data at all. As mentioned previously, the fraction of secondaries that can be lost through decay has been overestimated because it was assumed that no energy is carried by nucleons. If less of the energy is carried by mesons, the angular distribution will be flattened since decay is more likely at large zenith angles than at small zenith angles.

Another result of the model that lends support to the belief that the rate of loss to μ mesons is too high is demonstrated by the predicted proportion of μ

[21] K. Greisen and W. D. Walker, Phys. Rev. **90**, 915 (1953).
[22] G. Salvini and Y. Kim, Phys. Rev. **88**, 40 (1952).

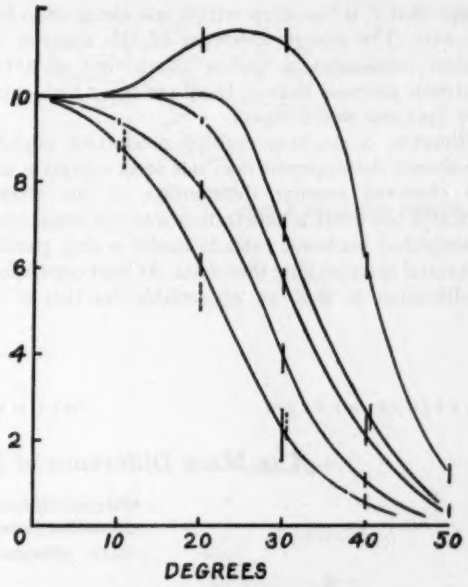

FIG. 7. Calculated space zenith-angle distributions. The curves were obtained for a single electron cascade with the vertical lines representing the effect of varying the power in the integral electron spectrum from 1.5 to 2.0. The curves are for shower sizes 3.2×10^4, 3.2×10^5, 10^6, 3.2×10^6, and 10^7 electrons. The dotted vertical lines represent the calculations for a nuclear cascade model; the results are not significantly altered as N goes from 3×10^5 to 2×10^6.

mesons, Table III. At Echo Lake (~700 g/cm²) the proportion of μ mesons would be about 2 percent. This is considerably greater than the results of measurements for somewhat smaller showers,[6] which indicate less than this for all heavy particles and less than 1 percent for μ mesons in particular.

Thus we see that the present nuclear cascade model does not give results that agree with the experiments, but the changes that would probably produce agreement are of the sort that one would make on other grounds as he improved the model.

Another interesting prediction from the model is that the proportion of N rays, which depends essentially on the number produced just above the apparatus, is about 0.5 percent at 700 g/cm² and increases to about 1.5 percent at 500 to 600 g/cm². These numbers agree roughly with the experiments.

VII. SUMMARY

The spatial and energy structure and the angular distributions of the showers studied in this experiment —showers containing from 1 to 30 or 40 times 10^6 electrons—are not consistent with a single-cascade model. Some of the showers exhibit a "lumpy" density distribution within a meter or two of the axis whereas the majority appear to vary smoothly with distance from the axis. The smooth variation is similar to that expected for an electronic cascade near its maximum

except that it is less steep within one meter or so from the axis. The energy spectrum of the electron and photon component is "softer" than that of a pure electronic cascade, that is, there are fewer high-energy rays than one would expect.

However, a one step multiple-production model of the shower development does not seem adequate since the observed angular distribution of the showers indicates too great a penetration into the atmosphere. A simplified nucleonic cascade model is only partially successful in reconciling these data. At least one required modification is that an appreciable fraction of the energy in a high-energy collision is transferred to nucleons so that the penetration of the cascade is not limited by the decay of pi mesons. This may occur because of a lack of complete inelasticity or because of increasing importance of nucleon-pair formation at high energies.

ACKNOWLEDGMENT

We are indebted to Allen J. McMahon and Daniel T. Anderson, who operated the ionization chamber equipment and assisted with the reduction of the data, and to Malcolm A. McLeod, who read much of the film.

PHYSICAL REVIEW VOLUME 93, NUMBER 3 FEBRUARY 1, 1954

The Mass Difference of Neutral and Negative π Mesons*

WILLIAM CHINOWSKY AND JACK STEINBERGER
Columbia University, New York, New York
(Received October 28, 1953)

The angular correlation of the decay γ rays from neutral π mesons produced in the reaction $\pi^-+p\rightarrow n+\pi^0$ has been measured, using counter techniques. Analysis of the observed correlation function yields a value of the $\pi^- - \pi^0$ mass difference $m_{\pi^-}-m_{\pi^0}=8.8\pm0.6m_e$.

I. INTRODUCTION

THE $\pi^- - \pi^0$ mass difference was first measured by Panofsky, Aamodt, and Hadley[1] in a study of the reactions of π^- mesons stopped in hydrogen. In this experiment hydrogen gas, inside the cyclotron chamber and under 3000-lb/in.^{2} pressure, was exposed to the secondary radiation from a target bombarded by 330-Mev protons. Measurement of the energy spectrum of the γ rays produced in the hydrogen disclosed two groups, one of them rather broad near 70 Mev. This was presumed due to the reaction $\pi^-+p\rightarrow n+\pi^0$, $\pi^0\rightarrow 2\gamma$. The width of the distribution is a measure of the velocity of the neutral meson. Assuming the π^- at rest, the mass difference was then calculated, $\delta=m_{\pi^-}-m_{\pi^0}=10.6\pm2.0m_e$.

Sachs and Steinberger[2] have verified the assumption that the low-energy group is due to the decay of neutral mesons produced by stopped negative mesons. Hydrogen was bombarded by a monochromatic external meson beam and the two γ rays from the neutral meson decay observed in coincidence.

In a similar experiment, but using the liquid hydrogen target previously described,[3] we have investigated the angular correlation of the two γ rays. This provides a measure of the π^0 velocity, as did the energy distribution of Panofsky *et al.*,[1] and therefore a new measurement of the $\pi^- - \pi^0$ mass difference.

II. KINEMATICS

A. Reaction Kinematics

Mesons coming to rest in liquid hydrogen become bound in the lowest Bohr orbit of a meson-proton atomic system in a time short compared to the mean life of $\pi-\mu$ decay.[4,5] The velocities in the bound state are negligible compared to the sensitivity of this experiment. The meson and proton are therefore considered to interact at rest. The process $\pi^-+p\rightarrow n+\pi^0$ gives a neutron and neutral meson, the sum of whose kinetic energies is then equal to the $\pi^- - \pi^0$ mass difference, minus the neutron-proton mass difference. From momentum and energy conservation,

$$\delta=m_{\pi^-}-m_{\pi^0}=[(m_{\pi^-}+m_p)^2\beta^2/(1-\beta^2)+m_n{}^2]^{\frac{1}{2}} - m_p/(1-\beta^2)^{\frac{1}{2}}-m_{\pi^-}[1/(1-\beta^2)^{\frac{1}{2}}-1],$$

where βc is the velocity of the neutral meson. For small β,

$$\delta=m_n-m_p+\tfrac{1}{2}\beta^2[m_{\pi^-}+m_{\pi^-}{}^2/m_n].$$

B. $\gamma-\gamma$ Correlation

In the π^0 rest system the two γ rays are emitted in opposite directions. Let ξ be the angle between the direction of motion of one of the γ rays in the rest system and the π^0 velocity in the laboratory system.

* This work was performed under the joint program of the U. S. Office of Naval Research and the U.S. Atomic Energy Commission.
[1] Panofsky, Aamodt, and Hadley, Phys. Rev. **81**, 565 (1951).
[2] A. Sachs and J. Steinberger, Phys. Rev. **82**, 973 (1951).
[3] Lindenfeld, Sachs, and Steinberger, Phys. Rev. **89**, 531 (1953).
[4] A. S. Wightman, Phys. Rev. **77**, 521 (1950).
[5] Sargent, Rinehart, and Lederman (private communication) have observed, in hydrogen gas at 18-atmos pressure, in a cloud chamber experiment, a ratio of $\pi-\mu$ decays to stoppings <15 percent. In liquid hydrogen the ratio is then $<\frac{1}{4}$ percent.

For the angle ϕ between the two γ rays in the laboratory system, we have

$$\sin(\phi/2)=(1-\beta^2)^{\frac{1}{2}}/[(1-\beta^2)\cos^2\xi+\sin^2\xi]^{\frac{1}{2}}.$$

Considering the isotropy of the γ-ray distribution in the rest system, the probability of observing a pair with correlation angle between ϕ and $\phi+d\phi$ is

$$P(\phi)d\phi=\frac{(1-\beta^2)\sin\phi d\phi}{(1-\cos\phi)^{\frac{1}{2}}\beta[(1-\cos\phi)/(1-\beta^2)-2]^{\frac{1}{2}}}.$$

This correlation function is shown in Fig. 1 for $\beta=0.2$. The smallest correlation angle at which γ-ray coincidences should be observed is

$$\phi_c=\cos^{-1}(2\beta^2-1).$$

For small velocities this cut-off angle is a linear function of β, with $\pi-\phi_c\cong 2\beta$. The error in β is therefore half the error ϵ_ϕ in the experimentally determined cut-off angle, and the error in the mass difference will be approximately $\frac{1}{2}m_\pi\beta\epsilon_\phi$.

III. EXPERIMENTAL PROCEDURE

The negative mesons produced at the internal target of the Columbia University cyclotron at Nevis are collimated in a channel of the 8-ft iron shielding wall and further sorted in momentum by a double-focusing magnet and the beam defining counters No. 1 and No. 2. See Fig. 2. Counter No. 1 is a liquid scintillator $4\frac{1}{2}$ in. in diameter by $\frac{3}{8}$ in. thick. Counter No. 2 is a stilbene crystal $2\frac{1}{4}$ in. horizontally by $2\frac{3}{4}$ in. vertically by $\frac{1}{8}$ in. in thickness. Between the two counters 5 g/cm² of carbon and 5 g/cm² of LiH are inserted to maximize the number of mesons stopped in the hydrogen. The liquid hydrogen container[3] is a vertical cylinder 3.1 in. in diameter and $4\frac{1}{2}$ in. high. However, only $3\frac{3}{4}$ in. vertically are exposed by the thin part (0.006-in. Al foil) of the vacuum chamber. The γ-ray detectors, counters No. 3 and No. 4, are liquid scintillators 4 in. horizontally by 8 in. vertically by 1 in. in thickness. The centers of the γ-ray detection counters are each $27\frac{1}{2}$ in. from the center of the hydrogen well and move in the horizontal plane through the target center.

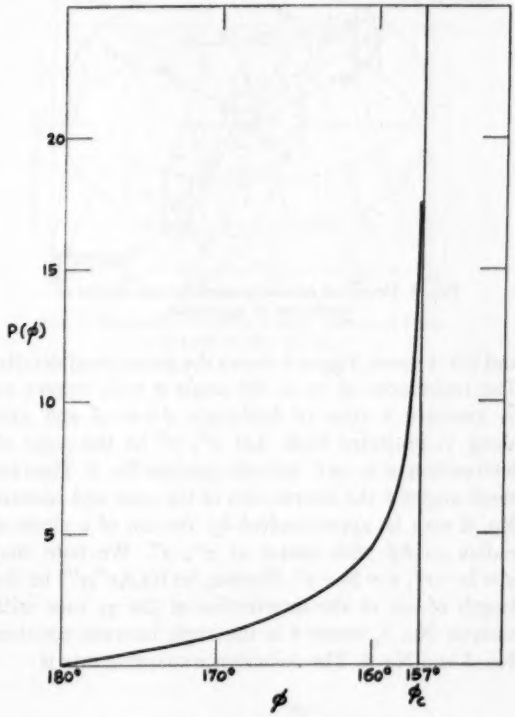

FIG. 1. γ-γ angular correlation function $P(\phi)$ vs ϕ for $\beta=0.2$.

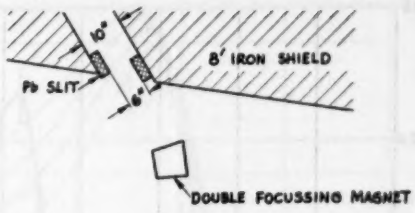

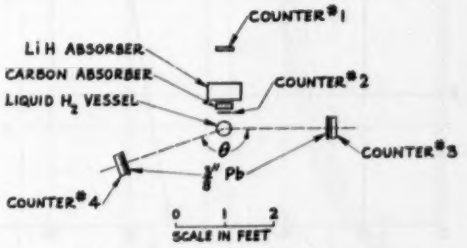

FIG. 2. Experimental geometry, top view.

To obtain the $\gamma-\gamma$ coincidence rates we measure the four counting rates:

(a) Pb converter in place, H_2 in well;
(b) Pb converter in place, no H_2 in well;
(c) Pb converter removed, H_2 in well;
(d) Pb converter removed, no H_2 in well.

The coincidence rate is then taken to be $(a-b)-(c-d)$. The rates without converter were however so small that they were usually omitted.

IV. EXPERIMENTAL RESULTS

Preliminary measurements were made with counters No. 3 and No. 4 at 10 in. from the hydrogen well to

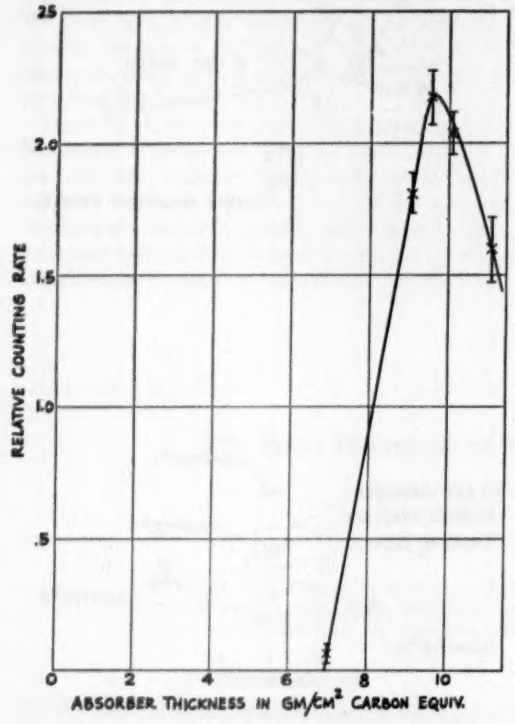

FIG. 3. Fourfold coincidence counting rates *vs* absorber thickness.

determine the most advantageous absorber thickness between counters No. 1 and No. 2. The results are shown in Fig. 3. The measurements were not extended to larger and smaller absorber thicknesses since it has already been shown that such coincidences are due to stopped mesons.[2]

Table I shows fourfold coincidences as a function of the angle θ between the γ-ray detectors, each counter at a fixed distance of $27\frac{1}{2}$ in. from the hydrogen cup. Incident beam intensity in the 1, 2 telescope was of the order of 2×10^5 counts per minute. Fourfold rates with hydrogen in the cup varied from about 2 counts/min at 165° to 0.1 count/min at 145°. Background rates varied from approximately 1 percent of hydrogen events to 25 percent at small angles. The data are presented in Fig. 3 in graphical form together with computed curves to be discussed below.

TABLE I. Experimental results. Variation of fourfold coincidence rates with θ, the angle between γ-ray detectors. Counts are per 2.048×10^6 monitor counts.

	Number counts hydrogen in cup	Number counts without hydrogen	Net due to hydrogen
180°	22.2±1.5	1.3±0.5	20.9±1.6
170°	21.6±1.5	1.3±0.7	20.3±1.7
165°	24.6±1.9	1.0±1.0	23.6±2.1
160°	22.4±1.4	0.9±0.9	21.3±1.7
155°	12.8±1.2	0.7±0.5	12.1±1.3
150°	6.5±0.8	0.8±0.6	5.7±1.0
145°	2.3±0.5	1.4±0.5	0.9±0.7

V. RESOLUTION OF APPARATUS

Quantitative evaluation of the cut-off angle ϕ_c requires a knowledge of the resolution of the detection system. To this end, consider counter No. 3 as fixed and the H_2 cylinder collapsed into a plane parallel to that of counter No. 3. Let $N(\phi)\sin\phi d\phi$ be the rate, per unit volume of well, of emission of γ rays with correlation angle between ϕ and $\phi+d\phi$, and per unit solid angle of one γ ray. The corresponding rate on the collapsed surface is then

$$n(x,y,\phi)dxdyd\phi=N(\phi)\sin\phi d\phi(r^2-x^2)^{\frac{1}{2}}dxdy.$$

Here r is the well radius, x and y, respectively, the horizontal and vertical displacements from the well center. Let x', y' be the coordinates of a point on counter No. 3, and let a pair of γ rays, γ_1 and γ_2, be emitted in $dxdy$, γ_1 striking counter No. 3 in $dx'dy'$. The rate for this process is $N(\phi)\sin\phi d\phi(r^2-x^2)^{\frac{1}{2}}dxdydx'dy'/R^2$. R is the radius of the right circular cylinder C, with axis coincident with the well axis, on which counters No. 3 and No. 4 move. Figure 4 shows the geometrical details. The trajectories of γ_2 at the angle ϕ with respect to γ_1 generate a cone of half-angle $\psi=\pi-\phi$ and axis along γ_1 projected back. Let x'', y'' be the point of intersection of γ_1 on C opposite counter No. 3. Then for small angles ψ the intersection of the cone and counter No. 4 may be approximated by the arc of a circle of radius $\rho=R\psi$ with center at x'', y''. We note that $x'=2x-x''$, $y'=2y-y''$. Further, let $l(\phi,\theta,x'',y'')$ be the length of arc of the intersection of the γ_2 cone with counter No. 4, where θ is the angle between counters No. 3 and No. 4. The coincidence counting rate is

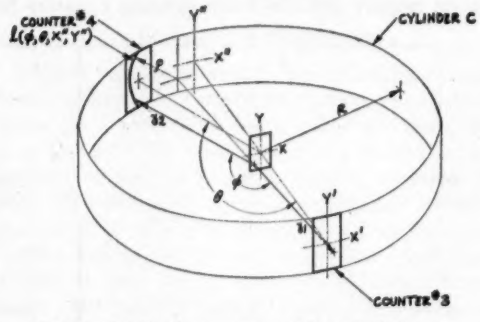

FIG. 4. Details of geometry used for calculation of resolution of apparatus.

$$C(\theta)=\int N(\phi)d\phi\times L(\theta,\phi),$$

where

$$L(\theta,\phi)=\int\int\frac{dx''dy''}{R^2}\frac{l(\theta,\phi,x'',y'')}{2\pi R}\int\int dxdy(r^2-x^2)^{\frac{1}{2}}$$

is the resolution function of the apparatus. The x, y integral is elementary. The x'', y'' integration was done numerically for a number of values of ϕ and θ by constructing regions in x'', y'' space with equal probability of being bombarded by γ_1 (given by the x, y integral$\times[\Delta x''\Delta y'']$) and summing the arc lengths l on a map measure fixed to a compass, the centers of the circles being placed in the various regions of x'', y'' space. The results, giving the resolution function $L(\theta,\phi)$ for several values of θ are shown in Fig. 5.

VI. THE $\pi^- - \pi^0$ MASS DIFFERENCE

The curves of counting rate *vs* θ shown in Fig. 6 were computed by performing, numerically, the integral

$$C(\theta)=\int_{\phi_1(\theta)}^{\phi_2(\theta)}L(\theta,\phi)\frac{(1-\beta^2)d\phi}{(1-\cos\phi)^{\frac{1}{2}}\beta[(1-\cos\phi)(1-\beta^2)^{-1}-2]^{\frac{1}{2}}}$$

for different values of β^2. All curves were normalized to the same area as that of the experimentally determined curve. The experimental resolution is seen to be somewhat poorer than the calculated resolution. This may be at least in part due to scattering of the conversion electrons in the edges of the lead foil. The best fit is obtained with $\beta^2=0.040$, and we estimate the limits on β^2 to be 0.0365 and 0.0435. The $\pi^- - \pi^0$ mass difference is then

$$m_{\pi^-}-m_{\pi^0}=8.8\pm0.6m_e.$$

This is in good agreement with the earlier result of Panofsky, Aamodt, and Hadley, $m_{\pi^-}-m_{\pi^0}=10.6\pm2m_e$.

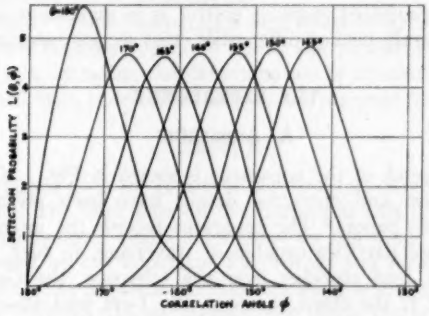

FIG. 5. Resolution function $L(\theta,\phi)$. Values of θ are indicated on the curves.

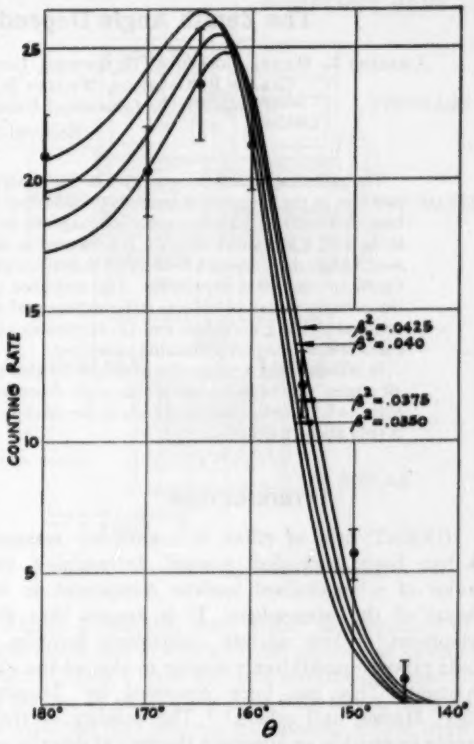

FIG. 6. Calculated and observed coincidence counting rates as a function of θ, the angle between γ-ray detectors. Errors shown are statistical.

The Zenith Angle Dependence of Cosmic-Ray Protons*

CHARLES E. MILLER, JOSEPH E. HENDERSON, DAVID S. POTTER, JAY TODD, JR., WAYNE M. SANDSTROM, GERALD R. GARRISON, WILLIAM R. DAVIS, AND FRANCIS M. CHARBONNIER
Applied Physics Laboratory,† University of Washington, Seattle, Washington

(Received October 13, 1953)

The proton spectrum for particles in the momentum band 0.4−1.0 Bev/c and the meson spectrum for particles in the momentum band 0.09−0.34 Bev/c at zenith angles 45° east, vertical, and 45° west have been obtained at 3.3-km elevation and magnetic latitude 48° north. The zenith angle dependence of protons, along with a simplified analysis, is presented as data on the nucleonic cascade. It is found that the gross zenith angle dependence will fit a $\cos^{3.2}\theta$ distribution at 45 degrees east and west, there being no statistically significant east-west asymmetry. The simplified calculation assumes that a unidirectional component of the primary radiation will (1) suffer exponential absorption along its original path with a path length for removal of 120 g/cm² of air and (2) acquire an ultimate distribution at 3.3 km due to scattering fitting a $\cos^n\omega$ law, n being an adjustable parameter.

It is found that a value of n of 6.5±0.7 yields a unidirectional distribution which, when integrated over all angles, results in a gross zenith angle dependence agreeing with $\cos^{3.2}\theta$. The $\cos^n\omega$ distribution with n equal to 6.5 is quite sharp and leads to the conclusion that the average projected scattering angle per collision is only about 6 degrees.

INTRODUCTION

A GREAT deal of effort in cosmic-ray research has been expended toward determining the behavior of a generalized nuclear component in its traversal of the atmosphere. It is known that the development of this nuclear component involves a cascade process qualitatively similar to that of the soft component. This has been discussed by Janossy, Heitler, Messel, and others.[1–3] The validity of their attempts to provide an adequate theoretical description of the cascade suffers from an almost complete lack of experimental knowledge of the cross sections of the many processes involved. Recent experiments on penetrating showers by Branch[4] and others have provided evidence to indicate that the differential cross sections in inelastic nucleon-nucleus collisions must be sharply peaked in the forward and backward directions.

In successively refined experiments[5] conducted by this Laboratory, a technique of proton-meson analysis of the cosmic radiation has been developed using a magnetic cloud chamber. This has been applied to the present study of the zenith angle dependence of the nonelectronic component of the ionizing radiation of range less than 15 cm of lead present at an altitude of 3.3 km. This radiation consists almost entirely of mu-mesons and protons. The ability of this apparatus to accept these particles in distinct momentum bands makes it possible to study the zenith angle dependence of protons alone.

A simple phenomenological analysis of this dependence of proton radiation on zenith angle has been made in an attempt to separate effects of nuclear scattering from the geometrical factors arising from the fact that contributions to the total radiation come from all directions of primary incidence. If the effect of exponential absorption is also taken into account, it is possible to arrive at a closer approximation to the angular distribution of secondaries due to nuclear collisions. From this distribution, it is found that the mean projected angle of scatter is in agreement with the sharply peaked differential cross section mentioned above.

THE EXPERIMENT

A. Apparatus

A sketch of the apparatus is shown in Fig. 1. Construction and operating details have been given in previous papers.[5] The apparatus records the intensity of those particles capable of traversing, in turn, the 2.5-cm lead absorber over the telescope, the Geiger tube $C1$, the cloud chamber, the 1-cm lead absorber over $C2$, $C2$ itself, but stopping in the 15-cm lead absorber at the bottom. Coincidence events of the type $C1+C2-A1-A2-A3$ are selected by suitable electronic circuits and initiate chamber expansion. Anticoincidence counters $A1$, lying outside the acceptance beam defined by $C1$ and $C2$, serve to limit the number of cases in which shower events are recorded, while the tubes $A2$ and $A3$, also in anticoincidence, establish the maximum range of particles accepted. As discussed before,[5] such range definition serves to resolve protons and mesons into distinct momentum bands. To the extent that scattering and nuclear interaction in the absorbers are ignored, the apparatus accepts protons in the momentum band 0.4−1.0 Bev/c.

Particles are deflected in the chamber by a magnetic field of 8200 gauss, and momentum measurements are obtained by photographing the chamber and comparing

* This work supported by U. S. Office of Naval Research.
† A division of the Department of Physics.
[1] W. Heitler and L. Janossy, Proc. Phys. Soc. (London) **A62**, 374 (1949).
[2] L. Janossy and H. Messel, Proc. Roy. Irish Acad. **A54**, 217, 245 (1949).
[3] H. Messel, Phys. Rev. **83**, 21, 26 (1951).
[4] G. M. Branch, Phys. Rev. **84**, 147 (1951).
[5] Miller, Henderson *et al.*, Phys. Rev. **79**, 459 (1950); **84**, 981 (1951).

the curvature of the projected image of the track with that of standard arc.

As in previous work, the 2.5-cm absorber above $A1$ serves to insure the recognition of electron showers. Such showers either actuate one of the counters $A1$, in which the case the event is not recorded, or else are recognized by the appearance of multiple tracks in the chamber.

The entire assembly sketched in Fig. 1 was so mounted that it could be rotated about an axis perpendicular to the plane of the page, so that the beam at any zenith angle up to 50° could be accepted.

B. Experiments Performed

Three sets of measurements were taken with this apparatus located at Climax, Colorado, elevation 3.3-km, magnetic latitude 48° north during the months of August, September, and October, 1951. Initial conjectures as to the results of the measurements led to the conclusion that appreciable differences in intensity would require rather large angles of observation. For this reason, an angle of 45° was chosen. The three sets of measurements differed only in the zenith angle to which the apparatus was tilted, a measurement being made at vertical incidence, at 45° to the east of the zenith and at 45° to the west. Accumulation of statistically meaningful data was too slow to allow measurements at other angles.

Nearly 12 000 photographs were taken, about equally divided between the three cases. The method of data analysis, including the determination of absolute rates quoted here, is described fully in the previous papers.

RESULTS

Figure 2 gives the results of the three sets of measurements. The dark bars on the horizontal axis indicate the momentum bands determined by the range limits imposed by the apparatus for protons and mesons as labeled. The negative distributions show a single peak, since they contain mu mesons only, while the positive distributions show a second maximum at the momentum expected for protons. The rapid cutoff of the negative distributions at high momentum insures that the positive curve contains very few mesons above 0.5 Bev/c. The high momentum tail of the positive curve indicates the strong nuclear interaction in the lead absorber characteristic of protons. From these graphs, it is apparent that the 45° east and 45° west spectra are identical within statistics for both protons and mesons, and that the vertical spectrum differs from the 45° spectra only by a scale factor of about 3.2. These results are better shown in Fig. 3, in which the solid curve is the vertical spectrum, while the plotted points are those of the 45° data averaged over east and west and multiplied by the scale factor of 3.2. This scale factor corresponds to an angular distribution described by $\cos^n\theta$, with $n=3.2\pm0.3$.

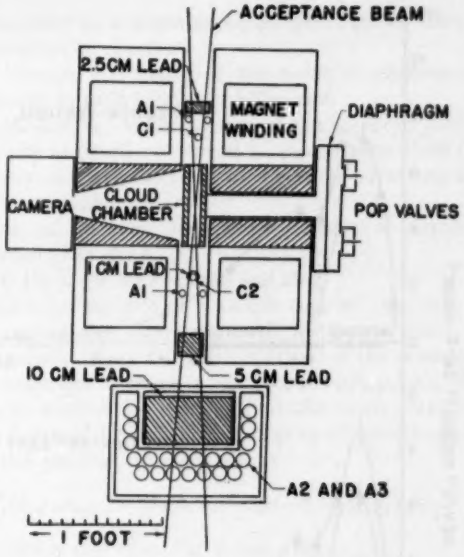

FIG. 1. Sketch of experimental apparatus.

Figure 3 indicates that, within the accuracy of the experiment and at this altitude, protons of momentum near 0.75 Bev/c show the same zenith angle dependence as mesons of momentum near 0.25 Bev/c. It is not to be expected that protons and mesons should show the same zenith angle dependence, since these particles are not closely related genetically, and the factors determining these zenith angle dependences are not at all similar. The present result must thus be considered fortuitous for the particular momentum and altitude investigated. Indeed, the results of another experiment[6] to be published soon show that at higher momentum (2 Bev/c), meson intensities in the vertical and 45° directions differ by a factor of only 2.

DISCUSSION

As compared to the meson radiation, the atmospheric development of the proton radiation (and the nucleonic radiation in general) is greatly complicated by nuclear interaction which here becomes the most important single process. The cascade is propagated through the atmosphere principally by protons and neutrons produced in successive penetrating showers. Pi mesons originating in these showers decay too quickly to have high probability of undergoing further nuclear interaction, while the mu mesons secondary to them do not undergo appreciable nuclear interaction at all and so take almost no part in further propagation of the cascade.

Absorption of the radiation which produces penetrating showers has been studied by Van Allen, Ber-

[6] F. M. Charbonnier *et al.* (to be published).

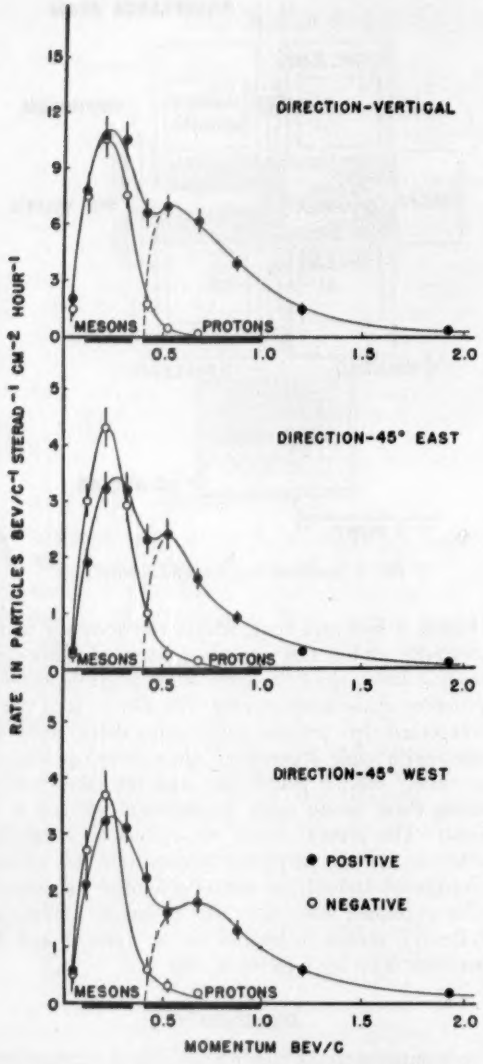

FIG. 2. Proton and meson momentum spectra for three zenith angles.

nardini, Rossi, and others[7–10] who find an exponential absorption with a coefficient of about 120 g/cm² of air. Studies of the absorption of radiation producing photographic stars as well as direct measurements by this Laboratory of the relative proton intensity between 3.3 km and sea level give similar absorption path lengths. It should be pointed out that an exponential absorption with this path length cannot hold to the top of the atmosphere, as in this case, the observed proton intensity at 3.3 km would be much too large, as compared with the primary intensity at the top of the atmosphere. In the following treatment of the angular spread of the proton radiation, a constant removal path length of 120 g/cm² is used. In making comparisons with observations made at 3.3 km, it is not necessary that this assumption hold to the top of the atmosphere, but rather that it be good from heights of 3.3 km to sea level. Protons observed in this investigation lie principally between 0.5 Bev/c and 1.0 Bev/c. On the basis of ionization loss alone, these protons must have had momenta greater by 2 Bev/c at the top of the atmosphere. As they will have undergone, on the average, several nuclear collisions, the primary energy must have been several times greater than this amount. For protons of momenta above 7.5 Bev/c the primary distribution is isotropic above the horizon, as shown by

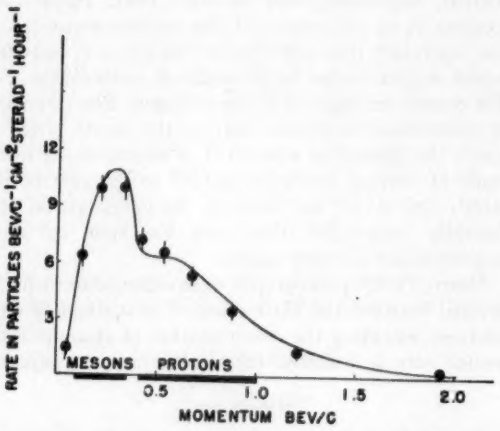

FIG. 3. Comparison of momentum spectra. Points plotted are for the 45° positive spectra averaged over east and west and multiplied by a scale factor of 3.2. The curve is the vertical positive spectrum.

the Lemaitre-Vallarta theory of the geomagnetic effect. It can be expected then that the protons observed at 3.3 km are derived mainly from an initially isotropic distribution. The radiation at 3.3 km then can be considered as the superposition of contributions at this altitude from equal primary intensities for all directions at the top of the atmosphere. The observed angular spread at 3.3 km depends in part on geometrical factors resulting from this superposition of contributions from many primary directions. It is clear, for example, that a primary radiation all of vertical incidence would not give rise to so great an angular spread at 3.3 km as that observed. Thus, the observed angular spread represents an upper limit to that due to nuclear scattering alone in traversing the atmosphere. We attempt to obtain a closer approximation to the angular spread due solely to the nuclear scattering through the following assumptions:

[7] H. E. Tatel and J. A. Van Allen, Phys. Rev. **73**, 87 (1948).
[8] Bernardini, Cortini, and Manfredini, Phys. Rev. **74**, 1878 (1948).
[9] B. Rossi, Revs. Modern Phys. **20**, 537 (1948).
[10] J. Tinlot, Phys. Rev. **73**, 1476 (1948).

(1) The primary proton intensity is the same at all angles of incidence.

(2) The intensity of secondaries at depth x due to primaries of zenith angle θ (independent of azimuth) depends only on the diagonal distance d in g/cm² as measured along this zenith direction.

(3) This intensity decreases exponentially with a path length of 120 g/cm².

(4) The angular spread of secondaries due to the primary radiation in a given direction is represented by a $\cos^n\omega$ law, centered about this direction, with n independent of depth.

The first assumption is completely justified for primary momenta above 7.5 Bev/c by the geomagnetic theory. As a result of the following computation the assumption that the primary radiation is isotropic for angles greater than 45° is found unnecessary. For this smaller angle, geomagnetic theory insures isotropy for momenta as low as 3.3 Bev/c.

The second assumption would be strictly true if there were no scattering. With scattering, the geometrical situation is not strictly the same for all zenith angles. A primary traversing a given path near the top of the atmosphere will produce secondaries at lower altitudes with lateral displacements from its original path. As compared to vertical incidence, minimum path lengths for these secondaries (from the point of observation to the top of the atmosphere) will be increased for 180° of azimuth and correspondingly decreased for the other 180°. Except for large zenith angles, since average path lengths are the same, the situation will not differ much from that for vertical incidence.

Assumption three conforms to the large body of experimental determinations of this attenuation. While, as has been pointed out, this cannot hold to the top of the atmosphere, for the present purpose it need only be a close approximation for atmospheric depths from about 700 to 1000 g/cm². Experimental evidence indicated its validity below 60 000 feet.[11]

With regard to assumption four, a $\cos^n\omega$ scattering law has no theoretical foundation. Its use conforms to usual practice, n being adjusted to give the experimentally determined rate of decrease. The assumption that n is a constant cannot be true over large ranges of distance. Again this need only be approximately true over a range of 700 to 1000 g/cm². As n will be a function of the proton energies involved, similarity of the proton spectra at 700 and 1000 g/cm² can be taken as a measure of the constancy of n. This evidence has been provided by Wilson.[12]

The various quantities used in the calculation are defined as follows:

$I_0(\theta_0,\varphi_0)$ denotes proton intensity at the top of the atmosphere in a direction θ_0, φ_0 (see Fig. 4). This is assumed to be constant.

x denotes the depth of the point of observation measured in path lengths of 120 g/cm².

$I_x(\theta_0,\varphi_0,\theta_x,\varphi_x)$ is the portion of the observed proton intensity at depth x at angles θ_x, φ_x contributed by the primary radiation incident at angles θ_0, φ_0 at the top of the atmosphere.

$I_x(\theta_x,\varphi_x)$ denotes the proton intensity at depth x observed at angles θ_x, φ_x.

ω is the angle between $d\Omega_0$ and $d\Omega_x$.

The counting rate of a Geiger counter telescope at the top of the atmosphere will be proportional to $I_0(\theta_0,\varphi_0)d\Omega_0$, where $d\Omega_0$ is the aperture of the telescope. The telescope at depth x will record $I_x(\theta_x,\varphi_x)d\Omega_x$. We wish to account for the fact that this latter rate falls by a factor of 3.2 from the vertical to 45° zenith angle. For this purpose, we assume that

$$I_x(\theta_0\varphi_0,\theta_x,\varphi_x)=kI_0(\theta_0,\varphi_0)[\exp(-x/\cos\theta_0)]\cos^n\omega.$$

We quickly find from Fig. 4 that

$$\cos\omega=\sin\theta_0\sin\theta_x\cos(\varphi_0-\varphi_x)+\cos\theta_0\cos\theta_x,$$

so that

$$I_x(\theta_x,\varphi_x)d\Omega_x=kI_0(\theta_0,\varphi_0)\int_{\Omega_0}[\cos\theta_0\cos\theta_x + \sin\theta_0\sin\theta_x\cos(\varphi_0-\varphi_x)]^n\exp(-x/\cos\theta_0)d\Omega_0 d\Omega_x,$$

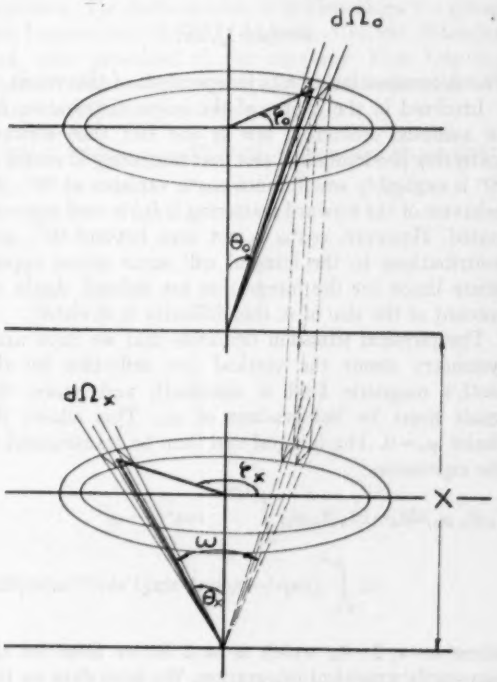

FIG. 4. Sketch of coordinate system used.

[11] M. Blau and H. Wambacher, Akad. Wiss. Wien **IIa, 146,** 623 (1937).

[12] M. G. Mylroi and J. G. Wilson, Proc. Phys. Soc. (London) **A64,** 417 (1951).

where k is a normalization factor, and Ω_0 is the upper hemisphere. The determination of k can be made immediately by noticing that

$$\int_{\Omega_x} I_x(\theta_0,\varphi_0,\theta_x,\varphi_x)d\Omega_x = kI_0(\theta_0,\varphi_0)\exp(-x/\cos\theta_0)\int_{\Omega_x}\cos^n\omega d\Omega_x d\Omega_0$$

must reduce to $I_0(\theta_0,\varphi_0)d\Omega_0$ for the case of no absorption, i.e., infinite removal path length. This means that x is zero and the exponential factor is unity. Thus, from

$$k\int_{\Omega_x}[\cos\theta_0\cos\theta_x+\sin\theta_0\sin\theta_x\cos(\varphi_0-\varphi_x)]^n d\Omega_x=1,$$

where Ω_x is again the upper hemisphere, k can presumably be found. The result, however, evidently depends on θ_0. This is to be expected, since for larger values of θ_0, the $\cos^n\omega$ distribution places particles outside the limits of integration. However, it will be shown immediately below that the exponent n is large enough so that the contributions to the above integral for values of θ_x greater than 90° are negligibly small for θ_0 less than 45°, which is the region of interest. Thus, it is legitimate to set $\theta_0=0$ with the result

$$k\int_0^{\pi/2}\int_0^{2\pi}\cos^n\theta_x\sin\theta_x d\varphi_x d\theta_x=1$$

or

$$k=(n+1)/2\pi.$$

The determination of n is independent of this result.

Involved in the choice of the $\cos^n\omega$ distribution for an assumed scattering law is the fact that forward scattering predominates and that scattering in excess of 90° is negligibly small. Since $\cos^n\omega$ vanishes at 90°, the behavior of the forward scattering is fairly well approximated. However, $\cos^n\omega$ is not zero beyond 90°, and contributions to the integral will occur unless appropriate limits for the integration are defined. Again on account of the size of n, this difficulty is obviated.

The physical situation demands that we have axial symmetry about the vertical (no deflection by the earth's magnetic field is assumed), and hence, the result must be independent of φ_x. This allows the choice $\varphi_x=0$. The integral can then be transformed to the expression:

$$I_x(\theta_x,\varphi_x)d\Omega_x=kI_0(\theta_0,\varphi_0)\int_0^{\pi/2+\alpha}\cos^n(\xi-\alpha)\times\int_0^{\pi}[\exp(-x/\sin\lambda\sin\xi)\sin^{n+1}\lambda d\lambda d\xi d\Omega_x,$$

where $\alpha=\pi/2-\theta_x$, which is in a better form for the necessarily graphical integration. We have data on this quantity for 2 directions of observation, and a determination of n can be had by computing the ratio

$$\rho=I_x(0,\varphi_x)/I_x(\pi/4,\varphi_x)$$

as a function of n and comparing with the experimental value of 3.2. Table I presents the results of this calculation. It is seen that ρ is a fairly sensitive function of n, and that n can be assigned the value 6.5. This is a sharp distribution, falling by a factor of nine from zero to 45° zenith angle, and is ample justification for the various approximations made in evaluating the integral, since contributions from primary radiation incident at zenith angles greater than 45° are less than 5 percent for n greater than 5.

The value of n so determined is dependent on the choice of path length. The sensitivity of the dependence is not great, however. The figure for the path length as determined by this laboratory is 125 ± 8 g/cm². Values from nuclear plate data[8] are somewhat higher (about 135 g/cm²) but refer to particles in much broader momentum bands. Within the region $L=100-140$ g/cm², n varies from 6.0 to 8.5. Within the region $L=125\pm8$ g/cm² and within the statistical accuracy of the experimental value of ρ, n has the value 6.5 ± 0.7.

TABLE I. Sharpness of assumed scattering distribution *vs* zenith angle dependence.

n	ρ
5	2.66
6	2.93
7	3.51
Inf.	9.70

The case of no scattering at all (n infinite) gives a value of ρ of 9.7, while the introduction of a distribution as sharp as $\cos^{6.5}\omega$ brings this ratio down by a factor of three. One might wonder whether attenuation alone might account for the ratio $\rho=3.2$. A short calculation shows that L would have to exceed 300 g/cm² of air, indicating that the effect of scattering cannot be neglected.

An approximation to the average projected angle of scatter may be had by a simple analysis. Protons in the atmosphere undergo nuclear collisions with a path length of about 60 g/cm²,[1] corresponding to the geometrical cross section. The distance from 3.3 km to the top of the atmosphere is then about 10 such path lengths. We can thus assume that observed protons are, on the average, in the tenth generation in the sense that the proton is separated by a total of ten collisions from its primary parent. The root-mean-square total angular deviation of a proton undergoing N collisions with an average scattering angle α, regarding this as a simple diffusion process, is given by

$$\bar{A}=\langle A^2\rangle^{\frac{1}{2}}=\alpha\sqrt{N}.$$

$\bar{A}$ for the $\cos^{6.5}\omega$ distribution is about 20°. With $N=10$, one finds $\alpha=6.3°$. This number is far removed from

the value 15–20 degrees predicted by Messel in early theoretical treatment of the cascade.

Branch[4] has determined the angular distribution about the shower axis of penetrating particles in extensive air showers. Such showers, of course, include, in addition to nucleons, many pi and mu mesons. A conclusion therefrom, relevant to this problem, is nevertheless possible, since Branch finds a root-mean-square angular deviation of emergent particles of about three degrees. This figure agrees fairly well with the figure 6.3 degrees presented here. Branch's result, which this experiment independently corroborates, has caused drastic changes in the nature of the cross section assumed in the theoretical papers by Green, Messel, and Chartres,[13,14] with the adoption of a distribution sharply peaked in the forward and backward directions.

Other published data concerned with the problem treated here is the work of Walker.[15] He performed a counter-absorber type of experiment at 3.26-km elevation and at sea level in which recorded events are those due to charged particles producing penetrating showers in blocks of lead absorber of varying thicknesses. After elaborate precautions to remove the soft and mesonic components, he is able to call such particles protons, but the method of selection only vaguely defined the accepted momentum. Walker's requirements for the lowest energy case are that a charged particle traverse two trays of counters separated by 12 inches, enter an eight-inch block of lead and produce a shower there, whose presence shall be indicated by the discharge of three or more counters in a tray located below the absorber. Knowledge of which counters in the upper two trays were discharged yields the zenith angle dependence to 25° in six steps. The only limit that can be placed on the extent of the accepted momentum band is a lower one, which, because of the requirement for shower production, is certainly very much higher than the 1-Bev/c maximum cutoff for this experiment. This fact is further substantiated by Walker's ratio of the intensity at elevation to that at sea level. This ratio is about four, which is far removed from the well-established ratio of about twenty as obtained by this laboratory, by Wilson[12] and by Whittemore and Shutt[16] for low momentum (less than 1 Bev/c) protons.

Walker finds that his data for 3.26 km can best be represented by a $\cos^n\theta$ distribution with n equal to 5.5 ± 0.7, while at sea level, the exponent is 3.4 ± 1.0.

The very high-energy radiation considered by Walker is certainly isotropic at the top of the atmosphere. Only absorption can lead to a sharper zenith angle dependence with increasing depth. Walker's zenith angle dependence at 3.26 km can be accounted for by an absorption path length of 130 g/cm^2 in the absence of scattering. With scattering, an even shorter path length is required. This is inconsistent with Walker's value of 4 for the intensity ratio between 3.26 km and sea level. Continued absorption with this path length (130 g/cm^2) without scattering would give a zenith angle dependence of $\cos^{8.5}\theta$ at sea level. The experimental value quoted by Walker ($n=3.4\pm1.0$) would indicate sharply increased scattering below 3.26 km which seems unlikely at these energies.

This experiment was performed at a site provided by the Climax Molybdenum Company at Fremont Pass in Colorado. The authors wish to acknowledge the generous cooperation of C. J. Abrams, General Manager, and other personnel of the company. Don Eng and Elmer Wright of our group are also responsible for many contributions to this research.

[13] Green, Messel, and Chartres, Phys. Rev. **88**, 1277 (1952).
[14] H. Messel and H. S. Green, Phys. Rev. **87**, 378, 738 (1952).
[15] W. D. Walker, Phys. Rev. **77**, 686 (1950).
[16] W. L. Whittemore and R. P. Shutt, Phys. Rev. **86**, 940 (1952).

Geomagnetic and Albedo Studies with a Čerenkov Detector at 40° Geomagnetic Latitude*

J. R. WINCKLER AND K. ANDERSON
University of Minnesota, Minneapolis, Minnesota
(Received September 9, 1953)

A Čerenkov detector consisting of a Lucite radiator optically sealed to a large-area side-window photomultiplier has been flown at $\lambda=40°$ at a depth of 25 g/cm² below the top of the atmosphere. The albedo was determined and is not more than 5 percent of the incident flux for particles of $\beta>0.7$ in any upward direction. The albedo observed is too small to account for the factor-of-two difference between the observed E–W asymmetry and that predicted from the primary spectrum and geomagnetic theory. Direct asymmetry measurements by the Čerenkov counter suggest that the earth shadow cone cutoff may start at larger zenith angles than theoretically predicted. A very rough relative abundance measurement of H:He:Li gives 1:0.08:0.02.

I. INTRODUCTION

THE present investigation is concerned with two discrepancies which have arisen from high-altitude cosmic-ray measurements. The first factor is the failure of the azimuthal effect at high altitudes of the total cosmic radiation to agree via the geomagnetic theory with the measured latitude effect. The other discrepancy is the failure of the total energy, computed on the basis of the incident particle flux and geomagnetic theory, to agree with the total energy measured by the atmospheric-ionization data.

The first discrepancy appeared as a result of a latitude survey at balloon altitudes[1] and also appears in data obtained with rockets above the atmosphere.[2,3] As pointed out in Table IV, reference 1, if one compares the east-west effect at a number of latitudes with the expected effect, using the vertical counting rate *vs* latitude and also using geomagnetic theory, one finds that the measured east-west effect is about one-half the predicted value. This comparison is independent of the nature of the primary radiation, except that it is assumed to be entirely positively charged, as the comparison is made entirely on the basis of the dimensionless Störmer variable in place of the energy. As was pointed out, the azimuthal effect might be decreased by the presence of splash albedo produced by primary particles incident on the atmosphere whose secondaries then went out again and were counted as primaries by the Geiger telescopes. In order to reduce the east-west effect enough by this means to make it consistent with the measurements, it was calculated that at $\lambda=0$, 33 percent, at $\lambda=20$, 25 percent, and at $\lambda=40$, 45 percent of the western flux at 60° zenith, would have to be projected out again in the eastern direction.[1] Presumably, that part of the splash albedo which consists of stable particles would leave the atmosphere, and if it had an energy less than the cut-off energy for entrance from infinity, according to geomagnetic theory, the particles would remain trapped in the earth's field and eventually would return to the earth. It has been pointed out by Treiman,[4] that if one considers the first integral of the Störmer theory, particles leaving in the vicinity of latitude λ, and fulfilling the condition that they do not escape to infinity and therefore constitute part of the albedo, would return to the earth close to that same latitude, or to the corresponding latitude in the opposite hemisphere over wide limits of the angle of emission X. This can be seen from the Störmer first integral

$$\alpha=-R\cos\lambda\cos X+(1/R)\cos^2\lambda, \qquad (1)$$

with the auxiliary conditions that $\alpha\geq 2$, $R\leq 1$. One should note that the angle of return of the albedo particle is not the same, in general, as the angle of departure. If one, however, measures the amount of radiation leaving the atmosphere or moving in an outward direction, one can then compute the magnitude of the effect.

Evidence for albedo above the atmosphere comes from rocket range-ionization measurements of Perlow and co-workers[5,6] in which it was shown that there is an appreciable amount of low-energy radiation, possibly electrons, above the atmosphere. Van Allen, Singer, and co-workers have also shown that the ratio of the omni-directional flux to vertical telescope flux values at a number of latitudes demonstrates that the average omni-directional value is higher than the vertical, whereas, according to theory, it should be lower if all the particles measured are primaries. Measurements with telescopes in rockets by this group at various zenith angles above the atmosphere support this conclusion by an increase in the flux towards the horizontal direction. It is somewhat difficult to assess the effects of these results on the balloon measurements near the top of the atmosphere at roughly 15 g/cm². The balloon equipment used to measure the asymmetry contained 3 cm of lead in the telescope plus the counter wall

* This work supported by the joint program of the U. S. Atomic Energy Commission and the U. S. Office of Naval Research.
[1] Winckler, Stix, Dwight, and Sabin, Phys. Rev. **79**, 656–669 (1950).
[2] J. A. Van Allen and A. V. Gangnes, Phys. Rev. **78**, 50 (1950); **79**, 51 (1950).
[3] S. F. Singer, Phys. Rev. **77**, 729 (1950); **80**, 47 (1950).
[4] S. Treiman, Phys. Rev. **91**, 432 (1953).
[5] G. J. Perlow and J. D. Shipman, Jr., Phys. Rev. **71**, 325 (1947).
[6] Perlow, Davis, Kissinger, and Shipman, Phys. Rev. **88**, 321 (1952).

thickness, which gave 36 g of lead equivalent or 19 g of air equivalent. At a 60° zenith angle there were 30 g/cm² of air above the equipment, which means that the total initial energy of a proton coming downward toward the telescope must have been 270 Mev or more to be detected, or when the proton reached the telescope it had to have 112 Mev remaining. These energy values are considerably above the threshold to which the rocket measurements were sensitive, particularly the single-counter rocket values, which go down to the order of a few Mev, so that almost certainly a large amount of extra radiation was measured in some of the rocket experiments not directly relevant to the balloon data. The above-the-atmosphere splash albedo may be more intense than that observed at 15- to 25-g/cm² depth, as the primary flux is larger in directions near the horizontal as one goes to smaller and smaller depths, and these primaries are more effective in producing albedo.

The second discrepancy which has been referred to comes from a comparison of the vertical telescope balloon or rocket data with the ionization measurements of Neher,[7] in which it is generally agreed that the flux calculations, although agreeing with the ionization data in the *form* of the primary-energy spectrum, give about twice the amount of incident energy. Energy is calculated from the balloon or rocket flux measurements by the equation

$$E(\lambda)=\int_{E_{\min}(\lambda)} N(E)EdE. \qquad (2)$$

The spectrum $N(E)$ is obtained over the geomagnetically sensitive region from the vertical balloon flux measurements and is extended to higher energies using the very high energy data obtained from the air showers, which in general agree in form with the high-energy spectra obtained by other means. The errors involved in this calculation cannot account for the factor-of-two differences, except for the uncertainty in the primary flux itself, which might arise from the albedo. It was therefore considered important to make measurements of the albedo at balloon altitudes and to study the possible effect of the albedo on the two discrepancies.

II. THE ČERENKOV DETECTOR

Preliminary attempts to detect the albedo using a lead-absorption method gave a nul result at $\lambda=55°$ at 20-g/cm² atmospheric depth.[8] In these measurements a large block of lead was alternately moved to and away from the lower side of a counter telescope, and the counting rates compared. There were obviously present showers from the equipment which changed with the position of the lead block, but, nevertheless, the effect observed was essentially zero.

[7] H. V. Neher, Phys. Rev. **83**, 650 (1951).
[8] J. R. Winckler, Phys. Rev. **85**, 1053–1054 (1952).

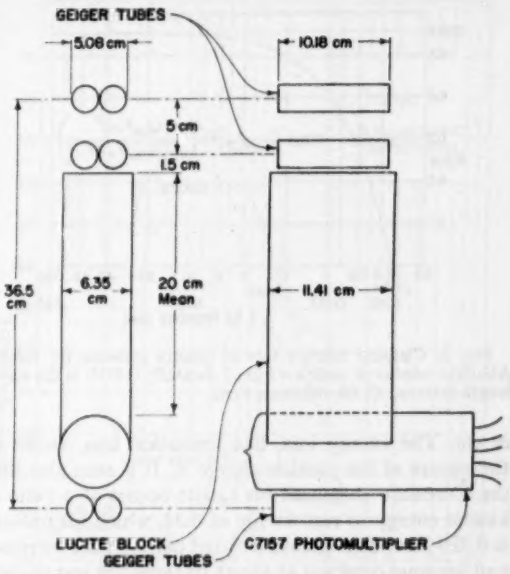

FIG. 1. Schematic diagram of the Čerenkov detector. The solid angle is 1.86 sterad-cm². The total detector stopping power is 30 g/cm².

The next experiment involved the use of a Čerenkov detector,[9] which in a preliminary form gave a small effect of upward relativistic particles at the top of the atmosphere at $\lambda=55°$. This early detector used an end-window photomultiplier tube optically connected to a side arm of a block of Lucite, which constituted the radiator. The device had strong directional properties but very poor light-collection efficiency, and was discarded in favor of a much-improved detector.[9] This detector is shown in Fig. 1 and consists of a block of Lucite to which is optically joined an RCA-type C-7157 developmental phototube. This phototube has a side window of 13 sq in. sensitive area, and four of these phototubes were obtained through the kindness of the U. S. Navy Department, Bureau of Ships. Of the original four, one was furnished with a cracked base, and one was lost because of the failure of a balloon during flight. The other two were flown successfully and results are reported in this paper.

The theory of the Čerenkov effect on a classical basis has been given by Frank and Tamm[10] following the original discovery in 1934 by Čerenkov.[11] In Fig. 2 is plotted the function $F(\beta,n)$, giving the relative number of quanta emitted for the case of Lucite, for a singly charged particle. The absolute number of quanta is obtained by multiplying $F(\beta,n)$ by $Z^2\Delta\omega l/137c$, where $\Delta\omega$ is the angular frequency region and l the thickness

[9] J. R. Winckler and K. Anderson, Rev. Sci. Instr. **23**, 765–66 (1952).
[10] I. Frank and I. Tamm, Compt. rend. acad. sci. U.R.S.S. **14**, 109 (1937).
[11] P. A. Čerenkov, Compt. rend. acad. sci. U.R.S.S. **8**, H51 (1934); Phys. Rev. **52**, 378 (1937).

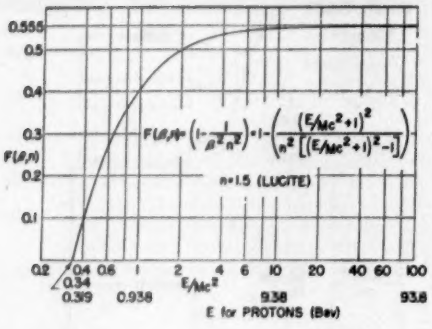

FIG. 2. Classical relative rate of quanta emission for Lucite. Absolute number of quanta $= F(\beta,n)\cdot 2\pi\Delta\lambda l Z^2/(137\lambda^2)$ in the wavelength interval $\Delta\lambda$ for thickness l cm.

in cm. The energy loss, like ionization loss, varies as the square of the particle charge Z. It is seen also that the Čerenkov threshold for Lucite occurs at a ratio of kinetic energy to rest energy of 0.34, which for protons is 0.319 Bev. The quanta emitted per cm then increases and becomes constant at about 10 times the rest energy. Considering the spectral response of the C-7157 photomultiplier, roughly 5000 usable quanta should be produced in the Lucite block by a very high energy, singly charged particle. The angle of emission θ also depends on the ratio of kinetic energy to rest energy of the particle, and reaches the limiting value of 48° for Lucite (see Fig. 3). This means that the radiation given out by a particle traversing the block from end to end will be almost entirely internally reflected and will proceed down the block in the direction of the particle. If this light is incident on the photo surface at the end, the pulse of light is recorded. If the particle proceeds the other way through the block, the light is absorbed in the blackened end and does not record. It has been pointed out by Huybrechts and Schönberg[12] that a correction term must be inserted in the classical formula to take into consideration the decreased emission in the high-frequency Čerenkov bands due to quantum-mechanical effects near the trajectory of the particles.

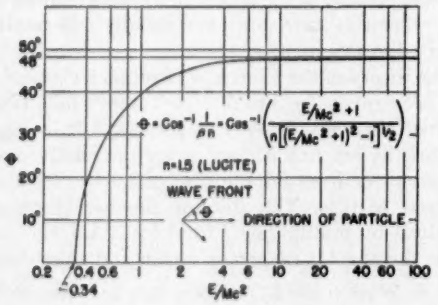

FIG. 3. Angle of emission of Čerenkov radiation for Lucite.

[12] M. Huybrechts and M. Schönberg, Nuovo cimento 9, 764 (1952).

Because Lucite has no absorption bands in the spectral response region of the photomultiplier, it appears that this correction does not influence the calculation for Lucite. It is evident that collision electrons produced in the Lucite block by the high-energy particle may themselves give Čerenkov radiation, if they are above the threshold. The calculation of this effect shows that for high-energy, singly charged particles, there will be an increase in the total quanta produced of about 10

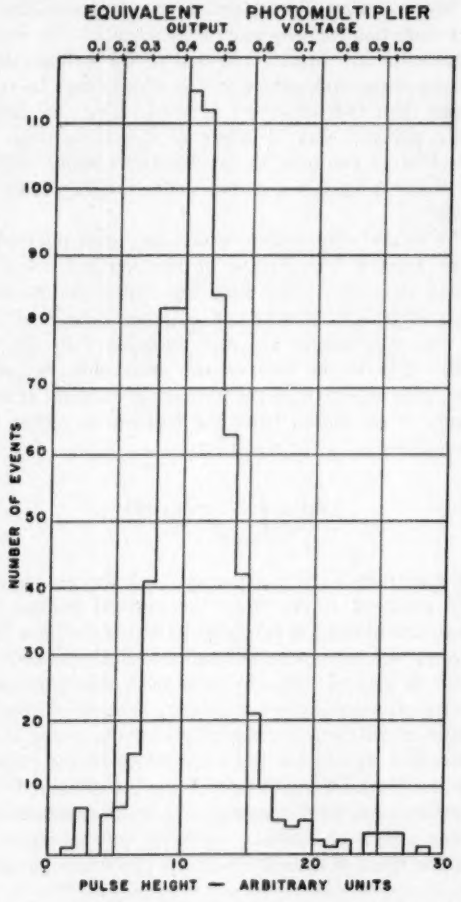

FIG. 4. Pulse-height distribution for sea-level mesons on equipment for flight E. Flight L gives very similar results.

percent and that this will add a tail to the pulse-height distribution on the high side. A typical pulse-height distribution for sea-level mesons is shown in Fig. 4. The mesons were required to traverse 6 inches of lead after passing through the Lucite block. The distribution was obtained for the tube used in flight E, referred to later, and has a half-width of about 50 percent, which is about twice that reported earlier.[9] The half-width appears to be sensitive to the photomultiplier itself, but the exact cause of the change in half-width has not been deter-

mined. This curve clearly shows a tail on the high-energy side associated with the collision electrons produced in the block.

The use of a Čerenkov detector for cosmic rays was first reported by Jelly[13] and was used by Duerden and Hyams[14] in an attempt to separate masses of slow particles. The ability of the Cerenkov detector to discriminate masses was also pointed out by one of us,[8] and comes from combining the Čerenkov emission characteristic, Fig. 2, with, say, a range determination on the particle. With the present instrument a proton of energy between 210 and 319 Mev can penetrate the block of Lucite, the phototube, and the associated Geiger counters, without producing Čerenkov radiation, which is not possible for an electron or a meson. The mass discrimination, however, is confined to a narrow energy region. The angle of emission of the radiation so far has not been utilized to advantage in cosmic-ray

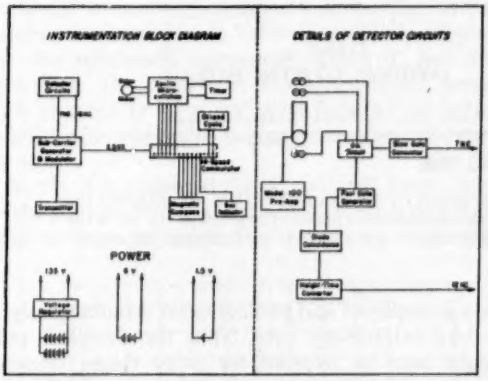

FIG. 5. Block diagram of Čerenkov detector and associate circuitry for use in the high-altitude albedo and geomagnetic studies.

experiments, because the large solid angle necessary to accumulate statistics makes the angular resolution poor; but in the case of an accelerator, one may use the angle of emission to get a very precise measurement of the beam energy, as has been demonstrated by Mather[15] and Marshall.[16] The latter also has utilized the Čerenkov radiation for very high speed counting devices because of the nature of the radiation itself. An attempt was made by Bianchi and Manducci[17] to measure the intensity as a function of energy to reproduce the classical curve, Fig. 2, using a range type of energy selector for sea-level mesons. The results seem to show a rise in the relativistic region above that predicted by classical theory. There has been no further verification of this work.

[13] J. V. Jelly, Proc. Phys. Soc. **A64**, 82 (1951).
[14] T. Duerden and B. D. Hyams, Phil. Mag. **43**, 717 (1952).
[15] R. L. Mather, Phys. Rev. **84**, 181 (1951).
[16] J. Marshall, Phys. Rev. **86**, 685 (1952).
[17] A. M. Bianchi and C. Manducci, Nuovo cimento **9**, 861 (1952).

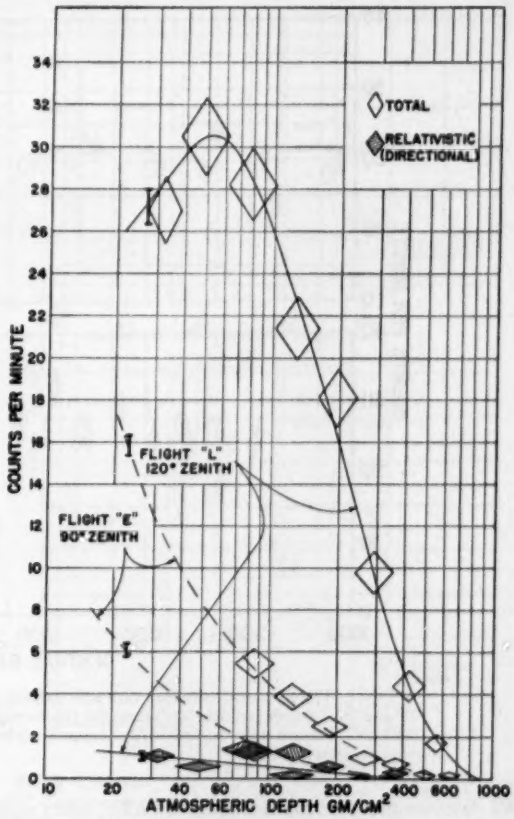

FIG. 6. Total and relativistic counting rates at 90° and 120° as a function of atmospheric depth.

III. EXPERIMENTAL DETAILS

The Čerenkov detector (Fig. 1) consists of the 2½-in. ×4½-in.×8-in. Lucite block with one end cut to a 1¼-in. radius concave to fit the C-7157 photomultiplier. An optical seal is made with Canada balsam. The opposite end of the Lucite is painted black to absorb all incident radiation. The detector is aligned in a threefold Geiger telescope composed of 3 pairs of tubes of 4-in. sensitive length and 1-in. diameter, with the extremities 14½ in. center-to-center. The solid angle is 1.86 sterad-cm². This telescope has a relatively small solid angle as necessitated by the phototube size, and long flights are necessary to accumulate meaningful directional data.

TABLE I. Level flight counting rate values.

		Pressure g/cm²	Counts/minute 0°	180°
Total	Flight *E*	23.6	20.8±.5	20.2
	Flight *L*	27.6	27.2	27.1
Relativistic	Flight *E*	23.6	17.4	1.1
	Flight *L*	27.6	21.4	1.4

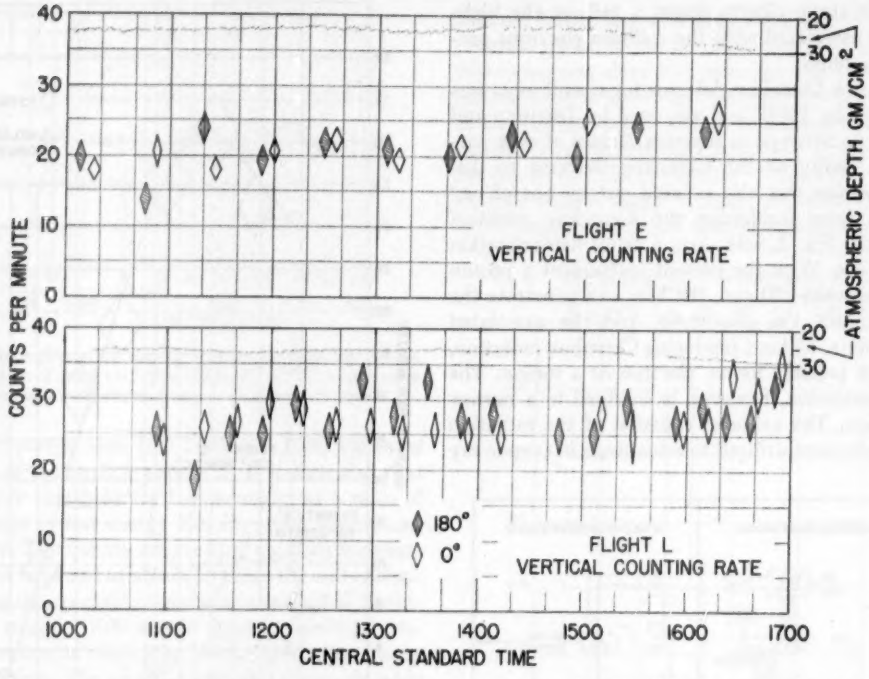

FIG. 7. Total vertical counting rate and balloon pressure height for the two flights. Data are taken for the 0° and 180° zenith positions for all events registering a Geiger telescope coincidence. The graph at the top is the balloon pressure-time record with pressure scale at right top in g/cm². Flux (particles/cm² sec sterad) = (counts/min)×0.009.

All data are given in counts/minute, which, when multiplied by 0.009, gives the flux in particles/cm² sec sterad. The total detector stopping power is 30 g/cm².

The electronics and circuit details are shown in Fig. 5. The Čerenkov pulse appears at a level of about 0.2 volt and 1 μsec in length for a singly charged, fast particle and is amplified 30 times by the model-100 preamplifier. This pulse enters the height-time converter, provided the fast gate is actuated by a signal from the Geiger telescope, and is converted into a square wave of length from 5 to 100 milliseconds. This square wave is transmitted by one of the telemetering subcarriers. The fast-gate signal is also transmitted as a suitable square wave 50 milliseconds in length on a second subcarrier. The detector is mounted so that the zenith position can be varied from straight up to straight down in steps located at 0°, 60°, 90°, 120°, and 180°, and programmed so that approximately 5 minutes are spent successively at each position. The complete gondola is also rotated about a vertical axis one turn every ten minutes. Compass readings and a sun reference photocell index the azimuth, and these data, together with the zenith position and balloon pressure height, are multiplexed on the third telemetering subcarrier. At the ground receiving station the square waves are integrated and the pulses recorded by photographing two cathode-ray tubes. The multiplexed data is displayed and photographed simultaneously on a third cathode-ray tube. Thus the Čerenkov pulse height may be recorded for every Geiger telescope event, and may be associated with the relevant direction in space indicated by the compass and zenith positions. The system is quite similar to that used previously for transmitting telescope and directional data.[1]

Two good flights, designated E and L, were obtained at $\lambda = 40°$ with separate gondolas. Flight E remained level at 23 g/cm² for about 6 hours, and flight L at 27 g/cm² for a similar time. Flight E could record a pulse-height range just up to the α-particle region at four times the pulse height of a singly charged particle, and on the ascending portion the zenith angle was set at 90°. Flight L could record pulses ten times that of a singly charged particle, which made it capable of detecting the Li component. Flight L ascended through the atmosphere in the 120° zenith position, to observe the atmospheric-depth dependence of the oblique-upward component.

IV. EXPERIMENTAL RESULTS

A. Atmospheric-Depth Variation

The data obtained on ascent in the two flights are shown in Fig. 6. The total Geiger telescope flux at 120° (or 60°) passes through a maximum and drops toward

small depths. However, telescope events accompanied by a detectable Čerenkov pulse, indicating a particle having $\beta > 0.7$ moving upward 30° above the horizontal, increase slowly to about 5 percent of the total. At 90° the situation changes markedly, where the relativistic component is a much larger fraction of the total. The total flux in this case does not seem to pass through a maximum, and constitutes a little more than half the 120° (or 60°) total. The values in Fig. 6 are averaged over 360° of azimuth.

B. Vertical Data at Ceiling Altitude

The total vertical (0° or 180°) counting rate for the two flights as a function of time is shown in Fig. 7. As can be seen, the 0° and 180° rates are equal on the average, and are constant with time for most of the flight. Near the end the rate increases somewhat, which is associated with both a slight increase in depth and a northerly component of balloon drift. The average values are summarized in Table I, which also separates out the relativistic component in the 0° and 180° directions. The relativistic flux extrapolated linearly with pressure to 15 g/cm² gives 0.08/cm² sec sterad, in good agreement with values obtained previously at $\lambda = 40°$.[1]

In Fig. 8 is presented the 0° and 180° zenith pulse-height distributions for flight *E* at 23.6 g/cm² for full range of the equipment. The dotted curve shows the

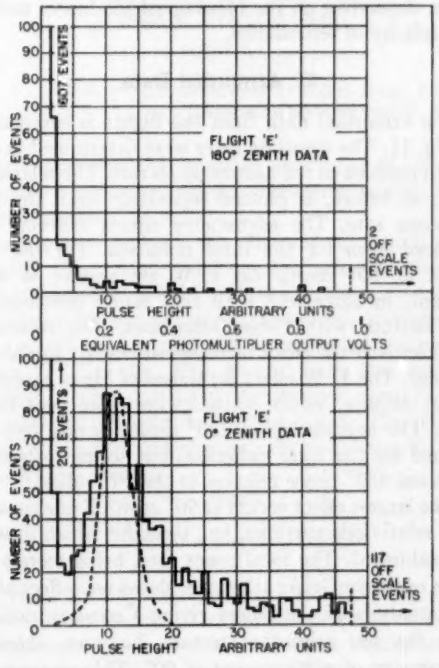

FIG. 8. Čerenkov pulse-height distributions for flight *E*, 0° and 180° direction at 23.6 g/cm². The dotted curve is for sea-level mesons.

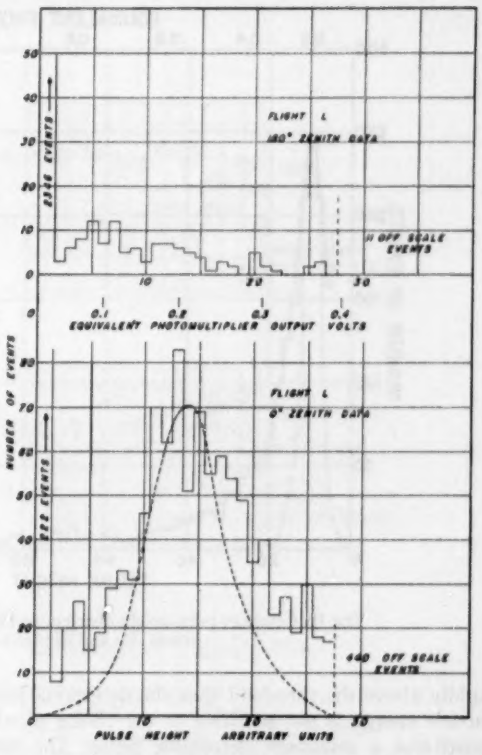

FIG. 9. Čerenkov pulse-height distributions for flight *L*, 0° and 180° direction at 27.6 g/cm². The dotted curve is for sea-level mesons. This is a magnified portion of full scale around proton peak.

distribution obtained for sea-level mesons penetrating 6 inches of Pb after the detector. A very similar set of curves is obtained for flight *L* at 27.6 g/cm² (Fig. 9) for the region near the singly charged particle peak. In both cases the high altitude curve for 0° is filled out above the sea-level curve on the low pulse-height side. There is also a fraction of events for which a particle traversal is recorded but for which *no* Čerenkov pulse is observed. These extra pulses are due to particles which are able to penetrate the block but which give Čerenkov radiation between the threshold and the maximum value. The velocity is then determined and corresponds to $0.34 < E/mc^2 < 4$. In accordance with the discussion in Sec. II, this fraction is assumed to be protons with $210 < E < 319$ Mev, or upward relativistic particles. The 180° distribution shows no peak at all, but indicates a small number of upward moving particles with $0.34 < E/mc^2 < 4$, and a large number of events giving no Čerenkov light. Most of these are the downward particles recorded in the 0° direction, the remainder the protons with $210 < E < 319$ Mev for which direction is not determined. From these data the up-and-down relativistic and the lower-energy proton flux may easily be computed. The Čerenkov light output increases so

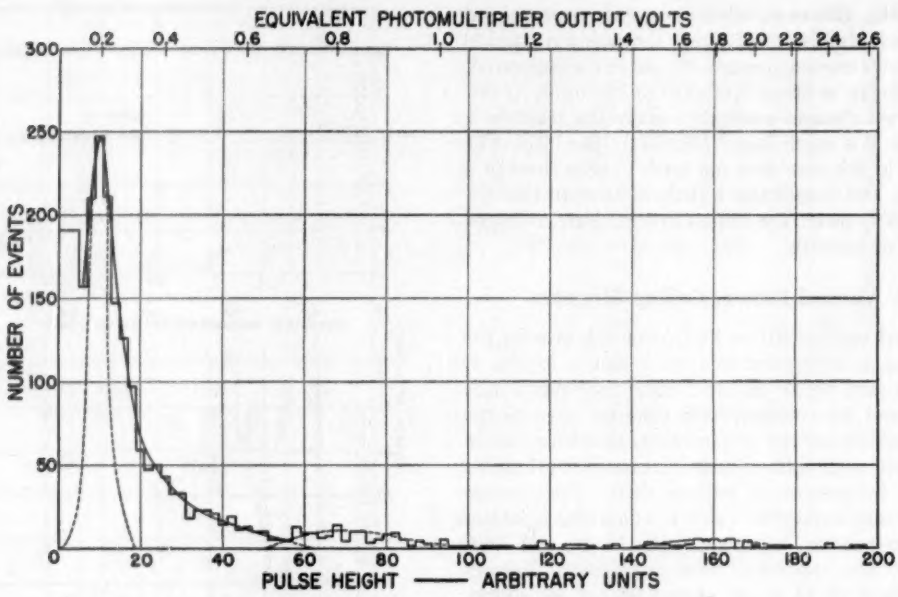

FIG. 10. Čerenkov pulse-height distribution for flight L, 0° direction, 27.6 g/cm² with wide scale, showing proton, He and Li peaks. Dotted curve is for sea-level mesons.

rapidly above the threshold that the determination of particle energy is not sensitive to the choice of what constitutes a minimum detectable pulse. The fill-in between the sea level and the high-altitude curves on the high side is to be associated with *nuclear* collisions, the electron collisions being already present in the sea-level curve. This effect is very pronounced, as would be expected for approximately 29 g/cm² of Lucite, or nearly half of a geometrical mean-free-path for protons. The Čerenkov effect comes from charged particles produced with $E/mc^2>0.34$ in the collisions. The multiplicity cannot be uniquely determined, as the residual path in the radiator is unknown for any particular event. Some of these pulses may be due to α particles or heavy nuclei of reduced velocity, but the principal contribution comes from nuclear collisions.

In Fig. 10 is shown the wide-range pulse-height distribution for flight L at 0° zenith. The singly charged peak is just resolved out of the width of the recording-oscilloscope background trace for this large scale (compare Fig. 9). There is a distinct peak at a voltage (read top scale) four times the singly charged peak, attributable to He, and a peak at nine times the singly-charged voltage attributable to Li. The latter is only two or three times background, so that the relative abundance figure is not very meaningful. However, we get the value H:He:Li=1:08:0.02 applicable at 27.6 g/cm² at $\lambda=40°$. The half-width of the He and Li peaks seems much smaller than the proton peak. Since all primaries have a value of E/mc^2 well up on the Čerenkov curve at this latitude, this is assumed to result from the improvement in photon statistics as the number of photons increases proportional to Z^2. For heavies, a nuclear collision may *decrease* or *increase* the output pulse, depending on the breakup of the heavy and the multiplicity of secondaries.

C. Azimuthal Data

The azimuthal data from the flights is summarized in Fig. 11. The counting rates were determined in each zenith position in ten azimuthal sectors. The relativistic data, as before, is plotted separately from the total telescope rate. The asymmetry effects are very pronounced even for the total radiation. For the total count at 60° zenith the E–W asymmetry is 30±5 percent, in agreement with that found previously at this latitude with Geiger telescopes.[1] For relativistic particles *only* the effect increases somewhat to about 35 percent. The E–W effect for pulses of He or larger size is not definite, as the statistics are quite poor in this case. The asymmetry at 120° zenith is not very well defined for the total radiation, but seems to bear the expected 180° phase relation to the 60° values.[18]

The largest effect occurs at 90° zenith if one considers *only* relativistic particles, i.e., those for which direction is established. The total count rate, being merely that of an ordinary Geiger telescope, shows *zero* effect at 90°. The analysis of the pulses giving Čerenkov radiation into the ten azimuthal sectors, however, shows an asymmetry of ≈80 percent at 90°. This measurement

[18] The gondola azimuth is referred to the telescope direction when pointing above the horizontal.

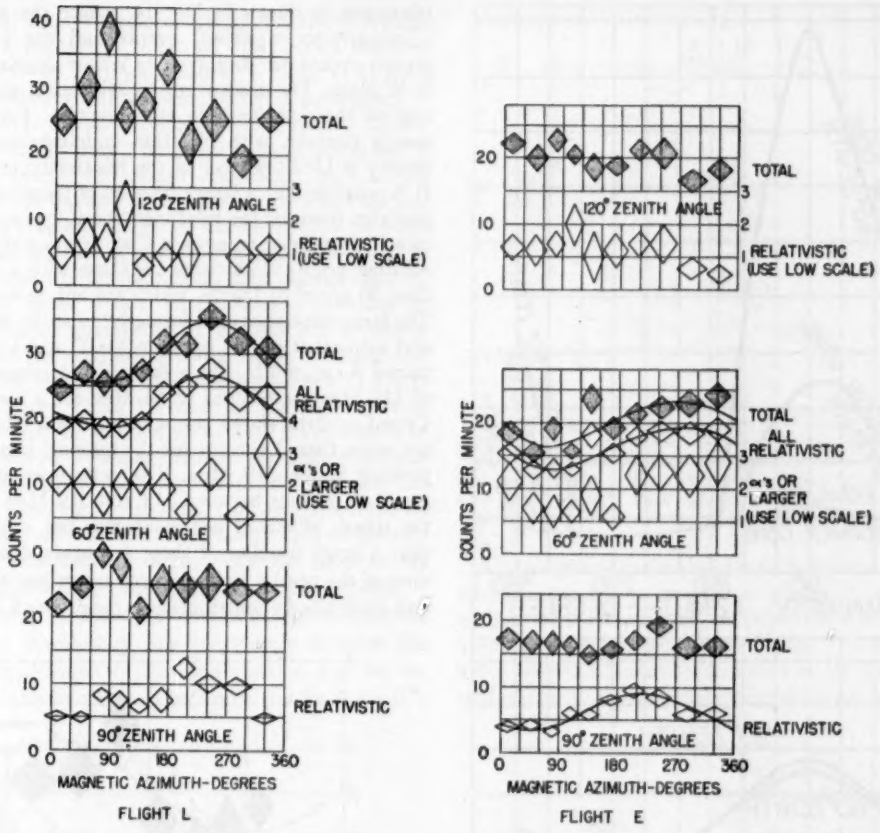

FIG. 11. Azimuthal data for flights E and L in 60°, 90°, and 120° zenith positions. The total and relativistic parts are plotted separately. At 60° zenith pulses ≥ 2 particles also are plotted.

in particular displays the great superiority of this type of detector over conventional telescopes for directional measurements.

Comparison between the observed azimuthal effect and the effect predicted from the primary spectrum and geomagnetic theory is shown in Figs. 12 and 13. The theoretical cut-off energy for protons at $\lambda = 40°$ for 40° and 60° zenith angles as a function of azimuth is shown in Fig. 12. This comes from the work of Schremp,[19] who computed the shadow cone for this latitude, and from simple Störmer theory. The Störmer variable, as a function of zenith (z) and azimuth (φ), is given by the relation

$$r_0 = \frac{\cos^2\lambda}{\gamma^2 + (\gamma^2 - \sin z \sin\varphi \cos^2\lambda)^{\frac{1}{2}}}. \qquad (3)$$

The value $\gamma = 1.0$ at $\lambda = 40°$ was used. Schremp's data are presented in the literature as projections of the allowed cone intersection with the unit hemisphere on the horizontal plane. From such figures the earth-shadow effect values were taken, with somewhat less accuracy than implied by the curves of Fig. 12. Figure 13 compares the predicted and observed curves for the azimuthal effect at $\lambda = 40°$ for 60° and 90° zenith. The comparison was made as follows. The applicable integral number-energy spectrum obtained from the vertical flux at 15 g/cm² (see reference 1) is $0.30E^{-0.90}$/cm² sec sterad, with the energies in Bev of kinetic energy for protons. From this spectrum and the curves of Fig. 12 the curves of Fig. 13 were constructed. The counting rates from the present experiments were normalized to have the same azimuthal average as the predicted curves and plotted, with magnetic azimuth kept on an absolute basis. The flux values of the present measurements were on the average too high because of the somewhat larger atmospheric depth (25 *vs* 15 g/cm²), hence the normalization. Although the primary energy is expressed in Bev for protons, the comparison is valid for any type primary nucleus, except that all positive primaries are assumed. As shown in Fig. 13, the present results agree rather well with the Störmer theory at 60° zenith and are in definite disagreement

[19] E. J. Schremp, Phys. Rev. **54**, 153, 158 (1938).

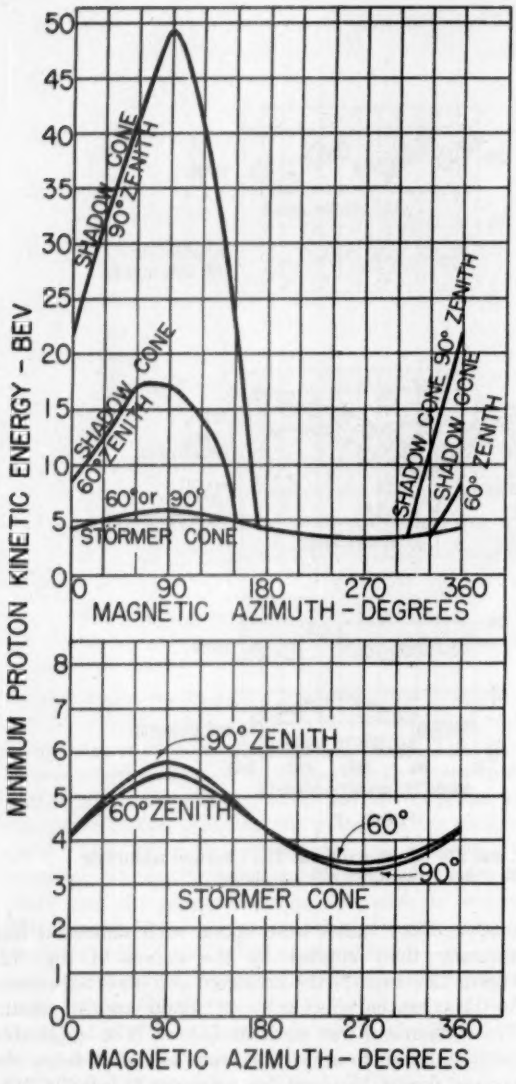

FIG. 12. Theoretical cut-off energy for $\lambda=40°$ considering Störmer theory (lower) and with the addition of the Schremp shadow cone calculation (above).

with the intensities predicted by the shadow-cone theory. At 90° zenith the present results lie *between* the simple Störmer and shadow-cone intensities. In the horizontal direction at 24 g/cm² there is 300 to 400 g/cm² of atmosphere ahead of the detector, so that the measurements are farther removed from the primaries. Nevertheless, the strong indication is that the shadow cones lie at somewhat larger zenith angles than predicted. Measurements at higher altitudes, say 5–6 g/cm², where large zenith-angle data are more meaningful, are essential to see if this conclusion is justified.

The albedo flux likely to affect ordinary Geiger telescopes is shown in Fig. 14, where the relativistic (Čerenkov-accompanied) events and the low-energy proton events are displayed as vector diagrams in the E–W plane. The upward relativistic flux is about 5 percent of the downward in any direction. For the low-energy protons, with direction undetermined, the intensity is 15–20 percent of the relativistic component. It is possible that a larger fraction of these are upward particles than for the relativistic case, but even in this case their number represents a low fraction of the total. Another group of particles are those with a range less than 30 g/cm² of Lucite, which are not detected at all. The large telescopes used formerly[1] to study the vertical and azimuthal effects between $\lambda=0°$ and $\lambda=40°$ contained 3 cm of Pb, which implied a minimum energy of 112 Mev for protons or 64 Mev for μ mesons. The Čerenkov data shows the splash albedo effects to be not more than 5 percent for the mesons, together with protons above 319 Mev. The telescopes included a group of protons between 112 and 319 Mev for which the splash albedo is not measured, but it is unlikely that a large fraction of these are upward moving, in view of the results for the energy range just above this, and their albedo contribution is hence small in relation

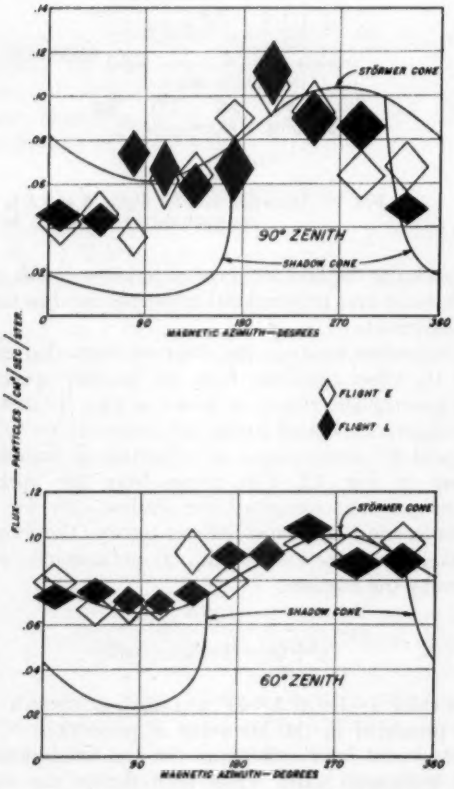

FIG. 13. Comparison of observed and predicted values of azimuthal effects at 60° and 90° zenith angles at $\lambda=40°$.

to the total flux. Therefore, the splash albedo values obtained, if applied to telescope experiments between $\lambda=0°$ and $\lambda=40°$, are too small by a factor of at least four to resolve the latitude-asymmetry disagreement.

Aside from its contribution to the splash albedo, which is probably small, the lower-energy proton flux is of interest even if 100 percent downward, as it affects the second discrepancy mentioned in the introduction, namely the absolute energy comparisons. Here we must consider the fraction of particles vertically detected at 15 g/cm² that are not primaries. The present data at ≈25 g/cm² show a flux that definitely contains at least 15 percent nonrelativistic protons which cannot be primaries. In addition, the relativistic counting rate is decreasing with decreasing depth between 27.6 and 23.6 g/cm² (see Table I), showing that part of this component may be secondaries as well. An extension of the present type of measurement to the highest obtainable altitude would be very useful in clarifying the situation. However, it appears that perhaps a 10–30 percent effect may be accounted for by such an investigation, but not a factor of two, as exists between the particle and ionization measurements of total energy.

It may now be stated in conclusion that neither the asymmetry discrepancy nor the energy balance discrepancy mentioned in the introduction can be explained by albedo effects at balloon altitudes at $\lambda=40°$.

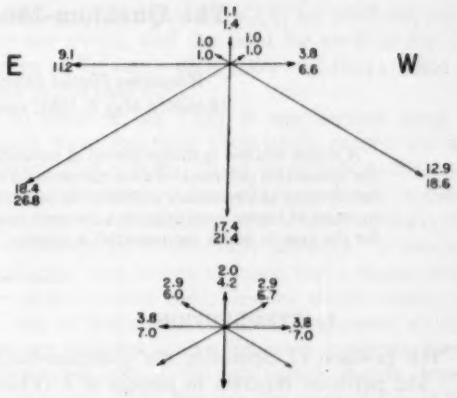

FIG. 14. Vector diagram in the E–W plane for relativistic particles (above) and protons of energy between 210 and 319 Mev (below). The upper numbers on each diagram refer to flight *E*, the lower to flight *L*. The values are in counts/minute. Statistical error ±10 percent. Flux (particles/cm² sec sterad) = (counts/min)×0.009.

A possible alternative explanation for the low asymmetries observed at $\lambda=40°$ is suggested by the azimuthal effects measured with the Čerenkov detector which are free of splash albedo effects. This is the possibility that the shadow-cone limits lie at larger zenith angles than those predicted by Schremp's calculation.

The Quantum-Mechanical Partition Function

G. V. CHESTER*
Wheatstone Physics Laboratory, King's College, London, England
(Received May 8, 1953; revised manuscript received August 7, 1953)

A simple method is demonstrated of expanding the quantum-mechanical partition function in powers of the interaction potential between the particles of the system. The result is valid for all types of statistics and for all types of interaction, provided the interaction potential is nonsingular. The general term is expressed, in terms of known quantities, in a compact form. It is shown that the series must be considerably modified for the case in which the potential is singular. The convergence of the series is discussed briefly.

I. INTRODUCTION

THE problem of expanding the quantum-mechanical partition function in powers of h (Planck's constant) has been discussed by various authors.[1-5] Several methods of obtaining the original expansions, due to Wigner and Kirkwood, have now been given. As these series are, however, only useful at sufficiently high temperatures, where quantum effects are comparatively small, efforts have been made to develop an expansion convergent at low temperatures. Thus, Green[4] has obtained the first two terms of an expansion in powers of the interaction potential between the particles of the system. His results are in an extremely cumbersome form and are, in any case, limited to the case of Boltzmann statistics, whereas the few calculations that have actually been carried out[6,7] at low temperatures definitely show that the type of statistics obeyed by the particles is of considerable importance. Goldberger and Adams[5] obtained the general term in the series proposed by Green. The final result was, however, left in an awkward operational form and the calculations were again limited to the case of Boltzmann statistics. Finally, Siegert[8] showed how the series could be obtained by solving an integral equation for the partition function by an iterative procedure. In this approach it is easy to take into account, in a formal manner, the type of statistics obeyed by the particles. The general term in the series was not, however, calculated in an explicit form. A knowledge of the general term is clearly of importance if we wish to discuss, even qualitatively, the convergence of the expansion.

The purpose of the present paper is to rederive, and to discuss the validity of, the expansion of the partition function in powers of the interaction potential. It is first shown that the series may be obtained by a straightforward application of Taylor's theorem to the partition function of the system. The calculation is quite general and is valid for all types of statistics. The general term is expressed, in terms of known quantities, in a compact form. In Sec. 3 we compare our work with that of previous authors. The equivalence of our expansion with that due to Goldberger and Adams is established. Lastly, the validity of the expansion is discussed. It is shown that the terms in the series must be considerably modified if the potential possesses any singularities. In fact, the series is only valid in this case if the particles of the system are considered to have finite (nonzero) incompressible cores. A condition is obtained for the convergence of the series.

II. THE EXPANSION IN POWERS OF THE POTENTIAL

The partition function (Z) of a system, is usually written as

$$Z=\sum_q \exp(-\beta\mathcal{E}_q), \tag{1.1}$$

where in Eq. (1.1), $\beta=1/kT$, and the $\mathcal{E}_q$ are the energy levels of the system. A well-known alternative form of Eq. (1.1) is

$$Z=\mathrm{Tr}[\exp(-\beta H)], \tag{1.2}$$

where H is the Hamiltonian of the system, and $\mathrm{Tr}(A)$, stands for the trace of the quantum-mechanical operator A. It is assumed, in what follows, that the Hamiltonian is independent of any spin coordinates of the particles.

The trace of any operator is invariant under change of representation. Consequently, any complete set of wave functions can be used to form the trace in Eq. (1.2).

For a system of N interacting particles, in an enclosure, H can be written H_0+gV, where H_0 is the translational energy and gV the potential energy of the mutual interactions. The partition function Z can now be thought of as a function of g. It will be shown that the Taylor series expansion of Z in powers of g is identical with the series proposed by Goldberger and Adams. We first write

$$\exp[-\beta(H_0+gV)]=\exp(-\beta H)=\sum_{\nu=0}^{\infty}\frac{(-1)^\nu}{\nu!}\beta^\nu H^\nu. \tag{1.3}$$

* Present address: Radar Research Establishment, Great Malvern, Worcestershire, England.

[1] E. P. Wigner, Phys. Rev. 40, 749 (1932).
[2] J. G. Kirkwood, Phys. Rev. 44, 31 (1933).
[3] J. E. Mayer and W. Band, J. Chem. Phys. 15, 141 (1947).
[4] H. S. Green, J. Chem. Phys. 19, 955 (1951).
[5] H. Goldberger and E. N. Adams, J. Chem. Phys. 20, 240 (1952).
[6] De Boer, Van Kranendonk, and Compaan, Physica 16, 545 (1950).
[7] J. H. De Boer and E. G. D. Cohen, Physica 17, 993 (1951).
[8] A. J. F. Siegert, J. Chem. Phys. 20, 572 (1952).

If Taylor's theorem is applied to the right-hand side of Eq. (1.3), it becomes

$$\exp(-\beta H)=\sum_{n=0}^{\infty} g^n/n!\sum_{\nu=0}^{\infty}(-1)^\nu\beta^\nu/\nu!\,[D^nH^\nu]_{g=0}, \quad (1.4)$$

where in Eq. (1.4) $D=\partial/\partial g$. Combining Eq. (1.4) with Eqs. (1.2) and (1.3),[9]

$$Z=Z(g)=\sum_{n=0}^{\infty} g^n/n!\sum_{\nu=0}^{\infty}(-1)^\nu\beta^\nu/\nu!\,\mathrm{Tr}\{[D^nH^\nu]_{g=0}\}. \quad (1.5)$$

Thus, the fundamental quantity to be calculated is $\mathrm{Tr}\{[D^nH^\nu]_{g=0}\}$. To carry out this calculation the following simple relations are needed:

$$D(H)=V, \quad D^n(H)=0, \ n>1, \text{ and } [H]_{g=0}=H_0. \quad (1.6)$$

It is now easily seen, using these relations, that $(D^nH^\nu)_{g=0}$ can be written as the sum of a number of terms of the form

$$H_0^{\nu_1'}VH_0^{\nu_2'}VH_0^{\nu_3'}\cdots H_0^{\nu_n'}VH_0^{\nu_{n+1}'}. \quad (1.7)$$

In the expression (1.7) the ν_k' are integers and can take on any values from 0 to $\nu-n$, subject to the condition that

$$\sum_{k=1}^{n+1}\nu_k{}'=\nu-n.$$

As we are only concerned with the trace of (1.7), the theorem that $\mathrm{Tr}(AB)=\mathrm{Tr}(BA)$ can be used to rewrite it as

$$H_0^{\nu_1}VH_0^{\nu_2}VH_0^{\nu_3}\cdots H_0^{\nu_n}V, \quad (1.8)$$

with precisely the same conditions on the ν_k. The complete expression for $(D^nH^\nu)_{g=0}$ can now be written down:

$$(D^nH^\nu)_{g=0}=(n-1)!\nu\sum_{(\nu k)}H_0^{\nu_1}VH_1^{\nu_2}\cdots H_0^{\nu_n}V, \quad (1.9)$$

where in Eq. (1.9) $\sum_{(\nu k)}$ means that the summation is to be taken over all sets of integers ν_k, satisfying the relation

$$\sum_{k=1}^{n}\nu_k=\nu-n.$$

The factor ν arises from the fact that the first differentiation gives rise to ν equal terms of the form $H_0^{\nu-1}V$, while the factor $(n-1)!$ arises because at the kth stage of forming the nth differential coefficient there are $k-1$ groups of H's, any one of which can be chosen as the operand for the kth operator. Thus, $(k-1)$ terms, each of which is identical with a typical term of the form (1.8), arise from the kth stage of forming D^nH^ν. In this way, the complete factor $(n-1)!$ is built up. The result, Eq. (1.9), holds for $n\geq 1$; for $n=0$ the calculations are trivial, and the term for $n=0$ in Eq. (1.5) reduces to $\mathrm{Tr}[\exp(-\beta H_0)]$. We can thus confine ourselves to the case $n\geq 1$.

The trace of Eq. (1.9) is now formed using free particle wave functions (Ψ_q) which satisfy the wave equation $H_0\Psi_q=E_q\Psi_q$. These wave functions must be correctly symmetrized (or antisymmetrized), according to whether we are dealing with a system which obeys Bose-Einstein or Fermi-Dirac statistics. If this symmetrization were not carried out, and a single product wave function were used, then we would merely have the case of Boltzmann statistics. However, all three cases are included in the following analysis; the difference arises only in the way certain matrix elements are calculated. Thus, forming the trace of Eq. (1.9),

$$\mathrm{Tr}(D^nH^\nu)_{g=0}=(n-1)!\nu\sum_{(q_j)}\sum_{(\nu k)}E_{q_1}{}^{\nu_1}E_{q_2}{}^{\nu_2}\cdots \times E_{q_n}{}^{\nu_n}V_{q_1q_2}\cdots V_{q_nq_1}, \quad (1.10)$$

where in Eq. (1.10), the E_{q_i} are the free particle energy levels, and the summation $\sum_{(q_j)}$ indicates that the summation is to be taken over all sets of the q_j. The $V_{q_iq_j}$ are the matrix elements of the interaction potential V, and are given by

$$V_{q_iq_j}=\int\Psi_{q_i}{}^*V\Psi_{q_j}d\mathbf{r}_1\cdots d\mathbf{r}_n. \quad (1.11)$$

The integration in Eq. (1.11) is to be taken over all the coordinates (including a summation over any spin coordinates) of the particles in the system, the limits being determined by the boundaries of the enclosure. As the E_{q_i} are the same, whether the Ψ_{q_i} are symmetrized or not, the only difference due to the statistics arises from (a) the enumeration of states Ψ_{q_i} in forming the sum $\sum_{(q_i)}$ and (b) in the form of the matrix elements, Eq. (1.11), according as the Ψ_{q_i} are symmetrized or antisymmetrized.

The sum over the sets (ν_k) in Eq. (1.10) can be carried out by using a generating function. Equation (1.10) is written as

$$\mathrm{Tr}[(D^nH^\nu)_{g=0}]=\nu(n-1)!\sum_{(q_j)}V_{q_1q_2}\cdots V_{q_nq_1} \times[\text{coeff. of } z^{\nu-n} \text{ in } \prod_{i=1}^{n}(1-zE_{q_i})^{-1}]. \quad (1.12)$$

The required coefficient can easily be picked out, if a technique due to Dingle[10] is used. The generating function is broken up into partial fractions, thus:

$$\prod_{i=1}^{n}(1-zE_{q_i})^{-1}=\sum_{j=1}^{n}A_j(1-zE_{q_j})^{-1}. \quad (1.13)$$

It is assumed, for the moment, that the E_{q_j} are unequal;

[9] This step involves the interchange of the operations of trace and summation. If any difficulty arises, in any particular case, from this interchange it can be regarded as being purely formal and the remainder of the analysis will still be valid.

[10] R. B. Dingle, Proc. Cambridge Phil. Soc. 45, 275 (1949).

then the A_j are given by

$$A_j=\prod_{i\neq j=1}^{n} E_{qj}{}^{n-1}(E_{qj}-E_{qi})^{-1}. \tag{1.14}$$

Combining Eqs. (1.14) and (1.13),

$$\prod_{i=1}^{n}(1-zE_{qi})^{-1}=\sum_{j=1}^{n}\left[\prod_{i\neq j}^{n}\frac{E_{qj}{}^{n-1}}{(E_{qj}-E_{qi})}\right](1-zE_{qj})^{-1}. \tag{1.15}$$

The coefficient of z^{r-n} in $(1-zE_{qj})^{-1}$ is $E_{qj}{}^{r-n}$, so finally,

$$\mathrm{Tr}[(D^nH^r)_{g=0}]=\nu(n-1)!\sum_{(qj)}V_{q_1q_2}\cdots V_{q_nq_1}$$

$$\times\sum_{j=1}^{n}E_{qj}{}^{r-1}\prod_{i\neq j}^{n}(E_{qj}-E_{qi})^{-1}. \tag{1.16}$$

The expansion of Z may now be written down, remembering that the term for $n=0$ requires special treatment; thus,

$$Z=Z_0+\sum_{n=1}^{\infty}g^nZ_n, \tag{1.17}$$

where in Eq. (1.17) Z_0 is given by,

$$Z_0=\sum_q\exp(-\beta E_q), \tag{1.18}$$

and Z_n is given by,

$$Z_n=-(\beta/n)\sum_{(qj)}V_{q_1q_2}\cdots V_{q_nq_1}$$

$$\times\sum_j[\exp(-\beta E_{qj})\Big/\prod_{i\neq j}^{n}(E_{qj}-E_{qi})]. \tag{1.19}$$

Thus, Eq. (1.19) gives an explicit expression for the nth term in the expansion of Z in powers of g, and also in powers of the matrix elements of the interaction potential. In the above derivation, it might be thought that the summation over the sets (q_j) should be restricted to unequal values of the q_j, because of terms with $(E_{qj}-E_{qi})$ in the denominator. Such a restriction is, however, unnecessary as it is easily shown that the numerators of these terms also vanish for $E_{qi}=E_{qj}$. By a careful passage to the limit $(E_{qi}\to E_{qj})$ a finite result is obtained. This result is identical with that obtained by allowing some of the E_{qj} in Eq. (1.13) to be equal.

III. COMPARISON WITH PREVIOUS WORK

Goldberger and Adams, in their paper,[5] quote the following result, due to Schwinger. If a and b are any two operators, then

$$\mathrm{Tr}[e^{-(a+b)}]=\mathrm{Tr}[e^{-a}]-\mathrm{Tr}[be^{-a}]$$

$$+\sum_{n=2}^{\infty}\frac{(-1)^n}{n}\int_0^1 s_1{}^{n-1}ds_1\int_0^1 s_2{}^{n-2}ds_2\cdots\int_0^1 ds_n$$

$$\times\mathrm{Tr}(be^{-(1-s_1)a}be^{-s_1(1-s_2)a}\cdots be^{-s_1\cdots s_na}). \tag{2.1}$$

If we identify a with βH_0 and b with βVg, then the left-hand side of Eq. (2.1) is merely the partition function of Sec. II. Formally, it is quite clear that this expansion is identical with that given above, both being expansions in powers of g. This can easily be verified by writing the general term in the series in Eq. (2.1) as

$$Z_n'=\frac{(-\beta)^ng^n}{n}\int_0^1 s_1{}^{n-1}ds_1\cdots\int_0^1 ds_n$$

$$\times\mathrm{Tr}(Ve^{-(1-s_1)\beta H_0}\cdots Ve^{-s_1s_2\cdots s_n\beta H_0}). \tag{2.2}$$

The trace in Eq. (2.2) is now formed, using the same wave functions as before; thus,

$$Z_n'=\frac{(-\beta)^ng^n}{n}\sum_{(qj)}V_{q_1q_2}\cdots V_{q_nq_1}$$

$$\times\int_0^1 s_1{}^{n-1}\exp(-\beta s_1E_{q_1})ds_1\cdots$$

$$\times\int_0^1 ds_n\exp(-\beta s_1s_2\cdots s_nE_{q_n}). \tag{2.3}$$

By direct integration it is easily shown that

$$Z_n'=-\frac{\beta g^n}{n}\sum_{(qj)}V_{q_1q_2}\cdots V_{q_nq_1}\sum_{j=1}^{n}\frac{\exp(-\beta E_{qj})}{\prod_{i\neq j}(E_{qj}-E_{qi})}; \tag{2.4}$$

thus Z_n' and g^nZ_n are identical. In this form, Eq. (1.19), the general term is expressed in terms of known quantities, E_{qj} and V_{qiqj}. This is a considerable advantage if we wish to estimate the order of magnitude of the terms in the series. In deriving the expansion, it was assumed initially that the Hamiltonian could be split into two parts H_0 and gV, one of which (H_0) had a very simple eigenvalue equation, the solutions of which were known. However it is obvious, from the method of derivation, that the expansion is valid for any partition of a general Hamiltonian, provided that the solutions of the eigenvalue equation of one of the parts are known, and these are used to form the trace in Eq. (1.5). Another formal method of generating the series is to substitute in the usual formula, Eq. (1.1), for the partition function, the perturbation expansion for the qth energy level, and then expand the resulting expression in powers of g. The procedure requires to be justified because of possible degeneracies in the energy levels. Our procedure avoids this.

It is of interest to compare the first-order term in the above series, with the same term in the series due to Goldberger and Adams[5] and Green.[4] In both these papers the series was generated by expanding the configurational distribution function, in a power series in the interaction potential, and then integrating term by term over all the coordinates. No account was taken of quantum statistics in either case. It was pointed out

by Goldberger and Adams that the first term in their series is identical with that given by Green. However, when the term is integrated over all the coordinates, the result is trivial, namely that

$$gZ_1 \propto Z_0. \tag{2.5}$$

This result follows at once from our expansion, for

$$gZ_1 = -\beta g \sum_q V_{qq} \exp(-\beta E_q), \tag{2.6}$$

and in the case of classical statistics V_{qq} is independent of q, and thus Eq. (2.6) at once reduces to Eq. (2.5). However, in the case of quantum statistics V_{qq} is not independent of q, and Eq. (2.6) is no longer trivial. In a later paper Green[11] has derived the general term in the form of an extremely complicated integral. This result is again limited to the case of classical (Boltzmann) statistics. It would seem, however, that if the series proves to be useful, it will be in the region of low temperatures, where the Kirkwood expansion is too slowly convergent to be of any use. In this region there is reason to believe that quantum statistics exert a marked influence on the properties of a system. Thus, the two isotopes of helium show markedly different properties at low temperatures. Likewise, De Boer's calculations[6,7] on the light isotope of helium again show up the importance of the statistics obeyed by the particles. Indeed, the discussion of the second term in the series, Eq. (2.6), completely confirms our statement.

It might seem, at first sight, that each term in the series is proportional to β. However, the general term Z_n consists of a sum of terms of the form $R(q_k)$, where (q_k) is the set of all summation indices $q_1 \cdots q_n$. It is easily shown that if any term $R(q_k)$ has r of these indices equal then it is proportional to β^r. Consequently, each term Z_n contains "sub terms" proportional to all powers of β up to β^n. This is contrary to Green's suggestion[4] that each successive term would be proportional to β.

IV. THE VALIDITY OF THE EXPANSION

In this section, the existence of the individual terms (Z_n) will be investigated first, and then the more difficult problem of the convergence of the series will be discussed.

In the deduction of the series, no account was taken of any singularities in the potential function V. In many cases, however, V will possess singularities, for instance, if it represents the interaction potential of a number of particles. This type of potential was assumed in Sec. II. The importance of such singularities is illustrated by considering the classical partition function. This is proportional to $\int_S \exp(-\beta V)dQ$, where S is the whole of configuration space, and Q stands for all the coordinates. If the exponential is expanded in powers of V, and V has any singularities, then there will be an n such that all integrals of the type $\int_s (\beta V)^p dQ (p \geq n)$ will diverge. Consequently, this expansion of the classical partition function is invalid. This state of affairs can easily be remedied, if the only kinds of singularity that V possesses are such that it becomes positively infinite. If this is assumed, then the range of integration (S) can be split up into two parts S_1 and S_2, such that S_1 constitutes the region where V is bounded, and S_2 consists of the remainder of configuration space. Then it is seen at once that the integral over the region S_2 vanishes, because $\exp(-\beta V)$ is identically zero in this region. The partition function is now proportional to $\int_{S_1} \exp(-\beta V)dQ$ and as V is bounded in the set of points S_1 all integrals of the type $\int_{S_1} (\beta V)^p dQ$ will be finite. Thus, if we wish to expand the partition function in powers of V, the range of integration of each term must exclude the points at which V is singular.

It will now be shown that precisely the same conclusion holds in the case of the quantum-mechanical partition function. First, it is easily seen that similar divergent integrals will occur in the quantum-mechanical case. For the expansion of $\exp(-\beta H)$ consists of a sum of terms of the form $H_0^{r_1} V \cdots H_0^{r_n} V$. Clearly, if any one of these operators is expanded, then there will always be one term of the type $V^n H_0^{r-n}$. When the trace of this term is formed, the integral that results will diverge for sufficiently large n. To avoid this difficulty, a similar method to that used above is employed. The following assumptions are first made about V: (a) if any pair of particles with position vectors $\mathbf{r}_i$ and $\mathbf{r}_j$ take up a configuration such that $|\mathbf{r}_i - \mathbf{r}_j| \leq 2r_0$, then V is to become positively infinite; (b) otherwise, V is to be continuous and bounded everywhere. The entire configuration space (S) of the system is again divided into two parts, S_1 which consists of S apart from the $N(N-1)/2$ regions such that $|\mathbf{r}_i - \mathbf{r}_j| \leq 2r_0$, while S_2 constitutes the remainder of S. These assumptions about the potential energy include all the types of interactions that are commonly met with in statistical mechanics. Thus, if V has no singularities r_0 is zero and S_2 is merely the null set. If V is singular at isolated points, then r_0 is again zero, and to proceed with the analysis, r_0 is replaced by ϵ, which is set equal to zero at the end of the calculations. Finally, if there are regions in which V is singular, then r_0 is finite. This would occur for the case in which the particles are supposed to have incompressible cores of radius r_0.

The partition function Z is given by

$$Z(\beta) = \int_S \sum_q \phi_q^*(Q)\phi_q(Q) \exp(-\beta E_q)dQ, \tag{4.1}$$

where in Eq. (4.1) $\phi_q(Q)$ is the qth eigensolution of the eigenvalue equation $H\phi_q = E_q\phi_q$, and Q stands for the set of all coordinates. The ϕ_q must, of course, be suitably symmetrized. Define $I(Q)$ by the equation,

$$I(Q) = \sum_q \phi_q^*(Q)\phi_q(Q) \exp(-\beta E_q). \tag{4.2}$$

[11] H. S. Green, J. Chem. Phys. **20**, 1274 (1952).

Then, $I(Q)dQ$ is the probability that at a temperature T the coordinates (Q) of the system have values lying between Q and $Q+dQ$. This statement follows immediately from the definition that $\phi_q^*(Q)\phi_q(Q)dQ$ is the probability that the coordinates of the system have values lying between Q and $Q+dQ$, when the system is in the state $\phi_q(Q)$. Now, it follows from a theorem due to Pauli[12] that $\phi_q^*(Q)\phi_q(Q)\tau(Q)\to 0$ as we approach any of the singularities of V, where dQ has been written as $\tau(Q)dr_1\cdots dr_N$, $\tau(Q)$ being the weight factor for dQ. If this were not so, then the Hamiltonian of the system would be no longer be Hermitian. Thus, in the set of points S_2 $I(Q)dQ$ is identically zero. That this must be so is obvious in the case of particles with incompressible cores, for the wave functions must be made to vanish in the region of the core. However, this type of potential requires special consideration; we will, therefore, suppose, for the moment, that the potential is only singular at isolated points. The function $I(Q)$ can be written in the form

$$I(Q)=\sum_q \phi_q^*(Q)\exp(-\beta H)\phi_q(Q). \tag{4.3}$$

The wave functions ϕ_q are now expanded in terms of the complete orthonormal (suitably symmetrized) set of free particle wave functions $\Psi_n(Q)$, and it is easily shown that Eq. (4.3) becomes

$$I(Q)=\sum_n \Psi_n^*(Q)\exp(-\beta H)\Psi_n(Q). \tag{4.4}$$

When Eqs. (4.4) and (4.1) are combined, it is found that

$$Z(\beta)=\int_{S_1+S_2} I(Q)dQ=\int_{S_1}\sum_n \Psi_n^*(Q)\exp(-\beta H)\Psi_n(Q). \tag{4.5}$$

If $\mathrm{Tr}'(A)$ stands for the trace of A, with the restriction that all the integrals are to be taken *only* over the set s_1, then Eq. (4.5) becomes

$$Z(\beta)=\mathrm{Tr}'(\exp-\beta H). \tag{4.6}$$

It is easily proved that the following results still hold:

$$\mathrm{Tr}'(AB)=\mathrm{Tr}'(BA), \tag{4.7}$$

and

$$\mathrm{Tr}'(ABC\cdots H)=\sum_{(qk)} A'_{q_1q_2}B'_{q_2q_3}\cdots H'_{q_nq_1}, \tag{4.8}$$

where in Eq. (4.8) the $A'_{q_1q_2}$, etc., are defined by equations of the type

$$A'_{q_1q_2}=\int_{S_1}\Psi_{q_1}^* A\Psi_{q_2}dQ. \tag{4.9}$$

We shall call matrix elements such as this "restricted matrix elements." If these results are used, then the whole of the previous analysis can be carried through again, the usual matrix elements V_{qnj} being replaced at each step by the restricted matrix elements V'_{qnj}. The zero-order term (Z_0) requires special attention. For when the trace of $\exp(-\beta H_0)$ is formed, the normalization integral $\int_{S_2}\Psi_n^*\Psi_n dQ$ has to be replaced by the integral $\int_{S_1}\Psi_n^*\Psi_n dQ$. This integral is, however, unity, because the set S_2 is a set of zero measure and the integrand is bounded in S_2. We thus have

$$Z=Z_0+\sum_{n=1}^{\infty} g^n Z_n', \tag{4.10}$$

where in Eq. (4.10),

$$Z_0=\textstyle\sum_q \exp(-\beta E_q) \tag{4.11}$$

and

$$Z_n'=-(\beta/n)\sum_{(qK)} V'_{q_1q_2}\cdots V'_{q_nq_1} \times\sum_j[\exp(-\beta E_{qj})/\prod_{i\neq j}(E_{qi}-E_{qj})]. \tag{4.12}$$

In the case in which V is singular only at isolated points, the set S_1 is defined by the parameter ϵ. Thus each of the Z_n is a function of ϵ. Clearly as $\epsilon\to 0$ each of the $Z_n'\to\infty$ for sufficiently large n, and no individual term in the series has any significance. In fact, it is only possible to pass to the limit after the series (or part of it at least) has been summed. Consequently, in this case, the series cannot be used term by term.

We next consider the terms in the expansion when the potential represents the interactions between particles that have incompressible cores. For this type of potential the transformation of $I(Q)$ from Eq. (4.3) to Eq. (4.4) is no longer valid. If we write $\phi_q(Q)=\sum_n a_{nq}\Psi_n$, then the transformation can only be carried out if $\sum_q a_{nq}a_{n'q}^*=\delta_{n,n'}$, that is, if

$$\sum_q\int_S\int_S \phi_q\phi_q^*\Psi_n(Q')\Psi_{n'}^*(Q)dQdQ'=\delta_{n,n'}. \tag{4.13}$$

Now $\sum_q\phi_q(Q)\phi_q^*(Q')=\delta(Q-Q')$ in S_1, and since the wave functions $\phi_q(Q)$ vanish identically in the set S_2, $\sum_q\phi_q(Q)\phi_q(Q')\equiv 0$ in S_2. Consequently, we must have

$$\delta_{n,n'}=\int_{s_1}\int_{S_1}\delta(Q-Q')\Psi_n(Q')\Psi_{n'}^*(Q)dQdQ' =\int_{S_1}\Psi_n(Q)\Psi_{n'}^*(Q)dQ. \tag{4.14}$$

This last relation is obviously not true because the Ψ_n are orthonormal over the whole of the configuration space, S_1 and S_2. This difficulty can, however, be overcome, if the ϕ_q are expanded in terms of the complete orthonormal set $\chi_n(Q)$, where the χ are the solutions of the wave equation for a system of N perfectly elastic spheres of radius r_0. These wave functions vanish identically in the set S_2, and obey the normalization condition that

$$\delta_{n,n'}=\int_{s_1}\chi_n(Q)\chi_{n'}(Q)dQ. \tag{4.15}$$

[12] W. Pauli, *Handbuch der Physik* (Springer, Berlin, 1933), second edition, Vol. 24, pp. 123–24.

With these wave functions instead of the Ψ_n, the transformation from Eq. (4.3) to Eq. (4.4) is obviously valid. Moreover, these wave functions satisfy the free particle wave equation $H_0\chi_n(Q)=E_n\chi_n(Q)$, in the set S_1. This means that the whole of the analysis of Sec. II is valid provided we replace the free particle wave functions $\Psi_n(Q)$ by the wave functions $\chi_n(Q)$. Thus, the expansion given by Eq. (1.17) is formally correct, if $V_{q_iq_j}$ is redefined by the equation:

$$V_{q_iq_j}=\int_{S_1}\chi_{q_i}^*(Q)V\chi_{q_j}(Q)dQ. \tag{4.16}$$

We must also take into account the fact the summations over the indices (q_j) are over all distinct accessible states. Now, the number of these states G_{q_j} that are associated with any energy level E_{q_j} will be different, according to whether we are dealing with free particle wave functions or elastic sphere wave functions. Consequently, even though the first term Z_0 *appears* to be identical in these two cases, it is, in fact, entirely different. It is clear from Eq. (4.16) that the $V_{q_jq_j}$ are finite.

It should be mentioned that the methods of Goldberger and Adams, and of Siegert, both require to be modified for this type of potential. Consider, for instance, the method of Goldberger and Adams. When the trace is formed in Eq. (2.2), it is not permissible to use free particle wave functions for the same reason as we have given above. The simplest suitable set is the set of elastic sphere wave functions $\chi_n(Q)$. When these wave functions are used, the series again becomes identical with that given in this paper. A similar consideration applies to the integral equation derived by Siegert.

It still remains to discuss the convergence of the sum in Eq. (4.12). Write

$$Z_n=-(\beta^n/n)\sum_{(q_k)}V_{q_1q_2}\cdots V_{q_nq_1}F_{(q_k)}, \tag{4.17}$$

where, if Eq. (2.3) is used,

$$F_{(q_k)}=\int_0^1 s_1^{n-1}ds_1\int_0^1 s_2^{n-2}ds_2\cdots\int^1 ds_n$$
$$\times\exp[-\beta(s_1E_{q_1}+s_2(1-s_1)E_{q_2}\cdots s_1\cdots s_nE_{q_n}]. \tag{4.18}$$

From this equation it is seen that $F_{(q_k)}>0$ for all (q_k) and β, and is moreover monotonically decreasing in all the summation indices q_k. If any one term in the multiple sum in Eq. (4.17) is considered, then it is easily shown that $F_{(q_k)}\leq\exp[-\beta(E_{q_k})_m]$ where $(E_{q_k})_m$ is the smallest value that E_{q_k} takes on for this particular term. If it is now assumed that the following multiple series S_n, where S_n is given by

$$S_n=-\beta^n\sum_{q_1}[\sum_{(q_k)\geq q_1}{}' V_{q_1q_2}\cdots V_{q_nq_1}]\exp(-\beta E_{q_1}), \tag{4.19}$$

converges, then it follows that the multiple series in Eq. (4.17) also converges. This is essentially because the $F_{(q_k)}$ are monotonic in all their indices q_k and are bounded by $\exp(-\beta(E_{q_k})_m)$ as $q_k\to\infty$. The symbol $\sum'_{(q_k)\geq q_1}$, in Eq. (4.18), means that the sum is to be over all sets of indices (q_k), omitting always the index q_1, and that the values of the other q_k are to be such that $q_k\geq q_1$. This seems to be as far as one can go rigorously. However, the unrestricted sum $\sum_{(q_k)}V_{q_1q_2}\cdots V_{q_nq_1}$ converges because the integral for $V_{q_1q_1}$ converges—this follows from the assumptions that were made about the potential V. This makes it very reasonable to suppose that the restricted sum converges as well, particularly as the unrestricted sum always converges, no matter in what order the summations are performed. Because of the factor $\exp(-\beta E_{q_1})$ the summation over the index q_1 will converge, provided the restricted sum is of order less than $\exp(-\beta E_{q_1})$.

The much more difficult question of the convergence of the series as a whole has still to be discussed. The classical analog of the series, Eq. (4.10), converges for all finite value of g—always granted the assumptions we have made about V. Unfortunately, it does not seem possible to establish a similar result in the quantum-mechanical case. However, the following remarks seem to be worth noting. Firstly, the convergence of the perturbation expansion in powers of g for the energy levels $\mathcal{E}_q$ does not guarantee the convergence of our series. Conversely, the convergence of our series does not guarantee the convergence of the perturbation expansion of any energy level $\mathcal{E}_q$. This is because in each case it is necessary to rearrange a double sum. Finally, it is quite easily shown that the series will be absolutely convergent for all finite g, if the series $\sum'_{(q_k)}V_{q_1q_2}\cdots V_{q_nq_1}$ is absolutely convergent for all q_1. This appears to be so restrictive on the potential V that it is unlikely to be very useful.

The following conclusions can be drawn from the preceding analysis. Firstly, if the interaction potential has no singularities (of the type discussed), then the original series [Eq. (1.17)] is valid. The existence of the individual terms being almost certainly quaranteed by the convergence of the integral for $V_{q_1q_1}$. Secondly, if the potential has regions in which it is positively infinite, then the original series must be modified and must be replaced by the series given by Eq. (1.17) and (4.16). In this case the existence of the individual terms again depends on the convergence of $V_{q_1q_1}$. If the potential is, however, singular at isolated points, then eventually the terms in the series become infinite, and the expansion is invalid. Finally, even in the cases in which the individual terms exist, we are unable to deduce any really useful criterion for the convergence of the series.

ACKNOWLEDGMENT

The author wishes to thank Mr. F. Booth for help in the preparation of the manuscript. He is also indebted to the Department of Scientific and Industrial Research, for a maintenance grant, without which this work would not have been possible.

Radiative Effects in Meson-Nucleon Scattering*

STANLEY DESER†
Harvard University, Cambridge, Massachusetts
(Received October 23, 1953)

An integral equation is derived which sums the contributions of a certain (infinite) set of radiative corrections to lowest-order meson-nucleon scattering. This equation for the S matrix is examined and an approximate treatment given. The resulting scattering amplitude is exhibited in the Thomson and high-energy limits.

INTRODUCTION

ONE of the shortcomings of perturbation theory has been that only finite subsets of the terms relevant to a given process can be evaluated in practice. On occasion it is possible to include an infinite subset and thus partially avoid the perturbation approach.

In the present account, such an infinite subset of the contributing terms to lowest-order meson-nucleon scattering will be summed to give an integral equation for the S matrix for the process. The terms in question will be seen to consist of all radiative corrections in which a number of mesons are emitted by the nucleon, the lowest-order scattering then taking place, followed by the reabsorption of the virtual quanta in inverse order to that of emission.

DERIVATION OF THE EQUATION

In order to derive the equation in question, we start with a quantity closely related to S, the Green's function of the meson-nucleon system. Its symbolic solution in terms of one-particle quantities has been previously shown to be, in the symmetric $ps(ps)$ theory[1] (which we shall use),

$$G_{MN}-\Delta_+G_+=-ig^2G_+\Delta_+[\gamma_5G_+\gamma_5' +\gamma_5'G_+\gamma_5+\delta\Gamma_5/\delta g\phi']\Delta_+G_+, \quad (1)$$

where G_+, Δ_+ are the modified nucleon and meson propagation functions, respectively, and Γ_5 is the vertex operator and is an isotopic spin vector.

More explicitly, Eq. (1) reads

$$(\xi_1|G_{MN}-\Delta_+G_+|\xi_2)=-ig^2G_+\int(d\eta)(d\eta')\Delta_+(\xi_1,\eta) \times[\Gamma_5(\eta)G_+\Gamma_5(\eta')+\Gamma_5(\eta')G_+\Gamma_5(\eta) +\delta\Gamma_5(\eta)/\delta g\phi(\eta')]\Delta_+(\eta',\xi_2)G_+. \quad (2)$$

The quantity inside the brackets is essentially the S matrix minus the unit matrix, $S-1$, which we shall denote by T.[2]

We now make our first approximation in taking the vertex operator, Γ_5, to satisfy[3]

$$\Gamma_5(\eta)=\gamma_5-ig^2\int(d\eta')(d\eta'')\gamma_5(\eta') \times G_+\Gamma_5(\eta)G_+\gamma_5(\eta'')\Delta_+(\eta'',\eta'), \quad (3)$$

from which it follows that

$$\delta\Gamma_5(\eta)/\delta g\phi(\eta')=-ig^2\int(d\xi)(d\xi')\gamma_5(\xi)G_+ \times[\Gamma_5(\eta')G_+\Gamma_5(\eta)+\Gamma_5(\eta)G_+\Gamma_5(\eta') +\delta\Gamma_5(\eta)/\delta g\phi(\eta')]G_+\gamma_5(\xi')\Delta_+(\xi',\xi). \quad (4)$$

We see that $\delta\Gamma_5/\delta g\phi$ reproduces the structure of T, and, therefore,

$$T=\Gamma_5G_+\Gamma_5'+\Gamma_5'G_+\Gamma_5-ig^2\int(d\xi)(d\xi') \times\gamma_5(\xi)G_+TG_+\gamma_5(\xi')\Delta_+(\xi',\xi). \quad (5)$$

This is the promised integral equation for the scattering. Its inclusion of the processes mentioned earlier may be verified by iteration, for example.

A further simplification will be made in replacing Γ_5 by γ_5. In coordinate space, Eq. (5) now reads

$$T_{ij}(x\xi,x'\xi')=\tau_i\tau_j\gamma_5G_+(x,x')\gamma_5\delta(x-\xi)\delta(x'-\xi') +\tau_j\tau_i\gamma_5G_+(x,x')\gamma_5\delta(x-\xi')\delta(x'-\xi) -ig^2\tau_k\gamma_5\int(dx'')(dx''')G_+(x,x'')T_{ij}(x''\xi;x'''\xi') \times G_+(x''',x')\gamma_5\tau_k\Delta_+(x,x'), \quad (6)$$

and its Fourier transform is

$$(2\pi)^{-4}T_{ij}(p_1p_2;\,p_1'p_2')=[\tau_i\tau_j\gamma_5G_+(p_1+p_2)\gamma_5 +\tau_j\tau_i\gamma_5G_+(p_1-p_2')\gamma_5]\delta(p_1+p_2-p_1'p_2') -ig^2(2\pi)^{-4}\tau_k\gamma_5\int(dk)G_+(p_1-k)(2\pi)^{-4} \times T_{ij}(p_1-k,\,p_2;\,p_1'-k,\,p_2')G_+(p_1'-k)\gamma_5\tau_k\Delta_+(k). \quad (7)$$

* Part of a doctoral thesis submitted to Harvard University.
† National Science Foundation Predoctoral Fellow, now at The Institute for Advanced Study, Princeton, New Jersey.
[1] S. Deser and P. Martin, Phys. Rev. **90**, 1075 (1953). The same notation will be used here.
[2] The connection between the Green's function and the S matrix in the meson-nucleon situation is worked out in detail by Karplus, Kivelson, and Martin, Phys. Rev. **90**, 1072 (1953).
[3] The assumption of Eq. (3) is equivalent to the inclusion of only those graphs for the vertex operator in which virtual mesons are emitted and reabsorbed by the nucleon in a "nesting" pattern about the vertex point. The equation has in fact been employed by S. F. Edwards, Phys. Rev. **90**, 284 (1953), in an attempt to determine Γ_5.

In the above, free-field G_+ and Δ_+ are used. In center-of-mass coordinates, $P=p_1+p_2$ and $p=\frac{1}{2}(p_1-p_2)$, the equation simplifies. Since T is a function of $x-x'$ only, in its center-of-mass dependence, or, alternately, since T is defined on the energy shell, we employ the fact that

$$T(p_1p_2;\,p_1'p_2')=T(pP;\,p'P')$$
$$=T(p,p';\,P)(2\pi)^4\delta(P-P') \quad (8)$$

to write our equation as

$$T_{ij}(p,p';\,P)=\tau_i\tau_j\gamma_5G_+(P)\gamma_5+\tau_j\tau_i\gamma_5G_+(p+p')\gamma_5$$
$$-ig^2(2\pi)^{-4}\gamma_5\tau_k\int G_+(\tfrac{1}{2}P+p-k)$$
$$\times T_{ij}(p-\tfrac{1}{2}k,\,p'-\tfrac{1}{2}k;\,P-k)G_+(\tfrac{1}{2}P+p'-k)$$
$$\times\gamma_5\tau_k\Delta_+(k)(dk). \quad (9)$$

In this form, the equation couples various spin and isotopic spin components of T_{ij}. The isotopic dependence may be separated out by writing

$$T_{ij}=\delta_{ij}T_1+\tfrac{1}{2}(\tau_i\tau_j-\tau_j\tau_i)T_2\equiv\delta_{ij}T_1+\tau_{ij}T_2. \quad (10)$$

Then, since

$$\tau_k\delta_{ij}\tau_k=3\delta_{ij};\quad \tau_k\tau_{ij}\tau_k=-\tau_{ij}, \quad (11)$$

the equation separates with regards to the isotopic spin

$$T_1=\gamma_5G_+(P)\gamma_5+\gamma_5G_+(p+p')\gamma_5$$
$$-3ig^2(2\pi)^{-4}\int\gamma_5G_+T_1G_+\gamma_5\Delta_+, \quad (12a)$$

$$T_2=\gamma_5G_+(P)\gamma_5-\gamma_5G_+(p+p')\gamma_5$$
$$+ig^2(2\pi)^{-4}\int\gamma_5G_+T_2G_+\gamma_5\Delta_+. \quad (12b)$$

A similar treatment might be employed for the spin parts; there, one obtains coupled equations for the various coefficients A, B, $\cdots$ of T in an expansion in the elements of the spinor algebra: $T=A\cdot 1+B_\mu\gamma^\mu+\cdots$. We shall make use of this breakup at a later stage.[4]

We now suppose that the effect of the radiative corrections can be approximated in the following way, as to structure: the scattering amplitudes T_i will become modulating, or scale, functions times the ordinary Born approximation amplitudes. The overall effects of the radiative corrections will then be contained in these scale functions. We assume then, for each T_i, that

$$T_i(p,p';\,P)=\lambda_i(p_2,p_2')T_i^{(0)}(p,p';\,P), \quad (13)$$

where

$$T_{1,2}^{(0)}=\gamma_5G_+(P)\gamma_5\pm\gamma_5G_+(2p)\gamma_5.$$

When this form for T is substituted under the integral in Eq. (12), the λ_i will not be functions of k so that the result will be[5]

$$T=\lambda T^{(0)}=T^{(0)}+\lambda\int KT^{(0)}. \quad (14)$$

K is the kernel as derived from Eq. (12). Thus,

$$\lambda=\left(1-\int KT^{(0)}/T^{(0)}\right)^{-1}, \quad (15)$$

which is the usual form obtained when damping effects are included.

The actual integrals occurring in Eq. (14) are not feasible in closed form in the general case.[6] We shall therefore restrict ourselves to two limiting cases in which they can be performed: the Thomson and the high-energy regions.

THE THOMSON LIMIT

Here the calculations needed have been performed, and the results given, by Ashkin, Simon, and Marshak.[7] Using these, we find that:

$$\int K_1T_1^{(0)}=1.2(2\pi)^{-2}(2m)^{-1}\alpha';$$
$$\int K_2T_2^{(0)}=-0.22(2\pi)^{-2}(2m)^{-1}\alpha' \quad (16)$$

$$T_1^{(0)}=-4m(4m^2-\mu^2)^{-1};\quad T_2^{(0)}=2\mu(4m^2-\mu^2)^{-1},$$

where $\alpha'\equiv g^2/4\pi$. Taking a conventional value for α' of 10, we find that

$$\lambda_1=0.87,\quad \lambda_2=0.73. \quad (17)$$

Thus, in the Thomson limit, the damping of the Born approximation result is relatively small, as might be expected in this nonrelativistic approximation in which all motion becomes negligible.

THE HIGH-ENERGY REGION

We now turn to the opposite extreme, that of high-energy incoming mesons. In this case we neglect the meson mass μ in comparison with its energy ω; such an approximation might be expected to hold above, say, $\omega=350$ Mev. In addition, we shall restrict ourselves to forward scattering; although this is not a necessary restriction,[8] it greatly simplifies the work. The quali-

[4] A possible treatment to be noted in this connection assumes that $T=\gamma_5 f(p,p';\,P)$. In this case, some progress may be made in actually solving the integral equation. This assumption seems unphysical, however.

[5] This form and that of Eq. (15) are to be understood symbolically, as the ordering of the Dirac matrices in the integral must be taken into account; in general, the λ_i will include such matrices as well.

[6] They are precisely those arising in the calculation of lowest-order radiative corrections to scattering, as is obvious from the fact that $\int KT^{(0)}$ is essentially the T for that process.

[7] Ashkin, Simon, and Marshak, Progr. Theoret. Phys. Japan 5, 634 (1950). The relevant quantities are C_I and C_{II}, which are given in Table IV, p. 658.

[8] The integrals occurring in the more complicated nonforward situation can also be done in closed form; they may be obtained, for example, from the work of L. M. Brown and R. P. Feynman,

tative features of the results will emerge in this case as well. At this stage, our equations reduce to:

$$T_1(p,P)=\gamma_5 G_+(p)\gamma_5+\gamma_5 G_+(2p)\gamma_5 - 3ig^2(2\pi)^{-4}\int (dk)k^{-2}\gamma_5 G_+(k+p_1) \times T_1(p+\tfrac{1}{2}k;\, P+k)G_+(k+p_1)\gamma_5,$$
$$T_2(p,P)=\gamma_5 G_+(P)\gamma_5-\gamma_5 G_+(2p)\gamma_5 + ig^2(2\pi)^{-4}\int (dk)k^{-2}\gamma_5 G_+(k+p_1) \times T_2(p+\tfrac{1}{2}k;\, P+k)G_+(k+p_1)\gamma_5. \tag{18}$$

Use will also be made of the facts that, for real nucleons and mesons, $\gamma p_1+m=0$, $p_1^2+m^2=0$, $p_2^2+\mu^2=0$.

In making the assumption (13) here, we must realize that the λ_i are, in general, Dirac matrices and take this requirement approximately into account[9] by writing

$$T_i=(\lambda_i+\gamma p_2\mu_i/m)T_i^{(0)}. \tag{19}$$

Taking the trace and then $tr\times\gamma p_2$ of the equation resulting when Eq. (19) is inserted into (18), we obtain two equations for λ and μ in each case, which will express these in terms of our integrals. These, in turn, can be written as functions of the single variable $\delta=2\omega/m$ in the lab system.

The integrals to be performed have the structure

$$\int \frac{(k_\mu;\, k_\mu k_\nu)(dk)}{k^2(k^2+2k\cdot p_1)^2(k^2+2k\cdot q+\Delta)}$$

or

$$\int \frac{(1;\, k_\mu)(dk)}{(k^2+2k\cdot p_1)^2(k^2+2k\cdot q+\Delta)}$$

and are straightforward. We merely quote the results:

$$\lambda_1^{-1}=1-\frac{3\alpha'}{2\pi}\left\{\frac{2\delta-4\delta^3}{(1-\delta^2)^2}\ln\delta-\frac{\delta}{1-\delta^2}-\frac{\delta}{2}+L(1-\delta) -\bar{L}(1+\delta)+\frac{6\alpha'}{\pi(1-3\alpha'\delta/4\pi)}\left[\frac{\delta^2}{1-\delta^2} -\frac{\delta^2-3\delta^4}{(1-\delta^2)^2}\ln\delta+\bar{L}(1+\delta)+L(1-\delta)-2L(1)\right] -i\pi\left[\ln(1+\delta)+\frac{2}{1+\delta}-\frac{1}{2(1+\delta)^2}-\frac{3}{2}\right] \times\left[1-\frac{6\alpha'}{\pi(1-3\alpha'\delta/4\pi)}\right]\right\}, \tag{20}$$

$$\mu_1=2\alpha'/\pi(1-3\alpha'\delta/4\pi)^{-1}\lambda_1,$$

and similar expressions for λ_2, μ_2. The L and $\bar{L}$ are Spence functions, as defined by Brown and Feynman (reference 8).

We note that the λ's and μ's are complex functions, as might be expected.[10] In the usual treatments of scattering, the imaginary part of the forward scattering amplitude gives the total cross section $[\sigma=4\pi k^{-1}f(0)]$ for scattering out of the initial state resulting from all possible transitions. In our approximation, and by the very nature of the ansatz made, only certain states contribute to the decay out of the initial state, rather than all of those into which our state can really decay, as would be the case in the rigorous treatment. In such a treatment, all higher order processes by means of which decay can take place would contribute to the imaginary part; here, however, only insofar as the ansatz simulates the rigorous solution is its imaginary part approximately valid.

We also remark that $T_i=(\lambda_i+\gamma p_2/m\mu_i)T_i^{(0)}\to\lambda_i T_i^{(0)}$ to within terms in μ^2, which have been neglected throughout. However, the form of λ is strongly influenced by the assumption (19). Had we merely taken $T=\lambda T^{(0)}$, an entirely different form of λ would follow.

An approximate estimate of the damping at $\delta=\frac{3}{4}$, corresponding to ω about 350 Mev,[11] again with $\alpha'=10$, yields

$$\lambda_1\approx 0.01(1-0.1i),$$
$$\lambda_2\approx 1-0.16i. \tag{21}$$

Thus, although the T_2 part is relatively unaffected, the T_1 is considerably damped at this energy. It may be mentioned that if μ_i had not been introduced, λ_2 would have been as strongly damped as the λ_1 quoted, whereas λ_1 would become an order of magnitude larger at the same energy.

DISCUSSION

We have seen that at low energies damping tends to be small, whereas at higher ones at least part of the amplitude tends to be very strongly decreased. It is obvious that the quantitative statements are not too trustworthy; the strong rise of the effect with energy, however, is suggestive of what may be expected of field reaction effects. Graphs in which many mesons are simultaneously present would seem to play an important role at higher energies. It should be of interest to compare our treatment with one including a different

Phys. Rev. 85, 231 (1952). As far as the integrations are concerned, our calculation is equivalent to the electrodynamic case treated there once the approximation $\mu=0$ is made.

[9] More rigorously, one would have to write λ_i as the sum of all 16 elements of the spinor algebra.

[10] The imaginary parts arise only from the parts of the ansatz (19) involving $G_+(P)$, corresponding to the reducibility of radiatively corrected "uncrossed" terms as against irreducibility of the "crossed" terms. Thus only the reducible diagrams have imaginary parts since there is no mode of decay in the irreducible case.

[11] Of course, both T_1 and T_2 give scattering in a mixture of isotopic spin $\frac{1}{2}$ and $\frac{3}{2}$ states; if the effects in the respective pure states are to be obtained, the proper linear combination of the two must be employed. T_1 and T_2 describe ordinary and charge exchange scattering, respectively.

(infinite) set of graphs: the ladder approximation arising from use of the meson-nucleon equation.[1] Such a calculation represents another extreme in approximation schemes: it drops terms with many mesons in the field in favor of higher order (iterated) scattering graphs. However, any method which arbitrarily neglects an infinite number of relevant terms is, of course, open to the objection that inclusion of these other graphs could vitiate all its conclusions.

ACKNOWLEDGMENT

I wish to thank Professor J. Schwinger for suggesting this investigation and for many helpful conversations during its progress.

PHYSICAL REVIEW VOLUME 93, NUMBER 3 FEBRUARY 1, 1954

The Theory of Quantized Fields. V

JULIAN SCHWINGER
Harvard University, Cambridge, Massachusetts
(Received October 26, 1953)

The Dirac field, as perturbed by a time-dependent external electromagnetic field that reduces to zero on the boundary surfaces, is the object of discussion. Apart from the modification of the Green's function, the transformation function differs in form from that of the field-free case only by the occurrence of a field-dependent numerical factor, which is expressed as an infinite determinant. It is shown that, for the class of fields characterized by finite space-time integrated energy densities, a modification of this determinant is an integral function of the parameter measuring the strength of the field and can therefore be expressed as a power series with an infinite radius of convergence. The Green's function is derived therefrom as the ratio of two such power series. The transformation function is used as a generating function for the elements of the occupation number labelled scattering matrix S and, in particular, we derive formulas for the probabilities of creating n pairs, for a system initially in the vacuum state. The general matrix element of S is presented, in terms of the classification that employs a time-reversed description for the negative frequency modes, with the aid of a related matrix Σ, which can be viewed as describing the development of the system in proper time. The latter is characterized as indefinite unitary, in contrast with the unitary property of S, which is verified directly. Two appendices are devoted to determinantal properties.

TIME-DEPENDENT ELECTROMAGNETIC FIELDS

THE previous paper in this series[1] dealt with the Dirac field, as coupled to a second prescribed Dirac field. We shall now discuss the effect of coupling with a prescribed Bose-Einstein field, using the example of the electromagnetic field. The Lagrange function and field equations of this system are presented in Eqs. (IV. 1, 2).

The simplest extension of the work of IV is obtained by supposing that the external electromagnetic field vanishes in the vicinity of the boundary surfaces σ_1 and σ_2, while assuming arbitrary values in the interior of this region. We shall retain the gauge $A_\mu=0$ to describe a zero field. The decomposition of the Dirac field into positive and negative frequency components on σ_1 and σ_2 can be performed as in IV, and the history of the system between σ_1 and σ_2 will be described by the transformation function $(\chi^{(-)'}\sigma_1|\chi^{(+)'}\sigma_2)$. The source substitution (IV. 33) produces the latter from the transformation function referring to zero eigenvalues,

$$(0\sigma_1|0\sigma_2)=\exp(i\mathcal{W}_0). \tag{1}$$

The dependence of $\mathcal{W}_0$ upon the source is expressed by [(IV. 37)]

$$\delta\mathcal{W}_0=\int_{-\infty}^{\infty}(dx)[\delta\bar{\eta}\langle\psi\rangle+\langle\bar{\psi}\rangle\delta\eta], \tag{2}$$

where now

$$\begin{aligned}\gamma_\mu[-i\partial_\mu-eA_\mu(x)]\langle\psi(x)\rangle+m\langle\psi(x)\rangle&=\eta(x),\\ [i\partial_\mu-eA_\mu(x)]\langle\bar{\psi}(x)\rangle\gamma_\mu+m\langle\bar{\psi}(x)\rangle&=\bar{\eta}(x),\end{aligned} \tag{3}$$

are the equations to be solved in conjunction with the boundary conditions (IV. 40, 41). The associated Green's function [Eqs. (IV. 42, 43)] thus obeys the differential equations

$$\begin{aligned}&\gamma_\mu[-i\partial_\mu-eA_\mu(x)]G_+(x,x')+mG_+(x,x')\\ &=[i\partial_\mu'-eA_\mu(x')]G_+(x,x')\gamma_\mu+mG_+(x,x')=\delta(x-x'),\end{aligned} \tag{4}$$

and the boundary condition that G_+ as a function of x, shall contain only positive frequencies for $x_0>x_0'$, A, and only negative frequencies for $x_0<x_0'$, A. We have indicated by $x_0>A$ and $x_0<A$ that the domain of non-vanishing field is confined, respectively, to earlier or later times than x_0. The same statements apply with x and x' interchanged.

The compatibility of these two forms of the boundary condition, for arbitrary A_μ, can be ascribed to the charge symmetry of the theory. If the second differ-

[1] J. Schwinger, Phys. Rev. 92, 1283 (1953).

ential equation for $G_+(x,x')$ is transposed with respect to the spinor indices and x interchanged with x', we obtain the differential equation for the charge conjugate Green's function

$$\gamma_\mu[-i\partial_\mu+eA_\mu(x)]\,{}_cG_+(x,x') +m\,{}_cG_+(x,x')=\delta(x-x'), \quad (5)$$

where

$${}_cG_+(x,x')=CG_+{}^{tr}(x',x)C^{-1} \quad (6)$$

and

$$\gamma_\mu{}^{tr}=-C^{-1}\gamma_\mu C. \quad (7)$$

The charge conjugate Green's function is thus obtained from G_+ by the substitution $A_\mu\rightarrow -A_\mu$. The relation inverse to (6),

$$G_+(x,x')=C\,{}_cG_+{}^{tr}(x',x)C^{-1}, \quad (8)$$

now shows that the boundary condition obeyed by $G_+(x,x')$, in its dependence on x', is the same as that of $G_+(x',x)$.

The integration of the differential expression (2) yields

$$\mathcal{W}_0=\int_{-\infty}^{\infty}(dx)(dx')\bar{\eta}(x)G_+(x,x')\eta(x')+w, \quad (9)$$

where w is the constant of integration, which characterizes the null eigenvalue transformation function in the absence of sources. We can no longer argue that this constant vanishes, in view of the presence of the external electromagnetic field. The resulting transformation function differs in form from (IV. 46, 47) only by the addition of w to $\mathcal{W}$. In particular,

$$(\chi^{(-)'}\sigma_1|\chi^{(+)'}\sigma_2)]_0 =\exp\left[iw+i\oint d\sigma_\mu\oint d\sigma_\nu'\bar{\psi}'(x) \times\gamma_\mu G_+(x,x')\gamma_\nu\psi'(x')\right], \quad (10)$$

where $]_0$ indicates the restriction to zero sources.

The dependence of w upon the electromagnetic field is expressed by

$$\delta_A w=\left\langle\int_{\sigma_2}^{\sigma_1}(dx)\delta_A\mathfrak{L}(x)\right\rangle\Big]_0 =\int_{-\infty}^{\infty}(dx)\delta A_\mu(x)\langle j_\mu(x)\rangle\Big]_0, \quad (11)$$

where

$$j_\mu(x)=e\tfrac{1}{2}[\bar{\psi}(x),\gamma_\mu\psi(x)] =-e\,\mathrm{tr}\gamma_\mu(\psi(x)\bar{\psi}(x'))_+\epsilon(x,x')]_{x'\rightarrow x}, \quad (12)$$

and we have used the notation of (IV. 35). In the second version of the current vector, it is understood that an average is taken of the two limiting forms obtained with $x_0-x_0'\rightarrow\pm 0$. The symbol tr expresses diagonal summation with respect to the spinor indices. Now

$$\delta_\eta\langle\psi(x)\rangle]_0=\int_{\sigma_2}^{\sigma_1}(dx')G_+(x,x')\delta\eta(x') =i\left\langle\int_{\sigma_2}^{\sigma_1}(dx')(\psi(x)\bar{\psi}(x')\delta\eta(x'))_+\right\rangle\Big]_0, \quad (13)$$

so that

$$i\langle(\psi(x)\bar{\psi}(x'))_+\rangle\epsilon(x,x')]_0=G_+(x,x'), \quad (14)$$

which reduces to (IV. 83) in the absence of an electromagnetic field. Accordingly,

$$\langle j_\mu(x)\rangle]_0=ie\,\mathrm{tr}\gamma_\mu G_+(x,x), \quad (15)$$

where $G_+(x,x)$ is defined by the same averaged limit as in (12). To construct w, we must integrate the differential expression

$$\delta w=\int_{-\infty}^{\infty}(dx)\,\mathrm{tr}ie\gamma_\mu\delta A_\mu(x)G_+(x,x), \quad (16)$$

with the initial condition that $w=0$ for $A_\mu=0$.

It should be noted that w is an even function of the external field, and therefore is an even function of e. This aspect of charge symmetry follows from the observation

$$\mathrm{tr}\gamma_\mu G_+(x,x)=\mathrm{tr}\gamma_\mu{}^{tr}G_+{}^{tr}(x,x) =-\mathrm{tr}\gamma_\mu\,{}_cG_+(x,x), \quad (17)$$

which shows that

$$\langle j_\mu(x)\rangle]_0=\tfrac{1}{2}ie\,\mathrm{tr}\gamma_\mu(G_+(x,x)-{}_cG_+(x,x)) \quad (18)$$

is an odd function of the external field. Hence, w is an even function. It is also worth remarking that w is a gauge invariant, Lorentz invariant quantity.

Infinite Determinants

To obtain explicit formal expressions for w, we introduce a notation in which the spinor indices and space-time coordinates are regarded as matrix indices. Thus, the differential equations for the Green's functions are written as

$$[\gamma(p-eA)+m]G_+=G_+[\gamma(p-eA)+m]=1, \quad (19)$$

and the differential expression for w becomes

$$\delta w=Tr(ie\gamma\delta AG_+)=Tr(G_+ie\gamma\delta A), \quad (20)$$

where Tr represents the complete diagonal summation, with respect to continuous coordinates and discrete spinor indices.

We shall employ the Green's function for the zero field situation, which obeys

$$(\gamma p+m)G_+{}^0=G_+{}^0(\gamma p+m)=1. \quad (21)$$

If we multiply the two equations of (19) with G_+^0, on the left and right, respectively, we get the integral equations

$$(1-G_+^0e\gamma A)G_+=G_+(1-e\gamma AG_+^0)=G_+^0, \quad (22)$$

which have the symbolic solution

$$G_+=(1-G_+^0e\gamma A)^{-1}G_+^0=G_+^0(1-e\gamma AG_+^0)^{-1}. \quad (23)$$

Hence,

$$\begin{aligned} i\delta w &= Tr[(1-e\gamma AG_+^0)^{-1}\delta(-e\gamma AG_+^0)] \\ &= Tr[(1-G_+^0e\gamma A)^{-1}\delta(-G_+^0e\gamma A)]. \end{aligned} \quad (24)$$

We thus encounter the differential expression

$$TrX^{-1}\delta X=\delta(\log \det X), \quad (25)$$

which, together with the initial condition, $\det 1=1$, completely defines the determinant[2] of a matrix (or operator). Therefore,

$$e^{iw}=\det(1-e\gamma AG_+^0)=\det(1-G_+^0e\gamma A). \quad (26)$$

The identity of the two forms expresses the determinantal property

$$\begin{aligned} \det(1-G_+^0e\gamma A) &= \det[G_+^0(1-e\gamma AG_+^0)(G_+^0)^{-1}] \\ &= \det(1-e\gamma AG_+^0). \end{aligned} \quad (27)$$

We have shown that w is an even function of e. Hence, we must have

$$e^{iw}=\det(1+e\gamma AG_+^0), \quad (28)$$

which can also be derived directly from the transposition property of determinants. An explicitly even formula now follows from the multiplication property,

$$e^{2iw}=\det(1-e^2\gamma AG_+^0\gamma AG_+^0), \quad (29)$$

which would be the result of constructing w from (18). The relation between the values of e^{iw} for two different fields can also be obtained by determinant multiplication. We first observe that (26) can be written

$$e^{iw}=\det[(G_+)^{-1}G_+^0]. \quad (30)$$

Hence,

$$\begin{aligned} &\exp(iw^{(1)})/\exp(iw^{(2)}) \\ &\quad = \det[(G_+^{(1)})^{-1}G_+^0]\det[(G_+^0)^{-1}G_+^{(2)}] \\ &\quad = \det[(G_+^{(1)})^{-1}G_+^{(2)}] \\ &\quad = \det[1-e\gamma(A^{(1)}-A^{(2)})G_+^{(2)}]. \end{aligned} \quad (31)$$

The matrices that enter in these determinants are of the form $1+\lambda K$. An infinitesimal change in the parameter λ yields, according to (25),

$$\delta \log \det(1+\lambda K)=Tr(1+\lambda K)^{-1}\delta\lambda K. \quad (32)$$

If we define the logarithm of the matrix $1+\lambda K$ by

$$\log(1+\lambda K)=\int_0^\lambda (1+\lambda' K)^{-1}d\lambda' K, \quad (33)$$

we find that

$$\det(1+\lambda K)=\exp[Tr \log(1+\lambda K)]. \quad (34)$$

Under appropriate circumstances, the matrix $\log(1+\lambda K)$ can be expanded in powers of λ and

$$Tr \log(1+\lambda K)=\sum_{n=1}^{\infty}(-1)^{n-1}\frac{1}{n}\lambda^n K_n, \quad (35)$$

where

$$K_n=TrK^n. \quad (36)$$

If we then expand the exponential in (34), we get

$$\det(1+\lambda K)=\sum_{n=0}^{\infty}\lambda^n d_n, \quad (37)$$

with

$$d_n=\sum_k \frac{(K_1)^{k_1}}{k_1!}\frac{(-\frac{1}{2}K_2)^{k_2}}{k_2!}\frac{(\frac{1}{3}K_3)^{k_3}}{k_3!}\cdots, \quad (38)$$

in which the summation is extended over all non-negative integers $k_1, k_2, \cdots$ such that

$$n=k_1+2k_2+3k_3+\cdots. \quad (39)$$

The direct expansion[3] of the determinant is expressed by the coefficient

$$d_n=\frac{1}{n!}\int (dx_1)\cdots(dx_n)\det{}_{(n)}K(x_i,x_j), \quad (40)$$

where the summation over spinor indices is understood. The identity of the two expressions, (38) and (40), is established by remarking that each of the $n!$ terms in the development of $\det_{(n)}K(x_i,x_j)$ consists of one or more cycles in the variables. Thus, for $n=6$, one of the terms is

$$-[K(x_1,x_1)][K(x_2,x_3)K(x_3,x_2)] \\ [K(x_4,x_5)K(x_5,x_6)K(x_6,x_4)].$$

On carrying out the integrations, this will yield the product of three traces, $-K_1K_2K_3$. In general, we shall find k_1 unary cycles, k_2 binary cycles, etc., and these integers are related to n by (39). The number of terms that have the magnitude $K_1^{k_1}K_2^{k_2}\cdots$ is

$$\frac{n!}{k_1!2^{k_2}k_2!3^{k_3}k_3!\cdots}, \quad (41)$$

[2] The equivalence of this definition with the customary one is shown in Appendix A.

[3] See, for example, E. T. Whittaker and G. N. Watson, *Modern Analysis* (Cambridge University Press, Cambridge, 1927), Sec. 11.2. A derivation, with the aid of operator methods, will be found in Appendix B.

where the powers of 2, 3, $\cdots$ express the cyclic symmetry of the traces. A binary cycle contains an odd permutation, and in general the sign factor is

$$(-1)^{k_2+k_3+\cdots}. \tag{42}$$

The resulting expression for (40) is just (38).

The quantity

$$\det'(1+\lambda K)=e^{-Tr\lambda K}\det(1+\lambda K) \tag{43}$$

is evidently obtained from $\det(1+\lambda K)$ by placing $K_1=0$. Accordingly, in the power series expansion

$$\det'(1+\lambda K)=\sum_{n=0}^{\infty}\lambda^n d_n', \tag{44}$$

the coefficients

$$d_n'=\frac{1}{n!}\int(dx_1)\cdots(dx_n)\det{}_{(n)}'K(x_i,x_j) \tag{45}$$

contain determinants which are obtained from those of d_n by omitting all unary cycles. This is equivalent to striking out the diagonal elements of the n-dimensional matrix. Similarly,

$$\det''(1+\lambda K)=\exp[-Tr\lambda K+\tfrac{1}{2}Tr\lambda^2K^2]\times\det(1+\lambda K) \tag{46}$$

has a power series expansion in terms of determinants from which all unary and binary cycles are omitted. However, the latter process cannot be represented by simply omitting elements of the matrix.

The modified determinant $\det'(1+\lambda K)$ obeys the fundamental inequality

$$|\det'(1+\lambda K)|^2\leq\exp[Tr\lambda K(\lambda K)^\dagger]. \tag{47}$$

To prove this, we first remark that

$$\begin{aligned}&|\det'(1+\lambda K)|^2\\&=\exp[-Tr\lambda K]\det(1+\lambda K)\exp[-Tr(\lambda K)^\dagger]\\&\qquad\times\det(1+\lambda K)^\dagger\\&=\exp[Tr\lambda K(\lambda K)^\dagger]\det'[(1+\lambda K)(1+\lambda K)^\dagger].\end{aligned} \tag{48}$$

If $H=1+A$ represents a Hermitian, non-negative matrix, we have

$$\det'H=\exp[Tr(\log(1+A)-A)]\leq 1, \tag{49}$$

since, for every eigenvalue $1+A'\geq 0$, there exists the inequality

$$\log(1+A')-A'\leq 0. \tag{50}$$

Hence,

$$\det'[(1+\lambda K)(1+\lambda K)^\dagger]\leq 1, \tag{51}$$

which establishes[4] (47).

We conclude from this inequality that $\det'(1+\lambda K)$ is devoid of singularities throughout the finite λ plane, provided that

$$TrKK^\dagger<\infty. \tag{52}$$

The modified determinant is then an integral function of λ, and we can assert that the Taylor series (44) converges for all λ. The same statements apply to $\det''(1+\lambda K)$, since

$$|TrK^2|\leq TrKK^\dagger. \tag{53}$$

The dependence of $\det'(1+\lambda K)$ upon the elements of the matrix K is described by

$$\begin{aligned}\delta_K\det'(1+\lambda K)&=\det'(1+\lambda K)Tr[((1+\lambda K)^{-1}-1)\lambda\delta K]\\&=-\det'(1+\lambda K)Tr[(1+\lambda K)^{-1}\lambda K\lambda\delta K],\end{aligned} \tag{54}$$

which indicates that the quantities

$$\begin{aligned}&\det'(1+\lambda K)(x|(1+\lambda K)^{-1}\lambda K|x')\\&\qquad=-(\delta/\delta\lambda K(x',x))\det'(1+\lambda K)\end{aligned} \tag{55}$$

are integral functions of λ. Now

$$(\delta/\delta K(x',x))d_2'=-K(x,x'), \tag{56}$$

and

$$\begin{aligned}&(\delta/\delta K(x',x))d_n'\\&=\frac{1}{n!}\int(dx_1)\cdots(dx_n)\sum_{i\neq j}\delta(x'-x_i)\delta(x-x_j)\\&\qquad\times(\partial/\partial K(x_i,x_j))\det{}_{(n)}'K(x_i,x_j)\\&=\frac{1}{(n-2)!}\int(dx_3)\cdots(dx_n)[(\partial/\partial K(x_2,x_1))\\&\qquad\times\det{}_{(n)}'K(x_i,x_j)]_{x_1=x,x_2=x'},\end{aligned} \tag{57}$$

so that

$$\begin{aligned}&\det'(1+\lambda K)(x|(1+\lambda K)^{-1}\lambda K|x')\\&=\lambda K(x,x')+\sum_{n=1}^{\infty}\lambda^{n+1}\frac{1}{n!}\int(dx_1)\cdots(dx_n)\\&\qquad\times\det{}_{(n+1)}'\begin{bmatrix}K(x,x'), & K(x,x_j)\\ K(x_i,x'), & K(x_i,x_j)\end{bmatrix}\end{aligned} \tag{58}$$

is a power series with an infinite radius of convergence, under the stated condition on K. We have employed a determinantal notation which corresponds to the partitioning of the $n+1$ dimensional array with respect to the elements of the first row and of the first column. The discarding of unary cycles here implies the omission of all diagonal elements save the first, $K(x,x')$.

In a similar way, we have

$$\begin{aligned}\delta_K\det''(1+\lambda K)&=\det''(1+\lambda K)Tr[((1+\lambda K)^{-1}-1+\lambda K)\lambda\delta K]\\&=\det''(1+\lambda K)Tr[(1+\lambda K)^{-1}\lambda^2K^2\lambda\delta K],\end{aligned} \tag{59}$$

[4] One can also prove (47) with the aid of Hadamard's inequality, R. Courant and D. Hilbert, *Methoden der Mathematischen Physik* (Interscience Publishers, Inc., New York, 1943), p. 31.

so that

$$\det''(1+\lambda K)(x|\,(1+\lambda K)^{-1}\lambda^2K^2|\,x') = (\delta/\delta\lambda K(x',x))\,\det''(1+\lambda k) \quad (60)$$

is an integral function of λ, which is represented by the convergent power series

$$\det''(1+\lambda K)(x|\,(1+\lambda K)^{-1}\lambda^2K^2|\,x') = -\sum_{n=1}^{\infty}\lambda^{n+1}\frac{1}{n!}\int(dx_1)\cdots(dx_n) \times \det{}_{(n+1)}''\begin{bmatrix} 0 & K(x,x_j) \\ K(x_i,x'), & K(x_i,x_j)\end{bmatrix}. \quad (61)$$

The omission of $K(x,x')$, in comparison with the series (58), corresponds to its origin by differentiation from the binary cycle term $\frac{1}{2}TrK^2$.

To employ these results, we first place

$$\lambda K = -e^2\gamma AG_+{}^0\gamma AG_+{}^0. \quad (62)$$

We shall show later that the condition (52) on K holds for a certain class of electromagnetic fields. Then

$$\det'(1-e^2\gamma AG_+{}^0\gamma AG_+{}^0) = \exp[e^2Tr\gamma AG_+{}^0\gamma AG_+{}^0]e^{2iw}$$

is an integral function of e, or of the parameter measuring the strength of the field. But, according to (26) and (46), we also have

$$\det''(1-e\gamma AG_+{}^0) = \exp[\tfrac{1}{2}e^2Tr\gamma AG_+{}^0\gamma AG_+{}^0]e^{iw}, \quad (64)$$

in which we have used the fact that

$$Tr\gamma AG_+{}^0 = -Tr\gamma A\,{}_cG_+{}^0 = 0, \quad (65)$$

since $G_+{}^0 = {}_cG_+{}^0$. Hence

$$\det'(1-e^2\gamma AG_+{}^0\gamma AG_+{}^0) = [\det''(1-e\gamma AG_+{}^0)]^2, \quad (66)$$

which shows that the power series expansion for $\det''(1-e\gamma AG_+{}^0)$ cannot have a finite radius of convergence, since this would contradict the integral function property of the left side in (66). Therefore (64) is an integral function of e, which is represented by the convergent power series

$$\exp(-ie^2w_1)e^{iw} = \det''(1-e\gamma AG_+{}^0) = 1+\sum_{n=2}^{\infty}e^{2n}\frac{1}{(2n)!}\int(dx_1)\cdots(dx_{2n}) \times \mathrm{tr}\left\{\prod_{i=1}^{2n}(\gamma_iA(x_i))\,\det{}_{(2n)}''G_+{}^0(x_i,x_j)\right\}. \quad (67)$$

We have exploited the known even character of this function, and written

$$w_1 = \tfrac{1}{2}iTr\gamma AG_+{}^0\gamma AG_+{}^0 \quad (68)$$

for the coefficient of e^2 in the expansion of w. Incidentally, since iw is the logarithm of an integral function, its Taylor series will, in general, have a finite radius of convergence, which is the magnitude of the smallest root possessed by the integral function (67).

With the knowledge that $\det''(1-e\gamma AG_+{}^0)$ is an integral function, we turn to (61) which provides information about the elements of the matrix

$$(1-e\gamma AG_+{}^0)^{-1}-1-e\gamma AG_+{}^0 = e\gamma A[G_+{}^0(1-e\gamma AG_+{}^0)^{-1}-G_+{}^0] = e\gamma A\,(G_+-G_+{}^0). \quad (69)$$

On removing the factor $e\gamma A(x)$ from both sides, we obtain the power series representation of the integral function

$$\det''(1-e\gamma AG_+{}^0)[G_+(x,x')-G_+{}^0(x,x')] = \sum_{n=1}^{\infty}(-e)^n\frac{1}{n!}\int(dx_1)\cdots(dx_n)\,\mathrm{tr}\left\{\prod_{i=1}^{n}(\gamma_iA(x_i)) \times \det{}_{(n+1)}''\begin{bmatrix} 0, & G_+{}^0(x,x_j) \\ G_+{}^0(x_i,x'), & G_+{}^0(x_i,x_j)\end{bmatrix}\right\}. \quad (70)$$

The Green's function $G_+(x,x')$ is thus obtained as the ratio of two integral functions,[5] which are each exhibited explicitly as infinite series. We can also present (70) in terms of the matrix I, defined by

$$G_+ = G_+{}^0+G_+{}^0IG_+{}^0, \quad (71)$$

or

$$G_+(x,x') = G_+{}^0(x,x')+\int(dx'')(dx''')G_+{}^0(x,x'') \times I(x'',x''')G_+{}^0(x''',x'). \quad (72)$$

Thus,

$$\det''(1-e\gamma AG_+{}^0)I(x,x') = \sum_{n=1}^{\infty}(-e)^n\frac{1}{n!}\int(dx_1)\cdots(dx_n)\,\mathrm{tr}\left\{\prod_{i=1}^{n}(\gamma_iA(x_i)) \times \det{}_{(n+1)}''\begin{bmatrix} 0, & \delta(x-x_j) \\ \delta(x_i-x'), & G_+{}^0(x_i,x_j)\end{bmatrix}\right\} \quad (73)$$

in which $\delta(x-x_j)$ and $\delta(x_i-x')$ also imply delta symbols for the suppressed spinor indices.

In discussing the condition (52), where λK is given by (62), it is well to notice that the value of $\det'(1+\lambda K)$ is not affected by replacing K with $f^{-1}Kf$, where f is an essentially arbitrary function of x, concerning which we only require that it exhibit the space-time localiza-

[5] This result can be identified with the solution of the integral equations (22) by the methods of Fredholm, Hilbert, and Poincaré. We have, in effect, developed the requisite parts of this theory directly from the differential form (25). Applications of the Fredholm procedure to the theory of scattering have been made by several authors [R. Jost and A. Pais, Phys. Rev. 82, 840 (1951); A. Salam and P. T. Matthews, Phys. Rev. 90, 690 (1953)].

tion of $A_\mu(x)$, consistent with the same property for $f(x)^{-1}A_\mu(x)$. Thus, we may say that $f(x)=(A(x))^{\frac{1}{2}}$, where $A(x)$ measures the magnitude of the potential vector for the external field. Then

$$Tr\lambda K(\lambda K)^{\dagger}=e^4\int(dx)(dx')(dx_1)(dx_2)$$
$$\times\mathrm{tr}[f(x)^{-1}\gamma A(x)G_+^0(x,x_1)\gamma A(x_1)G_+^0(x_1,x')$$
$$\times f(x')^2\gamma_0 G_-^0(x',x_2)\gamma A(x_2)$$
$$\times G_-^0(x_2,x)\gamma A(x)f(x)^{-1}\gamma_0], \quad (74)$$

and the integrations are all confined to the interior of the region occupied by the field. Conditions for the finiteness of this integral thus refer to the possible singular character of the field in the vicinity of a point (or points). Let us suppose that

$$A(x)\sim[(x-x_0)^2]^{-\frac{1}{2}(1-\beta)}=|x-x_0|^{-(1-\beta)} \quad (75)$$

in the vicinity of x_0. The convergence of the integral involves the behavior of $G_\pm^0(x,x')$ for $x\sim x'$. Since the Green's functions satisfy a first-order differential equation with a four-dimensional delta-function inhomogeneity, we have

$$x\sim x': \quad G_\pm^0(x,x')\sim|x-x'|^{-3}. \quad (76)$$

The sixteen fold integral (74) will converge about the point x_0, despite the singularities of the four A and the four G^0 provided that $16>4(1-\beta)+12$, or

$$\beta>0. \quad (77)$$

Hence $F(x)$, the measure of the field strength,

$$x\sim x_0: \quad F(x)\sim|x-x_0|^{-(2-\beta)}, \quad (78)$$

cannot be as singular as $|x-x_0|^{-2}$, which implies the integrability of $F(x)^2$. Accordingly, our discussion applies to those electromagnetic fields for which the space-time integrated energy density is finite.[6]

We must observe, finally, that

$$w_1=\tfrac{1}{2}i\int(dx)(dx')\ \mathrm{tr}[\gamma A(x)G_+^0(x,x')$$
$$\times\gamma A(x')G_+^0(x',x)]=\infty, \quad (79)$$

independently of the field. This stems from the coincidence of the singularities of $G_+^0(x,x')$ and $G_+^0(x',x)$ at $x=x'$. Since w_1 must be gauge invariant, the potential vectors always occur differentiated, and the singularity of each Green's function is effectively reduced to $|x-x'|^{-2}$. Hence the integral (79) is logarithmically divergent at $x-x'=0$. The explicit result obtained elsewhere[7] can be transformed without difficulty into

$$w_1=-\int(dx)(dx')\tfrac{1}{4}F_{\mu\nu}(x)w_1(x-x')F_{\mu\nu}(x'), \quad (80)$$

where

$$w_1(x-x')=\frac{1}{4\pi^2}\int_{2m}^{\infty}\kappa d\kappa[(1-(2m/\kappa)^2)^{\frac{1}{2}}$$
$$-\tfrac{1}{3}(1-(2m/\kappa)^2)^{\frac{3}{2}}]\mathcal{G}_+(x-x',\kappa), \quad (81)$$

and

$$\mathcal{G}_+(x-x',\kappa)=\frac{1}{(2\pi)^4}\int(dk)\frac{e^{ik(x-x')}}{k^2+\kappa^2-i\epsilon}, \quad \epsilon\to+0 \quad (82)$$

is the outgoing wave Green's function associated with the differential equation

$$(-\partial_\mu^2+\kappa^2)\mathcal{G}_+(x-x',\kappa)=\delta(x-x'). \quad (83)$$

The quantity κ, which appears as a mass parameter in the last equation, ranges from $2m$ to infinity, thereby producing the logarithmic divergence that we have already recognized.

The divergent part is separated by writing

$$\mathcal{G}_+(x-x',\kappa)=\kappa^{-2}\delta(x-x')+\kappa^{-2}\partial_\mu^2\mathcal{G}_+(x-x',\kappa), \quad (84)$$

which yields

$$w_1(x-x')=C\delta(x-x')+\partial_\mu^2\omega(x-x'), \quad (85)$$

where

$$C=\frac{1}{6\pi^2}(\log(\kappa/m)-\tfrac{5}{6})]_{\kappa\to\infty}, \quad (86)$$

and

$$\omega(x-x')=\frac{1}{4\pi^2}\int_{2m}^{\infty}\frac{d\kappa}{\kappa}[(1-(2m/\kappa)^2)^{\frac{1}{2}}$$
$$-\tfrac{1}{3}(1-(2m/\kappa)^2)^{\frac{3}{2}}]\mathcal{G}_+(x-x',\kappa). \quad (87)$$

Thus,

$$w_1=-C\int(dx)\tfrac{1}{4}F_{\mu\nu}^2(x)+\tfrac{1}{2}\int(dx)(dx')$$
$$\times\partial_\nu F_{\mu\nu}(x)\omega(x-x')\partial_\lambda' F_{\mu\lambda}(x'), \quad (88)$$

and the second term is finite for the class of fields to which our results refer. This follows from the remark that $\mathcal{G}_+(x-x',\kappa)\sim|x-x'|^{-2}f(\kappa|x-x'|)$, for $x\sim x'$. If the derivatives of the fields have the singularity $|x-x_0|^{-(3-\beta)}$, $\beta>0$, the integral

$$\int(dx)(dx')\partial_\nu F_{\mu\nu}(x)\mathcal{G}_+(x-x',\kappa)\partial_\lambda F_{\mu\lambda}(x')$$

is convergent, and behaves like $\kappa^{-2\beta}$ for $\kappa\to\infty$. The final integration is therefore convergent.

[6] This criterion is also stated by A. Salam and P. T. Matthews, reference 5.

[7] J. Schwinger, Phys. Rev. 82, 664 (1951). In Eqs. (6.26) and (6.29), the denominators printed as $4\pi^2$ should be $(4\pi)^2$.

Although w is divergent,

$$|e^{iw}|^2=e^{-2Imw} \tag{89}$$

is finite, since the divergent parameter C is real. We shall derive a useful determinantal expression for this quantity. The matrix I, which has been introduced in (71), is also defined by

$$e\gamma AG_+=IG_+^0, \quad G_+e\gamma A=G_+^0I, \tag{90}$$

or

$$I=e\gamma A(1-G_+^0e\gamma A)^{-1}=(1-e\gamma AG_+^0)^{-1}e\gamma A. \tag{91}$$

The adjoint matrix

$$\bar{I}=\gamma_0I^\dagger\gamma_0 \tag{92}$$

is characterized by the same equations, but with G_-^0, G_- replacing G_+^0, G_+. If we solve (91) and the analogous adjoint equations for $e\gamma A$, we find that

$$\begin{aligned}e\gamma A&=(1+IG_+^0)^{-1}I=I(1+G_+^0I)^{-1}\\&=\bar{I}(1+G_-^0\bar{I})^{-1}=(1+\bar{I}G_-^0)^{-1}\bar{I},\end{aligned} \tag{93}$$

which yields the important equations

$$I-\bar{I}=I(G_+^0-G_-^0)\bar{I}=\bar{I}(G_+^0-G_-^0)I. \tag{94}$$

The zero-field retarded and advanced Green's functions are given by

$$\begin{aligned}G_{ret}^0(x,x')&=G_+^0(x,x')+iS^{(-)}(x,x')\\&=G_-^0(x,x')+iS^{(+)}(x,x')\\&=\begin{cases}i[S^{(+)}(x,x')+S^{(-)}(x,x')], & x_0>x_0'\\0, & x_0\leq x_0',\end{cases}\end{aligned} \tag{95}$$

and

$$\begin{aligned}G_{adv}^0(x,x')&=G_+^0(x,x')-iS^{(+)}(x,x')\\&=G_-^0(x,x')-iS^{(-)}(x,x')\\&=\begin{cases}0, & x_0\geq x_0'\\-i[S^{(+)}(x,x')+S^{(-)}(x,x')], & x_0<x_0',\end{cases}\end{aligned} \tag{96}$$

in which we have written

$$\begin{aligned}S^{(+)}(x,x')&=\sum_{+,p}\psi_{\lambda p}(x)\bar{\psi}_{\lambda p}(x'),\\S^{(-)}(x,x')&=\sum_{-,p}\psi_{\lambda p}(x)\bar{\psi}_{\lambda p}(x').\end{aligned} \tag{97}$$

Now

$$\begin{aligned}1-G_{ret}^0e\gamma A&=(1-iS^{(-)}I)(1-G_+^0e\gamma A)\\&=(1+iS^{(+)}\bar{I})(1-G_-^0e\gamma A),\end{aligned} \tag{98}$$

and

$$\begin{aligned}1-G_{adv}^0e\gamma A&=(1+iS^{(+)}I)(1-G_+^0e\gamma A)\\&=(1+iS^{(-)}\bar{I})(1-G_-^0e\gamma A),\end{aligned} \tag{99}$$

from which we obtain

$$\begin{aligned}\det(1-G_{ret}^0e\gamma A)&=\det(1-iS^{(-)}I)\det(1-G_+^0e\gamma A)\\&=\det(1-iS^{(+)}\bar{I})\det(1-G_-^0e\gamma A)\end{aligned} \tag{100}$$

and

$$\begin{aligned}\det(1-G_{adv}^0e\gamma A)&=\det(1+iS^{(+)}I)\det(1-G_+^0e\gamma A)\\&=\det(1+iS^{(-)}\bar{I})\det(1-G_-^0e\gamma A).\end{aligned} \tag{101}$$

But

$$\det(1-G_{ret}^0e\gamma A)=\det(1-G_{adv}^0e\gamma A)=1, \tag{102}$$

since all cycles vanish when the matrix $K(x,x')$ is proportional to $G_{ret}^0(x,x')$ or $G_{adv}^0(x,x')$. In particular, unary cycles do not occur, in view of the definitions[8] of these Green's functions at $x_0=x_0'$.
Therefore,

$$\begin{aligned}e^{iw}=\det(1-G_+^0e\gamma A)&=[\det(1-iS^{(-)}I)]^{-1}\\&=[\det(1+iS^{(+)}I)]^{-1}\end{aligned} \tag{103}$$

and

$$\begin{aligned}e^{-iw^*}=\det(1-G_-^0e\gamma A)&=[\det(1+iS^{(-)}\bar{I})]^{-1}\\&=[\det(1-iS^{(+)}\bar{I})]^{-1}.\end{aligned} \tag{104}$$

On multiplying together corresponding expressions in (103) and (104) we encounter determinants of the matrices

$$\begin{aligned}(1-iS^{(-)}I)(1+iS^{(-)}\bar{I})&=1-iS^{(-)}(I-\bar{I})+S^{(-)}IS^{(-)}\bar{I}\\&=1+S^{(-)}IS^{(+)}\bar{I},\end{aligned} \tag{105}$$

and

$$(1+iS^{(+)}I)(1-iS^{(+)}\bar{I})=1+S^{(+)}IS^{(-)}\bar{I}, \tag{106}$$

in which we have used (94), written as

$$I-\bar{I}=iI(S^{(+)}-S^{(-)})\bar{I}=i\bar{I}(S^{(+)}-S^{(-)})I, \tag{107}$$

in virtue of the relation

$$G_+^0-G_-^0=i(S^{(+)}-S^{(-)}). \tag{108}$$

Hence

$$\begin{aligned}|e^{iw}|^2&=[\det(1+S^{(-)}IS^{(+)}\bar{I})]^{-1}\\&=[\det(1+S^{(+)}IS^{(-)}\bar{I})]^{-1}.\end{aligned} \tag{109}$$

Only matrix elements of I and $\bar{I}$ connecting positive and negative frequency modes are involved here. With an evident notation to designate these submatrices, we have

$$\begin{aligned}|e^{iw}|^2&=[\det(1+I_{-+}\bar{I}_{+-})]^{-1}\\&=[\det(1+I_{+-}\bar{I}_{-+})]^{-1}\end{aligned} \tag{110}$$

---

[8] The arbitrariness of the definitions for $x_0=x_0'$ is without influence on the final result. Let $G_{ret}^0(x,x')$, for example, be more generally defined at $x_0-x_0'=0$ as the numerical multiple $\mu(0\leq\mu\leq1)$ of the value for $x_0-x_0'=+0$, namely,

$$i\sum_{\lambda p}\psi_{\lambda p}(x)\bar{\psi}_{\lambda p}(x')[=i\gamma_0\delta(\mathbf{x}-\mathbf{x}')].$$

Then

$$\begin{aligned}\det(1-G_{ret}^0e\gamma A)&=\exp\left[-\int(dx)\,\mathrm{tr}G_{ret}^0(x,x)e\gamma A(x)\right]\\&=\exp\left[-i\mu\sum_{\lambda p}\int(dx)\bar{\psi}_{\lambda p}(x)e\gamma A(x)\psi_{\lambda p}(x)\right],\end{aligned}$$

which is of absolute value unity. This is the property actually employed in deriving (109).

and

$$I_{+-}=I_{-+}^*, \quad I_{-+}=I_{+-}^*. \tag{111}$$

Hence $I_{-+}I_{+-}$ and $I_{+-}I_{-+}$ are nonnegative Hermitian matrices, which possess nonnegative real eigenvalues, and

$$|e^{iw}|^2 \leq 1. \tag{112}$$

The Scattering Matrix

The history of the Dirac field under the influence of the external electromagnetic field is given by the transformation function (10), which we now employ as a generating function for the occupation number transformation function $(n\sigma_1|n'\sigma_2)$, according to

$$(\chi^{(-)'}\sigma_1|\chi^{(+)'}\sigma_2)=\sum_{n,n'}(\chi^{(-)'}|n)(n\sigma_1|n'\sigma_2)(n'|\chi^{(+)'}). \tag{113}$$

We shall represent this transformation function in terms of the matrix, referred to the standard surface, of a unitary operator S,

$$(n\sigma_1|n'\sigma_2)=\exp(iP(n)x_1)(n|S|n')\exp(-iP(n')x_2). \tag{114}$$

We can regard S as describing an equivalent disturbance which is localized on the standard surface.

On introducing the matrix I, according to (72), we get

$$\oint d\sigma_\mu \oint d\sigma_\nu' \bar{\psi}'(x)\gamma_\mu G_+(x,x')\gamma_\nu\psi'(x')$$

$$=\oint d\sigma_\mu \oint d\sigma_\nu' \bar{\psi}'(x)\gamma_\mu G_+^{\,0}(x,x')\gamma_\nu\psi'(x')$$

$$+\int (dx)(dx')\bar{\psi}'(x)I(x,x')\psi'(x'), \tag{115}$$

in which we have written at interior points, as in IV,

$$\psi'(x)=i\oint d\sigma_\mu' G_+^{\,0}(x,x')\gamma_\mu\psi'(x'),$$

$$\bar{\psi}'(x)=-i\oint d\sigma_\mu'\bar{\psi}'(x')\gamma_\mu G_+^{\,0}(x',x), \tag{116}$$

and, it should be noted, the Green's functions are those for zero external field. Hence,

$$(\chi^{(-)'}\sigma_1|\chi^{(+)'}\sigma_2)=(\chi^{(-)'}\sigma_1|\chi^{(+)'}\sigma_2)]_0 e^{iw}$$

$$\times\exp\left[i\int (dx)(dx')\bar{\psi}'(x)I(x,x')\psi'(x')\right], \tag{117}$$

where, in this section, $]_0$ designates the absence of an external electromagnetic field. It will be recalled that

$$(\chi^{(-)'}\sigma_1|\chi^{(+)'}\sigma_2)]_0$$
$$=\exp[\textstyle\sum_{\lambda p}\chi_{\lambda p}{}^{(-)'}e^{ipx_1}e^{-ipx_2}\chi_{\lambda p}{}^{(+)'}], \tag{118}$$

and that

$$\psi'(x)=\textstyle\sum_+\psi_{\lambda p}(x)e^{-ipx_2}\chi_{\lambda p}{}^{(+)'}+\sum_-\psi_{\lambda p}(x)e^{ipx_1}\chi_{\lambda p}{}^{(-)'},$$
$$\bar{\psi}'(x)=\textstyle\sum_-\bar{\psi}_{\lambda p}(x)e^{-ipx_2}\chi_{\lambda p}{}^{(+)'}+\sum_+\bar{\psi}_{\lambda p}(x)e^{ipx_1}\chi_{\lambda p}{}^{(-)'}. \tag{119}$$

On incorporating the phase factors e^{ipx_1}, e^{-ipx_2} into the eigenvalues, we arrive at the generating function for the scattering matrix, $(n|S|n')$,

$$\textstyle\sum(\chi^{(-)'}|n)(n|S|n')(n'|\chi^{(+)'})$$
$$=e^{iw}\exp[\sum_{++}\chi_{\lambda p}{}^{(-)'}(\delta_{\lambda p,\lambda' p'}+iI(\lambda p,\lambda' p'))\chi_{\lambda' p'}{}^{(+)'}$$
$$+\sum_{--}\chi_{\lambda p}{}^{(-)'}(\delta_{\lambda p,\lambda' p'}-iI(\lambda' p',\lambda p))\chi_{\lambda' p'}{}^{(+)'}$$
$$+\sum_{+-}\chi_{\lambda p}{}^{(-)'}iI(\lambda p,\lambda' p')\chi_{\lambda' p'}{}^{(-)'}$$
$$+\sum_{-+}\chi_{\lambda p}{}^{(+)'}iI(\lambda p,\lambda' p')\chi_{\lambda' p'}{}^{(+)'}], \tag{120}$$

where

$$I(\lambda p,\lambda' p')=\int (dx)(dx')\bar{\psi}_{\lambda p}(x)I(x,x')\psi_{\lambda' p'}(x'). \tag{121}$$

A simplified generating function that describes the transitions of a system known to be initially in the vacuum state, is obtained by placing the eigenvalues $\chi^{(+)'}$ equal to zero,

$$\textstyle\sum_n(\chi^{(-)'}|n)(n|S|0)$$
$$=e^{iw}\exp[i\sum_{+-}\chi_{\lambda p}{}^{(-)'}I(\lambda p,\lambda' p')\chi_{\lambda' p'}{}^{(-)'}]. \tag{122}$$

Hence,

$$(0|S|0)=e^{iw}, \tag{123}$$

and

$$(n_+n_-|S|0)=\delta_{n_+,n_-}e^{iw}i^{n^2}\det{}_{(n)}I(+,-), \tag{124}$$

where $n=n_+=n_-$ is the number of pairs of oppositely charged particles that are created, and the n-dimensional determinant is constructed from the elements $I(\lambda p,\lambda' p')$, where the row index λp ranges, in standard order, over the positive frequency modes that are occupied in the final state, and the column index similarly refers to the negative frequency modes. The factor $i^{n^2}(=1,\ n$ even; $=i,\ n$ odd) arises from i^n combined with $(-1)^{\frac{1}{2}n(n-1)}$, the latter being introduced on bringing the eigenvalues into standard order. The determinant can also be written as

$$\det{}_{(n)}I(+,-)=\frac{1}{(n!)^2}\int (dx_1)\cdots(dx_n)(dx_1')\cdots(dx_n')$$
$$\times(\det{}_{(n)}\bar{\psi}_+(x_i))(\det{}_{(n)}I(x_i,x_j'))$$
$$\times(\det{}_{(n)}\psi_-(x_j')). \tag{125}$$

The probability that the system persist in the vacuum state is thus given by

$$p(0,0)=|(0|S|0)|^2=|e^{iw}|^2, \tag{126}$$

while the probability for creating n pairs of particles in specified modes is

$$p(n_+n_-,0)=|e^{iw}|^2|\det_{(n)}I(+,-)|^2. \quad (127)$$

The total probability for the creation of n pairs is, therefore,

$$p_{n,0}=\sum_{n_++n_-=n}p(n_+n_-,0)$$
$$=|e^{iw}|^2\frac{1}{(n!)^2}\sum_{+-}(\det_{(n)}I(+,-))$$
$$\times(\det_{(n)}\bar{I}(-,+)), \quad (128)$$

in which the latter summation is extended independently over the n positive frequency modes, and the n negative frequency modes. The factor $1/(n!)^2$ thus removes the repetitious counting of final states. We insert (125), together with the analogous expression for $\det_{(n)}\bar{I}(-,+)$, and employ determinantal relations of the type

$$\frac{1}{n!}\sum_-(\det_{(n)}\psi_-(x_i))(\det_{(n)}\bar{\psi}_-(x_j))$$
$$=\det_{(n)}S^{(-)}(x_i,x_j'), \quad (129)$$

and

$$\frac{1}{n!}\int(dx_1')\cdots(dx_n')(\det_{(n)}I(x_i,x_j))$$
$$\times(\det_{(n)}S^{(-)}(x_j',x_k''))=\det_{(n)}(x_i|IS^{(-)}|x_k''). \quad (130)$$

This yields

$$p_{n,0}=|e^{iw}|^2\frac{1}{n!}\int(dx_1)\cdots(dx_n)$$
$$\times\det_{(n)}(x_i|S^{(+)}IS^{(-)}\bar{I}|x_j). \quad (131)$$

The probability for encountering the system in some final state is thus

$$\sum_{n=0}^{\infty}p_{n,0}=|e^{iw}|^2\sum_{n=0}^{\infty}\frac{1}{n!}\int(dx_1)\cdots(dx_n)$$
$$\times\det_{(n)}(x_i|S^{(+)}IS^{(-)}\bar{I}|x_j)$$
$$=|e^{iw}|^2\det(1+S^{(+)}IS^{(-)}\bar{I})$$
$$=1, \quad (132)$$

in virtue of the expression (109) for the quantity which is the vacuum-vacuum transition probability.

The general matrix element of S is advantageously presented in terms of the classification introduced in IV, which employs a time-reversed description for the negative frequency modes. We take the generating function (113) for the matrix of S and write

$$(\chi^{(-)'}|S|\chi^{(+)'})=e^{iw}[\bar{\psi}'|\sum|\psi'], \quad (133)$$

so that

$$[\bar{\psi}'|\sum|\psi']=\exp\Big[i\oint d\sigma_x\oint d\sigma_{x'}\bar{\psi}'(x)\gamma_x$$
$$\times G_+(x,x')\gamma_{x'}\psi'(x')\Big], \quad (134)$$

and it is understood that the eigenvalues on the right are to be referred to the standard surface. This expression serves as the generating function for the occupation number matrix of $\sum$, according to

$$[\bar{\psi}'|\sum|\psi']=\sum_{N,N'}[\bar{\psi}'|N][N|\sum|N'][N'|\psi']. \quad (135)$$

In virtue of the relation

$$(\chi^{(-)'}|n)(n'|\chi^{(+)'})=(-1)^{N_-}(-1)^{\frac{1}{2}(N_--N_-')(N_-+1-N_-')}$$
$$\times[\bar{\psi}'|N][N'|\psi'], \quad (136)$$

we have the following connection between the matrices of S and $\sum$:

$$(n|S|n')=e^{iw}(-1)^{N_-}(-1)^{\frac{1}{2}(N_--N_-')(N_-+1-N_-')}$$
$$\times[N|\sum|N']. \quad (137)$$

The occupation numbers $N=n_+,n_-'$ are associated with modes that propagate out of the region bounded by σ_1 and σ_2 (positive frequencies on σ_1, negative frequencies on σ_2), while the occupation numbers $N'=n_+',n_-$ are those of modes that propagate into the region (positive frequencies on σ_2, negative frequencies on σ_1). Hence $\sum$ connects an "initial" state described by incoming fields with a "final" state specified by outgoing fields. The sense of development is that of time for the positive frequency modes, but is reversed for the negative frequency modes. Without attempting to justify the term here, we speak of $\sum$ as describing the development of the system in proper time. It should be noted that the number of "particles" is conserved, $N=N'$, as is evident from the structure of the generating function (134). Thus, $n_++n_-'=n_+'+n_-$, or $n_+-n_-=n_+'-n_-'$; the conservation of particles in proper time is equivalent to the conservation of charge is conventional time.[9]

In the absence of an external field, we have $S=1$, and $\sum=\epsilon$, where, according to (IV. 96)

$$[\bar{\psi}'|\epsilon|\psi']=\exp[\sum\bar{\psi}_{\lambda p}'\epsilon(\lambda)\psi_{\lambda p}']$$
$$=\sum[\bar{\psi}'|N](-1)^N[N|\psi'], \quad (138)$$

so that

$$[N|\epsilon|N']=\delta_{N,N'}(-1)^{N_-}. \quad (139)$$

This also follows from (137). On using (115) and (138), the generating function (134) assumes the form

$$[\bar{\psi}'|\sum|\psi']=\exp[\sum\bar{\psi}_{\lambda p}'\sigma(\lambda p,\lambda'p')\psi_{\lambda'p'}'], \quad (140)$$

with

$$\sigma(\lambda p,\lambda'p')=\epsilon(\lambda)\delta_{\lambda p,\lambda'p'}+iI(\lambda p,\lambda'p'). \quad (141)$$

[9] See R. P. Feynman, Phys. Rev. 76, 749 (1949).

The general occupation number matrix element of $\sum$ is thereby obtained as

$$[N|\sum|N']=\delta_{N,N'}\det{}_{(N)}\sigma(\lambda p,\lambda' p'), \quad (142)$$

where λp and $\lambda' p'$ range, in standard order, over the occupied modes of the "final" and "initial" states, respectively.

We shall now use the connection between I and $\bar{I}$, Eq. (107), to prove that $\sum$ satisfies the relations

$$\sum^{\dagger}\epsilon\sum=\sum\epsilon\sum^{\dagger}=\epsilon. \quad (143)$$

This indefinite-unitary property will first be established for $\sigma(\lambda p,\lambda' p')$, which represents the sub-matrix of $\sum$ for single "particle" states. We combine (141) with

$$\sigma^{\dagger}(\lambda p,\lambda' p')=\epsilon(\lambda)\delta_{\lambda p,\lambda' p'}-i\bar{I}(\lambda p,\lambda' p'), \quad (144)$$

and construct

$$\sum_{\lambda'' p''}\sigma^{\dagger}(\lambda p,\lambda'' p'')\epsilon(\lambda'')\sigma(\lambda'' p'',\lambda' p')=\epsilon(\lambda)\delta_{\lambda p,\lambda' p'} +i[I(\lambda p,\lambda' p')-\bar{I}(\lambda p,\lambda' p')] + \sum_{\lambda'' p''}\bar{I}(\lambda p,\lambda'' p'')\epsilon(\lambda'')I(\lambda'' p'',\lambda' p'). \quad (145)$$

But (107) implies that

$$I(\lambda p,\lambda' p')-\bar{I}(\lambda p,\lambda' p') =i\sum_{\lambda'' p''}\bar{I}(\lambda p,\lambda'' p'')\epsilon(\lambda'')I(\lambda'' p'',\lambda' p'). \quad (146)$$

Therefore

$$\sum_{\lambda'' p''}\sigma^{\dagger}(\lambda p,\lambda'' p'')\epsilon(\lambda'')\sigma(\lambda'' p'',\lambda' p')=\epsilon(\lambda)\delta_{\lambda p,\lambda' p'}, \quad (147)$$

or, in matrix notation,

$$\sigma^{\dagger}\epsilon\sigma=\epsilon. \quad (148)$$

Since the fundamental relation between I and $\bar{I}$ is unaltered by the substitution $I\leftrightarrow-\bar{I}$, we also have

$$\sigma\epsilon\sigma^{\dagger}=\epsilon. \quad (149)$$

The general statement can be deduced from (142). With

$$[N|\sum{}^{\dagger}|N']=\delta_{N,N'}\det{}_{(N)}\sigma^{\dagger}(\lambda p,\lambda' p'), \quad (150)$$

we get

$$\sum_{N''}[N|\sum{}^{\dagger}\epsilon|N''][N''|\sum|N'] =\delta_{N,N'}\frac{1}{N!}\sum_{\lambda'' p''}\det{}_{(N)}(\sigma^{\dagger}(\lambda p,\lambda'' p'')\epsilon(\lambda'')) \times\det{}_{(N)}(\sigma(\lambda'' p'',\lambda' p')) =\delta_{N,N'}\det{}_{(N)}(\sum_{\lambda'' p''}\sigma^{\dagger}(\lambda p,\lambda'' p'')\epsilon(\lambda'')\sigma(\lambda'' p'',\lambda' p')) =\delta_{N,N'}(-1)^{N-}=[N|\epsilon|N'], \quad (151)$$

which establishes the first part of (143). The proof of the second part is based analogously upon (149). In a closely related derivation, we combine the partial generating functions

$$\sum_{N'}[N|\sum|N'][N'|\psi']=\prod_{\lambda p}(\sum_{\lambda' p'}\sigma(\lambda p,\lambda' p')\psi_{\lambda' p'})^{N}, \quad (152)$$

and

$$\sum_{N'}[\bar{\psi}'|N'][N'|\sum{}^{\dagger}\epsilon|N] =\prod_{\lambda p}(\sum_{\lambda' p'}\bar{\psi}_{\lambda' p'}\sigma^{\dagger}(\lambda' p',\lambda p)\epsilon(\lambda))^{N}, \quad (153)$$

into

$$[\bar{\psi}'|\sum{}^{\dagger}\epsilon\sum|\psi'] =\exp[\sum\bar{\psi}_{\lambda p}\sigma^{\dagger}(\lambda p,\lambda'' p'')\epsilon(\lambda'')\sigma(\lambda'' p'',\lambda' p')\psi_{\lambda' p'}] =\exp[\sum\bar{\psi}_{\lambda p}\epsilon(\lambda)\psi_{\lambda p}] \quad (154) =[\bar{\psi}'|\epsilon|\psi'].$$

The indefinite-unitary property of $\sum$ implies, in particular, that

$$\sum_{N}(-1)^{N-+N-'}|[N|\sum|N']|^2=1, \quad (155)$$

which indicates that $|[N|\sum|N']|^2$ is not necessarily less than unity. But this is to be anticipated from the significance of these quantities as relative, rather than absolute probabilities,

$$|[N|\sum|N']|^2=p(n,n')/p(0,0). \quad (156)$$

Consider, for example, the probability for no change in a single particle state, relative to the probability for the maintainance of the vacuum state,

$$p(1_{\lambda p},1_{\lambda p})/p(0,0)=|\sigma(\lambda p,\lambda p)|^2. \quad (157)$$

The one-particle version of (155),

$$\sum_{\lambda' p'}\epsilon(\lambda)\epsilon(\lambda')|\sigma(\lambda' p',\lambda p)|^2=1, \quad (158)$$

asserts that

$$|\sigma(\lambda p,\lambda p)|^2=1-\sum_{\lambda' p'\neq\lambda p}\epsilon(\lambda)\epsilon(\lambda')|\sigma(\lambda' p',\lambda p)|^2. \quad (159)$$

Thus, for $\lambda>0$, say, we have

$$p(1_{\lambda p},1_{\lambda p})/p(0,0)=1-\sum{}_{+}|I(\lambda' p',\lambda p)|^2 +\sum{}_{-}|I(\lambda' p',\lambda p)|^2, \quad (160)$$

where the positive frequency mode summation omits λp. These oppositely signed summations express the changes in the probability ratio, relative to unity, produced by transitions of the particle to other positive frequency modes, and by the exclusion principle suppression of pair creation in which a particle would have occupied the mode λp.

We shall now supply the explicit verification that S is a unitary operator. The proof is more involved than the elementary demonstration of the indefinite-unitary property possessed by $\sum$. This is attributable to the

non-conservation of the number of particles, as compared with the number of "particles." Our procedure begins with (117), written as

$$(\Phi(\chi^{(-)\prime})S\Psi(\chi^{(+)\prime}))=(\Phi(\chi^{(-)\prime})\Psi(x^{(+)\prime}))e^{iw}$$
$$\times\exp\left[i\int(dx)(dx')\bar{\psi}'(x)I(x,x')\psi'(x')\right], \quad (161)$$

with the usual understanding on referring eigenvalues to the standard surface. By introducing the operators that possess the eigenvalues $\chi_{\lambda p}{}^{(-)\prime}$ we can exhibit the vector $S\Psi(\chi^{(+)\prime})$, and thereby the adjoint vector $\Phi(\chi^{(-)\prime})S^{\dagger}$. We must then prove that the product $(\chi^{(-)\prime}|S^{\dagger}S|\chi^{(+)\prime})$ equals $(\chi^{(-)\prime}|\chi^{(+)\prime})$. The evaluation of this product is accomplished by bringing the operators to bear upon their eigenvectors, which will yield a function of the eigenvalues, multiplied into $(\chi^{(-)\prime}|\chi^{(+)\prime})$. This function of the eigenvalues can also be obtained by making the substitution $\chi_{\lambda p}{}^{(\pm)}\rightarrow\chi_{\lambda p}{}^{(\pm)}+\chi_{\lambda p}{}^{(\pm)\prime}$, and evaluating the null eigenvalue matrix element. Thus, the demonstration of $S^{\dagger}S=1$ is reduced to the verification that

$$|e^{iw}|^2(0|F|0)=1, \quad (162)$$

where

$$F=\exp\Big\{-i\int(dx)(dx')[\bar{\psi}'(x)+\textstyle\sum_{-}\bar{\psi}_{\lambda p}(x)\chi_{\lambda p}{}^{(+)}]$$
$$\times\bar{I}(x,x)[\psi'(x')+\textstyle\sum_{+}\psi_{\lambda' p'}(x')\chi_{\lambda' p'}{}^{(+)}]\Big\}$$
$$\times\exp\Big\{i\int(dx)(dx')[\bar{\psi}'(x)+\textstyle\sum_{+}\bar{\psi}_{\lambda p}(x)\chi_{\lambda p}{}^{(-)}]$$
$$\times I(x,x')[\psi'(x')+\textstyle\sum_{-}\psi_{\lambda' p'}(x')\psi_{\lambda' p'}{}^{(-)}]\Big\}. \quad (163)$$

The commutation properties of the operators $\chi_{\lambda p}{}^{(\pm)}$ should be noted. Since

$$(\chi^{(-)\prime}|\chi^{(+)\prime})=\exp(\textstyle\sum_{\lambda p}\chi_{\lambda p}{}^{(-)\prime}\chi_{\lambda p}{}^{(+)\prime}), \quad (164)$$

we have

$$\delta(\chi^{(-)\prime}|\chi^{(+)\prime})$$
$$(\chi^{(-)\prime}|\chi^{(+)\prime})\textstyle\sum_{\lambda p}(\delta\chi_{\lambda p}{}^{(-)\prime}\chi_{\lambda p}{}^{(+)\prime}+\chi_{\lambda p}{}^{(-)\prime}\delta\chi_{\lambda p}{}^{(+)\prime})$$
$$=(\chi^{(-)\prime}|\textstyle\sum_{\lambda p}(\delta\chi_{\lambda p}{}^{(-)}\chi_{\lambda p}{}^{(+)}+\chi_{\lambda p}{}^{(-)}\delta\chi_{\lambda p}{}^{(+)})|\chi^{(+)\prime}), \quad (165)$$

and therefore

$$G_{\chi^{(+)}}=i\sum_{\lambda p}\chi_{\lambda p}{}^{(-)}\delta\chi_{\lambda p}{}^{(+)}, \quad G_{\chi^{(-)}}=i\sum_{\lambda p}\chi_{\lambda p}{}^{(+)}\delta\chi_{\lambda p}{}^{(-)}. \quad (166)$$

The implied commutation relations are

$$\{\chi_{\lambda p}{}^{(+)},\chi_{\lambda' p'}{}^{(+)}\}=\{\chi_{\lambda p}{}^{(-)},\chi_{\lambda' p'}{}^{(-)}\}=0,$$
$$\{\chi_{\lambda p}{}^{(+)},\chi_{\lambda' p'}{}^{(-)}\}=\delta_{\lambda p,\lambda' p'}. \quad (167)$$

Naturally, the same results are obtained from the operator properties of ψ and $\bar{\psi}$.

Our first task is to demonstrate that the left side of (162) is independent of the eigenvalues. Now

$$(\delta_l/\delta\bar{\psi}'(x))F$$
$$=-i\int(dx')\bar{I}(x,x')(\psi'(x')+\textstyle\sum_{+}\psi_{\lambda p}(x')\chi_{\lambda p}{}^{(+)})F$$
$$+Fi\int(dx')I(x,x')(\psi'(x')+\textstyle\sum_{-}\psi_{\lambda p}(x')\chi_{\lambda p}{}^{(-)}). \quad (168)$$

Furthermore, for $\lambda>0$,

$$[\chi_{\lambda p}{}^{(+)},F]=(\partial_l/\partial\chi_{\lambda p}{}^{(-)})F$$
$$=Fi\int(dx)(dx')\bar{\psi}_{\lambda p}(x)I(x,x')$$
$$\times(\psi'(x')+\textstyle\sum_{-}\psi_{\lambda' p'}(x')\chi_{\lambda' p'}{}^{(-)}), \quad (169)$$

and, with $\lambda<0$,

$$[F,\chi_{\lambda p}{}^{(-)}]=(\partial_r/\partial\chi_{\lambda p}{}^{(+)})$$
$$=i\int(dx)(dx')\bar{\psi}_{\lambda p}(x)\bar{I}(x,x')$$
$$\times(\psi'(x')+\textstyle\sum_{+}\psi_{\lambda' p'}(x')\chi_{\lambda' p'}{}^{(+)})F. \quad (170)$$

The latter results can be expressed by

$$[\psi'(x)+\textstyle\sum_{+}\psi_{\lambda p}(x)\chi_{\lambda p}{}^{(+)},F]$$
$$=F\int(dx')(x|iS^{(+)}I|x')$$
$$\times(\psi'(x')+\textstyle\sum_{-}\psi_{\lambda' p'}(x')\chi_{\lambda' p'}{}^{(-)}), \quad (171)$$

and

$$[F,\psi'(x)+\textstyle\sum_{-}\psi_{\lambda p}(x)\chi_{\lambda p}{}^{(-)}]$$
$$=\int(dx')(x|iS^{(-)}\bar{I}|x')$$
$$\times(\psi'(x')+\textstyle\sum_{+}\psi_{\lambda' p'}(x')\chi_{\lambda' p'}{}^{(+)})F, \quad (172)$$

where $S^{(\pm)}(x,x')$ are defined in (97). On introducing the notation

$$(0|(\psi'(x)+\textstyle\sum_{+}\psi_{\lambda p}(x)\chi_{\lambda p}{}^{(+)})F|0)=(0|F|0)f_{+}(x),$$
$$(0|F(\psi'(x)+\textstyle\sum_{-}\psi_{\lambda p}(x)\chi_{\lambda p}{}^{(-)})|0)=(0|F|0)f_{-}(x), \quad (173)$$

(168) asserts that

$$(\delta_l/\delta\bar{\psi}'(x))(0|F|0)$$
$$=-(0|F|0)i\int(dx')[\bar{I}(x,x')f_{+}(x')$$
$$-I(x,x')f_{-}(x')], \quad (174)$$

while (171) and (172) supply the information

$$f_+(x)-\int(dx')(x|iS^{(+)}\bar{I}|x')f_-(x')=\psi'(x),$$
$$f_-(x)-\int(dx')(x|iS^{(-)}\bar{I}|x')f_+(x')=\psi'(x). \tag{175}$$

By subtracting the two equations in (175), we get (suppressing the indices)

$$(1+iS^{(-)}\bar{I})f_+=(1+iS^{(+)}I)f_-. \tag{176}$$

But, according to (107),

$$I(1+iS^{(-)}\bar{I})=(1+iIS^{(+)})\bar{I}, \tag{177}$$

while

$$I(1+iS^{(+)}I)=(1+iIS^{(+)})I. \tag{178}$$

Hence, if we multiply (176) with I, and remove the ensuing common factor, $1+iIS^{(+)}$, we are left with

$$\bar{I}f_+=If_-, \tag{179}$$

which shows that

$$(\delta_l/\delta\bar{\psi}'(x))(0|F|0)=0. \tag{180}$$

Evidently, $(0|F|0)$ is also independent of the eigenvalues $\psi'(x)$. The problem remaining is the demonstration of

$$|e^{i\omega}|^2(0|\exp[-i\sum_{-+}\chi_{\lambda p}{}^{(+)}\bar{I}(\lambda p,\lambda' p')\chi_{\lambda' p'}{}^{(+)}]$$
$$\times\exp[i\sum_{+-}\chi_{\lambda p}{}^{(-)}I(\lambda p,\lambda' p')\chi_{\lambda' p'}{}^{(-)}]|0)=1. \tag{181}$$

But this is just the statement that

$$(0|S^\dagger S|0)=\sum_n|(n|S|0)|^2=1, \tag{182}$$

the proof[10] of which has already been given, in (132). The substitution $I\leftrightarrow-\bar{I}$ convert this verification of $S^\dagger S=1$ into one for $SS^\dagger=1$.

The discussion of time-independent fields will be deferred to a subsequent paper.

APPENDIX A

We want to verify here that the differential form (25) correctly defines $\det X$. The integrability of this expression must be demonstrated first. By considering two independent variations, we confirm that

$$\delta_2 Tr(X^{-1}\delta_1 X)-\delta_1 Tr(X^{-1}\delta_2 X)$$
$$=-Tr(X^{-1}\delta_2 X\ X^{-1}\delta_1 X)$$
$$+Tr(X^{-1}\delta_1 X\ X^{-1}\delta_2 X)=0, \tag{1}$$

in virtue of the fundamental trace property, $TrXY=TrYX$. With infinite matrices, the applicability of this property requires suitable convergence of the traces. On using a discrete labelling of the matrix elements, we can express (25) as

$$(\partial/\partial X_{ij})\det X=(X^{-1})_{ji}\det X. \tag{2}$$

[10] For further discussion, see Appendix B.

A second differentiation with respect to an arbitrary element of the matrix yields

$$(\partial/\partial X_{ij})(\partial/\partial X_{kl})\det X=[(X^{-1})_{ji}(X^{-1})_{lk}$$
$$-(X^{-1})_{jk}(X^{-1})_{li}]\det X. \tag{3}$$

The right side reverses sign on interchanging the row indices i, k, and on interchanging the column indices j, l. Hence, the second derivative vanishes for equal row, or equal column indices. In particular,

$$(\partial^2/\partial X_{ij}{}^2)\det X=0. \tag{4}$$

We also conclude that

$$\sum_j X_{ij}(\partial/\partial X_{ij})\det X=\sum_j X_{ij}(X^{-1})_{ji}\det X$$
$$=\det X, \tag{5}$$

and that

$$\sum_i X_{ij}(\partial/\partial X_{ij})\det X=\det X. \tag{6}$$

Therefore $\det X$ is a linear, homogeneous function of the elements in each row, and in each column, which is antisymmetrical in the rows and in the columns of the matrix. This establishes the identity of $\det X$, as defined by (25) and the initial condition $\det 1=1$, with the conventional concept.

The multiplication property of determinants follows directly from the definition (25). Indeed,

$$Tr(XY)^{-1}\delta(XY)=TrX^{-1}\delta X+TrY^{-1}\delta Y \tag{7}$$

states that

$$\delta(\log\det XY)=\delta(\log\det X)+\delta(\log\det Y), \tag{8}$$

whence

$$\det XY=\det X\det Y. \tag{9}$$

The constant of integration has been fixed by the initial condition. Note also that the trace property

$$TrX=TrX^{tr} \tag{10}$$

leads immediately to

$$\det X=\det X^{tr}. \tag{11}$$

APPENDIX B

In this section we discuss the connection between determinants and ordered operators. Let $\chi_r{}^{(\pm)}$ be a set of operators that satisfy

$$\{\chi_r{}^{(+)},\chi_s{}^{(+)}\}=\{\chi_r{}^{(-)},\chi_s{}^{(-)}\}=0,$$
$$\{\chi_r{}^{(+)},\chi_s{}^{(-)}\}=\delta_{rs}, \tag{1}$$

and consider the ordered exponential

$$V=\exp[\sum_{rs}\chi_r{}^{(+)};\lambda K_{rs}\chi_s{}^{(-)}], \tag{2}$$

in which we have used the notation

$$\exp[A;B]=\sum_{n=0}^{\infty}\frac{1}{n!}A^nB^n. \tag{3}$$

We deduce the commutation properties

$$[\chi_r^{(+)},V]=-(\partial_r/\partial\chi_r^{(-)})V=-\sum_p \chi_p^{(+)}\lambda K_{pr}V, \quad (4)$$

and

$$[V,\chi_s^{(-)}]=-(\partial_l/\partial\chi_s^{(+)})V=-V\sum_t \lambda K_{st}\chi_t^{(-)}, \quad (5)$$

whence

$$\begin{aligned}\sum_p \chi_p^{(+)}(1+\lambda K)_{pr}V&=V\chi_r^{(+)},\\ V\sum_t(1+\lambda K)_{st}\chi_t^{(-)}&=\chi_s^{(-)}V,\end{aligned} \quad (6)$$

and

$$\begin{aligned}\chi_r^{(+)}V&=V\sum_p \chi_p^{(+)}[1/(1+\lambda K)]_{pr},\\ V\chi_s^{(-)}&=\sum_t[1/(1+\lambda K)]_{st}\chi_t^{(-)}V.\end{aligned} \quad (7)$$

On differentiating V with respect to λ, we get

$$\begin{aligned}(\partial/\partial\lambda)V&=\sum K_{rs}\chi_r^{(+)}V\chi_s^{(-)}\\ &=\sum V\chi_r^{(+)}(K/1+\lambda K)_{rs}\chi_s^{(-)}\\ &=V\sum(K/1+\lambda K)_{rr}\\ &\qquad-\sum V\chi_s^{(-)}\chi_r^{(+)}(K/1+\lambda K)_{rs}\\ &=VTr(K/1+\lambda K)\\ &\qquad-\sum \chi_s^{(-)}V\chi_r^{(+)}(K/(1+\lambda K)^2)_{rs},\end{aligned} \quad (8)$$

and the integration of the final form supplies the identity

$$\begin{aligned}\exp[\sum \chi_r^{(+)};\lambda K_{rs}\chi_s^{(-)}]&=\det(1+\lambda K)\\ &\times\exp[-\sum \chi_s^{(-)};\chi_r^{(+)}(\lambda K/1+\lambda K)_{rs}].\end{aligned} \quad (9)$$

The $(\chi^{(-)\prime}||\chi^{(+)\prime})$ matrix element of this operator relation states that

$$\begin{aligned}&(\chi^{(-)\prime}|\exp[\sum \chi_r^{(+)};\lambda K_{rs}\chi_s^{(-)}]|\chi^{(+)\prime})\\ &=\det(1+\lambda K)\exp\{\sum \chi_s^{(-)\prime}\chi_r^{(+)\prime}[1/(1+\lambda K)]_{rs}\},\end{aligned} \quad (10)$$

and, in particular, that

$$\det(1+\lambda K)=(0|\exp[\sum_{rs}\chi_r^{(+)};\lambda K_{rs}\chi_s^{(-)}]|0), \quad (11)$$

which exhibits $\det(1+\lambda K)$ as the matrix element of an operator. The derivation of this result requires no more than the first two rearrangements of (B8). Now

$$\begin{aligned}\exp[\sum \chi_r^{(+)};\lambda K_{rs}\chi_s^{(-)}]&=\sum_{n=0}^{\infty}\lambda^n\frac{1}{n!}\sum_{r,s}\chi_{r_1}^{(+)}\cdots\chi_{r_n}^{(+)}\\ &\times\prod_{i=1}^{n}K_{r_i s_i}\chi_{s_n}^{(-)}\cdots\chi_{s_1}^{(-)},\end{aligned} \quad (12)$$

and

$$\begin{aligned}\chi_{s_n}^{(-)}\cdots\chi_{s_1}^{(-)}\Psi(0)&=\epsilon_{s_1\cdots s_n}\Psi(n'),\\ \Psi(0)^\dagger\chi_{r_1}^{(+)}\cdots\chi_{r_n}^{(+)}&=\epsilon_{r_1\cdots r_n}\Psi(n)^\dagger,\end{aligned} \quad (13)$$

where the occupation number eigenvectors are preceded by alternating symbols, which are unity if the operators appear in some standard order. Therefore,

$$\det(1+\lambda K)=\sum_{n=0}^{\infty}\lambda^n\frac{1}{n!}\sum_r \det{}_{(n)}K_{r_i r_j}, \quad (14)$$

since the $s_1\cdots s_n$ must be some permutation of the $r_1\cdots r_n$, and the factor $\epsilon_{r_1\cdots r_n}\epsilon_{s_1\cdots s_n}$ is $+1$ or -1, according as the permutation is even or odd. The analogous result for a continuously labelled matrix is obtained with the substitution

$$K_{r_i r_j}\rightarrow(dx_i)^{\frac{1}{2}}K(x_i,x_j)(dx_j)^{\frac{1}{2}}, \quad (15)$$

namely,

$$\begin{aligned}\det(1+\lambda K)=\sum_{n=0}^{\infty}\lambda^n\frac{1}{n!}\int(dx_1)\cdots(dx_n)\\ \times\det{}_{(n)}K(x_i,x_j).\end{aligned} \quad (16)$$

It is of interest to consider the similar properties of ordered exponentials constructed from operators that obey the B.E. commutation relations

$$\begin{aligned}[\chi_r^{(+)},\chi_s^{(+)}]=[\chi_r^{(-)},\chi_s^{(-)}]&=0,\\ [\chi_r^{(+)},\chi_s^{(-)}]&=\delta_{rs}.\end{aligned} \quad (17)$$

Then the minus sign is to be omitted from (B4) and (B5), so that the sign of K is reversed in (B6) and (B7). This results in (B8) being replaced by

$$\begin{aligned}(\partial/\partial\lambda)V&=VTr(K/1-\lambda K)\\ &\quad+\sum \chi_s^{(-)}V\chi_r^{(+)}(K/(1-\lambda K)^2)_{rs},\end{aligned} \quad (18)$$

which yields the B.E. identity

$$\begin{aligned}\exp[\sum \chi_r^{(+)};\lambda K_{rs}\chi_s^{(-)}]&=[1/\det(1-\lambda K)]\\ &\times\exp\{\sum \chi_s^{(-)};\chi_r^{(+)}[\lambda K/(1-\lambda K)]_{rs}\}.\end{aligned} \quad (19)$$

Thus the B.E. analog of (B11) is

$$1/\det(1-\lambda K)=(0|\exp[\sum \chi_r^{(+)};\lambda K_{rs}\chi_s^{(-)}]|0). \quad (20)$$

In the expansion (B12), the order of left and right factors is now irrelevant, and repeated indices can occur. Thus (B13) is replaced by

$$\begin{aligned}\chi_{s_n}^{(-)}\cdots\chi_{s_1}^{(-)}\Psi(0)&=(\prod n_k'!)^{\frac{1}{2}}\Psi(n'),\\ \Psi(0)^\dagger\chi_{r_1}^{(+)}\cdots\chi_{r_n}^{(+)}&=(\prod n_k!)^{\frac{1}{2}}\Psi(n)^\dagger.\end{aligned} \quad (21)$$

The indices $s_1\cdots s_n$ must be some permutation of the $r_1\cdots r_n$, and each term carries the factor $\Pi n_k!$. Hence the expansion of (B20) is represented by

$$1/\det(1-\lambda K)=\sum_{n=0}^{\infty}\lambda^n\frac{1}{n!}\sum_r \mathrm{perm}_{(n)}K_{r_i r_j}, \quad (22)$$

where the so-called permanent is defined by

$$\mathrm{perm}_{(n)}K_{r_i r_j}=\sum_{s=r}\prod_{i=1}^{n}K_{r_i s_i}, \quad (23)$$

and the summation with respect to the s_i is extended over all $n!$ permutations of the r_i. This quantity differs from the corresponding determinant by the omission of

the alternating sign factor which, in the latter, enforces the nonoccurrence of identical rows or columns. In the continuous limit [Eq. (B15)], repeated indices produce no contribution and we get

$$1/\det(1-\lambda K)=\sum_{n=0}^{\infty}\lambda^n\frac{1}{n!}\int(dx_1)\cdots(dx_n)$$
$$\times\mathrm{perm}_{(n)}K(x_i,x_j). \quad (24)$$

This permanent coincides with a special case of the symmetrant defined in IV. The relation between the expansions (B14) and (B22) can be understood in terms of the expressions

$$\det(1+\lambda K)=\exp[Tr\log(1+\lambda K)] \quad (25)$$

and

$$1/\det(1-\lambda K)=\exp[-Tr\log(1-\lambda K)], \quad (26)$$

since the sign factors in (38) arise from the successive sign changes in the series (35), which are missing in

$$-Tr\log(1-\lambda K)=\sum_{n=1}^{\infty}\frac{1}{n}\lambda^n K_n. \quad (27)$$

Finally, we shall use operator techniques to prove that

$$(0|F_0|0)=\det(1+S^{(+)}IS^{(-)}\bar{I}), \quad (28)$$

where F_0 represents (163) with zero eigenvalues, thus verifying (181). The dependence of F_0 upon the quantities $\bar{I}(x,x')$ is given by

$$(\delta/\delta\bar{I}(x,x'))F_0=-i\sum\nolimits_{-}$$
$$\times\bar{\psi}_{\lambda p}(x)\chi_{\lambda p}{}^{(+)}\sum\nolimits_{+}\psi_{\lambda' p'}(x')\chi_{\lambda' p'}{}^{(+)}F_0. \quad (29)$$

Now, according to (171) and (172),

$$[\sum\nolimits_{+}\psi_{\lambda p}(x)\chi_{\lambda p}{}^{(+)},F_0]$$
$$=F_0\int(dx')(x|iS^{(+)}I|x')\sum\nolimits_{-}\psi_{\lambda' p'}(x')\chi_{\lambda' p'}{}^{(-)} \quad (30)$$

and

$$[F_0,\sum\nolimits_{-}\psi_{\lambda p}(x)\chi_{\lambda p}{}^{(-)}]$$
$$=\int(dx')(x|iS^{(-)}\bar{I}|x')\sum\nolimits_{+}\psi_{\lambda' p'}(x')\chi_{\lambda' p'}{}^{(+)}F_0, \quad (31)$$

which are combined in

$$\int(dx')(x|1+S^{(+)}IS^{(-)}\bar{I}|x')\sum\nolimits_{+}\psi_{\lambda p}(x')\chi_{\lambda p}{}^{(+)}F_0$$
$$=F_0\sum\nolimits_{+}\psi_{\lambda p}(x)\chi_{\lambda p}{}^{(+)}$$
$$+\int(dx')(x|iS^{(+)}I|x')\sum\nolimits_{-}\psi_{\lambda p}(x')\chi_{\lambda p}{}^{(-)}F_0. \quad (32)$$

We deduce that

$$(0|\sum\nolimits_{-}\bar{\psi}_{\lambda p}(x)\chi_{\lambda p}{}^{(+)}\sum\nolimits_{+}\psi_{\lambda' p'}(x')\chi_{\lambda' p'}{}^{(+)}F_0|0)$$
$$=(x'|(1+S^{(+)}IS^{(-)}\bar{I})^{-1}iS^{(+)}IS^{(-)}|x)(0|F_0|0), \quad (33)$$

and consequently

$$(\delta/\delta\bar{I}(x,x'))(0|F_0|0)$$
$$=(x'|(1+S^{(+)}IS^{(-)}\bar{I})^{-1}S^{(+)}IS^{(-)}|x)(0|F_0|0). \quad (34)$$

We thus arrive at the differential expression

$$\delta\log(0|F_0|0)=Tr[(1+S^{(+)}IS^{(-)}\bar{I})^{-1}$$
$$\times\delta(S^{(+)}IS^{(-)}\bar{I})], \quad (35)$$

which proves (B28).

Letters to the Editor

PUBLICATION of brief reports of important discoveries in physics may be secured by addressing them to this department. The closing date for this department is five weeks prior to the date of issue. No proof will be sent to the authors. The Board of Editors does not hold itself responsible for the opinions expressed by the correspondents. Communications should not exceed 600 words in length and should be submitted in duplicate.

Present Status of the Atomic Constants

J. A. BEARDEN, M. D. EARLE, J. M. MINKOWSKI, AND J. S. THOMSEN
The Johns Hopkins University, Baltimore, Maryland
(Received July 7, 1953; revised manuscript received December 10, 1953)

IN the course of evaluating the atomic constants by means of a least squares adjustment,[1] it became apparent that the values obtained depended strongly on the emphasis given to the fine structure separation as determined from the Lamb shift experiments[2,3] and to the hyperfine structure measurements in hydrogen.[4] Several sets of values have been computed in order to observe the effect of including or omitting these two experiments.

Figure 1 shows the values of h, e, and α^{-1} resulting from the various adjustments. There is a large difference between the 1950 values (BW[5] and DC[6]) and the presently computed ones using the hyperfine structure experiment. This difference is principally due to the fact that in the relation between α and the hyperfine structure separation a correction term of the order $Z\alpha^2$, whose magnitude is about 96 ppm (parts per million), is now included. If, as now believed, higher order correction terms in α are small, the principal uncertainty involved in the use of the experiment is

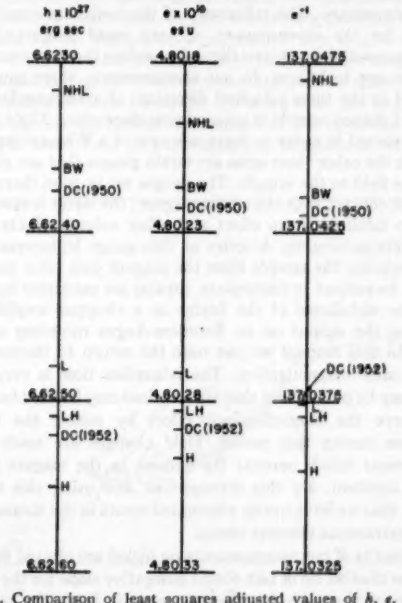

FIG. 1. Comparison of least squares adjusted values of h, e, and α^{-1}. NHL—values obtained without using either hyperfine structure or Lamb shift experiments; BW—Bearden and Watts values, July 1950; DC (1950)—DuMond and Cohen values, December 1950; (see reference 6) LH—values obtained using hyperfine structure and Lamb shift experiments; H—values obtained using hyperfine structure experiment, omitting Lamb shift experiment; DC (1952)—DuMond and Cohen values, 1952; L—values obtained using Lamb shift experiments, omitting hyperfine structure experiment.

primarily due to uncertainty involved in the effect of the proton structure on its magnetic moment. Reliable estimates[7-9] indicate that this may be of the order of 20 ppm. This uncertainty was not included in the H adjustment; but in the LH, in which both the hyperfine structure and Lamb shift experiments were used, the above figure was divided by two to obtain a probable error of 10 ppm. This, of course, decreases the weight given to the hyperfine structure measurement in the adjustment.

In the light of the good agreement between the L values and the H values, we see no choice at the present time but to include both the Lamb shift experiment and the hyperfine structure measurement (with the $Z\alpha^2$ correction term) and to accept the LH values. It should be clearly understood that the surprisingly large changes in the constants are principally due to the two experiments mentioned above, other revisions in the input data being a secondary importance. Unfortunately, there is a rather disturbing lack of consistency in the present adjustment. The ratio of error by external consistency to that by internal consistency, which was of the order of unity in the 1950 work, is now about 2.4.

The lack of consistency may be due to at least two causes:

(1) Errors in some of the experiments may have been seriously underestimated (see reference 12, Sec. 9).

(2) Theoretical formulas used in interpreting the hyperfine structure and Lamb shift experiments may be in error, or higher order terms in α may be of more importance than hitherto believed. This possibility is given support by the fact that the ratio of external to internal error in the NHL adjustment, with these two experiments omitted, is only about 1.8. However, the statistical evidence is by no means conclusive.

The good agreement between the Lamb shift experiment and the hyperfine structure experiment indicates that any theoretical error is probably common to both experiments. However, the only apparent source of such an error is the anomalous magnetic moment of the electron,[10] which is in good agreement with direct experimental results.[11]

Recently, DuMond and Cohen[12] have published values of the atomic constants which agree with our LH values within the limits of error. These authors have omitted the hfs experiment on the ground that its theoretical interpretation involves an uncertainty due to the unknown proton structure. As pointed out above, we have taken this into account by ascribing an error of 10 ppm to the original equation connected with this excellent experiment. This procedure would seem particularly justifiable in an adjustment using experiments with probable errors of the order of 54 ppm [Eq. (6.11) in the quoted DuMond and Cohen work].

The use of the fine structure separation (ΔE) from the Lamb shift experiments in the least squares adjustment seems to require a greater degree of justification than has been given to it by DuMond and Cohen.

ΔE is not a direct result of the measurement. The measured quantities are the magnetic field and frequency corresponding to transitions from the Zeeman levels $a^2S_{\frac{1}{2}}$ to $e^2P_{\frac{1}{2}}$ (or $f^2P_{\frac{1}{2}}$) and from $a^2S_{\frac{1}{2}}$ to $a^2P_{\frac{1}{2}}$. In order to get the separations ($2^2S_{\frac{1}{2}}-2^2P_{\frac{1}{2}}$) (Lamb shift S) and ($2^2S_{\frac{1}{2}}-2^2P_{\frac{1}{2}}$), ($\Delta E-S$) at zero field, Lamb's[13] formulas (164) to (167) must be applied.

In the actual computation, Dayhoff, Triebwasser, and Lamb use the Bearden and Watts 1950 values[5,13] of atomic constants, and their result for ΔE is 10 971.59±0.10 Mc/sec. It is this value which is subsequently used in the DuMond and Cohen adjustment.

Another objection to the use of the fine structure separation as determined by the Lamb shift experiments is connected with the fact that the magnetic field is calibrated by means of the proton resonance method, thus producing a correlation between these results and the experiment of Thomas, Driscoll, and Hipple on the absolute proton moment.

However, due to the particular arrangement of constants in formulas (164) to (167) of reference 13, it happens that the results are quite insensitive to whether the Bearden and Watts values or

the present LH values are used in the calculations. (It is not true that the results would be insensitive to any possible variation of the constants of comparable magnitude.) Also, since the term involving the Thomas, Driscoll, and Hipple experiment is only about 20 percent of ΔE, closer study shows that this correlation is not critical. Thus, despite the well-founded theoretical objections to using this extremely accurate experiment, it can probably be included without serious error.

[1] Bearden, Earle, Minkowski, and Thomsen, Phys. Rev. **91**, 482 (1953).
[2] Triebwasser, Dayhoff, and Lamb, Phys. Rev. **89**, 98 (1953).
[3] Dayhoff, Triebwasser, and Lamb, Phys. Rev. **89**, 106 (1953).
[4] P. Kusch and A. G. Prodell, Phys. Rev. **88**, 184 (1952).
[5] J. A. Bearden and H. M. Watts, Phys. Rev. **81**, 73, 160 (1951).
[6] J. W. M. DuMond and E. R. Cohen, Phys. Rev. **82**, 555 (1951).
[7] N. M. Kroll and F. Pollock, Phys. Rev. **86**, 876 (1952).
[8] E. E. Salpeter and W. Newcomb, Phys. Rev. **87**, 150 (1952).
[9] E. E. Salpeter (private communication).
[10] R. Karplus and N. M. Kroll, Phys. Rev. **77**, 536 (1950).
[11] Koenig, Prodell, and Kusch, Phys. Rev. **88**, 191 (1952).
[12] J. W. M. DuMond and E. R. Cohen, Revs. Modern Phys. **25**, 691 (1953).
[13] W. E. Lamb, Jr., Phys. Rev. **85**, 259 (1952).

Volume Magnetostriction in Nickel and the Bethe-Slater Interaction Curve

K. Azumi and J. E. Goldman
Carnegie Institute of Technology, Pittsburgh, Pennsylvania*
(Received December 10, 1953)

THE volume magnetostriction at high fields in ferromagnets can be related to the pressure dependence of the magnetization through the thermodynamic identity:

$$(\partial\omega/\partial H)_p = -(\partial(VM)/\partial p)_H, \tag{1}$$

where $\omega = \Delta V/V_0$. There are reasons for expecting a negative field dependence for the volume magnetostriction in nickel. (1) Recent experiments by Jones and Stacey[1] on the influence of pressure on magnetization show an increase in magnetization of the order of 10 percent at a pressure of 10 000 atmospheres which suggests that the left side of Eq. (1) should have negative sign. (2) Kornetzki[2] has related the volume magnetostriction to the pressure dependence of the Curie point in the following way:

$$\frac{1}{\theta}\frac{\partial\theta}{\partial p} = \frac{1}{T}\frac{\partial\omega}{\partial H}\Big/\left(\rho\frac{\partial\sigma}{\partial T} - \frac{3\alpha}{K}\frac{\partial\omega}{\partial H}\right), \tag{2}$$

where ρ and σ are the density and specific magnetization respectively, α is the thermal expansion, and K is the volume compressibility. The second term in the denominator may be neglected

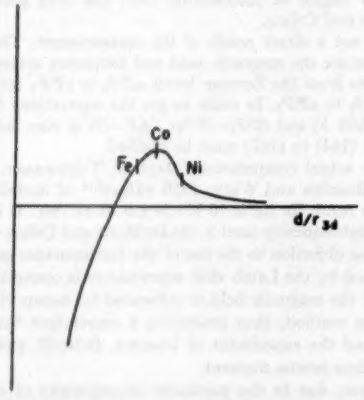

FIG. 1. The Sommerfeld and Bethe representation of Slater's interaction parameter in which the exchange energy J is plotted as a function of the ratio of the interatomic distance to the calculated radius of the 3*d* shell.

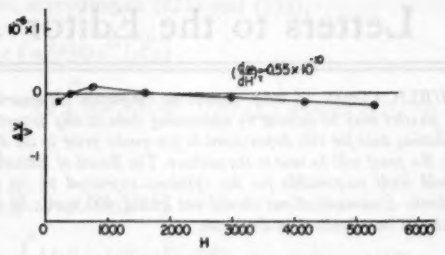

FIG. 2. Volume magnetostriction of nickel (isothermal) plotted as a function of applied magnetic field.

compared to the first, and it is seen that the latter is always negative. Patrick[3] finds $\partial\theta/\partial p$ to be positive which would require $\partial\omega/\partial H$ to be negative. It is considered improbable that the sign would change between room temperature and the Curie point. (3) The exchange interaction in ferromagnetic materials is usually represented by the "Bethe-Slater" curve shown in Fig. 1. There should be at least a qualitative correlation between the Curie points and the values of the ordinates for given metals on the curve (irrespective of the model employed), which lends support to the placement of nickel to the right of the maximum and would thus be in agreement with the observed effects of pressure and with the above supposition regarding the sign of the volume magnetostriction.

Previous investigators[4] have studied the volume magnetostriction of nickel using liquid dilatometers. All report positive values for $\partial\omega/\partial H$. Doring has pointed out the need for applying corrections to allow for expansions resulting from magnetocaloric heating, but his corrections are much larger than the measured quantities. By its very nature the liquid dilatometer as a method of measurement makes it difficult to eliminate errors due to magnetocaloric effects which in nickel are significant even at room temperature. The refinement of the resistance strain gauge method for the measurement of very small magnetostriction effects[5] suggested the desirability of repeating these measurements with the new technique. In our measurements, three gauges are mounted in the three principal directions of a rectangular parallelepiped shaped sample of approximate dimensions 22×6×6 mm and connected in series to form one arm of a Wheatstone bridge of which the other three arms are strain gauges that are placed in the same field as the sample. The gauges are in good thermal and magnetic contact with the electromagnet; the latter is essential in order to minimize form effect and other volume effects due to incomplete saturation. A series of thin-gauge high-permeability strips separate the sample from the magnet pole piece so that it will not be subject to constraints. Strains are measured by amplifying the unbalance of the bridge in a chopper amplifier and recording the output on an Esterline-Angus recording milliammeter. In this manner we can note the return to thermal equilibrium after magnetization. The relaxation time is very short, but it may be pointed out that this method may be used indirectly to observe the magnetocaloric effect by noting the thermal expansion during this period. Field changes are made by an arrangement which permits the current in the magnet coils to remain constant. By this arrangement and using this method, it is felt that we have nearly eliminated errors in the measurement due to extraneous thermal effects.

The results of our measurements on nickel are plotted in Fig. 2. It is seen that we do in fact obtain a negative slope for the volume magnetostriction as a function of magnetic field. The measured slope is 0.55×10^{-10} which we estimate to be accurate to approximately 10 percent. The agreement between our measurements and the more recent experiments on pressure effects appears to support the view that the exchange interaction in ferromagnetics can be represented by a curve of the type first suggested by Slater and

given by Sommerfeld and Bethe. A detailed description of the method of measurement and additional results on other ferromagnetic metals and some nickel-copper alloys will be presented in a later communication.

Acknowledgment is made of the assistance of William Bitler in making the measurements and of a post-doctoral grant to one of us (K. A.) from the Transportation Research Institute of Japan. We are also indebted to Dr. Lyle Patrick for the privilege of seeing his manuscript before publication.

* Supported by the U. S. Office of Naval Research.

[1] G. O. Jones and F. D. Stacey, Proc. Phys. Soc. (London) **B66**, 255 (1953).
[2] M. Kornetzki, Z. Physik **98**, 289 (1935); Physik. Z. **44**, 296 (1943).
[3] Lyle Patrick, thesis, University of Chicago (1953); this issue [Phys. Rev. **93**, 384 (1954)].
[4] M. Kornetzki (reference 2); J. L. Snoek, Physica **4**, 853 (1937); W. Doring, Z. Physik **103**, 560 (1936).
[5] J. E. Goldman, Phys. Rev. **72**, 529 (1947); J. phys. et radium **12**, 471 (1951).

Specific Heat of 96-Percent He^3 below 1°K*

G. DE VRIES AND J. G. DAUNT
Department of Physics and Astronomy, Ohio State University, Columbus, Ohio
(Received December 17, 1953)

WE have extended our previous measurements[1] of the specific heat of liquid He^3 (He^3 content 96 percent, 4-percent He^4) by observations down to 0.57°K. Calorimetric techniques as previously described[1,2] were used, the calorimeter holding 13-mm^3 liquid He^3. The calorimeter was cooled to temperatures below 1°K by a paramagnetic salt, the thermal connection being through a superconducting thermal valve which could be opened or closed magnetically, as described elsewhere.[3] Temperatures were measured with a carbon resistance thermometer calibrated against temperatures obtained from the susceptibility of the paramagnetic salt. Our preliminary results are shown in Fig. 1, which includes also our previous results obtained between 1.3°K and 2.3°K. The probable estimated error is ±10 percent. Details of the corrections which had to be applied for evaporation of the liquid during the heating cycles, etc., will be described in a fuller publication later. It might be noted that the largest corrections (at 1.3°K) totaled 17 percent of the observed specific heats. The lower limit of temperature of observation was determined in these experiments by the effective range of the type of resistance thermometer which we employed.

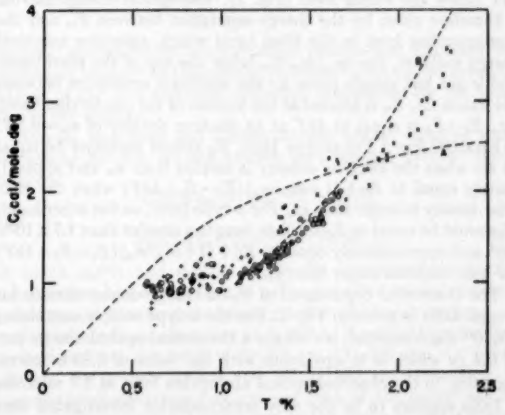

FIG. 1. The specific heat, C_{sat}, in cal/mole-deg of liquid He^3 (96-percent He^3) as a function of the absolute temperature T in °K. The crosses ✕ give our previously reported results,[1] the circles and crosses +, the new observations. The curve A gives the specific heat for an ideal Fermi-Dirac gas ($T_{deg}=4.85$°K). The curve B gives the formula $C_{sat}=0.68T+0.27^3$ cal/mole-deg derived from the vapor-pressure data [J. G. Daunt, Phil. Mag. Suppl. **1**, 209 (1952)].

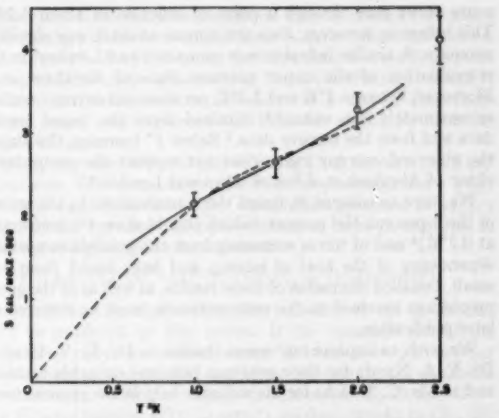

FIG. 2. The entropy S in cal/mole-deg of pure liquid He^3 as a function of the absolute temperature T in °K. The full curve gives the entropy curve derived from the measured specific heat. The circles give the values computed by Abraham *et al.* (see reference 5), the broken curve the computed entropy from the vapor-pressure data by Chen and London (see reference 6).

It will be seen from Fig. 1 that our new data between 1.3°K and 0.57°K form a smooth continuation of the specific heat curve at higher temperatures which we reported previously.[1] Although there is some scatter in the individual points, it seems clear that there is no marked anomaly of a discontinuous or λ-type nature over the whole range of observation. It is of interest to note, however, the marked flattening of the curve between 0.6°K and 1°K and the fact that no obvious extrapolation of the curve can be made to $T=0$°K.

We have drawn curve A also in Fig. 1, the specific heat to be expected for an ideal Fermi-Dirac system of particles of spin ½ with molecular weight and number density appropriate to liquid He^3. It is clear by comparing curve A with the experimental results that the specific heat of liquid He^3 cannot be approximated by that of an ideal Fermi-Dirac gas, a conclusion which we had previously reached.[1] Moreover, from the fact that the observed specific heat in the range 0.57°K to 1.7°K lies everywhere well below that of the Fermi-Dirac model (curve A), it appears that one should conclude that the pairing off or the correlation between the nuclear spins must either be completely removed at temperatures of 0.6°K and up, or that nearly all the spins must still be paired off even at temperatures as high as 2°K. The latter alternative is unacceptable in view of the classical behavior recently observed for the paramagnetic susceptibility of the He^3 spin system in the temperature range 1.2°K to 2.8°K by Fairbank *et al.*[4]

In order to gain further insight concerning the thermal behavior of liquid He^3, we have made computations of the entropy as a function of temperature. Since our observed specific heat does not allow any clear extrapolation to $T=0$°K we have computed only entropy differences. To obtain Fig. 2, however, we have arbitrarily assumed an exact value for the entropy of pure He^3 at 1.5°K and our results are shown by the full curve. The value chosen for S_{liq} at 1.5°K was 2.63 cal/mole-deg obtained from the vapor-pressure measurements by Abraham *et al.*[5] We wish to emphasize that although the specific heat measurements of Fig. 1 are for a 96 percent He^3 *mixture*, our computed entropy of Fig. 2 is, within the accuracy given by the experimental errors, that for *pure* liquid He^3. That this is so is evident from the fact that the entropy value of 2.63 cal/mole deg, chosen for $T=1.5$°K, does not include the entropy of mixing. (The classical entropy of mixing for a 96 percent He^3 mixture would be 0.15 cal/mole-deg.)

It is of interest to note in Fig. 2 that the entropy *versus* temper-

ature curve goes through a point of inflexion at about 1.25°K. This inflexion, however, does not appear to mark any significant anomaly. A similar inflexion was computed and London[6] in their re-evaluation of the vapor pressure data of Abraham *et al.*[5] Moreover, between 1°K and 2.3°K our observed entropy confirms approximately the values[5,6] obtained from the vapor pressure data and from the density data.[7] Below 1° however, the slope of the observed entropy curve does not support the computations either of Abraham *et al.*[5] or of Chen and London.[6]

We have considered in detail the contributions to the entropy of the 4-percent He[4] present (which should show a λ temperature at 0.2°K)[8] and of terms stemming from the possible temperature dependency of the heat of mixing, and have found them to be small. Detailed discussion of these results, as well as of the general procedures involved in the measurements, must be deferred to a later publication.

We wish to express our warm thanks to Dr. C. V. Heer and Dr. V. A. Nanda for their generous help and valuable discussion and to Mr. C. S. Ochs for his welcome help in the measurements.

* Assisted by a contract between the U. S. Atomic Energy Commission and the Ohio State University Research Foundation.

[1] G. de Vries and J. G. Daunt, Phys. Rev. **92**, 1572 (1953).
[2] Horowitz, Silvidi, Malaker, and Daunt, Phys. Rev. **88**, 1182 (1952).
[3] C. V. Heer and J. G. Daunt, Phys. Rev. **76**, 854 (1949).
[4] Fairbank, Ard, Dehmelt, Gordy, and Williams, Phys. Rev. **92**, 208 (1953).
[5] Abraham, Osborne, and Weinstock, Phys. Rev. **80**, 366 (1950).
[6] T. C. Chen and F. London, Phys. Rev. **89**, 1038 (1952).
[7] Grilly, Hammel, and Sydoriak, Phys. Rev. **75**, 1103 (1949).
[8] J. G. Daunt and C. V. Heer, Phys. Rev. **79**, 46 (1950).

Anomalous Optical Absorption Limit in InSb

ELIAS BURSTEIN
Crystal Branch, Metallurgy Division, Naval Research Laboratory, Washington, D. C.
(Received December 11, 1953)

TANENBAUM and Briggs[1] have recently encountered an anomalous dependence of the optical absorption limit on impurity content in InSb. They find that the room-temperature absorption limit of an intrinsic sample lies at 7.0 microns while that of a relatively impure sample lies at 3.2 microns. They suggest that the transmission in the region from 3.2 to 7.0 microns is due to an impurity effect. Optical measurements have also been carried out at this laboratory.[2] We find, for example, in agreement with Tanenbaum and Briggs, that the absorption limit of an n-type sample containing 5×10^{18} electrons/cm^3 lies at 3.2 microns, while that of an intrinsic sample lies at 7.2 microns. We believe, however, that there is a natural explanation for the anomalous behavior of the absorption limit which is based on the very small effective mass of the electrons in InSb, rather than on some specific impurity effect.

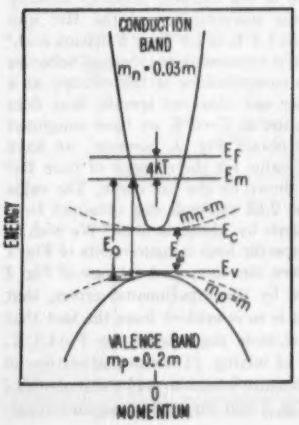

FIG. 1. Energy-momentum diagram of InSb based on $m_n = 0.03m$ and $m_p = 0.2m$ giving the position of the Fermi level and that of the lowest unfilled level in the conduction band for an n-type sample containing 5×10^{18} electrons/cm^3. The corresponding energy-momentum curves for a semiconductor for $m_n = m_p = m$ is shown in dotted lines.

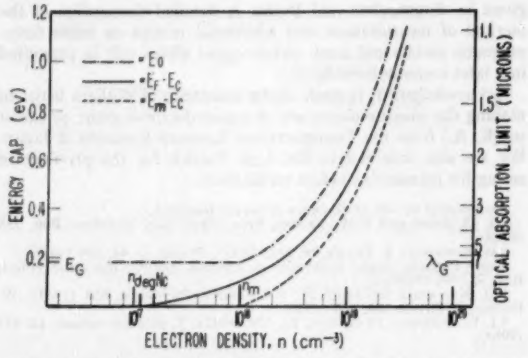

FIG. 2. The dependence of the Fermi level, the lowest unfilled level in the conduction band, and the optical energy gap on charge carrier density in n-type InSb.

By assuming that the thermal-energy gap at room temperature is equal to 0.18 ev, the optical energy gap for intrinsic materials, Tananbaum and Maita[3] obtain a value of $0.083m$ for the geometric mean of the effective masses of the electrons and holes in InSb. In addition, by assuming a $T^{-\frac{3}{2}}$ law for the hole mobilities at high temperatures, they obtain a value of approximately 85 for $(\mu_n/\mu_p)_L$, the ratio of electron to hole mobilities in the lattice scattering range of temperatures. Using the relation $(\mu_n/\mu_p)_L = (m_p/m_n)^{5/2}$ we obtain values of $0.03m$ and $0.2m$ for the effective masses of electrons and holes, respectively, in InSb. The very small effective mass of the electrons in InSb results from a sharp curvature at the bottom of the conduction band and is associated with a small effective density of states and with a small degeneracy concentration ($N_c = 1.6\times10^{17}$/cm^3 and $n_{deg} = 1.2\times10^{17}$/cm^3 at 300°K). Consequently, InSb becomes degenerate at relatively low electron densities, and in a degenerate sample the height of the Fermi level above the bottom of the conduction band, $E_f - E_c$, increases very rapidly with increasing electron density.

The optical absorption limit of a degenerate n-type sample involves vertical transitions from the filled band to the lowest unfilled level E_m in the conduction band, which lies approximately $4kT$ below the Fermi level (Fig. 1). The optical energy gap E_0 is therefore given by the energy separation between E_m and the corresponding level in the filled band which, assuming spherical energy surfaces, lies $(m_n/m_p)E_m$ below the top of the filled band, and is not just simply given by the minimum separation between the bands E_G. E_m is located at the bottom of the conduction band, i.e., $E_f - E_c$ is equal to $4kT$ at an electron density of $n_m = 6.5N_c = 1.0\times10^{18}$/cm^3.[4] For n-type InSb, E_0 should therefore be equal to E_G when the electron density is smaller than n_m and approximately equal to $E_G + (1+m_n/m_p)(E_f - E_c - 4kT)$ when the electron density is larger than n_m. For p-type InSb, on the other hand, E_0 should be equal to E_G for hole densities smaller than 1.7×10^{19}/cm^3, and approximately equal to $E_G + (1+m_p/m_n)(E_v - E_f - 4kT)$ for hole densities larger than p_m.

The theoretical dependence of E_0 on charge-carrier density for n-type InSb is given in Fig. 2. For the n-type sample containing 5×10^{18} electrons/cm^3, we obtain a theoretical optical energy gap of 0.4 ev which is in agreement with the value of 0.39 ev corresponding to the observed optical absorption limit at 3.2 microns.

InSb appears to be the only semiconductor investigated thus far in which the anomalous behavior of the absorption limit is observed. This may be attributed to the fact that the effective masses of the charge carriers in other semiconductors are much larger than the effective mass of the electrons in InSb, so that a much larger carrier density is needed to make them degenerate.

A shift in the absorption limit with charge-carrier density should also be observable at sufficiently high charge-carrier densities in other semiconductors. However, the absorption by free charge carriers at the high densities needed would, in general, mask the intrinsic absorption limit and thereby prevent the effect from being observed.

[1] M. Tanenbaum and H. B. Briggs, Phys. Rev. 91, 1561 (1953).
[2] I am indebted to W. Zimmerman for supplying the doped InSb samples; to Bertha W. Henvis for carrying out the optical measurements; and to G. Lerman for carrying out the Hall effect measurements. I am also grateful to Dr. M. Tanenbaum of the Bell Telephone Laboratories for supplying the intrinsic sample of InSb.
[3] M. Tanenbaum and J. P. Maita, Phys. Rev. 91, 1009 (1953).
[4] J. McDougall and E. C. Stoner, Trans. Roy. Soc. London **A237**, 67 (1938).

Origin of the Emission of the Oxygen Green Line in the Airglow*

MARCEL NICOLET
Ionosphere Research Laboratory, Pennsylvania State University, State College, Pennsylvania
(Received December 7, 1953)

IT is well known that the airglow emission of the oxygen green line at λ5577A cannot be attributed to the ordinary chemical sources if the altitude of the airglow layer is greater than that of the E layer. Furthermore, ionic recombinations involving negative ions in Region F are not sufficient to lead to an airglow emission. Finally, while the hypothesis of incoming particles exciting this emission has been put forward, it remains vague and cannot account for the variations which are observed.

According to the observational data,[1] the height of the emission layer is of the order of 250±50 km, and the maximum of intensity occurs at local midnight ±2.5 hours. The observed annual variation shows several maxima and indicates, therefore, a quite complex variation. Finally, the isophotal plots of the intensity changes of various parts of the sky suggest the presence of a definitive emission pattern in the high atmosphere.

In order to explain such an emission, recourse must be made to results obtained by Nicolet and Mange[2] on the vertical distribution of molecular oxygen. The charge-exchange process considered by Bates and Massey[3] can be applied in the following form in the F_2 layer:

$$O^+ + O_2 \rightarrow O + O_2^+. \tag{1}$$

The reaction (1) is followed by

$$O_2^+ + e \rightarrow O' + O'', \tag{2}$$

namely, a dissociative recombination process first discussed by Bates and Massey[3] and calculated by Bates.[4] Dissociative recombination of O_2^+ is a powerful excitation mechanism for the green line in the airglow.

Because molecular and atomic oxygen are in diffusive equilibrium at 200 km, we can assume the following vertical distributions:

$$n(O) = n_0(O) \exp[-(1+\beta)\zeta], \tag{3}$$

and

$$n(O_2) = n_0(O_2) \exp[-(2+\beta)\zeta], \tag{4}$$

in which $n_0(O)$ and $n_0(O_2)$ denote the concentrations at the reduced[5] height $\zeta=0$, $n(O)$ and $n(O_2)$ are the concentrations at height ζ, and β is the scale height gradient of atomic oxygen.

Numerical values[2] show that O_2 is still an important constituent in Region F; of the order of 5×10^7 cm^{-3} at 200 km, 5×10^6 at 250 km, 5×10^5 at 300 km and 10^5 at 350 km. According to ionospheric observations,[6] an average peak of the night-time F_2 layer may be considered at heights of the order of 300–350 km. The vertical distribution of the electron concentration n_e can be represented[5] by the following formula:

$$n_e = (n_e)_0 \exp\{\tfrac{1}{2}(1+\beta)[1-\zeta(1-\eta)-e^{-\zeta}]\}, \tag{5}$$

in which η denotes a parameter giving the form of the particular distribution. If $\eta=0$, the conventional form is obtained in which the total electron content of the layer is three times the content below the peak. If $\eta=1/(1+\beta)$, the recombination coefficient can be proportional to the pressure and the total electron content is six times the content below the peak. It is known that these extreme forms may represent the behavior of the F_2 layer[7] in winter and summer.

Ionization potentials of O and O_2 being 13.60 ev[8] and 12.04 ev,[9] respectively, O_2^+ obtained by (1) is in the electronic state ($^2\Pi_g$) from $v=0$ to $v=6$ at most. The dissociation potential of oxygen being 5.11 ev,[10] process (2) *a priori* leads to three possibilities as far as the energy balance is concerned:

$$O_2^+ + e \rightarrow 2O(^1S), \text{ or } O(^1S)+O(^1D), \text{ or } O(^1S)+O(^3P).$$

From this, one concludes that the emission of the green line might be produced by this means. If the complete use of the energy may yield two excited atoms ^1S, it must be pointed out that the rate of the emission processes depends on the repulsion curves of states leading to dissociation products ^1S, ^1D, and ^3P.

At F_2 layer heights, $n(O^+) > n(O_2^+)$, so that, thanks to (3), (4), and (5), we may deduce the following vertical distribution of the green line emission:

$$I_{5577} \propto \exp\left\{(1+\beta)\left[1-\zeta\left(\frac{2\beta+3}{1+\beta}-\eta\right)-e^{-\zeta}\right]\right\}. \tag{6}$$

The gradient of the scale height being $\beta=0.3$, the peak of the emission corresponds to a value of ζ varying from -1 to -2 below the peak of the electron concentration (300–350 km), i.e., an altitude of 250 km.

It follows from these calculations that an airglow emission in Region F is possible. A complete account of this work will be published elsewhere. This will show the interdependence of the emission of the green line and of the properties of an ionospheric layer in which molecular oxygen ions play an important part on account of vertical transport by diffusion.[11]

* The work reported in this note has been sponsored by the Geophysical Research Division of the Air Force Cambridge Research Center, Air Research and Development Command.
[1] Roach, Williams, and Pettit, J. Geophys. Research **58**, 73 (1953); Barbier, Dufay, and Williams, Ann. astrophys. **14**, 399 (1951).
[2] M. Nicolet and P. Mange, J. Geophys. Research **59**, 1 (1954).
[3] D. R. Bates and H. S. W. Massey, Proc. Roy. Soc. (London) **A192**, 1 (1947).
[4] D. R. Bates, Phys. Rev. **78**, 492 (1950).
[5] M. Nicolet, J. Atm. and Terrest. Phys. **1**, 141 (1951).
[6] G. R. White and I. S. Wachtel, J. Geophys. Research **54**, 239 (1949).
[7] F. G. Smith, J. Atm. and Terrest. Phys. **2**, 350 (1952).
[8] C. E. Moore, "Atomic Energy Levels," National Bureau of Standards Circular No. 467 (U. S. Government Printing Office, Washington, D. C., 1949).
[9] E. C. Y. Inn, Phys. Rev. **91**, 1194 (1953).
[10] G. Herzberg, Can. J. Phys. **32**, 1 (1954).
[11] M. Nicolet, *Rocket Research of the Upper Atmosphere* (Pergamon Press, London, 1954).

Threshold Energies for Sputtering and the Sound Velocity in Metals

GOTTFRIED K. WEHNER
Electronic Components Laboratory, Wright Air Development Center, Wright-Patterson Air Force Base, Dayton, Ohio
(Received December 7, 1953)

THE author has recently[1] described experiments which show that the minimum threshold energy for sputtering is a function of the angle of incidence of the bombarding ions. Previous attempts to measure threshold energies failed to give reliable results because they were made either in the glow discharge or with wires which are small compared to the ion sheath thickness;[2,3] in both cases, however, the angle of incidence is undetermined.

With a low gas pressure (1 micron) and a large sputtering electrode immersed in a plasma of high density (10^{11}–10^{12} per cm^3), it is possible to avoid collisions of the ions within the ion sheath and to approach the plane case with predominantly

TABLE I. $\Delta H_s(298)$ = Heat of vaporization[a] at 298°K [ev]. E = Modulus of elasticity[b] [kg/mm²]. μ = Poisson constant.[b] $v_s = [E(1-\mu)/\mu(1-\mu-2\mu^2)]^{\frac{1}{2}}$ = bulk sound velocity in 10^5 cm/sec. V_0^*(Hg) = Threshold energy for sputtering by Hg ions under normal incidence [ev], corrected for neutralization energy and work function. $M = 2(2em_g V_0^*)^{\frac{1}{2}} m_m/(m_g+m_m)$ = momentum transferred at V_0^* [ev-sec/cm].

	$\Delta H_s(298)$	E	μ	v_s	V_0^*(Hg)	$M \times v_s$
Al	3.26	7220	0.34	6.45	120–140	34 – 36.6
Si	3.91	11 500	0.42	11.2	60– 70	43 – 46.4
Ti	4.92	10 500	0.36	6.35	110–130	51.6– 56
V	5.2	15 000	0.35	6.24	120–130	56.2– 58.4
Cr	3.68	19 000	0.31	6.15	60– 80	37.6– 45.6
Fe	4.2	21 550	0.29	6.1	60– 70	41.6– 44.8
Co	4.56	20 380	0.31	5.6	80–100	46 – 51.4
Ni	4.41	19 700	0.32	5.6	70– 90	42.4– 48.4
Cu	3.56	12 500	0.35	4.7	50– 70	32.2– 36
Ge	3.4	8000	0.32	4.6	40– 50	31.2– 34.8
Zr	5.43	6970	0.37	4.33	120–130	60.4– 62.4
Cb	7.6	16 000	0.35	5.5	120–130	77.4– 80
Mo	6.75	33 630	0.31	6.7	80–100	78.4– 87.4
Rh	6.0	38 640	0.26	6.15	70– 80	70.8– 75.6
Pd	4.05	12 360	0.39	4.5	50– 80	44.6– 56.4
Ag	3.04	8160	0.37	3.68	40– 50	32.8– 36.6
Sb	2.74	5600	0.33	4.3	30– 40	36 – 41.2
Hf	7.4	8500	0.37	3.34	150–180	76.8– 83.6
Ta	8.7	18 820	0.35	4.25	120–140	89 – 96.6
W	8.75	41 520	0.30	5.36	80–100	92.8–104
Re	8.21	53 000	0.26	5.65	70– 80	91.4– 98
Pt	5.86	17 320	0.39	3.98	70– 90	66 – 75.2
Au	3.94	7900	0.42	3.22	40– 50	40.8– 45.6
Pb	2.02	1600	0.44	2.17	20– 40	20 – 28.2
Th	6.5	7970	0.26	2.89	120–140	68.6– 74
U	5.43	13 380	0.30	3.08	70– 80	56 – 60
B	3.91	—	—	(13.1–14.7)	200–250	(42.8)
C	7.45	—	—	(14.7–16)	500–600?	(82)?

[a] L. Brewer in *Chemistry and Metallurgy of Miscellaneous Materials, Thermodynamics* (McGraw-Hill Book Company, Inc., New York, 1950), National Nuclear Energy Series, Plutonium Project Record, Vol. 19B, Div. IV, p. 13.
[b] W. Köster in "General Metallurgy," *FIAT Review of German Science*, 1939–46 (1950), Vol. 31.

perpendicular impacts. The study of deposits, sputtered under these conditions, shows that a well-defined minimum ion energy (V_0^*) is characteristic for every gas-metal combination.

V_0^*(Hg), (normal incidence of Hg ions) was measured for 26 metals (Table I). These threshold energies cannot be brought into agreement with existing threshold theories.[2,4] It turns out, however, that they follow (so far without exception) a simple law: The product of the momentum transferred at V_0^* from the ion to the metal atom (central collision between free elastic spheres), with the bulk sound velocity of the metal, is proportional (factor ≈11.2) to the heat of sublimation (Fig. 1); hence, threshold energies can be calculated from

$$V_0^* = \left(\frac{1.68\times 10^5 (m_g+m_m)\phi}{m_g^{\frac{1}{2}} v_s m_m}\right)^2,$$

where V_0^* is in ev; m_g = atomic weight of ion; m_m = atomic weight of metal; v_s = bulk sound velocity of metal in cm/sec; and ϕ = heat of sublimation of metal in kcal/mol. Part of V_0^* is supplied by the neutralization energy V_i and part is used for overcoming the work function W of the material; hence, $V_0^* = V_0 + V_i - W$, where V_0 is identical with the measured voltage difference between sputtering electrode and plasma. A correction of v_s for temperature (200–300°C) is small enough in most cases to stay within the experimental error and is omitted.

This law is in good agreement with other experimental results, such as those for Pt in Xe,[5] and those from recent work of Bradley[6] concerning alkali metals in inert gases. Hence, there is reason to believe that this law is of a general nature and is applicable to all gas-metal combinations, as long as "physical" and not "chemical" sputtering (e.g., C in H_2) takes place.

The bulk sound velocity of boron, not listed in the literature, would hereby be determined to be 14×10^5 cm/sec (between Si and diamond). Measurements with C (graphite) seem to indicate that it is the maximal sound velocity which determines the threshold energy. Unfortunately, sufficient data concerning $v_{s\,max}$ from measurements in metal single crystals are not available in the literature for the introduction of this additional correction.

The significance of the sound velocity here, although not yet fully understood, is obviously to introduce the elastic constants of the material, which determine what part of the transferred energy with the momentum directed to the inside of the material arrives at the surface with a momentum reversed in direction. This part has to be at least equal to the binding energy of a surface atom before sputtering ensues.

A more detailed paper will be submitted later.

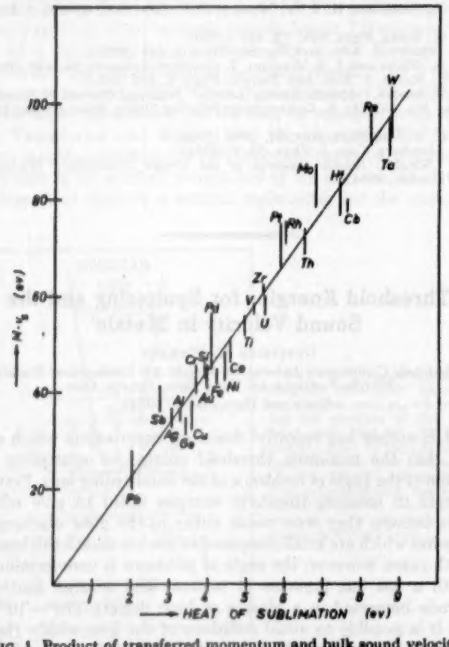

FIG. 1. Product of transferred momentum and bulk sound velocity *versus* heat of sublimation.

[1] G. Wehner, J. Appl. Phys. (to be published).
[2] K. H. Kingdon and I. Langmuir, Phys. Rev. **22**, 148 (1923).
[3] Research Staff of General Electric Company, Ltd., London, Phil. Mag. **45**, 98 (1923).
[4] E. S. Lamar and K. T. Compton, Science **80**, 541 (1934).
[5] G. Wehner and G. Medicus, J. Appl. Phys. (to be published).
[6] R. C. Bradley, paper presented at 1953 Conference on Gaseous Electronics, Washington, D. C. (unpublished).

Infrared Absorption of NiO

R. W. JOHNSTON AND D. C. CRONEMEYER
Electronics Laboratory, General Electric Company, Syracuse, New York
(Received December 10, 1953)

THE Verneuil method[1] (or flame-fusion method) of growing crystals is well known and has been utilized for some time in producing crystals of sapphire, rutile, etc. Recently this method has been used at this laboratory to produce single crystals of NiO. These crystals are dark green to black in color and are easily cleaved.[2] Their crystal structure is face-centered cubic with a lattice spacing of 4.17A which agrees with previously published data.[3] The melting point, as determined during the actual growth, is slightly above 1900°C.

The over-all resistivity at room temperature of these crystals, as measured by a megohm bridge, is 7.0×10^6 ohm cm, this value being somewhat less than the 10^9 ohm cm usually reported in the literature for NiO in the polycrystalline form.[3]

A $1\times 5\times 10$ mm plate was cleaved from the NiO single-crystal boule; infrared transmission in the wavelength range of 1μ to 15μ was observed with this specimen using a Perkin Elmer Model-112

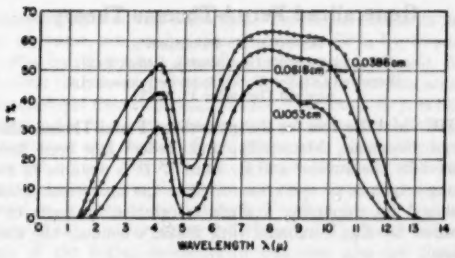

FIG. 1. Transmission spectrum of NiO from 1μ to 14μ for sample thickness 0.1053 cm, 0.0618 cm, and 0.0386 cm.

double-pass spectrophotometer. Since this finding pointed towards some interesting information concerning the semiconducting properties of NiO, a more careful study was begun. Because refractive index information is necessary to convert transmission to absorption coefficient, and few refractive index data are available,[4] the following technique was adopted to obtain both refractive index and absorption coefficient data from the transmission spectrum.

The transmission T of a plane parallel plate of thickness x can be expressed by the equation[5]

$$T=\frac{(1-R)^2e^{-\alpha x}}{1-R^2e^{-2\alpha x}}, \qquad (1)$$

where α is the absorption coefficient and R is the reflection coefficient defined as $R=[(n-1)/(n+1)]^2$, with n as the refractive index. The n and α values could be derived from an algebraic simultaneous solution of the equations for two different thicknesses; however, in this case, a graphical solution was used which combined the data on specimens of three different thicknesses. The graphical solution was obtained by plotting from Eq. (1), T *versus* αx with $n(R)$ as a parameter. Trial values of n then permitted the determination of α for known x and n; α and n values which were independent of thickness x were thereby chosen.

The 1×5×10 mm cleaved plate was ground and polished optically flat and parallel and the transmission spectrum obtained. This same plate was then ground and repolished for two thinner specimens. The transmission spectra (Fig. 1) for the three thicknesses (0.1053 cm; 0.0618 cm; 0.0368 cm) are replotted as absorption coefficient *versus* photon energy in Fig. 2, utilizing the graphical solution outlined above. Refractive index data obtained from the solution are also included and agree fairly well with those published.[4]

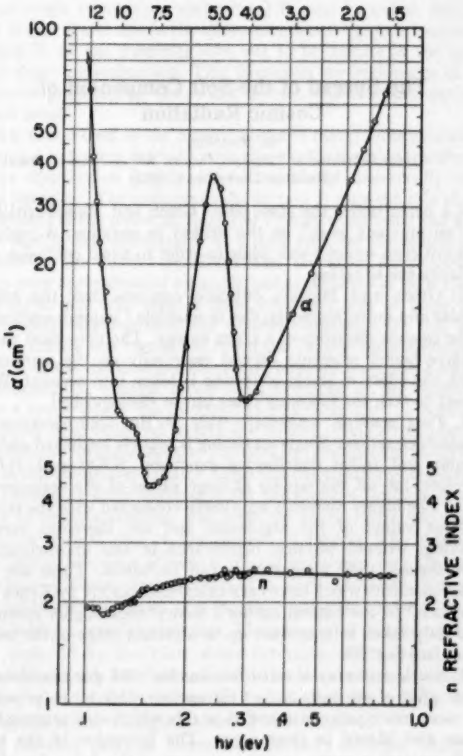

FIG. 2. Absorption coefficient α (cm⁻¹) and refractive index n of NiO *versus* photon energy in ev.

The branch of the curve for energy values greater than 0.3 ev may be the tail of the fundamental absorption which is to be expected at about 2 ev according to the electrical measurements of Wright and Andrews[6] on polycrystalline NiO. These authors present data indicating the existence of impurity optical activation energies between 0.3 and 0.6 ev. The 0.24-ev absorption peak may be an impurity ionization energy corresponding at least in order of magnitude to that expected above. There is also a satellite absorption peak at 0.13 ev. The increasing absorption coefficient below this peak is probably a lattice vibration absorption. The validity of this conclusion is enhanced by the suddenly decreasing refractive index at these low frequencies, a circumstance which probably would not result from impurity absorption.

We would like to thank Dr. G. G. Palmer, who supplied us with the NiO crystals, and Dr. F. G. Keihn, who made the x-ray determinations on them for us.

[1] A. Verneuil, Compt. rend. **135**, 791 (1902); Ann. chim. et phys. **3**, 20 (1904).
[2] H. P. Rooksby, Nature **152**, 304 (1943).
[3] E. J. W. Verwey, in *Semiconducting Materials* (Butterworths Scientific Publications Ltd., London, 1951), p. 155.
[4] C. J. Ksanda, Am. J. Sci. **22**, 131 (1931); A. Kundt, Sitzber. deut. Akad. Wiss. Berlin, 255–272 (1888).
[5] R. B. Barnes and M. Czerny, Phys. Rev. **38**, 338 (1931).
[6] R. W. Wright and J. P. Andrews, Proc. Phys. Soc. (London) **62**, 446 (1949).

Bulk Photoconductivity in Lead Sulfide*

D. E. SOULE AND R. J. CASHMAN
Department of Physics, Northwestern University, Evanston, Illinois
(Received December 7, 1953)

EXTENSIVE investigations have been carried out upon photoconducting evaporated and chemical layers of PbS (for a review see Smith[1]). Sosnowski *et al.*[2] and Gibson[3] have presented models of photoconductivity in evaporated layers based on the modulation of intercrystalline potential barriers. Experimental evidence of bulk photoconductivity in PbS crystals, however, has not been published to our knowledge. We have studied this property in three cleaved synthetic PbS crystals at liquid nitrogen temperature.

The dark conductivities at room temperature for samples S_{11}, S_{12}, S_{13} were 34, 21, and 23 ohm^{-1} cm^{-1}, respectively. All electrode and probe contacts to the crystals were made by electroplating them with rhodium and then soldering the lead wires to the rhodium. All samples showed slight internal rectification.

The potential difference developed between a probe fixed at the right electrode and a probe moved along the crystal S_{12} at room temperature is shown in Fig. 1(a). Two different traversing paths are represented. Potential barriers are present within the crystal at A, B, C, and D.

At 77°K the frequency response to chopped radiation from a tungsten source was taken over the range of 20 to 9000 cps to

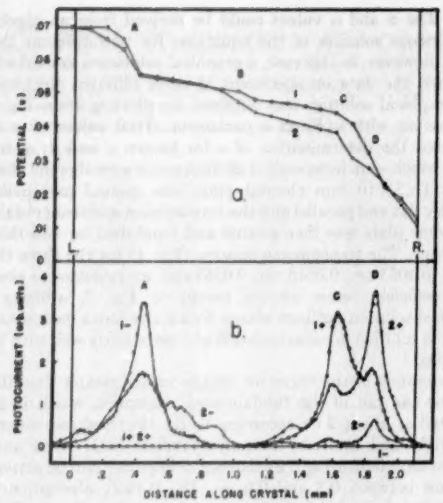

FIG. 1. (a) Potential *versus* distance along crystal at room temperature. 1 and 2 are different paths. (b) Photocurrent response at 77°K for light spot (width 75μ) scanned along crystal. Paths 1 and 2 correspond roughly to those in (a). Sign indicated is for the right electrode.

determine the possibility of a thermal contribution to the resultant current change. During the measurement the electrode-to-crystal junctions were masked. Throughout this frequency range the photoresponse remained constant to within ± 2.0 percent. An upper limit of 4 microseconds for the time constant was calculated assuming a maximum of 2.0 percent drop in amplitude at 9000 cps from that at 20 cps. All following photocurrent measurements were made with a tungsten source chopped at 90 cps with the crystal at 77°K.

The surface was then scanned with a light spot 75μ wide. A 0.54 v bias was applied in the back direction (right electrode positive) and 0.50 v in the forward direction. The resulting photocurrent is shown in Fig. 1(b) for both polarities of applied voltage and for two different traversing paths along S_{12} corresponding roughly to those followed in Fig. 1(a). No appreciable photoresponse appears to originate at the metal to semiconductor junctions of the electrodes at L and R. The photoresponse maxima located at A, C, and D correspond to the potential barriers at A, C, and D, respectively, in Fig. 1(a). For both paths where the right electrode is positive the left-hand maxima are depressed and vice versa. This behavior indicates that the barriers are asymmetrical and are modulated by the applied voltage. Thermoelectric probe measurements taken over the whole crystal surface showed it to be p type. Consequently, the carrier concentration across a barrier is probably a gradation in hole density.

The photocurrent dependence upon applied bias voltage with the total crystal illuminated showed maximum responses at 0.9 v for the right electrode positive and 0.7 v for the right electrode negative. The reason for this apparent saturation effect is not yet known.

It appears evident from these measurements that though these internal potential barriers may not necessarily be the original sites of the primary photoeffect they at least aid in rendering the photocurrent measurable.

This investigation is still in progress and a more complete report will be published at a later date.

* This work was sponsored by the U. S. Bureau of Ships, Department of the Navy, Washington, D. C.
[1] R. A. Smith, Advance in Physics **2**, 321 (1953).
[2] Sosnowski, Starkiewicz, and Simpson, Nature **159**, 818 (1947).
[3] A. F. Gibson, Proc. Phys. Soc. (London) **B64**, 603 (1951).

Generalized Fermi-Thomas Theory

MALCOLM K. BRACHMAN
Texas Instruments Incorporated, Dallas, Texas
(Received October 23, 1953; revised manuscript received December 11, 1953)

THE virial theorem for the generalized Fermi-Thomas theory of Feynman, Metropolis, and Teller[1] has been further discussed by the author[2] and by March.[3] It is possible to avoid the long sequence of operations used in the analytical proof of reference 1 by employing a single integration by parts of the expression for E_{kin} combined with Duffin's lemma,[4] the known relation

$$\partial I_\nu(\eta)/\partial\eta = \nu I_{\nu-1}(\eta)$$

and the known value of the pressure.[2]

Reference 2 treats a system of Z electrons moving in the field of a nucleus of charge Ze and infinite mass. The electrons interact with one another according to Coulomb's law and obey the Fermi-Dirac statistics. If we set the electronic charge e equal to zero so that the Coulomb interaction is omitted, we obtain the thermodynamic functions recently given by Singwi[5] for a system of particles obeying the Pauli exclusion principle but without further interactions; this corresponds to the model of liquid He^3 envisaged in reference 3. To complete the identification, we note that $R=Zk$ and $\rho=Z/v$. A general expression for the pressure is

$$p=\frac{2}{3}\frac{I_{\frac{3}{2}}(\eta)}{I_{\frac{1}{2}}(\eta)}\frac{RT}{v},$$

which reduces to the correct value $\frac{2}{3}\rho\epsilon_0$ when T tends to zero.

[1] Feynman, Metropolis, and Teller, Phys. Rev. **75**, 1561 (1949).
[2] M. K. Brachman, Phys. Rev. **84**, 1263 (1951).
[3] N. H. March, Phil. Mag. **43**, 1042 (1952); **44**, 346 (1953).
[4] R. J. Duffin, Phys. Rev. **47**, 421 (1935).
[5] K. S. Singwi, Phys. Rev. **87**, 540 (1952).

The Spread of the Soft Component of Cosmic Radiation

G. MOLIÈRE
Centro Brasileiro de Pesquisas Fisicas, Rio de Janeiro, Brazil
(Received December 8, 1953)

IN a paper under the same title,[1] Green and Messel criticized "all previous work" on the subject in question. A reply to their criticism seems worth while in order to avoid confusion and to clarify the situation.

(1) Green and Messel's criticism concerns first the higher angular and radial moments, due to multiple Coulomb scattering, of the cascade electrons of a given energy. The numerical values of these higher moments depend essentially on the manner in which the effect of single scattering is taken into account. With respect to this, the following cases can be distinguished.

A. Pure multiple scattering:—this is the approximation of Landau's equations. Single scattering is entirely neglected and the angular and radial distribution functions $f(E,\theta)$ and $f(E,r)$, therefore, fall off too rapidly at large values of the arguments θ and r. The higher moments are closely connected with the fall-off at large values of the arguments and are, therefore, strictly speaking, without physical significance in this approximation. Nevertheless, their computation can be useful. These are the higher moments which have been calculated exactly by Eyges and Fernbach.[2] In the present author's theory[3] these higher moments were duly taken into account up to a certain stage of the calculation (see Sec. B).

B. Single scattering is taken into account with due consideration of the effect of the finite size of the nuclei:—this is, in principle, the most exact procedure and it is this which was proposed by Green and Messel in their paper. The limitation of the large single scattering angles as a consequence of the finite size of the nucleus, may be taken into account (according to E. J. Williams)

by introducing a cut-off angle θ_{max}. The higher moments in this case, of course, are greater than in case A: ($\langle\theta^4\rangle_{Av}$ by 18 percent and $\langle\theta^6\rangle_{Av}$ by 45 percent, according to Green and Messel). But it is obvious that the higher moments in this case are very sensitive to the choice of the cut-off θ_{max}. On the other hand, E. J. Williams' expression for θ_{max} merely represents an estimation of the order of magnitude and the cut-off procedure as a whole, of course, is somewhat rough. (By a more rigorous treatment the largest scattering angles would not be entirely suppressed but only reduced in frequency by a factor Z^{-1} since in this region the protons of the nucleus scatter individually.) The exact numerical values of the higher moments in this case also are therefore physically meaningless. Moreover, the influence of the finite size of the nucleus is practically negligible in shower theory (see Sec. C). Finally, it may be stated that the method of calculating the distribution functions by means of the moments, as proposed by Green and Messel, seems not very suitable because a very large number of moments (strictly speaking, all of them), would be needed if one wished to obtain reasonable accuracy in the interesting region of small and medium arguments.[4]

C. Single scattering is taken into account neglecting the influence of the finite size of the nuclei:—in shower theory single scattering is altogether of little importance. This has been pointed out by Nishimura and Kamata[5] who have shown that the main contribution to strongly deflected electrons (i.e., those found at large values of θ and r), is due to multiple scattering of electrons slowed down by ionization loss rather than to single scattering. Large single scattering angles, in general, are rare events. The modification of the frequency of very large single scattering angles by the finite size of the nucleus, therefore, is of still less importance. [As an illustration, it may be estimated that the influence of the finite size of the nucleus on the distribution function $f(E,\theta)$ is not appreciable up to angles of about seven times the root-mean-square angle of multiple scattering.] It may be noted, further, that in case C and also in the above-mentioned rigorous treatment of case B, all the moments turn out to be infinite in the usual small-angle approximation. This illustrates the irrelevance of the moments proposed by Green and Messel which depend entirely on the cutoff.

Case C was used in the present author's theory,[3] the procedure being the following. Starting with case A, the Fourier-transforms of the distribution functions were calculated numerically with great accuracy. The moments valid in case A play the rôle of the coefficients of the power series of the Fourier-transforms and were duly used in this calculation. As a next step, for convenience in performing the Fourier-transformation, the exact Fourier-transforms were approximated by analytical expressions in such a way that stress was laid upon a good representation at large and intermediate arguments of the Fourier-transforms. In this way great accuracy was reached at small and intermediate arguments θ and r of the distribution functions resulting from the Fourier-transformation, whereas errors were admitted in the region of large θ and r where the distribution functions due to multiple scattering have fallen off practically to zero, these errors also influencing the higher moments. The criticism expressed in the literature in this connection (Blatt,[6] Eyges[7]) is not significant because in this domain of large arguments the distribution function is due solely to single scattering. The influence of the latter was determined in a final step of the theory, as follows. The resulting distribution functions of case A were decomposed into Gaussian functions ("Gauss transformation"), each Gaussian function associated with electrons of a certain "energetic history," characterized by a certain parameter. These Gaussian functions, then, were replaced by the more exact functions which contain the "single-scattering tail." Finally, by the inverse Gauss transformation, the distribution functions of shower theory duly containing the effect of single scattering were obtained.

(2) Another point of Green and Messel's criticism concerns the neglect of the variation of the atmospheric density in all previous theories. The influence of this variation of density is closely connected with the path length which is needed for equilibrium in the distribution in θ and r. As to this question, Green and Messel have given an example. They have calculated $\langle r^2\rangle_{Av}$ as a function of depth in a homogeneous layer of matter in the case of a primary (integral) power spectrum of exponent 1.5. From the figures given by them the conclusion may be drawn that in the case of a power 1.5 a path length of about 12 to 14 radiation lengths is needed for equilibrium in the radial distribution. Roughly, this means that the radial deviations of the electrons in the depth of observation have their origin mainly at a depth smaller by 6 to 7 radiation lengths. For showers observed at sea level, therefore, the inhomogeneity of the atmosphere can be roughly accounted for by using a value of the radiation length which is greater by 25 to 30 percent. For a power law with exponent 1, i.e., for air showers near the maximum, the situation is still better. It may be estimated that in this case 6 to 8 radiation lengths are sufficient to reach equilibrium, which means that a layer higher by 3 to 4 radiation lengths is responsible for the radial distribution. The radiation length, therefore, has to be increased by 15 to 20 percent for observation at sea level and by 30 to 40 percent for 5000 m.

A more exact computation of this correction, *viz.*, an improved theory taking into account the variation of density, would be useful. But the assertion of Green and Messel that the neglect of the effect of density variation would introduce errors as large as 5000 percent (!) cannot be understood. Presumably this large error would concern the higher moments and so is of no interest.

(3) In a further point in their paper, Green and Messel make the criticism that previous authors either consider only the maximum of showers or integrate over all depths. However, both the maximum and the integration over all depths are suitable starting points. Besides, Green and Messel seem to overlook the fact that in the meantime, Nishimura and Kamata[5] extended the theory to a shower age of 1.5.

The points 4 and 5 enumerated by Green and Messel need no commentary. The further criticism expressed by Green and Messel in the text of their paper, claiming that ionization loss has not been duly treated by previous authors, is also made obsolete by the work of Nishimura and Kamata, which seems to be unknown to them.

Finally it may be noted that the lateral spread of the electronic component of large air showers is only slightly modified by the contribution of the nucleon-meson component. This contribution is practically restricted to small distances from the center and consists in the formation of plural cores at separations of the order of some tens of centimeters from each other.[8]

[1] H. S. Green and H. Messel, Phys. Rev. **88**, 331 (1952). We are thankful to Professor W. Heisenberg for sending us a prepublication print of the paper.
[2] L. Eyges and S. Fernbach, Phys. Rev. **82**, 23 (1951).
[3] G. Molière, in *Cosmic Radiation*, edited by W. Heisenberg (Dover Publications, New York, 1946). The theory of the spread of large air showers will be presented in detail in the second edition of this book (Springer, Berlin, 1953).
[4] In their application of this method to the nucleonic cascade, Green and Messel [Phys. Rev. **87**, 738 (1952)] used an arbitrary extrapolation for the asymptotic behavior of the higher moments. As stated above, just this asymptotic behavior determines the shape of the distribution function.
[5] J. Nishimura and K. Kamata, Progr. Theoret. Phys. **6**, 262, 628 (1951); **7**, 185 (1952).
[6] J. M. Blatt, Phys. Rev. **75**, 1584 (1949).
[7] L. Eyges, quoted by Blatt, reference 6. See also Nordheim, Osborne, and Blatt, Echo-Lake Report, 1949 (unpublished).
[8] See H. Messel and H. S. Green, Phys. Rev. **87**, 738 (1952).

Total Interaction Cross Section of Pions with Protons and Deuterons at 1.0 Bev*

R. L. Cool, L. Madansky,† and O. Piccioni
Brookhaven National Laboratory, Upton, New York
(Received December 16, 1953)

THE total cross sections of negative pions with hydrogen and the deuterium-hydrogen difference have been measured at an average pion kinetic energy of 1.0 Bev. The apparatus described

TABLE I. The total interaction cross section of 1.0-Bev negative pions with H and (D–H). Measurements are listed for absorbers of various hydrogen or deuterium content and for several rms values θ_{rms} of the half-angle subtended by counter No. 5 at the absorber.

θ_{rms}	Absorber g cm^{-2} of H	$\sigma(\pi^-,p)$ mb	Absorber g cm^{-2} of D	$\sigma(\pi^-,d-p)$ mb
7.2°	8.27	39 ±3	13.34	17 ±3
5.4°	3.90	42 ±4.5	...	...
3.2°	12.17	49 ±3	...	...
2.7°	...	...	13.34	21.2±2.6
2.5°	3.90	47.5±5	...	...
2.2°	12.17	46 ±3.5	...	...

in a previous letter[1] was placed in the 1.1-Bev negative pion beam which, like the 1.55-Bev beam, is deflected by the Cosmotron magnet. The method for measuring the cross sections was the same as that described before.

In this beam the muon contamination was larger than at 1.55 Bev. It was determined by two arrangements; both make use of the strong-pion and weak-muon nuclear interaction so that, after passing through thick absorbers, the beam contains most of the initial muons and comparatively few pions. The counting rate beyond the absorber has to be corrected for the pions which remain and for the loss of muons by multiple Coulomb scattering in the absorber. In the first arrangement, an absorption curve in Al was obtained up to 307 g cm^{-2}, by placing the Al between counters 4 and 5. The correction for the loss of muons by scattering was calculated in this case to be 17 percent. In the second arrangement, counters 4 and 5 were arranged as for the CH_2-C measurements with the 73 g cm^{-2} of C in place. In addition, 372 g cm^{-2} of Fe was placed behind counter 5. A single large counter was placed behind the Fe and was used in several successive positions to integrate the remaining beam over an effective diameter of 14 in. In this arrangement, the loss of muons by scattering was negligible, but a somewhat greater uncertainty than that of the first method was involved in placing safe limits on the remaining pions. The result of the first method is $I_\mu/I_0 = 0.110\pm0.025$ while the second gives $I_\mu/I_0 = 0.117\pm0.012$.

Two thicknesses of absorber have been used in the CH_2-C measurements (12.17 and 3.9 g cm^{-2} of H). The thick absorber introduces less statistical uncertainty and an effectively larger muon correction than the thin absorber. The muon contamination produces a correction in $\sigma(\pi^-,p)$ of 8 mb for the thin absorber and 12 mb for the thick. The results are in agreement, and quoted errors include the uncertainty in evaluating the muon contamination. The electron contamination has been measured as at 1.5 Bev, and found to be less than 1 percent.

Several geometries have been used to check that the cross-section values obtained are equal to the total cross section; that is, that the fraction of events in which secondaries enter our last counter is, indeed, very small with the geometry most extensively used. Taking account of the differences in solid angle, the data reported in Table I show that $\sigma(\pi^-,p) = 48\pm4$ mb at 1.0 Bev, which is distinctly larger than the value of 27.5±6 mb obtained by Lindenbaum and Yuan[2] at 450 Mev and, with reasonable certainty, exceeds our value of 34±3.5 at 1.5 Bev.[1] The value of Shapiro, Leavitt, and Chen[3] of $\sigma(\pi^-,p) = 47\pm5$ mb at 850 Mev fits quite smoothly on a curve showing a broad maximum at roughly 1 Bev.

Another interesting feature shown by our data is the ratio between $\sigma(\pi^-,p)$ and $\sigma(\pi^-,d-p)$. $\sigma(\pi^-,d-p) = 21\pm3$ mb and should be equal to $\sigma(\pi^+,p)$ if the principle of charge symmetry and the additivity of cross sections in deuterium were rigorously correct. While actually some difference can be expected, principally because of the second assumption, the qualitative fact that $\sigma(\pi^-,p)$ is considerably larger than $\sigma(\pi^+,p)$ at 1 Bev can hardly be doubted. Preliminary measurements with positive pions at 800 Mev support our present conclusion.

From $\sigma(\pi^-,p)$ and $\sigma(\pi^+,p)$ one can derive the value of the cross section for the pure state having total isotopic spin of one-half: $\sigma(\pi^-,p)_{I=\frac{1}{2}} = \frac{3}{2}\sigma(\pi^-,p) - \frac{1}{2}\sigma(\pi^+,p)$. It is 62±7 mb at 1 Bev and about one-half of this value at both 0.45 Bev and 1.5 Bev. This state seems, therefore, to have a very marked maximum at about 1 Bev.

We acknowledge many stimulating conversations which we have had with R. Serber, C. N. Yang, W. Rarita, and H. S. Snyder. C. F. Woolley, Jr., has most valuably assisted us throughout these experiments.

* Research performed at Brookhaven National Laboratory under the auspices of the U. S. Atomic Energy Commission.
† On leave from The Johns Hopkins University, Baltimore, Maryland.
[1] Cool, Madansky, and Piccioni, Phys. Rev. 93, 249 (1954); Bull. Am. Phys. Soc. 28, No. 6, 14 (1953).
[2] S. Lindenbaum and L. Yuan, Phys. Rev. 92, 1578 (1953).
[3] Shapiro, Leavitt, and Chen, Phys. Rev. 92, 1073 (1953).

Transient Nuclear Induction Signals Associated with Pure Quadrupole Interactions*

M. BLOOM AND R. E. NORBERG
Department of Physics, University of Illinois, Urbana, Illinois
(Received December 17, 1953)

WE have observed transient "pure quadrupole" induction signals corresponding to the "Bloch decays" and echoes found in pulsed nuclear magnetic resonance experiments.[1] The induction signals arise from oscillating components of magnetization established along the axis of the applied rf magnetic field H_1. A quantum-mechanical calculation predicted that these transient components should occur even though, at equilibrium, the electric interaction $Q\cdot\nabla E$ produces no macroscopic magnetization. The presence of the induction decays had been suggested by Dean[2] to explain the anomalous signal to noise behavior of his quenched oscillator in an earlier investigation of pure quadrupole spectra. We have found the predicted induction signals in $NaClO_3$ single crystals and powders, following the application of rf pulses at the Cl^{35} pure quadrupole resonance frequency (29.920 Mc/sec at room temperature). We observe the effects of nuclear Zeeman splittings upon the induction signals by orienting the single crystals within a small magnetic field.

To develop a theoretical expression for the induction signals, we consider a Hamiltonian of the form $\mathcal{H} = Q\cdot\nabla E + \mu\cdot(H_0 + H_1\cos\omega t)$, where H_0 and H_1 are the amplitudes respectively of the applied dc and rf magnetic fields. We expand the wave function of the Cl nuclei (spin $\frac{3}{2}$) in terms of the eigenfunctions of the electric quadrupole term, $\psi = \Sigma C_m \exp(-iE_m t/\hbar)\psi_m$. The induction signals observed arise from the components along H_1 of the bulk magnetization $M_{x(y)}$, which is created transverse to the symmetry axis of ∇E. $M_{x(y)} \propto \bar{I}_{x(y)} = (\psi^*/I_{x(y)}/\psi)$, where the $I_{x(y)}$ are the transverse components of the nuclear angular momentum operator.

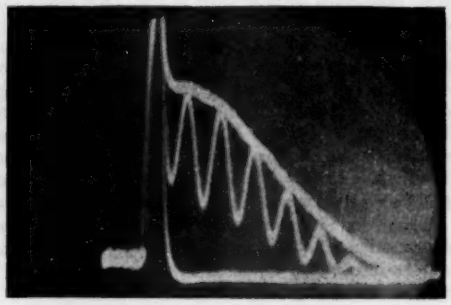

FIG. 1. Induction decay in a single crystal of $NaClO_3$. The sweep is 800 μsec long. The beat structure appears in the presence of a Zeeman field of 12 gauss applied, parallel to H_1, along (0,0,1).

For spin $\frac{3}{2}$, $I_{x(y)} \propto (C_{\frac{1}{2}}^* C_{\frac{1}{2}}(\pm) C_{-\frac{3}{2}}^* C_{-\frac{1}{2}}) \exp(i\omega t) + \text{complex conjugate}$, where $\omega = (E_{\frac{1}{2}} - E_{\frac{1}{2}})/\hbar = (E_{-\frac{1}{2}} - E_{-\frac{3}{2}})/\hbar$.

We solve the time-dependent Schroedinger equation in two intervals: during the pulse, in the presence of the rf field H_1, and following the pulse, where H_1 is zero. The effect of H_1 is then to induce only the transitions $\frac{3}{2} \rightleftharpoons \frac{1}{2}$ and $-\frac{3}{2} \rightleftharpoons -\frac{1}{2}$. Considering the Boltzmann surplus and assuming the system to be initially in the $\pm\frac{3}{2}$ state, the result (for $H_0 = 0$) is a time-independent induction signal following the pulse. We assume that the effect of the existence over the sample of differing ∇E (due to crystalline imperfections) or internal magnetic fields (due to dipolar interactions) is to dephase the precessing microscopic magnetization vectors and to cause the induction signals to decay in a time T_2. Figure 1 is a multiple exposure of decay signals in a $NaClO_3$ single crystal taken with and without an H_0. The decay envelope is Gaussian with T_2 equal to 425 μsec. A calculated T_2 of this order of magnitude results from a computation of the magnetic dipolar interaction of a Cl nucleus with the nuclear moments located within one lattice parameter.

To compute the Zeeman effects, we consider an H_0 applied at an angle θ_0 with respect to ∇E and an H_1 applied for a time t_w at an angle θ_1. The voltage induced in the coil for $t > t_w$ is then given by:

$$V(t) \propto \sin\theta_1 \sin(\sqrt{3}\Omega_1 t_w \sin\theta_1)\left[\frac{f-1}{f}\cos\left\{\frac{\Omega_0(3+f)\cos\theta_0}{2}t\right\} + \frac{f+1}{f}\cos\left\{\frac{\Omega_0(3-f)\cos\theta_0}{2}t\right\}\right], \quad (1)$$

where $\Omega_0 = \gamma H_0$, $\Omega_1 = \gamma H_1$, and $f = (1+4\tan^2\theta_0)^{\frac{1}{2}}$. The appearance, in general, of the two frequencies in square brackets in (1) arises from the mixing (in the presence of an H_0) of the $\frac{3}{2}$ and $-\frac{3}{2}m$ states, which splits the steady state resonance symmetrically into two pairs of lines.[2] Further calculations predict a spin-echo signal at 2τ (following the application of a second rf pulse at time τ). We have observed echoes and stimulated echoes in both the powders and single crystals. Hahn and Herzog (see following letter) report the behavior of the echoes as a function of H_0 and of crystal orientation.

In $NaClO_3$, ∇E lies along the symmetry axis of the molecule. The four molecules in a unit cell of the crystal are oriented with their symmetry axes along the body diagonals of the unit cube. [Direction cosines $(1/\sqrt{3}, 1/\sqrt{3}, 1/\sqrt{3}$; etc.)] The beat structure in Fig. 1 is that observed on the decay in a single crystal with H_1 and H_0 both applied along (0,0,1). In this orientation $\cos\theta_0 = 1/\sqrt{3}$ and $f = 3$ for each of the four molecules in the unit cell. A single-beat frequency $\sqrt{3}\gamma H_0/2\pi$ is then predicted by Eq. (1) and is found to agree with that observed. Figure 2 shows the more complex pattern observed with H_1 along (0,0,1) and H_0 along $(1/\sqrt{2},1/\sqrt{2},0)$. The voltage predicted by (1) is here proportional to $2\cos(\Omega_0 t) + 1.6\cos(0.53\Omega_0 t) + 0.4\cos(1.9\Omega_0 t)$, which agrees with the pattern of the observed decay. The echo exhibits a structure similar to that on the decay.

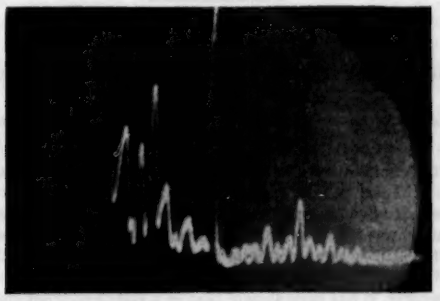

FIG. 2. Induction decay and echo found with H_1 along (0,0,1) and an H_0 of 12 gauss along $(1/\sqrt{2},1/\sqrt{2},0)$. The separation of the pulses is 900 μsec.

The single crystals of $NaClO_3$ were loaned by the Bell Telephone Laboratories. We are grateful to E. L. Hahn and B. Herzog for discussions of their results and have also benefited from conversations with C. P. Slichter and D. McCall. Much of our rf equipment was designed by H. W. Knoebel and L. S. Kypta.

* Supported in part by the U. S. Office of Naval Research and (M.B.) by a Province of Quebec Post Graduate Scholarship.

[1] E. L. Hahn, Phys. Rev. 80, 580 (1950).

[2] C. Dean, thesis, Harvard University (unpublished); Phys. Rev. 86, 607 (1952).

Anisotropic Relaxation of Quadrupole Spin Echoes

E. L. HAHN AND B. HERZOG
Watson Scientific Laboratory, International Business Machines Corporation, Columbia University, New York, New York

(Received December 17, 1953)

BY the pulsed nuclear induction method[1] we have observed the free Larmor precession of Cl^{35} and Cl^{37} nuclear moments, due only to the pure crystalline electric field gradient in single and powdered crystals of $NaClO_3$. When a small constant magnetic field H_0 is applied to the single crystal, the echo relaxation time due to spin-spin coupling is modified by the variation of the Zeeman splitting as the magnitude and direction of H_0 normal to the cubic axis of a $NaClO_3$ single crystal is varied. We refer the reader to the preceding letter by Bloom and Norberg which discusses their independent observations of the free quadrupole precession and theory of the Zeeman splitting.

The formation of nuclear signals following two rf pulses, as shown in Fig. 1, can be explained by the analogous mechanism of spin echo formation in large magnetic fields.[1] The chlorine quadrupole moment Q, with spin $I = \frac{3}{2}$, is aligned by an electric field gradient q which is assumed to be axially symmetric about the molecular bond (z axis) joining Na to Cl. The single quadrupole resonance transition frequency $\omega = eqQ/2\hbar$ is replaced in general by four separate resonance frequencies[2] as the degeneracy of the $m = \pm\frac{1}{2}$ and $m = \pm\frac{3}{2}$ states is removed by H_0. In the unit cell there are four chlorine nuclei with their z axes of quantization oriented along the body diagonals of the sub-cubic cells. There are two nonequivalent directions of Na-Cl axes with respect to H_0, and a pair of chlorine nuclei is assigned to each of these directions denoted by $+$ and $-$. Using a quantum-mechanical treatment applied in an earlier paper,[3] we obtain the solution for free precession in agreement with that given by Bloom and Norberg. The spin echo signal, described by a similar solution, appears symmetric about the time $t = 2\tau$, where τ is the separation between pulses. The observed signal is given by $V = V_+ + V_-$, where

$$V_\pm \propto \sin^3(\sqrt{3}\omega_1 t_w \sin\theta_\pm)\cos(\sqrt{3}\omega_1 t_w \sin\theta_\pm) \times\left\{\left(\frac{\beta_\pm - 1}{\beta_\pm}\right)\cos[(\omega_0\cos\theta_\pm)(3+\beta_\pm)(t-2\tau)/2] + \left(\frac{\beta_\pm + 1}{\beta_\pm}\right)\cos[(\omega_0\cos\theta_\pm)(3-\beta_\pm)(t-2\tau)/2]\right\} \times\exp\left\{-[(t-2\tau)^2/T_2'^2 + t^2/(T_2')^2(H_0,\beta_\pm)]\right\}.$$

θ is the angle between H_0 and the molecular axis, $\omega_0 = \gamma H_0$, $\omega_1 = \gamma H_1$, $\beta_\pm = (1+4\tan^2\theta_\pm)^{\frac{1}{2}}$, γ is the gyromagnetic ratio, and H_1 is the rf field. In terms of the angle φ which H_0 makes with respect to the 001 direction, $\cos\theta_\pm = \sqrt{\frac{2}{3}}\cos(\varphi \pm \pi/4)$ and $\sin\theta_\pm = [1 - \frac{2}{3}\cos^2(\varphi \pm \pi/4)]^{\frac{1}{2}}$. We infer from our observations that T_2' for each of the $+$ and $-$ groups is nearly the same. The total width of the echo at half-maximum is given by T_2 seconds (0.5 millisecond for Cl^{35}), which is equivalent to a static local magnetic dipole field inhomogeneity of $\Delta H \approx 2.6$ gauss for an assumed Gaussian distribution. For each setting of τ, with the spins initially at thermal equilibrium, the maximum of the echo amplitude is observed to be proportional to $\exp[-(2\tau)^2/T_2'^2(H_0,\varphi)]$

which describes the shape of the envelope of the echo maxima. The time constant T_2' is observed to be a function of φ and H_0 (see the polar plot in Fig. 2).[4] It appears that the Zeeman splitting modifies the extent to which time-varying local fields and spin-spin flipping are effective in destroying the phase coherence necessary for echo formation. The thermal relaxation times T_1 ($\sim$35 milliseconds) for both chlorine isotopes are independent of H_0 and play no role in the anisotropy of relaxation. A polar plot similar to that in Fig. 2 is obtained for Cl^{37}. Within experimental error, it appears that the T_2' values may be larger by a factor $1.3\sim\gamma Cl^{35}/\gamma Cl^{37}$ for large values of H_0. Except for the difference in magnetic moments, this is a rough indication that the relaxation due to the fluctuating local field distribution is approximately the same for both chlorine isotopes in spite of the difference in their abundance. As the overlap (due mainly to T_2) among the four quantum levels diminishes with increasing Zeeman splitting (a similar situation occurs for the sodium nuclei), there is less chance that a spin-spin flip with an accompanying change in dipole field will take place between like nuclear neighbors. T_2' has a particularly sensitive dependence on H_0, (a) when $1/T_2 \sim\gamma H_0$, and (b) when any of the possible resonance transitions cross or coincide as φ is varied. There are eight possible simultaneous resonance frequencies. Four are given by: $\omega(\pm) = eqQ/(2\hbar)+F$ and $\omega'(\pm)=eqQ/(2\hbar)-F$, where $F=(\gamma H_0/\sqrt{2}) \times\{\sqrt{3}\cos(\varphi-\pi/4)\pm[2-\cos^2(\varphi-\pi/4)]^{\frac{1}{2}}\}$. Another set of four frequencies is obtained by substituting $+\pi/4$ for $-\pi/4$ in F. When $\varphi=0°$, the eight resonances coalesce to three and the probability for coupling is a maximum, giving the shortest T_2' for a given H_0. In the region $0°<\varphi<45°$, T_2' becomes the largest because eight separate resonance transitions exist. At $\varphi=45°$ there are six resonances and a decrease in T_2' takes place. The plot repeats these conditions periodically with increasing φ. The round lobes arise from the effect of static line width or broadening of each of the Zeeman levels. At large H_0, where $\gamma H_0>1/T_2$, the magnitude of T_2' approaches a constant value.

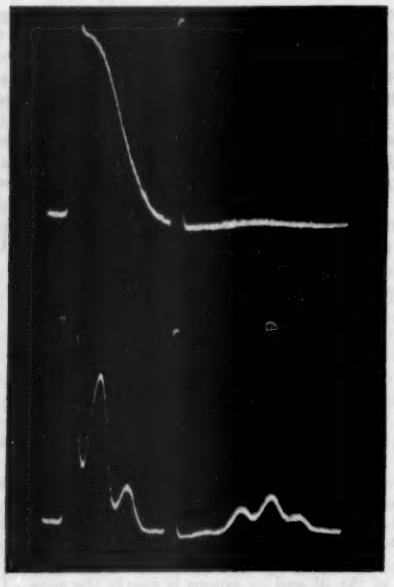

FIG. 1. Oscillographic display of free quadrupole precession of Cl^{35} in a single $NaClO_3$ crystal upon application of two rf pulses at the coadition $\sqrt{3}\omega t_w=\pi/2$. The total length of each sweep is 2.4 milliseconds. The upper photograph indicates the free precession after the first pulse and an almost completely attenuated echo in the absence of a magnetic field. The lower photograph indicates an echo and tail with accompanying Zeeman beat pattern for an applied $H_0=5.3$ gauss at $\phi=0°$ with all other conditions the same as in the upper photo.

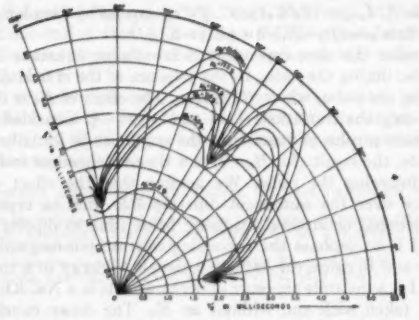

FIG. 2. T_2' for Cl^{35} in $NaClO_3$ as a function of H_0 and φ. In and near the critical regions ($\phi=0°$, 45°, and 90°), repeated measurements indicate the plotted quantitative behavior of T_2' within ±5 percent. Other regions of the plot are less accurate, to approximately ±10 percent.

We have been able to predict the general shape of the plots in Fig. 2 by considering all the possibilities for resonance coupling between a chlorine nucleus and all nearest neighbors. The net T_2' is then determined by all possible spin flips and accompanying dipole field fluctuations.[5] In a typical resonance formula, account is taken of the level broadening. The strengths of the local fields and transition probabilities are included by evaluating the squares of the matrix elements involving the Zeeman level wave functions.

One of us (ELH) wishes to acknowledge the benefit of early discussions with Dr. W. G. Proctor regarding physical features of quadrupole precession. We thank Dr. M. Bloom and Dr. R. E. Norberg for informative communications about their work. We thank Dr. T. Wang for his assistance and interest in the measurements, and Professor C. H. Townes for clarifying discussions. The $NaClO_3$ crystal in our experiment was kindly provided by Dr. A. L. Schawlow of the Bell Laboratories.

[1] E. L. Hahn, Phys. Rev. **80**, 580 (1950).
[2] B. T. Feld and W. E. Lamb, Phys. Rev. **67**, 28 (1945); C. Dean, thesis, Harvard University (unpublished).
[3] E. L. Hahn and D. E. Maxwell, Phys. Rev. **88**, 1070 (1952).
[4] The echo envelope lifetime T_2' referred to here accounts only for the incoherence of Larmor precession due to local dipole fields which fluctuate in time. It does not include static line broadening, whereas in steady state resonance measurements, "T_2" includes both of these effects. The time duration of any echo (or induction tail) would also be expected to depend upon both of these effects. However, we observe no significant change in this lifetime as T_2' changes with H_0. It appears, therefore, that as the rate of spin-spin flipping increases, for example, as $H_0\to0$, the otherwise static dipole fields of these coupled neighbors are averaged to a lower value, and the net observed lifetime of the individual signals tends to remain the the same. A rigorous analysis of this effect is being considered.
[5] The estimate of eqQ for Na would correspond to a frequency of $\lesssim1$ Mc/sec [C. H. Townes and B. P. Dailey, J. Chem. Phys. **20**, 35 (1952)]. If the condition $\gamma\hbar H_0\sim eqQ$ for the Na nuclear moment in our experiment is obeyed, the Na spin axis of quantization will no longer be along the molecular axis, and the Na dipole field at the Cl nucleus will be modified. We have not taken this possibility into account in our semi-empirical prediction of the anisotropy. Further investigation of this question is under way.

The Primeval Cosmic Abundance of Deuterium

G. BOATO*
Institute for Nuclear Studies, University of Chicago, Chicago, Illinois
(Received December 17, 1953)

NO definite answer has yet been given to the problem of the primeval cosmic abundance of deuterium. In stars deuterium has never been detected; in the sun an upper limit for the amount of deuterium was given in 1932 by Menzel[1] as 1.6×10^{-4} times the amount of hydrogen and more recently by Class[2] as 2.5×10^{-5} times the amount of hydrogen.

Moreover, it has been shown[3] that in a sufficiently hot star the deuterium is consumed very rapidly by nuclear reactions. The reaction starts in the center of the star, but convection currents

TABLE I. Isotopic composition of hydrogen in water and meteorites. Lake Michigan water, our working standard, has a D/H ratio of 1.48×10^{-4}; the values reported below are expressed in percent differences between the D/H ratio in the particular sample and in our standard. The over-all error of the measurements is ±0.5.

Ocean water	+ 4.5
Surface water range[a]	−13 to +5.5
Carbonaceous meteorites	
Orgueil, France	+29.0
Mokoia, New Zealand	+25.0
Yvuna, Tanganyika	+35.0
Murray, United States	+ 9.5
8 other samples	−13 to 0

[a] See reference 5.

may be established by the heat of reaction, with a rapid disappearance of the deuterium present in the surface layers.

There is hope that one will be able to measure the isotopic composition of hydrogen in the interstellar gases, in the cosmic ray primaries, and in the atmospheres of the Jovian planets. At present the only measurements are those on the surface of the earth: the best determinations indicate that the average isotopic composition of surface waters corresponds to approximately one part of deuterium in 6500 parts of hydrogen. This proportion was regarded by some authors as indicative of a strong enrichment of deuterium on the earth by diffusional separation processes during the formation of the planetary system. In the light of present evidence, such a process appears to be very improbable.[4]

Experiments were done by Friedman[5] and recently by Edwards[6] to determine the isotopic composition of the hydrogen contained in iron meteorites. The possibility of contamination by terrestrial water and the production of H and D by cosmic-ray stars makes these measurements somewhat uncertain.

Carbonaceous chondrites were chosen for this research not only because they contain up to 12 percent of water, but also because they may represent the original material from which the planets have been accumulated, as suggested by Urey. The carbonaceous chondrites are a rare type of meteorite of low-density and high-carbon and water content; in several of them the presence of organic compounds has been reported. All of them have been seen to fall and have been collected shortly afterwards, thus reducing the possibility of terrestrial contamination. Twenty of them are known; they are similar in appearance, physical properties, and chemical composition. Twelve of these stones were analyzed with a combustion method for the hydrogen and carbon content, and their isotopic composition was determined mass spectrometrically. The detailed results will be published elsewhere.[7] It was found that most of the water is strongly bound and does not exchange with external water also during a long period of time. In four meteorites the isotopic composition of the hydrogen was found to be definitely outside the range of the terrestrial variations, as is shown in Table I. It seems, therefore, quite impossible that, at least in four cases, the measured isotopic composition can be ascribed to water exchange or adsorption taking place on the earth after the fall of the meteorite.

One can conclude that there is no significant variation of the deuterium content of the carbonaceous chondrites in comparison with the earth. Since it appears likely that the meteorites must represent accumulation of cosmic material in a gravitational field much smaller than that of the earth and at a different distance from the sun,[8] the isotopic data indicate a rather uniform distribution of deuterium throughout the original dust cloud from which the planets condensed, with a concentration close to the terrestrial value. Thus, it appears that rather than representing a deuterium enrichment by some escape process, the discrepancy between the solar and terrestrial concentrations actually reflects the fact that the consumption of deuterium in the sun by nuclear reactions occurred after the differentiation process between planetary and solar matter, as postulated by Kuiper.[9] In the primordial solar nebula, isotopic equilibrium at low temperature was probably established between the large amount of hydrogen gas and the comparatively small amount of water. Since this equilibrium must have favored a concentration of deuterium in the water and since the hydrogen escaped completely during the process of accumulation of the planets, while some water was preserved, a D/H ratio of somewhat less than 1/6500 can be estimated for the hydrogen in the primeval cosmic material.

The author is greatly indebted to Dr. H. C. Urey for his continued and helpful interest during the course of this work.

* Present address: Istituto di Fisica dell'Università, Genova, Italy.

[1] D. H. Menzel, Publs. Astron. Soc. Pacific **44**, 41 (1932).
[2] W. I. Claas, Recherches Astronomiques de l'Observ. d'Utrecht **12**, 1 (1951).
[3] See for example E. E. Salpeter, Phys. Rev. **88**, 547 (1952).
[4] H. E. Suess, J. Geol. **57**, 600 (1949).
[5] I. Friedman, Geochim. et Cosmochim. Acta **4**, 89 (1953).
[6] G. Edwards (private communication). Work in progress in this laboratory.
[7] G. Boato, Geochim. et Cosmochim. Acta (to be published).
[8] H. C. Urey and H. Craig, Geochim. et Cosmochim. Acta **4**, 36 (1953).
[9] G. P. Kuiper, *The Atmospheres of the Earth and Planets* (University of Chicago Press, Chicago, 1952), second edition, pp. 318–19.

"Magnetic-Scanning" Method for Investigating Hyperfine Structure and Isotope Shift

S. MROZOWSKI
Department of Physics, University of Buffalo, Buffalo, New York
(Received December 14, 1953)

IN a recent letter Bitter *et al.*[1] reported some results obtained by exciting selectively hyperfine components in the resonance of mercury vapor. One of the σ Zeeman components of the line 2537A emitted axially by a Hg^{198} lamp in a magnetic field was isolated. In varying the magnetic field and observing the intensity of the excited resonance radiation, the relative positions of the hyperfine structure components were determined and found to agree with the well-known structure of the line 2527A. Unexpected results were obtained for the intensities, however. It was found that the intensity of the resonance is not a linear function of the partial pressure of mercury, but rather reaches a maximum at total vapor pressures corresponding to temperatures of about 0°C, the position of the maximum being different for different isotopes. In trying to interpret the results, the authors came to a surprising conclusion: that this effect is due to collisions of the second kind leading to the ground state or to the metastable state $^3P_0$. However, the cross section for collisions in which large amounts of energy are transformed into kinetic energy of motion is negligibly small. Thus, in pure mercury vapor or in the presence of rare gases, no quenching collisions leading to the ground state are observed. For collisions leading to the metastable state $^3P_0$, the cross sections are of the same order of magnitude as the gas-kinetic ones (molecular gases) or considerably smaller (monatomic gases).[2] It can therefore be seen immediately that the explanation proposed is untenable, since the lifetime in the excited state $^3P_1$ is 10^{-7} sec and the time between gas-kinetic collision in the saturated mercury vapor at 0°C is certainly longer than 10^{-4} sec; the difference is a factor of 10^3. Collisions with the walls become less frequent as the pressure increases and thus cannot be responsible for a decrease of the intensity of the resonance. Finally, for collisions with large change in kinetic energy, no measurable difference in behavior of different isotopes is to be expected.

It seems, therefore, that the intensity maxima are due to the method of observation adopted by these investigators and not to any real effect occurring in the mercury vapor. Unfortunately, insufficient details of the experimental arrangement are given to make possible an evaluation of their results. It can be assumed, however, that since their arrangement was basically the same as that used by Malinowski,[3] the intensity of the resonance was observed in a perpendicular direction to the illumination. In such a case, the depth of penetration of the exciting radiation into the resonance container decreasing with increase of pressure will produce a maximum of intensity for the laterally observed resonance from a definite region of the container. A simple estimate shows that

for a region located a few mm from the entrance window the maximum will, in fact, occur at around 0°C. (At such a pressure the fluorescent beam decreases in intensity by more than 25 percent in the first 5 mm of its path.[4]) In general, more strongly absorbed components should exhibit intensity maxima at lower pressures. Irrespective of the direction from which one observes the resonance, in order to draw any definite conclusions one has to make large corrections for the decay of the beam, shape of the exciting line, angle of observation, imprisonment of the radiation, distance from the observation window (reabsorption), and so forth.[5] As a result, no reasonably accurate results for the relative intensities can be expected without using a highly refined technique. It is for this reason that direct measurements of the absorption are superior to an indirect method consisting of a determination of the intensity of resonance fluorescence.

[1] Bitter, Plotkin, Richter, Teviotdale, and Young, Phys. Rev. 91, 421 (1953).
[2] A. C. G. Mitchell and M. W. Zemansky, *Resonance Radiation and Excited Atoms* (Cambridge University Press, Cambridge, 1934), see pp. 224 and 235–6.
[3] A. v. Malinowski, Ann. Physik 44, 935 (1914), Fig. 1 and pp. 951–2.
[4] Absorption coefficient data for 2537A are given, for instance, in M. W. Zemansky, Phys. Rev. 36, 219 (1930).
[5] A very good discussion of these corrections can be found in P. Kunze, Ann. Physik 85, 1013 (1928).

Internal Compton Effect in Ba^{137}

LARRY SPRUCH AND G. GOERTZEL
Physics Department, Washington Square College, New York University, New York, New York
(Received December 16, 1953)

CONTINUOUS gamma rays accompanying internal conversion were recently detected[1] for the first time. The process bears the same relationship to the Compton effect as internal pair production does to pair production, and will be referred to as the internal Compton effect. The ratio of the total number of gamma rays between 50 and 200 kev to the number of internally converted electrons was found to be in crude agreement with the ratio predicted by the only theory available, the semiclassical calculations of Wang Chang and Falkoff,[2] but the angular distribution differed markedly from the theoretical prediction. The disagreement is not surprising, for the theory neglects the recoil of the electron upon emission of the real gamma ray, an approximation which is not completely justifiable for the electron and gamma-ray momenta involved. The theory also ignores the mechanism by which the electron is ejected and is, therefore, independent of the multipole character of the virtual gamma ray and of the initial spatial distribution of the electron. Finally, it ignores the effect of the Coulomb field on the electron in the intermediate and final state.

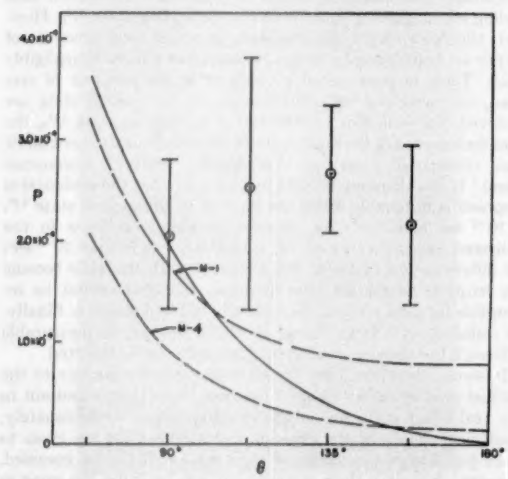

FIG. 1. Angular correlation between direction of conversion electron from Ba^{137m} and of the gamma ray of the continuous radiation. Circled points represent the experimental measurements of Brown and Stump; the solid curve is the value predicted on the basis of semiclassical theory. The dotted curves represent the values predicted for the actual case, an $M4$ transition, and, for comparison, for an $M1$ transition. P is the probability of emission of a gamma ray of the continuous radiation with an energy between 50 and 200 kev into a unit solid angle at an angle of $\theta°$ with respect to the electron.

All but the last defect are eliminated by a quantum calculation using the Born approximation. This latter approximation is still quite a serious one for Ba^{137}; in fact, the Born approximation calculation of the internal-conversion probability, which forms one of the two parts of the calculation, is only 0.4 of the true value. It would seem, though, that the ratio of continuous gamma rays to internally converted electrons should be more reliable than either calculation separately, since quite similar approximations are involved. Nevertheless, as seen from Fig. 1, the quantum calculations do not represent an improvement. The error is not due to the neglect of L shell conversion and it is highly unlikely that it is due to the neglect of $E5$ conversion. The source of the error must then be the neglect of the Coulomb field. It should be noted that in the experimental results the beta-decay bremsstrahlung background was subtracted off on the basis of a calculation which also ignored the effect of the Coulomb field.

The quantum calculations, which should be valid for small charge and large energy, have been performed for an arbitrary magnetic multipole. It is found that the ratio of continuous gamma rays to internally converted electrons is independent of the nuclear matrix element and *decreases* as the charge or the multipole increases. The transition rate for continuous gammas, however, increases as Z increases. The details of these calculations will be submitted for publication shortly.

[1] H. B. Brown and R. Stump, Phys. Rev. 90, 1061 (1953).
[2] C. S. Wang Chang and D. L. Falkoff, Phys. Rev. 76, 365 (1949).

Kinematic Criterion for Meson Production in Fundamental Particle Collisions*

R. M. STERNHEIMER
Brookhaven National Laboratory, Upton, New York
(Received December 10, 1953)

WHEN one or several mesons are made in a nucleon-nucleon or pion-nucleon collision at cosmotron energies,[1] the angle of recoil of the nucleons in the laboratory system cannot exceed a maximum value $\bar{\theta}_m$ which depends on the energy of the incident nucleon or pion and on the number of mesons produced. As an example, $\bar{\theta}_m$ is 68° for a collision of a 2.2-Bev neutron with a proton in which one pion is made. This result can be used to establish that a particle which goes off at an angle greater than $\bar{\theta}_m$ in an inelastic n-p collision cannot be a nucleon and must, therefore, be a pion (or a heavy meson). Such a criterion is useful in the analysis of cloud-chamber pictures.

In order to obtain $\bar{\theta}_m$, the maximum possible velocity of a nucleon in the center-of-mass system (c.m.s.) must be calculated. In order that the nucleon have maximum velocity, it is necessary that all of the other particles move in a direction opposite to the nucleon. The masses, momenta, velocities, and total energies of the particles in the c.m.s. will be denoted by m_i, p_i, v_i, and E_i, respectively; the subscript $i=1$ pertains to the nucleon considered; the other particles are labeled by $i=2, \cdots k$. In view of conservation of energy and momentum, v_1 is given by

$$v_1 = c^2 \sum_{i=2}^{k} p_i / (E - \sum_{i=2}^{k} E_i), \qquad (1)$$

where $E = \sum_{i=1}^{k} E_i$ is the total energy in the c.m.s. v_1 is to be

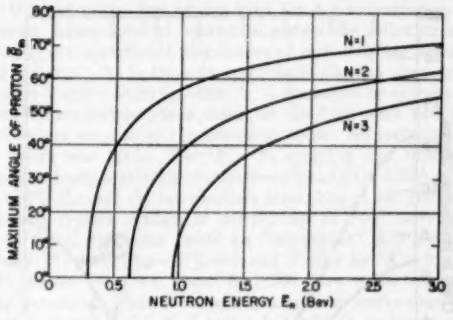

FIG. 1. Maximum angle $\bar{\theta}_m$ of recoil proton in n-p collision with production of N pions as a function of kinetic energy $\bar{E}_n$ of incident neutron in laboratory system.

maximized subject to the condition that

$$\sum_{i=1}^{k} E_i = \text{constant}.$$

This problem is equivalent to that of finding the extremum of

$$K = v_1 + \lambda \sum_{i=1}^{k} E_i, \tag{2}$$

where λ is a Lagrangian multiplier. K can be written

$$K = c^2 \sum_{i=2}^{k} p_i/(E - \sum_{i=2}^{k} E_i) + \lambda c\{[m_1^2c^2 + (\sum_{i=2}^{k} p_i)^2]^{\frac{1}{2}} + \sum_{i=2}^{k} (m_i^2c^2 + p_i^2)^{\frac{1}{2}}\}. \tag{3}$$

The extremum of K with respect to variations of $p_2, p_3, \cdots p_k$ is obtained from the conditions

$$\partial K/\partial p_j = 0. \quad (j = 2, 3, \cdots k) \tag{4}$$

In view of $\partial E_i/\partial p_j = v_j$, Eqs. (4) become

$$\frac{\partial K}{\partial p_j} = c^2/(E - \sum_{i=1}^{k} E_i) + c^2 \sum_{i=2}^{k} p_i v_j/(E - \sum_{i=1}^{k} E_i)^2 + \lambda[c^2 \sum_{i=2}^{k} p_i/(E - \sum_{i=1}^{k} E_i) + v_j] = 0. \quad (j = 2, 3, \cdots k) \tag{5}$$

In order that the $k-1$ equations (5) for λ be simultaneously satisfied, these equations must be identical, giving

$$v_2 = v_3 = \cdots = v_k. \tag{6}$$

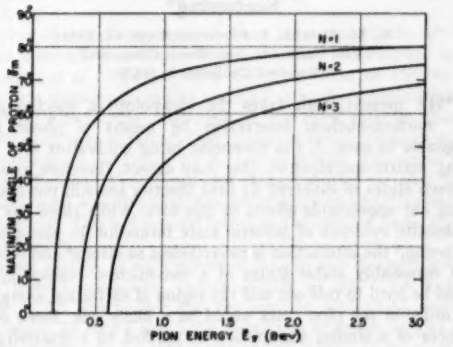

FIG. 2. Maximum angle $\bar{\theta}_m$ of recoil proton in pion-nucleon collision with production of N pions as a function of kinetic energy $\bar{E}_\pi$ of incident pion in laboratory system.

This result implies that particles 2, 3, $\cdots k$ move like a single particle of mass

$$m' = \sum_{i=2}^{k} m_i.$$

The momentum of m' is p_1, so that

$$(c^2p_1^2 + m_1^2c^4)^{\frac{1}{2}} + [c^2p_1^2 + (\sum_{i=2}^{k} m_i)^2c^4]^{\frac{1}{2}} = E. \tag{7}$$

Equation (7) can be solved for p_1, and hence for v_1, with the result

$$v_1 = c\left(\frac{A}{4E^2m_1^2 + A}\right)^{\frac{1}{2}}, \tag{8}$$

where

$$A = [(E + \sum_{i=2}^{k} m_ic^2)^2 - m_1^2c^4][(E - \sum_{i=2}^{k} m_ic^2)^2 - m_1^2c^4]. \tag{9}$$

The angle $\bar{\theta}$ of the nucleon in the laboratory system is given by

$$\tan\bar{\theta} = \frac{v_1(1 - V^2/c^2)^{\frac{1}{2}} \sin\theta}{V + v_1\cos\theta}, \tag{10}$$

where V is the velocity of the c.m.s. with respect to the laboratory, and θ is the angle between the directions of the nucleon and the incident particle in the c.m.s. The maximum value of $\bar{\theta}(=\bar{\theta}_m)$ is obtained from

$$d\tan\bar{\theta}/d\theta = 0, \tag{11}$$

which gives $\cos\theta = -v_1/V$. Upon inserting this result in Eq. (10), one finds

$$\tan\bar{\theta}_m = v_1(1 - V^2/c^2)^{\frac{1}{2}}/(V^2 - v_1^2)^{\frac{1}{2}}. \tag{12}$$

Equations (8) and (12) determine $\bar{\theta}_m$. Figure 1 shows $\bar{\theta}_m$ for production of $N=1$, 2, and 3 pions in n-p collisions as a function of the kinetic energy $\bar{E}_n$ of the incident neutron in the laboratory system. Figure 2 shows $\bar{\theta}_m$ for production of $N=1$, 2, and 3 pions in pion-nucleon collisions as a function of the kinetic energy $\bar{E}_\pi$ of the incident pion.

We note that Eqs. (8), (9), and (12) are general, and can be used for any particle m_1 when the total energy E and the masses $m_1, m_2, \cdots m_k$ are known.[2] These equations can be applied to find the maximum angle of a particle which results from the decay in flight of a meson or a V particle.

A further application of Eqs. (8) and (9) concerns the maximum possible momentum p_1 which a particle can have in the laboratory system as a function of the laboratory angle $\bar{\theta}_1$. Upon assuming a value of m_1, v_1 can be calculated, and p_1 is obtained from v_1 and V. If the observed momentum exceeds p_1, this fact can be used to aid in identifying the particle.

I would like to thank Dr. R. P. Shutt and Dr. H. S. Snyder for helpful discussions.

* Work done under the auspices of the U. S. Atomic Energy Commission.

[1] Fowler, Shutt, Thorndike, and Whittemore, Phys. Rev. 91, 758 (1953).

[2] Equations (8) and (9) are unchanged if an arbitrary number of γ rays or neutrinos accompany $m_1, m_2, \cdots m_k$. For it may be readily proved that the modification of Eq. (7) due to such massless particles yields a value of p_1 which is greatest when the total energy of the massless particles is zero.

Phase-Shift Analysis of High-Energy Nucleon-Nucleon Scattering*

R. M. THALER AND J. BENGSTON†
Yale University, New Haven, Connecticut
(Received December 7, 1953)

THE 240-Mev proton-proton scattering data[1] have been analyzed in terms of s-wave and p-wave anomalies.[2] If the s-wave phase shift $^1K_0$ is assumed to be $^1K_0 = 31.3°$,[3] then, neglecting Coulomb interaction, the combinations of p-phase shifts

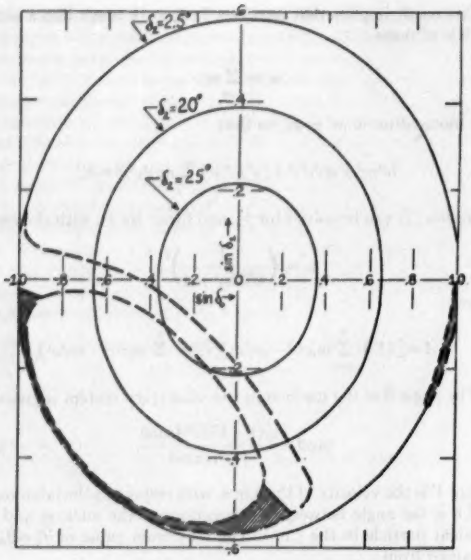

FIG. 1. Triplet p-phase shifts at 240 Mev ($\delta_2>0$) ${}^1K_0=31.3°$; dashed lines enclose regions admitted by large angle data; $\beta<0$ shown by cross hatch.

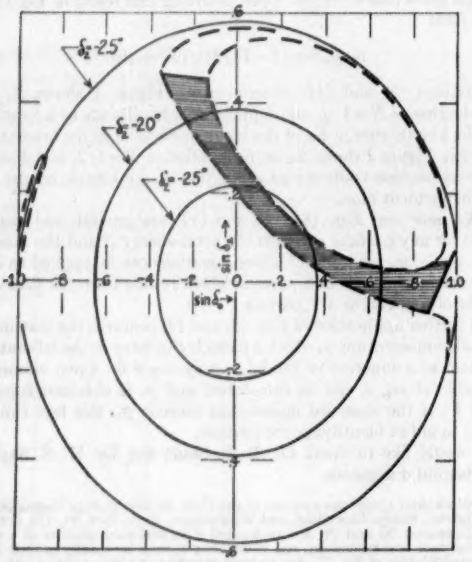

FIG. 2. Triplet p-phase shifts at 240 Mev ($\delta_2<0$). Otherwise as in Fig. 1.

δ_l yielding within experimental error an angle-independent $\sigma_\Omega\sim4.5$ mb/sterad are restricted to the regions between dashed lines shown in Figs. 1 and 2. The increase in σ_Ω shown by the Rochester data has been found to correspond to $\beta=\Sigma_l^3(2j+1)\times\sin\delta_l\cos\delta_l<0$, restricting possible δ_l to cross-hatched regions of Figs. 1 and 2. "Inverted" level position of ${}^3P_{0,1,2}$ gives $\delta_2>\delta_1>\delta_0$, a condition obtainable on the left of Fig. 1, which yields partial inversion as well. The fits are consistent with "charge independence," as in Fig. 3. Here n-p data[4] are fit with ${}^1K_0=30.9°$, ${}^1K_1=13.3°$, ${}^3K_0=50.8°$, ${}^3K_2=9.9°$, and the δ_l are from contour such as in Figs. 1 and 2 but for 260 Mev. The singlet phase shifts

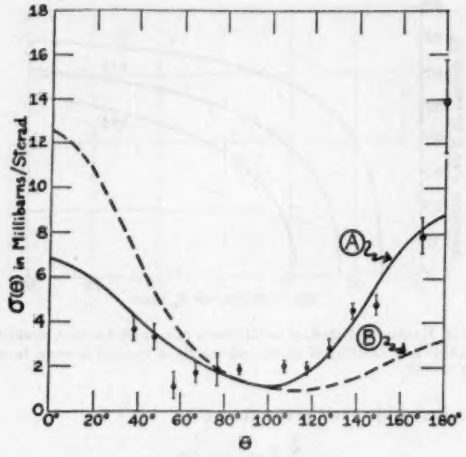

FIG. 3. n-p scattering cross section (see reference 4) at 260 Mev. ${}^1K_0$, ${}^1K_1=30.9°$, 13.3°; ${}^3K_0$, ${}^3K_2=50.8°$, 9.9°.

Curve A: δ_0, δ_1, δ_2, $\beta=13.5°$, 6.7°, $-25.7°$, -1.4.
Curve B: δ_0, δ_1, δ_2, $\beta=-13.5°$, $-6.7°$, 25.7°, 1.4.

$L=0,1$ are for Yukawa parameters $\mathcal{C}=89.8mc^2$, $a=0.42\hbar^2/mc^2$ while the ${}^3K_{0,2}$ are for $\mathcal{C}=132.4mc^2$, $a=0.42\hbar^2/mc^2$. Figure 3 shows that $\beta<0$ is also favored by n-p data. A more complete account of these calculations is in preparation.

The authors wish to thank Professor G. Breit, who initiated this work and guided the authors at every stage.

* Now at Oak Ridge National Laboratory, P. O. Box P, Oak Ridge, Tennessee.

† Assisted by the joint program of the U. S. Office of Naval Research and the U. S. Atomic Energy Commission, and by the Office of Ordnance Research.

[1] C. L. Oxley and R. D. Shamberger, Phys. Rev. 85, 416 (1952); O. A. Towler, Jr., Phys. Rev. 85, 1024 (1952).

[2] J. Bengston and R. M. Thaler, Phys. Rev. 91, 454 (1953). The results of this work were previously stated by G. Breit at the 1952 Rochester Conference in the discussion of calculations of Martin and Verlet. A. Garren, Phys. Rev. 92, 213 (1953).

[3] Calculated in first Born approximation for the meson well

$$V=-\mathcal{C}'(mc^2)[r/(\hbar^2/mc^2)a']^{-1}\exp[-[r/(\hbar^2/mc^2)a']],$$

with $\mathcal{C}'=89.8$ and $a'=0.42$.

[4] Kelly, Leith, Segrè, and Wiegand, Phys. Rev. 79, 96 (1950).

Effect of ${}^3P_2-{}^3F_2$ Coupling on Nucleon-Nucleon Scattering*

R. M. THALER, J. BENGSTON,† AND G. BREIT
Yale University, New Haven, Connecticut
(Received December 7, 1953)

THE present work takes the viewpoint[1] of specifying the nucleon-nucleon interaction by means of phase shifts assignable to each J, the viewpoint being equivalent to a scattering matrix specification. One may expect, therefore, coupling between states of different L; field theories are still powerless in ruling out appreciable effects of this sort. While there has been no definite evidence of isobaric state formation in pion-nucleon scattering,[2] the interaction is nevertheless so strong[3] and complex that reasonably stable states of a two-nucleon—meson system would be hard to rule out and the region of excitation energies of the order of the pion mass would be a likely one. Some consequences of a similar assumption as applied to s scattering are known not to be in contradiction with "low-energy" scattering.[4] It appeared desirable, therefore, to consider the consequences of assumed couplings of states of the same J and different L. The

$^3P_2-^3F_2$ case is the first of this kind for p-p scattering as J is increased. It appeared of interest to answer the following questions: (a) are appreciable magnitudes of such coupling admitted by experiment? (b) Is there an appreciable effect of the coupling on values of phase shifts for other $J-L$ demanded by experiment?

For p-p scattering, phase shifts for all $J\leq 2$ were admitted. The s waves were as in the preceding letter. No restriction on $^3P_{0,1}$ states was made. The $^3P_2-^3F_2$ coupling was treated in resonance-theory scattering-matrix formalism,[5] all of $\delta(^3F_2)$ arising from $\delta(^3P_2)$ through the intermediate state. Fits at 240 Mev were considered typical. Values of $K(^1D_2)$ up to $\sim 4°$ were used. It was found that one needs an "uncoupled" $\delta(^3P_2)<0$ for $T=\tan^{-1}[(\Gamma_1+\Gamma_3)/(E_R-E)]>0.1$ and $T<0.3$ for $^1K_2>0$. Here the Γ_1, Γ_3 are for $L=1, 3$ and $E_R\geq 300$ Mev is the resonance energy parameter. Thus the coupling considered works somewhat against inverted order of P terms but admits such order for $T<0.1$. Fits satisfying charge independence exist in a large range of parameters and fits giving an inverted order of P levels together with charge independence have been found.

It is believed, therefore, that calculations of P waves from pseudoscalar and related potentials may need additional adjustment for intermediate-state coupling. A more complete account will be published. Thanks are due Mr. Alvin Saperstein for checking some of the analytical work.

* Now at Oak Ridge National Laboratory, P. O. Box P, Oak Ridge, Tennessee.

† Assisted by the joint program of the U. S. Office of Naval Research and the U. S. Atomic Energy Commission, and by the U. S. Office of Ordnance Research.

[1] G. Breit, *Nuclear Physics, University of Pennsylvania Bicentennial Conference* (University of Pennsylvania Press, Philadelphia, 1941).
[2] K. A. Brueckner, Phys. Rev. **86**, 106 (1952); Anderson, Fermi, Long, and Nagle, Phys. Rev. **85**, 936 (1952); Anderson, Fermi, Nagle, and Yodh, Phys. Rev. **86**, 793 (1952).
[3] N. Austern, Phys. Rev. **87**, 208 (1952); B. T. Feld, Phys. Rev. **91**, 454 (1953).
[4] G. Breit and M. C. Yovits, Proc. Nat. Acad. Sci. **37**, 771 (1951).
[5] G. Breit, Phys. Rev. **58**, 1068 (1940).

The Branching Ratio of K^{40}†

G. J. WASSERBURG, *Institute for Nuclear Studies, University of Chicago, Chicago, Illinois*
AND
R. J. HAYDEN, *Argonne National Laboratory, Lemont, Illinois*
(Received December 9, 1953)

ATTEMPTS to measure the branching ratio of K^{40} by determining the A^{40}/K^{40} ratio in potassium minerals of supposedly known age were recently reported by Russell, Shilibeer, Farquhar, and Mousuf[1] and by Mousuf.[2] These results indicated a branching ratio of 0.06 ± 0.006. Other recent determinations of λ_K/λ_β by counting methods[3] and by determining the A^{40}/Ca^{40} ratio in geologically old potassium salts[4] are in agreement with a value of 0.13.

In view of this discrepancy, we have redetermined the A^{40}/K^{40} ratio in a sample of potassium feldspar which was supplied to us by Russell *et al.* This sample is listed by them as number 4.[1] Three runs were made on this material using an isotopic dilution technique. The feldspar was crushed and three samples coarser than 80 mesh were obtained. One aliquot of each of these samples was analyzed for potassium by K. Jensen and M. Sjoholm of the Argonne National Laboratory. An aliquot of this material finer than 180 mesh was also analyzed and a value of 10.43 percent K was obtained. This is 5 percent less than the amount found in the coarser fractions.

Another aliquot of each screened sample was dropped into a nickel furnace containing molten NaOH at 600°C. A known volume of A^{38} was added[5] and the reaction allowed to proceed for 24 hours. In runs 1 and 2 the tracer was added as soon as the reaction started. In run 3 the tracer was added 12 hours after the reaction began. The gases were then purified and the argon analyzed by means of a mass spectrometer with a 12-inch radius of curvature and 60° deflection. This instrument can completely resolve equal peaks separated in mass by one part in two thousand. Thus, possible hydrocarbon background peaks could be resolved from the argon. No such peaks were actually observed when the sample tube was kept at liquid air temperature.

TABLE I. Data for potassium feldspar sample No. 4, Pink Microcline, Bessner Mine, Lot 5 Con. B., Henvey Twp., Ontario.

Run	1	2	3
Sample weight (g)	14.522	27.283	6.902
Sieve size (mesh)	40–80	18–40	18–40
Percent K	11.00	10.92	10.92
A^{38}/A^{40}	$1.92\pm0.02\times10^{-4}$	$9.03\pm0.1\times10^{-4}$	$3.72\pm0.02\times10^{-4}$
A^{36}/A^{38}	0.0506 ± 0.001	0.044 ± 0.001	0.032 ± 0.001
Volume of A^{38} in tracer (cc stp)	$1.143\pm0.02\times10^{-3}$	$0.997\pm0.02\times10^{-3}$	$1.063\pm0.02\times10^{-3}$
Radiogenic A^{40} (cc stp) per g	$4.01\pm0.12\times10^{-4}$	$4.03\pm0.12\times10^{-4}$	$3.99\pm0.12\times10^{-4}$
A^{40}/K^{40}	0.0534 ± 0.0014	0.0541 ± 0.0014	0.0536 ± 0.0014

Considering the uncertainty in the age assigned to this locality, we feel that our results are essentially in agreement with a branching ratio of 0.13.

The data obtained are listed in Table I along with the sample weights. The A^{38}/A^{40} ratio in the tracer is 0.54 ± 0.01. The error given for the A^{40}/K^{40} ratio is the square root of the sum of the squares of the individual mean deviations and estimated errors.

The amount of atmospheric contamination is determined from the A^{36}/A^{38} ratio and is less than 3.3 percent in all runs. It is seen that the results of the three runs agree within two percent.

A sample of Opal glass and potassium feldspar obtained from the Bureau of Standards was analyzed along with an aliquot of feldspar used in run No. 2. The results obtained with the two standards agree with the values listed by the National Bureau of Standards[6] within one percent.

The value of A^{40}/K^{40} given by Russell *et al.* is 0.037 ± 0.004. The values which we have obtained is 0.0537 ± 0.0014. We have obtained 75 percent greater yields of radiogenic argon per gram of sample than they report and the potassium content which we have determined is greater than theirs by 17 percent.

Using a value of 0.54×10^{-9} year^{-1} for the decay constant and 0.060 for the branching ratio, we obtain an age of 12.6×10^8 years. The age which was assumed by Russell *et al.* was 9.4×10^8 years. This age was determined from the Pb^{206}/Pb^{207} ratio in a sample of uraninite from the same locality as the feldspar. The A^{40}/K^{40} age calculated for this feldspar, assuming our A^{40}/K^{40} ratio and a branching ratio of 0.13 is 7.0×10^8 years. Chemical analysis of this uraninite gave 5.57 percent lead and 52.76 percent uranium.[7] Using the isotopic analyses of Russell *et al.* and computing the contamination from Nier's values on the Bear Lake galena,[8] we obtain a Pb^{206}/U^{238} age of 6.9×10^8 years and a Pb^{207}/U^{235} age of 7.6×10^8 years. Nier[8] determined the lead-uranium and lead-thorium ages of a sample of Bessner uraninite. He obtained a Pb^{206}/U^{238} age of 7.65×10^8 years, a Pb^{207}/Pb^{206} age of 8.25×10^8 years, and a ThD/Th age of 7.87×10^8 years.

The authors are greatly indebted to Professor M. G. Inghram and to Professor H. C. Urey for their valuable guidance and suggestions during the progress of this work.

† This work was supported in part by the U. S. Atomic Energy Commission and in part by National Science Foundation Grant No. G-208.
[1] Russell, Shillibeer, Farquhar, and Mousuf, Phys. Rev. **91**, 1223 (1953).
[2] A. K. Mousuf, Phys. Rev. **88**, 150 (1952).
[3] W. R. Faust, Phys. Rev. **78**, 624 (1950); G. A. Sawyer and M. L. Wiedenbeck, Phys. Rev. **76**, 1535 (1949); Phys. Rev. **79**, 490 (1950); P. R. J. Burch, Nature **172**, 361 (1953).
[4] Inghram, Brown, Patterson, and Hess, Phys. Rev. **80**, 916 (1950).
[5] Richard J. Hayden and Mark G. Inghram in *Mass Spectroscopy in Physics Research*, National Bureau of Standards Circular 522 (U. S. Government Printing Office, Washington, D. C., 1953), p. 189.
[6] 1949 Supplement to National Bureau of Standards Circular 398; Standards Number 70 and 91.
[7] J. L. Kulp, Columbia University (private communication).
[8] A. O. Nier, Phys. Rev. **55**, 153 (1939).

Beta Decay of Np^{238}

HILDING SLÄTIS, JOHN O. RASMUSSEN, JR.,* AND HUGO ATTERLING
Nobel Institute of Physics, Stockholm, Sweden
(Received December 14, 1953)

WE have reinvestigated the beta and conversion electron spectrum of 2.1-day Np^{238} using a precision double-focusing spectrometer[1] and a high-transmission intermediate-image spectrometer.[2] The previous investigation of Freedman *et al.*[3] (with Mihelich's[4] reinterpretation of some low-energy conversion lines) showed gamma transitions of 43, 103, 983, and 1030 kev and a two-component beta spectrum, 47 percent with an end point of 1272 kev and 53 percent with 258 kev. The spectrum of the 1272-kev group was reported to have allowed shape. Decay schemes have been proposed by Freedman *et al.*[3] and by Asaro *et al.*[5] The fine structure observed in alpha decay[6] of Cm^{242} also gives valuable evidence regarding the low-lying levels of Pu^{238}.

Np^{238} was produced by bombardment of uranium metal with a 12.5-Mev internal proton beam. A uranium disk was placed in a cavity of a copper plate soldered to the water-cooled target holder. The uranium surface facing the beam was covered with a 0.015 mm thick platinum foil in order to prevent sputtering of uranium into the cyclotron chamber. Essentially weightless and chemically pure samples of neptunium were isolated using separation procedures previously described,[6] the final step involving separation of neptunium from lanthanum carrier by a cation exchange column elution with 13*M* HCl.

Table I summarizes the energies and intensities of observed conversion lines due to Np^{238} decay. The intensities of the lowest-energy conversion lines were corrected slightly for counter window transmission loss. Of greatest interest is the evidence for additional gamma transitions of 939 and 925 kev, although the latter was so weak as to be somewhat uncertain.

The agreement of energies from this work and from alpha spectroscopy of Cm^{242} indicates that the 44.1-kev transition is between the first excited state and ground state of Pu^{238}, while the 102.1-kev transition is between second and first excited states. The ratios of the *L* subshell conversion coefficients[7] point to *E*2 assignments for these transitions. The energy difference between the 1030- and 986-kev gamma rays is 44 kev, leading us to believe that both of these gamma rays arise from a common level and go to ground and first excited states, respectively. The 939-kev gamma ray evidently most come from a level with energy near that of the 1030-kev level. Although it does not seem possible to construct a unique decay scheme from the available data, it seems probable that both the hard and soft beta groups are themselves complex. We determined the ratio of the intensities of hard to soft beta groups as 55:45, in good agreement with the ratio 53:47 of Freedman *et al.*[3] The 44.1-kev transition, being *E*2, is almost totally converted, and from Table I the total conversion line intensity is 65 percent of total beta disintegrations. Hence, if more than 10 percent of the soft beta particles cascade through the 44.1-kev transition, that percentage excess must equal hard beta particles not cascading through it, that is, going to the ground state. The energy separation between possible hard beta components is not large enough to be clearly resolvable in our Fermi-Kurie plots from intermediate image spectrometer data. These plots do show some slight curvature near the end point consistent with beta groups of 1290 and 1246 kev, but the curvature could be instrumental and interpretation made as a single group of 1260 kev. Electron-electron coincidence studies are needed to clear up this question. Whether or not this complexity exists, the Fermi-Kurie plot for allowed shape is much straighter than that including the unique correction factor for $\Delta I=2$, yes-type spectra. The tables of Rose *et al.*[8] were used to determine the correction factor. The allowed shape determination confirms the finding of Freedman *et al.*[3] Our low-energy beta end point is about 271 kev but conversion lines obscure parts of the spectrum, so the determination is not precise.

TABLE I. Conversion lines in the beta spectrum of Np^{238}.

Interpretation of line	E_e^- (kev)	Electron binding energy[a] (kev)	E_γ (kev)[b]		Abundance of conversion electrons per 100 disintegrations
L_{II}	21.8	22.3	44.1	γ_1	28.7
L_{III}	25.9	18.1	44.0		21.0
M_{II}	38.7	5.6	44.2		15.2
M_{III}	39.5	4.6	44.1		
N	42.8	1.4	44.2		
O	43.6	0.3	43.9		
L_{II}	80.1	22.3	102.3	γ_2	1.4
L_{III}	84.1	18.1	102.1		0.9
$M_{II,III}$	96.6	5.0	101.6		0.7
(K_e)	802.8	121.7	925	(γ_3)	0.05
K_3	817.2	121.7	939	γ_4	0.10
K_1	864.4	121.7	986	γ_5	0.26
K_2	907.2	121.7	1029	γ_6	0.22
$L_{3,II}$	914	22.3	936	γ_4	0.06
$L_{1,II}$	963	22.3	985	γ_5	0.13
$M_{1,II}$	983	~5.6	988	γ_5	—
$L_{2,II}$	1008	22.3	1031	γ_6	0.08
$M_{2,II}$	1024	~5.6	1030	γ_6	0.06

[a] Hill, Church, and Mihelich, Rev. Sci. Instr. **23**, 523 (1952).
[b] The weighted mean energies of the gamma rays, in kev, are: γ_1, 44.1; γ_2, 102.0; γ_3, 925; γ_4, 939; γ_5, 986; γ_6, 1030.

The new high-energy gamma transitions indicate the presence of at least two levels near 1 Mev with spacings of the same order as the close-lying levels above the ground state. The strong surface-coupling model of Bohr and Mottelson[9] predicts rotational band spectra on higher excited states as well as on the ground state. It seems quite likely that the close-lying levels around 1 Mev in Pu^{238} represent such a rotational band system.

This investigation will be reported in more detail later.

One of us (J.O.R.) wishes to acknowledge a fellowship from the Nobel Institute of Physics during the time this work was carried out.

* Present address: University of California Radiation Laboratory, Berkeley 4, California.
[1] N. Svartholm and K. Siegbahn, Arkiv Mat. Astron. Fysik **A33**, No. 21 (1946); Hedgran, Siegbahn, and Svartholm, Proc. Phys. Soc. (London) **63**, 960 (1950); Hedgran, Arkiv Fysik **5**, No. 1 (1952).
[2] H. Slätis and K. Siegbahn, Arkiv Fysik **1**, 339 (1949).
[3] Freedman, Jaffey, and Wagner, Phys. Rev. **79**, 410 (1950).
[4] J. W. Mihelich, Phys. Rev. **87**, 646 (1952).
[5] Asaro, Thompson, and Perlman, Phys. Rev. **92**, 694 (1953).
[6] Magnusson, Thompson, and Seaborg, Phys. Rev. **78**, 363 (1950).
[7] Gellman, Griffith, and Stanley, Phys. Rev. **85**, 944 (1952).
[8] Rose, Perry, and Dismuke, Oak Ridge National Laboratory Unclassified Report ORNL-1459, February 1953 (unpublished).
[9] A. Bohr and B. R. Mottelson, Phys. Rev. **89**, 316 (1953); **90**, 717 (1953); Kgl. Danske Videnskab. Selskab, Mat.-fys. Medd. **27**, No. 16 (1953).

Influence of the Earth's Magnetic Field on the Extensive Air Showers

GIUSEPPE COCCONI
Cornell University, Ithaca, New York
(Received December 11, 1953)

THIS note is written to point out that the displacement from the rectilinear path produced by the action of the earth's magnetic field on the electrons ($\pm$) of an extensive air shower (e.a.s.) can be not negligible in comparison with the displacement due to Coulomb scattering.

Several elaborate calculations have been made by various authors to evaluate the lateral spread of e.a.s., but none, to our knowledge, takes this effect into account. A qualitative discussion is given here.

Most of the e.a.s. fall on the earth with small zenith angles; hence we shall consider here only the influence of the horizontal component of the magnetic field:[1] $H=0.31\cos\lambda$ gauss, where λ is the geomagnetic latitude. The corresponding radius of curvature

of an electron of energy $E(\gg mc^2)$ is

$$\rho = 1.08\times10^{-3}E/\cos\lambda \text{ cm} \quad (E \text{ in ev}).$$

When the displacement D_m due to the magnetic field is small in comparison with the length of the path T, as it always is in air, then

$$D_m = \int_0^T (T-t)dt/\rho.$$

D_m must be compared with D_s, the projected lateral displacement due to multiple Coulomb scattering, which is the main phenomenon responsible for the distribution of the electrons around the core of e.a.s. With sufficiently good accuracy

$$\langle D_s^2\rangle = \tfrac{1}{2}E_s^2\int_0^T \frac{(T-t)^2dt}{E^2X} = \mathfrak{D}_s^2,$$

where $E_s = 2.1\times10^7$ ev is a constant, and $X = (3\times10^4/P)$ cm (P = air pressure in atmospheres) is the characteristic radiation length in air.

If the energy losses can be neglected, E and ρ are constants, and if the atmospheric pressure is also taken as a constant, then

$$\frac{D_m}{\mathfrak{D}_s} = \frac{T^2}{2\rho}\Big/\left(\frac{E_s^2T^3}{6XE^2}\right)^{\frac{1}{2}} = 9.3\times10^{-4}(T/P)^{\frac{1}{2}}\cos\lambda \quad (T \text{ in cm}).$$

For $T = 1$ km and $P = 1$, the ratio, independent of energy, is already 0.3 cosλ.

A more specific case can be considered. Above the critical energy most of the electron energy losses are due to radiation. In a simplified model, the energy of an electron is reduced by a factor of 2 for each radiation length. The atmospheric pressure can be considered as a constant. Then $E(t) = E_T\exp[\alpha(T-t)]$, where E_T is the energy of the electron after crossing the thickness T, and $\alpha = (\log 2)/X = 2.3\times10^{-5}P$ cm^{-1}. One obtains

$$D_m = (e^{\alpha T} - \alpha T - 1)/(\rho_T\alpha^2e^{\alpha T}).$$

If $\alpha T > 1$, i.e., if $T > 1$ km at sea level,[2]

$$D_m \approx 1/(\rho_T\alpha^2) = 1.75\times10^{11}(\cos\lambda)/(E_TP^2) \text{ cm},$$

independent of T. With the same assumptions,

$$\mathfrak{D}_s = \frac{E_s}{(8X\alpha^2)^{\frac{1}{2}}E_T}\left[1 - \frac{(\alpha T+1)^2+\alpha^2T^2}{\exp(2\alpha T)}\right]^{\frac{1}{2}} \xrightarrow{\alpha T>1} \frac{E_s}{(8X\alpha^2)^{\frac{1}{2}}E_T} = \frac{3.9\times10^{11}}{E_TP} \text{ cm}.$$

The ratio is

$$D_m/\mathfrak{D}_s = 0.45(\cos\lambda)/P \quad (\text{for } \alpha T > 1).$$

Up to quite high latitudes the separation in the E–W direction of the negative electrons from the positive ones due to the earth's magnetic field is then about as large as the average lateral displacement due to scattering; the effect increases with altitude.

For electrons of energy smaller than the critical energy, the magnetic displacement presumably becomes small in comparison with that due to Coulomb scattering, because these electrons cannot travel very far in the air and are instead carried away from the axis of the shower mostly by single large-angle scatterings. Thus, the magnetic deflection modifies quite strongly the distribution around the core of the showers of high-energy electrons, and to a smaller extent that of the low-energy ones. At latitudes lower than ~50° and around sea level the distribution of vertical showers is not circular but, roughly speaking, elliptical, with the major axis in the E–W direction and almost two times longer than the small axis.

This phenomenon will make it difficult to analyze experiments on the distribution of high-energy electrons around the core of e.a.s. and in general all experiments whose interpretation depends on the electron lateral distribution.

Probably the magnetic deflection does not strongly affect the distribution of the other components of e.a.s., namely nucleons and mesons. In fact, the angle at which these particles are emitted in nuclear interactions is responsible for a lateral displacement much larger, in most cases, than that produced by the earth's magnetic field.

[1] A more detailed calculation should take into account the fact that the displacement due to the earth's magnetic field is a function of both zenith and azimuthal angles.

[2] D_m converges rapidly when T increases because the energy of the electron increases rapidly with altitude. This justifies the assumption P = constant.

PHYSICAL REVIEW VOLUME 93, NUMBER 3 FEBRUARY 1, 1954

Proceedings of the American Physical Society

Minutes of the Sixth Annual Conference on Gaseous Electronics, Sponsored Jointly by the Division of Electron Physics of the American Physical Society and the U. S. Office of Naval Research, Held at Washington, D. C., October 22–24, 1953

THE Sixth Annual Conference on Gaseous Electronics was held at the Shoreham Hotel, Washington, D. C., on October 22, 23, and 24, 1953. There were 228 registrants. One invited paper "Ultra-Violet Photons in the Decay of Metastable Argon Atoms" by L. Colli and U. Facchini of C.I.S.E., Milan, Italy, was presented *in absentia*. Abstracts of some of the forty-four contributed papers are printed below. A banquet was held on the evening of the 23rd. The guest speaker, Captain C. W. Shilling, Senior Medical Officer at the U. S. Naval Academy, presented an excellent address on the value of basic research, and cited numerous examples in the medical field. Also at the banquet, the conference committee for the forthcoming year was announced as follows: Professor W. P. Allis, *Chairman;* L. Fisher, *Secretary;* E. O. Johnson; W. Gruner; H. D. Hagstrum; M. A. Biondi; S. Githens; and M. Kuper.

A1. Calculated Values of the Parameters of Noble Gas Discharges. Walter J. Graham and Arthur J. Rühlig, *U. S. Naval Research Laboratory.*—Molar properties of gaseous discharges are determined by the transport cross section which is expressible in terms of the phase shifts defined in electron-atom scattering theory. $\sigma_1(v)$ was calculated for helium, neon, and argon using values of phase shifts η_0 to η_4 derived by

Westin[1] from existing scattering data. Druyvesteyn distribution functions were calculated for E/p from 0.1 to 1.0. Average values were then calculated for collision frequency, drift velocity, diffusion coefficient, and average energy. Also, collision frequency and elastic energy loss were calculated using Maxwell distributions for kT, up to 10 ev. These calculations are particularly useful at very low energy, where extrapolation of phase shifts is more reliable than of the experimental data. Values of σ_1 are compared with those of Barbiere (taken from direct scattering data); values of drift velocity are somewhat lower than Nielsen's data.

[1] Kgl. Norske Videnskab. Selskabs. Forh. 1946 Nr. 2.

A2. RF Noise from Low-Current, Atmospheric-Pressure Arc Discharges in Air. M. I. SKOLNIK, *The Johns Hopkins University.*—It was found that broad-band rf noise can be obtained from low-current dc arcs operated in air. Arc currents ranging from 20 to 200 ma and electrode separations from 0.01 in. to ½ in. were used. The largest amount of noise power was obtained with cold-cathode arcs using aluminum or copper cathodes. Noise power measurements were made over the frequency range from 38 to 4500 Mc. For arc currents of 50 ma, a noise factor (ratio of noise power actually obtained to the noise power theoretically available from a resistor at room temperature) of approximately 115 db was obtained at 40 Mc, and at 4500 Mc the noise factor exceeded 65 db. The maximum noise factor corresponds to an effective noise temperature of approximately 10^{14}°K. The noise output was reduced after approximately one-half hour with aluminum electrodes and after a few minutes operation with copper. When thermionic cathodes, such as tungsten or carbon, were used, little noise was produced. It was found that the noise was produced by a series of very narrow pulses of amplitude greater than 100 volts. The repetition rate was of the order of one or two megacycles and varied with the discharge current.

A3. Phenomena Associated with Small Temperature Variations of the Electron Gas in Discharge Plasmas around 300°K. Part I. Cross Modulation.* J. M. ANDERSON AND L. GOLDSTEIN, *University of Illinois.*—Investigation of guided microwave propagation through gaseous discharge plasmas has shown a "cross-modulation" effect[1] substantially the same as the "Luxembourg effect" observed in the ionosphere. The interaction of microwaves (X-band) in the essentially isothermal plasma is explained, to a first approximation, on the basis of a theory proposed by Bailey and Martyn.[2] A pulse-modulated, "disturbing" wave (450-milliwatt peak), was propagated in square wave guide at polarization orthogonal to that of a lower-power continuous "wanted" wave through a gaseous discharge tube contained in the wave guide. Measurements were made in the decaying plasmas established in the rare gases at 1 to 20 mm Hg pressure. The envelope of the transmitted wanted wave, to which the pulse modulation has been transferred, yields a value for G (Townsend energy loss factor $\sim 2m/M$). In general, the excess electron gas "temperature" resulting from the absorbed microwave energy has been calculated to be of the order of a few times 300°K. Cross modulation is enhanced when a constant magnetic field at the gyro-resonance intensity of the disturbing wave frequency is applied to the plasma.

* Supported by Air Force Cambridge Research Center and Wright Air Development Center.
[1] Goldstein, Anderson, and Clark, Phys. Rev. 90, 151 (1953).
[2] V. A. Bailey and D. F. Martyn, Phil. Mag. 18, 369 (1934).

A4. Phenomena Associated with Small Temperature Variations of the Electron Gas in Discharge Plasmas around 300°K. Part II. Afterglow Quenching. L. GOLDSTEIN AND J. M. ANDERSON, *University of Illinois.*—The observed interaction of simultaneously propagated low-level electromagnetic waves through an essentially isothermal discharge plasma suggested that all phenomena strongly dependent on the temperature of the electron gas should be affected by the absorption of low-level electromagnetic energy. Results of experimental verification and study of one such expected effect which concerns the recombination of electrons and positive ions will be reported. These studies are made by means of the visible recombination afterglow. Pulse-modulated (X-band) microwave energy was propagated through a discharge plasma as described in Part I. The visible afterglow intensity was observed by means of photomultipliers along the discharge tube, which was located in a wave guide. As a result of pulsed microwave energy absorption the temperature of the electron gas is raised above the equilibrium temperature presumed ~300°K. The increased electron temperature decreases the afterglow intensity. In the case of electron removal, due mainly to recombination with positive ions, this quenching is to be attributed to the decrease of the associated recombination coefficient. In the case of diffusion removal of electrons the afterglow quenching is in addition to be ascribed to the increased loss of electron density brought about by accelerated diffusion. These effects constitute rather sensitive means of detection of high-frequency e.m. energy.

A5. Microwave Measurements of the Properties of a DC Hydrogen Discharge.* BURTON J. UDELSON AND JOHN E. CREEDON, *U. S. National Bureau of Standards.*—By microwave methods, the variation of electron density was determined along the length of a dc discharge in 3-mm Hg of hydrogen, operating at currents of the order of 0.5 ma. A determination was also made of the variation of electron density and electron collision frequency (νc) as functions of both gas pressure and tube current in the positive column of a dc discharge. The method employed was the measurement of the change of resonant frequency and the change of voltage standing wave ratio at resonance produced by the introduction of a region of the discharge into the high field gap of a re-entrant S-band cavity. Discharge tubes of approximately 0.2-in. diameter and 0.01-in. wall thickness were employed. From these measurements, relative electron density and νc were calculated.[1] The resultant values of collision frequency ($\nu c = 4.4 \times 10^9 \times$gas pressure) agreed favorably with the values calculated from the data of collision probability obtained from Brode.[2]

* This work was sponsored by the U. S. Navy Bureau of Ships.
[1] D. J. Rose and S. C. Brown, J. Appl. Phys. 23, 1028 (1952).
[2] R. B. Brode, Revs. Modern Phys. 5, 257 (1933).

A6. A Microwave Measurement of the Velocity Dependence of the Collision Cross Section of Slow Electrons in Helium.* LAWRENCE GOULD,† *Massachusetts Institute of Technology.*—A microwave method previously reported[1] for determining the collision probability for momentum transfer of slow electrons has been modified so that a variation in average electron energy from 0.012 to 3 electron volts may be obtained. Measurements of the ratio of the real to the imaginary part of the complex conductivity, using a null method,[2] are made in the afterglow of a pulsed discharge. The average electron energy is varied by applying a microwave electric field in the afterglow, and, under appropriate assumptions, the average energy is determined theoretically from this field. Measurements from 0.012 to 0.052 electron volt are also obtained by varying the gas temperature from 95°K to 400°K. The value of the collision probability in helium is 18.3±2 percent from 0 to 0.75 electron volt and increases slowly to a peak value of 19.2±2 percent at 2.2 electron volts.

* This work has been supported in part by the U. S. Army Signal Corps, the Air Materiel Command, and the U. S. Office of Naval Research.
† Now at Microwave Associates, Boston, Massachusetts.
[1] Phelps, Fundingsland, and Brown, Phys. Rev. 84, 559 (1951).
[2] L. Gould and S. C. Brown, J. Appl. Phys. 24, 1053 (1953).

A7. The Excitation of Plasma Oscillations.* DUNCAN H. LOONEY† AND SANBORN C. BROWN, *Massachusetts Institute of Technology.*—A beam of high-energy electrons, injected into the plasma of a dc discharge from an auxiliary electron gun, excited oscillations in the plasma at the plasma electron oscillation frequency $\omega_p^2 = ne^2/m\epsilon_0$. A movable probe showed the existence of standing-wave patterns of the oscillatory energy in the region of the plasma in and around the electron beam. Nodes of the patterns coincided with the electrodes which limited the region of the plasma traversed by the beam. The standing-wave patterns were independent of the frequency of the oscillation. At any particular frequency, the standing-wave pattern was determined by the thickness of the ion sheaths on the bounding electrodes. The mechanism of the energy transfer from the electron beam to the oscillation of the plasma electrons was established as a velocity modulation process by the detailed behavior of the frequency of oscillation and the transitions in the standing-wave patterns as the sheath thickness was varied.

* This work has been supported in part by the U. S. Army Signal Corps, the Air Materiel Command, and the U. S. Office of Naval Research.
† Now at the Bell Telephone Laboratories, Inc., Murray Hill, New Jersey.

B1. On the Electron Current Saturation in a Ball-of-Fire Diode. G. MEDICUS, *Wright Air Development Center.*—The electron current saturation in a ball-of-fire discharge, as described by Medicus[1] can be understood as follows. The electrons constituting the anode current diffuse against a retarding field which surrounds the ball of fire, in the nonsaturated as well as in the saturated state. In the latter a thin Langmuir sheath along the anode develops which captures all the electrons that reach its edge by diffusion. So, regarding the electrons, the anode in principle behaves like a large plane probe with a good saturation characteristic. The ions in the nonsaturated state reach the anode by their mobility in the accelerating field. At electron current saturation, however, no ions can reach the anode because of the retarding field of the Langmuir sheath. In this case, the ions very probably are swept out from the space between anode and cathode onto the glass walls of the tube (and to the cathode housing) by an ion wind.

[1] G. Medicus, J. Appl. Phys. **24**, 233 (1953).

B2. Buildup Times of Glow Discharges in Air.* ALEX MAYER AND L. H. FISHER, *New York University.*—This constitutes a preliminary report on the buildup time of glow discharges in air. Two chambers of different diameters (three and six inches) were studied. The electrodes were two-inch circular disks of brass in both chambers and the dry air sample was shared from the same manifold. External ultraviolet illumination of the cathodes was provided to avoid statistical lags. At an electrode separation of 2 cm and a pressure of 1 mm of Hg the chambers give essentially identical results, the time lags being of the order of 1000 microseconds near threshold and 2 microseconds at an overvoltage of about 35 percent. For the same electrode separation and 0.1 mm of Hg (below the Paschen minimum) the tubes behave quite differently from each other. The breakdown voltage of the larger tube is considerably lower than that of the smaller tube. The formative time lag of the smaller tube is 0.1 second at an overvoltage of 24 percent and decreases to 9 microseconds at an overvoltage of 550 percent; in contrast, the time lag for the larger tube is 1350 microseconds at 0.5 percent overvoltage and decreases to 4 microseconds at 500 percent overvoltage. Results will be given for longer gaps.

* Supported by the U. S. Office of Naval Research and the Research Corporation.

B3. Formative Time Lags of Uniform Field Breakdown in Hydrogen.* I. LESSIN AND L. H. FISHER, *New York University.*—Formative time-lag measurements of spark breakdown in uniform fields[1] have been extended to hydrogen. The variation of formative time lags with percent overvoltage was studied for pressures between 200 mm of Hg and atmospheric, and for electrode separations ranging from 0.5 to 2.0 centimeters. The lags in hydrogen were found to be independent of pressure and to increase with increasing electrode separation. The pressure independence of the lags corresponds to the results in air and nitrogen, but is in marked contrast to the results in argon and oxygen. The time lags in hydrogen are of the same order of magnitude as those found in air and nitrogen but are somewhat longer at the higher overvoltages and somewhat shorter at the lower overvoltages. These results indicate once again a Townsend buildup before breakdown. Preliminary attempts to interpret the data quantitatively in the manner given by Kachickas and Fisher for air, nitrogen, and argon have not succeeded too well. Calculations have been hampered by unavailability of reliable α/p values in the E/p region in which most of the data lie. However, it is concluded that the secondary mechanism is a photoelectric effect at the cathode.

* Supported by the U. S. Office of Naval Research and the Research Corporation.
[1] L. H. Fisher and B. Bederson, Phys. Rev. **81**, 109 (1951); G. A. Kachickas and L. H. Fisher, Phys. Rev. **79**, 232 (1950); **88**, 878 (1952); **91**, 775 (1953).

B4. Current Growth in the Formative Time Lag of Sparks.* H. W. BANDEL, *University of California at Berkeley.*—Following the work of Fisher and associates[1,2] an oscilloscopic study has been made of the growth of current preceding streamer spark breakdown, during long formative time lags at low overvoltages. Time lags from 10–100 microseconds have been observed in dried air at 730-mm Hg. Currents have been observed from microamperes in the early part of the formative time rising to 10^{-3} amp just before breakdown. With heavy electron triggering a relatively consistent set of curves of current *vs* t/τ, where τ is the time lag, is obtained. Investigation with triggering of the order of 10 electrons per microsecond reveals that statistical factors cause great variations in the formative time lag and rate of current buildup.

* Supported by the U. S. Office of Naval Research and National Science Foundation funds, and a Research Corporation of America Fellowship.
[1] L. H. Fisher and B. Bederson, Phys. Rev. **81**, 109 (1951).
[2] G. A. Kachickas, Doctor's thesis, New York University.

B5. Hitherto Unrecognized Aspects of Breakdown Streamers.* LEONARD B. LOEB, *University of California at Berkeley.*—Oscilloscopic observations of streamers yield v_t the velocity of streamer tip advance, and n the number of positive ions left behind per cm advance which has remarkably constant values over the gap depending on streamer type. The fields X_s down the streamer must be sufficient to maintain conduction against charge loss, to yield a drift velocity v_s and to maintain the integral of X_s along the channel less than the applied potential V. This can only occur for observed values of v_t if $v_s = n/n_s v_t$, where n_s is the number of electrons per cm carrying current up the streamer, with a constant $n_s + n$ electrons and ions created per cm advance. The volume density produced by n ions per cm causes radial expansion of the space charge by indrawn avalanches leaving a transient expanding luminosity behind the streamer tip. This expanded ionization slowly decays the current being carried up the narrow channel of n_s electrons/cm which is followed by the return stroke. Further properties of preonset and breakdown streamers, and of stepped lightning leaders are presented.

* Part of the investigations involved were supported by the U. S. Office of Naval Research funds and a grant from the Research Corporation.

B6. Fast Time Analysis of Burst Pulse, Preonset Streamer, and Trichel Pulse Point-to-Plane Coronas.* M. R. AMIN, *University of California at Berkeley.* (Presented by L. B.

Loeb.)—By developing suitable oscillographic techniques using both electrical and photomultiplier cell studies the three common aspects of point-to-plane corona have been studied in detail. Burst pulse corona is initiated by a burst of 2×10^7 ions followed by a sequence of smaller pulses after dead times of 1–10 microseconds, with 10^6 ions each. As potentials increase above threshold, the sequences increase in length until interrupted by a gross space charge in the low field regions. This extinguishes the burst and a long clearing time follows. The whole sequence from threshold to steady corona is observed. Preonset streamers are shown to consist of a sharp peak followed by luminosity from radial expansion behind the tip. The tip velocity and ions per cm advance are observed and further details explained. The Trichel pulse corona at atmospheric pressure lasts less than 10^{-8} sec, depends on a photoelectric γ and is quenched by dissociative attachment of electrons to O_2 molecules yielding O^- ions within 0.05 cm of the point. At lower pressures the choking space charge forms further out in the gap; more ions and time are needed to quench. The longer discharge is sustained by a positive ion γ after starting with a photon γ. The variation of repeat rate with potential and current and the nature of conditioning of the point at higher currents are revealed.

* These studies were supported by the U. S. Office of Naval Research and later by a grant from the Research Corporation.

B7. Impulse Corona and Breakdown of a Point-Plane Gap. T. W. LIAO, *General Electric Company.*—Impulse corona currents of positive and negative point-plane gaps in air have been measured from corona-start to breakdown with 1.5×40 μsec voltage waves. The current pulse in the ground circuit represents essentially the electronic current for the positive point, but mostly the ionic current for the negative point. The negative-point corona current increases much more uniformly with the applied voltage from corona-start to breakdown than the positive point. The positive point of breakdown is a streamer process progressing from the point to the plane. The negative-point corona prior to breakdown produces negative space charge which retards the progression but gradually increases the field at the plane resulting in a "reverse-streamer" process. Calculations show that the field at the plane due to the space charge is about 5 to 10 times higher than the applied field for the critical breakdown condition. The time to breakdown increases with the gap spacing, extending as long as 37 μsec for a 6-in. gap.

B8. Further Studies of Photon Production in Externally Sustained Discharges.* D. S. BURCH, R. C. IRICK, AND R. GEBALLE, *University of Washington.*—A photocathode has been employed in more extensive studies of the dependence of photon production rates on E/p in several gases. In H_2, earlier measurements made with a Geiger detector[1] have been augmented, yielding results in agreement with published theoretical predictions.[2] In pure O_2 and N_2 the magnitudes of the observed effects are approximately equal and are small compared with H_2. The intensity is approximately constant over the range of E/p from 60 to 90 volts/cm/mm. In air and in a 4-percent mixture of O_2 and N_2 the effect is an order of magnitude larger than in the pure gases, and rises slowly with E/p in the range from 40 to 120 volts/cm/mm. Possible interpretations of these results will be presented.

* Partially supported by the Office of Ordnance Research, U. S. Army.
[1] R. Geballe and J. M. Templeman, Conference on Gaseous Electronics, Pittsburgh, 1949.
[2] R. W. Lunt and C. A. Meek, Proc. Roy. Soc. (London) **A157**, 146 (1936).

C1. Charge Transfer in the Upper Atmosphere. S. N. GHOSH, *Air Force Cambridge Research Center.*—Some charge transfer reactions appear to have higher reaction rates than that of any other collisional process in the upper atmosphere. For reactions involving Ca^+ emanating from the sun, the energy defects are large and, therefore, for near-adiabatic collisions the maximum probabilities occur long before these ions have lost all their energy by colliding with atmospheric gases. On the other hand, the energy defects are small for reactions involving solar protons which have reached the earth's atmosphere. These reactions have been tested for Wigner's spin conservation rule. The possible charge transfer reactions between neutral atoms and molecules with the ions present in the ionized layers of the upper atmosphere have also been discussed and tested for Wigner's rule. For the low-energy ions present in these layers, the cross sections are very low for nearly all reactions.

C2. Cross Sections for Charge Transfer Collisions of Low-Energy Ions in N_2 and O_2. ROY F. POTTER, *U. S. National Bureau of Standards.*—Measurements have been made of the cross sections for charge transfer collisions between the low-energy (9–250 ev) ions, N_2^+, O_2^+, O^+, and N^+, and the molecules N_2 and O_2. Two reactions (N^+, N_2; O^+, N_2) have been reported by other workers and will be compared with present work. The experimental method utilizes a radio-frequency mass spectrometer as an ion source. The ions are collimated and enter a weak radial electric field of cylindrical symmetry. The secondary ions are separated from the primary beam and the ratio of the two currents is measured as a function of pressure. Results will be discussed in terms of the adiabatic collision condition and possible internal energy states of the ions.

C3. Measurement of Dissociative Recombination in Nitrogen. A. C. FAIRE, O. T. FUNDINGSLAND,* AND A. L. ADEN, *Air Force Cambridge Research Center.*—Laboratory investigations of recombination of thermal electrons with molecular ions have been conducted in nitrogen using a microwave method previously reported.[1] By adding atomic helium to the molecular gas in such proportion as to maintain a total gas pressure high enough to subordinate ambipolar diffusion to the walls of a microwave cavity, measurements of the electron-positive ion recombination coefficient are extended to lower pressures than those previously reported by Biondi and Brown.[2] The electronic energy levels of helium all lie above the first ionization potential of nitrogen. Hence, during the discharge afterglow the helium serves mainly as a passive recoil agent to retard diffusion and to speed up the energy decay of free electrons to thermal equilibrium with the ions. For the purpose of this paper, the assumption is made that recombination does exist as a mode of decay when a linear curve results from a plot of reciprocal electron density as a function of time in the discharge afterglow. The value of the recombination coefficient obtained from the measurements was of the order of 10^{-6} cm³/sec.

* Now at the Electronic Defense Laboratories, Mountain View, California
[1] M. A. Biondi and S. C. Brown, Phys. Rev. **75**, 1700 (1949).
[2] M. A. Biondi and S. C. Brown, Phys. Rev. **76**, 1697 (1949).

C4. Doppler Broadening of Dissociative Recombination Lines. MANFRED A. BIONDI, *Westinghouse Research Laboratories.*—The extremely large electron-ion recombination cross sections observed in microwave afterglow studies have been attributed to the process of dissociative recombination, e.g.,

$$He_2^+ + e \rightarrow He^* + He + \text{kinetic energy}.$$

Previous attempts to verify this hypothesis by examination of the excited states formed in the recombination process gave inconclusive results.[1] The present investigation is based on a characteristic feature of the dissociative recombination reaction: the excited atom formed has kinetic energy in excess of thermal energy. If this fast excited atom undergoes a radia-

tive transition before losing its excess kinetic energy in collisions with gas atoms and before the excitation is transferred to a slow atom, then the line emitted is broader than the thermal Doppler width. At present, a shuttered Fabry-Perot interferometer is being used to determine the profiles of recombination lines emitted from helium afterglows. While the intensity problem is severe, preliminary data indicate that the experiment is feasible.

[1] M. A. Biondi and T. Holstein, Phys. Rev. **82**, 962 (1951); **83**, 1078 (1951).

C5. Time-Resolved Spectroscopy of Nitrogen and Hydrogen. C. F. HENDEE AND W. B. BROWN, *Philips Laboratories, Inc.*—The long decay time of the first positive bands of N_2 in a pulsed N_2 discharge[1] has been re-examined by the use of the pulsed photomultiplier technique. The decay times of individual bands were obtained because of the increased sensitivity of this method. The transition probabilities of these bands vary by a factor of ten.[2] However, only a slight variation of decay time was observed, giving substantiation to the process of indirect excitation through the $a'\pi$ level. The light from a H_2 thyratron has been studied with pulsed photomultipliers. The pulse shapes of the Balmer and band lines were similar for normal square-wave currents. When the current during the pulse oscillated at about 10 mc there was a modulation of the light during the first oscillation in each pulse. A time resolution of 0.03 μsec is inferred from the results. Under these conditions, the pulse shapes of the Balmer and singlet band lines differed from that of the triplet lines and continuum.

[1] C. F. Hendee, Conference on Gaseous Electronics (1951).
[2] Jarmain and Nicolls, University of Western Ontario, Scientific Report No. 4, Contract No. AF 19(122)-470.

C6. New Method for Exciting Metallic Spectra by Active Nitrogen. The Excitation of Xe. CARL KENTY, *Lamp Development Laboratory of General Electric Company.*—By passing condensed sparks across metallic gaps in 30-cm A plus 1-cm N_2, "flames"[1] have been produced of W, Ta, Mo, Pd, V, Cb, Cr, Co, Fe, Ni, Pt, Au, Ir, Rh, Zr, Ti, Be, Al, Cu, Ag, U, Th, and Re. Strongly colored flames are: V, red; Cb, yellow; Pd, green; W, blue; Cr, blue-violet; and Fe, violet. Photographs show that the spectra are metal arc lines of unusual intensity distribution. The metal atoms are sputtered off by the discharge and excited by some form of active nitrogen (A.N.). The spectra are identical using He or Ne and show minor differences using Xe, Kr, or A. Using Xe the flame is relatively weak. Using He, Ne, A, or Kr some yellow afterglow (Y.A.) is produced along with the flame but not with Xe. Xenon (3 cm) added to 30-cm A+1-cm N_2 with a weak discharge greatly weakens Y.A. and causes afterfluorescence of the Nonex wall, absent with the other rare gases, and indicating Xe molecular continuous radiation at 1700–1800 resulting from the excitation of Xe by A.N. Results indicate probably three carriers of energy: one, possibly $N_2(a'\pi_g)$ following Nicholls[2] excites $N_2(B^3\pi_g)$ i.e., Y.A. and also Xe (*s* states); another, possibly another N_2 singlet metastable,[3] excites Hg and Xe but not Y.A.; a third, probably mainly $N(^2P,3.57\,V)$, principally excites the metallic flames.

[1] C. Kenty, Phys. Rev. **89**, 339 (1953).
[2] R. W. Nicholls, J. Chem. Phys. **20**, 1040 (1952), and private communication.

D1. Photodetachment of the Hydrogen Negative Ion. LEWIS M. BRANSCOMB, *U. S. National Bureau of Standards,* AND WADE L. FITE, *University of Pennsylvania.*—The photodetachment of one electron from the hydrogen atomic negative ion H^- has been demonstrated experimentally and the cross section measured in a crossed beam experiment using an incandescent light source. This process was proposed in 1939 by Wildt to explain the gray-body character of solar radiation in the near infrared, and the proposal received strong support from solar observations. A beam of 200-volt H^- ions is generated in a glow discharge source and, after mass separation in a crossed field velocity selector, is passed through a very intense light beam in a region of high vacuum. The light beam is chopped at 450 cps, producing about 10^{-13} amp of alternating electron current, which is extracted from the ion beam by weak electric and magnetic fields. Using the measured intensity and spectral distribution of the light, the measured velocity of the ions, and the theoretical cross section, the theoretically expected ratio of detached electron current to ion current is calculated and compared with experiment. Preliminary measurements confirm the theoretical result of S. Chandrasekhar and his colleagues, who reported a cross section whose maximum value is 4.52×10^{-17} cm^2 at 8275A. The use of yellow and red filters also confirms the approximate spectral distribution of the theoretical cross section. The photodetachment of negative ions from an oxygen discharge has also been observed and is being investigated.

D2. Photoionization in Atmospheric Gases.* N. WAINFAN, W. C. WALKER, AND G. L. WEISSLER, *University of Southern California.*—Using methods described elsewhere[1] by the author[s],[2] the ionization limits, absorption coefficients, and the number of ion pairs appearing per 100 absorbed photons were determined for N_2 and O_2 in the wavelength range from 473A to 1100A. The first ionization limit of O_2 was found to be 12.1 ± 0.1 volts and that of N_2 to be 15.6 ± 0.1 volts. These results are in good agreement with those obtained by electron impact methods.[3] The absorption coefficients obtained were substantially the same as those reported previously.[4] In O_2, for wavelengths between 1019A and 700A, a region of strong absorption bands, the fraction of absorbed photons that yielded ion pairs varied rapidly. At wavelengths shorter than 700A the absorption mechanism was found to be entirely due to photoionization. For N_2 the fraction of absorbed photons producing photoionization rose rapidly from the ionization limit and for wavelengths shorter than 750A the entire absorption process appeared to be photoionization. Additional results for H_2O vapor, CO_2, and CH_4 will also be presented.

* The aid of the U. S. Office of Naval Research is gratefully acknowledged.
[1] Wainfan, Walker, and Weissler, J. Appl. Phys. (To be published).
[2] H. D. Hagstrum, Revs. Modern Phys. **23**, 185 (1951).
[3] G. L. Weissler and Po Lee, J. Opt. Soc. Am. **42**, 200 (1952); Weissler, Lee, and Mohr, J. Opt. Soc. Am. **42**, 82 (1952).

D3. Photoelectric Yields of some Metals in the Vacuum Ultraviolet.* W. C. WALKER, N. WAINFAN, AND G. L. WEISSLER, *University of Southern California.*—The absolute quantum yields of the noble metals Ag and Au and the transition metals Mo, Ni, Pd, Pt, Ta, and W in the wavelength region from 991A to 473A were measured for both untreated and heat-treated surfaces.[1] The photoyields of all the metals investigated were found to be smaller for heat-treated samples than those for untreated ones, but in no instance was the decrease found to be greater than a factor of three. All of the transition metals with the exception of Pd and Pt gave evidence of a spectral maximum in the wavelength region covered. The yields of a heated sample of Ni were the largest of any metal studied with values ranging from 0.09 electron per photon at 991A to 0.15 at the maximum which occurred at 640A. Platinum and palladium, which gave similar results, were found to have the smallest photoyields exhibiting a constant value of about 0.035 electron per photon over the entire wavelength region. More extensive work is now in progress on these and other metals.

* The aid of the Office of Ordnance Research, U. S. Army, is gratefully acknowledged.
[1] Wainfan, Walker, and Weissler, J. of Appl. Phys. **24**, 1318 (1953).

D4. Ionization Probability Curves near Threshold for Hg, Cd, and Zn. W. M. HICKAM, *Westinghouse Research Laboratories.*—Using the retarding potential difference method[1] with the 90° sectored type mass spectrometer, the ionization probability curves for Hg, Cd, and Zn have been obtained over the energy range from threshold to some four electron volts above. The Hg curve is in substantial agreement with that of Nottingham[2] and shows a hump at approximately 0.4 ev above threshold. A linear rise is observed in the Cd curve for some 3 ev at which point the slope increases followed by a hump at approximately 3.5 ev. The zinc curve rises linearly for approximately 1.3 ev and displays a plateau in the neighborhood of 2 ev above threshold. An attempt is made to correlate the observed structure with autoionization of atomic states identified by Beutler,[3] and other unidentified states. These states arise from excitation of a single inner electron [e.g., $3d^{10}4s^2 \rightarrow 3d^9 4s^2(^2D_{5/2})4p$ in the case of Zn]. Autoionization from the identified levels seems insufficient to explain the obtained results.

[1] Fox, Hickam, and Kjeldaas, Phys. Rev. **69**, 555 (1953).
[2] W. B. Nottingham, Phys. Rev. **55**, 203 (1939).
[3] H. Beutler, Z. Physik **86**, 710 (1933).

D5. Electron Ejection by Slow Positive Ions Incident on Flashed and Gas-Covered Metallic Surfaces. JAMES H. PARKER, JR., *University of California at Berkeley.*—A direct measurement of the ejected electron yield (γ_i) for A^+ incident on flashed and H_2-, N_2-, and O_2-treated Ta and Pt and for the singly charged hydrogen, nitrogen, and oxygen ions incident on Ta and Pt after treatment with the respective parent gas has been made for the kinetic energy range of 5 to 150 ev. The gas treatment for Pt consisted of an exposure to the molecular gas at a pressure of a few mm of Hg while the treatment for Ta consisted of an exposure plus a glow discharge in which the Ta surface served as the cathode. In general, gas treatment of Ta and Pt was found to effect large decreases in γ_i for A^+ ions, with the effect increasing with decreasing ion energy. For both Ta and Pt the O_2 treatment was found to be the most effective in reducing γ_i while the H_2 treatment was found to be the least effective. γ_i for nitrogen ions on N_2-treated Ta and Pt showed a unique behavior at low ion energy in that it was found to increase with decreasing ion energy. This behavior was not observed for the other ions in this study.

D6. Reflection of Ions as Ions or as Metastable Atoms at a Metal Surface. HOMER D. HAGSTRUM, *Bell Telephone Laboratories.*—In a small fraction of the encounters of a noble gas ion with a metal surface the ion does not decay completely to the ground state of the atom but is reflected either as an ion or as a metastable atom. Measurements have been made which yield values of the reflection coefficients for normal incidence of ions to ions, R_{ii}, and of ions to metastable atoms, R_{im}. By the use of a retarding field between target and collector and a magnetic field in the vicinity of the target it has been possible to determine the magnitude of reflected ion current, the tertiary electron currents ejected from the collector by reflected ions and metastable atoms, and finally the coefficients R_{ii} and R_{im}. R_{ii} for He^+ on W is found to remain approximately constant at 0.015, independent of ion energy, whereas R_{im} rises steadily from zero to near 0.10 in the ion energy range 50 to 1000 ev. Both reflection coefficients are smaller the heavier the incident ion. For an ion-target combination for which resonance neutralization is impossible the present results appear to require the possibility of ions becoming metastable atoms very close to the metal surface. It can then be shown that the observed rise in R_{im} with ion energy is to be expected. The approximate constancy of R_{ii} depends upon what appears to be a reasonable balance between loss and gain of ions which do not partake in the Auger processes in the vicinity of the metal surface. If resonance neutralization is possible, detailed analysis of the results becomes very difficult.

D7. An Improved Optical Absorption Technique for the Study of Metastable Atoms. A. V. PHELPS AND J. L. PACK, *Westinghouse Research Laboratories.*—An improved optical absorption technique has been developed for the study of the decay of the metastable atom density following a pulsed discharge. Light from a capillary source is passed through the discharge tube. The intensity of one of the lines which is absorbed by the metastable atoms is measured using an interference filter and a gated photomultiplier. The photomultiplier gate occurs at twice the discharge pulse frequency so that alternate pulses of the photomultiplier output are reduced by absorption. The component of the photomultiplier output at the discharge frequency is proportional to the absorption and can be measured with a narrow-band amplifier and synchronous detector. Since the time resolution of the system is determined by the width of the photomultiplier gate, the response of the synchronous detector can be made slow enough to average the absorption signal over many decay periods. Fluctuations in the number of electrons leaving the cathode of the photomultiplier limit the useful sensitivity of the present system to approximately 0.02-percent absorption. Using this apparatus, the cross section for the conversion of helium singlet metastables into triplet metastables as a result of collisions with thermal electrons is found to be approximately 3×10^{-14} cm^2.

D8. Time Constants of Self-Sustained Townsend Discharges. W. S. HUXFORD, *Northwestern University.*—Comparison of measured ionization coefficients of argon in parallel plate phototubes with parameters of self-sustained discharges in the same tube confirms the hypothesis of volume ionization of metastables. Calculations based on space-charge considerations do not account for the negative potential characteristics. Variation of time constants with current were obtained by applying a small modulating voltage to the dc discharge and measuring the frequency response with an oscilloscope. Tubes having cesium-silver and cesium-antimony cathodes were used filled with argon and with helium at pressures from 0.25 to 3.0 mm Hg. Time constants in argon have values from 0.001 to 0.01 sec for currents in the range from 1 to 20 microamperes and vary inversely with current density. Space-charge effects set in at currents above a critical value causing a sudden change in current density and a rapid decrease in the observed time constants. When helium-filled tubes are irradiated with the 2.058μ helium line from an intense arc a current decrease occurs. Time constants obtained by chopping or amplitude modulating this radiation agree with those obtained by means of electrical modulation.

E1. Statistical Mechanics of Cathode Sputtering. DON E. HARRISON, JR.,* *Yale University.*—The author has developed a statistical mechanical treatment of the sputtering process. Most of the problems inherent in such an approach have been overcome or bypassed, so that the remaining complications are chiefly mathematical. The process may be described in terms of four interacting distribution functions which are assumed to satisfy the Boltzmann transport equation. Using mathematical methods developed in the study of neutron diffusion, it is possible to obtain exact solutions of the two fundamental integro-differential equations when the masses of the ions and metallic atoms are equal. The theory is developed assuming that the lattice atoms are at rest and that the particles interact like elastic hard spheres. Comparison of the theory with the available experimental data indicates that the curves are of the same general form. The sputtering

threshold, used as a fitting parameter, has a reasonable value. Work is in progress to obtain solutions where the masses are unequal. The general form of these results can be predicted by comparison with similar problems studied in neutron diffusion theory.

* Now at the University of Louisville.

E2. Sputtering of Alkali Metals by Inert Gas Ions of Low Energy. R. C. BRADLEY, *University of California at Berkeley.*—Direct measurements of sputtering have been made using sodium and potassium targets bombarded by the ions He^+, Ne^+, A^+, and Xe^+; the sputtered atoms being counted by a surface ionization detector. The energy range covered was 0–1800 ev. Secondary electron coefficients were measured simultaneously. Over most of the energy range covered the measured sputtering coefficient (number of atoms reaching the detector per ion incident on the target) was linear in $\ln E$ for He^+ and Ne^+ and in $\sqrt{E}$ for A^+ and Xe^+, where E is the ion energy. At energies less than about 150 volts the coefficient appeared to depend only on the amount of kinetic energy which could on the average be transferred to a single surface atom in a direct two-body collision. Thus, at low energies Ne^+ produced the most sputtering from a sodium target and A^+ the most from a potassium target. At high energies the sputtering rate was in the same order as (but not proportional to) the mass of the ion. Absolute sputtering coefficients (total number of sputtered atoms per incident ion) could not be measured directly but were estimated from the geometry. The effect of surface contamination was also studied.

E3. Sputtering by Ion Bombardment—A Momentum Transfer Problem. GOTTFRIED K. WEHNER, *Wright Air Development Center.*—By studying the deposits from a sputtered metal strip immersed in a plasma of high density and low gas pressure, it can be shown that sputtering under oblique-angle ion bombardment starts at lower ion energies than with perpendicularly incident ions; and momentum is transferred from obliquely incident ions to the sputtered atoms. Both results are considered to be a strong argument against the evaporation theory. Every gas-metal combination exhibits a characteristic ion threshold energy (function of angle of incidence) for starting sputtering. Threshold energies V_0 for 23 metals under perpendicular mercury ion bombardment were determined and found to range from 35 volts for silver to 165 volts for hafnium and 230 volts for boron. V_0 follows a simple law: The momentum transferred at V_0 to a metal atom (collision between elastic spheres) multiplied with the velocity of sound in the metal is proportional (factor 5) to the heat of sublimation.

E4. X-Ray Absorption Processes in Proportional Counter Gases. C. S. DUFFENDACK AND C. F. HENDER, *Philips Laboratories, Inc.*—When a medium x-ray photon is absorbed by a gas atom, a photoelectron is emitted. Subsequently, the absorbing atom emits a characteristic fluorescent x-ray photon or an Auger electron. If the fluorescent photon escapes from the counter gas, only a fraction of the incident energy is utilized in creating ion pairs. This process gives rise to the "escape" peak in the pulse-height distribution of a proportional counter. The "main" peak is formed by complete utilization of the incident energy. The energy gap between "main" and "escape" peak is equal to the emission energy of the absorbing gas atom (characteristic fluorescence). The positions of the K and L "escape" peaks in the pulse-height distribution for argon, krypton, and xenon are discussed. The ratio of the number of counts in the "escape" peak to the total number is a measure of the fluorescent yield of the gas atom. The "escape" peak should exhibit a fine structure, due to the fluorescence of the absorbing gas atom in the K or L series lines. Indications are that the "escape" peak, though long neglected, is of greater interest than the "main" peak in many applications of proportional counters.

E5. Proportional Counter "Escape" Peak Resolution and Fine Structure. S. FINE, *Philips Laboratories, Inc.*—An extension of some unpublished work of O. R. Frisch indicates that the half-widths of the peaks in pulse-height distributions of proportional counters decrease with decreasing pulse height. This is evident from the results obtained with some counters developed for medium x-ray detection. Pulse-height distributions indicate that the energy gaps between "main" and "escape" peaks are an intrinsic characteristic of the absorbing atom and that more precise information concerning the fluorescence yield may be obtained with higher atomic number of gases where the escape peaks are more resolved. With the optimum combination of absorbing gas and incident energy, values of the fluorescence yields of the $K\alpha$, $K\beta$ emission have been obtained using the escape peak. Work with radiations simulating the characteristic fluorescence of two contiguous rare earths shows that separation and identification may be accomplished only in the "escape" peak region.

F1. High-Pressure Arc Anode Phenomena. J. D. COBINE AND E. E. BURGER, *General Electric Research Laboratory.*—A study has been made of the more important processes occurring at the anode of the high-pressure, high-current arc. In these arcs, the anode current density may be from 10 000 to 50 000 amp/cm². The input power density at the anode spot may be in the range 60 000 to 500 000 watts/cm². It is shown that under these conditions evaporation is the most important process in the energy balance at the anode spot. Evaporation probably maintains a substantially constant temperature at the spot surface. The heat flow into the metal from the active area appears to be of the order of 10 percent of the anode energy input in one-half cycle (60 cps). The amount of energy radiated from the spot is quite small. Experimental data on electrode erosion permit a rather good estimate to be made of the anode spot temperature. For example, copper with an erosion rate of 86.5 grams/cm²/sec has a probable spot temperature of 2650°K. Other probable spot temperatures are approximately 2300°K for Ag, 3300°K for Al, 3650°K for Ni, 3600°K for Fe, and 4750°K for Ti.

F2. Retrograde Motion of Cathode Spot in Transverse Magnetic Fields. ROBERT ST. JOHN AND J. G. WINANS, *University of Wisconsin.*—Experiments on motion of cathode spot in mercury arcs in transverse magnetic fields have given results consistent with previous observations.[1,2] With constant arc current and no foreign gas the retrograde velocity increases smoothly up to about 11 000 oersteds after which it increases very rapidly to nearly double its previous velocity as observed by Smith.[1] The field strength needed for the rapid increase in velocity is lowered by increasing the arc current. The spectrum of the cathode spot showed strong atomic lines and a continuum which was not like that from Hg_2 molecules. At low magnetic field strengths (H L 1000 oersteds) the spectrum of the negative glow showed only Hg I lines but at high magnetic field strengths (about 11 000 oersteds) both Hg I and Hg II lines appeared. Smith[1] observed also Hg III lines. The potential drop across the arc changed from about 12 to about 15 volts with change in field strength from 1000 to 11 000 oersteds. The addition of helium eliminated all of the Hg II lines and made the cathode spot more diffuse.

[1] C. G. Smith, Phys. Rev. **83**, 194 (1951); **84**, 1075 (1951).
[2] C. J. Gallagher, "The Retrograde Motion of the Arc Cathode Spot." Special publication by General Electric Company.

F3. Orderly Subdivision of a Mercury Arc Cathode Spot. CHARLES G. SMITH, *Raytheon Manufacturing Company.*—

Arc currents above approximately two amperes split the cathode spot. Division is here studied in rapidly moving "anchored arcs." A polished molybdenum cylinder, 1.2 cm diameter, axis vertical, projects ½ cm above a mercury pool of an arc tube. Above and larger than the molybdenum stump is a disk-shaped anode having a radial slot above which is an ion collector. A vertical magnetic field of 5000 oersteds races the arc spot 120 meters per second in the retrograde direction around the molybdenum cylinder to which the arc is anchored. Passage of arc under the anode slot shows a signal on the ion collector. The oscillograph pattern shows a steep front followed by a tapering off portion. Below two amperes there is a smooth pattern. Increased current causes a sharp nick in the steep wave front. More current deepens and widens the nick. "Cathode spot" becomes a close double. More current makes more spots. Splitting is a reproducible function of current. It shows that a part of the spot influences a remote part.

F4. Motion of the Arc Cathode Spot in a Magnetic Field. C. G. MILLER AND N. L. SANDERS,* *University of California at Santa Barbara.*—The motion of the arc spot on liquid metal cathodes subjected to a transverse magnetic field has been investigated using various ambient gases. A number of workers[1–4] have observed that the arc spot moves in a retrograde direction (opposite to that of the electromagnetic force) in a restricted range of ambient temperatures and pressures when in a magnetic field. The present work indicates that there may be two modes of operation of the arc, and that the arc when traveling in the retrograde direction depends on gas or vapor ionization near the cathode. The two modes of operation may occur simultaneously; the arc spots of each mode when moving may pass through each other without losing their identity. The p.d. across the arc differs for the two modes; when the modes coexist, the larger p.d. governs.

* Now at University of Southern California, Los Angeles, California.
[1] N. Minorski, J. de phys. radium **9**, 127 (1928).
[2] C. G. Smith, Phys. Rev. **62**, 48 (1942); **69**, 96 (1946); **73**, 543 (1948).
[3] C. J. Gallagher, J. Appl. Phys. **21**, 768 (1950).
[4] G. J. Himler and G. I. Cohn, Elec. Eng. **67**, 1148 (1948).

F5. An Equation for the V-I Curve of the High Current Argon Arc. T. B. JONES, *The Johns Hopkins University,* AND J. W. DZIMIANSKI, *Allis-Chalmers Manufacturing Company.*—A study was made of the fundamental properties of the high current dc arc in argon at atmospheric pressure as the electrode materials were varied. Rod electrodes of tungsten, tantalum, molybdenum, titanium, iron, and copper were used over current ranges of 25 to 100 amperes for precise measurements and 25 to 200 amperes for free burning measurements. These arc studies made it possible to develop a new empirical equation which depicts the electrical characteristics of the arcs investigated over a wide range of currents including the positive slope region of the V-I curves. With this equation as a basis the distribution of power and voltage in the arc was calculated. The melting rate data seemed to support the conclusion that in arcs of this type over the current range studied the anode drop is zero or extremely small whereas the cathode drop may be affected materially by deposition of anode metal on the cathode surface. For each of the metals tested the appropriate constants were calculated for insertion in the empirical equation. These constants showed that variation of the electrode materials had a significant effect on the electrical characteristics of the arc but this effect was not nearly so great as that caused by different inert gases.

Author Index to Papers Presented at the Conference on Gaseous Electronics in Washington, D. C.

Aden, A. L.—C3
Amin, M. R.—B6
Anderson, J. M.—A3, A4
Bandel, H. W.—B4
Biondi, M. A.—C4
Bradley, R. C.—E2
Branscomb, L. M.—D1
Brown, S. C.—A7
Brown, W. B.—C5
Burch, D. S.—B8
Burger, E. E.—F1
Cobine, J. D.—F1
Creedon, J. E.—A5
Duffendack, C. S.—E4
Dzimianski, J. W.—F5
Faire, A. C.—C3
Fine, S.—E5
Fisher, L. H.—B2, B3
Fite, W. L.—D1
Fundingsland, O. T.—C3
Geballe, R.—B8
Ghosh, S. N.—C1
Goldstein, L.—A3, A4
Gould, L.—A6
Graham, W. J.—A1
Hagstrum, H. D.—D6
Harrison, D. E., Jr.—E1
Hendee, C. F.—C5, E4
Hickam, W. M.—D4
Huxford, W. S.—D8
Irick, R. C.—B8
Jones, T. B.—F5
Kenty, C.—C6
Lessin, I.—B3
Liao, T. W.—B7
Loeb, L. B.—B5
Looney, D. H.—A7
Mayer, A.—B2
Medicus, G.—B1
Miller, C. G.—F4
Pack, J. L.—D7
Parker, J. H., Jr.—D5
Phelps, A. V.—D7
Potter, R. F.—C2
Ruhlig, A. J.—A1
Sanders, N. L.—F4
Skolnik, M. I.—A2
Smith, C. G.—F3
St. John, R.—F2
Udelson, B. J.—A5
Wainfan, N.—D2, D3
Walker, W. C.—D2, D3
Wehner, G. K.—E3
Weissler, G. L.—D2, D3
Winans, J. G.—F2